



UNIVERSITAT POLITÈCNICA
DE CATALUNYA
BARCELONATECH

Active flow control optimization on Selig Donovan 7003 airfoil

Navid Monshi Tousi

ADVERTIMENT La consulta d'aquesta tesi queda condicionada a l'acceptació de les següents condicions d'ús: La difusió d'aquesta tesi per mitjà del repositori institucional UPCommons (<http://upcommons.upc.edu/tesis>) i el repositori cooperatiu TDX (<http://www.tdx.cat/>) ha estat autoritzada pels titulars dels drets de propietat intel·lectual **únicament per a usos privats** emmarcats en activitats d'investigació i docència. No s'autoritza la seva reproducció amb finalitats de lucre ni la seva difusió i posada a disposició des d'un lloc aliè al servei UPCommons o TDX. No s'autoritza la presentació del seu contingut en una finestra o marc aliè a UPCommons (*framing*). Aquesta reserva de drets afecta tant al resum de presentació de la tesi com als seus continguts. En la utilització o cita de parts de la tesi és obligat indicar el nom de la persona autora.

ADVERTENCIA La consulta de esta tesis queda condicionada a la aceptación de las siguientes condiciones de uso: La difusión de esta tesis por medio del repositorio institucional UPCommons (<http://upcommons.upc.edu/tesis>) y el repositorio cooperativo TDR (<http://www.tdx.cat/?locale-attribute=es>) ha sido autorizada por los titulares de los derechos de propiedad intelectual **únicamente para usos privados enmarcados** en actividades de investigación y docencia. No se autoriza su reproducción con finalidades de lucro ni su difusión y puesta a disposición desde un sitio ajeno al servicio UPCommons No se autoriza la presentación de su contenido en una ventana o marco ajeno a UPCommons (*framing*). Esta reserva de derechos afecta tanto al resumen de presentación de la tesis como a sus contenidos. En la utilización o cita de partes de la tesis es obligado indicar el nombre de la persona autora.

WARNING On having consulted this thesis you're accepting the following use conditions: Spreading this thesis by the institutional repository UPCommons (<http://upcommons.upc.edu/tesis>) and the cooperative repository TDX (<http://www.tdx.cat/?locale-attribute=en>) has been authorized by the titular of the intellectual property rights **only for private uses** placed in investigation and teaching activities. Reproduction with lucrative aims is not authorized neither its spreading nor availability from a site foreign to the UPCommons service. Introducing its content in a window or frame foreign to the UPCommons service is not authorized (*framing*). These rights affect to the presentation summary of the thesis as well as to its contents. In the using or citation of parts of the thesis it's obliged to indicate the name of the author.

Active Flow Control Optimization on Selig Donovan 7003 Airfoil



Navid Monshi Tousi

Fluid Mechanics Department

Supervisors

Dr. Josep Maria Bergadà Granyó

Dr. Fernando Pablo Mellibovsky Elstein

Universitat Politècnica de Catalunya

A thesis submitted for the degree of

Doctor of Philosophy

March 2023

Acknowledgements

I would like to extend my deepest gratitude to the individuals who have played a crucial role in the successful completion of my Ph.D. thesis. Their unwavering support, guidance, and encouragement have been invaluable, and I am deeply grateful for their contributions.

First and foremost, I would like to give my deepest appreciation to my esteemed supervisors, Prof. Josep M. Bergadà and Prof. Fernando Mellibovsky, for their unparalleled expertise, guidance, and support that have been instrumental in shaping my research and ensuring its success. Their faith in my abilities and constant encouragement inspired me to pursue excellence and provided the foundation for my academic growth.

A special thanks to my friend Reda El Mansy for his unwavering support and friendship during the last five years. The days we spent together working in the lab were the best. Without his companionship, this journey would have been far more challenging.

I am also thankful to Mr. Marti Coma for his collaboration on the studies we carried out together. Also, I would like to thank Lidia Caros and Christian Jane for their great assistance during the first stages of the work.

I would also like to extend my thanks to Mr. Toni Castillo. His valuable technical support with computers and clusters throughout the Ph.D. was beyond helpful.

My heartfelt thanks go to my parents, Mohammad and Hayedeh, and my brother, Omid, for their unwavering love, guidance, and spiritual

support throughout my academic journey. Their constant encouragement provided me with the strength and determination to reach my objectives. I am forever grateful for their presence in my life.

Finally, I would like to thank the Barcelona Supercomputing Center for providing the advanced computer resources necessary to conduct my research.

تقدیم به هایده و محمد

Contents

0.1	Introduction	1
1	Active Flow Control Optimisation on SD7003 Airfoil at Pre and Post-stall Angles of Attack using Synthetic Jets	7
1.1	Abstract	7
1.2	Introduction	8
1.3	Numerical Method	13
1.3.1	Equations and flow solver	13
1.3.2	Domain and Boundary Conditions	14
1.3.3	Non-dimensional parameters	15
1.3.4	Mesh sensitivity study	17
1.3.5	Baseline computations and numerical validation	19
1.4	Optimisation of AFC parameters	22
1.4.1	Optimisation method	24
1.4.2	Objective functions and Design variables definitions	27
1.5	Results	31
1.5.1	Pre-stall angles of attack of $4^\circ, 6^\circ$ and 8°	31
1.5.2	Post-stall angle of attack of 14°	40
1.6	Discussion	46
1.6.1	Boundary layer thickness for different AoA and actuation cases	46
1.6.2	Further investigation on AoA of 14°	47
1.6.3	Energy assessment	49
1.6.4	Flow structures	51
1.7	Conclusions	57
1.8	appendix	58

1.8.1	Full Pareto Front results, at all AoA	58
1.9	References	62
2	Large Eddy Simulation of Optimal Synthetic Jet Actuation on a SD7003 airfoil in post-stall conditions	70
2.1	Abstract	70
2.2	Introduction	71
2.3	Governing equations and numerical modeling	76
2.4	Domain, boundary conditions and mesh validation	78
2.5	Results	84
2.5.1	RANS-SA vs LES comparison of optimally actuated cases	89
2.5.2	Baseline vs optimally actuated case comparison.	94
2.6	Conclusions	98
2.7	References	100
3	Spalart-Allmaras turbulence parameter tuning for active flow control applications	107
3.1	Abstract	107
3.2	Introduction	108
3.3	Governing equations	111
3.4	Domain, boundary conditions and mesh	113
3.5	Results	115
3.6	Conclusions	121
3.7	References	122
4	A New Hybrid Optimization Method, application to a Single Objective Active Flow Control Test Case	128
4.1	Abstract	128
4.2	Introduction	129
4.3	Hybrid Method Description	131
4.4	Numerical Results	137
4.4.1	Test Case Description	138
4.4.2	Results from the Optimizations Methods	140
4.4.3	Results Based on the Fluid Flow Performance	143

4.5	Discussion	145
4.6	References	146
5	Discharge coefficients of a heavy suspension nozzle	150
5.1	Abstract	150
5.2	Introduction	151
5.3	Experimental test rig	155
5.4	Mathematical equations and analytical process followed to determine the physical variables.	159
5.5	Dynamic computational fluid dynamic simulations	162
5.6	Results and discussion	164
5.7	Conclusions	178
5.8	References	178
6	Appendix	183
6.1	Published Journal Papers	183
6.2	Conference Papers	259

List of Figures

1.1	(a) 2D Computational domain and (b) synthetic jet geometrical design parameters	15
1.2	(a) Overall mesh view, (b) leading edge's and (c) trailing edge's zoomed views of the mesh	17
1.3	Distributions of (a) pressure coefficient and (b) skin friction coefficient, for four meshes at $\alpha = 8^\circ$	19
1.4	(a) Lift and (b) drag coefficients as well as (c) aerodynamic efficiency versus the angle of attack and their comparison with some of the numerical and experimental results. Exp 89 [38], Exp 95 [39], ILES [40], LES [32], the standard k- ω SST and the k- ω SST LR, [43, 44] .	20
1.5	Distributions of pressure (left column) and skin friction coefficients on the upper surface (right column) for the baseline cases at all angles of attack and their comparison with previous available results. Figures (a) and (b), corresponds to AoA of 4° , figures (c) and (d) characterises the results at 6° , figures (e) and (f) are defining the information at 8° and the information for AoA of 14° is found in figure (g) and (h).	21
1.6	Mesh view nearby the jet, automatically generated.	28
1.7	Evolution of the objective functions as the number of simulated cases increase (a and c). Pareto Front history at several generations (b and d). AoA of 8° is represented in figures (a and b). Figures (c and d) characterise the results at AoA 14°	29

1.8	Aerodynamic efficiency η versus non-dimensional frequency F^+ , momentum coefficient C_μ , jet angle θ° , jet position x/C and jet width h/C for all the CFD cases at AoA of 4° , 6° and 8° are presented in left to right columns respectively. The horizontal dashed line represents the baseline case efficiency for each AoA.	32
1.9	Pareto Front at angles of attack of (a) 4° , (b) 6° and (c) 8° . The blue dots represent the efficiency versus lift coefficient for the baseline cases at different AoA.	34
1.10	Distributions of pressure coefficient (C_p) and skin friction coefficient (C_f) for the baseline (black solid lines), maximum efficiency (red dashed lines) and maximum lift (blue dotted lines) cases at three pre-stall AoA. (a), (b) AoA 4° ; (c), (d) AoA 6° ; (e), (f) AoA 8° . . .	37
1.11	Streamlines of the temporal average velocity field and contours of turbulence viscosity at the three pre-stall AoA. (a) 4° , (b) 6° and (c) 8° . The baseline, maximum lift and maximum efficiency cases are introduced as the top, central and bottom panel in each sub-figure, respectively.	38
1.12	aerodynamic efficiency versus (a) non-dimensional frequency, (b) momentum coefficient, (c) jet angle, (d) jet position, (e) jet width and (f) lift coefficient at $\alpha = 14^\circ$. The horizontal dashed line and the blue dot represent the baseline case efficiency.	42
1.13	Streamlines of the temporal average velocity field and contours of turbulence viscosity at the post-stall AoA. of 14° . The baseline, maximum lift and maximum efficiency cases are introduced as the top, central and bottom panel, respectively.	43
1.14	Distributions of (a) pressure coefficient and (b) skin friction coefficient for the baseline (black solid lines), maximum efficiency (red dashed lines) and maximum lift (blue dotted lines) cases at 14° . . .	45

1.15	Mean streamwise velocity profiles at several streamwise locations, (a) from $x/C=0.1$ to $x/C=0.5$ and (b) from $x/C=0.6$ to $x/C=1$, as a function of the normalised wall normal distance. Individual profiles are separated by horizontal offset of 2 with the corresponding zero lines located at 2, 4, 6, 8, 10. The black solid, red dashed and blue dotted lines represent the baseline, maximum efficiency and maximum lift cases, respectively.	46
1.16	Boundary layer thickness as a function of the chord length and for the four AoA studied cases; (a) 4° , (b) 6° , (c) 8° and (d) 14° . The black solid, red dashed and blue dotted lines represent the baseline, maximum efficiency and maximum lift cases, respectively.	47
1.17	Comparison of the two Pareto Fronts obtained at AoA 14° with the restricted and unrestricted momentum coefficient.	49
1.18	Instantaneous velocity streamlines at different phases of synthetic jet for the maximum efficiency case at AoA 6° with $F^+ = 9.2$, $C_\mu = 0.0194$, $\theta = 124^\circ$, $x/C = 0.25$ and $h/C = 0.019$	52
1.19	instantaneous velocity streamlines at different phases of synthetic jet for the maximum lift case at AoA 6° with $F^+ = 9.1$, $C_\mu = 0.0195$, $\theta = 15^\circ$, $x/C = 0.308$ and $h/C = 0.006$	54
1.20	Instantaneous velocity streamlines at different phases of synthetic jet for the maximum efficiency case at AoA 14° with $F^+ = 2.4$, $C_\mu = 0.0055$, $\theta = 18^\circ$, $x/C = 0.0097$ and $h/C = 0.005$. Restricted momentum coefficient.	55
1.21	Instantaneous velocity streamlines at different phases of synthetic jet for the maximum efficiency case at AoA 14° with $F^+ = 5.2$, $C_\mu = 0.039$, $\theta = 15^\circ$, $x/C = 0.02764$ and $h/C = 0.005$. Unrestricted momentum coefficient.	56
2.1	(a) Computational domain. (b) Synthetic jet parameters.	79
2.2	An overview of LES baseline mesh along with a zoomed view of its near-wall and wake regions	80
2.3	Resolved k_{res} and b) modeled k_{sgs} parts of the turbulent kinetic energy (TKE). c) Resolved-to-total TKE ratio $k_{\text{sgs}}/k_{\text{tot}}$	82

2.4	Spanwise- and time-averaged chord distributions of (a) pressure C_p and (b) skin friction C_f coefficients along the SD7003 surface(s) at $Re = 6 \times 10^4$ and $\alpha = 14^\circ$. Shown are the present LES (solid red), the LES case by Rodriguez et al. [2] (dashed green), ILES by Galbraith and Visbal [42] (dashed black) and SA RANS by Tousei et al. [1] (dashed blue).	83
2.5	Optimisation procedure and optimal cases in objective function space (C_l, η) space.	85
2.6	Results sensitivity to free-stream preturbulence levels as prescribed by $\tilde{\nu}/\nu$. (a) Average lift coefficient C_l . (b) Average drag coefficient C_d . Baseline (squares), maximum lift (up-pointing triangles) and maximum aerodynamic efficiency (down-pointing triangles) SJA setups are shown for both RANS-SA (blue) and LES (red) computations.	88
2.7	Optimal SJA vs baseline (a) Pressure C_p and (b) skin friction C_f coefficient distributions. Shown are the LES-baseline (dashed red), the LES- η^{\max} (solid red), RANS SA- $\eta^{\max}(\tilde{\nu})$ (solid blue) and sub-optimal actuated LES-act case by Rodriguez et al. [2] (dash-dotted green).	90
2.8	Spanwise-averaged $\langle u'v' \rangle$ component of the Reynolds stress tensor and time- and spanwise-averaged streamlines. (a) RANS-SA-baseline (top) and RANS-SA- $\eta^{\max}(\tilde{\nu})$ (bottom). (b) LES-baseline (top) and LES- η^{\max} (bottom).	91
2.9	Evolution of the upper-surface boundary layer along the airfoil. Time- and spanwise-averaged streamwise velocity profiles $\langle u(x, y, z; t) \rangle_{t,z}$ at streamwise coordinates (a) $x/C = 0.1$ through $x/C = 0.5$ and (b) $x/C = 0.6$ through $x/C = 1$, as a function of wall-normal distance. Shown are the baseline (dashed) and actuated (solid) cases, for both LES (red) and RANS-SA (blue) simulations. The actuated cases are LES- η^{\max} and SA- $\eta^{\max}(\tilde{\nu})$	92

2.10	Evolution of boundary layer characteristic properties along the upper surface of the airfoil for actuated cases LES- η^{\max} (red lines) and RANS-SA- $\eta^{\max}(\tilde{\nu})$ (blue). (a) Boundary layer (δ_τ , dotted), displacement (δ_1 , solid), and momentum (δ_2 dashed) thicknesses. (b) Shape factor H	94
2.11	Power Spectral Density (PSD) of the streamwise velocity signal as recorded from spanwise probe arrays P ₂ and P ₅ . (a) LES-baseline spanwise-averaged $\langle u'v' \rangle$ colourmap showing the location of the five probe-arrays. Three probes are placed along the shear layer, while the other two are in the very near wake. The PSD of the signals from probes P ₂ (x, y) = (0.098, 0.08) and P ₅ (x, y) = (1.1, 0.08) are represented for the (b) LES-baseline, (c) LES- C_l^{\max} and (d) LES- η^{\max} cases. Shown are the spectra for the signal read from P ₅ (black) and P ₂ (light gray), which has been further filtered (dark gray).	95
2.12	Instantaneous vortical structures visualised through iso-surfaces of the Q-criterion $Q = 30U_\infty^2/C^2$, coloured by streamwise velocity u . (a) LES-baseline. (b) LES- C_l^{\max} . (c) LES- η^{\max}	97
3.1	(a) Computational domain. (b) Synthetic jet parameters.	113
3.2	Mesh overview and zoomed views around the airfoil and leading edge	115
3.3	Results sensitivity to the jet preturbulence levels ($i_D j_D$, red) and its comparison with the results sensitivity analysis to the inlet preturbulence level ($i_D j_N$, blue) [2]. For the latter, the turbulence level obtained after the simulations at the jet ($\tilde{\nu}_j/\nu$) is shown by the yellow circles ($i_D j_N, (\tilde{\nu}_j/\nu)$). The horizontal back lines are the LES result [2]. (a) Average lift coefficient C_l . (b) Average drag coefficient C_d	116
3.4	Skin friction coefficient (a) and pressure coefficient (b) for <i>jet-optimal</i> (red), <i>jet-suboptimal</i> (grey), <i>inlet-optimal</i> (blue) and <i>LES</i> (black). The zoomed view shows the separation locations for different cases.	118

3.5	Spanwise-averaged $\langle u'v' \rangle$ component of the Reynolds stress tensor and time- and spanwise-averaged streamlines. (a) <i>LES</i> (top) and <i>inlet-optimal</i> (bottom). (b) <i>jet-suboptimal</i> (top) and <i>jet-optimal</i> (bottom).	119
3.6	Evolution of the upper-surface boundary layer along the airfoil. Time- and spanwise-averaged streamwise velocity profiles $\langle u(x, y, z; t) \rangle_{t,z}$ at streamwise coordinates $x/C = 0.1$ through $x/C = 1$, as a function of wall-normal distance. Shown are the <i>LES</i> (black), <i>inlet-optimal</i> (blue), <i>jet-optimal</i> (red) and <i>jet-suboptimal</i> (grey).	120
4.1	General algorithm of the tested Hybrid Method.	137
4.2	Full mesh of the domain (a) and Mesh nearby the Synthetic Jet actuator (b).	140
4.3	Averaged streamlines and pressure field of baseline case ($C_l = 0.80$).	140
4.4	Comparative of the convergence of the different optimization methods.	141
4.5	Averaged streamlines and pressure field of the Case 1 ($C_l = 0.81$).	144
4.6	Averaged streamlines and pressure field of case 2 ($C_l = 1.39$).	144
4.7	Averaged streamlines and pressure field of case 3 ($C_l = 1.49$).	145
4.8	Averaged streamlines and pressure field of case 4 ($C_l = 1.52$).	145
4.9	Averaged streamlines and pressure field of case 5 ($C_l = 1.54$).	145
5.1	Scheme of a typical heavy vehicle suspension.	151
5.2	(a) Test rig main view; (b) The two reservoirs with their pressure and temperature transducers; (c) schematic view of the reservoirs and the transducers localization.	157
5.3	(a) Reservoirs main mesh; (b) T shape nozzle section mesh; (c) T shape nozzle mesh general view.	164
5.4	Measured temporal pressure variation in both reservoirs, comparison between experimental and CFD results. (a) Flow from large to small reservoir. (b) Flow from small to large reservoir. Five different pressure decays are considered for each flow direction, see Table 5.1.	166

5.5	Numerical temperature evolution in the upstream and downstream reservoirs. (a) The flow goes from the large to the small reservoir. (b) The flow goes from the small to the large reservoir.	167
5.6	Experimentally based and numerical temperature decay in the upstream reservoir. (a) The flow goes from the large to the small reservoir. (b) The flow goes from the small to the large reservoir.	168
5.7	Temporal mass variation in each reservoir based on experimental data and for all pressures studied. (a) Flow from large to small reservoir. (b) Flow from small to large reservoir.	169
5.8	Mass flow between reservoirs, based on experimental data and for all pressures studied. (a) Flow from large to small reservoir. (b) Flow from small to large reservoir.	170
5.9	Temporal evolution of the maximum Mach number obtained at the nozzle separating the two reservoirs. Comparison between the numerical results and the experimentally based ones. (a) Flow from large to small reservoir. (b) Flow from small to large reservoir.	171
5.10	Nozzle discharge coefficient based on experimental data and for all pressures studied. (a) Flow from large to small reservoir. (b) Flow from small to large reservoir.	173
5.11	Velocity contours of all CFD cases studied and at three instants, 0.02, 0.5 and 1 second. The first and second rows, represent the fluid evolution when the fluid goes from the L-to-S reservoir, the respective upstream/downstream initial pressures are 0.4MPa-0.1MPa and 1.1MPa-0.1MPa. The third and fourth rows, characterise the two cases when the flow goes from S-to-L reservoir, being the upstream/downstream initial pressures of 0.6MPa-0.1MPa and 1.2MPa-0.4MPa, respectively.	176

List of Tables

1.1	Time-averaged LSB characteristics and airfoil aerodynamic coefficients for different meshes at $\alpha = 8^\circ$	18
1.2	Aerodynamic coefficients of actuated cases using present S-A model and their comparison with other turbulent models employed by other researchers. The Reynolds number is $Re=6 \times 10^4$	22
1.3	Parameters of the Genetic Algorithm.	27
1.4	AFC Design variables and their evaluation ranges for the different angles of attack.	29
1.5	Optimum five synthetic jet parameters associated with the maximum lift and maximum efficiency cases at pre-stall angles of attack of $4^\circ, 6^\circ$ and 8°	35
1.6	Optimum five synthetic jet parameters associated with the maximum lift and maximum efficiency cases at a post-stall angle of attack of 14° (small momentum coefficient range). 600 CFD cases .	41
1.7	Optimum five synthetic jet parameters associated with the maximum lift and maximum efficiency cases at a post-stall angle of attack of 14° (large momentum coefficient range). 400 CFD cases .	48
1.8	Power ratio obtained for the maximum efficiency case and at pre and post stall AoA.	51
1.1	All the Optimum cases of Pareto Front at 4°	58
1.2	All the Optimum cases of Pareto Front at 6°	59
1.3	All the Optimum cases of Pareto Front at 8°	60
1.4	All the Optimum cases of Pareto Front at 14° (restricted momentum coefficient)	61

1.5	All the Optimum cases of Pareto Front at 14° (unrestricted momentum coefficient)	62
2.1	Literature review of the aerodynamic performances of the SD7003 airfoil at $Re = 6 \times 10^4$ and $\alpha = 14^\circ$. L_x , L_y and L_z are the domain size in the streamwise, cross-stream and spanwise directions, respectively, in units of C . N_{xy} and N_z are the in-plane and spanwise resolutions, and T the time-span of the simulations in C/U_∞ units.	82
2.2	Baseline case, and optimal SJA actuation cases corresponding to maximum lift C_l^{\max} and maximum aerodynamic efficiency η^{\max} . The values of the five actuation parameters (jet frequency f_j , jet momentum coefficient C_μ , jet inclination angle with respect to the airfoil surface θ_j , jet streamwise location from leading edge x_j and jet slot width h_j) are listed alongside the resulting aerodynamic performances.	86
3.1	Aerodynamic coefficients for the <i>jet-optimal</i> , <i>jet-suboptimal</i> , <i>inlet-optimal</i> and <i>LES</i> cases	117
4.1	Parameters of the Genetic Algorithm.	136
4.2	Parameters of the conjugate gradient algorithm.	136
4.3	Active Flow Control design variables and their evaluation ranges.	139
4.4	Best lift coefficient of each optimization case, means and standard deviation.	143
4.5	Values of the lift coefficient and design variables of the five labeled cases.	143
5.1	Initial absolute pressure at both reservoirs for all different experimental tests performed and for all CFD simulations undertaken.	158
5.2	Constant values of the discharge coefficient equation for two different range of Reynolds number and different flow directions, large to small reservoirs and vice versa.	174

0.1 Introduction

The present thesis focuses on investigating the impact of Synthetic Jet Actuator (SJA) as an Active Flow Control (AFC) device on the Selig Donovan (SD) 7003 airfoil at Reynolds 60,000 and different angles of attack (AoA) using Computational Fluid Dynamics (CFD) simulations. By conducting an optimization study, the optimal SJA design parameters for each studied AoA (4, 6, 8, and 14) are determined. The optimization process is performed by coupling an in-house Genetic Algorithm (GA) optimizer with a CFD solver (OpenFOAM) and a mesh generator (GMSH) using python scripts, which allows for the automatic meshing, execution, and post-processing of the CFD simulations until finding the optimal at each AoA. For the CFD simulations, the Reynolds-Averaged Navier-Stokes (RANS) with Spalart-Allmaras (SA) turbulence model was employed since is computationally affordable in comparison to the Large Eddy Simulation (LES) and Direct Numerical Simulation (DNS). The effect of actuation was found to be more pronounced at a post-stall AoA of 14 degrees. Therefore to validate the accuracy of the RANS-SA results at this AoA, the LES was conducted on the optimal cases, maximum lift and maximum efficiency. A comprehensive comparison of the RANS-SA results with the LES results was performed. In addition, the sensitivity of the RANS-SA results to the inlet and jet turbulence levels are thoroughly analyzed using parametric studies.

This Thesis comprises five chapters. The first three serve as the backbone of the thesis with a focus on AFC and chapters four and five reflect our collaboration with other researchers in separate studies implementing CFD simulations. The following sections provide a brief overview of each chapter.

Chapter 1.

The first chapter provides details on the main core of the research. We explore the potential of SJA as an AFC device to influence the forces on the SD7003 airfoil at a Reynolds number of $Re = 6 \times 10^4$. Our goal is to find the optimum SJA parameters (jet's location, width, momentum coefficient, pulsating frequency and injection angle) at pre- and post-stall AoAs (4, 6, 8, and 14 degrees) for which the lift and

aerodynamic efficiency of the airfoil is maximum. To accomplish this, we coupled an in-house GA optimizer to a CFD solver and a mesh generator using python and run over 2200 2D CFD simulations until finding the optimals. The RANS with SA turbulence model was selected due to its computational affordability.

The results revealed that as the angle of attack increases, the benefits of AFC become more apparent, resulting in enhanced aerodynamic efficiency. The mechanism necessary for maximum efficiency was found to differ between pre-stall and post-stall angles of attack. At AoA of $\alpha = 14^\circ$, a 251% increase in aerodynamic efficiency was observed compared to the baseline case, while at AoA of $\alpha = 8^\circ$ a mere 39% increase in aerodynamic efficiency was achieved. The interaction between the incoming flow and the pulsating synthetic jet at different injection angles was also analyzed, providing valuable insight into the mechanism of AFC.

Chapter 2.

In this chapter, the focus is placed on the same Reynolds number and only the post-stall AoA of 14 degrees since the AFC is shown to be more effective on a fully separated boundary layer. To assess the reliability of our RANS-SA optimization, we conduct LES with a Wall-Adapting Local Eddy-viscosity (WALE) sub-grid scale (SGS) model for the two optimal cases, maximum lift and maximum efficiency.

Our findings indicate that our LES, which employs the optimal SJA parameters obtained through Genetic Algorithms and SA turbulence model, surpasses the suboptimal actuated LES reported by other researchers. Their SJA parameters were not determined through pre-optimization studies, underscoring the need for such studies before conducting costly LES in AFC research.

Furthermore, we compare RANS-SA against LES and find that while LES is more accurate, SA can still provide reasonably accurate lift and drag coefficient predictions when its turbulent parameter, $\tilde{\nu}$, is tuned at the domain inlet. We conducted a parametric study to obtain the optimal $\tilde{\nu}$ at the domain inlet, and results show that the average flow behavior of RNAS-SA is comparable with a good level of agreement to the LES if $\tilde{\nu}/\nu$ falls within the range of $[10^{-6}, 10^{-3}]$, being ν the fluid kinematic viscosity.

Finally, we examine the flow topology and wake dynamics of both the baseline and actuated cases to gain a better understanding of the aerodynamic improvement.

Chapter 3.

In the third chapter, we delve deeper into the sensitivity of the RANS-SA maximum efficiency actuated case's results to different $\tilde{\nu}$ boundary conditions applied at the inlet and, more specifically, at the jet. In the previous chapter, we conducted a parametric study solely at the inlet, while the Neumann BC remained fixed at the jet boundary in all cases. Here we aim to minimize the impact of inlet turbulence level by setting $\tilde{\nu}/\nu$ to 10^{-20} (a laminar upstream flow) and explore the variation of the results as a function of different $\tilde{\nu}/\nu$ at the jet. We analyze the results and compare them with the previous chapter's parametric study and LES.

The findings indicate that by setting the jet $\tilde{\nu}/\nu$ value two orders of magnitude higher than the one used at the inlet in the previous parametric study, the same force coefficients, C_l and C_d , can be obtained. This time, the optimal $\tilde{\nu}/\nu$ (to get results closer to the LES) value falls within a range of $[10^{-4}, 10^{-1}]$. This discovery suggests that utilizing zero-gradient (Neumann) at the jet may not have been the most effective approach. Essentially, we were indirectly introducing a value at the jet by manipulating the inlet BC and relying on the boundary layer instability to amplify the value at the jet boundary. To achieve a realistic baseline turbulence level in the boundary layer that promotes transition and facilitates the proper interaction between the jet and boundary layer, it is imperative to introduce turbulence through the jet rather than relying on the upstream flow. This approach yields a more natural and genuine outcome.

Chapter 4.

In this chapter, we present a hybrid optimization method that combines the strengths of Genetic Algorithms (GA) and gradient based methods. This method aims to overcome the limitations of both methods, such as slow convergence of GA and lack of robustness in gradient based methods. The performance of the Hybrid

Method is compared with a gradient based method and a GA, both used alone. The rate of convergence is used as a metric to compare the performance, and the robustness is evaluated by executing each method multiple times with different starting points and random seeds. The Hybrid Method is tested on an Active Flow Control (AFC) optimization problem on a 2D Selig–Donovan 7003 (SD7003) airfoil at Reynolds number 6×10^4 and a 14 degree angle of attack. Five design variables are considered, and the objective function is to minimize the lift coefficient ($-C_l$). The Hybrid Method is capable of working with multiple optimization algorithms, objective functions, and design variables per optimization algorithm.

Chapter 5.

In this chapter, we investigate the discharge coefficient of a T-shaped nozzle used in heavy vehicle suspensions. The study determines the discharge coefficients under compressible dynamic real flow conditions using experimental data with air as the working fluid.

The results show that the discharge coefficients depend on both the pressure gradient between chambers and the flow direction. CFD simulations were also carried out to understand the dynamic discharge coefficients, considering air as a compressible and ideal fluid. The comparison of the experimental results with the CFD results validated both the experimental procedure and numerical methodologies presented. The information gathered in this study will be used to mathematically characterize the dynamic performance of a real suspension.

Publications

Conferences

- Tousi NM, Bergadà Granyó JM, Rodríguez Pérez IM. "Active flow control on SD7003 airfoil using synthetic jets." In Fifth International conference on advances in mechanical engineering: ICAME 2019: Istanbul, Turkey: December 17-19, 2019: proceedings book 2019 (pp. 344-352).

- Coma, M.; Tousi, N.; Pons-Prats, J.; Bergadà, J.M.; Bugada, G., Performance of hybrid optimization methods applied to active flow control devices, AeroBest, July 2021.
- Monshi Tousi, Navid, Reda El Mansy, Fernando Mellibovsky Elstein, and Josep Maria Bergadà Granyó. "Optimization of synthetic jet actuation on a SD7003 airfoil in stall conditions." In 1st Spanish Fluid Mechanics Conference: Cádiz, Spain: June 19-22, 2022: book of abstracts. 2022.
https://sfmc22.uca.es/wp-content/uploads/2022/06/ABSTRACT_36.pdf
- El Mansy, Reda, Navid Monshi Tousi, Josep Maria Bergadà Granyó, and Fernando Mellibovsky Elstein. "Square cylinder downstream of two different-velocity streams." In 1st Spanish Fluid Mechanics Conference: Cádiz, Spain: June 19-22, 2022: book of abstracts. 2022.
https://sfmc22.uca.es/wp-content/uploads/2022/06/ABSTRACT_37.pdf

Published Journal Papers

- Tousi NM, Coma M, Bergadà JM, Pons-Prats J, Mellibovsky F, Bugada G. Active flow control optimisation on SD7003 airfoil at pre and post-stall angles of attack using synthetic jets. *Applied Mathematical Modelling*. 2021 Oct 1;98:435-64.
<https://doi.org/10.1016/j.apm.2021.05.016>
- Tousi NM, Bergadà JM, Mellibovsky F. Large Eddy Simulation of optimal Synthetic Jet Actuation on a SD7003 airfoil in post-stall conditions. *Aerospace Science and Technology*. 2022 Aug 1;127:107679.
<https://doi.org/10.1016/j.ast.2022.107679>
- Coma M, Tousi NM, Pons-Prats J, Bugada G, Bergada JM. A New Hybrid Optimization Method, Application to a Single Objective Active Flow Control Test Case. *Applied Sciences*. 2022 Apr 12;12(8):3894.
<https://doi.org/10.3390/app12083894>

- Rio-Cano C, Tousi NM, Bergada JM, Comas A. Discharge coefficients of a heavy suspension nozzle. Applied Sciences. 2021 Mar 15;11(6):2619. <https://doi.org/10.3390/app11062619>

Journal Papers In the Process of Submission

- Spalart-Allmaras turbulence parameter tuning for active flow control applications

Chapter 1

Active Flow Control Optimisation on SD7003 Airfoil at Pre and Post-stall Angles of Attack using Synthetic Jets

1.1 Abstract

The use of Active Flow Control (AFC) technologies to modify the forces acting on streamlined bodies is one of the most active research fields in aerodynamics. For each particular application, finding the optimum set of AFC parameters which maximises lift, minimises drag or maximises lift-to-drag ratio (aerodynamic efficiency), has become a necessary design requirement. In the present paper, the AFC technology was applied to the Selig-Donovan 7003 (SD7003) airfoil at Reynolds number 6×10^4 . Synthetic jets were employed to modify the lift and drag forces acting on the airfoil. Four angles of attack (AoA) of 4° , 6° , 8° and 14° were considered, alongside five AFC parameters: jet position, jet width, momentum coefficient, forcing frequency and jet inclination angle. A multi objective optimisation based on genetic algorithms (GA) was performed for each angle of attack to find the optimum combination of AFC parameters. Each GA generation was simulated using Computational Fluid Dynamics (CFD). A home-made GA package was linked with a mesh generator and the CFD solver, and the results were automatically fed back to the GA code. Over 2200 CFD simulations

were performed in two dimensions, using the Spalart-Allmaras turbulent model. The motivation behind the current study is to understand the dependence of the optimum set of AFC parameters on the AoA. Results show that, as AoA is increased, the potential benefits of AFC become more pronounced, which allows for considerable improvement in aerodynamic efficiency. The physics involved in the interaction between the main flow and synthetic jet are clearly presented and clarifies that the physical phenomenon to obtain maximum efficiency is completely different at pre-stall and post-stall AoA. In particular, the aerodynamic efficiency was increased by 251% from baseline (no actuation) by using a moderate/finite momentum coefficient at AoA=14°, while a mere 39% increase was obtained at AoA=8°. In addition, the interaction between the incoming flow and the synthetic jet pulsating flow at different injection angles has been thoroughly investigated.

1.2 Introduction

Increasing lift and reducing drag have major effects on fuel usage, stability, durability and maneuverability of aircraft. Active Flow Control (AFC) technology consists of adding/subtracting momentum to/from the main flow in particular locations in order to interact with the boundary layer, and delay or promote its separation. Moreover, it has the advantage over passive flow control techniques of not introducing drag penalty in off-design conditions. When defining the AFC technique, special care should be taken to assess the energy balance, i.e. the net energy saved due to drag reduction, after the subtraction of the energy required to actuate the AFC device. A very useful classification of AFC strategies was proposed by Cattafesta and Sheplak [1] by dividing AFC techniques into three different classes. 1) Moving body actuators, whose purpose consists in inducing local fluid motion without the need of adding mass [2]. 2) Plasma actuators, which generate jets of ionized fluid with very fast temporal response [3, 4]. The reader can also check other references on Dielectric Barrier Discharge (DBD) also called plasma actuator devices [5, 6], where the authors proposed the combination of DBD plasma actuator experiments with numerical optimisation. And finally, 3) fluidic actuators (FA), which are the most common type of actuators, and whose working principle consists in injecting/sucking fluid to/from the boundary layer.

Recent research has set the focus on elucidating the origin of the self-sustained oscillations [7, 8]. Recent references also include the outcome of two European projects; namely MARS (Manipulation of Reynolds Stress for Separation Control and Drag Reduction) and DRAGY (Drag Reduction in Turbulent Boundary Layer via Flow Control). The two projects were devoted to mature the AFC technology in views of future industrial applications. Several AFC methods were assessed and the results obtained from the projects were outlined in [9, 10], where a review of the major AFC technologies and their applications on airplanes were presented.

Among the different fluidic actuators, Synthetic Jet Actuators (SJA), also called Zero Net Mass Flow Actuators (ZNMFA), have gained particular attention because of their simplicity and high capabilities in controlling flow separation (see for example, [11, 12, 13, 14]). Moreover, when studying the effectiveness of different AFC actuators on a stator compressor cascade, it was concluded that Synthetic Jet (SJ) actuators were more efficient than Continuous Jet Actuators (CJA) at comparable power input levels [15, 16, 17, 18]. Unlike CJAs, SJAs do not require external fluid supply. In SJA, an oscillating membrane is located inside a tiny cavity housed right beneath the surface. The role of the membrane is to inject momentum into the near-wall flow by alternatively sucking low momentum fluid into the chamber and then blowing it back with increased momentum.

During the last two decades, SJA-AFC has been implemented on different airfoils and studied both experimentally and numerically. The focus has been mostly set on assessing the effect of two important parameters related to these jets, namely the non-dimensional frequency ($F^+ = fC/U_\infty$, with f the dimensional frequency, C the airfoil chord and U_∞ the free-stream velocity) and the momentum coefficient (C_μ). In the case of SJAs, this latter is defined as $C_\mu = (h\rho_{jet}(U_j^2) \sin \theta)/(C\rho_\infty(U_\infty^2))$, where h is the jet width, ρ_{jet} and ρ_∞ are the jet and far field densities, respectively, U_j is the maximum jet velocity and θ is the jet inclination angle with respect to the adjacent surface.

Amitay et al. [19] investigated experimentally the effects of momentum coefficient, frequency and position of a synthetic jet actuator employed to control flow separation from an unconventional symmetric airfoil. They realised that by placing the actuator closer to the separation position, a lower momentum coefficient was needed to reattach the separated flow. In a second paper [20], they

discussed the role of actuation frequency on the reattachment of the controlled flow and found that, when the non-dimensional actuation frequency was of the same order of magnitude as the shedding frequency of vortices in the wake of the stalled airfoil ($F^+ \mathcal{O}(1)$), unsteady reattachment was achieved, whereas full flow reattachment was obtained when the actuation frequency was well above shedding frequency ($F^+ \mathcal{O}(10)$). Gilarranz et al. [21] applied SJA on a NACA0015 airfoil at $Re = 8.96 \times 10^5$ experimentally. They managed to increase the stall angle of airfoil from 12° to 18° and realised that actuation effectiveness widely improved beyond $AoA > 10^\circ$. They also observed that higher actuation frequencies were required to obtain remarkable effects at $AoA > 25^\circ$. You and Moin [22] performed a Large Eddy Simulation (LES) for the same airfoil and Reynolds number as Gilarranz et al. [21]. They used an actuation with $C_\mu = 0.0123$, $F^+ = 1.284$ and $\theta = 30.2^\circ$ and succeeded in delaying separation, which entailed a lift increase of 70%. Tuck and Soria [23] experimentally studied the effect of using SJA on a NACA0015 profile at $Re = 3.9 \times 10^4$. They observed that optimal actuation frequencies were $F^+ = 0.7$ and 1.3 , and that the highest one was most effective with an optimum for $C_\mu = 0.0123$. Under this forcing conditions, the stall AoA improved from 10° to 18° . Kitsios et al. [24] conducted a LES study using the same airfoil and Reynolds number previously analysed by Tuck and Soria [23]. They realised that the optimal frequencies found in the experiments actually coincided with the baseline shedding frequency (f_{wake}) and its first harmonic ($2f_{wake}$). This was also experimentally confirmed by Buchmann et al. [25]. Kim and Kim [26] numerically investigated flow separation control with SJAs on a NACA23012 at $Re = 2.19 \times 10^6$. They observed maximum lift happened when $F^+ = 1$ and the jet was located in the close vicinity of the separation point. The small rolling vortices generated by the actuator at this low frequency were very unstable and therefore were easily affected by external disturbances, a conclusion previously reported by Amitay and Glezer [20]. Monir et al. [27] used a RANS model to study the effect of SJA parameters on the performance of a NACA23012 wing profile at $Re = 2.19 \times 10^6$. They found that applying SJA tangentially yielded better results than doing it normal to the surface. They concluded that momentum injection into the boundary layer was more efficient in this new configuration. Goodfellow et al. [28] studied experimentally the effects of SJA on separation control and wake topology on a NACA0025 airfoil

at $Re = 10^5$ and $AoA=5^\circ$ and realised that momentum coefficient was the primary control parameter, and that exceeding a given threshold caused a drag decrease of almost 50%. Feero et al. [29] examined the exact same airfoil and Reynolds number, but at $AoA=10^\circ$. They noticed that the required momentum coefficient to reattach the flow was one order of magnitude lower for excitation frequencies in the range of the vortex shedding frequency than for high frequency. In a later study [30] of the same airfoil and at the same Reynolds number but at $AoA=12^\circ$, they focused on understanding the effect of jet position in controlling the separation. They found that, placing the jet slot close to the separation point, either downstream or upstream, yielded effective results, with a mild advantage for the upstream configuration. Zhang and Samtaney [31] performed a direct numerical simulation (3D-DNS) on a NACA0018 airfoil at $AoA=10^\circ$ and at $Re = 1000$. They studied the effect of three different non-dimensional frequencies ($F^+ = 0.5, 1$ and 4) on airfoil performance. Performances improved in all three cases, the optimum corresponding to $F^+ = 1$. Perhaps one of the latest simulations of SJA applied to airfoils is the one done by Rodriguez et al. [32]. They studied the SD7003 airfoil at $Re = 6 \times 10^4$ at three $AoA=4^\circ, 11^\circ$ and 14° . They observed an aerodynamic efficiency (lift-to-drag ratio) increase of 124% at the highest $AoA=14^\circ$.

In all the studies just cited, the effects of synthetic jets were assessed via parametric analysis, which is a very limited and time consuming approach, particularly so when optimum values of the parameters are sought. In what follows, some of the latest research involving optimisation methods are briefly presented.

Duvigneau and Visonneau [33] coupled the flow solver with an automatic optimisation, which relies on the derivative-free multi-directional search algorithm introduced by Torczon [34], to optimise three parameters of SJA; namely, non-dimensional frequency, velocity amplitude and jet angle. The study was performed on a NACA0015 airfoil at $Re = 8.96 \times 10^5$ and for a range of $AoA \in [12^\circ, 24^\circ]$. By setting the control parameters to their optimal values, the maximum lift was increased by 34%, and the stall angle delayed from 19° to 22° . In a further study [35], they used a derivative-free algorithm to find the optimal SJA location on a NACA0012 airfoil at $Re = 2 \times 10^6$. They considered two $AoA=18^\circ, 20^\circ$ across stall. The results showed that, at an $AoA=20^\circ$ the influence of jet location on lift increase (by 57%) was more noticeable than at $AoA=18^\circ$. Kamari et al. [36]

studied the optimisation of four AFC parameters when using constant blowing and sucking on the SD7003 airfoil at $Re = 6 \times 10^4$, they coupled Genetic Algorithms (GA) with Artificial Neural Networks (ANN). They concluded that constant sucking was more effective than using constant blowing. In a further study, using the same methodology, airfoil and Reynolds number, Tadjfar and Kamari [37] optimised five SJA parameters. Two injection configurations, tangent and normal to the boundary layer as well as two AoA=13° and 16° were considered, aerodynamic efficiency was the only objective function. A maximum aerodynamic efficiency of 591% was obtained at AoA=13° using the tangent injection configuration.

The airfoil and Reynolds number chosen for the present study are respectively the Selig-Donovan 7003 (SD7003) and $Re = 6 \times 10^4$. This is due to the fact that for this airfoil and Reynolds number many numerical and experimental data are available in the literature (see for example, [38, 39, 40, 41, 42, 43, 44]). SD7003 is a thin airfoil with a thickness-to-chord ratio of 8.5% ($t/C=0.085$) which is often employed in micro air vehicles (MAV). One of the particularities of this airfoil at such a low Reynolds number is the formation of a laminar separation bubble (LSB) on its suction side. LSB is formed when, due to the strong adverse pressure gradient, the laminar boundary layer initially separates from the upper surface and after a laminar-to-turbulent transition, reattaches further downstream. As the angle of attack increases, LSB moves towards the leading edge and reduces its length. Ultimately, at a critical angle, stall AoA, downstream reattachment is not occurring and causes a large recirculation zone which is accompanied by a sudden drop in the lift and a sharp increase in the drag. In the present study, via using a Genetic Algorithm optimisation method, the focus has been placed on demonstrating how different AoA, from pre-stall (4°, 6°, 8°) to post-stall (14°), can affect the optimum set of parameters associated with the synthetic jet actuator. For the present airfoil and Reynolds number, it is the first time five SJA parameters are being optimised at these four AoA. The optimisation methodology presented in this paper is completely novel and consists of linking, via using an in-house program developed in Python, a mesh generator (GMSH), a CFD package (OpenFOAM) and a Genetic Algorithm optimiser developed by the authors. After obtaining the two objective functions (maximum lift and maximum efficiency) determined by the CFD simulations, and once transferred to the GA optimiser, the optimiser

generates a new set of five Active Flow Control (AFC) parameters, which are being used to automatically create a new mesh and to reset the boundary conditions in the CFD package. Due to the new methodology employed to optimise the AFC parameters, which involved performing over 2200 2D-CFD simulations, it was not possible to perform the simulations in 3D. Nevertheless, as the main aim of the paper was to optimise five AFC parameters for each AoA, the resulting optimised AFC parameters presented in this manuscript are having the maximum possible degree of accuracy.

The remainder of the paper is structured as follows. The problem formulation and numerical methods are presented in section §1.3, followed by an overview of the optimisation methods in section §1.4. Results are presented in section §1.5 and discussed in section §1.6. Section §1.7 summarises the main conclusions of the study.

1.3 Numerical Method

1.3.1 Equations and flow solver

The present study is based on a large number of simulations aiming to optimise the flow around an airfoil at different AoA in order to minimise or maximise the forces acting over it. Although some authors have applied Direct Numerical Simulation (DNS) or Large Eddy Simulation (LES) for the simulation of AFC applications [45]. The use of 3D models for the optimisation study presented in this paper is not feasible due to the extreme demand in computational power. To overcome this drawback, a 2D unsteady Reynolds Averaged Navier-Stokes model (URANS) has been used. To perform all the simulations a finite volume CFD solver (OpenFOAM) was employed. Also a second order discretization method was used for all parameters. For pressure-velocity coupling the Pressure-Implicit with Splitting of Operators (PISO) scheme [46] was chosen due to its capability in handling unsteady flow. When considering the Navier-Stokes equations under incompressible flow conditions, after substituting each variable by its average and fluctuating values, the resulting averaged continuity and momentum equations are expressed as:

$$\nabla \cdot \bar{u} = 0 \quad (1.1)$$

$$\rho \frac{\partial \bar{u}}{\partial t} + \rho \bar{u} \cdot \nabla \bar{u} = -\nabla \bar{p} + (\mu + \mu_t) \nabla^2 \bar{u} \quad (1.2)$$

where \bar{u} and \bar{p} respectively represent the ensemble-averaged velocity and pressure, and μ_t is the turbulence viscosity, which expresses the effects of the fluctuating component of velocity on the averaged field. The Spalart-Allmaras (S-A) one-equation turbulent model [47] has been employed for all the simulations performed.

1.3.2 Domain and Boundary Conditions

A sketch of the computational domain containing the SD7003 airfoil with a chord length C is shown in Fig. 1.1a. The leading edge was placed at the origin of the coordinate system, and the horizontal distance between this point and the inlet was set to $15C$. The outlet domain was located $19C$ downstream of the airfoil trailing edge. The wing profile was fixed at zero degree and the different angles of attack were achieved by tilting the free-stream velocity. For the cases where the active flow control technology is implemented, a groove across which a synthetic jet flows is needed. A generic synthetic jet implementation is sketched in Fig. 1.1b where a section of the airfoil upper surface, nearby the leading edge, along with the synthetic jet and its geometrical design parameters, jet angle (θ), position (x) and width (h), is presented.

The boundary conditions employed were defined as follows. At the inlet, which was located along the curve connecting the points A and B in anticlockwise direction, see Fig. 1.1a, a constant velocity profile was imposed and its components were set to $(u, v) \equiv (U_\infty \cos \alpha, U_\infty \sin \alpha)$. Neumann boundary conditions for pressure were employed. Non-slip boundary conditions for velocity and Neumann for pressure were applied on the airfoil surface. At the outlet, which comprises the upper curve between points A and B in Fig. 1.1a, wound in clockwise direction, Dirichlet boundary conditions for pressure and Neumann boundary conditions for velocity were chosen. Whenever the SJA was implemented, Neumann boundary

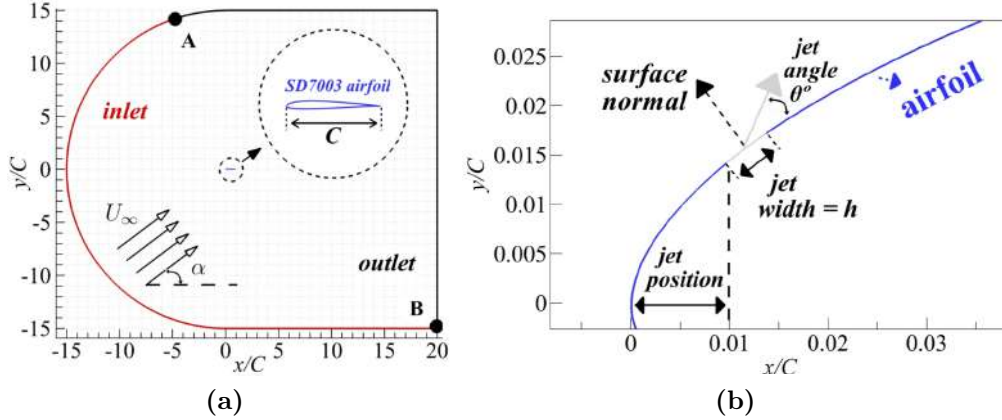


Figure 1.1: (a) 2D Computational domain and (b) synthetic jet geometrical design parameters

condition for pressure and Dirichlet boundary condition for velocity were considered. The time dependent velocity profile of the synthetic jet actuator has been defined according to

$$u_j = U_j \sin(2\pi ft) \quad (1.3)$$

where U_j is the maximum jet velocity, f is the dimensional jet frequency and t is the dimensional time. Notice that the top-hat velocity profile chosen for the SJA is widely used in the literature, see for example [16, 18, 37]. The evaluation of how different SJ spatial velocity profiles affect the AFC parameters optimisation was left as future work. In order to properly capture the laminar separation bubble (LSB), the free stream turbulence was set as proposed by Catalano and Tognaccini [43].

1.3.3 Non-dimensional parameters

The non-dimensional groups employed in the present manuscript are introduced in this section.

The definition of the Reynolds number is:

$$Re = \frac{U_\infty C}{\nu} \quad (1.4)$$

where C is the chord length, U_∞ characterises the free-stream velocity and ν is the kinematic viscosity. The non-dimensional wall coordinate (y^+) is defined as:

$$y^+ = \frac{yu_\tau}{\nu}, \quad u_\tau = \sqrt{\frac{\tau_w}{\rho}} \quad (1.5)$$

where y is the distance to the wall, u_τ is the friction velocity, ρ stands for the free-stream fluid density and the term τ_w characterises the wall shear stresses. Drag and lift coefficients respectively, are defined as:

$$C_d = \frac{2D}{\rho CU_\infty^2} \quad (1.6)$$

$$C_l = \frac{2L}{\rho CU_\infty^2} \quad (1.7)$$

In these equations, D and L are the dimensional drag and lift forces per unit span, respectively. The aerodynamic efficiency is as follows:

$$\eta = L/D = C_l/C_d \quad (1.8)$$

The definition of the pressure coefficient is given by:

$$C_p = \frac{p - p_\infty}{\frac{1}{2}\rho U_\infty^2} \quad (1.9)$$

where p is the pressure at any given point and p_∞ is the free-stream pressure. The skin friction coefficient is obtained using the following expression:

$$C_f = \frac{\tau_w}{\frac{1}{2}\rho U_\infty^2} \quad (1.10)$$

The momentum coefficient associated with the pulsating jet is given by:

$$C_\mu = \frac{h\rho_j U_j^2 \sin \theta}{C\rho U_\infty^2} \quad (1.11)$$

where h and ρ_j respectively represent the jet width and the pulsating flow fluid density, θ characterises the jet inclination angle with respect to the airfoil surface. The non-dimensional frequency is defined as:

$$F^+ = fC/U_\infty \quad (1.12)$$

being f the dimensional frequency. The equation characterising the advective time is expressed as:

$$T = tU_\infty/C \quad (1.13)$$

For the present study, the chord length is taken as one ($C = 1$), the free-stream velocity is equal to one ($U_\infty = 1$), the densities of the synthetic jet and the incoming flow are the same ($\rho_j = \rho = 1$) and the Reynolds number remains constant and equal to $Re = 6 \times 10^4$.

1.3.4 Mesh sensitivity study

In order to make sure the final CFD results were independent of the employed grid, a mesh sensitivity study was performed for an AoA of 8° . Four different meshes having different resolutions, A, B, C and D (see Table 1.1), were considered. To properly solve the boundary layer around the airfoil, a hybrid mesh was used to be able to generate a highly refined mesh near the airfoil without drastically increasing the total number of cells. Fig. 1.2a, shows the full computational domain, Figs. 1.2b and 1.2c represent zoom views of the mesh refinement nearby the airfoil surface leading and trailing edges, respectively.

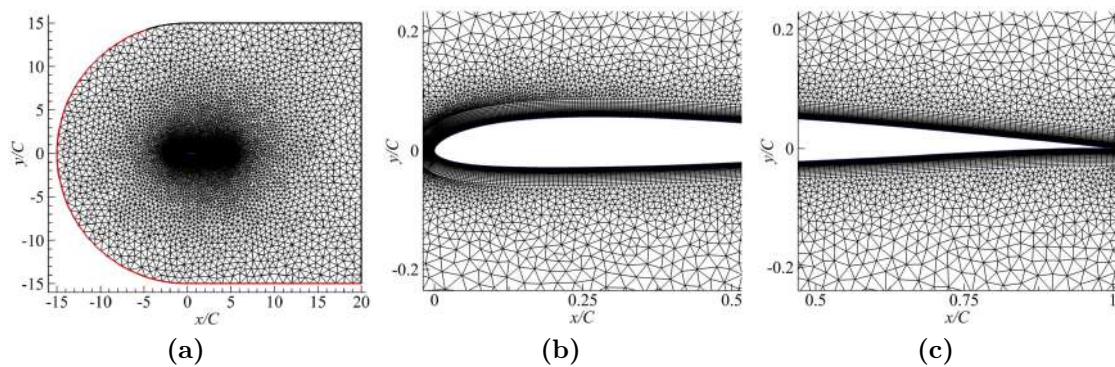


Figure 1.2: (a) Overall mesh view, (b) leading edge's and (c) trailing edge's zoomed views of the mesh

In Table 1.1, the main characteristics of the four different considered meshes (A, B, C and D) are introduced. The coarsest mesh consisted of 26256 cells, while the finest one was made of 92504 cells. The third column of Table 1.1 presents the

Mesh	N_{cell}	y^+	x_s/C	x_t/C	x_r/C	C_l	C_d	η
A	26256	4.0	0.033	0.154	0.228	0.941	0.0332	28.30
B	34448	1.0	0.040	0.165	0.246	0.938	0.0329	28.49
C	45466	0.3	0.041	0.170	0.250	0.934	0.0327	28.56
D	92504	0.1	0.041	0.170	0.250	0.934	0.0327	28.56

Table 1.1: Time-averaged LSB characteristics and airfoil aerodynamic coefficients for different meshes at $\alpha = 8^\circ$

maximum y^+ value of the first cell layer away from the airfoil surface, as computed after the simulations. The next three columns present the location along the chord where separation, transition to turbulence and reattachment occur, respectively. The separation point is gauged by cancellation of the friction coefficient. This is a particularly important point, as AFC effectively critically depends on its location relative to separation. The separated boundary layer undergoes a turbulent transition, gets re-energised, and reattaches further downstream. The reattachment point can be identified by a second change of sign of the wall shear stress. All these locations can be identified from the skin friction and pressure coefficients distribution presented in Fig. 1.3, where they are initially introduced. The airfoil lift and drag are reported, alongside the aerodynamic efficiency, in columns 7 through 9 of Table 1.1. All four meshes, exception made of mesh A, produce very similar results in terms of aerodynamic performances and LSB characteristic properties. Furthermore, C_p and C_f distributions are indistinguishable from one another among meshes B, C and D, as shown in Fig. 1.3. Quantitatively, mesh C yielded three significant digits accuracy of all parameters considered with about half the resolution of mesh D, rendering it a particularly good choice in terms of compromise between accuracy and computational requirements. This mesh consists of 16800 quadrilateral cell, distributed in 40 layers of 420 cells around the airfoil surface. The first layer thickness has a maximum y^+ below 0.3, which is well within the viscous sublayer as required by the wall treatment of the Spalart-Allmaras turbulence model.

Three time steps of 7×10^{-5} , 5×10^{-5} and 2×10^{-5} were tested with identical results for the converged solutions. In order to accurately resolve AFC cases, the lowest time step has been chosen and the convergence criterion set to 10^{-6} , such

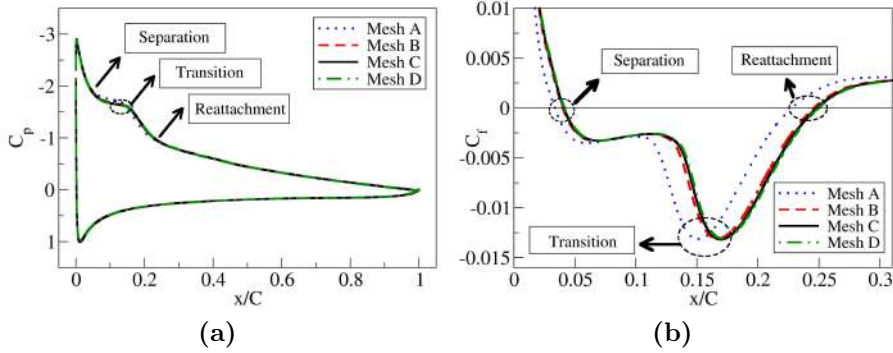


Figure 1.3: Distributions of (a) pressure coefficient and (b) skin friction coefficient, for four meshes at $\alpha = 8^\circ$

that all residuals are required to fall below this value. Convergence was always achieved before 30 time units, so that the maximum time horizon was set to $T = 30$ for all simulations.

1.3.5 Baseline computations and numerical validation

Once the mesh has been chosen, it is essential to validate the baseline performances at all AoA. To do so, initially the temporal averaged lift and drag coefficients as a function of AoA are presented in Fig. 1.4. These graphs compare two sets of experimental results, Exp 89 [38], Exp 95 [39], and four CFD ones, ILES [40], LES [32], the standard $k-\omega$ SST and the $k-\omega$ SST LR, both from Catalano and Tognaccini [43, 44]. The comparison with the results from the present work shows very good agreement. Ranges of pre and post-tall AoA are depicted in Fig. 1.4a. The lift is properly captured at pre-stall AoA, at post-stall, nevertheless, it generates a lower value than the ILES and LES ones. When comparing the drag coefficient (see Fig. 1.4b), we realised that the S-A model under-estimates the values versus the ones obtained using LES and ILES. In fact, the present drag coefficient values are especially similar to the ones gathered using the $k-\omega$ SST model. As a result, the aerodynamic efficiency (see Fig. 1.4c), at pre-stall AoA, presents the same differences as observed in the drag coefficient but at post-stall AoA, it has a good agreement with the previous introduced studies.

Fig. 1.5 shows the comparison of the pressure and skin friction coefficients

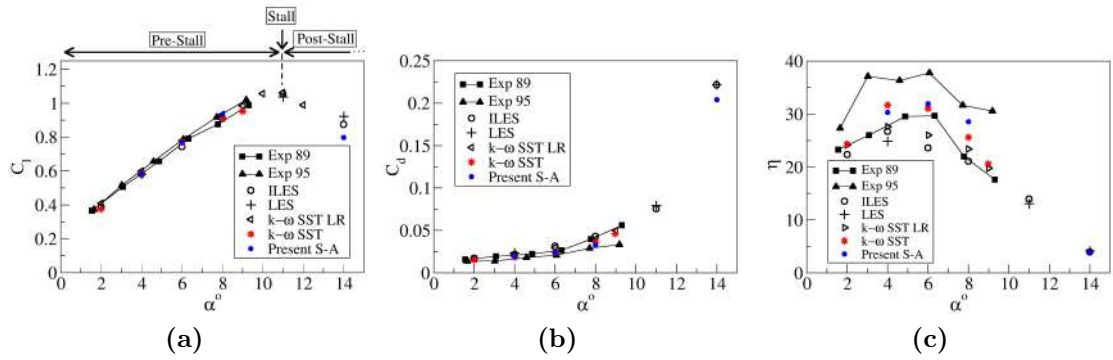


Figure 1.4: (a) Lift and (b) drag coefficients as well as (c) aerodynamic efficiency versus the angle of attack and their comparison with some of the numerical and experimental results. Exp 89 [38], Exp 95 [39], ILES [40], LES [32], the standard k- ω SST and the k- ω SST LR, [43, 44]

from the present study, for the baseline cases at AoA 4° , 6° , 8° and 14° , with the numerical ones available in the literature. At pre-stall AoA of 4° , 6° and 8° , it is observed that as the AoA increases, the separation and reattachment points keep moving upstream and the laminar bubble reduces its length. Notice that the friction coefficient maximum and minimum values increase with the AoA increase. It is observed that the results of the current S-A model have a very good agreement with the ones presented by Catalano and Tognaccini [43] when using the k- ω SST turbulent model. Larger differences are observed in the transition-to-turbulent region and the location of the reattachment point between these two RANS models and the 3D ones [40, 32]. These differences were expected, then as stated by Catalano and Tognaccini [43, 44], in order to properly capture the reattachment point, pre-definition of the transition location needs to be implemented. For the present study, it is particularly relevant to determine the location of the separation point, which is very well captured at all AoA (see the right column of Fig. 1.5). For an AoA of 14° , the present 2D simulation results were compared with the only available results [40, 32], see the two bottom graphs in Fig. 1.5. Despite the fact that at this AoA the flow is fully separated and 3D, the present results agree very well with the ILES ones performed by Galbraith and Visbal [40]. Small differences are observed when comparing with the LES one [32]. It can be seen that when the flow is fully separated, the present RANS model is capable of quite precisely

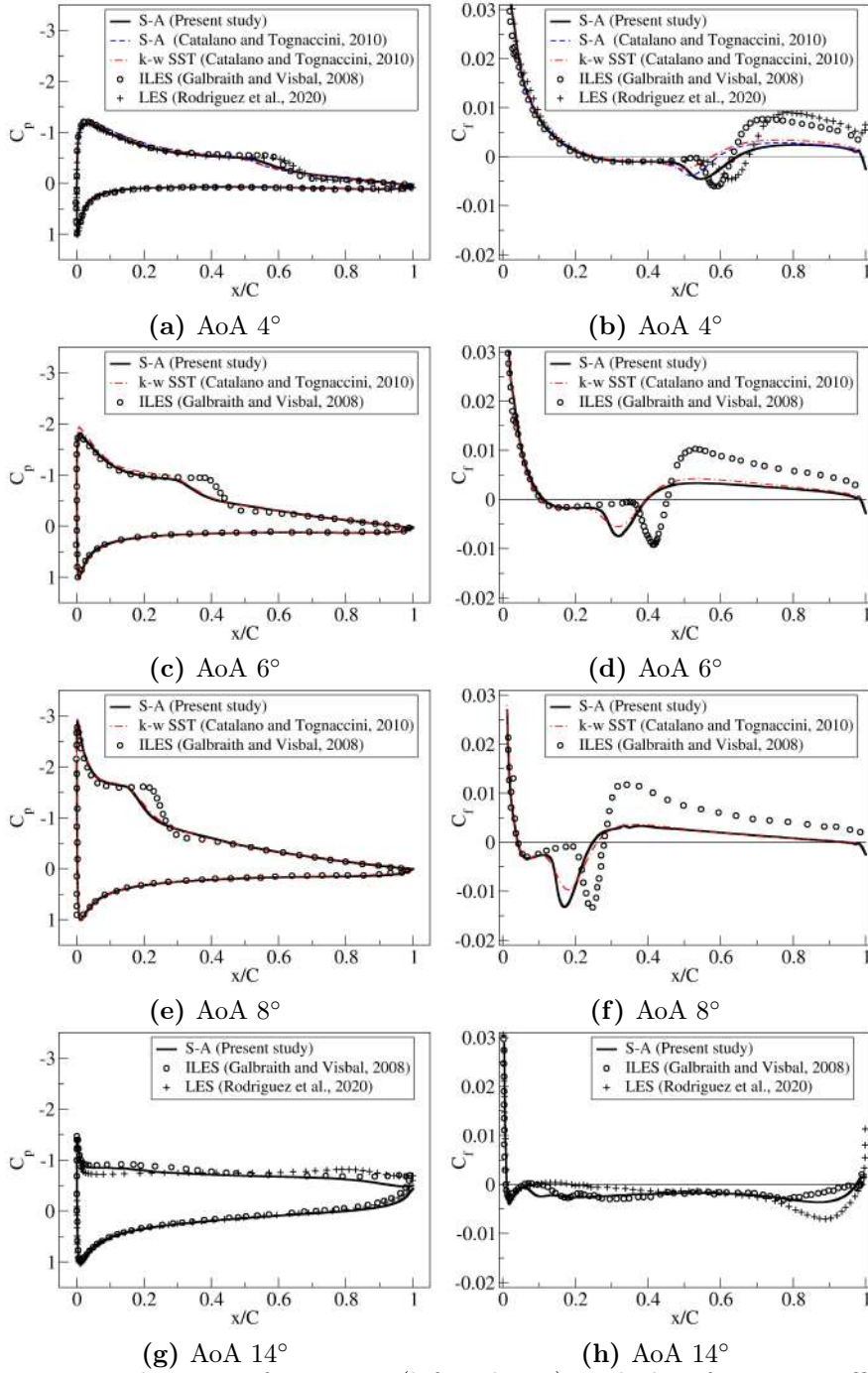


Figure 1.5: Distributions of pressure (left column) and skin friction coefficients on the upper surface (right column) for the baseline cases at all angles of attack and their comparison with previous available results. Figures (a) and (b), corresponds to AoA of 4°, figures (c) and (d) characterises the results at 6°, figures (e) and (f) are defining the information at 8° and the information for AoA of 14° is found in figure (g) and (h).

determining the airfoil pressure and skin friction coefficients. The separation point is properly predicted, fully matching the previous researchers work.

In order to further assess the results under actuation condition, the different SJA parameters along with the boundary conditions used by Rodriguez et al. [32] and Tadjfar and Kamari [37] were implemented and studied using our S-A model. The resulting lift and drag coefficients as well as the aerodynamic efficiency were compared in Table 1.2. ϵ represents the relative error which is defined as $\epsilon_x = (x_{presentS-A} - x_{literature})/x_{literature}$, where x characterises any of the aerodynamic coefficients presented. The comparisons at post-stall AoA of 14° with Rodriguez et al. [32] gave differences of less than 3.6% in all these three parameters. When comparing our results with the ones from Tadjfar and Kamari [37] at AoA 13° , the lift was exactly the same, while the maximum error regarding the drag coefficient was around 14%. The drag coefficient difference is likely due to the different turbulent models used in these two studies and the differences in the mesh density employed to perform this particular simulation.

α°	Cases	F^+	C_μ	θ°	x/C	h/C	C_l	$\epsilon_{C_l}(\%)$	C_d	$\epsilon_{C_d}(\%)$	η	$\epsilon_\eta(\%)$
14	LES [32]	1.0	0.0030	90.00	0.007	0.0070	1.078	—	0.129	—	08.35	—
	Present S-A						1.116	03.52	0.130	00.77	08.58	02.70
13	k- ω SST $\gamma - Re_\theta$ [37]	3.8	0.0424	23.57	0.040	0.0029	1.432	—	0.057	—	25.12	—
	Present S-A						1.432	00.00	0.065	14.03	22.03	12.30

Table 1.2: Aerodynamic coefficients of actuated cases using present S-A model and their comparison with other turbulent models employed by other researchers. The Reynolds number is $Re=6 \times 10^4$.

Based on all the comparisons presented in this section, it can be concluded that the 2D simulations performed generate results fully reliable at these four studied angles of attack, therefore allowing to the present researchers to proceed with the optimisation implementation of the active flow control jets (synthetic jets) on the baseline cases, and study the effects of the five different AFC parameters on the airfoil lift and efficiency.

1.4 Optimisation of AFC parameters

The selection of the values corresponding to the different AFC parameters can be performed through the use of an optimisation method. Optimisation problems are

addressed from many different approaches. The classical optimisation techniques are useful in finding the optimum solutions of functions that are continuous and differentiable. These methods use differential calculus techniques, are fast and accurate, but lack the capacity to deal with non-differentiable functions, either objective or restriction functions, which limits their application [48]. Other methods include linear programming (LP) [49], which are a set of techniques to find the best solution of a problem with a linear objective function (single objective problems), and linear equalities and inequalities as restrictions. Their application is limited by the linearity of the functions they require to use. For problems involving AFC applications, it is not possible to use (LP) for this same reason. Nonlinear optimisation methods appear to be more appropriate [50, 51, 52].

Among the methods capable of handling non-linearities are the gradient-based methods [53], they use information of the function gradient to select the search direction and, iteratively converge to the optimum solution. These methods can get stuck on local optima and are highly dependent on the starting solution of the iterative method. They are usually efficient, fast and accurate. Their efficiency increases with the accuracy associated with the gradient information computed. Different methods have been proposed to estimate the gradient whenever it can not be directly computed.

Stochastic strategies are those which use random or pseudo-random methods to define the variables along the iterations. They are capable of performing multi-objective optimisation and do not impose restrictions on the objective functions or restrictions behaviour. Their robustness is probably one of the most interesting aspects of these methods and do not usually require gradient information, although some methods can be improved using such information. In comparison with other methods, their main drawback is that they usually need a larger amount of iterations to converge [54, 55, 56, 57, 58]

Usually, optimisation methods when coupled with CFD packages are computationally very expensive. When considering the optimisation methods and in order to save computational time, the use of surrogate models is often a typical solution [59]. Artificial Neural Networks or Kriging models are, among many others, two of these surrogate models [60, 61]. The results obtained from a surrogate model

are often based on a set of previously CFD computed samples and require a training process to ensure an accurate outcome. The accuracy of the results obtained when using a surrogate model is usually lower than the one gathered when performing a CFD simulation. A recent application of a surrogate model in AFC can be found in [37]. In the present paper and in order to guarantee the maximum accuracy of the results the authors decided not to use any surrogate model. All results are gathered from CFD simulations, this could be done thanks to the large computational power available. The computational time required to complete all simulations needed for a given AoA (considering 400 2D-CFD cases) was about 18 days, using a single node of 48 cores in a supercomputer based on two 24 cores Intel Xeon Platinum processor.

A general description of the optimisation method and the configuration chosen is presented in the following sub-section.

1.4.1 Optimisation method

The problem under study requires the definition of a multi-objective optimisation. Two different strategies can be used to solve such a problem. On one hand, a temporary objective function can be calculated as the weighted sum of the real objective functions. In this way, the multi-objective problem is expressed as a single objective one. The weight values multiplying each original function require a decision, which can greatly affect the final result of the analysis. One should also consider the fact that to obtain the Pareto Front [62], several runs of the optimiser with different weight values will be required. On the other hand, the authors are proposing to use a pure multi-objective approach, which will enable to identify the whole Pareto Front at once, and therefore the best solutions regarding the combination of the whole set of objective functions. A multi-objective optimisation problem can be defined in its minimisation form as Eq. 1.14.

$$\left\{ \begin{array}{l} \min(f_1(\vec{x}), f_2(\vec{x}), \dots, f_k(\vec{x})), \quad k = 1, \dots, K \\ \text{Subject to:} \\ g_l(\vec{x}) \geq 0, \quad l = 1, \dots, L \\ h_m(\vec{x}) = 0, \quad m = 1, \dots, M \\ \text{Where:} \\ \vec{x} \in X, \quad X \text{ feasible set of decision variables.} \end{array} \right. \quad (1.14)$$

In order to clarify the nomenclature, the following definitions are stated:

Design Variables (DVs) are the set of decision variables, the independent variables of the optimisation problem: $\vec{x} \in X$.

Objective Functions (FOs) are the set of fitness functions. The functions that express the aptitude of a set of DVs: $f_1(\vec{x}), f_2(\vec{x}), \dots, f_K(\vec{x})$. Being K the number of objectives functions.

Constraints (Ctrts) are the set of expressions that need to be satisfied in order to consider the DVs as feasible. It includes both types, inequality g_l and equality h_m expressions. Being L and M the numbers of inequality and equality constraints, respectively.

In this study a Genetic Algorithm (GA) is used. The reason to use a GA is to capture the Pareto Front in a single optimisation. It is also a very robust method that usually works well regardless of the objective space shape which is unknown for this case. Furthermore, it is also robust enough to treat configurations that fail and can not be computed due to problems in the automatic mesh generation or any of the automation process involved in the numerical evaluation of each case. Genetic Algorithms were initially proposed by Holland [63] and further developed by Goldberg and Holland [64]. Their methodology is inspired by the natural evolution process, which selects the best fitted individuals to generate new offspring. The GA, including the steps performed to modify the geometry, boundary conditions and mesh for the design variables, is presented in Algorithm 1.

Initially, in the *InitialisePopulation()* function, a random population is generated. The size of all populations is 20 individuals, which has been considered a

Algorithm 1: Genetic algorithm

```
InitialisePopulation();  
while Stopping criteria is not met do  
    ObjectiveFunctionsCalculation();  
    BoundaryConditionsDefinition();  
    GeometryCreation();  
    MeshGeneration();  
    CFD-Calculations();  
    PostProcess();  
    Selection();  
    Crossover();  
    Mutation();
```

good trade-off between performance of the method and computational cost. Then the population is prepared and computed in the *ObjectiveFunctionsCalculation()* function, which obtains the objective functions for each individual in the population, as it will be explained later in §1.4.2. Each individual is prepared using an in-house Python script that links the mesh generator (GMSH), the CFD package (OpenFoam) and the GA. This script automates the process of translating the format of the different packages, modify the mesh and apply the boundary conditions. After the population is computed, the optimisation operators are applied, these are *Selection()*, *Crossover()* and *Mutation()*. In the implementation used in this study the *Selection()* operator employs a $\mu + \lambda$ strategy with a Crowded-Comparison Operator [62]. For the *Crossover()* operator, a Simulated Binary Crossover (SBX) [65] is used and the *Mutation()* operator is performed with Polynomial Mutation [66]. It is important to notice that the optimiser tracks the individuals that survive to the next generation without altering their design variables and does not compute again its objective functions, which is not uncommon when using genetic algorithms. Those individuals beat the odds and pass the crossover and mutation operators without suffering any modifications. In applications that are highly demanding in computational resources and time consuming, it is very important to take this behaviour into account to avoid repeating the CFD analysis. The values of the parameters of the GA used are presented in Table 1.3.

Parameter	Value
Population size	20
Probability of crossover	0.9
Probability of mutation	0.1

Table 1.3: Parameters of the Genetic Algorithm.

In the next section the detail of the objective functions and the design variables definition as well as the range employed for each design variable are presented.

1.4.2 Objective functions and Design variables definitions

The aim of this study is to maximise the lift coefficient and the aerodynamic efficiency of an airfoil at different angles of attack. The GA used solves the optimisation problem as a minimisation problem, which means it will minimise the objective functions. Taking this into account, two objective functions f_1 and f_2 were defined, which are minimised when the lift coefficient and the efficiency were maximum:

$$f_1 = -C_l \quad (1.15)$$

$$f_2 = -\eta \quad (1.16)$$

The optimisation was performed at four angles of attack, 4° , 6° , 8° and 14° , being four independent optimisation analysis defining the design variables as five AFC parameters associated with the synthetic jet. These parameters were the non-dimensional frequency (F^+), momentum coefficient (C_μ), jet angle (θ), jet position (x/C) and jet width (h/C). A scheme representing the geometrical design parameters was introduced in Fig. 1.1b. Fig. 1.6 shows a zoomed view around the jet position introduced in Fig. 1.1b for one of the automatic generated meshes. In the function *BoundaryConditionsDefinition()* from Algorithm 1, the first three design variables (F^+ , C_μ and θ) were selected. In the next step, using the function *GeometryCreation()*, and according to the two last design variables (x/C) and (h/C), a new geometry was created using the GMSH program. Once the new

geometrical changes were applied, the function *MeshGeneration()* created a new mesh, deciding as well the number of cells required along the groove width in order to guarantee a good mesh quality. At this point the CFD simulations were ready to start, the function *CFD-Calculations()* was doing so. Finally, the two objective functions were post-processed in *PostProcess()* function and the results were transferred to the three GA operators, already discussed in §1.4.1.

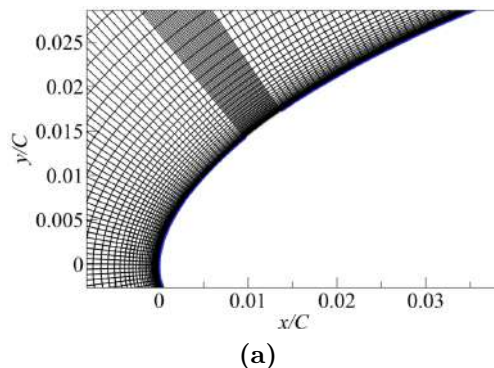


Figure 1.6: Mesh view nearby the jet, automatically generated.

The process just described was repeated until the stopping criteria was met. In the present study the stopping criteria used consisted in computing a minimum of 400 individuals. The reason why 400 individuals were sufficient is detailed in Fig. 1.7, which shows the convergence evolution and the Pareto Front history at a pre-stall AoA of 8° and at the post-stall AoA of 14° . At low angles of attack of 4° , 6° and 8° , the number of CFD simulations required to minimise the two objective functions (f_1) and (f_2), or in other words, to maximise the lift coefficient (C_l) and the aerodynamic efficiency (η), was around 400. Notice from Fig. 1.7a that after 300 simulations the two objective functions show a negligible improvement. In order to assure a full convergence of the two objective functions at post-stall AoA, it was initially decided to run 600 simulations (see Fig. 1.7c), but it was realised that after 400 simulations the objective functions suffered minor modifications. The same conclusion can be reached from the observation of the Pareto Front history's presented in Figs. 1.7b and 1.7d for 8° and 14° respectively. Notice that after 15 generations in Fig. 1.7b and 28 generations in Fig. 1.7d, the Pareto Front curves suffer minor variations.

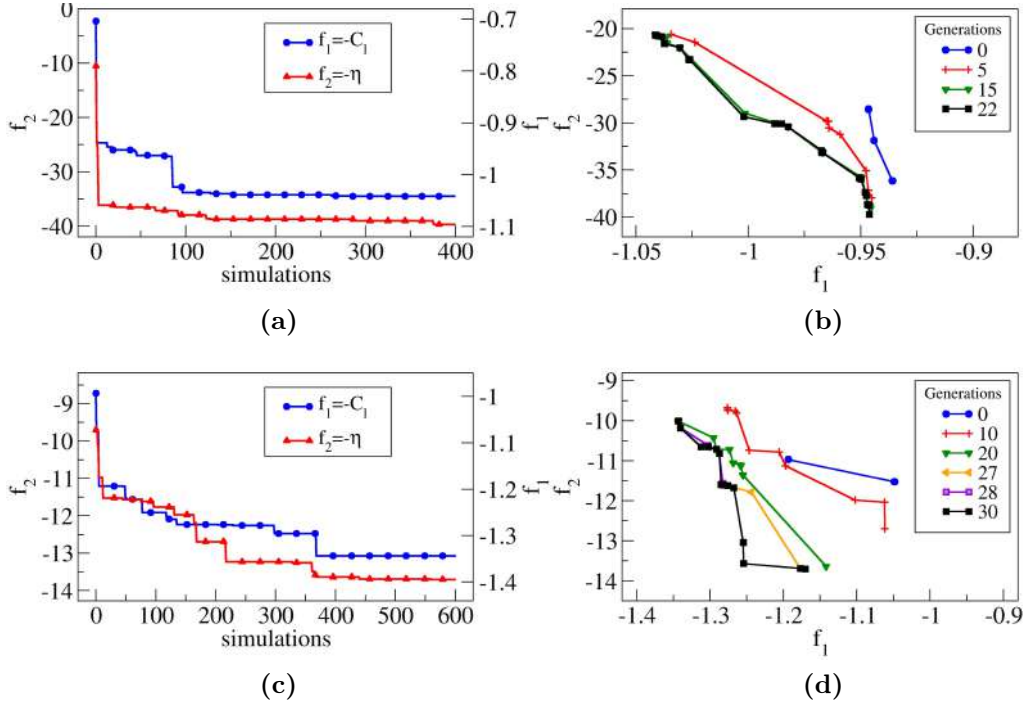


Figure 1.7: Evolution of the objective functions as the number of simulated cases increase (a and c). Pareto Front history at several generations (b and d). AoA of 8° is represented in figures (a and b). Figures (c and d) characterise the results at AoA 14°

The ranges of evaluation for the five AFC design variables and for the four different AoA, are presented in Table 1.4. At AoA of 4° , 6° and 8° , the ranges of the different variables were $F^+ \in [0.1, 10]$, $C_\mu \in [0.0001, 0.02]$, $\theta^\circ \in [15, 165]$, $x/C \in [0.015, 0.32]$ and $h/C \in [0.005, 0.02]$. The reason for selecting these particular ranges is upon several previous studies. For example, in the literature, frequencies around $F^+ = 1$ are commonly used for the pulsating flows (see for example, [32]).

α°	F^+	C_μ	θ°	x/C	h/C
4,6,8	0.1-10	0.0001-0.02	15-165	0.015-0.320	0.005-0.020
14	0.1-10	0.0001-0.02	15-165	0.0001-0.04	0.005-0.015
14	0.1-10	0.0001-0.10	15-165	0.0001-0.04	0.005-0.015

Table 1.4: AFC Design variables and their evaluation ranges for the different angles of attack.

In the present study and considering that the pulsating frequency is an important parameter to activate the boundary layer, we decided to set the limits, ten times smaller and bigger than the baseline one. Regarding the range of momentum coefficients, the upper limit was set based on the maximum momentum coefficient used in the experimental work done by Gilarranz et al. [21] and Goodfellow et al. [28]. In the case of jet width (h/C), we decided to use a larger upper limit in comparison to the one used by Kamari et al. [36] ($h/C = 0.003$). This is due to the fact that after checking their results, we noticed that the optimum solution for this parameter was located around 0.003. The range chosen for the jet position (x/C) was such that the separation point, at each AoA, was always located inside the chosen margins. For the pulsating jet inclination angle (θ°), Kamari et al. [36] set a range varying from 1 to 180 degrees. Since their optimum solutions were located in a region between 65 and 94.6 degrees, we decided to limit the upper and lower bounds of the jet angle to 15 and 165 degrees, respectively. This decision was also taken to reduce the computational cost.

At 14° , initially the same ranges for F^+ , C_μ and θ were employed, but smaller modifications were allowed on the ranges of position (x/C) and width (h/C) of the jet, see the second line of Table 1.4. The reason for this is that, at an angle of attack of 14° , separation occurs very close to the airfoil leading edge, and as the position of the groove as well as its width have to be placed around the separation point, the ranges of the groove location and width need to be accordingly restricted. Consequently, at 14° , only the initial 4% of the chord length was evaluated by the optimiser. Due to the physical restrictions just explained and to the high curvature of the airfoil near the leading edge, the maximum non-dimensional jet width at 14° was set to a size of $h/C = 0.015$, which is 25% smaller than the maximum jet width employed at pre-stall AoA. As it will be explained in the next sections, the present authors observed that, the maximum efficiency obtained when employing the AFC parameters just defined for AoA 14° , was lower than what other researchers obtained in similar investigations. In order to increase the maximum aerodynamic efficiency, a second set of optimisation tests at 14° was carried out (see the third line of Table 1.4). All AFC parameters remained unchanged except the momentum coefficient range, in this second optimisation evaluation C_μ was allowed to change in the range $0.0001 < C_\mu < 0.1$. In other

words, the maximum momentum coefficient was allowed to be five times larger than the one employed in the previous optimisation case.

1.5 Results

In the following sections, the optimum AFC parameters to maximise the airfoil lift and efficiency, at three pre-stall angles of attack (4° , 6° and 8°) and also at one post-stall angle of attack (14°), are presented. The main idea of studying the optimum AFC parameters at all these angles of attack is to be able to evaluate how each AFC parameter is changing as the AoA increases, with the hope of finding a pattern which could be used in future applications.

1.5.1 Pre-stall angles of attack of 4° , 6° and 8°

The aerodynamic efficiency for each of the 400 CFD studied cases at all pre-stall AoA and versus each AFC parameter is shown in Fig. 1.8. Each column represents the aerodynamic efficiency as a function of the different AFC parameter at given AoA. From left to right, AoA= 4° , 6° and 8° . The evolution of the aerodynamic efficiency as a function of a given AFC parameter, for several different AoA, can be observed at each row of Fig. 1.8. The first row characterises the efficiency versus the non-dimensional frequency for the three studied AoA. Maximum efficiencies are obtained at pulsating frequencies F^+ around 9. Lower frequencies appear of minor interest in terms of having high efficiency. For comparison, the horizontal line introduced in all graphs shows the baseline case efficiency at each AoA. The efficiency values for each particular baseline case is found in Table 1.5. The second row of graphs presents the efficiency as a function of the momentum coefficient C_μ . For AoA of 4° and 6° , the optimum C_μ is around 0.019 and the momentum coefficient is reduced to about 0.015 as the AoA increases to 8° . This small reduction of the momentum coefficient at 8° is likely to be due to the particularly successful groove location. The next row in Fig. 1.8 introduces the aerodynamic efficiency as a function of the jet inclination angle θ . The origin of the angular position was presented in Fig. 1.1b. The optimum jet injection angle is about 130° at AoA 4° and decreases to about 125° as the AoA increases to 8° . What it is particularly

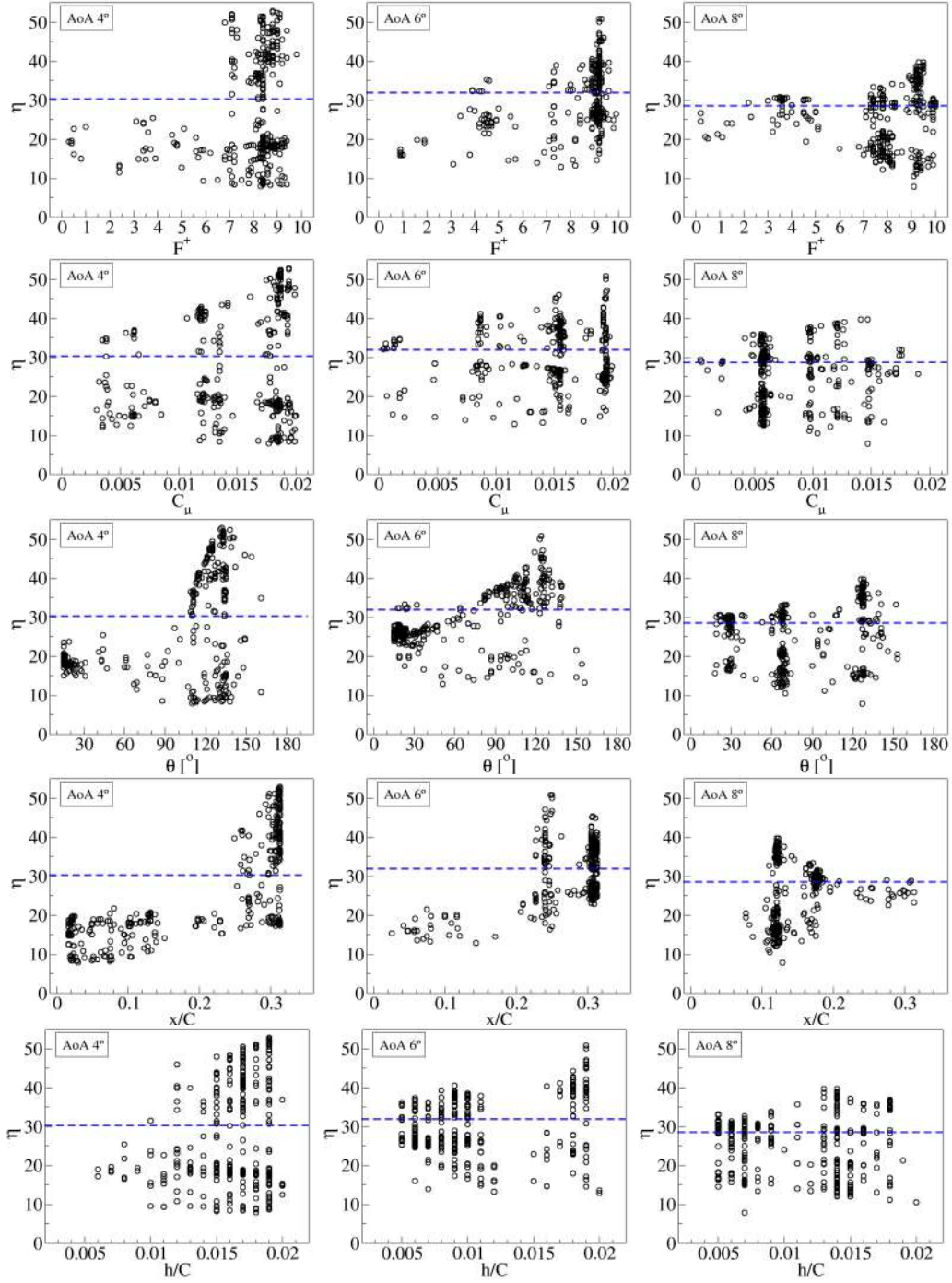


Figure 1.8: Aerodynamic efficiency η versus non-dimensional frequency F^+ , momentum coefficient C_μ , jet angle θ° , jet position x/C and jet width h/C for all the CFD cases at AoA of 4° , 6° and 8° are presented in left to right columns respectively. The horizontal dashed line represents the baseline case efficiency for each AoA.

interesting to observe is that regardless of the pre-stall AoA chosen, the flow is injected facing upstream. This fact needs to be understood in combination of the groove location, which is presented in the next row of Fig. 1.8. Groove location clearly moves upstream as the AoA increases, the optimum groove location at 4° , 6° and 8° is respectively $x/C = 0.313$, $x/C = 0.250$ and $x/C = 0.122$. In fact, this evolution was expected. Then, as explained in §1.3.5, the separation point moves upstream with the increase of AoA. The respective separation and reattachment points for the different studied AoA were, $x/C = 0.2436$ and $x/C = 0.66$ for and AoA of 4° , $x/C = 0.1125$ and $x/C = 0.3958$ at 6° , and $x/C = 0.04$ and $x/C = 0.248$ for an AoA of 8° . As it will be clarified in Fig. 1.10, the optimum groove location (maximum efficiency) falls inside the laminar bubble for all pre-stall studied AoA. What appears to be more interesting is to observe that the groove location versus the location of the separation point for each AoA, further moves downstream as the AoA increases. The location of the groove is displaced about 29% downstream versus the separation point at AoA 4° , this displacement increases to 122% when the AoA is of 6° and reaches a 205% for an AoA of 8° . The authors observed that when the groove is located just before the transition to turbulence point, for the present study this is particularly happening at 8 degrees AoA, the momentum needed to trigger the flow reattachment can be lower. The final row of Fig. 1.8 shows the aerodynamic efficiency as a function of the groove width h/C . Optimum groove widths at 4° and 6° are around $h/C = 0.19$ and decrease to $h/C = 0.13$ at 8° AoA. For an AoA of 8° , this reduction appears to be triggered by the advantageous location of the groove inside the laminar bubble, where the transition occurs. In this region, the boundary layer becomes turbulent and it requires a smaller amount of energy to be activated.

Fig. 1.9, for the three pre-stall AoA, characterises the two objective functions considered in this study, the aerodynamic efficiency and the lift coefficient. In each figure, over 400 points defining each of the CFD simulations are presented. The red broken line represented on the right hand side of each figure is the so called Pareto Front, which indicates the optimum values of the AFC parameters to obtain maximum efficiency, maximum lift and the optimum combination of both. The blue dot shown in each figure represents the airfoil baseline case characteristics associated with each studied AoA. For an AoA of 4° the Pareto Front is almost

vertical, the efficiency increase is mostly due to a decrease of the average drag. As the AoA raises, aerodynamic efficiency improvement is due to the lift increase and drag decrease.

The first three tables presented in 1.8.1 summarise the values of each of the five AFC parameters corresponding to each point of the Pareto Front for AoA 4° , 6° and 8° , respectively introduced in Fig. 1.9. Descending in the tables, lift and drag coefficients decrease and efficiency increases. The first and the last rows of each table are underlined and correspond to the maximum lift and maximum efficiency, respectively. For an AoA of 8° , the highest obtained efficiency was 39.71, see Table 1.3 in 1.8.1. Notice that the point of maximum efficiency corresponds to the point of minimum drag. When comparing with the baseline case efficiency, an increase of almost 39% is observed. The values related to the five AFC parameters which generate the maximum aerodynamic efficiency are; non-dimensional frequency $F^+ = 9.3$, momentum coefficient $C_\mu = 0.0147$, jet angle 126° , jet position $12\%C$, $x/C = 0.12$ and jet width $1.3\%C$, $h/C = 0.013$. The values characterising AFC parameters capable of generating the maximum lift are; $F^+ = 8$, $C_\mu = 0.0058$, $\theta = 67^\circ$, $x/C = 0.116$ and $h/C = 0.015$. A maximum lift increase versus the baseline case of around 11% could be obtained. Comparing the lift coefficients of all points defined in the Pareto Front with the baseline case one $C_l = 0.934$ at AoA 8° , see Table 1.3 in 1.8.1, it is seen an improvement in all optimum cases, whereas when considering the drag coefficient, an improve-

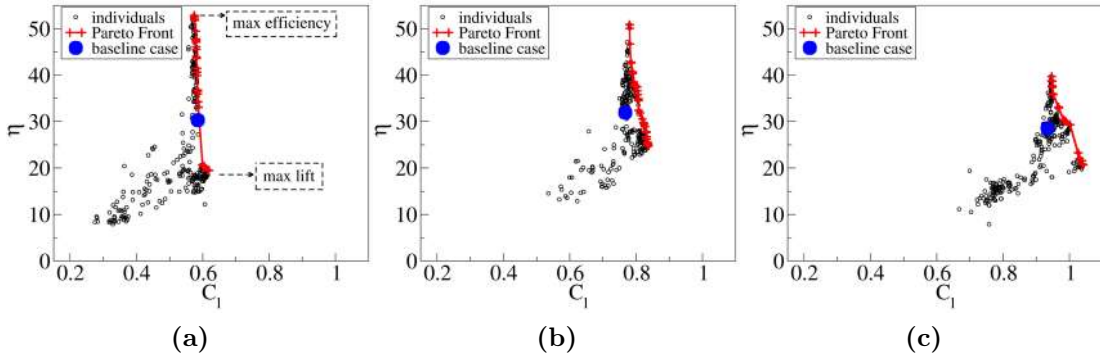


Figure 1.9: Pareto Front at angles of attack of (a) 4° , (b) 6° and (c) 8° . The blue dots represent the efficiency versus lift coefficient for the baseline cases at different AoA.

α°	cases	F^+	C_μ	θ°	x/C	h/C	C_l	$C_l\%$	C_d	η	$\eta\%$
4	max lift	9.4	0.0193	015	0.021	0.013	0.6185	+5.76	0.0317	19.51	-35.61
	max efficiency	8.8	0.0194	132	0.313	0.019	0.5740	-1.84	0.0108	52.86	+74.45
	baseline	—	—	—	—	—	0.5848	—	0.0193	30.30	—
6	max lift	9.1	0.0195	015	0.308	0.006	0.8371	+9.14	0.0338	24.76	-22.50
	max efficiency	9.2	0.0194	124	0.250	0.019	0.7802	+1.72	0.0153	50.85	+59.15
	baseline	—	—	—	—	—	0.7670	—	0.0240	31.95	—
8	max lift	8.0	0.0058	067	0.116	0.015	1.0413	+11.45	0.0504	20.66	-27.66
	max efficiency	9.3	0.0147	126	0.122	0.013	0.9460	+1.28	0.0238	39.71	+39.00
	baseline	—	—	—	—	—	0.9340	—	0.0327	28.56	—

Table 1.5: Optimum five synthetic jet parameters associated with the maximum lift and maximum efficiency cases at pre-stall angles of attack of $4^\circ, 6^\circ$ and 8°

ment (reduction of drag force), only happens when the lift coefficients are below $C_l = 0.985$. In other words, increasing the lift coefficient a value of higher than 0.985 introduces a drag penalty higher than in the non-actuated case. A similar effect is observed at the other two pre-stall studied AoA, see Tables 1.1 and 1.2 in 1.8.1.

Table 1.5 presents the aerodynamic coefficients (C_l , C_d and η) as well as five SJA parameters (F^+ , C_μ , θ , x/C and h/C) associated with the maximum lift and maximum efficiency cases. These cases represent two points of the Pareto front at each AoA (4° , 6° and 8°). When comparing these optimum cases with the baseline ones, the first thing to realise is that aerodynamic efficiencies can be increased by over 39% for all pre-stall AoA. The maximum efficiency was found to decrease with the AoA increase. During the simulations it was observed that the efficiency increase was linked to the low average value of the drag coefficient. Regardless of AoA, the lift coefficient associated with the highest efficiency cases suffered a variation smaller than $\pm 2\%$ versus the baseline case. The maximum lift coefficient, in percentage versus the baseline case, raised with the AoA increase. For an AoA of 4° the maximum lift coefficient increase was of around 5.7%, reaching a value of about 11.5% when the AoA was 8° . When comparing the jet inclination angles θ required to obtain maximum lift and maximum efficiency, it is observed that the maximum lift is associated with small jet inclination angles, maximum efficiencies are linked with high θ . To understand why it is so, it is needed to study the interaction between the incoming flow and the pulsating jet. This study

is presented in §1.6.4. Regarding the AFC parameters and based on the results presented, maximum aerodynamic efficiencies are linked with high injection angles, high momentum coefficients and high pulsating frequencies. At AoA 8° , the differences in the AFC parameters characterising the maximum lift and the maximum efficiency cases are mostly coming from the angle of the jet and the momentum coefficient. The rest of the parameters are almost in the same range. For the AoA of 4° and 6° the differences in AFC parameters to obtain maximum lift and maximum efficiency reside in the jet inclination angle, the groove width and the groove position.

In reality the effects of the groove location x/C are better observed in Fig. 1.10. For each pre-stall AoA studied, it is presented the pressure and friction coefficients as a function of the chord length. The comparison between the baseline, maximum efficiency and maximum lift cases is also introduced. From the friction coefficient curves and regardless of the AoA, it is observed that the optimum groove location to obtain the maximum efficiency as well as the maximum lift falls inside the laminar bubble. The only exception is observed at 4° , where the maximum lift is reached when locating the groove almost at the airfoil leading edge. For AoA 6° , the location of the groove to obtain the highest efficiency is slightly upstream than the one needed to obtain maximum lift. At AoA 8° the groove location remains approximately unchanged, for both the maximum efficiency and lift cases. From the friction coefficient curves and considering the highest efficiency cases (red lines), regardless of the AoA, it is observed that the length of the bubble appearing on the airfoil upper surface reduces whenever AFC is applied.

The effect of the AFC parameters on the pressure coefficient can clearly be seen in Figs. 1.10a, 1.10c and 1.10e. Notice that regardless of the AoA, the application of AFC tends to maintain the flow pretty much attached downstream of the AFC jet groove location and therefore, slightly decreasing the pressure at the airfoil upper surface. Such decrease is particularly relevant between the leading edge and synthetic jet location. The pressure is especially low at the groove location, generating as well a decrease on the friction coefficient. In some cases, the use of AFC generates small alternative vortices emanating from the interaction of the main stream with the synthetic jet, and they roll downstream on the airfoil upper surface. Under these conditions, the pressure on the upper airfoil surface decreases,

increasing the lift as well as the drag. Evolution of vortical structures on the airfoil surface will be further discussed in §1.6.

To further understand the effect of actuation on the airfoil upper surface for the three pre-stall AoA of 4° , 6° and 8° , the streamlines along with the turbulence

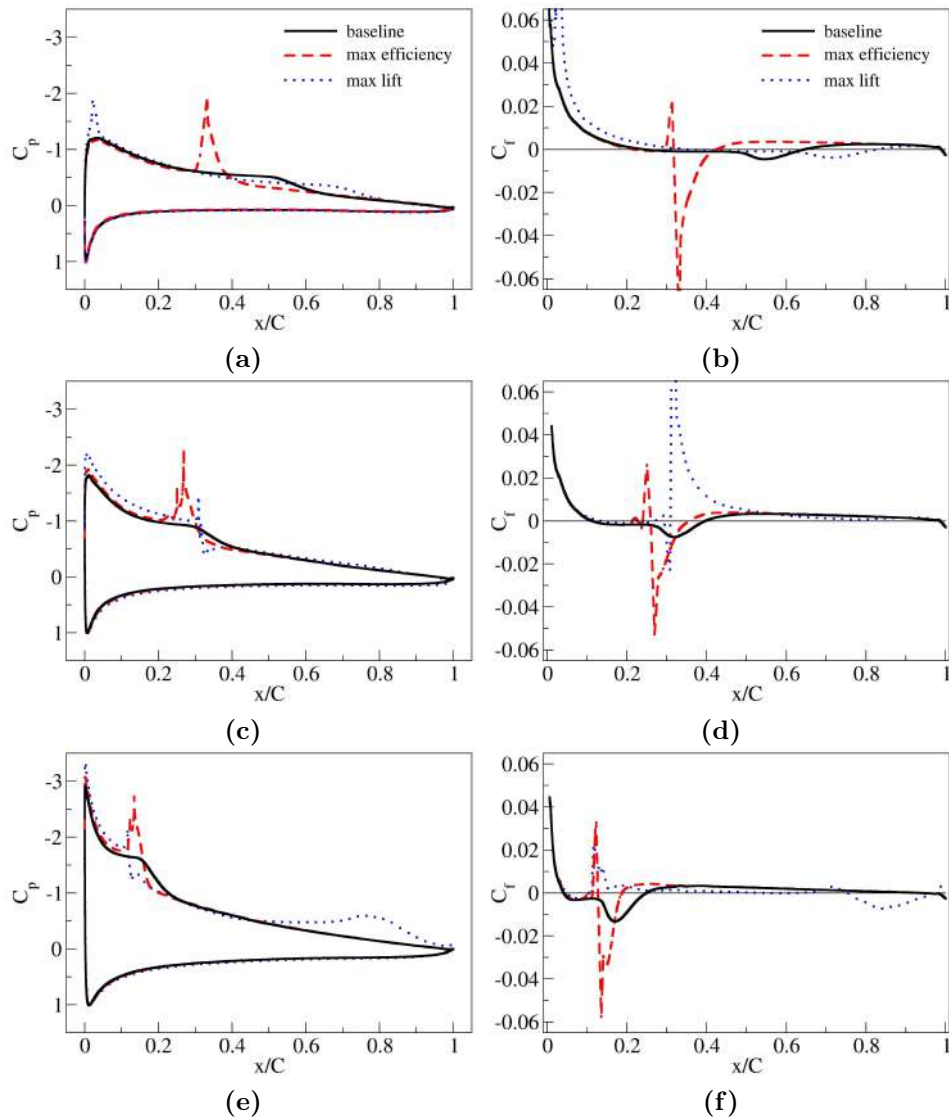


Figure 1.10: Distributions of pressure coefficient (C_p) and skin friction coefficient (C_f) for the baseline (black solid lines), maximum efficiency (red dashed lines) and maximum lift (blue dotted lines) cases at three pre-stall AoA. (a), (b) AoA 4° ; (c), (d) AoA 6° ; (e), (f) AoA 8° .

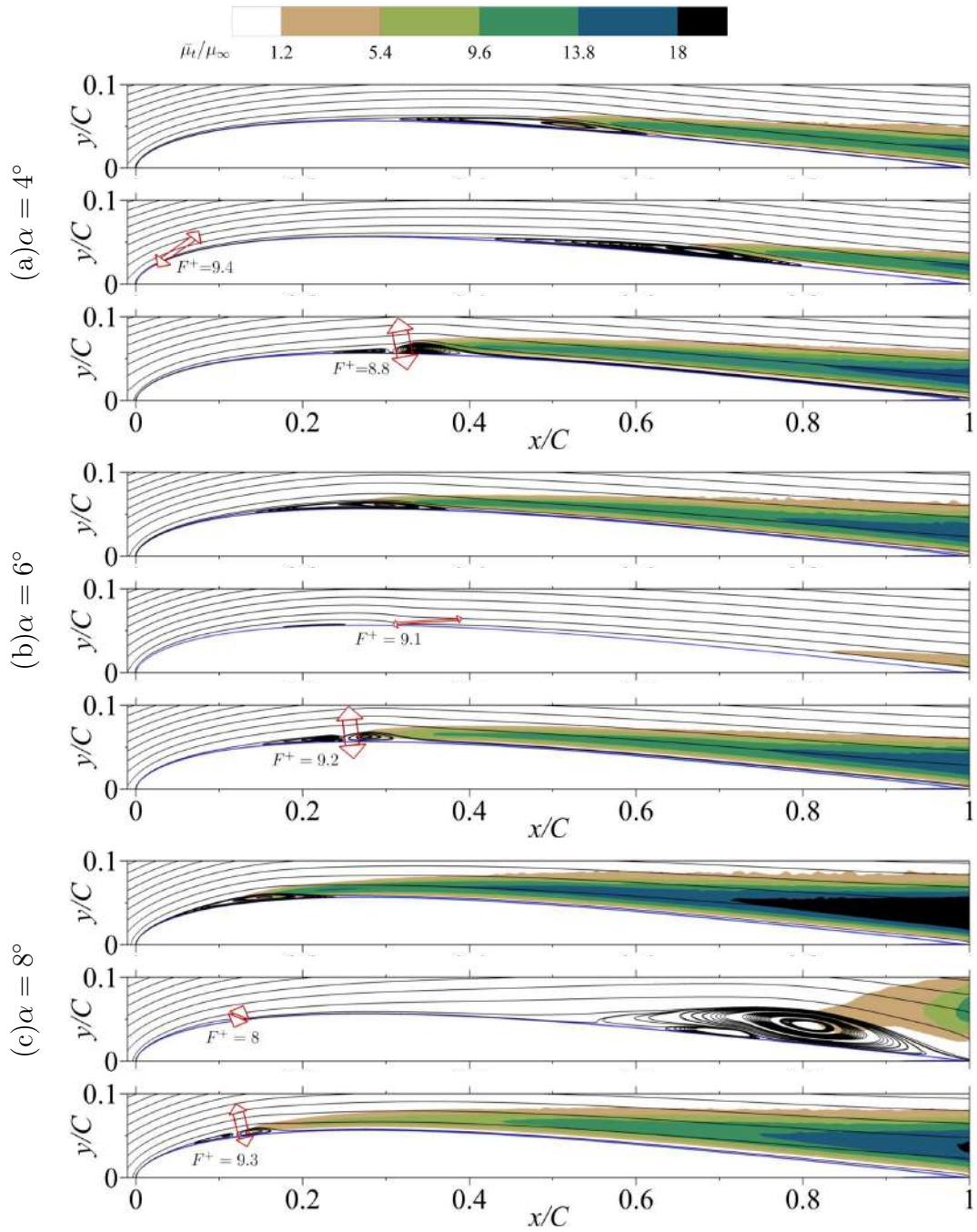


Figure 1.11: Streamlines of the temporal average velocity field and contours of turbulence viscosity at the three pre-stall AoA. (a) 4° , (b) 6° and (c) 8° . The baseline, maximum lift and maximum efficiency cases are introduced as the top, central and bottom panel in each sub-figure, respectively.

viscosity contours for the baseline and actuated cases are presented in Fig. 1.11. Regardless of the AoA, all baseline cases show a laminar bubble appearing just after the separation point. Notice that as previously explained in Fig. 1.10, the laminar bubble length decreases with the AoA increase. For an AoA 8° the bubble appears almost near the leading edge. For all cases, the flow remains reattached downstream of the separation bubble. When observing the highest lift cases (central panel in each sub-figure), a bubble is seen on the airfoil upper surface. This bubble is related to the pressure distribution introduced in Fig. 1.10, from where it can be concluded that the highest lift is achieved due the low pressure distribution along the airfoil upper surface. This pressure is lower than the one for the rest of the cases studied and it is particularly observed upstream of the groove location and also downstream of this point, where the bubble is generated. For an AoA of 4° , this is being accomplished via displacing the laminar bubble further downstream. At 6° , the laminar bubble is drastically reduced respective the baseline case one. At 8° , the lowest upper surface pressure is obtained when removing the laminar separation bubble at the leading edge and generating a large separation bubble around the airfoil position $x/C = 0.8$, the bubble origin and end are respectively located at $x/C = 0.6$ and $x/C = 1$. This large bubble explains the drag increase and the decrease of efficiency in this particular case. It must be kept in mind that, having low pressures at the airfoil upper surface, always tends to increase the drag. The length of the arrows observed in the central and bottom panels characterises the Synthetic Jet momentum coefficient, while their width is proportional to the groove width and their inclination represents the injection angle. The three bottom panels in each sub-figure show the streamlines configuration when the maximum aerodynamic efficiency is obtained. At all AoA, the maximum efficiency is reached when the flow is attached along the entire airfoil chord and just a small bubble appears downstream of the synthetic jet location. This vortical structure is larger at small AoA. Therefore it seems that at all pre-stall AoA the same physical phenomenon is controlling the flow reattachment. One of the details which is important to highlight is the relationship between the vortical structures observed in Fig. 1.11 and the evolution of the pressure and friction coefficients presented in Fig. 1.10. This relation can be clearly seen when observing that the position of the vortical structures presented in the maximum efficiency cases of

Fig. 1.11. Such a position coincides with the sudden drop of the friction coefficient and the sharp increase of the pressure coefficient observed in Fig. 1.10. From the contours of turbulence viscosity presented in Fig. 1.11, it is observed that under all conditions studied, the turbulence begins to grow inside the laminar separation bubble and then develops along the upper surface of the airfoil. As soon as transition to turbulence occurs, a turbulent boundary layer is developed and extends until the end of the chord. Flow reattachment occurs after the laminar separation bubble as a consequence of the transition to turbulence.

1.5.2 Post-stall angle of attack of 14°

In this subsection, the results obtained from the optimisation at the post-stall AoA 14° are presented. Fig. 1.12, from (a) to (e), introduces the aerodynamic efficiency as a function of each five AFC parameters evaluated in the present manuscript, the AoA was kept constant at 14° . When comparing the aerodynamic efficiency versus the non-dimensional frequency F^+ , Fig. 1.12a, the maximum efficiency appears at frequencies around $2.5 < F^+ < 3.5$. Notice that at pre-stall conditions, the optimum frequencies were around $F^+ \approx 9$. The aerodynamic efficiency as a function of the momentum coefficient C_μ is presented in Fig. 1.12b. Maximum efficiency is obtained for momentum coefficients around 0.005, when comparing this C_μ with the optimum ones at pre-stall AoA, it can be concluded the C_μ needed for the present case is over three times lower than the ones previously required. The explanation of why it is so needs to be found when analyzing the injection angle, which is introduced in Fig. 1.12c, along with the groove location. At post-stall AoA the optimum injection angle is around 18° , indicating the fluid is injected almost tangentially. This is completely different than the optimum jet angles at pre-stall AoA, which were around 120° . This injection angle as well as the momentum coefficient differences, along with the fact that at post-stall AoA there is no laminar bubble, direct the attention to different flow phenomenon to achieve flow attachment. Due to the fact that at post-stall AoA the AFC jet is injected almost tangentially, to further understand the coupling between the main flow and the injected pulsating one, the relation of the main flow reattachment with the Coanda effect should be further studied. At pre-stall AoA the interaction between

the AFC jet and the boundary layer flow generates small vortical structures which are alternatively shed downstream, lowering the local pressure and promoting fluid reattachment. The position of the groove, which is introduced in Fig. 1.12d, appears to be optimum at around 1% of the chord, which is just the location of the flow separation point. It seems at high AoA, the jet injection needs to be implemented where the separation point is, while at low AoA the optimum position is located further downstream, inside the laminar bubble. From Fig. 1.12e, it is observed that groove widths around $h/C = 0.005$ seem to be the optimum ones at 14° . These widths are three to four times smaller than the ones needed at pre-stall AoA. Finally the Pareto Front curve characterising the maximum efficiency and maximum lift coefficient points, as well as the optimum combination of them, is presented in Fig. 1.12f. In order to understand which is the effect of the different AFC parameters on the main flow, the relation between the instantaneous streamlines at different jet pulsating instants and the boundary layer evolution will be further discussed, in §1.6.4.

The optimum AFC parameters to obtain the maximum efficiency and maximum lift for an AoA of 14° , obtained from the optimisation process and after performing 600 CFD simulations, is presented in Table 1.6. All optimum points characterising the full Pareto Front curve are introduced in Table 1.4, 1.8.1. From Tables 1.6 and 1.4 it is observed that the AFC parameters required for maximum lift and maximum efficiency are very similar. The highest variation appears at the jet inclination angle θ , which is of 44° for the maximum lift and reduces to 18° for the maximum efficiency. The second AFC parameter suffering high variations is the F^+ , which for the maximum lift condition decreases by 37% versus the F^+ required for the maximum efficiency. Regarding the groove position, for maximum

α°	cases	F^+	C_μ	θ°	x/C	h/C	C_l	$C_l\%$	C_d	η	$\eta\%$
14	max lift	1.5	0.0051	44	0.0082	0.005	1.3435	+68.36	0.1343	10.00	+156.41
	max efficiency	2.4	0.0055	18	0.0097	0.005	1.1702	+46.64	0.0854	13.70	+251.28
	baseline	—	—	—	—	—	0.7980	—	0.2040	03.90	—

Table 1.6: Optimum five synthetic jet parameters associated with the maximum lift and maximum efficiency cases at a post-stall angle of attack of 14° (small momentum coefficient range). 600 CFD cases

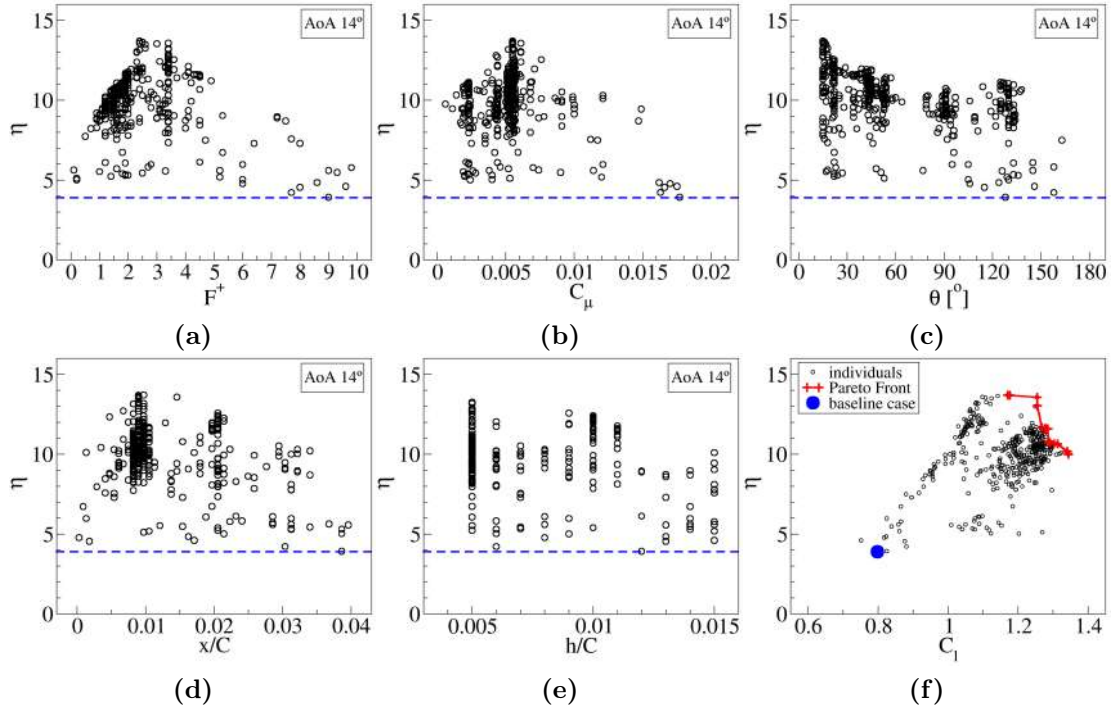


Figure 1.12: aerodynamic efficiency versus (a) non-dimensional frequency, (b) momentum coefficient, (c) jet angle, (d) jet position, (e) jet width and (f) lift coefficient at $\alpha = 14^\circ$. The horizontal dashed line and the blue dot represent the baseline case efficiency.

lift it is displaced upstream about 15% when compared with the groove position required for maximum efficiency. Table 1.6 shows that a maximum aerodynamic efficiency increase of about 251% can be obtained. When comparing Tables 1.5 and 1.6 it becomes clear that efficiency at the pre-stall AoA slightly decreases with the AoA increase, but at post-stall conditions it sharply increases. At post-stall AoA and considering the baseline case, due to the large vortical structure generated above the airfoil, see Fig. 1.13 top panel, considerable efficiency improvements can be obtained when implementing the AFC technology. In fact, from Table 1.6 it is observed a lift increase of 46% and a drag decrease of 58%, therefore explaining the large efficiency increase at AoA 14° . From the comparison of Tables 1.5 and 1.6 it is seen, for the pre-stall AoA the optimum jet inclination angles to obtain the maximum aerodynamic efficiency are around 120° , while at post-stall the jet inclination angles are of around 18° . But at pre-stall AoA the jet injection angles

to obtain maximum lift are similar to the ones to obtain maximum lift and or efficiency at post-stall AoA. When analysing the momentum coefficient, jet injection angle and groove location required at pre and post-stall AoA, clear differences are observed between them, suggesting that the interaction between the incoming flow and the synthetic jet one may be characterised by a different physical phenomenon, further research is required in this regard.

The time averaged streamlines and contours of turbulence viscosity on the airfoil top surface for the baseline, maximum lift and maximum efficiency cases at AoA 14° is presented in Fig. 1.13. The baseline case (top panel) is characterised by a large separation bubble, which is drastically reduced for the maximum lift and efficiency cases (middle and bottom panels respectively). For the highest lift condition, a small vortex is alternatively generated at a position around $x/C = 0.1$, which keeps rolling downstream onto the airfoil surface, creating a particularly low pressure on the airfoil upper surface and therefore producing the maximum lift. For the maximum efficiency case, a very small vortical structure alternatively appears at the groove location. It seems the boundary layer is slightly separating and

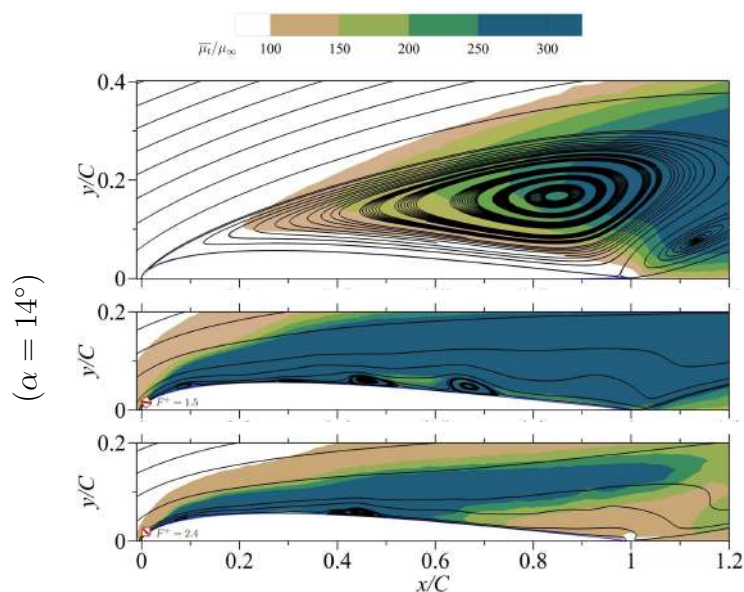


Figure 1.13: Streamlines of the temporal average velocity field and contours of turbulence viscosity at the post-stall AoA. of 14° . The baseline, maximum lift and maximum efficiency cases are introduced as the top, central and bottom panel, respectively.

reattaching again, maintaining the vortical structure locked in the same position. The same performance was previously observed at 13° AoA by Tadjfar and Kamari [37]. Airfoil profile and Reynolds number were the same in both cases. When comparing the contours of turbulence viscosity at this post-stall AoA with the ones presented at pre-stall AoA, (see Figs. 1.13 and 1.11) it is realised that at post-stall AoA the maximum turbulence viscosity is about an order of magnitude higher. This is due to the fact that at 14° AoA (baseline case) the flow is fully separated. At this post-stall AoA and for the actuated cases, the boundary layer becomes turbulent just after the Synthetic Jet location, the high level of turbulence viscosity associated with the fluid inside the turbulent boundary layer maintains the flow attached along the entire chord length.

The effects on the pressure and friction coefficients when using the optimum AFC parameters at 14° are introduced in Fig. 1.14. The comparison with the baseline case is also presented. For both optimum AFC cases, on the initial 50% of the chord, the pressure on the upper airfoil surface is drastically reduced, and then increases to a higher value than the one associated with the baseline case. The friction coefficient shows that, for both optimum actuated cases, at around 50% of the chord, a small vortical structure appears. Such structure is already seen in Fig. 1.13, highlighting the point where the pressure coefficient is beginning to have a value higher than the baseline case one. For both actuated cases, friction coefficient suffers a particular decrease at a position $x/C = 0.1$, which is the point where the small laminar bubble is generated just after the jet, see Figs. 1.13b and 1.13c. When comparing Fig. 1.14 with Fig. 1.10, it can be concluded that at post-stall AoA, the pressure and friction coefficients suffer large variations versus the baseline case ones. These changes are minor at pre-stall AoA, therefore explaining the relatively small efficiency variations.

The evolution of the mean streamwise velocity profiles at several streamwise locations, from $x/C=0.1$ to $x/C=1$, as a function of the normalised wall normal distance and for an AoA 14° , is introduced in Fig. 1.15. The comparison between the baseline, maximum lift and maximum efficiency cases is presented in the same figure. A drastic reduction of the boundary layer thickness is observed when the AFC cases are considered. For the baseline case and when moving downstream, the flow is separated, the vertical position at which negative velocity distribution exists

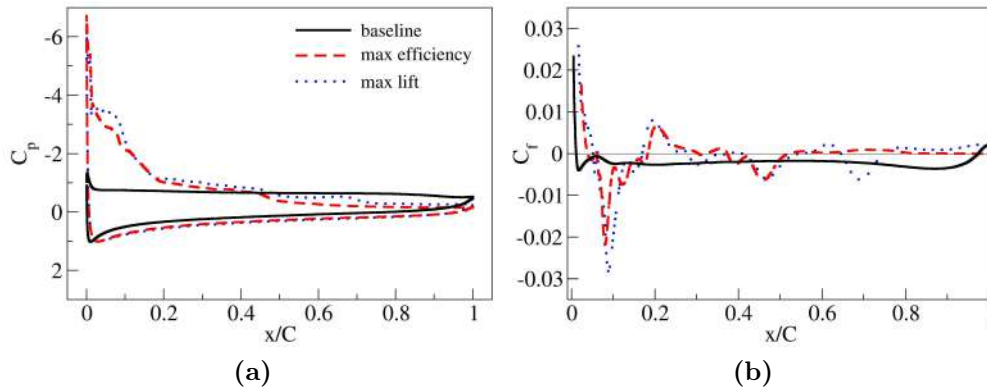


Figure 1.14: Distributions of (a) pressure coefficient and (b) skin friction coefficient for the baseline (black solid lines), maximum efficiency (red dashed lines) and maximum lift (blue dotted lines) cases at 14°

keeps growing therefore indicating the existence of a large vortical structure located onto the airfoil surface, as observed in Fig. 1.13. For any of the optimum AFC cases presented in Fig. 1.15 and regardless of the streamwise location chosen, fluid velocity remains always positive, indicating there is no boundary layer separation. Small differences are observed between maximum lift and maximum efficiency cases. At the airfoil trailing edge ($x/C=1$) and for the baseline case, the velocity profile nearby the surface shows a positive velocity sign (see Fig. 1.15b). This behaviour is linked to the existence of a relatively small vortical structure, turning anticlockwise, and located at the airfoil trailing edge, such structure can be seen in Fig. 1.13.

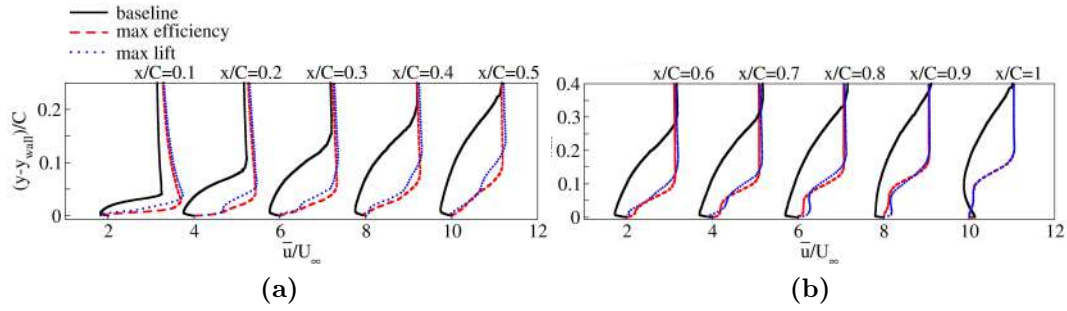


Figure 1.15: Mean streamwise velocity profiles at several streamwise locations, (a) from $x/C=0.1$ to $x/C=0.5$ and (b) from $x/C=0.6$ to $x/C=1$, as a function of the normalised wall normal distance. Individual profiles are separated by horizontal offset of 2 with the corresponding zero lines located at 2, 4, 6, 8, 10. The black solid, red dashed and blue dotted lines represent the baseline, maximum efficiency and maximum lift cases, respectively.

1.6 Discussion

In this section, some physical characteristics of the flow which helps in understanding the implementation effects of the AFC technology are introduced.

1.6.1 Boundary layer thickness for different AoA and actuation cases

The non-dimensional boundary layer thicknesses as a function of the non-dimensional abscissa axis for AoA of 4° , 6° , 8° and 14° are represented in Fig. 1.16. The thicknesses for the maximum lift, maximum efficiency and baseline cases are introduced in each figure, except at AoA 14° , where the curve representing the boundary layer thickness for the baseline case is not presented, as the flow is fully separated. The first thing to realise is that for the pre-stall AoA, the boundary layer thickness decreases with the AoA increase. Under these conditions, the AFC technology slightly modifies the boundary layer thicknesses versus the respective baseline cases ones, yet a clear reduction of the BL thickness is observed at AoA 6° under the maximum lift conditions. For AoA of 14° and 8° , the highest efficiency case is characterised by a boundary layer thickness thinner than the one observed for the maximum lift case. At AoA of 4° and 6° the opposite happens, high lift conditions have associated thinner boundary layers than the ones observed at high efficiency

conditions. In fact, the streamlines presented in Figs. 1.11 and 1.13 help in clarifying the evolution of the boundary layer thicknesses. The location of the groove along with the different jet injection angles could further explain the different trend in boundary layer thicknesses. Further research to understand the mixing phenomenon is needed.

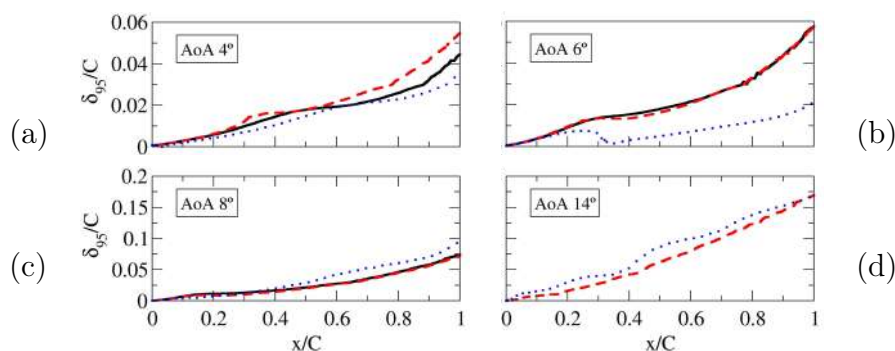


Figure 1.16: Boundary layer thickness as a function of the chord length and for the four AoA studied cases; (a) 4°, (b) 6°, (c) 8° and (d) 14°. The black solid, red dashed and blue dotted lines represent the baseline, maximum efficiency and maximum lift cases, respectively.

1.6.2 Further investigation on AoA of 14°

Recalling now the work done by Tadjfar and Kamari [37], where they studied the same airfoil profile at the same Reynolds number and for post-stall AoA of 13° and 16°, they obtained efficiencies much higher than what it is obtained in the present paper at 14° (see Tables 1.6 and 1.4). These differences seem to be mostly due to the 4 times higher momentum coefficient they employed in their study. In the present work the maximum momentum coefficient was limited to avoid using large amounts of energy to drive the synthetic jet. Yet, in order to check if the use of a higher momentum coefficient could further increase the aerodynamic efficiency, a second set of 400 CFD optimisation cases was run. The ranges of the different AFC parameters used for this second set of tests were already presented in the last line of Table 1.4. Notice that the only difference in the range of the different AFC parameters defined for the new case at 14° introduced in Table 1.4, resides in the larger momentum coefficient range allowed for this second optimisation process.

From now on, this second case will be called the unrestricted momentum coefficient case.

Table 1.7 introduces the optimised AFC parameters to obtain the new maximum lift and efficiency. When comparing the results presented in Table 1.7 with the ones previously presented in Table 1.6, it is observed the efficiency has increased from the previous 251% to the actual 460%. The groove width h/C remains unchanged, the jet injection angle θ has reduced to 15° clearly indicating that tangential injections lead to higher efficiencies, the position of the groove has moved around 180% further downstream, the injection frequency has doubled and the momentum coefficient has increased by over 600%. Based on this information it can be concluded that, for post-stall AoA the momentum coefficient as well as the groove location are essential to obtain high aerodynamic efficiencies. The flow needs to be injected almost tangentially. Under these conditions the aerodynamic efficiency is perfectly comparable with the one obtained by Tadjfar and Kamari [37], being the AFC parameters of a similar order of magnitude.

α°	cases	F^+	C_μ	θ°	x/C	h/C	C_l	$C_l\%$	C_d	η	$\eta\%$
14	max lift	6.7	0.0985	15	0.02854	0.005	1.7635	+121.00	0.0966	18.24	+367.69
	max efficiency	5.2	0.0390	15	0.02764	0.005	1.5690	+096.61	0.0717	21.86	+460.5
	baseline	—	—	—	—	—	0.7980	—	0.2040	03.90	—

Table 1.7: Optimum five synthetic jet parameters associated with the maximum lift and maximum efficiency cases at a post-stall angle of attack of 14° (large momentum coefficient range). 400 CFD cases

To further visualise the advantages obtained when using an unrestricted momentum coefficient, Fig. 1.17 is introduced. It compares the former Pareto Front obtained with the restricted momentum coefficient and initially presented in Fig. 1.12f, with the new Pareto Front obtained with the unrestricted momentum coefficient. The advantages of employing quite unrestricted momentum coefficients are clearly stated. The full values of the new Pareto Front are presented in Table 1.5 in 1.8.1. In the next subsection the comparison between the different flow structures obtained over the airfoil and generated due to the interaction of the main flow stream and the synthetic jet, are presented and discussed.

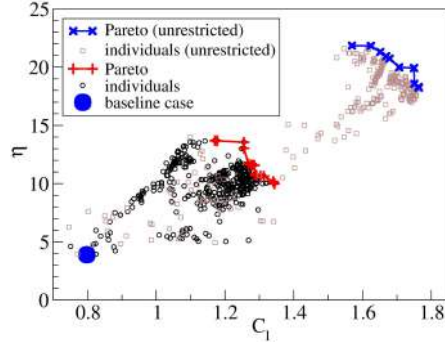


Figure 1.17: Comparison of the two Pareto Fronts obtained at AoA 14° with the restricted and unrestricted momentum coefficient.

1.6.3 Energy assessment

In the present section in order to determine the effectiveness of the AFC technology, the power per unit length used by the SJA (W_j) and the one gained after the actuation (W_G), at each AoA and for the optimum case of maximum efficiency, is calculated and presented in Table 1.8. The power required by the synthetic jet is defined in Equation 1.17.

$$W_j = \frac{1}{2} \rho_j A_j \sin(\theta) \overline{u_j^3} \quad (1.17)$$

where $A_j = hl$ is the cross-sectional flow area of the synthetic jets, in the present study as the spanwise length of the airfoil is equal to unity $l = 1$, the area is equivalent to the jet width h . As previously introduced in §1.3.3, θ is the jet inclination angle with respect to airfoil surface.

The time dependent velocity profile of the synthetic jet actuator to the power three, $\overline{u_j^3}$, has been defined according to [15, 17].

$$\overline{u_j^3} = \frac{1}{T/2} \int_0^{T/2} U_j^3 \sin^3(2\pi ft) dt = \frac{4}{3\pi} U_j^3 \quad (1.18)$$

where U_j represents the maximum jet velocity. The power saved due to the reduction of the drag force when AFC is applied can be given as:

$$W_G = U_\infty (D_{\text{baseline}} - D_{\text{actuated}}) = \frac{\rho U_\infty^3 C}{2} (C_{d_{\text{baseline}}} - C_{d_{\text{actuated}}}) \quad (1.19)$$

where D and C_d represent the drag force and drag coefficient respectively. The parameter representing the power ratio when AFC is applied reads:

$$W_G/W_j \tag{1.20}$$

Whenever this parameter becomes negative, it indicates the drag coefficient after the actuation is bigger than the one generated at the baseline case. When this value is positive but smaller than one, it means that despite a drag reduction being observed when AFC is implemented, the energy saved is lower than the one needed to actuate the synthetic jet. Also when the power ratio has values higher than the unity, there is energy saving. All related information is summarised in Table 1.8 from where it can be stated that under the maximum efficiency conditions at nearly all AoA the power ratio is higher than one. At AoA 14° the power ratio is particularly high. This is perfectly understandable when considering that at this AoA the flow is fully separated under baseline conditions, the application of AFC reattaches the flow drastically reducing the drag forces acting over the airfoil. Nevertheless, if the unrestricted momentum coefficient is employed, (see the row of $14^\circ(u)$ from Table 1.8) the power ratio drops, although the airfoil is still energetically efficient.

In conclusion, it is interesting to notice that although the AFC technology is effective in modifying lift and drag forces, under some conditions it is energetically efficient. In fact, at the three pre-stall AoA, under baseline conditions, the flow is attached to the airfoil and the application of AFC slightly improves the flow conditions. The drag is slightly increased but the energy used to do so is almost the same as the amount saved (considering the maximum efficiency conditions). At post-stall AoA, the situation is completely different as the flow is fully separated (before actuation). Whenever AFC is applied the flow attaches to the airfoil, causing a large drag reduction. As a result, the energy used is much smaller than the amount saved. From the energy point of view, the conclusion of this subsection is that Synthetic Jet Actuators are efficient at high AoA and specially at post-stall AoA.

cases	α°	U_j [m/s]	A_j [m ²]	θ°	W_j [W]	W_G [W]	W_G/W_j
	4	1.17	0.019	132	0.00479	0.00425	0.885
	6	1.11	0.019	124	0.00457	0.00435	0.951
max efficiency	8	1.18	0.013	126	0.00366	0.00445	1.213
	14	1.89	0.005	018	0.00221	0.05930	26.789
	14 (<i>u</i>)	5.49	0.005	015	0.04544	0.06615	1.455

Table 1.8: Power ratio obtained for the maximum efficiency case and at pre and post stall AoA.

1.6.4 Flow structures

In the present subsection it will be explained for AoA 6° and 14° , how the vortical structures created by the interaction of the AFC synthetic jet and the main flow, generate, collapse and are being shed downstream. Two injection angles θ of 124° and 15° , which respectively correspond to the cases of maximum efficiency and maximum lift for an AoA of 6° are initially analyzed, see Figs. 1.18 and 1.19. For an AoA of 14° , the two maximum efficiency cases corresponding to the restricted and unrestricted momentum coefficient ones are respectively presented in Figs. 1.20 and 1.21. In all these figures, a full jet oscillation period is divided in eighth equally spaced time periods. The initial four time periods correspond to the blowing phase, and the remaining four time periods obey to the suction phase. At phase $1/8T$ the synthetic jet has just started to blow fluid and therefore has associated a low injection velocity, the maximum blowing velocity will be reached in the next time period $2/8T$. The time periods $5/8T$ and $6/8T$ characterise the initial and maximum sucking velocities respectively, which are equivalent to the $1/8T$ and $2/8T$ blowing periods. The time periods $4/8T$ and $8/8T$ define the final blowing and sucking periods respectively. At these two time periods the synthetic jet velocity is zero.

Fig. 1.18, represents the case characterised by an AoA of 6° and an injection angle of $\theta = 124^\circ$. During the blowing phase, at the initial time period $1/8T$, the interaction between the external flow and the low synthetic jet velocity facing upstream generates a small laminar bubble just before the groove location. An even thinner bubble is created just upstream of this one. Downstream of the groove lo-

cation, at a distance about $x/C = 0.05$ versus the groove position, a third laminar bubble of a size slightly larger than the previous two ones is observed. When the time period is $2/8T$ the blowing velocity is maximum, the two upstream attached vortical structures have decrease in length while slightly increasing in thickness. This is due to the slightly increase of the boundary layer thickness at the groove location. Downstream of the groove location, the former third laminar separation bubble still remains in the same position and directly after the groove, a fourth vortical structure is generated. At the next time period $3/8T$, the synthetic jet blowing velocity is the same as at $1/8T$. This decrease of velocity versus the previous time period enhances the growth of the four vortical structures. A particular large growth is observed on the eddy located just downstream of the jet. The maximum dimension of the vortical structures is observed at $4/8T$, the two upstream structures, which where connected in the previous time periods are now quite independent. The two downstream structures are rather joined and the eddy located just downstream of the jet has now moved upstream into the jet area while considerably increasing its dimension. The external flow simply passes over

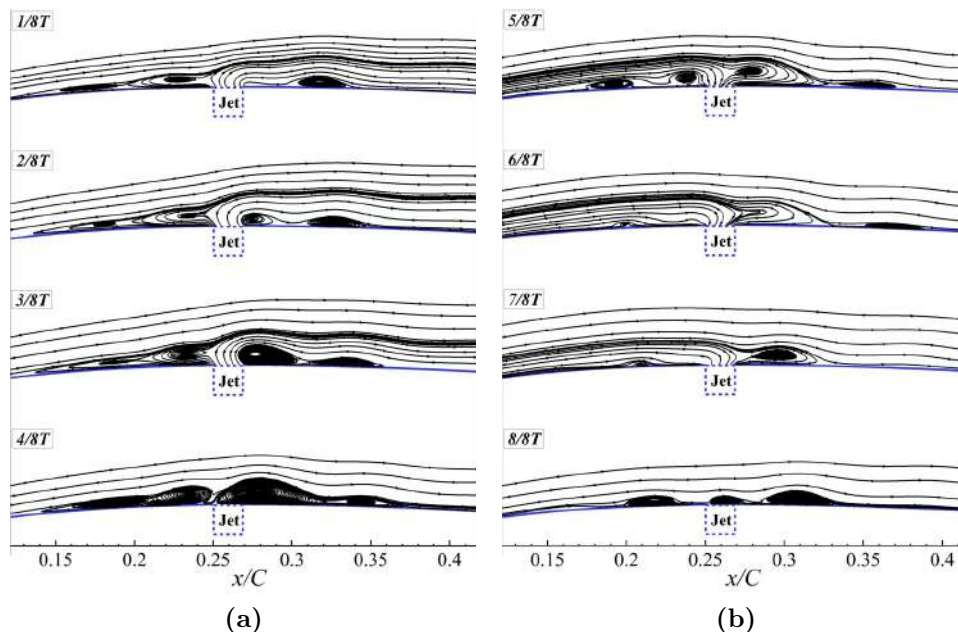


Figure 1.18: Instantaneous velocity streamlines at different phases of synthetic jet for the maximum efficiency case at AoA 6° with $F^+ = 9.2$, $C_\mu = 0.0194$, $\theta = 124^\circ$, $x/C = 0.25$ and $h/C = 0.019$.

the four eddy structures drastically reducing the downstream perturbed zone. As soon as the suction phase starts, at time $5/8T$, the former four vortical structures drastically reduce in size while maintaining their central core position. In the next time period $6/8T$, the sucking velocity is maximum, the two upstream structures have almost completely disappeared and the structure just downstream of the jet still remains, although it is largely being dragged into the groove. Finally, the further downstream structure is being pushed slightly downstream. As the time period increases to $7/8T$, and due to the low sucking velocity, the almost dragged downstream structure is regaining intensity and places again just downstream of the groove. The further downstream structure completely collapses while the remaining of one of the upstream structures can still be seen. The last time period characterises the end of the sucking phase, where the sucking velocity is zero, the former upstream and downstream structures have grown in size and a third smaller structure has been created just on the groove zone. This smaller structure will be blown away in the next time period, blowing phase.

Taking the blowing and suction phases globally and when the jet injection angle is of 124° , it can be said that the synthetic jet is creating around the jet zone several small laminar bubbles which keep appearing and disappearing while maintaining the flow outside this area rather attached to the airfoil. All information presented here is based on the 2D CFD RANS simulations. In fact, a further 3D-DNS set of simulations are needed to carefully evaluate the flow interaction just outlined in the present manuscript.

When maintaining the AoA at 6° but changing the jet injection angle to $\theta = 15^\circ$, which characterises the maximum lift case, the evolution of the flow around the jet area is presented in Fig. 1.19. From the comparison of Figs. 1.18 and 1.19 three main details are initially observed. When injecting at small angles, the groove position needs to be moved downstream, the groove width is reduced by over 66% and the eddies previously observed in Fig. 1.18, are now largely reduced. In fact, the vortical structures previously seen downstream of the groove are now completely gone. Regarding the upstream structures, two to three rather elongated eddies having a very small thickness are observed during the blowing phase, such structures almost disappear during the suction phase. Fig. 1.19 indicates the boundary layer thickness has to be thinner for the maximum lift case than for the

maximum efficiency case, which was analysed in Fig. 1.18, and this is exactly what Fig. 1.16 shows for this AoA.

The analysis of the vortex shedding phenomenon for the maximum efficiency case at AoA 14° and when the momentum coefficient was restricted to a maximum value of $C_\mu = 0.02$ is presented in Fig. 1.20. Blowing and suction phases are characterised by a set of vortical structures generated just downstream of the synthetic jet and rolling onto the airfoil surface. Their dimension grows as they move downstream and once the vortices reach the trailing edge they separate from the airfoil and are being shed downstream. From the observation of time periods between $1/8T$ and $4/8T$, it is seen that during the blowing phase the vortical structures simply move downstream. Very small vortical structures seem to be appearing at the end of the blowing phase. Seen from the airfoil leading edge, the first, rather circular, and the second, much elongated, vortical structures observed at $1/8T$, are approaching each other as they roll downstream, finally joining at time period $5/8T$, which is the beginning of The suction phase. At this particular time period, an elongated laminar bubble is observed just downstream

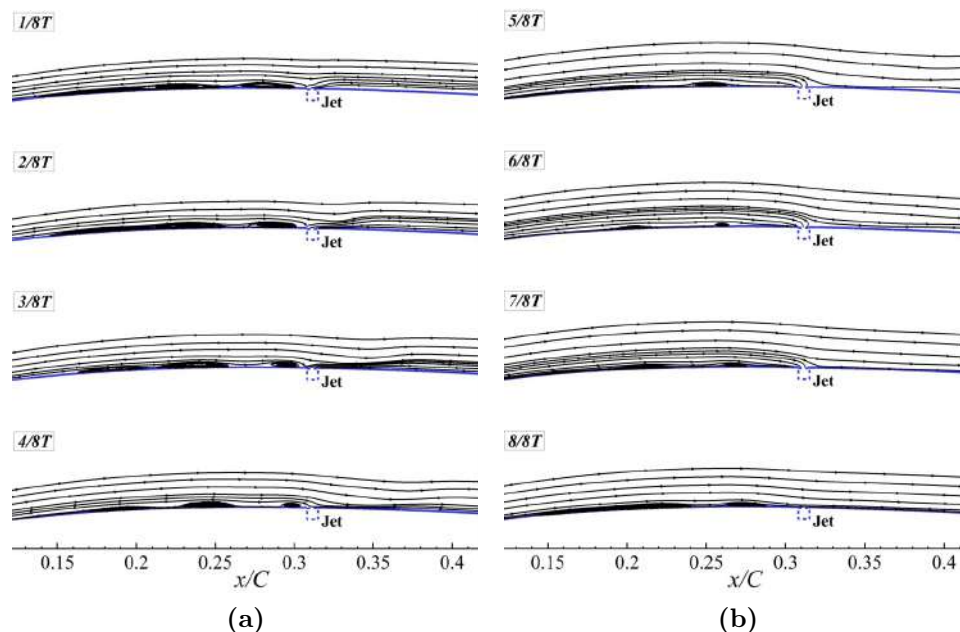


Figure 1.19: instantaneous velocity streamlines at different phases of synthetic jet for the maximum lift case at AoA 6° with $F^+ = 9.1$, $C_\mu = 0.0195$, $\theta = 15^\circ$, $x/C = 0.308$ and $h/C = 0.006$.

of the jet. In fact, this laminar bubble was initially observed as $3/8T$ and kept growing until reaching the actual time period. On the next time period, $6/8T$, where the suction velocity is maximum, the elongated laminar bubble previously seen wraps up generating a high intensity rounded vortex, which rolls downstream faster than the three smaller vortical structures initially generated at time period $2/8T$ and clearly seen downstream of the laminar bubble at $5/8T$. At time period $8/8T$ the high intensity vortical structure generated at $6/8T$, has already caught one of the three smaller vortical structures initially generated at $2/8T$, and it will take a full synthetic jet oscillation period until it will catch the remaining two small vortical structures, until reaching the time period $5/8T$. It can be concluded that the formation of the main vortical structures which will be shed downstream is due to the merging process of several small eddies initially generated at time period $2/8T$, with a higher intensity one generated at time period $6/8T$. This merging process takes a full synthetic jet oscillation cycle, counted from the moment the higher intensity vortex is created.

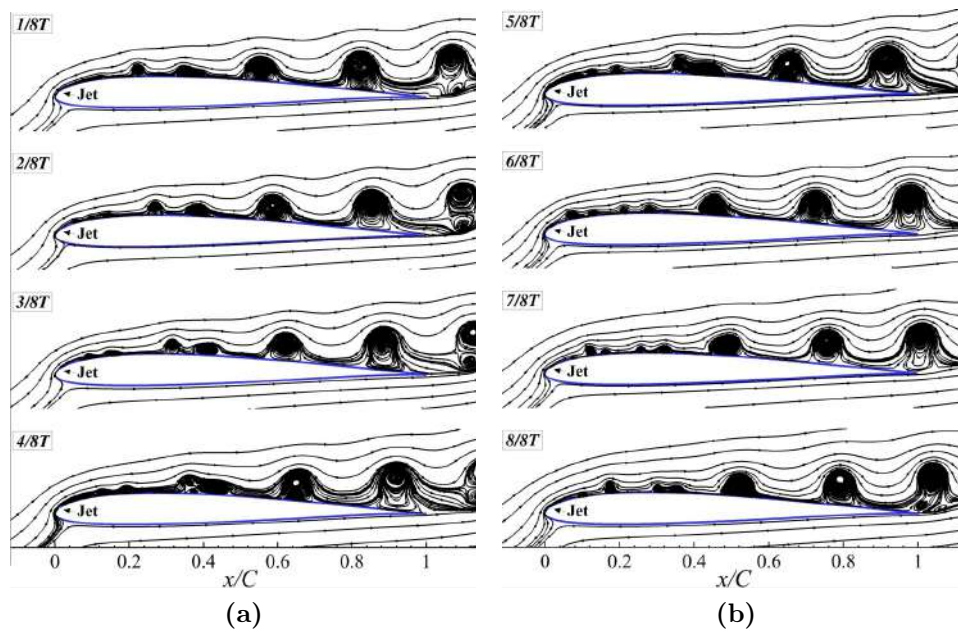


Figure 1.20: Instantaneous velocity streamlines at different phases of synthetic jet for the maximum efficiency case at AoA 14° with $F^+ = 2.4$, $C_\mu = 0.0055$, $\theta = 18^\circ$, $x/C = 0.0097$ and $h/C = 0.005$. Restricted momentum coefficient.

The final results presented in this paper, Fig. 1.21, characterise the maximum

efficiency case at AoA 14° but with the unrestricted momentum coefficient. In Table 1.7 it was already stated that for this particular case, the efficiency increase versus the baseline one was of 460%, notice that the efficiency increase associated with Fig. 1.20 was of 251%. Fig. 1.21 shows that regardless of the blowing or suction phase chosen, the streamlines are completely attached to the airfoil, just a small elongated laminar bubble slightly changing in size appears upstream of the jet groove. One of conclusions from this figure which is one of the conclusions of the present study is that if large momentum coefficients can be employed, the flow can be completely reattached to the airfoil surface. Nevertheless, we observed that the amount of energy required by this AFC actuation was not compensated by the energy saving due to the improved profile performance.

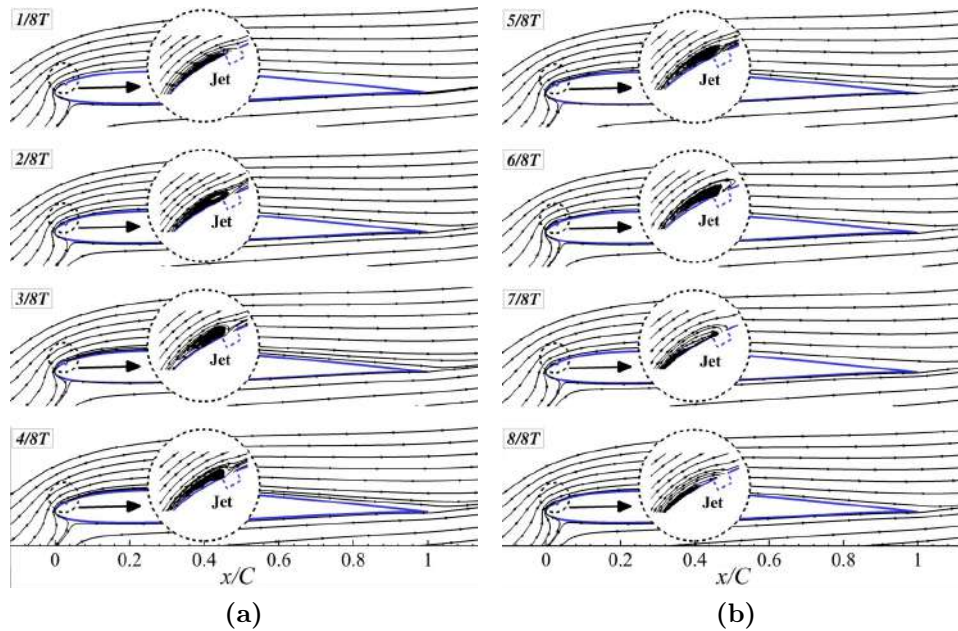


Figure 1.21: Instantaneous velocity streamlines at different phases of synthetic jet for the maximum efficiency case at AoA 14° with $F^+ = 5.2$, $C_\mu = 0.039$, $\theta = 15^\circ$, $x/C = 0.02764$ and $h/C = 0.005$. Unrestricted momentum coefficient.

1.7 Conclusions

The paper evaluates five AFC parameters and optimises their combination to obtain the maximum lift and efficiency for the SD7003 airfoil at three pre-stall and one post-stall AoA. The Reynolds number is kept constant at 6×10^4 .

The paper presents the results of over 2200 2D RANS simulations. 400 CFD cases were run for each of pre-stall AoA, 4° , 6° and 8° . 600 CFD cases were run at 14° with a restricted momentum coefficient and another 400 CFD cases were run at AoA 14° with an unrestricted momentum coefficient. A Genetic algorithm optimiser was linked with a mesh generator and a CFD solver in order to automatically perform the simulations for each new Genetic algorithm generation.

The use of an optimisation tool considering two objective functions, lift coefficient and efficiency, has allowed to obtain for each of the four studied AoA, a Pareto Front which contains all the optimum set of AFC parameters characterising the maximum efficiency, the maximum lift and their optimum combinations.

The use of AFC has improved the efficiency and lift coefficient under all studied angles of attack. The percentage of improvement of both parameters versus the baseline case values is particularly relevant at post-stall AoA.

An aerodynamic efficiency increase of almost 39% was obtained for an AoA of 8° . This efficiency was related to the following values for the different AFC parameters, non-dimensional frequency $F^+ = 9.3$, momentum coefficient $C_\mu = 0.0147$, jet angle 126° , jet position $12\%C$, $x/C = 0.12$ and jet width $1.3\%C$, $h/C = 0.013$. The efficiency increased to 251% when the AoA was 14° and using a restricted momentum coefficient, the AFC parameters associated were, $F^+ = 2.4$; $C_\mu = 0.0055$; $\theta = 18^\circ$, $x/C = 0.0097$ and $h/C = 0.005$. When using an unrestricted momentum coefficient at AoA of 14° , the efficiency increased to 460%, being the AFC parameters $F^+ = 5.2$; $C_\mu = 0.039$; $\theta = 15^\circ$, $x/C = 0.02764$ and $h/C = 0.005$.

To obtain a maximum aerodynamic efficiency, the synthetic jet optimum inclination angles at pre-stall AoA are about 125° . The jet inclination angles to obtain the maximum lift are around 15° . At post-stall AoA maximum lift and maximum efficiency are obtained when employing jet inclination angles around 18°

At pre-stall AoA the optimum position of the synthetic jet, to obtain the maximum efficiency, is inside the laminar separation bubble corresponding to each angle of attack. For the momentum coefficient restricted case at post-stall AoA, the groove needs to be located just where the separation point is. The momentum coefficient required is several times lower than the one needed at pre-stall AoA, yet the efficiency increase is much higher. For the unrestricted case at 14° , the jet location has moved further downstream, the required momentum coefficient is about seven times larger the one needed for the restricted case at the same AoA and the efficiency has now increased to 460% versus the base case one.

Large momentum coefficients are associated with high frequencies and vice-versa. The required jet width at post-stall AoA is about one third of the one required at pre-stall AoA.

The physics phenomenon characterising the interaction between the boundary layer and the pulsating jet flow is highly dependent on the jet inclination angle and the airfoil angle of attack. Despite the fact the simulations are two dimensional, a further insight into the interaction between the synthetic jet and the external flow is obtained. At pre-stall AoA and when using large injection angles, injecting upstream, a set of small vortical structures are observed. But when the injection angle is facing downstream, downstream vortical structures completely disappear. At post-stall AoA it has been demonstrated that injecting almost tangentially and employing large momentum coefficients completely reattaches the flow to the airfoil, hugely increasing its efficiency.

1.8 appendix

1.8.1 Full Pareto Front results, at all AoA

Table 1.1: All the Optimum cases of Pareto Front at 4°

F^+	C_μ	θ°	x/C	h/C	C_l	$C_l\%$	C_d	η	$\eta\%$
9.4	0.0193	15	0.021	0.013	0.6185	5.76	0.0317	19.51	-35.61
8.4	0.0183	15	0.020	0.013	0.6141	5.01	0.0314	19.56	-35.44
8.4	0.0134	16	0.111	0.012	0.6047	3.40	0.0297	20.34	-32.84
8.4	0.0134	15	0.131	0.012	0.6019	2.92	0.0295	20.37	-32.75

8.7	0.0121	15	0.131	0.013	0.5987	2.39	0.0289	20.70	-31.70
8.4	0.0135	111	0.307	0.015	0.5867	0.32	0.0177	33.09	9.20
8.4	0.0121	111	0.307	0.012	0.5854	0.10	0.0170	34.26	13.07
8.3	0.0178	110	0.313	0.018	0.5846	-0.03	0.0162	35.94	18.62
8.8	0.0193	109	0.313	0.018	0.5845	-0.04	0.016	36.54	20.59
8.2	0.0177	111	0.313	0.017	0.5843	-0.07	0.0158	36.77	21.35
8.2	0.0178	111	0.313	0.017	0.5843	-0.07	0.0158	36.81	21.51
7.2	0.0193	115	0.313	0.013	0.5826	-0.36	0.0145	39.92	31.76
8.7	0.019	114	0.313	0.018	0.5821	-0.44	0.0143	40.58	33.93
8.5	0.0193	114	0.313	0.017	0.5821	-0.44	0.0143	40.64	34.14
8.8	0.019	115	0.313	0.017	0.5820	-0.46	0.0140	41.46	36.85
8.8	0.0185	119	0.313	0.015	0.5809	-0.65	0.0133	43.64	44.02
8.8	0.0185	119	0.309	0.016	0.5803	-0.75	0.0132	43.66	44.12
8.8	0.0185	120	0.308	0.015	0.5802	-0.77	0.0132	43.92	44.97
9.2	0.0184	121	0.313	0.019	0.5800	-0.80	0.0127	45.53	50.29
7.3	0.0199	123	0.313	0.017	0.5799	-0.83	0.0125	46.07	52.05
8.7	0.0185	123	0.313	0.019	0.5795	-0.89	0.0122	47.15	55.61
8.8	0.0194	123	0.313	0.017	0.5795	-0.90	0.0122	47.43	56.53
9.4	0.0199	123	0.313	0.017	0.5790	-0.99	0.0121	47.78	57.69
8.8	0.0194	125	0.313	0.019	0.5787	-1.04	0.0117	49.45	63.21
7.1	0.0187	133	0.313	0.019	0.5754	-1.60	0.0111	51.78	70.91
7.1	0.0187	133	0.312	0.019	0.5752	-1.63	0.0110	51.95	71.48
7.1	0.0187	133	0.311	0.019	0.5748	-1.70	0.0110	52.02	71.68
8.8	0.0194	131	0.313	0.019	0.5747	-1.71	0.0109	52.54	73.41
8.8	0.0194	132	0.313	0.019	0.5740	-1.84	0.0108	52.86	74.45
baseline					0.5848		0.0193	30.30	

Table 1.2: All the Optimum cases of Pareto Front at 6°

F^+	C_μ	θ°	x/C	h/C	C_l	$C_l\%$	C_d	η	$\eta\%$
9.1	0.0195	15	0.308	0.006	0.8371	9.14	0.0338	24.76	-22.50
9.1	0.0195	15	0.308	0.007	0.8370	9.13	0.0337	24.79	-22.41
9.1	0.0192	15	0.308	0.006	0.8363	9.03	0.0336	24.88	-22.13
9.1	0.0195	19	0.308	0.006	0.8360	9	0.0332	25.17	-21.22
9.1	0.0195	23	0.307	0.006	0.8345	8.80	0.0327	25.46	-20.31
9.1	0.0195	24	0.313	0.007	0.8344	8.79	0.0327	25.48	-20.25
9.1	0.0192	23	0.307	0.006	0.8337	8.70	0.0326	25.58	-19.93
9.1	0.0195	34	0.307	0.006	0.8311	8.36	0.0317	26.21	-17.96
9.1	0.0198	40	0.307	0.006	0.8310	8.34	0.0310	26.73	-16.33

9	0.0199	47	0.308	0.006	0.8307	8.31	0.0300	27.68	-13.36
9.1	0.0195	47	0.308	0.006	0.8297	8.17	0.0297	27.87	-12.77
9.1	0.0195	55	0.308	0.006	0.8263	7.73	0.0286	28.90	-9.55
9.1	0.0195	59	0.308	0.006	0.8241	7.44	0.0280	29.43	-7.88
9.1	0.0194	59	0.308	0.006	0.8238	7.40	0.0279	29.46	-7.79
9.1	0.0195	62	0.308	0.006	0.8220	7.17	0.0276	29.78	-6.79
9.2	0.0194	66	0.311	0.006	0.8183	6.68	0.0267	30.56	-4.35
9.1	0.0158	64	0.308	0.005	0.8121	5.88	0.0254	31.88	-0.22
9.1	0.0144	64	0.308	0.005	0.8076	5.29	0.0249	32.39	1.38
9.3	0.0194	82	0.311	0.007	0.8071	5.22	0.0233	34.54	8.10
9.3	0.0194	83	0.311	0.007	0.8066	5.16	0.0231	34.84	9.05
9.3	0.0177	82	0.311	0.007	0.8050	4.95	0.0230	34.92	9.29
9.2	0.0158	82	0.308	0.008	0.8046	4.90	0.0225	35.76	11.92
9.2	0.0158	85	0.305	0.009	0.8031	4.70	0.0219	36.58	14.49
9.2	0.0194	91	0.309	0.008	0.8027	4.65	0.0214	37.47	17.27
9.2	0.0194	94	0.311	0.009	0.7989	4.16	0.0212	37.63	17.78
9.2	0.0155	94	0.311	0.009	0.7952	3.68	0.0211	37.67	17.90
9.2	0.0154	95	0.306	0.009	0.7948	3.62	0.0209	37.95	18.78
9.2	0.0155	99	0.309	0.010	0.7918	3.23	0.0205	38.55	20.66
9.2	0.0192	105	0.305	0.018	0.7895	2.93	0.0195	40.34	26.26
9.2	0.0192	106	0.305	0.018	0.7890	2.87	0.0193	40.73	27.48
9.2	0.0192	112	0.305	0.018	0.7849	2.33	0.0184	42.59	33.30
9.2	0.0192	113	0.305	0.018	0.7840	2.21	0.0183	42.77	33.86
9.2	0.0194	119	0.250	0.019	0.7810	1.82	0.0167	46.69	46.13
9.2	0.0194	123	0.250	0.019	0.7805	1.76	0.0155	50.07	56.71
<u>9.2</u>	<u>0.0194</u>	<u>124</u>	<u>0.250</u>	<u>0.019</u>	<u>0.7802</u>	<u>1.72</u>	<u>0.0153</u>	<u>50.85</u>	<u>59.15</u>
baseline					0.767	0.0240	31.95		

Table 1.3: All the Optimum cases of Pareto Front at 8°

F^+	C_μ	θ°	x/C	h/C	C_l	$C_l\%$	C_d	η	$\eta\%$
<u>8</u>	<u>0.0058</u>	<u>67</u>	<u>0.116</u>	<u>0.015</u>	<u>1.043</u>	<u>11.45</u>	<u>0.0504</u>	<u>20.66</u>	<u>-27.66</u>
8	0.0058	68	0.114	0.015	1.040	11.42	0.0502	20.72	-27.47
7.8	0.0056	68	0.120	0.014	1.039	11.20	0.0498	20.85	-27.02
8.1	0.0058	69	0.120	0.014	1.037	11.02	0.0480	21.57	-24.50
7.8	0.0057	68	0.120	0.007	1.030	10.27	0.0468	22.01	-22.96
7.4	0.0057	68	0.120	0.007	1.026	9.89	0.0440	23.27	-18.55
7.4	0.0056	68	0.120	0.007	1.026	9.85	0.0440	23.30	-18.44
9.9	0.0147	31	0.173	0.007	1.002	7.28	0.0341	29.33	2.66

9.9	0.011	30	0.169	0.013	0.988	5.78	0.0328	30.08	5.28
7.4	0.0104	26	0.173	0.006	0.985	5.46	0.0327	30.08	5.28
7.4	0.0098	30	0.173	0.006	0.982	5.14	0.0323	30.41	6.44
7.7	0.0059	67	0.167	0.005	0.967	3.53	0.0293	32.92	15.22
7.7	0.0058	69	0.166	0.005	0.967	3.53	0.0291	33.14	15.99
7.7	0.0059	71	0.166	0.005	0.967	3.53	0.0291	33.15	16.03
9.3	0.0049	128	0.122	0.014	0.950	1.71	0.0265	35.82	25.37
9.1	0.0056	128	0.122	0.016	0.950	1.71	0.0264	35.97	25.90
9.3	0.0096	126	0.122	0.014	0.948	1.50	0.0253	37.37	30.80
9.4	0.0098	128	0.120	0.014	0.947	1.40	0.0251	37.71	31.99
9.2	0.0121	127	0.123	0.014	0.947	1.40	0.0245	38.65	35.28
9.4	0.0121	128	0.121	0.013	0.946	1.28	0.0244	38.74	35.59
<u>9.3</u>	<u>0.0147</u>	<u>126</u>	<u>0.122</u>	<u>0.013</u>	<u>0.946</u>	<u>1.28</u>	<u>0.0238</u>	<u>39.71</u>	<u>39</u>
baseline					0.934		0.0327	28.57	

Table 1.4: All the Optimum cases of Pareto Front at 14° (restricted momentum coefficient)

F^+	C_μ	θ°	x/C	h/C	C_l	$C_l\%$	C_d	η	$\eta\%$
1.5	0.0051	44	0.0082	0.005	1.3435	68.36	0.1343	10	156.41
1.5	0.0052	44	0.0082	0.005	1.3433	68.33	0.1343	10	156.41
1.5	0.0061	43	0.0082	0.005	1.3403	67.96	0.1318	10.17	60.77
1.5	0.0054	43	0.0082	0.005	1.3123	64.45	0.1232	10.65	173.07
1.5	0.0052	43	0.0082	0.005	1.3025	63.22	0.1223	10.65	173.07
1.6	0.0052	54	0.0089	0.005	1.2914	61.83	0.1207	10.70	174.35
1.6	0.0068	54	0.0089	0.005	1.2873	61.32	0.1190	10.81	177.18
2	0.0056	29	0.0097	0.005	1.2850	61.03	0.1108	11.59	197.18
2	0.0056	34	0.0097	0.005	1.2815	60.59	0.1104	11.60	197.43
2	0.0056	33	0.0097	0.005	1.2761	59.91	0.1099	11.61	197.69
2	0.0056	38	0.0097	0.005	1.2678	58.87	0.1086	11.67	199.23
2.3	0.0061	15	0.0089	0.005	1.2547	57.23	0.0962	13.04	234.36
2.4	0.0061	15	0.0089	0.005	1.2544	57.19	0.0925	13.56	247.69
2.4	0.0055	15	0.0089	0.005	1.1769	47.48	0.0859	13.69	251.02
<u>2.4</u>	<u>0.0055</u>	<u>18</u>	<u>0.0097</u>	<u>0.005</u>	<u>1.1702</u>	<u>46.64</u>	<u>0.0854</u>	<u>13.70</u>	<u>251.28</u>
baseline					0.798		0.204	3.90	

Table 1.5: All the Optimum cases of Pareto Front at 14° (unrestricted momentum coefficient)

F^+	C_μ	θ°	x/C	h/C	C_l	$C_l\%$	C_d	η	$\eta\%$
6.7	0.0985	15	0.0285	0.005	1.764	121	0.0966	18.24	367.69
6.8	0.098	15	0.0285	0.005	1.763	120.86	0.09625	18.31	369.48
4.7	0.0965	25	0.0285	0.005	1.750	119.32	0.09419	18.58	376.41
4.9	0.0965	25	0.0223	0.005	1.749	119.22	0.08777	19.93	411.02
6.7	0.0740	15	0.0276	0.005	1.706	113.79	0.08530	20.00	412.82
6.8	0.0645	15	0.0276	0.005	1.678	110.30	0.08091	20.74	431.79
6.7	0.0615	15	0.0276	0.005	1.668	109.06	0.07967	20.94	436.92
6.7	0.0565	15	0.0276	0.005	1.651	106.90	0.07748	21.31	446.41
7.4	0.0490	15	0.0285	0.005	1.624	103.48	0.07434	21.84	460
5.2	0.0390	15	0.0276	0.005	1.569	96.61	0.0717	21.86	460.5
baseline					0.798		0.204	3.90	

1.9 References

- [1] Louis N. Cattafesta and Mark Sheplak. Actuators for active flow control. Annual Review of Fluid Mechanics, 43(1):247–272, jan 2011. doi: 10.1146/annurev-fluid-122109-160634.
- [2] Li Wang and Fang bao Tian. Numerical simulation of flow over a parallel cantilevered flag in the vicinity of a rigid wall. Physical Review E, 99(5), may 2019. doi: 10.1103/physreve.99.053111.
- [3] Young-Chang Cho and Wei Shyy. Adaptive flow control of low-Reynolds number aerodynamics using dielectric barrier discharge actuator. Progress in Aerospace Sciences, 47(7):495–521, oct 2011. doi: 10.1016/j.paerosci.2011.06.005.
- [4] Saeed Foshat. Numerical investigation of the effects of plasma actuator on separated laminar flows past an incident plate under ground effect. Aerospace Science and Technology, 98:105646, mar 2020. doi: 10.1016/j.ast.2019.105646.

- [5] Nicolas Benard and Eric Moreau. Electrical and mechanical characteristics of surface AC dielectric barrier discharge plasma actuators applied to airflow control. Experiments in Fluids, 55(11), nov 2014. doi: 10.1007/s00348-014-1846-x.
- [6] N Benard, Jordi Pons-Prats, Jacques Periaux, Gabriel Bugada, P Braud, JP Bonnet, and E Moreau. Turbulent separated shear flow control by surface plasma actuator: experimental optimization by genetic algorithm approach. Experiments in Fluids, 57(2), jan 2016. doi: 10.1007/s00348-015-2107-3.
- [7] Masoud Baghaei and Josep M Bergada. Analysis of the forces driving the oscillations in 3d fluidic oscillators. Energies, 12(24):4720, dec 2019. doi: 10.3390/en12244720.
- [8] Masoud Baghaei and Josep M Bergada. Fluidic oscillators, the effect of some design modifications. Applied Sciences, 10(6):2105, mar 2020. doi: 10.3390/app10062105.
- [9] Ning Qin, Jacques Periaux, and Gabriel Bugada, editors. Advances in Effective Flow Separation Control for Aircraft Drag Reduction. Springer International Publishing, 2020. doi: 10.1007/978-3-030-29688-9.
- [10] Adel Abbas, Gabriel Bugada, Esteban Ferrer, Song Fu, Jacques Periaux, Jordi Pons-Prats, Eusebio Valero, and Yao Zheng. Drag reduction via turbulent boundary layer flow control. Science China Technological Sciences, 60(9): 1281–1290, 2017.
- [11] Ari Glezer and Michael Amitay. Synthetic jets. Annual review of fluid mechanics, 34(1):503–529, 2002.
- [12] Christopher Rumsey, Thomas Gatski, William Sellers, Veer Vatsa, and Sally Viken. Summary of the 2004 cfd validation workshop on synthetic jets and turbulent separation control. In 2nd AIAA Flow Control Conference, page 2217, 2004.
- [13] Israel Wygnanski. The variables affecting the control of separation by periodic excitation. In 2nd AIAA Flow Control Conference, page 2505, 2004.

- [14] N Findanis and NA Ahmed. The interaction of an asymmetrical localised synthetic jet on a side-supported sphere. Journal of Fluids and Structures, 24 (7):1006–1020, oct 2008. doi: 10.1016/j.jfluidstructs.2008.02.002.
- [15] MG De Giorgi, CG De Luca, A Ficarella, and F Marra. Comparison between synthetic jets and continuous jets for active flow control: Application on a NACA 0015 and a compressor stator cascade. Aerospace Science and Technology, 43:256–280, jun 2015. doi: 10.1016/j.ast.2015.03.004.
- [16] S Traficante, MG De Giorgi, and A Ficarella. Flow separation control on a compressor-stator cascade using plasma actuators and synthetic and continuous jets. Journal of Aerospace Engineering, 29(3):04015056, 2016.
- [17] Maria Grazia De Giorgi, Stefania Traficante, Carla De Luca, Daniela Bello, and Antonio Ficarella. Active flow control techniques on a stator compressor cascade: a comparison between synthetic jet and plasma actuators. In Turbo Expo: Power for Land, Sea, and Air, volume 44748, pages 439–450. American Society of Mechanical Engineers, 2012.
- [18] Hongxin Zhang, Shaowen Chen, Yun Gong, and Songtao Wang. A comparison of different unsteady flow control techniques in a highly loaded compressor cascade. Proceedings of the Institution of Mechanical Engineers, Part G: Journal of Aerospace Engineering, 233(6):2051–2065, 2019.
- [19] Michael Amitay, Douglas R Smith, Valdis Kibens, David E Parekh, and Ari Glezer. Aerodynamic flow control over an unconventional airfoil using synthetic jet actuators. AIAA Journal, 39:361–370, jan 2001. doi: 10.2514/3.14740.
- [20] Michael Amitay and Ari Glezer. Role of actuation frequency in controlled flow reattachment over a stalled airfoil. AIAA Journal, 40:209–216, jan 2002. doi: 10.2514/3.15052.
- [21] JL Gilarranz, LW Traub, and OK Rediniotis. A new class of synthetic jet actuators—part i: Design, fabrication and bench top characterization. Journal of Fluids Engineering, 127(2):367–376, mar 2005. doi: 10.1115/1.1839931.

- [22] Donghyun You and Parviz Moin. Active control of flow separation over an airfoil using synthetic jets. Journal of Fluids and Structures, 24(8):1349–1357, nov 2008. doi: 10.1016/j.jfluidstructs.2008.06.017.
- [23] Ashley Tuck and Julio Soria. Separation control on a NACA 0015 airfoil using a 2d micro ZNMF jet. Aircraft Engineering and Aerospace Technology, 80(2):175–180, mar 2008. doi: 10.1108/00022660810859391.
- [24] Vassili Kitsios, Laurent Cordier, Jean-Paul Bonnet, Andrew Ooi, and Julio Soria. On the coherent structures and stability properties of a leading-edge separated aerofoil with turbulent recirculation. Journal of Fluid Mechanics, 683:395–416, aug 2011. doi: 10.1017/jfm.2011.285.
- [25] NA Buchmann, C Atkinson, and Julio Soria. Influence of ZNMF jet flow control on the spatio-temporal flow structure over a NACA-0015 airfoil. Experiments in Fluids, 54(3), feb 2013. doi: 10.1007/s00348-013-1485-7.
- [26] Sang Hoon Kim and Chongam Kim. Separation control on NACA23012 using synthetic jet. Aerospace Science and Technology, 13(4-5):172–182, jun 2009. doi: 10.1016/j.ast.2008.11.001.
- [27] H Esmaili Monir, M Tadjfar, and A Bakhtian. Tangential synthetic jets for separation control. Journal of Fluids and Structures, 45:50–65, feb 2014. doi: 10.1016/j.jfluidstructs.2013.11.011.
- [28] Sebastian D Goodfellow, Serhiy Yarusevych, and Pierre E Sullivan. Momentum coefficient as a parameter for aerodynamic flow control with synthetic jets. AIAA Journal, 51(3):623–631, mar 2013. doi: 10.2514/1.j051935.
- [29] Mark A Feero, Sebastian D Goodfellow, Philippe Lavoie, and Pierre E Sullivan. Flow reattachment using synthetic jet actuation on a low-Reynolds-number airfoil. AIAA Journal, 53(7):2005–2014, jul 2015. doi: 10.2514/1.j053605.
- [30] Mark A Feero, Philippe Lavoie, and Pierre E Sullivan. Influence of synthetic jet location on active control of an airfoil at low Reynolds number. Experiments in Fluids, 58(8), jul 2017. doi: 10.1007/s00348-017-2387-x.

- [31] Wei Zhang and Ravi Samtaney. A direct numerical simulation investigation of the synthetic jet frequency effects on separation control of low-Re flow past an airfoil. Physics of Fluids, 27(5):055101, may 2015. doi: 10.1063/1.4919599.
- [32] Ivette Rodriguez, Oriol Lehmkuhl, and Ricard Borrell. Effects of the actuation on the boundary layer of an airfoil at Reynolds number $Re = 60000$. Flow, Turbulence and Combustion, 105(2):607–626, may 2020. doi: 10.1007/s10494-020-00160-y.
- [33] Régis Duvigneau and Michel Visonneau. Simulation and optimization of stall control for an airfoil with a synthetic jet. Aerospace Science and Technology, 10(4):279–287, may 2006. doi: 10.1016/j.ast.2006.01.002.
- [34] Virginia Joanne Torczon. Multidirectional search: a direct search algorithm for parallel machines. PhD thesis, Rice University, 1989. URL <https://hdl.handle.net/1911/16304>.
- [35] Régis Duvigneau, A Hay, and M Visonneau. Optimal location of a synthetic jet on an airfoil for stall control. Journal of Fluids Engineering, 129(7):825–833, jan 2007. doi: 10.1115/1.2742729.
- [36] Dj Kamari, M Tadjfar, and A Madadi. Optimization of sd7003 airfoil performance using tbl and cbl at low reynolds numbers. Aerospace Science and Technology, 79:199–211, 2018.
- [37] Mehran Tadjfar and Dj Kamari. Optimization of flow control parameters over SD7003 airfoil with synthetic jet actuator. Journal of Fluids Engineering, 142(2), oct 2020. doi: 10.1115/1.4044985.
- [38] Michael S Selig, John Francis Donovan, and David B Fraser. Airfoils at low speeds. HA Stokely, 1989.
- [39] M Selig, JJ Guglielmo, AP Broeren, and P Giguere. Summary of low-speed airfoil data summary of low-speed airfoil data. Tech. rep., University of Illinois, 1995.

- [40] Marshall Galbraith and Miguel Visbal. Implicit large eddy simulation of low Reynolds number flow past the SD7003 airfoil. In 46th AIAA Aerospace Sciences Meeting and Exhibit, page 225. American Institute of Aeronautics and Astronautics, jan 2008. doi: 10.2514/6.2008-225.
- [41] Sebastian Burgmann and W Schröder. Investigation of the vortex induced unsteadiness of a separation bubble via time-resolved and scanning piv measurements. Experiments in fluids, 45(4):675, 2008.
- [42] Wei Zhang, Rainer Hain, and Christian J Kähler. Scanning piv investigation of the laminar separation bubble on a sd7003 airfoil. Experiments in Fluids, 45(4):725–743, 2008.
- [43] P Catalano and R Tognaccini. Turbulence modeling for low-Reynolds-number flows. AIAA Journal, 48(8):1673–1685, aug 2010. doi: 10.2514/1.j050067.
- [44] P Catalano and R Tognaccini. Rans analysis of the low-reynolds number flow around the sd7003 airfoil. Aerospace Science and Technology, 15(8):615–626, 2011.
- [45] Wei Wang, Spiridon Siouris, and Ning Qin. Hybrid RANS/LES for active flow control. Aircraft Engineering and Aerospace Technology, 86(3):179–187, apr 2014. doi: 10.1108/aeat-01-2013-0012.
- [46] Joel H Ferziger, Milovan Perić, and Robert L Street. Computational methods for fluid dynamics, volume 3. Springer, 2002.
- [47] Philippe Spalart and Steven Allmaras. A one-equation turbulence model for aerodynamic flows. In 30th aerospace sciences meeting and exhibit, page 439, 1992. doi: 10.2514/6.1992-439.
- [48] Hans-Paul Schwefel. Numerical Optimization of Computer Models. John Wiley & Sons, Inc., USA, 1981. ISBN 0471099880.
- [49] David G Luenberger, Yinyu Ye, et al. Linear and nonlinear programming, volume 2. Springer, 1984. doi: 10.1007/978-3-319-18842-3.

- [50] Dong-Seop Lee, Jacques Periaux, Jordi Pons-Prats, Gabriel Bugada, and Eugenio Oñate. Double shock control bump design optimization using hybridised evolutionary algorithms. In Evolutionary Computation (CEC), 2010 IEEE Congress on, pages 1–8. IEEE, 2010. doi: 10.1109/cec.2010.5586379.
- [51] Dong-Seop Lee, Jacques Periaux, Eugenio Onate, Luis F Gonzalez, and N Qin. Active transonic aerofoil design optimization using robust multiobjective evolutionary algorithms. Journal of Aircraft, 48(3):1084–1094, may 2011. doi: 10.2514/1.c031237.
- [52] DS Lee, LF Gonzalez, Jacques Periaux, and Gabriel Bugada. Double-shock control bump design optimization using hybridized evolutionary algorithms. Proceedings of the Institution of Mechanical Engineers, Part G: Journal of Aerospace Engineering, 225(10):1175–1192, jul 2011. doi: 10.1177/0954410011406210.
- [53] A Kendell Atkinson. An introduction to numerical analysis, 1988.
- [54] David Edward Goldberg. Genetic Algorithms in Search, Optimization and Machine Learning. Addison-Wesley, Reading, Massachusetts, January 1989.
- [55] Kalyanmoy Deb, Amrit Pratap, and T. Meyarivan. Constrained test problems for multi-objective evolutionary optimization. In Lecture Notes in Computer Science, pages 284–298. Springer Berlin Heidelberg, 2001.
- [56] DongSeop Lee, Luis Felipe Gonzalez, Jacques Periaux, Karkenahalli Srinivas, and Eugenio Onate. Hybrid-game strategies for multi-objective design optimization in engineering. Computers and Fluids, 47(1):189 – 204, 2011. ISSN 0045-7930. doi: <http://dx.doi.org/10.1016/j.compfluid.2011.03.007>.
- [57] Dong-Seop Lee, Luis F Gonzalez, Jacques Periaux, and Kavita Srinivas. Evolutionary optimisation methods with uncertainty for modern multidisciplinary design in aeronautical engineering. In Notes on Numerical Fluid Mechanics and Multidisciplinary Design, pages 271–284. Springer Berlin Heidelberg, 2009.

- [58] DongSeop Lee, Luis Felipe Gonzalez, Jacques Periaux, and Karkenahalli Srinivas. Efficient hybrid-game strategies coupled to evolutionary algorithms for robust multidisciplinary design optimization in aerospace engineering. IEEE Transactions on Evolutionary Computation, 15(2):133–150, apr 2011. doi: 10.1109/tevc.2010.2043364.
- [59] Roberto Lopez and Eugenio Oñate. A variational formulation for the multi-layer perceptron. In Artificial Neural Networks – ICANN 2006, pages 159–168. Springer Berlin Heidelberg, 2006.
- [60] David JJ Toal, Neil W Bressloff, and Andy J Keane. Kriging hyperparameter tuning strategies. AIAA Journal, 46(5):1240–1252, may 2008. doi: 10.2514/1.34822.
- [61] David JJ Toal and Andy J Keane. Efficient multipoint aerodynamic design optimization via cokriging. Journal of Aircraft, 48(5):1685–1695, sep 2011. doi: 10.2514/1.c031342.
- [62] Kalyanmoy Deb, Amrit Pratap, Sameer Agarwal, and TAMT Meyarivan. A fast and elitist multiobjective genetic algorithm: NSGA-II. IEEE transactions on evolutionary computation, 6(2):182–197, Apr 2002. ISSN 1089-778X. doi: 10.1109/4235.996017.
- [63] John Henry Holland. Adaptation in natural and artificial systems: an introductory analysis with applications to biology, control, and artificial intelligence. MIT Press, Cambridge, Massachusetts, January 1992.
- [64] David E Goldberg and John Henry Holland. Genetic algorithms and machine learning. Machine Learning, 3:95–99, 1988. doi: 10.1023/A:1022602019183.
- [65] Kalyanmoy Deb and Ram Bhushan Agrawal. Simulated binary crossover for continuous search space. Complex systems, 9(2):115–148, 1995.
- [66] Kalyanmoy Deb. Multi-objective optimization using evolutionary algorithms, volume 16. John Wiley & Sons, Chichester, UK, 2001.

Chapter 2

Large Eddy Simulation of Optimal Synthetic Jet Actuation on a SD7003 airfoil in post-stall conditions

2.1 Abstract

Aerodynamic performances may be optimised by the appropriate tuning of Active Flow Control (AFC) parameters. For the first time, we couple Genetic Algorithms (GA) with an unsteady Reynolds-Averaged Navier-Stokes (RANS) solver using the Spalart-Allmaras (SA) turbulence model to maximise lift and aerodynamic efficiency of an airfoil in stall conditions [1], and then validate the resulting set of optimal Synthetic Jet Actuator (SJA) parameters against well-resolved three-dimensional Large Eddy Simulation (LES). The airfoil considered is the SD7003, at the Reynolds number $Re = 6 \times 10^4$ and the post-stall angle of attack $\alpha = 14^\circ$. We find that, although SA-RANS is not quite as accurate as LES, it can still predict macroscopic aggregates such as lift and drag coefficients, provided the free-stream turbulence is prescribed to reasonable values. The sensitivity to free-stream turbulence is found to be particularly critical for SJA cases. Baseline LES simulation agrees well with literature results, while RANS-SA would seem to remain a valid model to a certain degree. For optimally actuated cases, our LES simulation predicts far better performances than obtained by suboptimal SJA LES computations

as reported by other authors [2] for the same airfoil, Re and α , which illustrates the applicability and effectiveness of the SJA optimisation technique applied, despite using the less accurate yet computationally faster SA-RANS. The flow topology and wake dynamics of baseline and SJA cases are thoroughly compared to elucidate the mechanism whereby aerodynamic performances are enhanced.

2.2 Introduction

Active Flow Control (AFC) may be applied to airfoils and wings to suppress or postpone flow separation thereby improving aerodynamic performance. One of the main advantages of AFC as compared to passive flow control is that no drag penalty is incurred in off-design conditions. AFC techniques usually fall in one of three different categories [3], namely moving body, plasma and fluidic actuation. Moving body actuators act on the geometry of the body to inject momentum into the flow [4]. Plasma actuators generate fast temporal response jets of ionized fluid by applying large electric potential differences [5, 6, 7, 8, 9]. Fluidic actuators (FA), which are by far the most common, inject/suck fluid to/from the boundary layer.

Among fluidic actuators, Synthetic Jet Actuators (SJA, sometimes also called Zero Net Mass Flow Actuators ZNMFA) are of particular interest because of their simplicity and demonstrated capability of suppressing flow separation [10, 11, 12, 13, 14]. For instance, SJAs have been shown more effective than Continuous Jet Actuators (CJA) at comparable power input levels in improving the performances of a stator compressor cascade [15, 16, 17, 18, 19]. SJAs do not require an external fluid supply, since their zero net mass flux can be simply obtained with an oscillating membrane (or reciprocating piston) housed inside a tiny cavity just beneath the surface. The back and forth displacement of the membrane alternatively sucks low momentum fluid from the near-wall and injects the fluid back with increased momentum.

A large number of numerical and experimental studies involving SJA implementation on airfoils has been published over the last couple of decades. Most of the research focuses on assessing the combined effect of two SJA parameters, namely the actuation frequency f_j and the jet momentum coefficient C_μ . The

former is nondimensionalised with the airfoil chord C and the free-stream velocity U_∞ following $f_j/(U_\infty/C)$, while the momentum coefficient is defined as $C_\mu = (\rho_j U_j^2 h_j \sin \theta_j)/(\rho_\infty U_\infty^2 C)$, with h_j the jet width, ρ_j and ρ_∞ the jet and far field fluid densities, respectively, U_j the maximum jet velocity and θ_j the jet inclination angle with respect to the surface.

One of the first experimental studies looking into the effect on flow separation over an unconventional symmetric airfoil of the momentum coefficient, frequency and position of a synthetic jet actuator was undertaken by Amitay et al. [19], Amitay and Glezer [20]. They found that placing the actuator close to the boundary layer separation point minimised the momentum coefficient required for flow reattachment. Actuating with frequencies of the same order of magnitude as the natural von Kármán vortex-shedding frequency ($f_j \sim f_{vK} \simeq 0.7U_\infty/C$) produced unsteady reattachment, while full flow reattachment could be obtained by actuating at about ten times the vortex-shedding frequency ($f_j/f_{vK} \sim \mathcal{O}(10)$).

The effect of SJA on a NACA0015 airfoil at $Re = 8.96 \times 10^5$ was studied experimentally by Gilarranz et al. [21] and numerically (using LES) by You and Moin [22]. In the experiments, while actuation was rather ineffective below $\alpha \leq 10^\circ$, its effectiveness was seen to largely improve at higher values of α , managing to push the stall angle of attack from $\alpha_s = 12^\circ$ to 18° . At $\alpha > 25^\circ$ the required actuation frequencies needed to obtain high lift coefficients were particularly large. Numerical simulations produced a 70% lift increase for SJA AFC parameters $C_\mu = 0.0123$, $f_j = 1.284U_\infty/C$ and $\theta_{revPj} = 30.2^\circ$ with respect to baseline. The same airfoil was experimentally analysed by Tuck and Soria [23] at the lower $Re = 3.9 \times 10^4$, and then simulated numerically via LES [24]. Maximum efficiency was obtained for SJA frequencies $f_j = 0.65U_\infty/C$ and 1.3 in the experiments, intermediate values being not quite so effective. The combination of $C_\mu = 0.0123$ momentum coefficient with the highest frequency delayed stall from $\alpha_s = 10^\circ$ for baseline to 18° . The numerical simulations revealed that the optimal frequencies coincided with the baseline shedding frequency (f_{vK}) and its first harmonic ($2f_{vK}$). The same particulars were observed again by Buchmann et al. [25] in their high-repetition-rate PIV experiments. Itsariyapinyo and Sharma [26] revisited the same airfoil at $Re = 1.1 \times 10^5$ with LES simulations of SJA acting tangentially to the surface precisely at the trailing edge. The lift coefficient was seen to increase

linearly when raising the momentum coefficient up to a certain threshold, beyond which point further improvement slowed down and saturated.

Kim and Kim [27] applied flow separation control to a NACA23012 airfoil at $Re = 2.19 \times 10^6$ and $\alpha \in [6^\circ, 22^\circ]$ in 5 different slat/flap/jet configurations using the Reynolds-averaged Navier-Stokes (RANS) equations and the $k-\omega$ SST turbulence model. Low actuation frequencies were found the most adequate to the reduction of the large separated regions, while the jet momentum coefficients required were large. They proposed the implementation of multi-array/multi-location SJA to reduce the required jet velocity, a solution that was successful. The same airfoil and Reynolds number were addressed by Monir et al. [28] in two different configurations using RANS and the Spalart-Allmaras turbulence model. They found that while SJA actuation at $\theta_j = 43^\circ$ could improve aerodynamic efficiency substantially, tangential actuation was by far the optimum.

Experimental studies to evaluate the effects of SJA on separation control and wake topology on a NACA0025 airfoil at $Re = 10^5$ and $\alpha = 5^\circ$ were undertaken by Goodfellow et al. [29]. They noticed that momentum coefficient was the primary control parameter, and obtained up to 50% drag decrease with C_μ above a certain threshold. The same airfoil at the same Reynolds number was analyzed by Feero et al. [30], but at the higher $\alpha = 10^\circ$. They reported that momentum coefficients required for flow reattachment were one order of magnitude lower for excitation frequencies about the vortex shedding frequency than for high frequencies. In a later study they considered the effects of jet location at the still larger $\alpha = 12^\circ$ [31]. Flow control was all the more effective by locating the jet slot in the vicinity of the natural separation point. Zhang and Samtaney [32] investigated the dependence of SJA efficacy on excitation frequency for a NACA0018 airfoil at $\alpha = 10^\circ$ and ultralow $Re = 1000$ using three-dimensional Direct Numerical Simulation (DNS). Three different frequencies were assessed ($f_j = 0.5U_\infty/C$, 1 and 4) and, although aerodynamic performances improved in all cases, $f_j = 1U_\infty/C$ was found the optimal.

As an airfoil specifically designed for low Reynolds number applications, the Selig-Donovan 7003 (SD7003) [33, 34] has been recently investigated at $Re = 6 \times 10^4$ employing LES [35, 36, 2]. Breuer [35] tested several inlet turbulence

intensities, ranging from nil to $Tu = 11\%$, at $\alpha = 4^\circ$ with the object of understanding its impact on the Laminar Separation Bubble (LSB). He concluded that high Tu values managed to reduce and even suppress the LSB, thereby enhancing aerodynamic performance. Freestream unsteadiness effects were also assessed by Qin et al. [36], this time by exploring different inlet velocity oscillation amplitudes and frequencies, at the same $\alpha = 4^\circ$. Flow separation was delayed and even suppressed during the acceleration phase, while the separation point progressed upstream towards the leading edge in the deceleration phase. Rodriguez et al. [2] applied SJA AFC to the SD7003 in their LES simulations at $\alpha = \{4^\circ, 11^\circ, 14^\circ\}$ and obtained an aerodynamic efficiency increase of up to $\Delta\eta/\eta = 124\%$ at the highest α , actuation being less effective at pre-stall angles of attack.

All research on SJA AFC application to airfoils discussed so far was limited to straightforward parametric explorations merely intended to elucidate the separate effects of the various actuation parameters on aerodynamic performance. There exist, however, a number of studies aiming at systematic optimisation. Duvigneau and Visonneau [37] optimised SJA non-dimensional frequency, velocity amplitude and injection angle on a NACA0015 airfoil at $Re = 8.96 \times 10^5$ and for a range of $\alpha \in [12^\circ, 24^\circ]$. To do so, they coupled their flow solver with an optimisation algorithm first developed by Torczon [38]. An optimum choice of the three SJA parameters produced a lift increase of 34% and a stall angle delay from $\alpha_s = 19^\circ$ to 22° . A study of SJA on a NACA0012 airfoil at $Re = 2 \times 10^6$ and $\alpha = \{18^\circ, 20^\circ\}$ followed shortly after that employed a derivative-free algorithm to find the optimal location for actuation [39]. The influence of jet location on lift was remarkable at $\alpha = 20^\circ$, with up to 57% increase, but not so noticeable at 18° .

Kamari et al. [40] optimised constant blowing and constant suction on the SD7003 airfoil at $Re = 6 \times 10^4$ by coupling Genetic Algorithms (GA) with Artificial Neural Networks (ANN) previously trained with a set of almost 45 CFD runs. Optimal constant suction was shown more effective. The same numerical methods were applied to the same airfoil, at the same Reynolds number and SJA parameters by Tadjfar and Kamari [41], but at $\alpha = 13^\circ$ and 16° and with two alternative injection configurations, namely tangent and normal to the airfoil surface. Aerodynamic efficiency was the objective/target function. Optimal tangent

injection at $\alpha = 13^\circ$, produced an astonishing maximum aerodynamic efficiency increase of 591%.

Perhaps the latest, and possibly the most extensive, research in the field of AFC application to airfoils is the one undertaken by Tousi et al. [1]. Five SJA parameters were optimised in a coupled fashion for a SD7003 airfoil at $Re = 6 \times 10^4$ and several pre- and post-stall $\alpha = \{4^\circ, 6^\circ, 8^\circ, 14^\circ\}$ using GA and RANS. The key difference between Tadjfar and Kamari [41] and Tousi et al. [1] resides in the methodology employed. While the former used ANN to estimate most of the SJA AFC parameters, the latter based the entire optimization process on precise RANS-CFD simulations with the Spalart-Allmaras (SA) turbulence model, which enhances the accuracy of the results at the cost of incurring a high computational burden. This is the first time, to the best of our knowledge, that genetic algorithms have been coupled with an unsteady RANS CFD solver with the aim of optimally tuning a set of SJA AFC parameters to maximise aerodynamic performances of an airfoil in stall conditions. The resulting optimals could not at the time undergo validation against experiments or well-resolved simulations, nor were the flow mechanisms responsible for optimally enhancing aerodynamic performances examined in any detail.

The study presented here builds up on the optimal SJA AFC configurations found by Tousi et al. [1]. Their analysis implicitly relied on the dubious accuracy of RANS-SA simulations of massively detached wake flows and/or deploying SJA AFC. Literature recommendations as to the setup of computations in regards to the tuning of turbulence model parameters and the prescription of free-stream turbulent viscosity boundary conditions were blindly followed. Here we undertake the ensuing natural step and put the optimization results thus obtained to the test. We analyse optimal SJA on the SD7003 at $Re = 6 \times 10^4$, at a single post-stall $\alpha = 14^\circ$, with accurate, well-resolved, 3D-LES computations. The object is two-fold. On one side, we evaluate the reliability of RANS-SA simulation in assessing SJA application to airfoils in post-stall conditions at moderate Reynolds numbers. On the other hand, we exploit the higher accuracy of LES simulation to better understand the physics behind SJA AFC application to the SD7003 airfoil.

A wealth of numerical and experimental data is available on the literature for the SD7003 airfoil [see, for example, 33, 34, 42, 43, 44, 45, 46], which makes it a

particularly convenient choice for the study of AFC. The SD7003 is a thin airfoil with a thickness-to-chord ratio $t/C = 8.5\%$ that is often employed in micro air vehicles (MAV) intended to fly at moderate Reynolds numbers. A LSB forms on the suction side at low Reynolds number, even for low to moderate values of α . The strong adverse pressure gradient existing beyond the suction peak on the upper surface causes the laminar boundary layer to detach, but separation is shortly followed by turbulent transition and this induces reattachment. The LSB drifts towards the leading edge and shrinks as α increases. Above a critical value of α , however, the reattachment ceases to occur and the recirculation region bursts and extends into the wake, which results in a sharp drop of lift and a dramatic surge of aerodynamic drag.

The remainder of the paper is structured as follows. The governing equations for LES and RANS-SA turbulence models are presented in §2.3. Section §2.4 is devoted to the computational domain, boundary conditions and grid assessment. The results and conclusions are presented in §2.5 and §2.6, respectively.

2.3 Governing equations and numerical modeling

The Navier-Stokes equations for an incompressible Newtonian fluid of density ρ and dynamic viscosity μ ($\nu \equiv \mu/\rho$ is the kinematic viscosity) read

$$\nabla \cdot \mathbf{u} = 0, \quad (2.1)$$

$$\rho \frac{\partial \mathbf{u}}{\partial t} + \rho(\mathbf{u} \cdot \nabla)\mathbf{u} = -\nabla p + \nabla \cdot (\mu \nabla \mathbf{u}). \quad (2.2)$$

The advection term can be expressed in conservation form by applying the vector calculus identity $(\mathbf{u} \cdot \nabla)\mathbf{u} = \nabla \cdot (\mathbf{u} \otimes \mathbf{u}) - (\nabla \cdot \mathbf{u})\mathbf{u}$, where \otimes denotes the outer product and the divergence term cancels out due to incompressibility. Taking the ensemble average of the Navier-Stokes equation or applying spatial filtering, yields

$$\nabla \cdot \bar{\mathbf{u}} = 0, \quad (2.3)$$

$$\rho \frac{\partial \bar{\mathbf{u}}}{\partial t} + \rho \nabla \cdot (\bar{\mathbf{u}} \otimes \bar{\mathbf{u}} + \overline{\mathbf{u} \otimes \mathbf{u}}) = -\nabla \bar{p} + \nabla \cdot (\mu \nabla \bar{\mathbf{u}}), \quad (2.4)$$

where the linear averaging/filtering operator commutes with all operators but the nonlinear term. Switching back to the non-conservation form of the ensemble

averaged/filtered advective term following $\nabla \cdot (\bar{\mathbf{u}} \otimes \bar{\mathbf{u}}) = (\bar{\mathbf{u}} \cdot \nabla)\bar{\mathbf{u}} + (\nabla \cdot \bar{\mathbf{u}})\bar{\mathbf{u}}$ and rearranging terms, results in

$$\nabla \cdot \bar{\mathbf{u}} = 0, \quad (2.5)$$

$$\rho \frac{\partial \bar{\mathbf{u}}}{\partial t} + \rho(\bar{\mathbf{u}} \cdot \nabla)\bar{\mathbf{u}} = -\nabla \bar{p} + \nabla \cdot (\mu \nabla \bar{\mathbf{u}} - \overline{\rho \mathbf{u} \otimes \mathbf{u}}). \quad (2.6)$$

Here, $-\overline{\rho \mathbf{u} \otimes \mathbf{u}}$ is the Reynolds stress tensor, which must be modeled using a turbulence model for RANS or a subgrid scale (SGS) model in the case of LES. The turbulence models used in the present RANS and LES are the Spalart-Allmaras (SA) [47] and the Wall-Adapting Local Eddy-Viscosity (WALE) [48], respectively. The accuracy of the former was assessed as acceptable in an earlier study [1], but the choice of LES in the present study is based on its demonstrated capabilities in dealing with turbulent transition as well as unstructured grids [48]. The WALE model is based on a tensor invariant that reproduces correctly wall asymptotic behaviour.

Both turbulence models used by either of the CFD methods employed here approximate the Reynolds stress tensor using the Boussinesq hypothesis, which states that the deviatoric part of the tensor can be written as

$$-\overline{\mathbf{u} \otimes \mathbf{u}} - \frac{1}{3}(\nabla \cdot \mathbf{u})\mathbf{I} = -2\nu_t \mathbf{S}. \quad (2.7)$$

\mathbf{I} denotes the identity matrix, $\mathbf{S} = 1/2 (\nabla \bar{\mathbf{u}} + \nabla(\bar{\mathbf{u}})^T)$ is the rate-of-strain tensor, and ν_t is the turbulent kinematic viscosity scalar field, which is the target of the so-called turbulent viscosity models.

The RANS SA model solves a single transport equation for a modified form of the turbulent kinetic viscosity $\tilde{\nu}$ that is the same with ν_t everywhere but in the near-wall region where viscosity effects dominate. Both turbulent viscosities are related by $\nu_t = \tilde{\nu} f_{v1}$, where $f_{v1} = \chi^3 / (\chi^3 + C_{v1}^3)$, $\chi = \tilde{\nu} / \nu$ and $C_{v1} = 7.1$. On the other hand, the LES WALE model, instead of solving a transport equation for ν_t , it models it via SGS, based on the following expression

$$\nu_t = \nu_{sgs} = (C_w \Delta)^2 \frac{(\mathcal{S}^d : \mathcal{S}^d)^{3/2}}{(\mathbf{S} : \mathbf{S})^{5/2} + (\mathcal{S}^d : \mathcal{S}^d)^{5/4}} \quad (2.8)$$

where $\mathcal{S}^d = \frac{1}{2} [(\nabla \bar{\mathbf{u}})^2 + (\nabla(\bar{\mathbf{u}})^T)^2] - \frac{1}{3}(\nabla \cdot \bar{\mathbf{u}})^2 \mathbf{I}$ is the traceless symmetric part of the square of the velocity gradient tensor, $\Delta = \sqrt{\Delta x \Delta y \Delta z}$ is the cut-off width

used for filtering the flow field, and Δx , Δy and Δz denote grid sizing along the three orthonormal coordinates. The sole parameter of the model has been set to $C_w = 0.325$, which is a standard choice [49, 50]. For the RANS-SA optimisation simulations we initially set the free-stream turbulent viscosity to a very low value $\tilde{\nu}/\nu = 10^{-20}$ following Catalano and Tognaccini [51], who claimed that this was required to properly capture the LSB at low pre-stall α , only to find out at the end that the choice was not the most appropriate for post-stall actuated cases.

Numerical computations have been carried out using the OpenFOAM [52] computational fluid dynamics (CFD) solver, which is based on the finite volume method (FVM). LES has been implemented on an unstructured grid using the Linear-Upwind Stabilized Transport (LUST) [52] scheme in discretising the non-linear advective term. This scheme stabilizes the solutions while retaining second-order accuracy. Second-order central-differences has been employed for the diffusive term, and an implicit second-order Backward Euler method has been chosen for evolving the equations in time. The pressure-velocity coupling problem has been tackled by the Pressure-Implicit algorithm with Splitting of Operators (PISO) [53]. The stopping criteria for both the pressure and velocity residuals was 10^{-6} .

For the RANS SA simulations, the same discretization methods were used as for the preliminar optimisation study by Tousi et al. [1]. These were second order discretization schemes for all parameters, and the pressure-velocity coupling PISO scheme, which can cope with transient simulations as required. The averaged solutions presented in the results section, obtained from either LES or SA simulations, are all considered after all initial transients have been overcome.

Each one of the 360 RANS computations required about 84CPUh of supercomputing time at Marenstrum IV – Barcelona Supercomputing Centre, while LES cases consumed 660kCPUh apiece.

2.4 Domain, boundary conditions and mesh validation

For simplicity, the SD7003 chord length has been taken as $C = 1$ and the free-stream velocity as $U_\infty = 1$ so that the Reynolds number is simply set as $Re =$

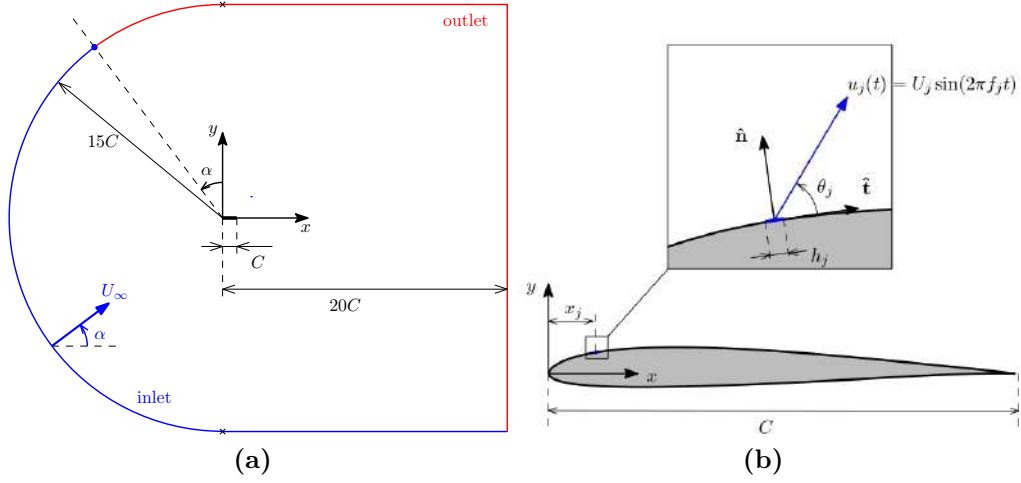


Figure 2.1: (a) Computational domain. (b) Synthetic jet parameters.

$U_\infty C/\nu = 1/\nu = 6 \times 10^4$ and all simulation parameters (including time and space coordinates) and results are already non-dimensional with length and time-scales C and C/U_∞ , respectively. The computational domain used for both LES and RANS simulations is depicted in Fig. 2.1. The airfoil (thick black line) is placed with its chord line horizontal and its leading edge at the coordinate origin $(x, y, z) \equiv (0, 0, 0)$. The two-dimensional spanwise projection of the domain is delimited upstream by a half circle of radius $R = 15$ and centered at the origin, two horizontal lines above and below at $y = \pm 15$ and a vertical line downstream at $x = 20$. The angle of attack is prescribed by tilting the inlet velocity, so that the inlet (blue line) and outlet (red) boundaries are not coincident with the geometrical elements just described (Figure 2.1a). For the 3D LES computations, a periodic span of 0.2 has been considered, as this size was shown sufficient for capturing the largest spanwise length scales of the flow at $\alpha = 14^\circ$ and $Re = 6 \times 10^4$ [42, 2].

The usual boundary conditions have been applied. At inlet (blue line), a uniform velocity profile of free-stream velocity $U_\infty = 1$ and tilt $\alpha = 14^\circ$ has been prescribed, along with zero normal pressure gradient ($\nabla p \cdot \hat{\mathbf{n}} = 0$). At outlet, the roles of pressure and velocity are reversed, so that homogeneous Dirichlet boundary condition is used for pressure ($p = 0$) and homogeneous Neumann ($\nabla \mathbf{u} \cdot \hat{\mathbf{n}} = \mathbf{0}$) for velocity. The airfoil surface is treated as an impermeable no-slip wall by setting

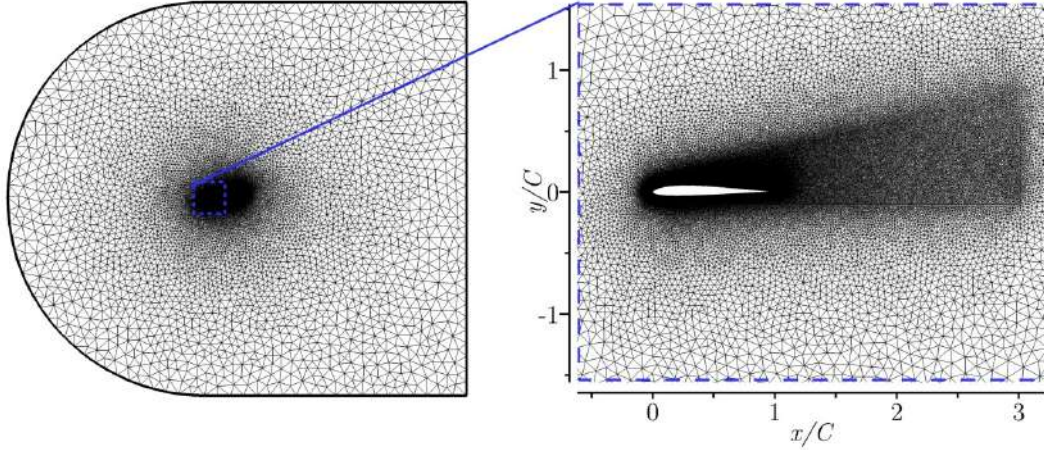


Figure 2.2: An overview of LES baseline mesh along with a zoomed view of its near-wall and wake regions

both velocity ($\mathbf{u} = 0$) and the normal gradient of pressure to zero. On the upper surface of the airfoil, a short portion of length the jet slot width h is cut straight and switched to inlet-type boundary conditions at the jet location for the actuated cases. Here, the time-dependent jet velocity $u_j = U_j \sin(2\pi f_j t)$ is prescribed, with $2U_j$ the jet velocity amplitude and f_j the actuation frequency. The jet velocity is tilted at an angle θ_j with respect to the airfoil surface and the velocity profile simply taken as a top-hat function in the streamwise direction and uniform along the wing span. Homogeneous Neumann boundary conditions are used for pressure at the jet boundary. Finally, periodic boundary conditions are enforced to the lateral boundaries of the domain for three-dimensional simulations.

A sketch representing the synthetic jet design parameters is presented in Fig. 2.1b. These parameters are the jet location along the chord x_j , the jet width h_j , and the jet angle θ_j (with respect to the airfoil surface), frequency f_j , and momentum coefficient $C_\mu = (h_j \rho_j U_j^2 \sin \theta_j) / (C \rho U_\infty^2)$, with the jet fluid density $\rho_j = \rho = 1$ the same as free-stream density on account of incompressibility.

An unstructured computational grid, consisting of about 28.7 million control volumes has been employed for the LES unactuated baseline case. The mesh was highly refined around the airfoil and along the wake, but left to coarsen in the far-field, as shown in Fig. 2.2. For the actuated cases, cell count has been increased to nearly 30 million due to the higher grid resolution required to resolve the jet. The

spanwise length has been discretised into 48 layers, as shown adequate by previous simulations for this same airfoil at the same Reynolds number and angle of attack [42].

According to Piomelli and Chasnov [54], the near-wall mesh resolution required for wall-resolved LES simulations involving mainly attached boundary layers is $\Delta x^+ = \mathcal{O}(50 - 150)$, $\Delta y^+ < 2$, and $\Delta z^+ = \mathcal{O}(15 - 40)$, where the $+$ superscript denotes wall units. The first cell layer thickness in wall units is $\Delta y^+ = y u_\tau / \nu$, where y is the dimensional normal distance to the wall, $u_\tau = \sqrt{\tau_w / \rho}$ is the friction velocity and τ_w the wall shear stress. Δx^+ and Δz^+ characterise the wall-grid spacing in the streamwise and spanwise directions, respectively, and are obtained from dimensional grid spacing in the same way as Δy^+ . The maximum Δx^+ , Δy^+ and Δz^+ on the upper surface of the airfoil are about 0.2, 0.5 and 18, respectively. The excess resolution in the streamwise wall-parallel direction could have been avoided by resolving the near-wall region with a structured mesh of prisms, which would have resulted in a lower cell count, but due to the massively separated nature of the baseline flow we deemed it prudent to keep cells short.

The resolved-to-total turbulent kinetic energy (TKE) ratio ($k_{\text{res}}/k_{\text{tot}}$ where $k_{\text{tot}} = k_{\text{res}} + k_{\text{sgs}}$, the total kinetic energy, is the sum of the resolved and modelled parts) provides yet another means of assessing LES mesh quality. The resolved component of TKE is obtained from the velocity field fluctuations of the resolved scales as $k_{\text{res}} = (\langle u'u' \rangle + \langle v'v' \rangle + \langle w'w' \rangle) / 2$, whereas the modelled component is $k_{\text{sgs}} = \nu_{\text{sgs}} / C_k \Delta$. The model parameter was set to a standard $C_k = 0.094$, which combined with the also standard value for $C_\epsilon = 1.048$ results in the classic value for the Smagorinsky constant $C_s = C_k^3 / C_\epsilon = 0.1677$. Sound LES simulations should resolve at least 80% of TKE [55], and this is the case of our baseline simulation, as clearly shown in Fig. 2.3. The mesh was sufficiently fine to resolve above 95% of TKE in all cases, leaving less than 5% to the sub-grid scale model in the most critical regions, namely the proximal part of the shear layer after boundary layer separation.

The Courant-Friedrichs-Levy number was limited to $\text{CFL} < 0.8$ by means of an adaptive time-stepper.

The mesh-independence and time-resolution analyses for the 2D RANS-SA simulations were performed and reported in an earlier study [1], concluding that

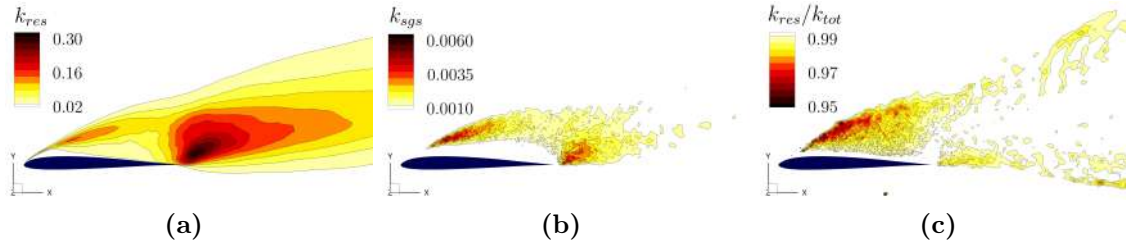


Figure 2.3: Resolved k_{res} and b) modeled k_{sgs} parts of the turbulent kinetic energy (TKE). c) Resolved-to-total TKE ratio $k_{\text{res}}/k_{\text{tot}}$.

	domain	$L_x \times L_y$	L_z	N_{xy}	N_z	T	C_l	C_d	f_{vK}	η
LES FVM (Present)	C-grid	35×30	0.2	597,916	48	35	0.895	0.239	0.69	3.744
LES FEM [2]	H-grid	15×16	0.2	467,812	64	65	0.886	0.238		3.726
ILES FDM [42]	O-grid	30×30	0.2	47,565	101	15	0.875	0.221		3.960
2D-RANS-SA [1]	C-grid	35×30	-	45,466	-	60	0.798	0.204		3.911

Table 2.1: Literature review of the aerodynamic performances of the SD7003 airfoil at $Re = 6 \times 10^4$ and $\alpha = 14^\circ$. L_x , L_y and L_z are the domain size in the streamwise, cross-stream and spanwise directions, respectively, in units of C . N_{xy} and N_z are the in-plane and spanwise resolutions, and T the time-span of the simulations in C/U_∞ units.

a hybrid mesh of 45,466 cells and a time step $\Delta t = 2 \times 10^{-5}$ was sufficient to properly capture the flow dynamics and to resolve boundary layers down to the viscous sublayer. The mesh truncation error was estimated at about 0.01% (see table 1 of that paper).

The baseline LES case has been validated against the simulations by Rodriguez et al. [2] and Galbraith and Visbal [42], both corresponding to the same airfoil at the same Reynolds number and angle of attack. The former study employed LES on a grid of nearly 30 million nodes, while the latter used Implicit LES (ILES) on a more modest mesh of about 5.7 million grid points. The values of time-averaged lift (C_l) and drag (C_d) coefficients, along with aerodynamic efficiency ($\eta = C_l/C_d$) and the Strouhal number or von Kármán frequency of vortex shedding (f_{vK}), are presented in Table 2.1. Current baseline simulation shows very good agreement with Rodriguez et al. [2] (within 1%) and a fairly good match with ILES simulations by Galbraith and Visbal [42]. The mesh and numerical approaches undertaken are sufficiently different that the mesh truncation error can be trusted to be contained within reported discrepancies for average aerodynamic performance

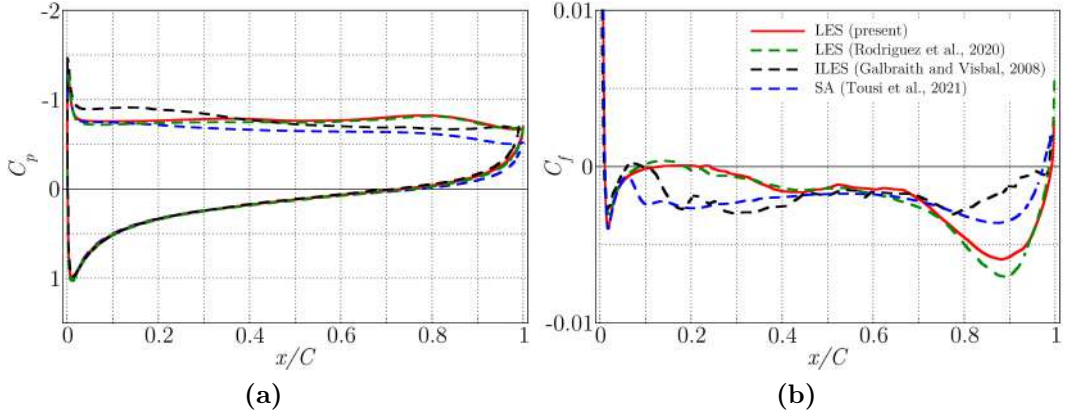


Figure 2.4: Spanwise- and time-averaged chord distributions of (a) pressure C_p and (b) skin friction C_f coefficients along the SD7003 surface(s) at $Re = 6 \times 10^4$ and $\alpha = 14^\circ$. Shown are the present LES (solid red), the LES case by Rodriguez et al. [2] (dashed green), ILES by Galbraith and Visbal [42] (dashed black) and SA RANS by Tousi et al. [1] (dashed blue).

parameters and, therefore, amount to less than 1%. RANS-SA results, however, tend to underestimate both aerodynamic force coefficients, particularly so C_d .

Aggregate quantities such as forces are always prone to misleading conclusions due to unnoticed compensation. Local quantities convey a better degree of appreciation as to whether the flow dynamics are being adequately captured. Fig. 2.4a depicts the chord distribution of the spanwise averaged pressure coefficient $C_p = (p - p_\infty)/(0.5\rho U_\infty^2)$ along both upper and lower surfaces. No apparent differences exist among the various simulations considered for the C_p distribution on the lower surface, except perhaps very slightly in the vicinity of the trailing edge. On the upper surface, the match between present results and Rodriguez et al. [2] is remarkably accomplished, while the ILES of Galbraith and Visbal [42] and the 2D RANS-SA by Tousi et al. [1] are fair but not excellent due to the less precise computational methods employed and the coarser grids. The aforementioned compensation effect is clear for the simulation by Galbraith and Visbal [42], which clearly transfers some lift from the back of the airfoil to the front. The resulting C_l is about the same obtained in the LES simulations, but at the cost of a nose-up shift of the pitching moment coefficient C_m . The skin friction coefficient $C_f = \tau_w/0.5\rho U_\infty^2$ again shows a fair agreement with Rodriguez et al.

[2]. The boundary layer separation on the upper surface is, on average, located at $x_{\text{sep}} \simeq 0.011$, and is also fairly well predicted by ILES and RANS-SA simulations, although downstream from the separation point these present noticeable discrepancies with respect to the two LES simulations. This may challenge the alleged capabilities of RANS-SA to properly reproduce highly separated flows, at least from a quantitative point of view, but since actuation is intended to reduce or even suppress separation, the method might still work acceptably for actuated cases.

2.5 Results

An optimisation procedure was employed by Tousi et al. [1] to determine optimal SJA parameters in terms of maximising both C_l and η . The set of five SJA parameters, the design variables of the optimisation problem, comprises the actuation frequency f_j , the jet inclination angle with respect to the airfoil surface θ_j , the slot streamwise location measured from the airfoil leading edge x_j , the jet slot width h_j and the jet momentum coefficient $C_\mu \equiv (\rho_j U_j^2 h_j \sin \theta_j) / (\rho_\infty U_\infty^2 C)$. The method coupled a scripted mesh generator (GMSH [56]), a CFD package (OpenFOAM) and a Genetic Algorithm (GA). The GA population size was set to 20 individuals (each one consisting in a CFD case with a different set of prescribed SJA parameters) per generation/iteration, which was considered a reasonable trade-off between method performance and computational cost. The first generation was initialised with a random set of individuals, and all CFD cases run. The two objective functions, C_l and η , were obtained for each of the simulations and passed onto the GA optimiser, where the *Selection*, *Crossover* and *Mutation* operators were applied to produce a new set of values for the five SJA parameters defining the individuals for the next generation. The Selection phase employed a $\mu + \lambda$ strategy with a *Crowded-Comparison* Operator [57]. Simulated Binary Crossover (SBX) [58] (with a probability of 0.9) and Polynomial Mutation [59] (with a probability of 0.1) were adopted for the Crossover and Mutation phases, respectively. This process was repeated until having completed 18 generations (360 CFD simulations), the overall improvement being found marginal after the sixteenth generation. For a detailed account of the optimisation method used, we refer the reader to Tousi et al. [1].

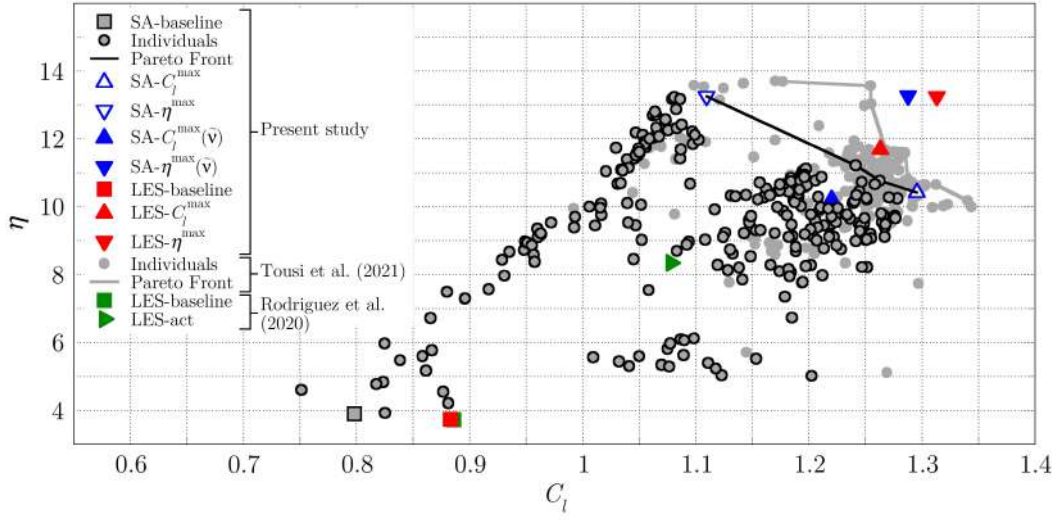


Figure 2.5: Optimisation procedure and optimal cases in objective function space (C_l, η) space.

Each additional individual requires a full CFD simulation, such that aspiring to be overly accurate results in unfeasible optimisation time spans. For this reason, a compromise was done by using two-dimensional RANS simulations with the Spalart-Allmaras model.

Fig. 2.5 presents a summary of the results obtained along the optimization process, as seen in objective function space. The 2D RANS-SA baseline case (gray-filled black square) starts at low values of both C_l and η . Actuated cases (gray-filled black circles corresponding to the 360 cases run) progressively move to higher lift coefficient and aerodynamic efficiency values to finally delineate a multi-objective Pareto front (black line) with optimum C_l (up-pointing empty blue triangle) and maximum η (down-pointing empty blue triangle). The optimisation was run further by Tousi et al. [1] by increasing the initial set of 360 cases with an additional 240 runs thus reaching a final population of up to 600 individuals (gray circles and gray line for the second Pareto front), but the final results were still not available by the time the present study began, and the further refinement obtained was anyway expected to be within the accuracy limits of RANS-SA. The LES baseline case (red square), as for Rodriguez et al. [2] (green square), has a larger C_l than the 2D RANS-SA case, as already pointed out, so that it is to be expected that some discrepancies might be encountered when switching from

	SJA parameters					Aerodynamic performance parameters				
	f_j	C_μ	θ_j (°)	x_j	h_j	C_l	C_d	η	$\Delta C_l/C_l$	$\Delta\eta/\eta$
Baseline										
SA [1]						0.798	0.204	3.91		
LES (present)						0.895	0.239	3.74		
LES [2]						0.886	0.238	3.72		
Actuated										
SA- C_l^{\max}						1.295	0.129	10.42	+62.3%	+157.4%
SA- $C_l^{\max}(\tilde{\nu})$	1.6	0.0053	53	0.0097	0.005	1.220	0.1194	10.21	+52.9%	+161.1%
LES- C_l^{\max}						1.263	0.108	11.69	+41.1%	+212.5%
SA- η^{\max}						1.109	0.083	13.25	+31.1%	+239.7%
SA- $\eta^{\max}(\tilde{\nu})$	2.6	0.0055	18	0.0089	0.005	1.288	0.097	13.27	+61.4%	+239.4%
LES- η^{\max}						1.313	0.094	13.96	+46.7%	+273.2%
LES-[2]	1.0	0.0030	90	0.0070	0.007	1.078	0.129	08.35	+21.6%	+124.4%

Table 2.2: Baseline case, and optimal SJA actuation cases corresponding to maximum lift C_l^{\max} and maximum aerodynamic efficiency η^{\max} . The values of the five actuation parameters (jet frequency f_j , jet momentum coefficient C_μ , jet inclination angle with respect to the airfoil surface θ_j , jet streamwise location from leading edge x_j and jet slot width h_j) are listed alongside the resulting aerodynamic performances.

RANS-SA to LES for the optimally actuated cases. In any case, the LES non-optimised actuated case run by Rodriguez et al. [2] (green triangle) falls largely short of the results expected from the optimisation.

The optimum SJA parameters at either end of the Pareto Front, corresponding to cases SA- C_l^{\max} and SA- η^{\max} , and the resulting aerodynamic performances are presented in Table 2.2. The case featuring maximum lift achieved a considerable improvement $\Delta C_l/C_l = 62.3\%$ with respect to baseline. Beside improving lift, this actuation setup also enhances aerodynamic efficiency by $\Delta\eta/\eta = 157.4\%$. Meanwhile, the maximum aerodynamic efficiency case boosted it by an impressive $\Delta\eta/\eta = 239.7\%$, retaining still an appreciable $\Delta C_l/C_l = 31.1\%$ increase in lift. Three of the SJA parameters, namely $C_\mu \simeq 0.005$, $x_j \simeq 0.009$ (just upstream of the separation point) and $h_j \simeq 0.005$, take essentially the same value for the two optimal cases considered. The main differences concern the actuation frequency f_j and injection angle θ_j . Maximum efficiency is obtained by actuating almost tangentially with $\theta_j = 18^\circ$ at frequency $f_j = 2.6$, while maximum lift requires larger actuation angle $\theta_j = 53^\circ$ and lower frequency $f_j = 1.6$.

Since the optimally actuated RANS-SA cases might be afflicted by the same shortcomings that plague the baseline run, two LES simulations at the same optimal set of actuation parameters were also undertaken. The results are indicated in Fig. 2.5 (up-pointing and down-pointing red triangles for the C_l^{\max} and η^{\max} cases, respectively) and accordingly listed in Table 2.2. While both LES simulations outperformed amply the unoptimised actuated case by Rodriguez et al. [2], the results notably differ from the 2D RANS-SA estimation. While the maximum lift case produced slightly lower C_l and somewhat higher η , the maximum aerodynamic efficiency case yielded remarkably higher C_l without notably modifying η . As a result, the latter case became at once optimal in terms of both C_l and η .

It must be born in mind that optimisation techniques for non-linear problems, GA being no exception, provide no guarantee that the best SJA configuration found is indeed optimal, let alone the absolute optimum. The configurations selected here as *optimal* are thus tagged in the weaker sense that nearly doubling the GA population of RANS-SA individuals did not produce better aerodynamic performances [1] than those obtained here for the two LES cases tested and, more importantly, that the well-resolved simulations widely outperformed available sub-optimal results for the same airfoil and flight conditions.

The discrepancies between 2D RANS-SA and LES simulations, also for the actuated cases, disputes the applicability of the former to low Reynolds number aerodynamics past airfoils at post-stall conditions, even in situations for which boundary layers remain attached through the action of SJA. RANS is specifically designed for turbulent flow conditions, and performs reasonably provided the model parameters are appropriately tuned. Some models can deal with laminar-turbulent transition, but their reliability is largely dependent on parameter tuning. In the case of the SA turbulence model, this sensitivity extends crucially to the free-stream boundary conditions for the unique turbulent field $\tilde{\nu}$. Following Catalano and Tognaccini [45, 51], which states that free-stream turbulent viscosity must be sufficiently low so as to properly capture the LSB at pre-stall α , we set $\tilde{\nu}/\nu = 10^{-20}$ for the SJA optimisation RANS simulations. As it happens, the optimisation process was run in post-stall conditions and with a time-dependent fluidic actuation that crucially acts on the LSB. Such a low turbulent viscosity might be artificially stabilising the laminar flow region and thus inducing wrong

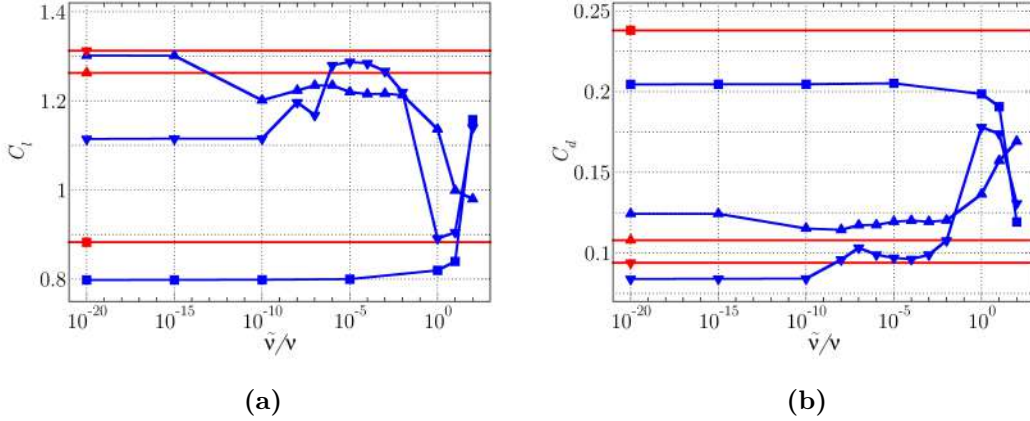


Figure 2.6: Results sensitivity to free-stream preturbulence levels as prescribed by $\tilde{\nu}/\nu$. (a) Average lift coefficient C_l . (b) Average drag coefficient C_d . Baseline (squares), maximum lift (up-pointing triangles) and maximum aerodynamic efficiency (down-pointing triangles) SJA setups are shown for both RANS-SA (blue) and LES (red) computations.

results. To check sensitivity to free-stream preturbulence levels, the baseline, maximum lift and maximum aerodynamic efficiency cases were run for a wide range $\tilde{\nu}/\nu \in [10^{-20}, 10^2]$. The results are presented in Fig. 2.6. Unrealistically high free-stream turbulent viscosity of the order of the fluid viscosity and above ($\tilde{\nu}/\nu \geq 1$) produce unphysical results and must be discarded. At the low-values end of the range, RANS-SA results (blue lines) are fairly stable but diverge considerably from LES (red horizontal lines). Not much is gained at intermediate levels of $\tilde{\nu}/\nu$ for the baseline case, which produces pretty stable but wrong C_l and C_d values all along. The actuated cases, however, traverse a regime $\tilde{\nu}/\nu \in [10^{-6}, 10^{-3}]$ with RANS-SA C_l and C_d values decently close to LES results. The aerodynamic performance of the maximum lift and maximum aerodynamic efficiency cases for $\tilde{\nu}/\nu = 10^{-5}$ are shown in Fig. 2.5 (filled blue symbols) and listed in Table 2.2 as $\text{SA-}C_l^{\max}(\tilde{\nu})$ and $\text{SA-}\eta^{\max}(\tilde{\nu})$, respectively. If not quite on top of the LES results, they at least are much closer and clearly align with the trend. The deviation from the original RANS-SA optimals as obtained from a reduced population of 360 individuals serves as an *a-posteriori* justification for not having waited for the completion of the 600 runs before starting the two *optimal* LES cases. It is clear enough that the error incurred by using RANS-SA in the optimisation process is sufficiently large and unsystematic to consider both Pareto fronts, the preliminar and the refined,

as not significantly distinct. The reason for this better agreement between RANS-SA and LES at intermediate values of the free-stream turbulent viscosity, only for actuated cases, remains a mystery. Unfortunately, the apparent improvement of the RANS-SA model with a more appropriate choice for $\tilde{\nu}$ was not known at the time the optimisation process was run and it was later thought inexpedient, on cost-benefit grounds, to re-run it anew. Besides, there is no guarantee that this same value of $\tilde{\nu}/\nu$ will produce accurate results at other post-stall flight regimes or under different SJA operating conditions. A thorough parametric exploration, far beyond the scope of this study, will be required to cast light on the issue. Breuer [35] observed that high inlet turbulent intensities tend to reduce and even suppress the LSB on the upper surface of the unactuated airfoil. This would explain the sharp drop of C_d and the surge of C_l we observe for the baseline case when high values of $\tilde{\nu}$ are prescribed at inlet. The LSB shrinks and vanishes and the airfoil performs as in pre-stall conditions on account of the turbulent boundary layer and the delay in its separation. For actuated cases, too high free-stream $\tilde{\nu}$ over-rides the SJA capabilities and the airfoil behaves much as in the baseline case, all the more so for maximum efficiency SJA.

In the remaining of the manuscript, RANS-SA optimal cases have been considered for $\tilde{\nu}/\nu = 10^{-5}$ instead of the original runs used for optimisation. Furthermore, since the maximum aerodynamic efficiency case outperforms the maximum lift efficiency case in all respects when assessed with these new RANS-SA or LES simulations, only the corresponding set of SJA parameter values will be considered further, as an absolute optimum.

2.5.1 RANS-SA vs LES comparison of optimally actuated cases

The pressure and skin friction coefficient distributions along the upper and lower surfaces corresponding to the maximum efficiency SJA set of parameters are plotted in Fig. 2.7 alongside baseline LES results (dashed red line). As expected, SJA manages to reattach the flow over a large portion of the upper surface. The separation point, identified by $C_f = 0$, is retarded for all three actuated simulations, LES- η^{\max} (solid red), SA- $\eta^{\max}(\tilde{\nu})$ (solid blue) and the sub-optimal LES-act case

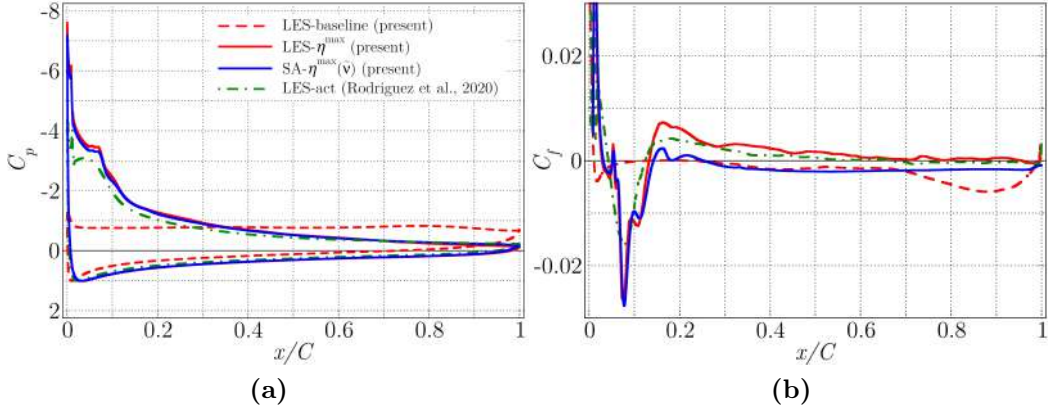


Figure 2.7: Optimal SJA vs baseline (a) Pressure C_p and (b) skin friction C_f coefficient distributions. Shown are the LES-baseline (dashed red), the LES- η^{\max} (solid red), RANS SA- $\eta^{\max}(\tilde{\nu})$ (solid blue) and sub-optimal actuated LES-act case by Rodriguez et al. [2] (dash-dotted green).

by Rodriguez et al. [2] (dash-dotted green), with respect to baseline (dashed red line) The separation bubble, though, is short and reattachment is effected shortly behind the jet location. The reattachment contributes to slightly increasing the pressure on the lower surface and, more notably, to enhancing the suction effect on the upper surface, particularly so along the front half of the airfoil. Suction on the back half is reduced but the net effect is that of a lift increase and a sharp pressure drag reduction. All three SJA cases show similar features. In particular, the SA- $\eta^{\max}(\tilde{\nu})$ and LES- η^{\max} computations, run with the same SJA parameter values, present very similar pressure distributions, which indicates that the main flow features are being appropriately dealt with also by the less accurate RANS-SA model when free-stream turbulent viscosity is appropriately prescribed to a moderate realistic value. The sub-optimal LES-act produces less suction in the front part of the upper surface and therefore lower lift, as a result of its being suboptimal. Friction distributions are very similar for the LES- η^{\max} and LES-act cases except around the actuation location, where the different actuation parameters produce very different local outcomes. The SA- $\eta^{\max}(\tilde{\nu})$ reproduces quite accurately the behaviour of C_f in the front part of the airfoil, as comparison with the LES- η^{\max} simulation avows, but the reattachment is not properly fulfilled and the friction remains negative over most of the upper surface when it should in reality be small

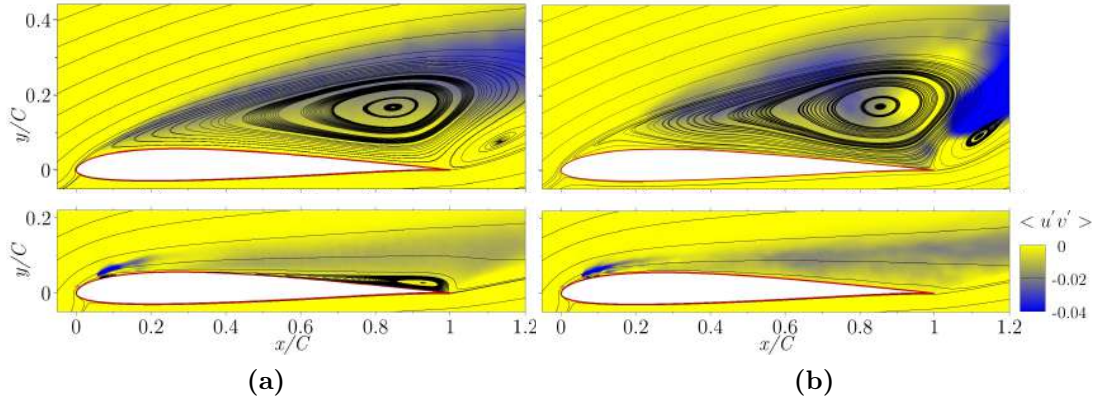


Figure 2.8: Spanwise-averaged $\langle u'v' \rangle$ component of the Reynolds stress tensor and time- and spanwise-averaged streamlines. (a) RANS-SA-baseline (top) and RANS-SA- $\eta^{\max}(\tilde{\nu})$ (bottom). (b) LES-baseline (top) and LES- η^{\max} (bottom).

but positive and decisively contribute to friction drag. The effect on total net drag is however not noticeable, as form drag largely dominates. All in all, 2D RANS-SA simulation seems an appropriate cost-effective tool for extensive optimisation of SJA parameters provided an adequate amount of turbulent viscosity is allowed at the inlet of the domain, and final optimal results are further refined with LES (or DNS if feasible).

Fig. 2.8 shows colourmaps of the $\langle u'v' \rangle$ component of the Reynolds stress tensor along with a collection of time- and spanwise-averaged streamlines for the baseline and maximum aerodynamic efficiency actuated cases. The baseline separation bubble exhibits similar topologies for the LES-baseline and RANS-SA-baseline simulations. The dynamical behaviour, as represented by $\langle u'v' \rangle$, is however quite different. Streamwise-cross-stream cross-correlation is evenly distributed along the shear layer bounding the separation bubble at the top for RANS-SA-baseline, while it is much more concentrated in the vortex formation region at the back of the airfoil for LES-baseline. The RANS-SA model is not expected to behave particularly well in post-stall conditions. Once actuation is switched on, the quality of RANS-SA results improves remarkably. The RANS-SA- $\eta^{\max}(\tilde{\nu})$ and LES- η^{\max} cases display a very similar distribution of $\langle u'v' \rangle$. These are particularly high in the region of the jet as it bends downstream, blown by the incoming flow. Also stream-

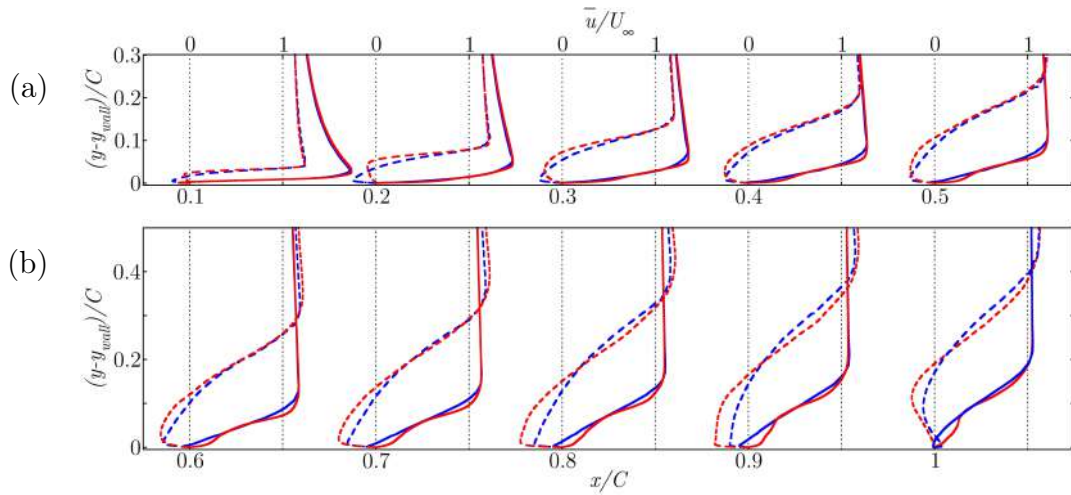


Figure 2.9: Evolution of the upper-surface boundary layer along the airfoil. Time- and spanwise-averaged streamwise velocity profiles $\langle u(x, y, z; t) \rangle_{t,z}$ at streamwise coordinates (a) $x/C = 0.1$ through $x/C = 0.5$ and (b) $x/C = 0.6$ through $x/C = 1$, as a function of wall-normal distance. Shown are the baseline (dashed) and actuated (solid) cases, for both LES (red) and RANS-SA (blue) simulations. The actuated cases are LES- η^{\max} and SA- $\eta^{\max}(\tilde{\nu})$

lines reveal a fairly comparable pattern, except that RANS-SA does not manage to completely suppress the separation bubble and a narrow but relatively long recirculation region extends on the upper surface from the trailing edge upstream. The boundary layer is therefore attached for LES but not for RANS-SA. However, the effects on the pressure distribution are not large, and although the friction on the aft portion of the upper surface differs notably, the net lift and drag, which are pressure dominated, do not suffer exceedingly from the inaccuracies incurred by the RANS-SA model.

To clarify the evolution of the boundary layer along the upper surface of the airfoil, the time- and span-averaged velocity profiles are presented in Fig. 2.9 at several streamwise locations. The baseline case (dashed lines) has the boundary layer already separated at $x = 0.1$, as clear from the reverse flow in the close proximity of the wall. The LES simulation (red), however, features lower recirculation velocity than the RANS-SA computation (blue), but spread over a wider cross-section. The peak of reverse flow is indeed located further from the wall for LES. These differences between the two methods region remain as the sepa-

rated cross-section widens downstream all the way down to $x = 0.5$, beyond which point RANS-SA starts underpredicting negative streamwise velocity with respect to LES. Maximum aerodynamic efficiency actuation (solid lines) suppresses separation, notably at $x = 0.2$ and beyond. The reattached boundary layer is very similar for LES and RANS-SA, an indication that the latter method is properly capturing the effects of SJA. The match is very good for $x \leq 0.2$ and gradually deteriorates downstream. Nonetheless, agreement remains acceptable in all respects except for the slight flow reversal RANS-SA predicts in the immediate proximity of the wall over most of the upper surface.

To better characterise the boundary layer in terms of the viscous blockage, the displacement (δ_1) and momentum (δ_2) thicknesses help quantify the near-wall mass-flow and momentum deficits resulting from the effects of viscosity. These are computed following

$$\delta_1 = \int_0^\delta \left(1 - \frac{\hat{u}}{\hat{u}_e}\right) d\hat{y}, \quad (2.9)$$

$$\delta_2 = \int_0^\delta \frac{\hat{u}}{\hat{u}_e} \left(1 - \frac{\hat{u}}{\hat{u}_e}\right) d\hat{y}, \quad (2.10)$$

where \hat{y} is the local wall-normal coordinate, \hat{u} the streamwise (wall-parallel) velocity component, \hat{u}_e its value at the boundary layer edge, and δ the boundary layer thickness, formally infinite but in practice the wall-normal distance required to reach the virtually inviscid flow region. As boundary layer thickness we have used $\delta = \delta_\tau$, defined as the wall-normal distance where the shear $\|\tau\|$ is seen to decay a 95% with respect to the maximum value recorded on the airfoil surface τ_w^{\max} ($\|\tau\| < 0.05\tau_w^{\max}$). The evolution of δ_τ , δ_1 , δ_2 and the shape factor $H \equiv \delta_1/\delta_2$ along the upper surface is shown in Fig. 2.10 for both the LES- η^{\max} and RANS-SA- $\eta^{\max}(\tilde{\nu})$ cases. All three thicknesses grow steadily along the chord but are much reduced in relation to baseline (not shown in the figure) following the suppression of boundary layer separation. RANS-SA slightly overestimates δ_1 over the aft half of the airfoil and underestimates δ_2 on the last third. As a result, shape factor is larger in this region for the RANS-SA simulation than for LES. The separation bubble visible in Fig. 2.8 must be held responsible for the discrepancies. It is also interesting to observe that both actuated cases show particularly large Reynolds

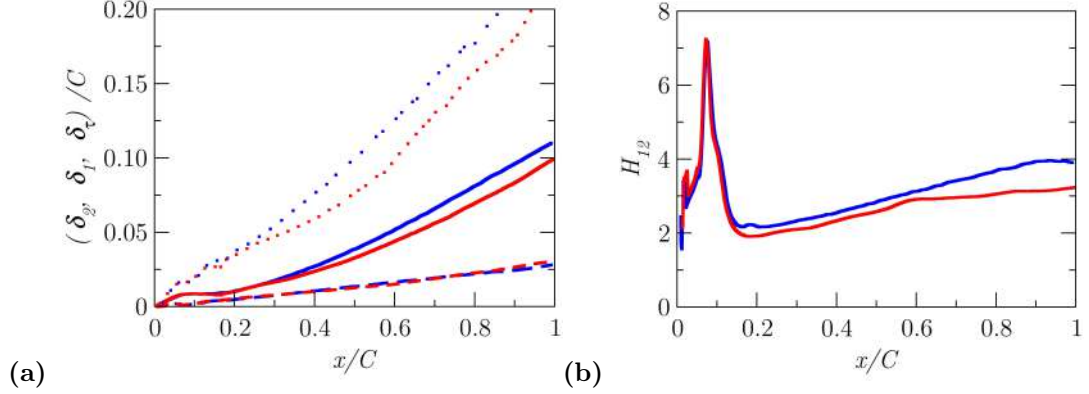


Figure 2.10: Evolution of boundary layer characteristic properties along the upper surface of the airfoil for actuated cases LES- η^{\max} (red lines) and RANS-SA- $\eta^{\max}(\bar{\nu})$ (blue). (a) Boundary layer (δ_τ , dotted), displacement (δ_1 , solid), and momentum (δ_2 dashed) thicknesses. (b) Shape factor H .

stresses values at the injection/suction zone, Reynolds stresses are also observed along the airfoil upper surface especially in the LES-*max* η case. This fact explains why the boundary layer remains reattached under these conditions.

2.5.2 Baseline vs optimally actuated case comparison.

The three LES simulations for baseline, (allegedly) maximum lift and maximum aerodynamic efficiency cases have been minutely analysed to elucidate the flow mechanism whereby SJA attains enhanced aerodynamic performances at post-stall angles of attack. In order to characterise the time dependence of the flow, five probe arrays were deployed in the flow field as indicated in Fig. 2.11a. All five probe lines are located in regions where high fluctuation levels are expected, as indicated by the high values of $\langle u'v' \rangle$. Three are distributed along the shear layer resulting from the early separation of the boundary layer, and the remaining two in the very near wake region. The streamwise ($u_{(x,y)}(z, t)$) velocity signal along spanwise probe arrays P₂ (within the shear layer at $(x,y)=(0.098,0.08)$, gray lines) and P₅ (in the near wake at $(x, y) = (1.1, 0.08)$, black) have been Fourier-transformed to obtain the Power Spectral Density (PSD) $|\hat{u}_{(x,y)}(z, f)|$ and then spanwise averaged into panels Fig. 2.11b-d for the LES-baseline, LES- C_l^{\max} and LES- η^{\max} cases, respectively. Quadratic interpolation pinpoints the main frequency peaks in the spectrum. For

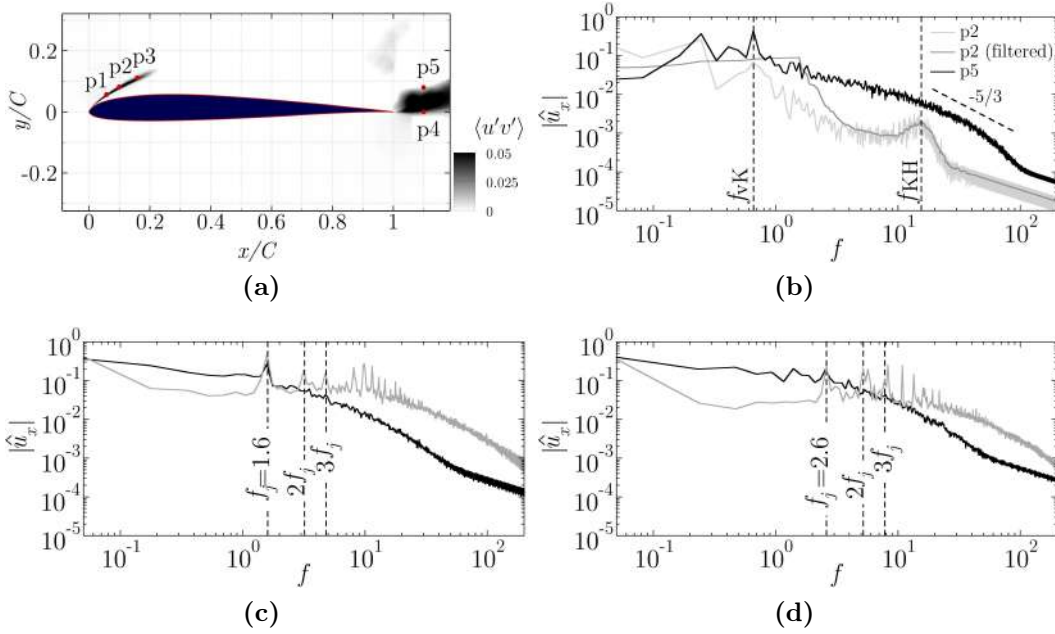


Figure 2.11: Power Spectral Density (PSD) of the streamwise velocity signal as recorded from spanwise probe arrays P₂ and P₅. (a) LES-baseline spanwise-averaged $\langle u'v' \rangle$ colourmap showing the location of the five probe-arrays. Three probes are placed along the shear layer, while the other two are in the very near wake. The PSD of the signals from probes P₂ (x, y) = (0.098, 0.08) and P₅ (x, y) = (1.1, 0.08) are represented for the (b) LES-baseline, (c) LES- C_l^{\max} and (d) LES- η^{\max} cases. Shown are the spectra for the signal read from P₅ (black) and P₂ (light gray), which has been further filtered (dark gray).

the baseline case, the Strouhal frequency associated with the vortex-shedding of Kármán vortices is identifiable at $f_{vK} = 0.69$, both at locations P_2 and P_5 . The $-5/3$ energy slope that is typical of the inertial range of developed turbulence is also noticeable despite the transitional nature of the flow considered here. Probe P_2 also detects a broadband peak at about $f_{KH} = 15.5$ that may be associated with the passage of Kelvin-Helmholtz vortices. In order to precisely detect the f_{KH} , the filtered signal from probe P_2 is represented as a dark-gray line in Fig. 2.11b. Probes P_1 and P_3 also record the same phenomenon, albeit with decreasing intensity, while P_4 and P_5 do not in the least reflect it. This is clearly suggestive of a local instability that develops precisely along the shear layer, i.e. a Kelvin-Helmholtz instability.

Actuating with $f_j = 2.6$, as corresponds to the LES- η^{\max} case, the jet frequency is imprinted on the flow and recorded at all probes. The vortex-shedding frequency is superseded by actuation, and no wake vortices are discernible. Several harmonics of the jet actuation frequency are also visible in the spectrum of signals recorded close to the actuation location. The same happens for the LES- C_l^{\max} , albeit with the reduced frequency $f_j = 1.6$. Again, the main peak is detected at all probes, while harmonics -a large number of them- are only detected by probes that are sufficiently close to the jet location. The actuation frequency for maximum aerodynamic efficiency (and incidentally also lift) is about 4 times larger than the natural vortex-shedding frequency.

Fig. 2.12 displays instantaneous vortical structures through Q-criterion iso-surfaces coloured by streamwise velocity. The LES-baseline case (panel a) is characterised by the early separation of the boundary layer and the clear development of Kelvin-Helmholtz vortices along the detached shear layer. These vortices remain predominantly two-dimensional as do all large-scale structures in the vicinity of the airfoil, and are subsumed downstream within the Kármán vortices forming at the top of the wake. The separated region is massive and determines the size of the Kármán vortices that are shed into the wake. The sinuous arrangement of vortices, connected by braids is clearly recognisable and streamwise-cross-stream vortices populate the braid region already one chord distance downstream from the trailing edge.

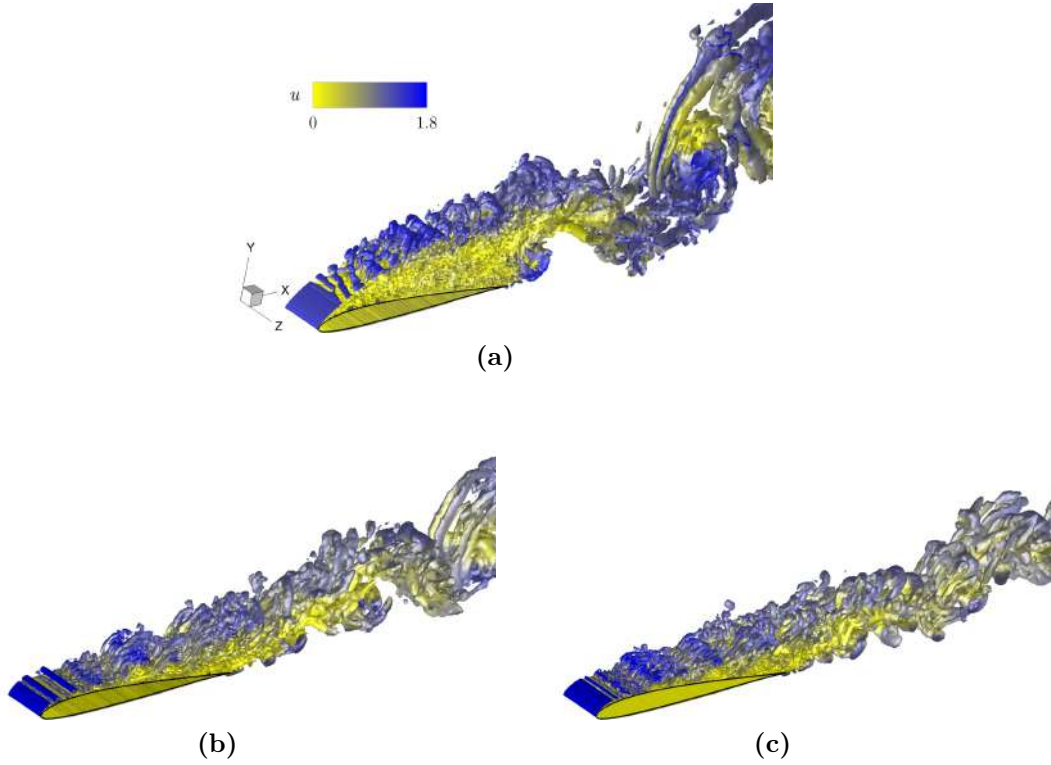


Figure 2.12: Instantaneous vortical structures visualised through iso-surfaces of the Q-criterion $Q = 30U_\infty^2/C^2$, coloured by streamwise velocity u . (a) LES-baseline. (b) LES- C_l^{\max} . (c) LES- η^{\max} .

Actuation drastically reduces the low-speed region above the airfoil and, with it, the width of the wake. Accordingly, lift is enhanced and pressure drag, and along with it total drag, greatly reduced. The SJA-generated spanwise vortices are clearly visible downstream from the jet location as fairly two-dimensional spanwise structures and govern the flow dynamics. They are somewhat more spaced for the LES- C_l^{\max} (panel b) than for the LES- η^{\max} case (panel c), on account of the lower actuation frequency of the latter as compared with the former. Kármán vortex-shedding is completely suppressed for LES- η^{\max} , and highly attenuated for LES- C_l^{\max} , for which case smaller-scale spanwise vortices are visible in the wake that become synchronised with the high-frequency vortices induced by the actuator. Two videos showing the vortical structures for the LES-baseline and LES- η^{\max} are provided as supplementary data.

2.6 Conclusions

Following the Synthetic jet Actuation parameters optimisation undertaken by Tousi et al. [1] on the SD7003 airfoil at moderate $Re = 6 \times 10^4$ and post-stall $\alpha = 14^\circ$, we have analysed, using Large Eddy Simulation, the aerodynamic performances and flow properties of optimally actuated scenarios. The original optimisation study, coupled a RANS solver that used the Spalart-Allmaras turbulence model with a Genetic Algorithm specifically devised for maximising either lift or aerodynamic efficiency.

Our Large Eddy Simulation of the baseline case reasonably validated the baseline RANS-SA computation, not without conspicuous discrepancies attributable to the inadequacy of the latter model for the simulation of massively separated flow configurations. However, the two optimal Active Flow Control LES cases, while still producing impressive enhancement of aerodynamic performances, did not align with RANS-SA results as expected. In point of fact, the maximum aerodynamic efficiency case outdoes the other alleged optimum both in terms of aerodynamic efficiency and lift, in this sense constituting an absolute optimum. And not only this, but it also further improves on RANS-SA estimations, with increases from baseline of $\Delta C_l/C_l = 46.7\%$ and $\Delta \eta/\eta = 273.2\%$.

The problem being highly nonlinear, there is no guarantee that the SJA configurations reported here as optimal are indeed absolute optima. They do, however, amply outperform the one SJA study available on the SD7003 airfoil at the same Re and α [2] and produce aerodynamic performances improvements with respect to baseline broadly comparable to those reported in the literature for other airfoils and post-stall flight regimes using alternative optimisation techniques.

A parametric study varying the free-stream turbulent viscosity prescribed at the inlet boundary for actuated simulations with the RANS-SA model reveals that flow topology and aerodynamic performance parameters are highly sensitive, unlike what happens for the baseline case. Turbulent-to-fluid viscosity ratios of around $\tilde{\nu}/\nu \sim 10^{-5}$ enable RANS-SA simulations to better reproduce the actual flow past the actuated airfoil. For these levels of free-stream turbulence, RANS-SA simulation of actuated cases aligned comfortably with LES results, thus proving the convenience of the former for AFC optimisation given their sufficient accuracy

and cost-effectiveness. Setting the right amount of free-stream turbulence is however essential, as too low or too large values result in unrealistic flows, possibly due to the poor capabilities of the SA turbulence model for predicting turbulent transition.

The application of optimal (or quasi-optimal) SJA suppresses the boundary layer separation from the upper surface and the shedding of von Kármán vortices in the wake. Actuation-jet-induced spanwise vortices pervade the flow and help maintain quasi-two-dimensionality over a long distance. They also replace the Kelvin-Helmholtz vortices that naturally arise with $f_{KH} \simeq 15.5$ from a shear layer instability of the separated boundary layer for the baseline case. The jet actuation frequency dominates the spectrum of velocity signals far downstream from the jet location, which indicates that actuation is governing the time- and length-scales of the vortical structures in the flow. Kármán vortices, originally shed with a frequency $f_{vK} = 0.69$ for the baseline case are no longer present in the wake nor imprint their periodicity on the spectrum of any of the probe signals.

The dependence of the optimum set of SJA parameters on the angle of attack is a matter worth considering, as also is the sensitivity of aerodynamic performances to suboptimal configurations. Some of the parameters, such as actuation frequency, amplitude and, possibly, injection angle, can be adjusted dynamically, while others must be necessarily fixed (slot location and width). For these latter, the sensitivity analysis is particularly relevant, as the one-size-fits-all solution is a must. Also, actuation cannot in practice be continuously distributed along the span, as we have considered here. A discrete number of actuators must instead be distributed along the span with a prescribed spacing, and each could potentially be endowed with a different amplitude, phase or even frequency, such that the set of optimisation parameters can be enlarged unboundedly. These detailed analyses will require extremely costly parametric explorations that are beyond the scope of the present study.

2.7 References

- [1] Navid Monshi Tousi, Marti Coma, Josep Maria Bergada, Jordi Pons-Prats, Fernando Mellibovsky, and Gabriel Bugada. Active flow control optimisation on sd7003 airfoil at pre and post-stall angles of attack using synthetic jets. Applied Mathematical Modelling, 2021. doi: <https://doi.org/10.1016/j.apm.2021.05.016>.
- [2] Ivette Rodriguez, Oriol Lehmkuhl, and Ricard Borrell. Effects of the actuation on the boundary layer of an airfoil at Reynolds number $Re = 60000$. Flow, Turbulence and Combustion, 105(2):607–626, may 2020. doi: [10.1007/s10494-020-00160-y](https://doi.org/10.1007/s10494-020-00160-y).
- [3] Louis N. Cattafesta and Mark Sheplak. Actuators for active flow control. Annual Review of Fluid Mechanics, 43(1):247–272, jan 2011. doi: [10.1146/annurev-fluid-122109-160634](https://doi.org/10.1146/annurev-fluid-122109-160634).
- [4] Li Wang and Fang bao Tian. Numerical simulation of flow over a parallel cantilevered flag in the vicinity of a rigid wall. Physical Review E, 99(5), may 2019. doi: [10.1103/physreve.99.053111](https://doi.org/10.1103/physreve.99.053111).
- [5] Young-Chang Cho and Wei Shyy. Adaptive flow control of low-Reynolds number aerodynamics using dielectric barrier discharge actuator. Progress in Aerospace Sciences, 47(7):495–521, oct 2011. doi: [10.1016/j.paerosci.2011.06.005](https://doi.org/10.1016/j.paerosci.2011.06.005).
- [6] Saeed Foshat. Numerical investigation of the effects of plasma actuator on separated laminar flows past an incident plate under ground effect. Aerospace Science and Technology, 98:105646, mar 2020. doi: [10.1016/j.ast.2019.105646](https://doi.org/10.1016/j.ast.2019.105646).
- [7] Nicolas Benard and Eric Moreau. Electrical and mechanical characteristics of surface AC dielectric barrier discharge plasma actuators applied to airflow control. Experiments in Fluids, 55(11), nov 2014. doi: [10.1007/s00348-014-1846-x](https://doi.org/10.1007/s00348-014-1846-x).

- [8] N Benard, Jordi Pons-Prats, Jacques Periaux, Gabriel Bugea, P Braud, JP Bonnet, and E Moreau. Turbulent separated shear flow control by surface plasma actuator: experimental optimization by genetic algorithm approach. Experiments in Fluids, 57(2), jan 2016. doi: 10.1007/s00348-015-2107-3.
- [9] Maria Grazia De Giorgi, Valentina Motta, and Antonio Suma. Influence of actuation parameters of multi-dbd plasma actuators on the static and dynamic behaviour of an airfoil in unsteady flow. Aerospace Science and Technology, 96:105587, 2020.
- [10] Ari Glezer and Michael Amitay. Synthetic jets. Annual review of fluid mechanics, 34(1):503–529, 2002.
- [11] Christopher Rumsey, Thomas Gatski, William Sellers, Veer Vatsa, and Sally Viken. Summary of the 2004 cfd validation workshop on synthetic jets and turbulent separation control. In 2nd AIAA Flow Control Conference, page 2217, 2004.
- [12] Israel Wygnanski. The variables affecting the control of separation by periodic excitation. In 2nd AIAA Flow Control Conference, page 2505, 2004.
- [13] N Findanis and NA Ahmed. The interaction of an asymmetrical localised synthetic jet on a side-supported sphere. Journal of Fluids and Structures, 24(7):1006–1020, oct 2008. doi: 10.1016/j.jfluidstructs.2008.02.002.
- [14] LIU Zhiyong, LUO Zhenbing, LIU Qiang, and ZHOU Yan. Modulation of driving signals in flow control over an airfoil with synthetic jet. Chinese Journal of Aeronautics, 33(12):3138–3148, 2020.
- [15] MG De Giorgi, CG De Luca, A Ficarella, and F Marra. Comparison between synthetic jets and continuous jets for active flow control: Application on a NACA 0015 and a compressor stator cascade. Aerospace Science and Technology, 43:256–280, jun 2015. doi: 10.1016/j.ast.2015.03.004.
- [16] S Traficante, MG De Giorgi, and A Ficarella. Flow separation control on a compressor-stator cascade using plasma actuators and synthetic and continuous jets. Journal of Aerospace Engineering, 29(3):04015056, 2016.

- [17] Maria Grazia De Giorgi, Stefania Traficante, Carla De Luca, Daniela Bello, and Antonio Ficarella. Active flow control techniques on a stator compressor cascade: a comparison between synthetic jet and plasma actuators. In Turbo Expo: Power for Land, Sea, and Air, volume 44748, pages 439–450. American Society of Mechanical Engineers, 2012.
- [18] Hongxin Zhang, Shaowen Chen, Yun Gong, and Songtao Wang. A comparison of different unsteady flow control techniques in a highly loaded compressor cascade. Proceedings of the Institution of Mechanical Engineers, Part G: Journal of Aerospace Engineering, 233(6):2051–2065, 2019.
- [19] Michael Amitay, Douglas R Smith, Valdis Kibens, David E Parekh, and Ari Glezer. Aerodynamic flow control over an unconventional airfoil using synthetic jet actuators. AIAA Journal, 39:361–370, jan 2001. doi: 10.2514/3.14740.
- [20] Michael Amitay and Ari Glezer. Role of actuation frequency in controlled flow reattachment over a stalled airfoil. AIAA Journal, 40:209–216, jan 2002. doi: 10.2514/3.15052.
- [21] JL Gilarranz, LW Traub, and OK Rediniotis. A new class of synthetic jet actuators—part i: Design, fabrication and bench top characterization. Journal of Fluids Engineering, 127(2):367–376, mar 2005. doi: 10.1115/1.1839931.
- [22] Donghyun You and Parviz Moin. Active control of flow separation over an airfoil using synthetic jets. Journal of Fluids and Structures, 24(8):1349–1357, nov 2008. doi: 10.1016/j.jfluidstructs.2008.06.017.
- [23] Ashley Tuck and Julio Soria. Separation control on a NACA 0015 airfoil using a 2d micro ZNMF jet. Aircraft Engineering and Aerospace Technology, 80(2):175–180, mar 2008. doi: 10.1108/00022660810859391.
- [24] Vassili Kitsios, Laurent Cordier, Jean-Paul Bonnet, Andrew Ooi, and Julio Soria. On the coherent structures and stability properties of a leading-edge separated aerofoil with turbulent recirculation. Journal of Fluid Mechanics, 683:395–416, aug 2011. doi: 10.1017/jfm.2011.285.

- [25] NA Buchmann, C Atkinson, and Julio Soria. Influence of ZNMF jet flow control on the spatio-temporal flow structure over a NACA-0015 airfoil. Experiments in Fluids, 54(3), feb 2013. doi: 10.1007/s00348-013-1485-7.
- [26] Pititit Itsariyapinyo and Rajnish N Sharma. Large eddy simulation of a naca0015 circulation control airfoil using synthetic jets. Aerospace Science and Technology, 82:545–556, 2018.
- [27] Sang Hoon Kim and Chongam Kim. Separation control on NACA23012 using synthetic jet. Aerospace Science and Technology, 13(4-5):172–182, jun 2009. doi: 10.1016/j.ast.2008.11.001.
- [28] H Esmaili Monir, M Tadjfar, and A Bakhtian. Tangential synthetic jets for separation control. Journal of Fluids and Structures, 45:50–65, feb 2014. doi: 10.1016/j.jfluidstructs.2013.11.011.
- [29] Sebastian D Goodfellow, Serhiy Yarusevych, and Pierre E Sullivan. Momentum coefficient as a parameter for aerodynamic flow control with synthetic jets. AIAA Journal, 51(3):623–631, mar 2013. doi: 10.2514/1.j051935.
- [30] Mark A Feero, Sebastian D Goodfellow, Philippe Lavoie, and Pierre E Sullivan. Flow reattachment using synthetic jet actuation on a low-Reynolds-number airfoil. AIAA Journal, 53(7):2005–2014, jul 2015. doi: 10.2514/1.j053605.
- [31] Mark A Feero, Philippe Lavoie, and Pierre E Sullivan. Influence of synthetic jet location on active control of an airfoil at low Reynolds number. Experiments in Fluids, 58(8), jul 2017. doi: 10.1007/s00348-017-2387-x.
- [32] Wei Zhang and Ravi Samtaney. A direct numerical simulation investigation of the synthetic jet frequency effects on separation control of low-Re flow past an airfoil. Physics of Fluids, 27(5):055101, may 2015. doi: 10.1063/1.4919599.
- [33] Michael S Selig, John Francis Donovan, and David B Fraser. Airfoils at low speeds. HA Stokely, 1989.

- [34] M Selig, JJ Guglielmo, AP Broeren, and P Giguere. Summary of low-speed airfoil data summary of low-speed airfoil data. Tech. rep., University of Illinois, 1995.
- [35] Michael Breuer. Effect of inflow turbulence on an airfoil flow with laminar separation bubble: An les study. Flow, Turbulence and Combustion, 101(2): 433–456, 2018.
- [36] Shiwei Qin, Manoochehr Koochesfahani, and Farhad Jaber. Large eddy simulations of unsteady flows over a stationary airfoil. Computers & Fluids, 161: 155–170, 2018.
- [37] Régis Duvigneau and Michel Visonneau. Simulation and optimization of stall control for an airfoil with a synthetic jet. Aerospace Science and Technology, 10(4):279–287, may 2006. doi: 10.1016/j.ast.2006.01.002.
- [38] Virginia Joanne Torczon. Multidirectional search: a direct search algorithm for parallel machines. PhD thesis, Rice University, 1989. URL <https://hdl.handle.net/1911/16304>.
- [39] Régis Duvigneau, A Hay, and M Visonneau. Optimal location of a synthetic jet on an airfoil for stall control. Journal of Fluids Engineering, 129(7):825–833, jan 2007. doi: 10.1115/1.2742729.
- [40] Dj Kamari, M Tadjfar, and A Madadi. Optimization of SD7003 airfoil performance using TBL and CBL at low reynolds numbers. Aerospace Science and Technology, 79:199–211, 2018.
- [41] Mehran Tadjfar and Dj Kamari. Optimization of flow control parameters over SD7003 airfoil with synthetic jet actuator. Journal of Fluids Engineering, 142(2), oct 2020. doi: 10.1115/1.4044985.
- [42] Marshall Galbraith and Miguel Visbal. Implicit large eddy simulation of low Reynolds number flow past the SD7003 airfoil. In 46th AIAA Aerospace Sciences Meeting and Exhibit, page 225. American Institute of Aeronautics and Astronautics, jan 2008. doi: 10.2514/6.2008-225.

- [43] Sebastian Burgmann and W Schröder. Investigation of the vortex induced unsteadiness of a separation bubble via time-resolved and scanning piv measurements. Experiments in fluids, 45(4):675, 2008.
- [44] Wei Zhang, Rainer Hain, and Christian J Kähler. Scanning piv investigation of the laminar separation bubble on a sd7003 airfoil. Experiments in Fluids, 45(4):725–743, 2008.
- [45] P Catalano and R Tognaccini. Turbulence modeling for low-Reynolds-number flows. AIAA Journal, 48(8):1673–1685, aug 2010. doi: 10.2514/1.j050067.
- [46] P Catalano and R Tognaccini. Rans analysis of the low-reynolds number flow around the sd7003 airfoil. Aerospace Science and Technology, 15(8):615–626, 2011.
- [47] Philippe Spalart and Steven Allmaras. A one-equation turbulence model for aerodynamic flows. In 30th aerospace sciences meeting and exhibit, page 439, 1992. doi: 10.2514/6.1992-439.
- [48] Franck Nicoud and Frédéric Ducros. Subgrid-scale stress modelling based on the square of the velocity gradient tensor. Flow, turbulence and Combustion, 62(3):183–200, 1999.
- [49] O Lehmkuhl, I Rodríguez, A Baez, A Oliva, and CD Pérez-Segarra. On the large-eddy simulations for the flow around aerodynamic profiles using unstructured grids. Computers & Fluids, 84:176–189, 2013.
- [50] Anuj Kumar Shukla and Anupam Dewan. Flow and thermal characteristics of jet impingement on a flat plate for small nozzle to plate spacing using les. International Journal of Thermal Sciences, 145:106005, 2019.
- [51] Pietro Catalano and Renato Tognaccini. Influence of free-stream turbulence on simulations of laminar separation bubbles. In 47th AIAA Aerospace Sciences Meeting Including The New Horizons Forum and Aerospace Exposition, page 1471, 2009.

- [52] Christopher J Greenshields. Openfoam user guide version 6. The OpenFOAM Foundation, page 237, 2018.
- [53] Raad I Issa. Solution of the implicitly discretised fluid flow equations by operator-splitting. Journal of computational physics, 62(1):40–65, 1986.
- [54] Ugo Piomelli and Jeffrey Robert Chasnov. Large-eddy simulations: theory and applications. In Turbulence and transition modelling, pages 269–336. Springer, 1996.
- [55] Stephen B Pope. Ten questions concerning the large-eddy simulation of turbulent flows. New journal of Physics, 6(1):35, 2004.
- [56] Christophe Geuzaine and Jean-François Remacle. Gmsh: A 3-d finite element mesh generator with built-in pre-and post-processing facilities. International journal for numerical methods in engineering, 79(11):1309–1331, 2009.
- [57] Kalyanmoy Deb, Amrit Pratap, Sameer Agarwal, and TAMT Meyarivan. A fast and elitist multiobjective genetic algorithm: NSGA-II. IEEE transactions on evolutionary computation, 6(2):182–197, Apr 2002. ISSN 1089-778X. doi: 10.1109/4235.996017.
- [58] Kalyanmoy Deb and Ram Bhushan Agrawal. Simulated binary crossover for continuous search space. Complex systems, 9(2):115–148, 1995.
- [59] Kalyanmoy Deb. Multi-objective optimization using evolutionary algorithms, volume 16. John Wiley & Sons, Chichester, UK, 2001.

Chapter 3

Spalart-Allmaras turbulence parameter tuning for active flow control applications

3.1 Abstract

The current study employs previously optimized Synthetic Jet Actuator (SJA) parameters obtained by Tousi et al. [1, 2] to evaluate the suitability of Reynolds-averaged Navier-Stokes (RANS), using the Spalart Allmaras turbulence model (SA), in the optimization of synthetic jet actuator parameters. This is achieved through a comparison of results obtained from the SA-RANS model against those obtained from Large Eddy Simulations (LES) on a SD7003 airfoil, at a post-stall angle of attack of $\alpha = 14^\circ$ and with a Reynolds number of $Re = 6 \times 10^4$. The aim is to assess the accuracy of the 2D-RANS-SA turbulence model in Active Flow Control (AFC) applications by tuning the turbulent parameter $\tilde{\nu}$ at the computational domain inlet and at the AFC groove outlet.

Although SA-RANS is not as accurate as LES, it can still predict macroscopic aggregates such as lift and drag coefficients quite accurately, providing that the jet turbulence level is adequate. This study emphasizes the critical role played by the jet turbulence level in obtaining the correct flow behavior in the boundary layer of the optimal actuated case.

3.2 Introduction

The application of the Active Flow Control (AFC) technology to airfoils or any bluff-body is mend postpone or even suppress flow separation thereby improving aerodynamic performance. AFC techniques fall into one of three different categories [3], namely moving body, plasma and fluidic actuation. Moving body actuators act on the geometry of the body to inject momentum into the flow [4]. Plasma actuators generate fast temporal response jets of ionized fluid by applying large electric potential differences [5, 6, 7, 8, 9]. Fluidic actuators (FA), inject/-suck fluid to/from the boundary layer, they are by far the most common sort of actuators, some recent advances towards the understanding of such devices can be found in [10, 11, 12].

Among the fluidic actuators, Synthetic Jet Actuators (SJA) also called Zero Net Mass Flow Actuators (ZNMFA) are particularly used due to their simplicity and capability of suppressing flow separation [13, 14, 15, 16, 17]. SJAs do not require an external fluid supply, since their zero net mass flux can be simply obtained with an oscillating membrane housed inside a tiny cavity just beneath the surface. SJAs have proven to be more effective than Continuous Jet Actuators (CJA), at comparable power input levels, in improving the performances of a stator compressor cascade [18, 19, 20, 21, 22].

Most of the previous research studied the combined effect of two SJA parameters, the actuation frequency f_j and the jet momentum coefficient C_μ . The former is nondimensionalised with the airfoil chord C and the free-stream velocity U_∞ following $f_j/(U_\infty/C)$, while the momentum coefficient is defined as $C_\mu = (\rho_j U_j^2 h \sin \theta)/(\rho_\infty U_\infty^2 C)$, with h the jet width, ρ_j and ρ_∞ the jet and far field fluid densities, respectively, U_j the maximum jet velocity and θ_j the jet inclination angle with respect to the surface.

Among the first experimental studies on the effects of the momentum coefficient, frequency and position of a synthetic jet actuator over a symmetric airfoil was undertaken by [22, 23]. They observed that locating the actuator close to the boundary layer separation point minimised the momentum coefficient required for flow reattachment. Actuating with frequencies of the same order of magnitude as the natural vortex shedding one produced unsteady reattachment, while

full flow reattachment could be obtained when actuating at about ten times the vortex-shedding frequency.

Experimental and numerical studies on a NACA0015 airfoil at $Re = 8.96 \times 10^5$ were carried on by Gilarranz et al. [24] and You and Moin [25], respectively, in both cases SJA's were employed. The effectiveness of the actuation was rather low at angles of attack below $\alpha \leq 10$, but rather high at α values around $\alpha = 12^\circ$. For angles of attack $\alpha > 25^\circ$ the actuation frequencies required to obtain high lift coefficients were particularly large. When using the following AFC parameters $C_\mu = 0.0123$, $f_j = 1.284U_\infty/C$ and $\theta = 30.2^\circ$, the lift increase versus the baseline case obtained by the numerical simulations was of 70%. The same airfoil but at a lower Reynolds number $Re = 3.9 \times 10^4$ was experimentally studied by Tuck and Soria [26], and simulated numerically via LES by Kitsios et al. [27]. Maximum efficiency was obtained for SJA nondimensional frequencies around 1.3 in the experiments. The combination of a momentum coefficient value of $C_\mu = 0.0123$ with the highest frequency, delayed stall from $\alpha_s = 10^\circ$ baseline case, to 18° . Numerical simulations revealed that the optimal frequencies coincided with the baseline shedding frequency (f_{vK}) and its first harmonic ($2f_{vK}$). Via PIV experimentation Buchmann et al. [28] obtained the same conclusion. Itsariyapinyo and Sharma [29] numerically studied via LES the same airfoil at $Re = 1.1 \times 10^5$, SJA was placed tangentially to the surface at the airfoil trailing edge. The lift coefficient increased linearly with the momentum coefficient up to a certain threshold, a further increase of the momentum coefficient tended to a lift coefficient saturation.

Reynolds-averaged Navier-Stokes (RANS) equations and the $k-\omega$ SST turbulence model on a NACA 23012 airfoil at $Re = 2.19 \times 10^6$ and $\alpha \in [6^\circ, 22^\circ]$ was applied by Kim and Kim [30] to analyse the flow separation control using 5 different slot/flap/jet configurations. Low actuation frequencies and large momentum coefficients were found the most adequate to reattach the boundary layer in large separated regions. They proposed multi-array/multi-location SJA implementation to reduce the required jet velocity magnitude. Via using the RANS-Spalart-Allmaras turbulence model, the same airfoil and Reynolds number were studied by Monir et al. [31]. Aerodynamic efficiency was substantially increased when using SJA actuation at $\theta_j = 43^\circ$, but tangential actuation was by far the optimum.

The effect of SJA on a NACA0025 airfoil at $Re = 10^5$ and $\alpha = 5^\circ$ was experimentally studied by Goodfellow et al. [32]. They realized that the momentum coefficient was the primary flow control parameter, obtaining up to 50% drag decrease when the momentum coefficient C_μ overcome a certain threshold. The same airfoil and Reynolds number but at $\alpha = 10^\circ$ and $\alpha = 12^\circ$ were respectively assessed by Feero et al. [33, 34]. When using excitation frequencies around the vortex shedding one, the momentum coefficients required for flow reattachment were one order of magnitude lower than when employing higher frequencies. Flow control was more effective when pacing the jet slot nearby the baseline case temporal averaged boundary layer separation point. The effect of AFC excitation frequency on a NACA0018 airfoil at $\alpha = 10^\circ$ and $Re = 1000$ using three-dimensional Direct Numerical Simulation (DNS) was investigated by Zhang and Samtaney [35]. Three different non-dimensional frequencies were assessed ($f_j = 0.5U_\infty/C$, 1 and 4), being $f_j = 1U_\infty/C$ the optimal one.

The Selig-Donovan 7003 (SD7003) [36, 37] airfoil was designed for low Reynolds number applications, and it has been recently studied at $Re = 6 \times 10^4$ via LES [38, 39, 40]. Using an angle of attack of $\alpha = 4^\circ$, Breuer [38] evaluated several inlet turbulence intensities, ranging from nil to $Tu = 11\%$, with the aim of understanding its impact on the LSB. They observed that high turbulence intensity values could reduce and even suppress the LSB, thereby enhancing aerodynamic performance. Different inlet velocity oscillation amplitudes and frequencies at the same $\alpha = 4^\circ$ were analysed by Qin et al. [39]. Flow separation was delayed during the acceleration phase while progressing upstream towards the leading edge in the deceleration phase. LES simulations at $\alpha = \{4^\circ, 11^\circ, 14^\circ\}$ and using SJA were performed by Rodriguez et al. [40]. Aerodynamic efficiency increase of up to $\Delta\eta/\eta = 124\%$ at $\alpha = 14^\circ$, actuation effectiveness largely decreased at pre-stall angles of attack.

Recent research in the field of AFC application to airfoils has been extensive, with notable contributions made by Tousi et al. [1, 2]. The study conducted by these authors involved the optimization of five SJA parameters for a SD7003 airfoil at a Reynolds number of 6×10^4 and at various pre- and post-stall angles of attack ($\alpha = 4^\circ, 6^\circ, 8^\circ, 14^\circ$) using Genetic Algorithm (GA) and the RANS with Spalart-Allmaras turbulence model.

A key difference between the research of [41] and that of [1] is the methodology employed. While the former utilized an Artificial Neural Network (ANN) to predict the majority of the AFC parameters, the latter relied on precise CFD simulations for the entire optimization process, resulting in higher accuracy of the results at the expense of increased computational cost.

Further comparisons between LES and RANS-SA simulations are presented in [2], where it was necessary to modify the turbulence parameter $\tilde{\nu}$ at the inlet of the computational domain to maximize the performance of the SA turbulence model in AFC applications. The primary focus of this paper is to examine the impact of the turbulence parameter $\tilde{\nu}$ defined at the jet and inlet boundaries, with the aim of optimizing the results obtained by the SA turbulence model in AFC applications.

The rest of the paper is structured as follows. The governing equations for the RANS-SA model are presented in §3.3. Section §3.4 introduces numerical modeling. The results and conclusions are respectively presented in sections §3.5 and §3.6.

3.3 Governing equations

The CFD simulations, performed in the optimization study [1], were all based on the Unsteady Reynolds-Averaged Navier-Stokes (URANS) with Spalar-Allmaras (SA) turbulence model [42]. Employing Direct Numerical simulations (DNS) or Large Eddy Simulations (LES) was not feasible due to their massive computation power requirement. The Navier-Stokes equations for incompressible flow take the form of,

$$\frac{\partial u_i}{\partial x_i} = 0 \quad (3.1)$$

$$\frac{\partial u_i}{\partial t} + \frac{\partial u_i u_j}{\partial x_j} = -\frac{1}{\rho} \frac{\partial p}{\partial x_i} + \nu \frac{\partial^2 u_i}{\partial x_j \partial x_j} \quad (3.2)$$

Calling $\phi(x, t)$ any generic flow variable, it can be written as the sum of its mean $\bar{\phi}(x, t)$ and fluctuating components $\phi'(x, t)$, being $\phi(x, t) = \bar{\phi}(x, t) + \phi'(x, t)$. After substituting each variable by its mean and fluctuating components in the Navier-Stokes equations and taking the time average, the following Reynolds-averaged Navier–Stokes equations are obtained.

$$\frac{\partial \bar{u}_i}{\partial x_i} = 0 \quad (3.3)$$

$$\frac{\partial \bar{u}_i}{\partial t} + \frac{\partial \bar{u}_i \bar{u}_j}{\partial x_j} = -\frac{1}{\rho} \frac{\partial \bar{p}}{\partial x_i} + \nu \frac{\partial^2 \bar{u}_i}{\partial x_j \partial x_j} - \frac{\partial \overline{u'_i u'_j}}{\partial x_j} \quad (3.4)$$

The term $\overline{u'_i u'_j}$ is called the Reynolds stress tensor and it is usually denoted by R_{ij} . Considering the Boussinesq hypothesis, the deviatoric part of the tensor is represented as.

$$R_{ij} - \frac{1}{3} R_{kk} \delta_{ij} = -2\nu_t \bar{S}_{ij} \quad (3.5)$$

where ν_t is the kinematic eddy viscosity that needs to be modeled using a RANS turbulence model.

As stated earlier, the turbulence model selected for the present applications was the Spalart-Allmaras (SA). This model was proposed by [42] and solves a single transport equation for the modified form of the turbulent kinetic energy called $\tilde{\nu}$. This new parameter is identical to ν_t except in the viscous-affected region nearby the wall.

$$\nu_t = \tilde{\nu} \left(\frac{\chi^3}{\chi^3 + C_{v1}^3} \right) \quad (3.6)$$

The transport equation of $\tilde{\nu}$ is expressed as:

$$\frac{\partial \tilde{\nu}}{\partial t} + u_j \frac{\partial \tilde{\nu}}{\partial x_j} = \frac{1}{\sigma} \left[\frac{\partial}{\partial x_j} \left((\nu + \tilde{\nu}) \frac{\partial \tilde{\nu}}{\partial x_j} \right) + C_{b2} \frac{\partial \tilde{\nu}}{\partial x_i} \frac{\partial \tilde{\nu}}{\partial x_i} \right] + C_{b1} (1 - f_{t2}) \tilde{S} \tilde{\nu} - \left[C_{w1} f_w - \frac{C_{b1}}{\kappa^2} f_{t2} \right] \left(\frac{\tilde{\nu}}{d} \right)^2 \quad (3.7)$$

where:

$$\begin{aligned} f_\omega &= g \left[\frac{1+C_\omega^6}{g^6+C_\omega^6} \right]^{1/6}, \quad g = r + C_{\omega 2}(r^6 - r), \quad r = \min \left[\frac{\tilde{\nu}}{S \kappa^2 d^2}, 10 \right] \\ \tilde{S} &= \Omega + \frac{\tilde{\nu}}{\kappa^2 d^2} f_{v2}, \quad f_{t2} = C_{t3} \exp(-C_{t4} \chi^2), \quad f_{v2} = 1 - \frac{\chi}{1+\chi f_{v1}} \\ f_{v1} &= \frac{\chi^3}{\chi^3 + C_{v1}^3}, \quad \chi = \frac{\tilde{\nu}}{\nu} \end{aligned} \quad (3.8)$$

Being d the distance from a given point to the nearest wall, and Ω the magnitude of the vorticity. The model constants have the following default values:

$$\begin{aligned}
C_{b1} &= 0.1355, & C_{b2} &= 0.622, & \sigma &= \frac{2}{3}, & C_{\omega1} &= \frac{C_{b1}}{\kappa^2} + \frac{(1+C_{b2})}{\sigma} \\
C_{\omega2} &= 0.3, & C_{\omega3} &= 2.0, & C_{v1} &= 7.1, & \kappa &= 0.4187, & C_{t3} &= 1.2 \\
C_{t4} &= 0.5
\end{aligned} \tag{3.9}$$

3.4 Domain, boundary conditions and mesh

This section explores the numerical modeling approach employed, including key aspects like domain specifications, boundary conditions, and mesh details.

Fig. 3.1a shows the computational domain encompassing the SD7003 airfoil with a chord length of C . The leading edge is located at the origin of the coordinate system and the horizontal distance between this point and the computational domain inlet (blue curve) is set to $15C$. The computational domain outlet (red line) is located $19C$ downstream of the airfoil trailing edge. The wing profile is set horizontally, and the 14 degrees angle of attack is achieved by tilting the free-stream velocity. For the cases where the SJA is implemented, a groove through which the fluid is injected/sucked is required. Fig. 3.1b depicts the airfoil with a generic synthetic jet implementation on the upper surface nearby the leading edge. The synthetic jet geometrical design parameters, jet angle (θ), position (x) and width (h), are shown in the zoomed view.

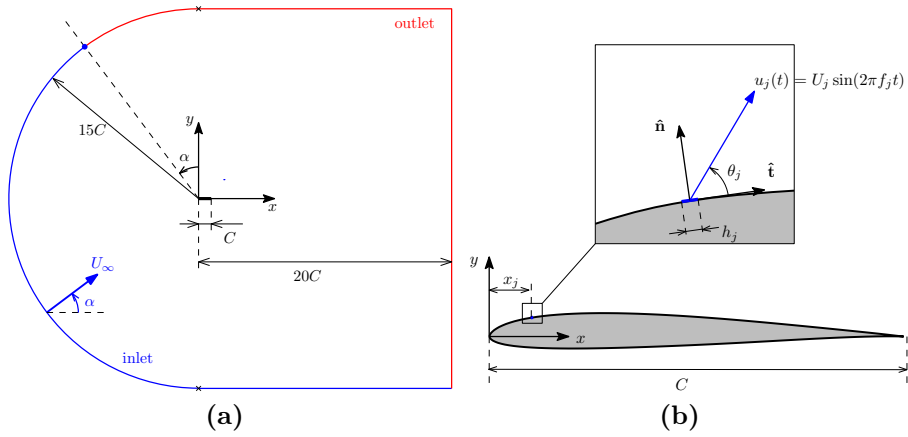


Figure 3.1: (a) Computational domain. (b) Synthetic jet parameters.

The boundary conditions (BC) used for the velocity and pressure are as follows. At the inlet, a constant velocity profile is imposed; its components are set to $(u, v) \equiv (U_\infty \cos \alpha, U_\infty \sin \alpha)$ where α is the angle of attack. Neumann BC are prescribed for the inlet pressure. At the outlet, Dirichlet for pressure and Neumann for velocity is considered. At the wall, no-slip condition for velocity and Neumann for pressure is applied. In active flow control cases, the jet BC is specified by a time-varying velocity profile and a Neumann BC for pressure. Specifically, the velocity profile is given by $u_j = U_j \sin(2\pi ft)$, where U_j is the maximum jet velocity, f is the dimensional frequency of the jet oscillations, and t is the dimensional time. The top-hat velocity profile is chosen for the SJA, as already employed in [19, 21].

In the previous section, it was demonstrated that the SA model contains a single turbulence parameter, $\tilde{\nu}$, for which boundary conditions must be defined at all boundaries. In [2], it was observed that actuated cases at $\alpha = 14^\circ$ are heavily influenced by the free-stream turbulent level prescribed at the inlet. To investigate this relationship, the researchers conducted a parametric study by exploring a wide range of $\tilde{\nu}/\nu \in [10^{-20}, 10^2]$ at the inlet while employing Neumann boundary conditions at the jet and outlet boundaries. They also imposed $\tilde{\nu} = 0$ at the wall, as no wall function was used.

The aim of this paper is to further investigate the impact of utilizing different combinations of $\tilde{\nu}$ boundary conditions at the jet and inlet boundaries. To simplify the discussion, we have labeled these combinations as $i_D j_D$, $i_N j_N$, and $i_N j_D$, where i and j denote the inlet and jet boundaries, and D and N refer to the Dirichlet and Neumann boundary conditions, respectively. It is worth noting that the $i_D j_N$ configuration has already been analyzed in [2].

The mesh assessment was performed in [1], where it was concluded that a hybrid mesh with 45,466 cells and $y^+=0.3$ was capable of yielding mesh-independent results; a general overview of the mesh is shown in Fig. 3.2. Another study [2] demonstrated the efficacy of an unstructured grid with 28.7 million cells for LES. The mesh was determined to produce aerodynamic coefficients consistent with those reported in the literature and was fine enough to accurately resolve over 95% of the turbulent kinetic energy, leaving less than 5% to be modeled by the sub-grid scale model.

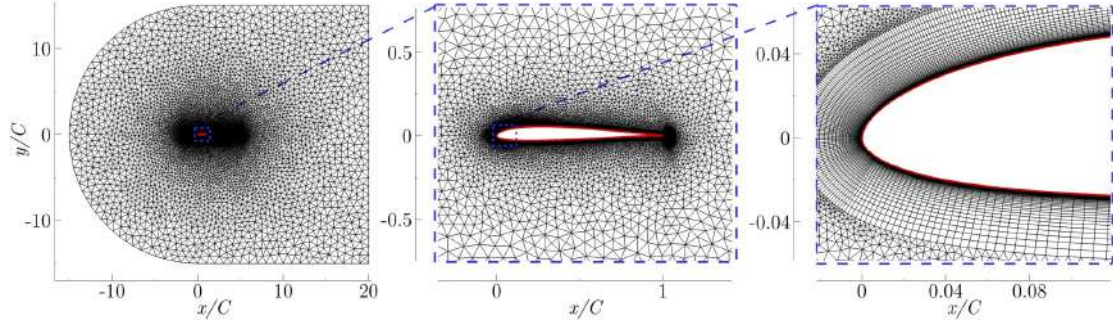


Figure 3.2: Mesh overview and zoomed views around the airfoil and leading edge

3.5 Results

As stated earlier, the optimization of synthetic jet actuator (SJA) parameters applied to the SD7003 airfoil at $Re = 60,000$ and 14-degree angle of attack was undertaken using RANS-SA in [1], where the optimum jet parameters with which maximum lift and efficiency achieved were reported. In a subsequent study [2], the previously obtained optimals were simulated anew using wall-resolved large eddy simulation (LES), demonstrating that the RANS-SA requires turbulence parameter adjustment to attain decently similar results to the LES. A parametric analysis of the RANS-SA turbulent viscosity ratio at the inlet was conducted in the same study, covering a wide range of $\tilde{\nu}/\nu$ values ranging from 10^{-20} to 10^2 while maintaining the jet to Neumann boundary conditions ($i_D j_N$). It was observed that for the optimum AFC cases (maximum lift and efficiency) prescribing $\tilde{\nu}/\nu \in [10^{-6}, 10^{-3}]$ at the domain inlet and Neumann boundary conditions at the jet outlet yield comparable aerodynamic coefficients to the respective LES cases.

Here, we mainly focus on the $i_D j_D$ configuration applied to the RANS-SA maximum efficiency case. To minimize the free-stream turbulence effect the inlet $\tilde{\nu}/\nu$ is fixed at 10^{-20} for all the cases and the sensitivity of results to the different jet values, $\tilde{\nu}/\nu \in [10^{-20}, 10^2]$, is thoroughly assessed.

It is worth noting that the other two remaining $\tilde{\nu}/\nu$ boundary condition combinations, namely $i_N j_N$ and $i_N j_D$, are also evaluated. It was observed that considering zero gradient BC at both inlet and jet boundaries ($i_N j_N$) is not an effective adjustment since under this condition, SA model fails in triggering the correct

value of $\tilde{\nu}/\nu$ in the boundary layer, and the results show sensitivity to the $\tilde{\nu}/\nu$ initial condition. On the other hand, i_Nj_D configuration shows a similar behavior as the i_Dj_D setup, indicating that the effect of inlet turbulence level can be minimized by setting $\tilde{\nu}/\nu$ BC to either a low value of 10^{-20} or a Neumann BC. Under these conditions, jet turbulence level plays a decisive role in flow dynamics around the airfoil.

Fig. 3.3 shows the C_d and C_l values obtained for the i_Dj_D ($\tilde{\nu}_i/\nu = 10^{-20}$ and $\tilde{\nu}_j/\nu \in [10^{-20}, 10^2]$) (red circles) and compare them with the ones of i_Dj_N ($\tilde{\nu}_i/\nu \in [10^{-20}, 10^2]$ and $\tilde{\nu}_j/\nu = zeroGradient$) (blue circles) [2]. For the latter configuration, the levels of $\tilde{\nu}/\nu$ at the jet outlet are read after the simulations and depicted as yellow circles in this figure.

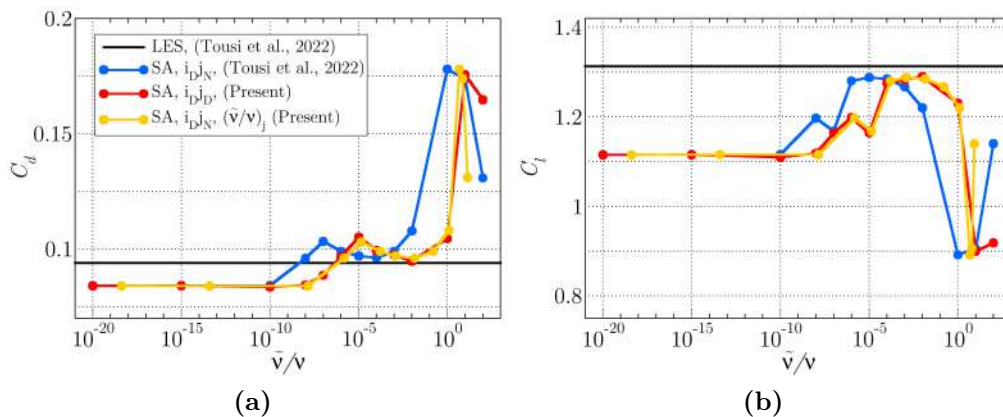


Figure 3.3: Results sensitivity to the jet preturbulence levels (i_Dj_D , red) and its comparison with the results sensitivity analysis to the inlet preturbulence level (i_Dj_N , blue) [2]. For the latter, the turbulence level obtained after the simulations at the jet ($\tilde{\nu}_j/\nu$) is shown by the yellow circles (i_Dj_N , ($\tilde{\nu}_j/\nu$)). The horizontal back lines are the LES result [2]. (a) Average lift coefficient C_l . (b) Average drag coefficient C_d .

The first thing that draws attention is the coincidence of the $\tilde{\nu}/\nu$ values obtained at the jet (yellow circles) with the given $\tilde{\nu}/\nu$ at the jet in the present study (blue circles). This indicates that employing Neumann BC at the jet boundary [2] was like introducing a value at the jet but doing so indirectly by acting on the inlet BC and letting the value at the jet be boosted by the boundary layer instability. Furthermore, comparing the i_Dj_D trend line (blue) against the LES

(black line) reveals that for the RANS-SA maximum efficiency case, a range of $\tilde{\nu}/\nu \in [10^{-4}, 10^{-1}]$ at the jet is sufficient to deliver comparable results to the LES.

It is also noteworthy to mention that the impact of high turbulence levels on the behavior of eddies generated by a jet. Specifically, when a turbulence intensity level greater than the kinematic viscosity ratio ($\tilde{\nu}/\nu > 1$) is induced, the eddies originating from the jet are swiftly suppressed at the outlet. This leads to a reduction in the momentum exchange between these eddies and the boundary layer. Consequently, this phenomenon effectively negates the beneficial effects of actuation, resulting in a fully separated flow, diminished lift, and increased drag.

In the remaining of the manuscript, the focus has been placed on the RANS-SA cases with $\tilde{\nu}_j/\nu = 10^{-3}$ (*jet-optimal*), $\tilde{\nu}_j/\nu = 10^{-5}$ (*jet-suboptimal*) and $\tilde{\nu}_i/\nu = 10^{-5}$ (*inlet-optimal*) [2]. The accuracy of their results is assessed with respect to the *LES* [2]. The aerodynamic coefficients of these cases are summarised in Table. 3.1

Case	Turbulence model	$\tilde{\nu}/\nu$		C_l	C_d	$\frac{C_l}{C_d}$
		inlet	jet			
<i>LES</i> [2]	LES	-	-	1.313	0.094	13.96
<i>inlet-optimal</i> [2]		1e-05	<i>zeroGradient</i>	1.288	0.097	13.27
<i>jet-optimal</i> (present)	RANS-SA	1e-20	1e-03	1.283	0.097	13.17
<i>jet-suboptimal</i> (present)		1e-20	1e-05	1.164	0.105	11.06

Table 3.1: Aerodynamic coefficients for the *jet-optimal*, *jet-suboptimal*, *inlet-optimal* and *LES* cases

Fig. 3.4 shows the mean pressure coefficient $C_p = 2(p - p_\infty)/\rho u_\infty^2$ and skin-friction coefficient $C_f = 2\tau_w/\rho u_\infty^2$ distribution along the upper surface of the airfoil obtained by *jet-optimal* (red), *jet-suboptimal* (gray), *inlet-optimal* (blue) and *LES* (black).

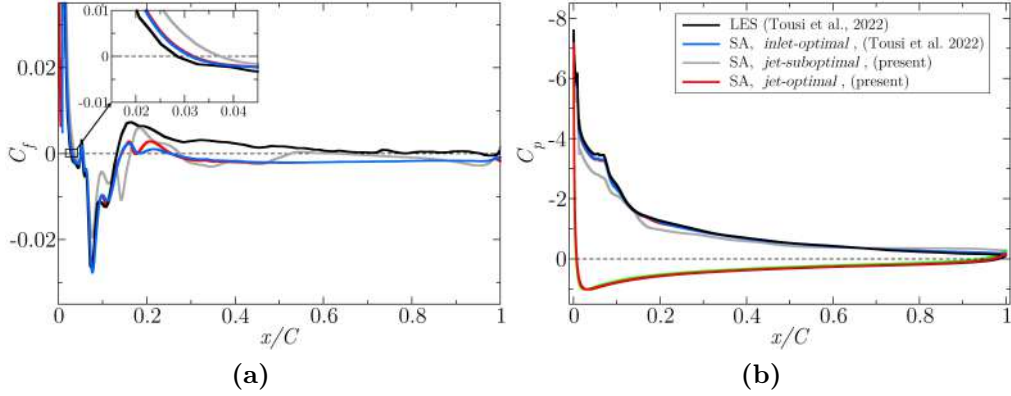


Figure 3.4: Skin friction coefficient (a) and pressure coefficient (b) for *jet-optimal* (red), *jet-suboptimal* (grey), *inlet-optimal* (blue) and *LES* (black). The zoomed view shows the separation locations for different cases.

The *jet-optimal* and *inlet-optimal* simulations, unlike *jet-suboptimal*, are able to accurately reproduce the C_f in the front part of the airfoil. They captured the separation and reattachment point locations ($x_s = 0.031$ and $x_r = 0.14$) rather close to the LES ones ($x_s = 0.028$ and $x_r = 0.132$), whereas *jet-suboptimal* detect these locations with larger discrepancies further downstream ($x_s = 0.037$ and $x_r = 0.162$). After the reattachment, the friction coefficient should remain positive ($C_f > 0$) until the trailing edge, indicating the attached boundary layer across the airfoil. However, the RANS-SA cases do not properly emulate such a trend. While C_f in *jet-optimal* and *inlet-optimal* remain a small and negative value across the major part of the airfoil, in *jet-suboptimal* delivers a wavy trend, indicating consecutive separations and reattachments over the airfoil. The reason for such behavior in the latter is likely because of the passage of vortical structures originating from the jet and shedding downstream. These structures ideally have to be modeled by the turbulence model, but due to insufficient turbulence injection through the jet, the eddies are not properly modeled and in return contaminate the average flow field.

Pressure distributions on the pressure side of the airfoil obtained by RANS-SA coincide with the LES. On the suction side, *jet-optimal* and *inlet-optimal* cases are able to replicate the LES distribution, except for a small portion near the transition region where the suction is slightly less in RANS-SA cases than LES.

The jet-suboptimal, on the other hand, presents larger discrepancies across the entire upper surface. Significantly lower suction in the front portion and slightly higher at the back half causes the net effect of a lift decrease and sharp pressure drag increase.

The time- and span-averaged streamlines, as well as colormaps of the negative Reynolds shear stress $\langle u'v' \rangle$ for LES and three RANS-SA simulations are displayed in Fig. 3.5.

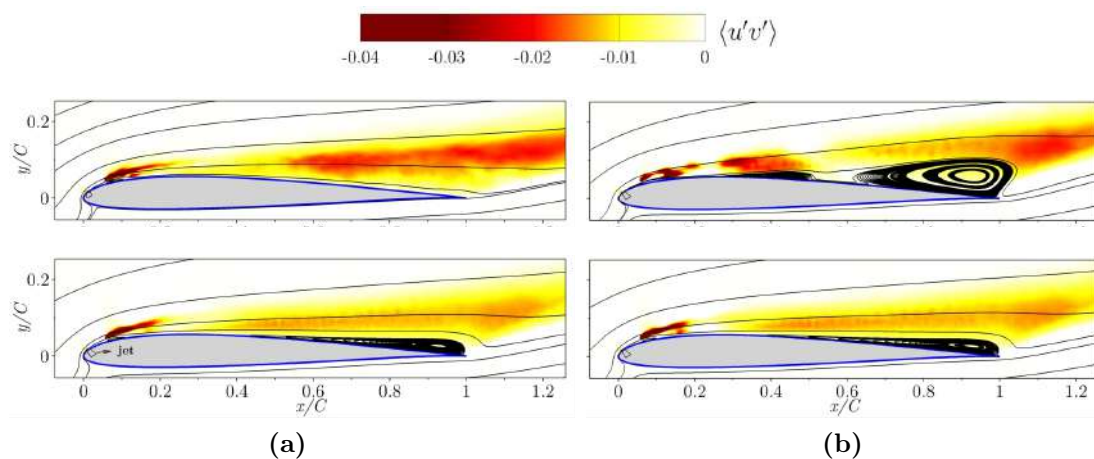


Figure 3.5: Spanwise-averaged $\langle u'v' \rangle$ component of the Reynolds stress tensor and time- and spanwise-averaged streamlines. (a) *LES* (top) and *inlet-optimal* (bottom). (b) *jet-suboptimal* (top) and *jet-optimal* (bottom).

Negative shear-stress values are associated with a positive and a negative fluctuation term, whether streamwise fluctuation velocity is positive ($u' > 0$) and the cross-stream one is negative ($v' < 0$), or vice-versa. It characterizes the areas where a large momentum interchange between fluid particles exists, and represents the exchange of momentum that occurs between the separated shear layer and the outside inviscid flow, as well as between the shear layer and the inner recirculation zone. Notice that such a large momentum interchange is particularly large around the jet injection area. From the streamlines plot and considering the LES simulation, it can be seen that the boundary layer remains attached to the upper surface of the airfoil, whereas it accompanies several consecutive separations and reattachments when using the RANS-SA model, this is particularly seen in sub-optimal turbulence conditions. In all cases near the leading edge, a small bubble

forms right after the jet location due to the interaction between the freestream and jet stream flows. This region is characterized by high-shear stress which despite the inducement of high friction drag, it contributes to boundary layer reattachment, reducing the drag pressure term and increasing the lift. When analyzing the downstream area, the averaged flow patterns obtained from the different RANS cases deviate from the LES one. In optimal conditions, a thin and elongated separation bubble covers almost the second half of the airfoil. On the other hand, the sub-optimal RANS generates two separated bubbles, one in the middle and one larger at the trailing edge. One possible explanation for such behavior is that the turbulence intensity associated with the AFC jet is insufficient to reattach the boundary layer.

Fig. 3.6 introduces the variation of the mean streamwise velocity profiles at various streamwise positions, from $x/C = 0.1$ to $x/C = 1$, as a function of the normalized wall normal distance.

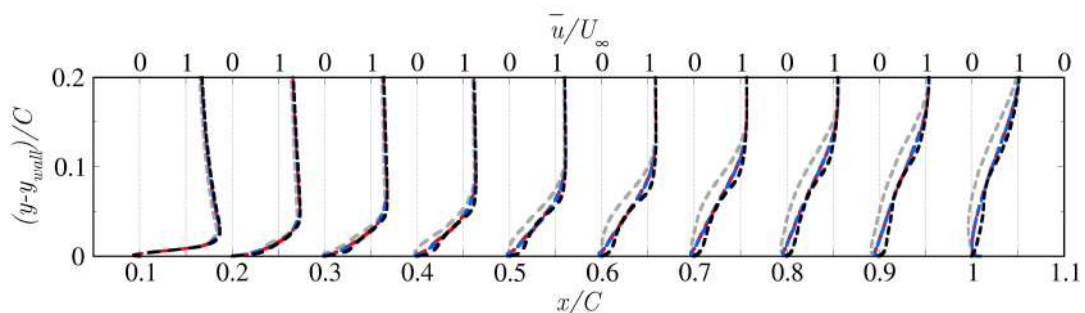


Figure 3.6: Evolution of the upper-surface boundary layer along the airfoil. Time- and spanwise-averaged streamwise velocity profiles $\langle u(x, y, z; t) \rangle_{t,z}$ at streamwise coordinates $x/C = 0.1$ through $x/C = 1$, as a function of wall-normal distance. Shown are the *LES* (black), *inlet-optimal* (blue), *jet-optimal* (red) and *jet-suboptimal* (grey).

The flow profiles obtained from LES indicate that the boundary layer remains attached over the majority of the upper surface due to the influence of the synthetic jet actuator. The only instance of flow separation, manifesting as a negative flow profile, occurs at $x = 0.1$, where a small bubble is generated downstream of the jet location, as previously depicted in Fig. 3.5. The velocity profiles obtained by inlet-optimal (blue) and jet-optimal (red) are identical along the entire surface, further reinforcing the notion that the appropriate setting of the jet turbulence

level is critical for a realistic boundary layer flow behavior. These velocity profiles are in good agreement with those obtained from LES, particularly so in the front portion of the airfoil. However, as the flow moves downstream from $x = 0.4$, a small negative velocity in close proximity to the wall is observed that is corresponding to the thin recirculation bubble depicted in Fig. 3.5. On the other hand, the velocity profiles obtained from the suboptimal jet turbulence level (gray), show significant discrepancies as compared to the LES results.

3.6 Conclusions

In previous studies, [1, 2] performed the optimization of synthetic jet actuator parameters to obtain the maximum lift and efficiency on the SD7003 airfoil at a $Re = 60,000$ and 14° angle of attack. The Reynolds-Averaged Navier-Stokes with Spalart-Allmaras turbulence model was used for the optimization; the suitability of this model was assessed by conducting Large Eddy Simulations over optimals. It was concluded that when actuation is switched on, the SA results are sensitive to the inlet turbulence level defined by the $\tilde{\nu}$ parameter. A parametric study revealed that the optimum $\tilde{\nu}/\nu$ at the inlet falls within $[10^{-6}, 10^{-3}]$ range. In that study, the $\tilde{\nu}$ at the jet boundary was kept to zero gradient BC (Neumann) for all the simulations.

Here, we explore the impact of various $\tilde{\nu}$ boundary condition combinations at the jet and inlet boundaries. We observed that employing Neumann BC at both the inlet and jet boundaries is not an effective approach since the results become dependent on the $\tilde{\nu}$ initial condition. On the other hand, adapting Dirichlet BC at both boundaries seems to be the most appropriate method. We study $\tilde{\nu}/\nu \in [10^{-20}, 10^2]$ range at the jet boundaries while fixing the inlet $\tilde{\nu}/\nu$ to a very low value (10^{-20}) in all cases i.e minimizing the inlet turbulence effect. It was observed that for a range of $\tilde{\nu}/\nu \in [10^{-4}, 10^{-1}]$ at the jet, the results are exactly the same as the [2] work with an optimum range of $\tilde{\nu} \in [10^{-6}, 10^{-3}]$ imposed at the inlet. This finding suggests that utilization of zero gradient at the jet may not have been the most effective approach. Essentially, it is like indirectly introducing a value at the jet by manipulating the inlet BC and relying on the boundary layer instability to amplify the value at the boundary.

To achieve a realistic baseline turbulence level in the boundary layer that promotes transition and facilitates the proper interaction between the jet and upstream flow, it is imperative to introduce turbulence through the jet rather than relying on the upstream flow.

3.7 References

- [1] Navid Monshi Tousi, Marti Coma, Josep Maria Bergada, Jordi Pons-Prats, Fernando Mellibovsky, and Gabriel Bugada. Active flow control optimisation on sd7003 airfoil at pre and post-stall angles of attack using synthetic jets. Applied Mathematical Modelling, 2021. doi: <https://doi.org/10.1016/j.apm.2021.05.016>.
- [2] NM Tousi, JM Bergadà, and F Mellibovsky. Large eddy simulation of optimal synthetic jet actuation on a sd7003 airfoil in post-stall conditions. Aerospace Science and Technology, page 107679, 2022.
- [3] Louis N. Cattafesta and Mark Sheplak. Actuators for active flow control. Annual Review of Fluid Mechanics, 43(1):247–272, jan 2011. doi: 10.1146/annurev-fluid-122109-160634.
- [4] Li Wang and Fang bao Tian. Numerical simulation of flow over a parallel cantilevered flag in the vicinity of a rigid wall. Physical Review E, 99(5), may 2019. doi: 10.1103/physreve.99.053111.
- [5] Young-Chang Cho and Wei Shyy. Adaptive flow control of low-Reynolds number aerodynamics using dielectric barrier discharge actuator. Progress in Aerospace Sciences, 47(7):495–521, oct 2011. doi: 10.1016/j.paerosci.2011.06.005.
- [6] Saeed Foshat. Numerical investigation of the effects of plasma actuator on separated laminar flows past an incident plate under ground effect. Aerospace Science and Technology, 98:105646, mar 2020. doi: 10.1016/j.ast.2019.105646.

- [7] Nicolas Benard and Eric Moreau. Electrical and mechanical characteristics of surface AC dielectric barrier discharge plasma actuators applied to airflow control. Experiments in Fluids, 55(11), nov 2014. doi: 10.1007/s00348-014-1846-x.
- [8] N Benard, Jordi Pons-Prats, Jacques Periaux, Gabriel Bugeada, P Braud, JP Bonnet, and E Moreau. Turbulent separated shear flow control by surface plasma actuator: experimental optimization by genetic algorithm approach. Experiments in Fluids, 57(2), jan 2016. doi: 10.1007/s00348-015-2107-3.
- [9] Maria Grazia De Giorgi, Valentina Motta, and Antonio Suma. Influence of actuation parameters of multi-dbd plasma actuators on the static and dynamic behaviour of an airfoil in unsteady flow. Aerospace Science and Technology, 96:105587, 2020.
- [10] Masoud Baghaei and Josep M Bergada. Analysis of the forces driving the oscillations in 3d fluidic oscillators. Energies, 12(24):4720, dec 2019. doi: 10.3390/en12244720.
- [11] Masoud Baghaei and Josep M Bergada. Fluidic oscillators, the effect of some design modifications. Applied Sciences, 10(6):2105, mar 2020. doi: 10.3390/app10062105.
- [12] Josep M Bergadà, Masoud Baghaei, Bhanu Prakash, and Fernando Mellibovsky. Fluidic oscillators, feedback channel effect under compressible flow conditions. Sensors, 21(17):5768, 2021.
- [13] Ari Glezer and Michael Amitay. Synthetic jets. Annual review of fluid mechanics, 34(1):503–529, 2002.
- [14] Christopher Rumsey, Thomas Gatski, William Sellers, Veer Vatsa, and Sally Viken. Summary of the 2004 cfd validation workshop on synthetic jets and turbulent separation control. In 2nd AIAA Flow Control Conference, page 2217, 2004.
- [15] Israel Wygnanski. The variables affecting the control of separation by periodic excitation. In 2nd AIAA Flow Control Conference, page 2505, 2004.

- [16] N Findanis and NA Ahmed. The interaction of an asymmetrical localised synthetic jet on a side-supported sphere. Journal of Fluids and Structures, 24(7):1006–1020, oct 2008. doi: 10.1016/j.jfluidstructs.2008.02.002.
- [17] LIU Zhiyong, LUO Zhenbing, LIU Qiang, and ZHOU Yan. Modulation of driving signals in flow control over an airfoil with synthetic jet. Chinese Journal of Aeronautics, 33(12):3138–3148, 2020.
- [18] MG De Giorgi, CG De Luca, A Ficarella, and F Marra. Comparison between synthetic jets and continuous jets for active flow control: Application on a NACA 0015 and a compressor stator cascade. Aerospace Science and Technology, 43:256–280, jun 2015. doi: 10.1016/j.ast.2015.03.004.
- [19] S Traficante, MG De Giorgi, and A Ficarella. Flow separation control on a compressor-stator cascade using plasma actuators and synthetic and continuous jets. Journal of Aerospace Engineering, 29(3):04015056, 2016.
- [20] Maria Grazia De Giorgi, Stefania Traficante, Carla De Luca, Daniela Bello, and Antonio Ficarella. Active flow control techniques on a stator compressor cascade: a comparison between synthetic jet and plasma actuators. In Turbo Expo: Power for Land, Sea, and Air, volume 44748, pages 439–450. American Society of Mechanical Engineers, 2012.
- [21] Hongxin Zhang, Shaowen Chen, Yun Gong, and Songtao Wang. A comparison of different unsteady flow control techniques in a highly loaded compressor cascade. Proceedings of the Institution of Mechanical Engineers, Part G: Journal of Aerospace Engineering, 233(6):2051–2065, 2019.
- [22] Michael Amitay, Douglas R Smith, Valdis Kibens, David E Parekh, and Ari Glezer. Aerodynamic flow control over an unconventional airfoil using synthetic jet actuators. AIAA Journal, 39:361–370, jan 2001. doi: 10.2514/3.14740.
- [23] Michael Amitay and Ari Glezer. Role of actuation frequency in controlled flow reattachment over a stalled airfoil. AIAA Journal, 40:209–216, jan 2002. doi: 10.2514/3.15052.

- [24] JL Gilarranz, LW Traub, and OK Rediniotis. A new class of synthetic jet actuators—part i: Design, fabrication and bench top characterization. Journal of Fluids Engineering, 127(2):367–376, mar 2005. doi: 10.1115/1.1839931.
- [25] Donghyun You and Parviz Moin. Active control of flow separation over an airfoil using synthetic jets. Journal of Fluids and Structures, 24(8):1349–1357, nov 2008. doi: 10.1016/j.jfluidstructs.2008.06.017.
- [26] Ashley Tuck and Julio Soria. Separation control on a NACA 0015 airfoil using a 2d micro ZNMF jet. Aircraft Engineering and Aerospace Technology, 80(2):175–180, mar 2008. doi: 10.1108/00022660810859391.
- [27] Vassili Kitsios, Laurent Cordier, Jean-Paul Bonnet, Andrew Ooi, and Julio Soria. On the coherent structures and stability properties of a leading-edge separated aerofoil with turbulent recirculation. Journal of Fluid Mechanics, 683:395–416, aug 2011. doi: 10.1017/jfm.2011.285.
- [28] NA Buchmann, C Atkinson, and Julio Soria. Influence of ZNMF jet flow control on the spatio-temporal flow structure over a NACA-0015 airfoil. Experiments in Fluids, 54(3), feb 2013. doi: 10.1007/s00348-013-1485-7.
- [29] Pititit Itsariyapinyo and Rajnish N Sharma. Large eddy simulation of a naca0015 circulation control airfoil using synthetic jets. Aerospace Science and Technology, 82:545–556, 2018.
- [30] Sang Hoon Kim and Chongam Kim. Separation control on NACA23012 using synthetic jet. Aerospace Science and Technology, 13(4-5):172–182, jun 2009. doi: 10.1016/j.ast.2008.11.001.
- [31] H Esmaeili Monir, M Tadjfar, and A Bakhtian. Tangential synthetic jets for separation control. Journal of Fluids and Structures, 45:50–65, feb 2014. doi: 10.1016/j.jfluidstructs.2013.11.011.
- [32] Sebastian D Goodfellow, Serhiy Yarusevych, and Pierre E Sullivan. Momentum coefficient as a parameter for aerodynamic flow control with synthetic jets. AIAA Journal, 51(3):623–631, mar 2013. doi: 10.2514/1.j051935.

- [33] Mark A Feero, Sebastian D Goodfellow, Philippe Lavoie, and Pierre E Sullivan. Flow reattachment using synthetic jet actuation on a low-Reynolds-number airfoil. AIAA Journal, 53(7):2005–2014, jul 2015. doi: 10.2514/1.j053605.
- [34] Mark A Feero, Philippe Lavoie, and Pierre E Sullivan. Influence of synthetic jet location on active control of an airfoil at low Reynolds number. Experiments in Fluids, 58(8), jul 2017. doi: 10.1007/s00348-017-2387-x.
- [35] Wei Zhang and Ravi Samtaney. A direct numerical simulation investigation of the synthetic jet frequency effects on separation control of low-Re flow past an airfoil. Physics of Fluids, 27(5):055101, may 2015. doi: 10.1063/1.4919599.
- [36] Michael S Selig, John Francis Donovan, and David B Fraser. Airfoils at low speeds. HA Stokely, 1989.
- [37] M Selig, JJ Guglielmo, AP Broeren, and P Giguere. Summary of low-speed airfoil data summary of low-speed airfoil data. Tech. rep., University of Illinois, 1995.
- [38] Michael Breuer. Effect of inflow turbulence on an airfoil flow with laminar separation bubble: An les study. Flow, Turbulence and Combustion, 101(2): 433–456, 2018.
- [39] Shiwei Qin, Manoochehr Koochesfahani, and Farhad Jaber. Large eddy simulations of unsteady flows over a stationary airfoil. Computers & Fluids, 161: 155–170, 2018.
- [40] Ivette Rodriguez, Oriol Lehmkuhl, and Ricard Borrell. Effects of the actuation on the boundary layer of an airfoil at Reynolds number $Re = 60000$. Flow, Turbulence and Combustion, 105(2):607–626, may 2020. doi: 10.1007/s10494-020-00160-y.
- [41] Mehran Tadjfar and Dj Kamari. Optimization of flow control parameters over SD7003 airfoil with synthetic jet actuator. Journal of Fluids Engineering, 142(2), oct 2020. doi: 10.1115/1.4044985.

- [42] Philippe Spalart and Steven Allmaras. A one-equation turbulence model for aerodynamic flows. In 30th aerospace sciences meeting and exhibit, page 439, 1992. doi: 10.2514/6.1992-439.

Chapter 4

A New Hybrid Optimization Method, application to a Single Objective Active Flow Control Test Case

4.1 Abstract

Genetic Algorithms (GA) are useful optimization methods for exploration of the search space, but they usually have slowness problems to exploit and converge to the minimum. On the other hand, gradient based methods converge faster to local minimums, although are not so robust (e.g., flat areas and discontinuities can cause problems) and they lack exploration capabilities. This article presents a hybrid optimization method trying to combine the virtues of genetic and gradient based algorithms, and to overcome their corresponding drawbacks. The performance of the Hybrid Method is compared against a gradient based method and a Genetic Algorithm, both used alone. The rate of convergence of the methods is used to compare their performance. To take into account the robustness of the methods, each one has been executed more than once, with different starting points for the gradient based method and different random seeds for the Genetic Algorithm and the Hybrid Method. The performance of the different methods is tested against an optimization Active Flow Control (AFC) problem over a 2D Selig–Donovan 7003 (SD7003) airfoil at Reynolds number 6×10^4 and a 14 degree angle of attack.

Five design variables are considered: jet position, jet width, momentum coefficient, forcing frequency and jet inclination angle. The objective function is defined as minus the lift coefficient ($-C_l$), so it is defined as a minimization problem. The proposed Hybrid Method enables working with N optimization algorithms, multiple objective functions and design variables per optimization algorithm.

4.2 Introduction

Optimization methods usually excel in exploration or exploitation, they have to make a trade-off between those characteristics. The balance between exploration and exploitation capabilities will affect the usability of the optimization method. A method that excels in exploitation may lack the capacity to find the candidate regions and get stuck in local minima. On the other hand, a method that excels in exploration may lack the capacity to quickly converge to a refined solution, but it can find the candidate regions efficiently. Evolutionary bio-inspired methods usually excel in exploration capabilities and gradient based methods usually excel in exploitation capabilities.

Traditionally, bio-inspired optimization methods provide good exploration capabilities with robustness in providing global minimum. Nevertheless, this requires a large number of evaluations of the objective functions, this being its main drawback, especially when dealing with applications to industry and engineering. We can see examples of this type of solution using particle swarm optimization algorithms in microwave engineering at A. Lalbakhsh and Smith [1], or resonator antennas at A. Lalbakhsh and Esselle [2]. Genetic Algorithms have also been used on environmental sensing problems at Lalbakhsh et al. [3], or improving satellite darkness at Lalbakhsh et al. [4]. Gray Wolf Optimization has been used for the solution of flow measurement and instrumentation problems at [5].

In practice, one could think in a sequential combination of different optimization methods in order to combine their main advantages and to overcome the different limitations of each one. For instance, first use an evolutionary algorithm (e.g., a Genetic Algorithm) to perform an exploration and, next, use its results to start a gradient based method (e.g., a conjugate gradient) to exploit the interesting

regions found by the evolutionary algorithm. If we do that with all the individuals provided by the evolutionary method, the total computational cost would be even more prohibitive. However, one could also think of applying a deterministic improvement with only a reduced set of promising individuals. This is considered a form of hybridization. An example of this kind of hybridization can be found at Kelly Jr and Davis [6], which proposes a combination of a Genetic Algorithm and a k-nearest neighbors classification algorithm. Another example of hybridization with multiple algorithms is proposed at Jih and Hsu [7]. In this case, a Genetic Algorithm and dynamic programming is used to address vehicle routing optimization problems. Other examples can be found at El-Mihoub et al. [8], Kulcke and Lorenz [9].

Other forms of hybridization are the definition of new operators, including multi-population methods. A multi-population Hybrid Method was proposed in Lee et al. [10] where games strategies were combined with bio-inspired optimization methods. In this approach there are different players, all of them using Genetic Algorithms applied to the solution of different complementary optimization problems.

This approach was used for the optimization of aeronautic shape configurations in Lee et al. [10], Lee et al. [11] and D. S. Lee and Srinivas [12]. This was applied in the optimization of composite structure design at Lee et al. [13].

In this paper, an extended implementation of this approach combining a player using a Genetic Algorithm with another player using a conjugate gradient is presented and tested against a single objective problem on an Active Flow Control device optimization. The performance of this approach is compared with the use of the Genetic Algorithm and the conjugate gradient methods used alone.

There are two players:

- One population-based for exploration, which could be an evolutionary algorithm or swarm intelligence.
- One which tries to improve a selection of the most promising individuals coming from the population of the bio-inspired algorithm which uses a deterministic gradient based method.

4.3 Hybrid Method Description

In this section, the proposed Hybrid Method is described. Hybrid Methods have been researched by Lee et al. [10] among others. In the work of Lee et al. [10], there are different optimization algorithms inside the Hybrid Method that are also called *players*, as it uses the Nash games concepts and hybridizes a Nash game with a global Pareto player. In Lee et al. [10], the authors use Genetic Algorithms for all optimization algorithms (i.e., players) which compound the Hybrid Method. When working with two objective functions, it uses three players. The first one is the Pareto player or global player and it deals with the whole problem, two objective functions and all design variables. The other two players are the Nash players, and each one only deals with one objective function. The design variables are also split between the two Nash players, resulting in each Nash player working with a subset of the search space.

The proposed Hybrid Method, which has been derived from the one proposed by Lee et al. [10], enables working with N players, multiple objective functions and design variables per player, and a different optimization algorithm for each player. The structure of the method is divided into three main components:

- **General Algorithm:** It contains the initialization of the player, the main optimization loop and the post-process of the optimization. It is not intended to be changed for different variants of the Hybrid Method.
- **Migration epoch algorithm:** It is the function that defines the exchange of information between the different players. It defines which individuals are migrated between players, under which circumstances, etc.
- **Immigrate methods:** The immigrate method is a function that has to be defined for each type of player. The way each optimization algorithm used as a player can incorporate and use an individual highly depends on the internal algorithm of each type of player. This function defines how each type of player incorporates the individuals that emigrate into them.

The Hybrid Method interlaces the execution of its internal optimization algorithms. Each player runs one iteration of its optimization algorithm, then a

migration epoch occurs before the other method runs one iteration of its own algorithm. The migration epoch is the mechanism that allows the exchange of information between players. The information exchanged by the players are the design variables of a selection of individuals. The migration epoch implementation is what defines the main functionality of the Hybrid Method. The general algorithm of the Hybrid Method is described in Algorithm 2.

Algorithm 2: General algorithm of the Hybrid Method

```

foreach player do
  | player-Initialize;
while not stop criteria is met do
  | foreach player do
  | | player-Generate;
  | | player-Compute;
  | | MigrationEpoch(players[i] );
foreach player do
  | player-PostProcess;
  PostProcess;

```

In this article, the optimization method selected to perform the exploration is a Genetic Algorithm based on the NSGAI [14]. Other population based optimization algorithms, such as differential evolution, particle swarm optimization, etc., could also be used here. The Genetic Algorithm is known for its robustness and exploration capabilities and it is one of the most widely used optimization algorithms for complex problems. It should perform the task well in exploring the full search space. On the other hand, the method selected for the exploitation is a conjugate gradient [15]. As shown in Algorithm 2, first of all, the *Initialize* process for each player is called. These methods are called once and are used to initialize each optimization algorithm. After the initialization of each optimization algorithm, the optimization loop is started. Inside the loop, as mentioned above, each optimization player runs one iteration before the migration epoch. One iteration consists of generating a set of new individuals (i.e., a set of design variables) and computing them. For the Genetic Algorithm player, the genetic operators of selection, crossover and mutation are performed inside the *Generate* process,

which yields a new population, known as the offspring. After the population is computed, the *MigrationEpoch* process is called, and after that the conjugate gradient runs an iteration of its algorithm starting with the migrated individual, and the process repeats until the stop criteria is met.

The *MigrationEpoch* process is responsible for managing the exchange of information between the different players. The definition of this process is what defines most of the hybrid algorithm. For example, it defines the criteria of which individuals migrate between players, how often they migrate, etc. The internal algorithm of the *MigrationEpoch* process that describes the Hybrid Method presented and tested in this article is detailed in Algorithm 3.

Algorithm 3: Hybrid Method With Gradient Game

After computing a full iteration of a player the MigrationEpoch(this-player) function does:

```

if iter = 0 then
  foreach player do
    player-Immigrate(this-player-Bestfits);
else
  if this-player-Bestfits < players[0]-Bestfits then
    foreach player do
      player-Immigrate(this-player-Bestfits);
  else
    GetMinBestfits;
    this-player-Immigrate(Bestfit);

```

The tested Hybrid Method combines two players (i.e., optimization algorithms). One player is intended to perform the exploration of the full search space. The second player is responsible for the exploitation of the promising regions found by the first one. The Hybrid Method shares information between the two players, in a bidirectional way, to overcome the main drawbacks of the optimization algorithms that is formed of. It tries to achieve a fast rate of convergence and to avoid getting stuck at local minimums.

The Hybrid Method initially runs the Genetic Algorithm player. After the

first iteration, the best individual found by the Genetic Algorithm is transferred to the conjugate gradient player (first *if* of the Algorithm 3). The *player-Bestfits* is the individual with the best objective function found so far, and it is stored for each player. It is updated every time a better individual is found. The conjugate gradient player will use this individual as the starting point of its internal algorithm for its own iteration. The iteration of the conjugate gradient consists of computing the gradient at the location of the starting point and performing a line search in the direction of the gradient. After the iteration of the conjugate gradient, another migration epoch occurs. If the best individual found by the conjugate gradient outperforms the best individual found by the Genetic Algorithm, then the best individual of the conjugate gradient is sent to the Genetic Algorithm.

If the first conditional is not met, a second *if* condition is evaluated, taking into account the values of the objectives functions achieved so far. The inner *if* condition compares the objective function of the last evaluated player (*this-player*) against the objective function of the first player, which in this case is a Genetic Algorithm. The condition $this-player-Bestfits < players[0]-Bestfits$ is clear in a single-objective optimization case, as it is a direct comparison between values of the objective function. If the objective function of *this-player* is better (lower) than the first player, this individual is migrated to the other player.

If the objective function of *this-individual* is not better, the inner *else* part of the algorithm is conducted. In the function *GetMinBestfits*, a search for the best individual (*Bestfit*) among all players is performed, and the individual is migrated to *this-player*, the last player that was executed.

For the full comprehension of the hybrid algorithm, it is important to specify the *Immigrate* process. This process is defined for each player, and its implementation depends on the type of optimization algorithm, and it affects the general hybrid algorithm. It has one input parameter, the individual that has been selected to migrate into this player. The *Immigrate* process is responsible for incorporating the individual into the player. The *Immigrate* process of the Genetic Algorithm substitutes the design variables of the last individual of its internal population with the one that comes from the conjugate gradient. This introduces the genetic information of this individual into the population. In the next iteration, the design variables of this individual will be used in the genetic operators.

In order not to repeat computations, the conjugate gradient player only performs a new iteration when the Genetic Algorithm one provides a best individual different than in the previous global iteration.

On the other hand, the Genetic Algorithm player always incorporates to the population the best individual coming from the conjugate gradient, even if it is the same as in any previous global iteration. The stochastic nature of the Genetic Algorithm can benefit from maintaining the best individual in the population at each iteration. There is a probability that the best individual is not selected in the genetic operators, and to keep the best individual in the population, keeping its genetic information can help to converge in that region. One could think about problems with elitism, but the method only forces one individual to remain in the population, the absolute best so far. If this happens for too long, most probably the optimization has converged, and in case it is not converged, the algorithm should still be capable to explore other regions with the mutation operator and the stochastic nature of the Genetic Algorithm.

For more clarity, the general algorithm with two players, the Genetic Algorithm as the first player and the conjugate gradient as the second one, is schematized at Figure 4.1. As mentioned previously, a migration epoch occurs after each iteration of each player. This executes the process detailed in the Algorithm 3, enabling the possibility of exchanging information between the two players.

The configuration of the Genetic Algorithm is specified in Table 4.1 and the configuration of the conjugate gradient is specified in Table 4.2. The configuration of both optimization algorithms is the same when running alone and when running as a player of the Hybrid Method.

One of the main drawbacks of the proposed Hybrid Method, using both population and gradient-based optimization methods, is that it requires the independent configuration of each optimization method for each player. In this case, the configuration of the Hybrid Method requires the configuration of the Genetic Algorithm and the conjugate gradient players. On the other hand, it also enables the possibility to fine-tune the players to perform better, but in cases with high computational costs, it is difficult to perform tests with different configuration values. Another drawback of the Hybrid Method is that the parallelization of the evaluations of the individuals can become more ineffective because each method may have its

Parameter	Value
Crossover operator	Simulated Binary Crossover [16]
Mutation operator	Polynomial Mutation [17]
Selection operator	$\mu + \lambda$ & Crowded-Comparison Operator [14]
Probability of crossover	0.9
Probability of mutation	0.1
Population size	20

Table 4.1: Parameters of the Genetic Algorithm.

Parameter	Value
Search Direction Method	Fletcher-Reeves [18]
Optimal Step Size Method	Golden Section [19]
Epsilon for numerical differentiation	1.0×10^{-6}
First step size	1.0×10^{-3}
Optimal step size tolerance	1.0×10^{-3}

Table 4.2: Parameters of the conjugate gradient algorithm.

optimum number of CPUs which may be different for each method. For example, in this case, the evaluation of the Genetic Algorithm population can benefit from using 20 CPUs, one for each individual of the population because they can be computed at the same time. On the other hand, to evaluate the individuals of the conjugate gradient, the parallelization is not that clear. The individuals to compute the gradient can be evaluated at the same time, in this case there are eleven individuals, the central point plus two for each design variable. The line search could also be parallelized, but it is not in the implementation used in this study. The difference in the parallelization capabilities between players could result in an under utilization of the computational resources at some stages of the process.

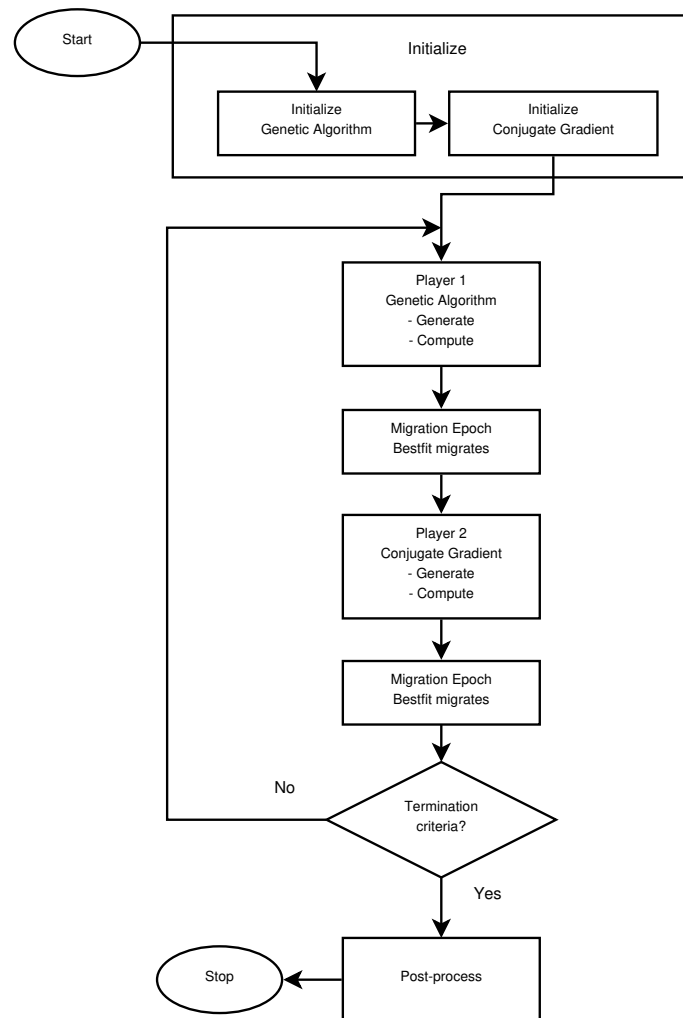


Figure 4.1: General algorithm of the tested Hybrid Method.

4.4 Numerical Results

In order to evaluate the performance of the proposed Hybrid Method, it has been compared against two classical optimization methods, a plain conjugate gradient and a plain Genetic Algorithm. The conjugate gradient method is the same as that which forms part of the Hybrid Method, but running on its own. The Genetic Algorithm used to compare the hybrid algorithm is also the same that forms part of the Hybrid Method, but also running alone. To take into account the random component of the Genetic Algorithm and the strong dependence on the starting

point of the conjugate gradient, multiple optimizations with each algorithm have been conducted.

Two optimizations have been conducted with the Genetic Algorithm, starting with different random populations. The Hybrid Method was also run twice, starting with the same random populations as the Genetic Algorithm, so both methods started with the same populations. Finally, the conjugate gradient was run six times, starting with six individuals of the first random population generated by one of the Genetic Algorithms.

All the optimization methods have been tested against the same test case. The test case consists of a single objective optimization of an Active Flow Control optimization problem based on the work of Tousi et al. [20]. The objective of that work is to determine the optimum parameters of the Synthetic Jet actuator design at different angles of attack in a multiple objective optimization problem. The test case details for the comparison of optimization algorithms are presented in Section 4.4.1.

4.4.1 Test Case Description

The test case focuses on the optimization of an Active Flow Control device, more precisely, a Synthetic Jet actuator. The device is tested on a SD7003 airfoil at an angle of attack of 14 degrees. For the comparison between the optimization algorithms, which is the main objective of this work, a single optimization problem with five design variables has been used. The objective function is to maximize the lift coefficient, and to do so the objective function is set to:

$$f = -C_l$$

At high angles of attack, the Synthetic Jet can greatly affect the flow structure, improving the lift coefficient. The Synthetic Jet actuator, if set properly, can help to reattach the flow to the airfoil or to almost avoid the detachment of the flow.

The design variables are the same as the previous work by Tousi et al. [20]. For a full explanation and detail of the Synthetic Jet actuator design variables meaning refer to [20]. The five design variables are:

F^+ Non-dimensional frequency.

C_μ Momentum coefficient.

θ Jet inclination angle.

x/C Non-dimensional jet position.

h/C Non-dimensional jet width.

The evaluation range of each design variable is shown in Table 4.3. The same ranges are used with all optimization algorithms.

Design Variable	Minimum Value	Maximum Value
F^+	0.1	10
C_μ	0.0001	0.02
θ°	5	175
x/C	0.001	0.3
h/C	0.005	0.015

Table 4.3: Active Flow Control design variables and their evaluation ranges.

The flow has been solved with an unsteady Reynolds averaged Navier–Stokes model (URANS), using the OpenFOAM software. Other models, like direct numerical simulation (DNS) or large eddy simulation (LES) could be used to solve the Synthetic Jet simulation, but their computational cost is too high to perform so many optimizations with the available resources. In addition, there is no need to use such precise solvers to evaluate the performance of the Hybrid Method. More details on the solver used can be consulted at [20], as this study uses the same model.

The mesh used, see Figure 4.2a, is one of the meshes previously evaluated in [20], although having a smaller number of cells (34,448) than the final one employed in that paper, the maximum y^+ after the simulation was $y^+ = 1$. The mesh nearby the Synthetic Jet actuator is presented in Figure 4.2b. The run time of the simulation has been adjusted to 30 time units, which as shown in [20] is sufficient to reach convergence. It is important to note that this study is not about the Synthetic Jet actuator optimization, but to compare the optimization algorithms in a real world application with a significant computational cost and

complexity. The study of the physical problem is not the main purpose of this study, which justifies reducing the precision of each CFD simulation in order to reduce the overall computational cost.

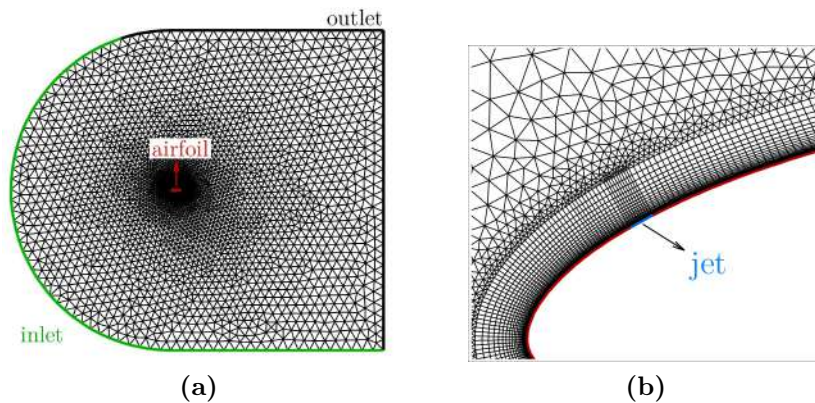


Figure 4.2: Full mesh of the domain (a) and Mesh nearby the Synthetic Jet actuator (b).

In Figure 4.3, the temporal averaged streamlines and pressure field for the non-actuated case is presented. This configuration is called the baseline. From the streamlines, it can be seen that the flow is fully separated and the airfoil is under stall conditions.

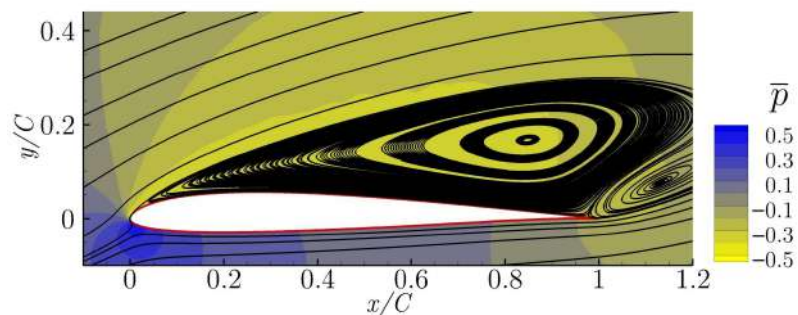


Figure 4.3: Averaged streamlines and pressure field of baseline case ($C_l = 0.80$).

4.4.2 Results from the Optimizations Methods

This section introduces the results obtained for the proposed comparison. The convergence of the different optimization algorithms are shown in Figure 4.4. The results shown in the graph of Figure 4.4 reflect the problems encountered by the

gradient based method. Most runs of the conjugate gradient initially improve faster than the Genetic Algorithm but then get stuck between $C_l \approx 1.35$ and $C_l \approx 1.45$ (except for two runs that get stuck at $C_l \approx 0.8$ and $C_l \approx 1.25$, respectively). Those lift coefficient values are achieved with almost 100 evaluations of the objective function for each optimization of the conjugate gradient. The strong dependence of the conjugate gradient on the starting point is also reflected on these results, as it presents very different solutions between runs than the other methods. In all cases, the conjugate gradient method was stopped because the algorithm found a local minimum and could not compute the gradient to further improve the results.

On the other hand, the Genetic Algorithm provides optimal solutions similar to the conjugate gradient, but with a higher computational cost, approximately four times higher. Both runs of the Genetic Algorithm achieve values of the objective function in the range of the conjugate gradient results. One of the runs achieves a better objective function than all of the conjugate gradient runs, with a value of $C_l = 1.49$. It is important to note that the Genetic Algorithm optimizations could run additional iterations and achieve better results, but with a high computational cost.

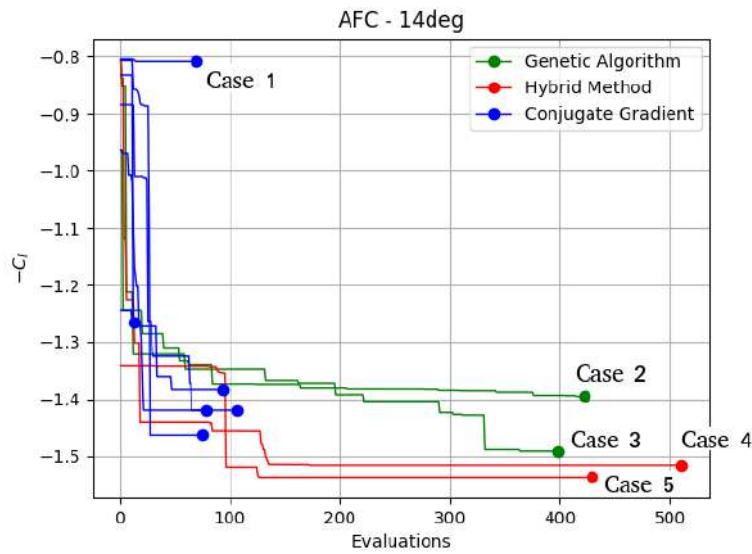


Figure 4.4: Comparative of the convergence of the different optimization methods.

The Hybrid Method is the method that achieved better results, outperforming

all runs of the other algorithms in both of its runs. During the first iterations, it achieved a convergence rate similar to the conjugate gradient. However, the improvement of the solution has continued, avoiding being trapped in any local minimum. It is also the most robust, as both runs are very similar in their performance. Both Hybrid Method runs outperformed all the other optimization methods with a $C_l = 1.52$ and $C_l = 1.54$. One run of the Genetic Algorithm achieved a comparable solution ($C_l = 1.49$), but it took more than twice the computational cost of the Hybrid Method. Case 3, with a lift coefficient of $C_l = 1.49$, obtained by the Genetic Algorithm with around 375 objective function evaluations, improves the baseline lift coefficient by 86%. Cases 4 and 5, obtained by the Hybrid Method runs, achieved a lift coefficient of $C_l = 1.52$ and $C_l = 1.54$, respectively. Both runs needed around 125 objective function evaluations, which is 67% the number of evaluations of case 3, with an increase in the lift coefficient of 90% and 93%, respectively, from the baseline. The best lift coefficient achieved by each optimization is presented in Table 4.4. The mean ($\overline{C_l}$) and standard deviation (σ) of the lift coefficient achieved by each optimization method is also presented. The Hybrid Method presents the best lift coefficient mean ($C_l = 1.53$) followed by the Genetic Algorithm ($C_l = 1.44$) and the conjugate gradient ($C_l = 1.29$). The conjugate gradient is the least robust, with a standard deviation of $\sigma = 0.2458$, but four of the six optimizations achieved similar results than the Genetic Algorithm with less computational effort.

Looking at these results, one can conclude that the proposed Hybrid Method performs much more robustly than the conjugate gradient method and much faster than the Genetic Algorithm.

	Genetic Algorithm	Hybrid Method	Conjugate Gradient
C_l	1.39	1.52	0.81
			1.26
	1.49	1.54	1.38
			1.42
			1.46
$\overline{C_l}$	1.44	1.53	1.29
σ	0.07071	0.01414	0.2458

Table 4.4: Best lift coefficient of each optimization case, means and standard deviation.

4.4.3 Results Based on the Fluid Flow Performance

This subsection provides a comparison between the characteristics of the flow field corresponding to each of the optimal solutions labeled in Figure 4.4. The lift coefficient and design variables of each of the optimal solutions are presented in Table 4.5. For a full explanation of the flow structure and details on the Synthetic Jet actuator performance, the reader is directed to [20].

Case	C_l	F^+	C_μ	θ°	x/C	h/C
1	0.81	8.6	1×10^{-4}	136	3×10^{-1}	5×10^{-3}
2	1.39	0.3	1.47×10^{-2}	24	1×10^{-3}	1.4×10^{-2}
3	1.49	3.2	1.92×10^{-2}	8	2×10^{-2}	5×10^{-3}
4	1.52	6.7	2×10^{-2}	7	2.6×10^{-2}	5×10^{-3}
5	1.54	9.9	2×10^{-2}	5	1.97×10^{-2}	5×10^{-3}

Table 4.5: Values of the lift coefficient and design variables of the five labeled cases.

As explained in the Section 4.4.1, the flow without the Synthetic Jet actuator is fully detached, see Figure 4.3. The objective of the Synthetic Jet actuator is to prevent or minimize flow separation. The averaged streamlines and pressure field of the optimized cases are presented and discussed in this section. The flow field corresponding to Case 1 is presented in Figure 4.5. Despite the fact that the flow

separation is slightly delayed versus the baseline case, a large vortical structure is still observed over the airfoil.

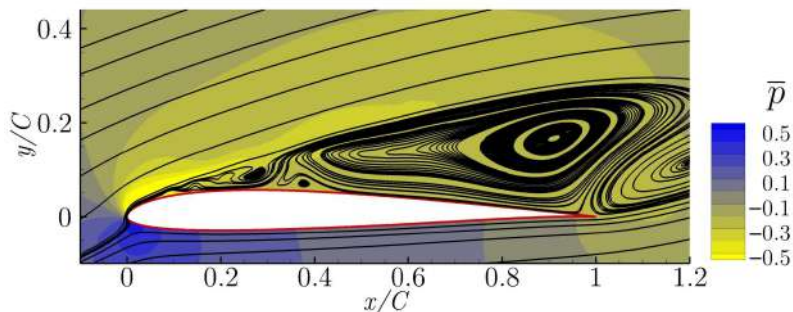


Figure 4.5: Averaged streamlines and pressure field of the Case 1 ($C_l = 0.81$).

In Figure 4.6, the averaged streamlines and pressure field obtained from case 2 is presented. It shows a late reattachment of the flow, which improves the lift coefficient of the baseline by 74%. This solution has been obtained by one of the Genetic Algorithm's runs, with around 400 evaluations of the objective function. The resulting lift coefficient is $C_l = 1.39$.

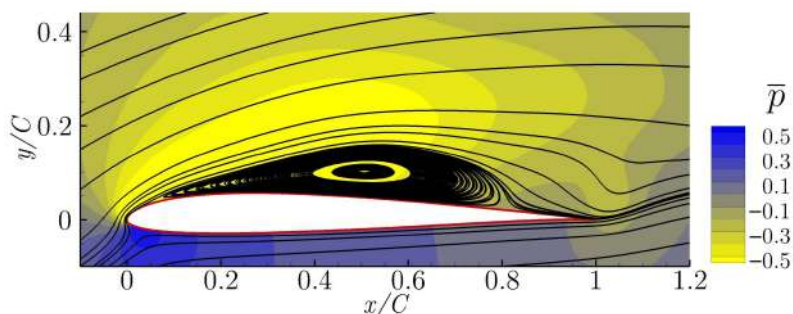


Figure 4.6: Averaged streamlines and pressure field of case 2 ($C_l = 1.39$).

The averaged streamlines and pressure fields of cases 3, 4 and 5 are presented in Figures 4.7–4.9, respectively. All of them show a complete flow reattachment, with very minor differences in the size of the laminar bubble appearing close to the airfoil leading edge. The bubbles are in fact located near the Synthetic Jet position, just downstream of it, as can be seen in the above mentioned figures. The optimization of the flow control actuation parameters has managed to successfully reattached the flow along the entire airfoil chord.

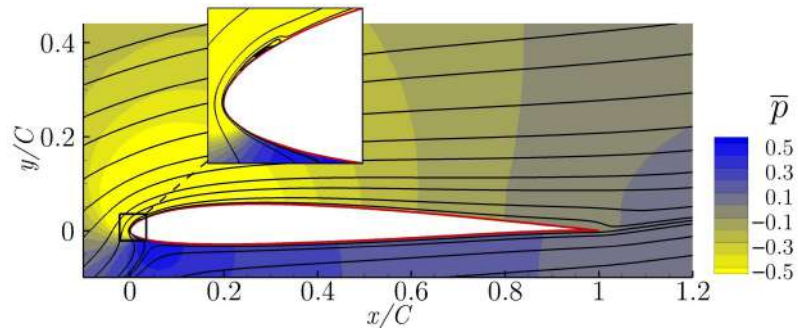


Figure 4.7: Averaged streamlines and pressure field of case 3 ($C_l = 1.49$).

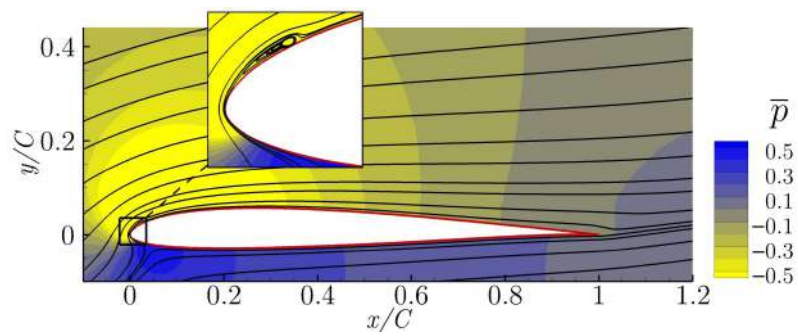


Figure 4.8: Averaged streamlines and pressure field of case 4 ($C_l = 1.52$).

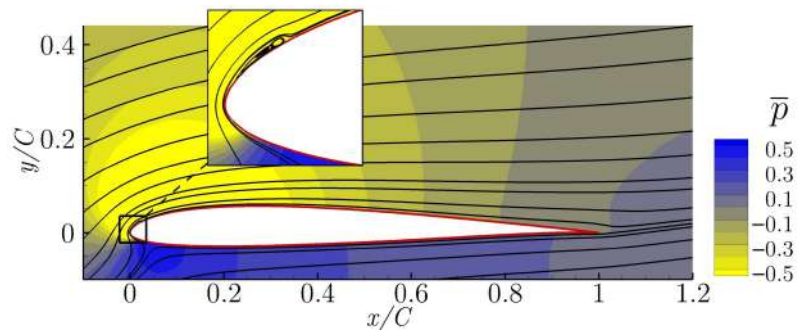


Figure 4.9: Averaged streamlines and pressure field of case 5 ($C_l = 1.54$).

4.5 Discussion

This article presents a new Hybrid Method which combines two optimization methods (a Genetic Algorithm and a conjugate gradient) of a very different nature.

The test case used to evaluate the performance of the new Hybrid Method is a single objective optimization with five design variables associated with a Synthetic Jet actuator. The CFD simulations are solved using a URANS model, which has proven precise enough to capture the active flow actuator effect and to compare between different designs. For the test case of the Synthetic Jet actuator, the Hybrid Method has outperformed both of the traditional optimization algorithms. The new Hybrid Method successfully combines the best characteristics of both optimization algorithms. It shows a great convergence rate, like a gradient based method, but without the lack of robustness that usually comes with gradient based methods and complex applications. The increase in robustness is provided by the Genetic Algorithm player which avoids local minimums. The strategy to exchange information between the two optimization algorithms proposed in this Hybrid Method has proven efficient to overcome the main drawbacks of both classical optimization methods, and the result is an optimization method capable of exploring and exploiting the full search space.

The future work aims to further test the new Hybrid Method in a multi-objective optimization problem such as the one introduced in Tousi et al. [20]. In high CPU-demanding applications, such a Synthetic Jet actuator optimization is important when working with optimization algorithms that require a low number of evaluations of the physical model, and the new Hybrid Method has proven a good option.

4.6 References

- [1] K. P. Esselle A. Lalbakhsh, M. U. Afzal and S. Smith. Design of an artificial magnetic conductor surface using an evolutionary algorithm. In Proceedings 2017 International Conference on Electromagnetics in Advanced Applications (ICEAA), volume 1, pages 885–887. IEEE, 2017.
- [2] M. U. Afzal A. Lalbakhsh and K. P. Esselle. Multiobjective particle swarm optimization to design a time-delay equalizer metasurface for an

- electromagnetic band-gap resonator antenna. IEEE Antennas and Wireless Propagation Letters, 16:912–915, 2017. ISSN 1536-1225. doi: <https://doi.org/10.1109/LAWP.2016.2614498>. URL <https://ieeexplore.ieee.org/document/7579622>.
- [3] Ali Lalbakhsh, Roy B.V.B. Simorangkir, Nima Bayat-Makou, Ahmed A. Kishk, and Karu P. Esselle. Chapter 2 - advancements and artificial intelligence approaches in antennas for environmental sensing. In Mohsen Asadnia, Amir Razmjou, and Amin Beheshti, editors, Artificial Intelligence and Data Science in Environmental Sensing, Cognitive Data Science in Sustainable Computing, pages 19–38. Academic Press, 2022. ISBN 978-0-323-90508-4. doi: <https://doi.org/10.1016/B978-0-323-90508-4.00004-6>. URL <https://www.sciencedirect.com/science/article/pii/B9780323905084000046>.
- [4] A. Lalbakhsh, A. Pitcairn, K. Mandal, M. Alibakhshikenari, K. P. Esselle, and S. Reisenfeld. Darkening low-earth orbit satellite constellations: A review. IEEE Access, 10:24383–24394, 2022. ISSN 2169-3536. doi: <https://doi.org/10.1109/ACCESS.2022.3155193>. URL <https://ieeexplore.ieee.org/document/9722840>.
- [5] Alimohammad Karami, Gholam Hossein Roshani, Ehsan Nazemi, and Sobhan Roshani. Enhancing the performance of a dual-energy gamma ray based three-phase flow meter with the help of grey wolf optimization algorithm. Flow Measurement and Instrumentation, 64:164–172, 2018. ISSN 0955-5986. doi: <https://doi.org/10.1016/j.flowmeasinst.2018.10.015>. URL <https://www.sciencedirect.com/science/article/pii/S0955598618301857>.
- [6] James D Kelly Jr and Lawrence Davis. A hybrid genetic algorithm for classification. In IJCAI, volume 91, pages 645–650, 1991.
- [7] Wan-Rong Jih and J Yung-Jen Hsu. Dynamic vehicle routing using hybrid genetic algorithms. In Proceedings 1999 IEEE International Conference on Robotics and Automation (Cat. No. 99CH36288C), volume 1, pages 453–458. IEEE, 1999.

- [8] Tarek A El-Mihoub, Adrian A Hopgood, Lars Nolle, and Alan Battersby. Hybrid genetic algorithms: A review. Engineering Letters, 13(2):124–137, 2006.
- [9] Matthias Kulcke and Wolfgang E. Lorenz. Utilizing gradient analysis within interactive genetic algorithms. In eCAAD, volume 2, pages 359–364, 2016.
- [10] DongSeop Lee, Luis Felipe Gonzalez, Jacques Periaux, Karkenahalli Srinivas, and Eugenio Onate. Hybrid-game strategies for multi-objective design optimization in engineering. Computers & Fluids, 47(1):189–204, 2011.
- [11] D. Lee, J J. Periaux, Pons-Prats, G. Bugada, and E. Oñate. Double shock control bump design optimization using hybridised evolutionary algorithms. In Proceedings IEEE Congress on Evolutionary Computation, volume 1, pages 1–8. IEEE, 2010.
- [12] J. Périaux D. S. Lee, L. F. Gonzalez and K. Srinivas. Efficient hybrid-game strategies coupled to evolutionary algorithms for robust multidisciplinary design optimization in aerospace engineering. IEEE Transactions on Evolutionary Computation, 15:133–150, 2011. ISSN 1089-778X. doi: <https://doi.org/10.1109/TEVC.2010.2043364>. URL <https://ieeexplore.ieee.org/document/5735238>.
- [13] D.S. Lee, C. Morillo, G. Bugada, S. Oller, and E. Onate. Multilayered composite structure design optimisation using distributed/parallel multi-objective evolutionary algorithms. Composite Structures, 94(3):1087–1096, 2012. ISSN 0263-8223. doi: <https://doi.org/10.1016/j.compstruct.2011.10.009>. URL <https://www.sciencedirect.com/science/article/pii/S0263822311003722>.
- [14] Kalyanmoy Deb, Amrit Pratap, Sameer Agarwal, and Tamt Meyarivan. A fast and elitist multiobjective genetic algorithm: NSGA-II. IEEE transactions on evolutionary computation, 6(2):182–197, Apr 2002. ISSN 1089-778X. doi: [10.1109/4235.996017](https://doi.org/10.1109/4235.996017).

- [15] Jonathan Richard Shewchuk et al. An introduction to the conjugate gradient method without the agonizing pain, 1994.
- [16] Kalyanmoy Deb and Ram Bhushan Agrawal. Simulated binary crossover for continuous search space. Complex systems, 9(2):115–148, 1995.
- [17] Kalyanmoy Deb. Multi-objective optimization using evolutionary algorithms, volume 16. John Wiley & Sons, Chichester, UK, 2001.
- [18] Roger Fletcher. Practical methods of optimization. John Wiley & Sons, 2013.
- [19] Richard P Brent. Algorithms for minimization without derivatives. Courier Corporation, 2013.
- [20] N.M. Tousi, M. Coma, J.M. Bergadà, J. Pons-Prats, F. Mellibovsky, and G. Bugada. Active flow control optimisation on sd7003 airfoil at pre and post-stall angles of attack using synthetic jets. Applied Mathematical Modelling, 98:435–464, 2021. ISSN 0307-904X. doi: <https://doi.org/10.1016/j.apm.2021.05.016>. URL <https://www.sciencedirect.com/science/article/pii/S0307904X21002614>.

Chapter 5

Discharge coefficients of a heavy suspension nozzle

5.1 Abstract

The suspensions used in heavy vehicles often consist of several oil and two gas chambers. In order to perform an analytical study of the mass flow transferred between two gas chambers separated by a nozzle and when considering the gas as compressible and real, it is usually needed to determine the discharge coefficient of the nozzle. The nozzle configuration analysed in the present study consist of a T shape and it is used to separate two nitrogen chambers employed in heavy vehicle suspensions. In the present study, under compressible dynamic real flow conditions and at operating pressures, discharge coefficients were determined based on experimental data. A test rig was constructed for this purpose, air was used as working fluid. The study clarifies that discharge coefficients for the T shape nozzle studied not only depend on the pressure gradient between chambers but also on the flow direction. Computational fluid dynamic (CFD) simulations using air as working fluid and when flowing in both nozzle directions were as well undertaken, the fluid was considered as compressible and ideal. The CFD results deeply helped in understanding why the dynamic discharge coefficients were dependent on both the pressure ratio and flow direction, clarifying at which nozzle location and for how long choked flow was to be expected. Experimentally based results were compared with the CFD ones, validating both the experimental procedure and numerical methodologies presented. The information gathered in the present study

is aimed to be used to mathematically characterise the dynamic performance of a real suspension.

5.2 Introduction

Hydro-pneumatic suspensions consist on two or more oil chambers and a couple of gas ones. During the alternative displacement of the suspension, oil and gas flows back and forth between two consecutive chambers often separated by one or several nozzles or valves, therefore generating the smooth suspension displacement characteristic of such devices. Figure 5.1 introduces a typical heavy vehicle suspension, where several oil and gas chambers can be observed. To mathematically evaluate the dynamic fluid variations associated with the compression and extension of a given suspension, it is required to obtain the dynamic discharge coefficient of the different nozzle shapes separating the gas chambers. The discharge coefficient is defined as $c_d = \frac{\dot{m}}{\dot{m}_t}$, where \dot{m} characterises the real mass flow flowing through the nozzle while \dot{m}_t is the mass flow obtained using a theoretical equation. For the suspension configuration presented in Figure 5.1, the gas chambers consist of a constant volume chamber and a variable volume one. Compressible gas, generally nitrogen, flows between two chambers through a narrow passage of constant cross-section, a nozzle. In the suspension of the present study, the pressure in both nitrogen chambers is time dependent, this the reason why it is important to determine the discharge coefficient variation for a real compressible flow under transient conditions.

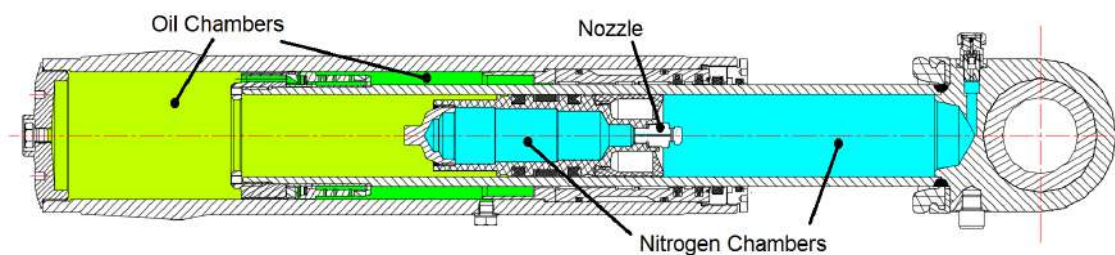


Figure 5.1: Scheme of a typical heavy vehicle suspension.

The main advantage of knowing the discharge coefficient of a given nozzle, is that it allows to determine the real mass flow through the nozzle via employing the-

oretical equations. From the existing literature, several traditional experimental procedures [1, 2] are described to experimentally determine the discharge coefficients on nozzles under real flow compressible conditions. The accuracy of these methods is good for a limited range of pressures, but it is jeopardized in applications involving high pressure metering. One of the most relevant early papers on non-ideal gas flow through orifices is the work undertaken by Johnson [3], where an expression for one-dimensional real flow through nozzles and based on the Beattie-Bridgeman equation was developed. The specific heat ratio was considered to be constant. Air at room temperature and for 10 MPa pressure differential was used as working fluid and he observed a deviation of 3.5 percent for critical flow in nozzles when employing real versus ideal gas equations. Bober and Chow [4], using Methane as working fluid and for a pressure differential of 23 MPa between chambers, compared the ideal and real gas flow performance through a venturi shaped nozzle using the Redlich-Kwong equation. Under choked flow conditions, the difference between ideal and real gas models was about 20%. Based on these early papers, it became clear that real gas effects had to be considered if precision metering was required.

Kouremenos et al. [5] and Kouremenos and Antonopoulos [6], based on the Lee-Kesler and Redlich-Kwong equations of state, described a constant entropy process via using three isentropic exponents. A set of simulations and experimental measurements of real compressible flow through convergent divergent nozzles, at very high pressure differentials, were recently undertaken by Kim et al. [7, 8] and Nagao et al. [9, 10]. They observed that for a given range of Reynolds numbers the discharge coefficient exceeded unity. This fact was previously reported by Nakao [11] experimentally. They realised that the molecules' vibrational energy had to be considered in the non-equilibrium thermodynamic process. Working with hydrogen, Ding et al. [12] observed the discharge coefficient was not just dependent on the Reynolds number but also on the throat diameter, stagnation pressure and stagnation temperature. They realised that the compressibility factor (Z) was changing in opposite direction than the discharge coefficient and concluded that the compressibility factor was likely the most important parameter when studying the discharge coefficient. They also noticed that, due to real gas effects, the fluid density at the nozzle throat became smaller than the theoretical one. In most of

the research undertaken previously, the theoretical work was not supported by an experimental method, which could allow working directly with the experimental data. These aspects were covered in [13], where for constant section short nozzles an expression defining the discharge coefficient was developed using an experimental method and a gas flow model based on the Lee-Kesler equation of state [14]. Experimental results were compared with the ones obtained from the new developed equation, observing that for tests performed using nitrogen up to 7.6 MPa pressure differential, a good correlation was obtained.

Computational Fluid Dynamic (CFD) applications are gaining reliability every day. The consideration of the gas as real and compressible, under sonic or supersonic flow conditions, is still not fully extended. In reality, turbulent models quite often have some difficulties in dealing with such kind of flows. Nevertheless, there are many industrial applications where sonic and even supersonic flow is used. CFD simulations on compressible flow through valves, whether purging or relief ones, have recently been performed in [15, 16]. The modelling of flow ejectors under sonic flow conditions was considered in [17, 18, 19, 20, 21]. Some of the recent papers simulating compressible flow conditions at high Mach numbers inside nozzles are [22, 23, 24, 25].

From all these studies it is particularly relevant to highlight the work done by Farzaneh-Gord et al. [15] where they numerically evaluated the exit flow of natural gas through a purging valve, during its opening time. They considered the gas as real and compressible, being the maximum pressure differential of 3.5 MPa. As a turbulent model the standard $k - \epsilon$ was selected. They concluded supersonic flow was to be expected at the pipe outlet. García-Todolí et al. [16] performed CFD simulations on air valves under compressible flow condition. They showed how CFD models are efficient to represent the behavior of air entering and leaving the valve. The maximum pressure differential studied was 0.1MPa. In their analysis, they used the realizable $k - \epsilon$ turbulent model and their results matched very well with the experimental data. Mazzelli et al. [17] performed numerical and experimental analyses in order to check the effectiveness of the commonly-used computational techniques when predicting ejector flow characteristics at supersonic flow conditions. For the numerical part, they considered the working fluid as an ideal gas. They tested different Reynolds-averaged Navier–Stokes (RANS) turbulent

models, among them the $k - \omega$ SST and $k - \epsilon$ realizable ones, and observed that in general all turbulent models generated very similar results, although epsilon-based models were more accurate at low pressure differentials, (around 0.2MPa). The different pressure differentials they evaluated were of, 0.2, 0.35 and 0.5MPa. On the other hand, they stated that the main differences between the numerical and experimental results appeared when comparing 2D and 3D models. Lakzian et al. [18] performed a compressible 2D RANS simulation on an air ejector pump. In their analysis they assumed the working fluid as ideal gas and the walls were treated as adiabatic. Pressure differentials of 0.5, 0.6, 0.7 and 0.8MPa were considered. They used a $k - \epsilon$ realizable turbulent model along with a wall function and a very good agreement with experimental data was obtained. They concluded that the main sources of entropy are the mixing and normal shock occurred in the mixing chamber and diffuser, respectively. Arias and Shedd [21] used CFD to develop a 3D model of compressible flow across a venturi in which obstacles were located inside. Air was considered as compressible and was treated as ideal gas. The turbulent model they used was RNG $k - \epsilon$ and the maximum pressure differential was about 0.1MPa. The results showed that the obstacles located at the converging nozzle of the venturi causes negligible pressure losses, while other obstacles that generate wakes in the flow are responsible for the largest pressure drop. Discharge coefficients of critical nozzles used for flow measurement under compressible flow conditions were evaluated by Ding et al. [22]. Fluid was considered as real, the standard $k - \epsilon$ turbulent model with a wall function was employed in all simulations. Nozzle roughness was considered, being the maximum pressure differential between nozzle inlet-outlet of 120MPa. They observed that when the nozzle roughness was very small and for pressure differentials until 1MPa, the effect on the discharge coefficient was negligible. Sonic and supersonic flow inside micro/nanoscale nozzles was studied by Darbandi and Roohi [23]. They used a density-based solver (rhoCentralFoam) employed in OpenFOAM. Second order spatial discretisation scheme along with a first order Euler-scheme for time integration were implemented. They observed supersonic flow was impossible to set in nanoscales once Knudsen number exceeded a given value. Zhao et al. [24] numerically studied the fuel flow in a nozzle considering the fuel compressibility. They

used the RANS method with a Realizable k-epsilon turbulent model and they investigated the effect of injection pressure on the fuel flow under fuel compressibility conditions. They concluded that the nozzle discharge coefficient for compressible flow was larger than when fluid was considered as incompressible.

According to the authors knowledge, the nozzle configuration studied in the present paper, which has a T shape, has not been previously studied under real gas compressible flow conditions, just the work done by Farzaneh-Gord et al. [15] presents some similarities. In fact under incompressible flow conditions a similar shape was studied by [26, 27], where it was stated the discharge coefficient was highly dependent on the flow direction. The present study consists of the following parts, initially the test rig employed to do all experimental tests is introduced, then the mathematical equations used to analytically determine the flow parameters are presented. In a third stage, the Computational Fluid Dynamics (CFD) methodology employed to numerically evaluate the compressible flow between the two tanks is introduced. Next the experimentally based and numerical results are presented and compared. Finally the discharge coefficients as a function of the Reynolds number and for both flow directions are presented and discussed, the paper ends with the conclusions.

5.3 Experimental test rig

Since the primary idea in the present paper was to experimentally determine the directional dynamic discharge coefficients for a real gas, air, the test rig introduced in Figure 5.2 was created. Figures 5.2a and 5.2b, respectively, shows a general view of the test rig and the two reservoirs. Figure 5.2c presents a schematic view of the two reservoirs' central section with the different transducers employed. Apart from the two reservoirs, the test rig consisted of a stopper cylinder, which was employed to displace the shutter valve located inside the large reservoir, see Figure 5.2c. When this valve was closed, it prevented the fluid from flowing between the two reservoirs, allowing to pressurize each of them independently. The volume of each reservoir was of 2288.48 and 700.18 cm^3 . Notice that the volume of the large reservoir was slightly increasing as the shutter valve was opening. Therefore in order to know at each instant which was the real volume, a position transducer

was attached to the stopper cylinder. The pressure multiplier in conjunction with the pressurize-depressurize valve was connected to the large reservoir and allowed to set the required pressure in the reservoir chambers. Static and dynamic pressure transducers were connected to each reservoir, this was done due to the uncertainty of the static transducer in properly measuring the dynamic pressure variations. The fluid temperature was aimed to be measured by several dynamic thermocouples placed on the internal reservoir walls, one of them was located in the large reservoir and three were placed on the smaller one, then larger temperature variations were expected in there.

It is important to notice that the dynamic thermocouples were welded to the internal walls of the reservoirs, therefore the measured temperature was in reality the internal wall temperature, which may not be exactly the same as the fluid temperature, specially under dynamic conditions. Considering known the dynamic temperature at the upstream reservoir, Kagawa et al. [2] identified the susceptibility of the pressure response to temperature changes in a reservoir at natural conditions, and suggested the use of an upstream isothermal chamber to guarantee no temperature variation. This idea appears to be a good solution since it reduces the number of variables, and assuming pressure is a known variable, it would be possible to mathematically determine the temperature, heat transfer and the mass flow downstream by means of integration. The main difficulty lies in achieving no upstream temperature variation during the discharge, Kagawa et al. [2] suggested stuffing extremely thin steel wool or copper wire in the upstream reservoir to obtain isothermal conditions. For the present experimental test rig and in order to tend to achieve isothermal conditions during experimentation, both reservoirs walls were constructed with a thickness of 35mm.

The main characteristics of the different transducers were: the static pressure sensors were from Keller series model 21/21PRO, capable of measuring pressures of 10 MPa and having a resolution of 100Pa. To properly evaluate the dynamic pressure, Kistler transducers model 601A were used, their resolution was of 100Pa and the time response was of $1\mu s$. Dynamic temperature was measured using low inertia Nammac thermocouples model E6-20, their resolution was of $0.01^{\circ}C$. The transducer used to measure the position of the shutter valve was a LVDT type, model CGA-2000 from TE connectivity, its resolution was of 0.001mm. The

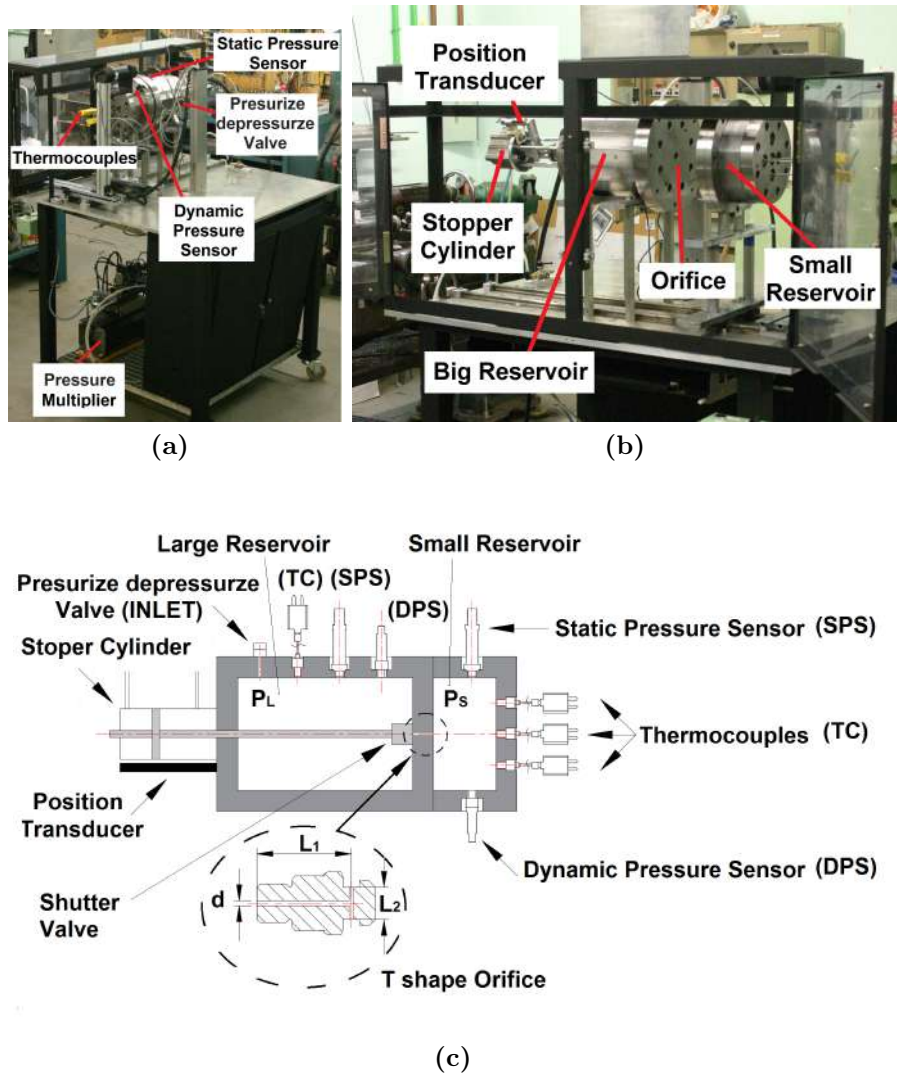


Figure 5.2: (a) Test rig main view; (b) The two reservoirs with their pressure and temperature transducers; (c) schematic view of the reservoirs and the transducers localization.

dynamic variables were recorded thanks to an in-house LabVIEW program specifically developed for this application. Table 5.1 introduces the initial absolute pressure on both reservoirs employed in each experimental test as well as in each CFD case. The main dimensions of the T shape nozzle are defined in Figure 5.2c. The constant section nozzle diameter of both the horizontal and vertical nozzle branches was $d = 1.5mm$, the horizontal branch length (L_1) was $L_1 = 29.5mm$

and the length of the vertical branch (L_2) was $L_2 = 10mm$.

The process followed to perform the simulations was a function of the flow direction, it was depending on which of the two reservoirs was initially pressurized. In other words, if the discharge was from the large to the small reservoir (L-to-S) or from the small to the large (S-to-L) one. It is important to notice that the T shape nozzle was always kept in the same position regardless of the flow direction.

Pressure large reservoir [MPa]	0.4	0.6	0.9	1.1	1.2	0.1	0.1	0.1	0.1	0.4	0.4	1.1	0.1	0.4
Pressure small reservoir [MPa]	0.1	0.1	0.1	0.1	0.4	0.4	0.6	0.9	1.1	1.2	0.1	0.1	0.6	1.2
											CFD	CFD	CFD	CFD

Table 5.1: Initial absolute pressure at both reservoirs for all different experimental tests performed and for all CFD simulations undertaken.

The measurements were done when the large reservoir was pressurized, started with the shutter valve open and both reservoirs at the atmospheric pressure, 0.1MPa absolute pressure. Under these conditions, the shutter valve was closed and the large reservoir was filled with air, passing through the pressurize-depressurize valve, until reaching the required pressure. Then, the pressurize-depressurize valve was closed. The last step consisted in opening the shutter valve, which was accomplished by pressurizing the stopper cylinder, and the flow was allowed to go from the large to the small reservoir. The stopper cylinder position, the static and dynamic pressure as well as the internal wall temperature on both reservoirs were recorded using an external computer and thanks to a labVIEW program. For tests at which the fluid was going from the small reservoir to the large one, the same procedure was used but initially, both reservoirs were pressurized at the pressure required for the small reservoir. After closing the shutter valve and using the pressurize-depressurize valve, the pressure at the large reservoir was decreased until obtaining the one needed. It is important to highlight at this point that each test was done ten times, the resulting curves presented in the results section are the average value of the ten measurements done for each variable.

5.4 Mathematical equations and analytical process followed to determine the physical variables.

From the experimental tests, it was soon realised that as the temperature transducers were welded to the reservoirs internal walls, in reality they were measuring the temperature of the wall and not the fluid temperature at each reservoir. The measured temperature was almost constant in both reservoirs and it was used to instantaneously estimate the heat transferred through the walls. Therefore, providing that the only trustworthy dynamic information in both reservoirs was the temporal pressure evolution, the methodology employed to determine the mass flow between reservoirs, was based on the following equations, developed by the authors in a former paper [13]. Equation (5.1) was obtained from the application of the energy equation in the upstream reservoir, it characterises the temporal mass variation in the upstream reservoir, $\frac{dm_u}{dt}$, as a function of the tank's temperature T_u , the heat transferred to the fluid $\frac{dQ_u}{dt}$, the upstream pressure temporal variation $\frac{dp_u}{dt}$, the variation of the compressibility factor versus the temperature and specific volume $\frac{\partial Z_u}{\partial T}$; $\frac{\partial Z_u}{\partial \nu}$, the mass of the fluid in the upstream reservoir m_u , the enthalpy h_u and the internal energy u_u associated with the upstream fluid. The heat transferred across the walls of the reservoir was estimated based on the Fourier equation $Q = -\lambda \frac{dT}{dx} \Big|_{x=0}$, being the value of the thermal conductivity $\lambda = 54 \left(\frac{W}{mK}\right)$. Equations (5.2) and (5.3) arise from the differentiation of the real gas equations applied to the upstream and downstream reservoirs, $p_u \forall_u = Z_u m_u R_u T_u$; $p_d \forall_d = Z_d m_d R_d T_d$, they link the pressure, volume, temperature, mass flow and compressibility factor temporal variations existing in the respective upstream and downstream reservoirs. Equation (5.4) simply characterises the mass transfer balance. In all these equations, sub-indices u and d stand for upstream and downstream, respectively.

$$\frac{dm_u}{dt} = \frac{\frac{1}{p_u} \frac{dp_u}{dt} - \frac{1}{m_u c_v} \left[\frac{1}{T_u} + \frac{1}{Z_u} \left(\frac{\partial Z_u}{\partial T} \right)_\nu \right] \frac{dQ_u}{dt}}{\frac{1}{m_u} - \frac{1}{Z_u} \left(\frac{\partial Z_u}{\partial \nu} \right)_T \frac{\forall_u}{(m_u)^2} + \frac{1}{m_u c_v} \left[\frac{1}{T_u} + \frac{1}{Z_u} \left(\frac{\partial Z_u}{\partial T} \right)_\nu \right] [RT_u^2 \left(\frac{\partial Z_u}{\partial T} \right)_\nu - (h_u + u_u)]} \quad (5.1)$$

$$\frac{dT_u}{dt} = \frac{T_u}{p_u} \frac{dp_u}{dt} + \frac{T_u}{\forall_u} \frac{d\forall_u}{dt} - \frac{T_u}{m_u} \frac{dm_u}{dt} - \frac{T_u}{Z_u} \frac{dZ_u}{dt} \quad (5.2)$$

$$\frac{dT_d}{dt} = \frac{T_d}{p_d} \frac{dp_d}{dt} + \frac{T_d}{\forall_d} \frac{d\forall_d}{dt} - \frac{T_d}{m_d} \frac{dm_d}{dt} - \frac{T_d}{Z_d} \frac{dZ_d}{dt} \quad (5.3)$$

$$\frac{dm}{dt} = \frac{dm_d}{dt} = -\frac{dm_u}{dt} \quad (5.4)$$

An in-house computer program was created to solve the preceding equations Equation (5.1) to Equation (5.4) with a Runge-Kutta method based on DVERK from the IMSL library. The air density was determined every time step using the Lee-Kesler equation iteratively as performed by Plocker and Knapp [28]. According to this equation, the compressibility factor as a function of the reduced parameters, can be expressed as:

$$Z^{(r)} = \left(\frac{P_r \nu_r}{T_r} \right) = 1 + \frac{B}{\nu_r} + \frac{C}{\nu_r^2} + \frac{D}{\nu_r^5} + \frac{c_4}{T_r^3 \nu_r^2} \left(\beta + \frac{\gamma_1}{\nu_r^2} \right) e^{\frac{-\gamma_1}{\nu_r^2}} \quad (5.5)$$

The parameters B, C, D, c_4 , β and γ_1 for various gases can be determined from reference [5]. P_r , T_r and ν_r stand for reduced pressure, reduced temperature and reduced specific volume, respectively.

According to Lee and Kesler [14], the compressibility factor can be defined as:

$$Z = Z^{(0)} + \frac{\omega}{\omega^{(R)}} (Z^{(R)} - Z^{(0)}) \quad (5.6)$$

where $Z^{(R)}$ and $Z^{(0)}$ are the compressibility factors for a reference fluid and simple fluid, respectively, while $\omega^{(R)}$ and ω stand for the acentric factors of the reference and working fluids.

Considering known the pressure and temperature in a given location and time, the following steps were used to calculate the fluid compressibility factor. Initially the reduced upstream pressure and temperature (P_r and T_r) were obtained based on the working fluid critical properties (P_c ; T_c) and the values of the pressure and temperature. When introducing the values of P_r and T_r in equation Equation (5.5), introducing as well the values of the parameters given for a simple fluid and obtained from reference [5], the value of ν_r could be determined. Substituting

the value of ν_r in the same equation Equation (5.5), the corresponding compressibility factor for a simple fluid $Z^{(0)}$ was obtained. Following the same procedure just described, but using the values of the parameters characterising the reference fluid, which for the present study was n-octane, values obtained from [5], the value of $Z^{(R)}$ was determined. Substituting the compressibility factors $Z^{(0)}$ and $Z^{(R)}$ in equation Equation (5.6) and considering the acentric factor values $\omega^{(R)}=0.3978$ and $\omega=0.039$, the compressibility factor for the working fluid could finally be obtained. This procedure allows to determine the compressibility factor and the fluid density at any position and time, just the values of the pressure and temperature are required at the generic location where the information is needed.

To be able to determine the instantaneous mass at each reservoir, the pressure evolution was measured in both reservoirs at any time, the volume of both reservoirs was also known and the fluid temperature as well as the compressibility factor were estimated based on the previous equations. The variation of the fluid mass between two consecutive time steps allowed to calculate the instantaneous mass flow leaving one reservoir and entering the other one. The only problem associated with this methodology was that the fluid temperature had to be estimated. As previously defined by Kagawa et al. [2] and Comas et al. [13], if the reservoirs were large enough, the fluid temperature was likely to remain constant. Yet, which were the required dimensions to fulfil this condition for each particular case was not clearly stated.

Based on the previous information, the instantaneous space averaged fluid velocity at the nozzle minimum section $S = \frac{\pi d^2}{4}$ was determined as presented in equation Equation (5.7). The fluid velocity at the critical section was determined based on the experimentally based mass flow \dot{m} , the nozzle section S and the fluid downstream density ρ_d .

$$v = \frac{\dot{m}}{S\rho_d} \quad (5.7)$$

To determine the Mach number, the sound speed was initially obtained from equation Equation (5.8), when substituting equations Equation (5.7) and Equation (5.8) in equation Equation (5.9), the Mach number at the nozzle critical section was obtained.

$$c^2 = \left(\frac{\partial p}{\partial \rho} \right)_s = -v^2 \left(\frac{\partial p}{\partial v} \right)_s \quad (5.8)$$

$$M = \frac{\vartheta}{c} \quad (5.9)$$

On the other hand and due to the fact that the pressure differential between both reservoirs was relatively small, see table Table 5.1, the following equation was employed to calculate the theoretical mass flow.

$$\dot{m}_t = \frac{\pi D^2}{4} \sqrt{\frac{2\gamma}{\gamma-1} p_u \rho_u \left(\left(\frac{p_d}{p_u} \right)^{\frac{2}{\gamma}} - \left(\frac{p_d}{p_u} \right)^{\frac{\gamma+1}{\gamma}} \right)} \quad (5.10)$$

The instantaneous discharge coefficient was determined at each time step by comparing the real and theoretical mass flows. Actually, the discharge coefficient at each time step was obtained according to equation Equation (5.11).

$$c_d = \frac{\dot{m}}{\dot{m}_t}; \quad (5.11)$$

Where \dot{m} is the real mass flow obtained based on the temporal variation of the mass in the upstream reservoir. Which was determined from the experimental upstream and downstream pressure evolution, the initial fluid temperature and after calculating the compressibility factor as well as the fluid temperature evolution at each time step. \dot{m}_t is the mass flow obtained via using equation Equation (5.10).

At each instant, the Reynolds number was determined using the following equation.

$$Re = \frac{4\dot{m}}{\pi D \mu}; \quad (5.12)$$

Where μ is the fluid dynamic viscosity.

5.5 Dynamic computational fluid dynamic simulations

In order to be able to analyse the dynamic flow evolution between the two reservoirs, several 3D Computational Fluid Dynamic (CFD) simulations were undertaken. The working fluid was air and it was considered as ideal and compressible.

Some recent papers in which the fluid was considered as ideal and compressible and working under similar pressure differentials are [18, 17]. In the present paper, the simulations were performed under dynamic conditions therefore matching the experimental test conditions.

Figure 5.3 shows the two reservoirs separated by the T shape nozzle, the dimensions of both reservoirs and the T shape nozzle were the same as the ones used in the experimental tests. The only difference was the shutter valve needed in the experimental test rig, see Figure 5.2c, which was not required in the CFD simulations. The mesh employed was generated using GMSH, it was unstructured and consisted of 126633 cells. The OpenFOAM software was used for all 3D simulations, finite volumes is the approach OpenFOAM uses to discretise Navier Stokes equations. The solver rhoCentralFoam was used for all tests, the spatial discretisation was set to second order being the first order Euler scheme the one used for time discretisation. The maximum Courant number was kept below 0.8, being the time step around 5e-8s. Turbulence intensity was set to 0.05% in all cases. The realizable $k - \epsilon$ turbulent model along with a wall function, as previously used by Lakzian et al. [18], were employed in all the simulations. The maximum y^+ on the wall of the nozzle was about 90. Volumetric Dirichlet pressure and temperature boundary conditions were initially set in both reservoirs, Newman boundary conditions for pressure and temperature were set in all walls, Dirichlet boundary conditions for velocity were established in all walls. Regarding the heat transfer, all walls were set as adiabatic. To compare with the experimental results four simulations were performed, in two of them the flow was going from the large to the small reservoir, the respective L-to-S reservoirs pressures were, 0.4-0.1MPa and 1.1-0.1MPa. In the other two simulations the fluid was flowing from the small to the large reservoir, being the S-to-L reservoirs pressures respectively of, 0.6-0.1MPa and 1.2-0.4MPa, see Table Table 5.1.

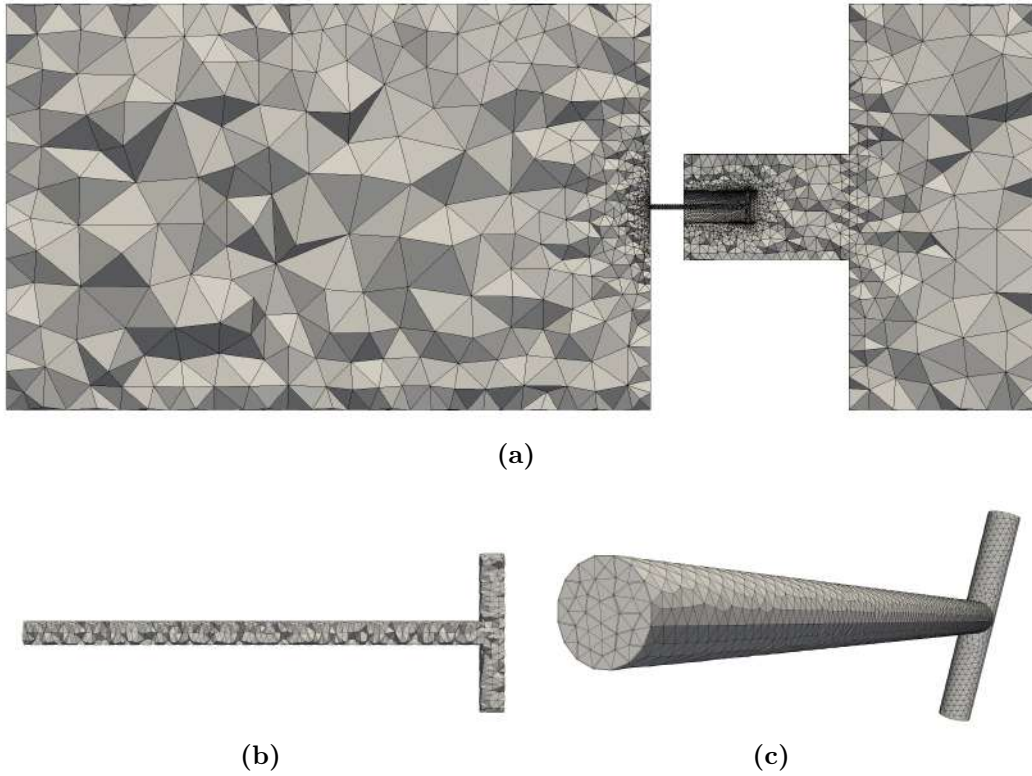


Figure 5.3: (a) Reservoirs main mesh; (b) T shape nozzle section mesh; (c) T shape nozzle mesh general view.

5.6 Results and discussion

In the present section, initially the measured temporal pressure evolution inside the reservoirs is compared with the ones obtained from the CFD simulations. The same is later being done with the temporal temperature at the upstream reservoirs. Next the time dependent mass at each reservoir is also compared between CFD and experimentally based results, which is followed by the temporal mass flow comparison. The time dependant Mach numbers at the respective critical sections and the discharge coefficients versus the Reynolds number are presented next. At the end of this section, a figure showing the flow inside the nozzle and for both flow directions is introduced. In this figure, the critical sections where the flow becomes sonic and the locations where supersonic flow is to be expected are clearly stated.

Figure 5.4 presents the temporal pressure variation measured in both reservoirs for the different initial pressure differentials introduced in Table Table 5.1. Each curve is in reality the average one obtained after performing each test ten times. Although not presented in Figure 5.4, the standard deviation of each point was smaller than 1% for all tests performed. From Figure 5.4a, it is observed the discharge lasts about two seconds regardless of the initial pressure differential existing between the two reservoirs. In fact the time needed to complete the discharge, suffers an increase of about 22.5% when comparing the discharge from 0.4 to 0.1 MPa with the 1.1 to 0.1 MPa one. This phenomenon is clearly understandable then the higher the upstream pressure the higher is the mass to be transferred from one reservoir to the other. Notice that the initial mass of fluid in the downstream reservoir is the same for all cases presented in Figure 5.4a, except the case at which the initial downstream pressure is of 0.4MPa, being the upstream pressure of 1.2MPa. This case shows clear differences versus the rest of the discharges, then the time required to complete the discharge is about 10% shorter than the one needed to complete the discharge when the upstream/downstream reservoir pressures were 0.4 and 0.1 MPa, respectively. In fact, the discharge time is directly related to the initial fluid density ratio $\rho_{upstream}/\rho_{downstream}$ between reservoirs. Given the rest of the parameters, reservoirs volumes and initial fluid temperature as constant, the smaller the initial upstream/downstream density ratio $\rho_{upstream}/\rho_{downstream}$, the shorter the discharge time.

From the observation of the temporal pressure decay when the flow goes from the small reservoir to the large one, Figure 5.4b, it is realised that the discharge time obeys the same upstream/downstream density rule just presented. It is as well interesting to observe that when comparing discharge times for the same pressure differential and opposite flow directions, the discharge time is larger when the fluid goes from the small to the large reservoir. This is likely linked to the resistance the T shape nozzle is presenting when the fluid flows in such a direction. The time the flow remains under choked conditions it is expected to depend on such resistance. This point is to be clarified in the remaining part of the paper. Figure 5.4 also compares the pressure decay and increase measured experimentally with the ones obtained from the CFD simulations, two cases are compared for each flow direction. The comparison shows a very good agreement, generating the same

discharge times and final pressures as the ones measured experimentally. Small discrepancies are observed in the final pressure values when the flow goes from the small to the large reservoir, a discrepancy of 4.4% is observed for a discharge from 1.2 to 0.4 MPa, the variation reaches 11.3% for a discharge from 0.6 to 0.1 MPa. Such relatively small discrepancies are understandable when considering that in the CFD simulations the process is considered adiabatic, the fluid is considered as ideal and the large volume remains constant.

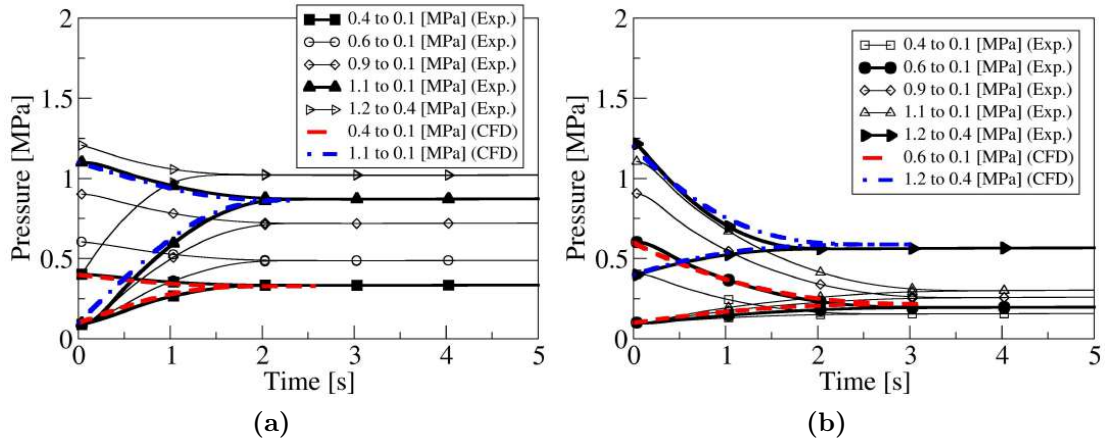


Figure 5.4: Measured temporal pressure variation in both reservoirs, comparison between experimental and CFD results. (a) Flow from large to small reservoir. (b) Flow from small to large reservoir. Five different pressure decays are considered for each flow direction, see Table 5.1.

Figure 5.5 presents the fluid temperature evolution in both reservoirs and for the four cases numerically evaluated. When the discharge is from the large to the small reservoir, Figure 5.5a, the fluid temperature on the large reservoir suffers a decrease of less than 20° , the increase of the fluid temperature in the small reservoir lies between 55° and 85° , such large increase is perfectly understandable when considering the reduced volume of this particular reservoir and that the walls are considered adiabatic. Notice as well that the temperature decrease and increase are directly dependent on the pressure ratio between reservoirs. When the flow goes from the small to the large reservoir, Figure 5.5b, the temperature decrease in the small tank oscillates between 50° and 70° , a maximum temperature rise of around 30° is observed in the large reservoir.

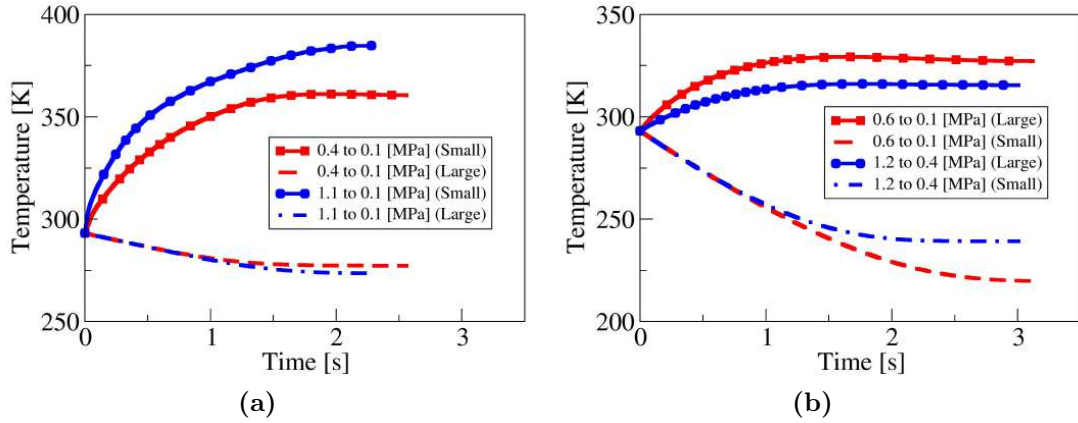


Figure 5.5: Numerical temperature evolution in the upstream and downstream reservoirs. (a) The flow goes from the large to the small reservoir. (b) The flow goes from the small to the large reservoir.

A point which needs to be considered and which could help explaining why the discharge from the small to the large reservoir takes longer than the one in the opposite direction is that, regardless of the flow direction the temperature variation at the small reservoir is several times larger than the one observed at the large one. Another possible explanation, needs to be found in the possible existence of a flow restriction under these conditions, therefore reducing the effective flow section. In fact, the most plausible explanation is likely to be the different nozzle resistance the fluid is facing when flowing in opposite directions. These hypotheses will be analysed in the remaining part of the paper.

Figure 5.6, introduces the experimentally based fluid temperature temporal variation on both reservoirs for the two flow directions and for all pressure differentials evaluated, see Table 5.1. Figures 5.6a and 5.6b, characterise the temperature decrease in the large and small reservoirs when the flow goes from the large to the small and from the small to the large reservoirs, respectively. The fluid temperature evolution in both reservoirs obtained from the CFD simulations is also presented for comparison.

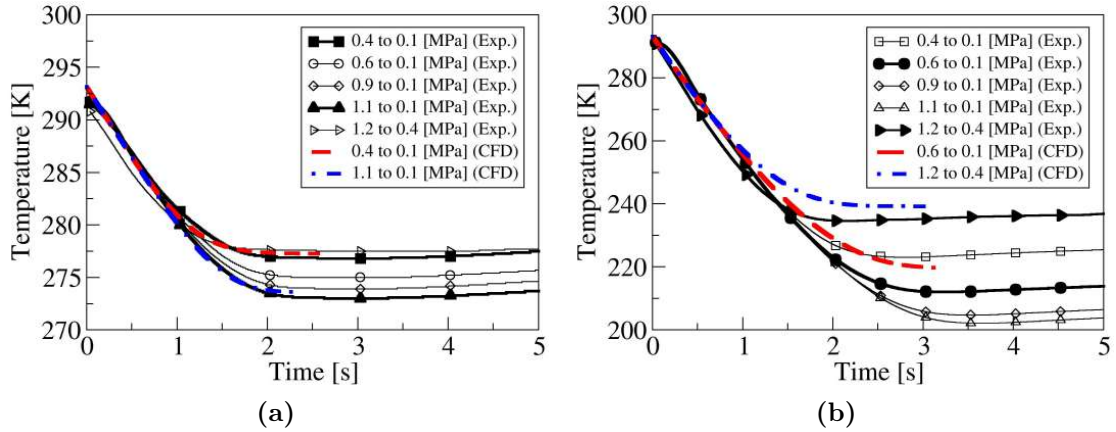


Figure 5.6: Experimentally based and numerical temperature decay in the upstream reservoir. (a) The flow goes from the large to the small reservoir. (b) The flow goes from the small to the large reservoir.

The first thing to be observed is that the fluid temperature decay is proportional to the initial pressure ratio between reservoirs, the higher the pressure ratio the higher the fluid temperature decay in the upstream reservoir. As previously observed, the temperature drop is particularly high in the small reservoir. Temperatures decrease of over 50° are observed in the small reservoir, such decrease is of less than 20° in the large one. When comparing the temperature evolution experimentally based with the CFD one, it is observed a particularly good agreement in the large reservoir, a maximum difference between experimental and numerical results of about 3.3% is observed in the small reservoir when the discharge is from 0.6 to 0.1 MPa. The experimentally based results generate final temperatures, slightly lower than the ones obtained via CFD simulations. As the walls were assumed adiabatic in the CFD simulations, Figure 5.6 confirms this assumption then the heat transferred through the walls appears to be negligible.

Based on the experimental pressure temporal evolution and the calculated temperature, the temporal mass variation at each reservoir for both flow directions and for all different pressures studied is presented in Figure 5.7. The same figure presents as well the mass decay/increase obtained via CFD. Figures 5.7a and 5.7b introduce the reservoirs temporal mass variation when the air flows from the L-to-S and S-to-L reservoirs, respectively. As previously observed, when the discharge

is from 1.2 to 0.4MPa, the discharge time is minimum, this is due to the small density ratio associated to the fluid. Regardless of the flow direction, the curves representing the temporal mass variation on both reservoirs are, for the discharge initial first second, having a constant pendent, but during the next 1.5 discharge seconds the curves are rounded. The constant pendent is likely to indicate choked flow conditions. The curves of the Mach number versus time should clarify this hypothesis.

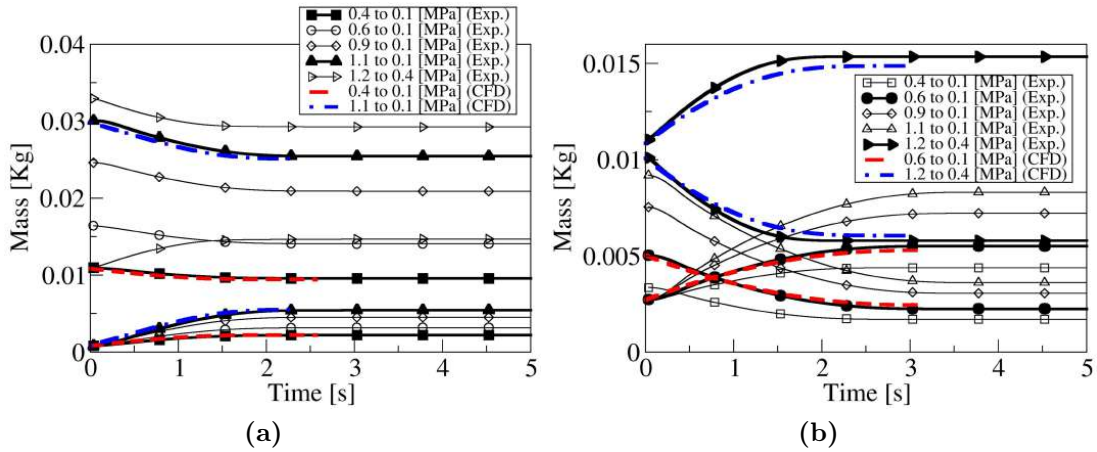


Figure 5.7: Temporal mass variation in each reservoir based on experimental data and for all pressures studied. (a) Flow from large to small reservoir. (b) Flow from small to large reservoir.

The instantaneous mass flow flowing between the two reservoirs for all pressures studied and for both flow directions, is presented in Figure 5.8. Notice that the information presented in this figure was directly extracted from Figure 5.7. For each pressure ratio, Figure 5.7 is presenting two curves, representing the mass decrease in one reservoir and the mass increase in the other, therefore each of the mass flow curves could be obtained twice, considering the mass decrease and increase in the respective reservoirs. Since both mass flow curves were almost identical, in Figure 5.8 just the curves representing the mass flow decrease in the upstream reservoir are presented. Figure 5.8a, characterises the mass flow between reservoirs when the fluid is going from the large to the small reservoir. Notice that as the pressure ratio increases, the mass flow also increases. In reality this mass

flow increase associated with the pressure ratio increase is due to the upstream fluid density increase. It is as interesting to see that as the pressure ratio increases the overall discharge time and the time at which the flow remains under sonic conditions, also increases, Figure 5.9 shall further clarify this point. Figure 5.8b presents the mass flow for the fluid going from the small to the large reservoir. It is interesting to realise that regardless of the pressure ratio evaluated, the discharge time lasts almost a second longer than when the flow goes in opposite direction. As already observed in Figure 5.8a, for a discharge from 1.2 to 0.4 MPa, the pendent of the mass flow curve is much higher than for the rest of the cases evaluated, clearly showing that, the initial downstream density plays an important role when considering the discharge temporal evolution and final time, such time decreases with the density ratio decrease.

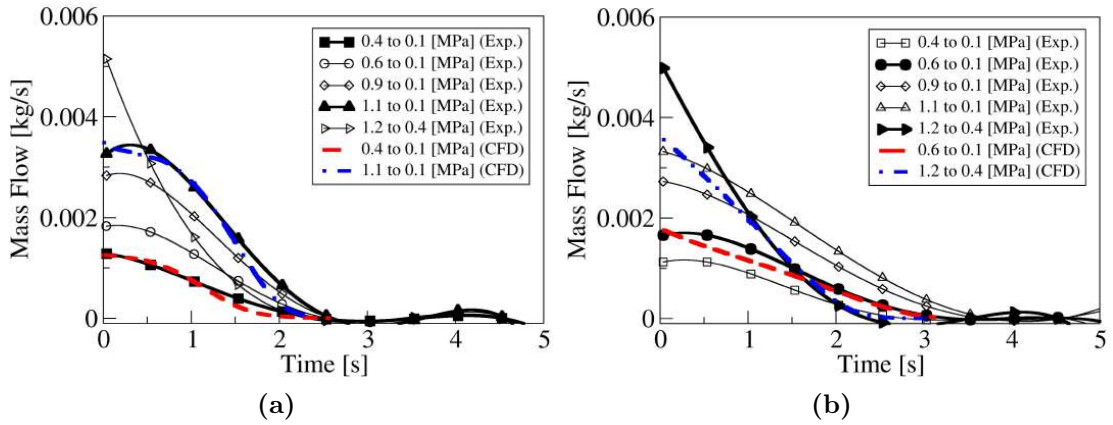


Figure 5.8: Mass flow between reservoirs, based on experimental data and for all pressures studied. (a) Flow from large to small reservoir. (b) Flow from small to large reservoir.

Figure 5.8 also compares the mass flow obtained experimentally with the numerical one, the agreement appears to be very good for all cases studied, just when the discharge is from 1.2 to 0.4 MPa and the flow goes from the small to the large reservoir, the pendent of the mass flow during the initial 0.5 seconds show some discrepancy. In fact already in Figure 5.7b, clear differences in the temporal mass evolution is observed for this particular discharge. When comparing Figures 5.8a and 5.8b for any given pressure differential, it is observed that at time zero the

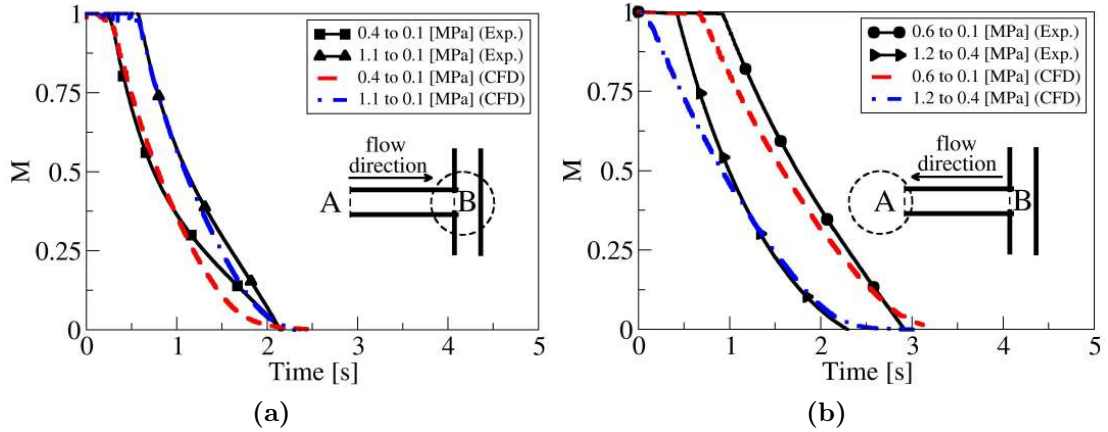


Figure 5.9: Temporal evolution of the maximum Mach number obtained at the nozzle separating the two reservoirs. Comparison between the numerical results and the experimentally based ones. (a) Flow from large to small reservoir. (b) Flow from small to large reservoir.

mass flow when the fluid goes from L-to-S is slightly larger than when the fluid goes from the S-to-L. This is indicating the flow is seeing a higher restriction when the fluid is going from S-to-L reservoir.

Figures 5.9a and 5.9b, introduce the Mach number temporal evolution at the nozzle minimum section as a function of the pressure differential and for the two flow directions, L-to-S and S-to-L reservoirs, respectively. The information presented obeys to the cases where numerical and experimentally based results can be compared. When the fluid goes from the large to the small reservoir, the flow is initially sonic, the time during which the flow remains under sonic conditions increases with the pressure ratio increase, Figure 5.9a. When the fluid is flowing from the small to the large reservoir and for initial respective pressures of 1.2MPa and 0.4MPa, the discharge is sonic during a very small time. But when the initial reservoirs pressure is of 0.6MPa and 0.1MPa, respectively, the time at which the flow remains sonic is of nearly 1 second, which is almost the same time observed when the fluid goes from the large to the small reservoir and for a respective pressure of 1.1MPa and 0.1MPa, compare figures Figures 5.9a and 5.9b.

The reason why the fluid remains sonic during a longer time, when the flow goes from S-to-L reservoirs, is likely to be caused by the sudden flow restriction the fluid

is suffering when the flow enters the horizontal section of the nozzle and coming from the two T shape branches. The two T shape branches promote the existence of a flow restricted section at the horizontal nozzle inlet, restricting as well the entrance of the fluid from a vertical plane, the fluid can only move vertically in the two vertical branches of the T nozzle. In reality this effect is creating a smaller effective section of the flow in this case than when flow goes from large to small reservoir. In other words, the nozzle resistance to the fluid is larger when the flow goes from the small to the large reservoir and therefore the mass flow is also smaller. In fact, when comparing the mass flow curves for the same pressure drop presented in Figures 5.8a and 5.8b, it can be clearly seen that the mass flow is higher during the initial times when the fluid goes from the L-to-S reservoir. At this point it must be highlighted that the location where the Mach number values are computed is always where the spatially averaged Mach number is maximum. Such location is at the end of the horizontal nozzle, beginning of the T junction, when the flow goes from L-to-S reservoir and at the end of the horizontal nozzle and beginning of the large tank, when the flow goes from the S-to-L reservoir. Such different locations were expected, then regardless of the flow direction the fluid at the entrance of the horizontal nozzle has to be subsonic and accelerates along it.

The temporal discharge coefficients as a function of the Reynolds number and for the four cases at which CFD and experimentally based results are generated is presented in Figure 5.10. The variations of the discharge coefficient when the flow goes from the large to the small tank and vice-versa is given in Figures 5.10a and 5.10b, respectively. For both flow directions, the numerical and experimentally based results are presented for the pressure differentials studied using both methodologies.

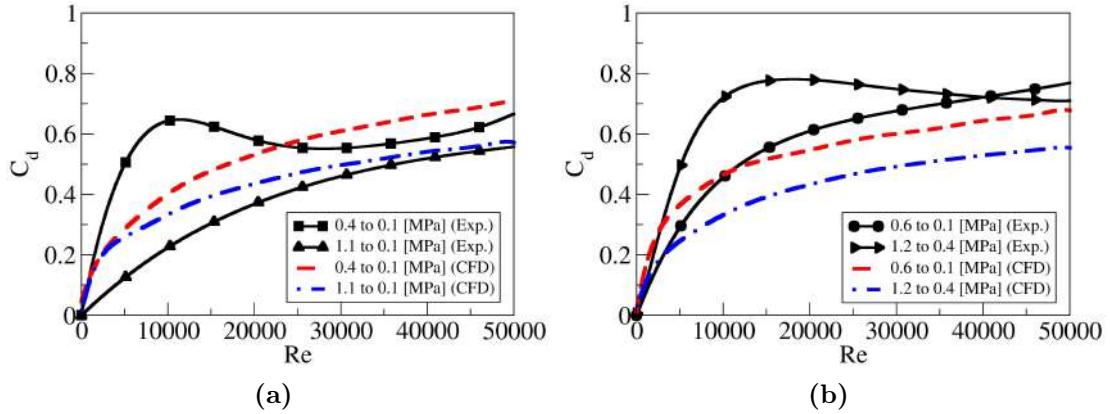


Figure 5.10: Nozzle discharge coefficient based on experimental data and for all pressures studied. (a) Flow from large to small reservoir. (b) Flow from small to large reservoir.

The first thing to notice is that for a given flow direction, the discharge coefficient shows a very similar temporal trend regardless of the pressure ratio evaluated. In fact this is to be expected then the discharge coefficient depends on the Reynolds number, but not on the pressure ratio between reservoirs. Some differences are observed between the discharge coefficients obtained numerically and the ones obtained based on experimental data, particularly at low Reynolds numbers. Authors believe such differences are due to the differences in fluid temperature between experimental and CFD results appearing at the end of the discharge. However for a given flow direction, the asymptotic values of the discharge coefficients are almost the same regardless of the methodology employed to calculate them. The discharge coefficients obtained when the flow is going from the large to the small reservoir are slightly higher than the ones obtained when the flow is going in the opposite direction. This supports what has been presented until the moment, which is the time required to discharge from the small to the large reservoir is larger than the one needed when the discharge is from the large to the small tank. In other words, the fluid is finding more resistance to flow from the small to the large reservoir than in opposite direction. As explained before, this must be due to the restriction the fluid is observing when flowing from the two T branches and entering the horizontal one.

In order to obtain a single curve representing the evolution of the discharge coefficient as a function of the Reynolds number and for each flow direction, at each Reynolds number the average discharge coefficient was determined. The mathematical equation of the resulting curves is presented in Equation (5.13), which represents the generic equation for the discharge coefficient as a function of the Reynolds number and for both flow directions. The parameters a_0, \dots, a_{10} characterising the discharge coefficient curve for each flow direction, are defined in Table 5.2. Notice that as in Figure 5.10b the maximum Reynolds number is 50000, the parameters given in the first two rows of Table 5.2 are valid for this Reynolds number range. Nevertheless, based on the results from the CFD simulations, a second set of parameters valid for a Reynolds number range $1000 \leq Re \leq 130000$ are also presented in the last two rows of Table 5.2.

$$C_d = a_0 + a_1 Re + a_2 Re^2 + \dots + a_{10} Re^{10} \quad (5.13)$$

Reynolds range	flow direction	a_0	a_1	a_2	a_3	a_4	a_5	a_6	a_7	a_8	a_9	a_{10}
1 to 50 000	L to S	1.470e-01	2.625e-05	-9.852e-10	3.077e-14	-8.131e-19	1.774e-23	-2.904e-28	3.252e-33	-2.300e-38	9.184e-44	-1.572e-49
	S to L	3.608e-02	1.053e-04	-5.156e-09	-1.795e-13	3.144e-17	-1.407e-21	2.351e-26	1.988e-31	-1.406e-35	2.063e-40	-1.047e-45
1000 to 130 000	L to S	1.480e-01	2.566e-05	-8.676e-10	1.981e-14	-2.541e-19	7.886e-25	2.838e-29	-4.980e-34	3.824e-39	-1.481e-44	2.350e-50
	S to L	6.400e-02	5.258e-05	-4.250e-09	2.382e-13	-8.453e-18	1.909e-22	-2.779e-27	2.594e-32	-1.499e-37	4.884e-43	-6.857e-49

Table 5.2: Constant values of the discharge coefficient equation for two different range of Reynolds number and different flow directions, large to small reservoirs and vice versa.

One of the advantages of performing 3D-CFD simulations is that it allows to carefully analyse the flow evolution inside the nozzle. The flow field dynamics given as instantaneous velocity contours at both ends of the horizontal pipe, for both flow directions, reservoir pressures and at three different time instants, 0.02s, 0.5s and 1s, is introduced in Figure 5.11. Each column characterises the time at which the velocity field is presented. The initial two rows of Figure 5.11 show the flow field at both horizontal nozzle ends when the fluid goes from the L-to-S reservoir, the initial upstream-downstream pressure on each tank is 0.4MPa-0.1MPa, and 1.1MPa-0.1 MPa respectively. The final two rows show the velocity field when the flow goes from the S-to-L reservoir, the upstream-downstream initial pressures are 0.6MPa-0.1MPa and 1.2MPa-0.4MPa, respectively.

When the fluid goes from the large to the small reservoirs and for the two pressure ratios studied, during the initial milliseconds, $t = 0.02s$, the fluid reaches

sonic conditions at the horizontal nozzle outlet just before the T junction, supersonic flow conditions are observed as the fluid expands to the two lateral vertical branches, see the first and second rows of Figure 5.11. At $t = 0.5s$ and for upstream-downstream initial pressures of 0.4MPa-0.1MPa, the fluid has become subsonic at all points, the maximum spatial averaged velocity is 239m/s, which corresponds to $M=0.74$, and the fluid still remains detached when entering the T junction. After 1 second of the origin of the discharge, the maximum fluid velocity has decreased to 120m/s but the flow keeps being detached at the T junction entrance. But, when the L-to-S reservoirs initial pressure is of 1.1MPa and 0.1MPa, respectively, after 0.5 seconds the flow is still under sonic conditions, the Mach number and the associated spatial averaged velocities at the inlet and outlet of the horizontal pipe are of $M=0.53$ (176 m/s) and $M=0.99$ (310 m/s), respectively. The respective values of the Mach number in these two pipe locations are of 0.45 and 0.56, after the initial second of the discharge.

The discharge when the fluid flows from the small to the large reservoir at initial pressures of 0.6MPa and 0.1MPa, respectively, is presented in the third row of Figure 5.11. Now, the maximum Mach number appears at the entrance of the large reservoir, horizontal pipe outlet, as expected according to the theory [29, 30]. At time $t = 0.02s$, the respective Mach numbers and spatial averaged fluid velocities at the horizontal pipe inlet and outlet are $M=0.6$ (198 m/s) and $M=1$ (353 m/s). For these particular initial pressures, and after 0.5 seconds, the flow still remains under sonic conditions, the inlet and outlet Mach numbers and fluid velocities are $M=0.59$ (190 m/s) and $M=1$ (317 m/s), respectively. At this point it is important to realise that under sonic conditions, the spatial averaged fluid velocity depends on the instantaneous fluid temperature. When comparing these figures with the ones characterising the initial pressure drop of 1.2MPa to 0.4MPa, presented as the bottom row of figure Figure 5.11, it is realised that now just at the initial instants, $t = 0.02s$, the flow is sonic, but the pressure drop is not large enough to generate a supersonic expansion as the fluid enters the large reservoir. After 0.5s, the discharge is completely subsonic, being the horizontal pipe inlet and outlet Mach numbers and associated spatial averaged fluid velocities of $M=0.57$ (182 m/s) and $M=0.73$ (230 m/s), respectively. At this point it is interesting to observe the agreement between the CFD results presented in Figure 5.11 and in

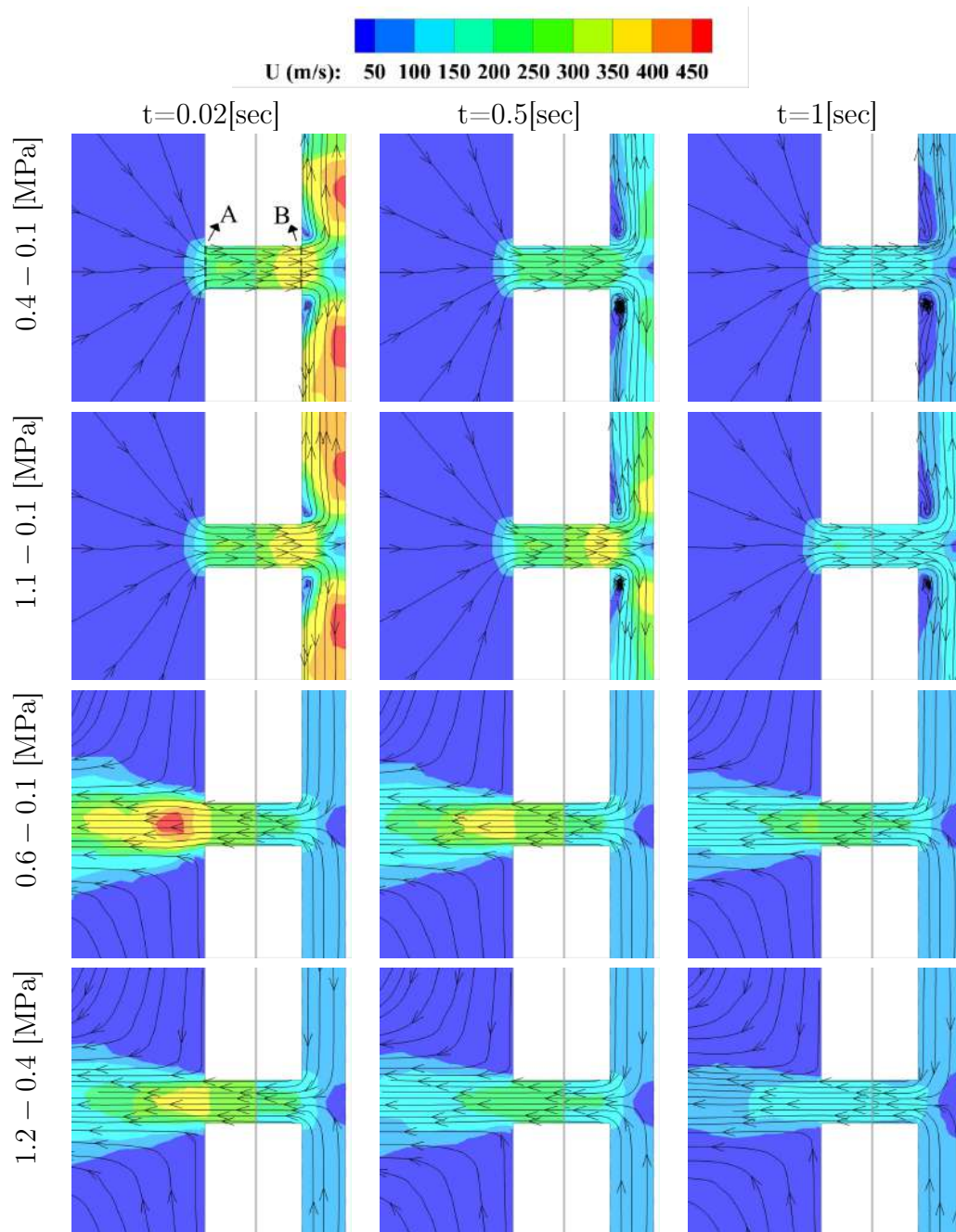


Figure 5.11: Velocity contours of all CFD cases studied and at three instants, 0.02, 0.5 and 1 second. The first and second rows, represent the fluid evolution when the fluid goes from the L-to-S reservoir, the respective upstream/downstream initial pressures are 0.4MPa-0.1MPa and 1.1MPa-0.1MPa. The third and fourth rows, characterise the two cases when the flow goes from S-to-L reservoir, being the upstream/downstream initial pressures of 0.6MPa-0.1MPa and 1.2MPa-0.4MPa, respectively.

Figure 5.9, notice that the time during which flow is sonic has a perfect match for all pressures studied.

The observations made in Figure 5.11 are clarifying why during the experimental tests and CFD simulations, the discharge time was larger when the flow was flowing from the S-to-L reservoir than when flowing in the opposite direction, see all figures between Figure 5.4 and Figure 5.8. Notice as well from Figure 5.8 that the maximum mass flow at time zero is always larger when the flow is going from the L-to-S reservoir than when going from the S-to-L one, clearly indicating the added difficulty for the fluid to flow from the small to the large reservoir. This difficulty can be understood when analysing the inlet section under both flow conditions. When the flow goes from the large to small reservoir, the flow enters the horizontal nozzle from any direction, 360 degrees, but when the flow goes from the small to the large reservoir, initially the fluid needs to enter from the two ends of a T branch and then the fluid needs to enter the horizontal nozzle from the two sides of the T branch, therefore facing a particularly narrow inlet when compared to the opposite fluid direction. The effects of this higher flow restriction, when the fluid is going from the small to the large reservoir, can also be observed when analysing the discharge coefficients in both flow directions. Notice that the discharge coefficient when the fluid is going from the S-to-L reservoir is asymptotically smaller than what when the fluid flows from the L-to-S reservoir, see Equation 13 and Table 2.

The work presented in the present manuscript consisted in evaluating the discharge coefficient of a T shape nozzle under compressible flow conditions. Experimental and numerical analyses were performed. Numerical simulations clarified where the sonic conditions are to be expected. Discharge coefficients were dependent on the flow direction and the Reynolds number, they agree well with the ones obtained by Comas et al. [13] and Nagao et al. [9], specially when considering the different nozzle length to diameter ratio. In the CFD simulations, the fluid was considered as ideal, similar CFD simulations were performed by Lakzian et al. [18] and Mazzelli et al. [17], where the fluid was as well considered as ideal and studied under similar pressure differentials and the same turbulence model. From the comparison of the present study with references [9, 13, 18, 17], it can be concluded

that the error generated by the CFD simulations is small and acceptable under the engineering applications point of view.

5.7 Conclusions

The discharge time is proved to be directly related to the upstream/downstream density ratio. The discharge coefficients on both flow directions of a T shape nozzle and considering the fluid as compressible and real, were obtained in the present manuscript based on experimental data. The same information was obtained from CFD simulations. The CFD simulations performed showed a good match with the experimental results, and allowed to understand the differences of the temporal flow evolution inside the nozzle at different flow directions. The exact locations where the flow was sonic and even supersonic were detected, allowing to further modify the T shape nozzle design in future applications. The theoretical methodology presented was based on the experimental data and proved to be very accurate and reliable, particularly when temporal pressure and temperature were known. The final equations characterising the discharge coefficient as a function of the Reynolds number and for both flow directions are provided.

5.8 References

- [1] ISO6358. Pneumatic fluid power-components using compressible fluids. determination of low-rate characteristics. Technical report, ISO Standards Org, 1989.
- [2] T Kagawa, T Wang, Y Ishii, Y Terashima, T Morozumi, T Mogami, and N Oneyama. Determination of flow rate characteristics of small pneumatic valves using isothermal chamber by pressure reponse. 7th Symp. on Fluid Control Measurement and Visualization. Sorrento, Italy, 2003.

- [3] Robert C Johnson. Calculations of real-gas effects in flow through critical-flow nozzles. Journal of Basic Engineering, Trans. ASME, Series D, 86(3):519–526, 1964.
- [4] W Bober and WL Chow. Nonideal gas effects for the venturi meter. ASME J. Fluid. Eng., 113(2):301–304, 1991.
- [5] DA Kouremenos, KA Antonopoulos, and XK Kakatsios. A correlation of the isentropic exponents of real gases. International journal of heat and fluid flow, 9(4):410–414, 1988.
- [6] DA Kouremenos and KA Antonopoulos. Sound velocity and isentropic exponents of real air on its compressibility chart. International Journal of Heat and Fluid Flow, 12(2):137–141, 1991.
- [7] HD Kim, JH Lee, KA Park, T Setoguchi, and S Matsuo. A study of the critical nozzle for flow rate measurement of high-pressure hydrogen gas. Journal of Thermal Science, 16(1):28–32, 2007.
- [8] Jae-hyung Kim, Heuy-dong Kim, Toshiaki Setoguchi, and Sigeru Matsuo. Computational study on the critical nozzle flow of high-pressure hydrogen gas. Journal of propulsion and power, 24(4):715–721, 2008.
- [9] Junji Nagao, Shigeru Matsuo, Mamun Mohammad, Toshiaki Setoguchi, and Heuy Dong Kim. Numerical study on characteristics of real gas flow through a critical nozzle. Int. J. Turbo Jet-Engines, 29(1):21–27, 2012.
- [10] Junji Nagao, Shigeru Matsuo, Shotaro Suetsugu, Toshiaki Setoguchi, and Heuy Dong Kim. Characteristics of high reynolds number flow in a critical nozzle. International Journal of Hydrogen Energy, 38(21):9043–9051, 2013.
- [11] S Nakao. Development of critical nozzle flow meter for high pressure hydrogen gas flow measurements. Proceedings of JSME, fluid dynamics section, Kanazawa, Japan G, 201:2005, 2005.

- [12] Hongbing Ding, Chao Wang, and Yakun Zhao. Flow characteristics of hydrogen gas through a critical nozzle. international journal of hydrogen energy, 39(8):3947–3955, 2014.
- [13] A Comas, Carlos Rio-Cano, and JM Bergada. A novel method to determine the discharge coefficient of constant section nozzles under compressible dynamic flow conditions. Journal of Fluids Engineering, 141(7), 2019.
- [14] Byung Ik Lee and Michael G Kesler. A generalized thermodynamic correlation based on three-parameter corresponding states. AIChE Journal, 21(3):510–527, 1975.
- [15] Mahmood Farzaneh-Gord, Mohammad Sadegh Pahlevan-Zadeh, Amir Ebrahimi-Moghadam, and Saied Rastgar. Measurement of methane emission into environment during natural gas purging process. Environmental Pollution, 242:2014–2026, 2018.
- [16] Salvador García-Todolí, Pedro L Iglesias-Rey, Daniel Mora-Meliá, F Javier Martínez-Solano, and Vicente S Fuertes-Miquel. Computational determination of air valves capacity using cfd techniques. Water, 10(10):1433, 2018.
- [17] Federico Mazzelli, Adrienne B Little, Srinivas Garimella, and Yann Bartosiewicz. Computational and experimental analysis of supersonic air ejector: Turbulence modeling and assessment of 3d effects. International Journal of Heat and Fluid Flow, 56:305–316, 2015.
- [18] Esmail Lakzian, Masoud Hajian, and Ali Farahmand. The entropy generation rate minimization for a proposed air ejector for the carpet industry. Meccanica, 53(1):145–159, 2018.
- [19] Jacek Smolka, Zbigniew Bulinski, Adam Fic, Andrzej J Nowak, Krzysztof Banasiak, and Armin Hafner. A computational model of a transcritical r744 ejector based on a homogeneous real fluid approach. Applied Mathematical Modelling, 37(3):1208–1224, 2013.

- [20] Ll Macia, R Castilla, Pedro Javier Gamez-Montero, Sergi Camacho, and E Codina. Numerical simulation of a supersonic ejector for vacuum generation with explicit and implicit solver in openfoam. Energies, 12(18):3553, 2019.
- [21] Diego A. Arias and Timothy A. Shedd. CFD analysis of compressible flow across a complex geometry venturi. Journal of Fluids Engineering, 129(9):1193–1202, apr 2007. doi: 10.1115/1.2754321. URL <https://doi.org/10.1115%2F1.2754321>.
- [22] Hongbing Ding, Chao Wang, and Yakun Zhao. Surface roughness effect on flow measurement of real gas in a critical nozzle. Measurement, 68:82–91, 2015.
- [23] Masoud Darbandi and Ehsan Roohi. Study of subsonic–supersonic gas flow through micro/nanoscale nozzles using unstructured dsmc solver. Microfluidics and nanofluidics, 10(2):321–335, 2011.
- [24] Jianhui Zhao, Weilong Liu, Jialu Zhao, and Leonid Grekhov. Numerical investigation of gas/liquid two-phase flow in nozzle holes considering the fuel compressibility. International Journal of Heat and Mass Transfer, 147:118991, 2020.
- [25] Aishvarya Kumar, Ali Ghobadian, and Jamshid M Nouri. Assessment of cavitation models for compressible flows inside a nozzle. Fluids, 5(3):134, 2020.
- [26] A Lichtarowicz, RK Duggins, and E Markland. Discharge coefficients for incompressible non-cavitating flow through long orifices. Journal of Mechanical Engineering Science, 7(2):210–219, 1965.
- [27] J Bergadà and E Codina. Discharge coefficients for a four nozzle two flapper servovalve. In Proc. of the 46th National Conference on Fluid Power, volume 1, pages 213–218, 1994.
- [28] UJ Plocker and H Knapp. Save time in computing density. Hydrocarbon Processing, 55(5):199–201, 1976.

- [29] MJ Zucrow and JD Hoffman. Gas dynamics, vol 1 john wiley & sons. Hoboken, New Jersey, 1976.
- [30] Josep María Bergada Grañó. Mecánica de fluidos: breve introducción teórica con problemas resueltos. Universitat Politècnica de Catalunya. Iniciativa Digital Politècnica, 2012.

Chapter 6

Appendix

6.1 Published Journal Papers



Active flow control optimisation on SD7003 airfoil at pre and post-stall angles of attack using synthetic jets



N.M. Tousi^{a,a,*}, M. Coma^{b,d}, J.M. Bergadà^a, J. Pons-Prats^{b,d}, F. Mellibovsky^b, G. Bugeda^{c,d}

^a Department of Fluids Mechanics, Universitat Politècnica de Catalunya, Barcelona, 08034, Spain

^b Department of Physics, Aeronautics Division, Universitat Politècnica de Catalunya, Barcelona, 08034, Spain

^c Department of Civil and Environmental Engineering, Universitat Politècnica de Catalunya, Barcelona, 08034, Spain

^d International Centre for Numerical Methods in Engineering (CIMNE), Universitat Politècnica de Catalunya, Barcelona, 08034, Spain

ARTICLE INFO

Article history:

Received 11 January 2021

Revised 7 May 2021

Accepted 16 May 2021

Available online 10 June 2021

Keywords:

Active flow control

Synthetic jet

Optimization

Aerodynamic efficiency

Flow structure

ABSTRACT

The use of Active Flow Control (AFC) technologies to modify the forces acting on streamlined bodies is one of the most active research fields in aerodynamics. For each particular application, finding the optimum set of AFC parameters which maximises lift, minimises drag or maximises lift-to-drag ratio (aerodynamic efficiency), has become a necessary design requirement. In the present paper, the AFC technology was applied to the Selig-Donovan 7003 (SD7003) airfoil at Reynolds number 6×10^4 . Synthetic jets were employed to modify the lift and drag forces acting on the airfoil. Four angles of attack (AoA) of 4° , 6° , 8° and 14° were considered, alongside five AFC parameters: jet position, jet width, momentum coefficient, forcing frequency and jet inclination angle. A multi objective optimisation based on genetic algorithms (GA) was performed for each angle of attack to find the optimum combination of AFC parameters. Each GA generation was simulated using Computational Fluid Dynamics (CFD). A home-made GA package was linked with a mesh generator and the CFD solver, and the results were automatically fed back to the GA code. Over 2200 CFD simulations were performed in two dimensions, using the Spalart-Allmaras turbulent model. The motivation behind the current study is to understand the dependence of the optimum set of AFC parameters on the AoA. Results show that, as AoA is increased, the potential benefits of AFC become more pronounced, which allows for considerable improvement in aerodynamic efficiency. The physics involved in the interaction between the main flow and synthetic jet are clearly presented and clarifies that the physical phenomenon to obtain maximum efficiency is completely different at pre-stall and post-stall AoA. In particular, the aerodynamic efficiency was increased by 251% from baseline (no actuation) by using a moderate/finite momentum coefficient at $\text{AoA}=14^\circ$, while a mere 39% increase was obtained at $\text{AoA}=8^\circ$. In addition, the interaction between the incoming flow and the synthetic jet pulsating flow at different injection angles has been thoroughly investigated.

© 2021 Elsevier Inc. All rights reserved.

* Corresponding author.

E-mail address: navid.monshi.tousi@upc.edu (N.M. Tousi).

1. Introduction

Increasing lift and reducing drag have major effects on fuel usage, stability, durability and maneuverability of aircraft. Active Flow Control (AFC) technology consists of adding/subtracting momentum to/from the main flow in particular locations in order to interact with the boundary layer, and delay or promote its separation. Moreover, it has the advantage over passive flow control techniques of not introducing drag penalty in off-design conditions. When defining the AFC technique, special care should be taken to assess the energy balance, i.e. the net energy saved due to drag reduction, after the subtraction of the energy required to actuate the AFC device. A very useful classification of AFC strategies was proposed by Cattafesta and Sheplak [1] by dividing AFC techniques into three different classes. 1) Moving body actuators, whose purpose consists in inducing local fluid motion without the need of adding mass [2]. 2) Plasma actuators, which generate jets of ionized fluid with very fast temporal response [3,4]. The reader can also check other references on Dielectric Barrier Discharge (DBD) also called plasma actuator devices [5,6], where the authors proposed the combination of DBD plasma actuator experiments with numerical optimisation. And finally, 3) fluidic actuators (FA), which are the most common type of actuators, and whose working principle consists in injecting/sucking fluid to/from the boundary layer. Recent research has set the focus on elucidating the origin of the self-sustained oscillations [7,8]. Recent references also include the outcome of two European projects; namely MARS (Manipulation of Reynolds Stress for Separation Control and Drag Reduction) and DRAGY (Drag Reduction in Turbulent Boundary Layer via Flow Control). The two projects were devoted to mature the AFC technology in views of future industrial applications. Several AFC methods were assessed and the results obtained from the projects were outlined in [9,10], where a review of the major AFC technologies and their applications on airplanes were presented.

Among the different fluidic actuators, Synthetic Jet Actuators (SJA), also called Zero Net Mass Flow Actuators (ZNMFA), have gained particular attention because of their simplicity and high capabilities in controlling flow separation (see for example, [11–14]). Moreover, when studying the effectiveness of different AFC actuators on a stator compressor cascade, it was concluded that Synthetic Jet (SJ) actuators were more efficient than Continuous Jet Actuators (CJA) at comparable power input levels [15–18]. Unlike CJAs, SJAs do not require external fluid supply. In SJA, an oscillating membrane is located inside a tiny cavity housed right beneath the surface. The role of the membrane is to inject momentum into the near-wall flow by alternatively sucking low momentum fluid into the chamber and then blowing it back with increased momentum.

During the last two decades, SJA-AFC has been implemented on different airfoils and studied both experimentally and numerically. The focus has been mostly set on assessing the effect of two important parameters related to these jets, namely the non-dimensional frequency ($F^+ = fC/U_\infty$, with f the dimensional frequency, C the airfoil chord and U_∞ the free-stream velocity) and the momentum coefficient (C_μ). In the case of SJAs, this latter is defined as $C_\mu = (h\rho_{jet}(U_j^2 \sin\theta))/(C\rho_\infty(U_\infty^2))$, where h is the jet width, ρ_{jet} and ρ_∞ are the jet and far field densities, respectively, U_j is the maximum jet velocity and θ is the jet inclination angle with respect to the adjacent surface.

Amitay et al. [19] investigated experimentally the effects of momentum coefficient, frequency and position of a synthetic jet actuator employed to control flow separation from an unconventional symmetric airfoil. They realised that by placing the actuator closer to the separation position, a lower momentum coefficient was needed to reattach the separated flow. In a second paper [20], they discussed the role of actuation frequency on the reattachment of the controlled flow and found that, when the non-dimensional actuation frequency was of the same order of magnitude as the shedding frequency of vortices in the wake of the stalled airfoil ($F^+ \mathcal{O}(1)$), unsteady reattachment was achieved, whereas full flow reattachment was obtained when the actuation frequency was well above shedding frequency ($F^+ \mathcal{O}(10)$). Gilarranz et al. [21] applied SJA on a NACA0015 airfoil at $Re = 8.96 \times 10^5$ experimentally. They managed to increase the stall angle of airfoil from 12° to 18° and realised that actuation effectiveness widely improved beyond $AoA > 10^\circ$. They also observed that higher actuation frequencies were required to obtain remarkable effects at $AoA > 25^\circ$. You and Moin [22] performed a Large Eddy Simulation (LES) for the same airfoil and Reynolds number as Gilarranz et al. [21]. They used an actuation with $C_\mu = 0.0123$, $F^+ = 1.284$ and $\theta = 30.2^\circ$ and succeeded in delaying separation, which entailed a lift increase of 70%. Tuck and Soria [23] experimentally studied the effect of using SJA on a NACA0015 profile at $Re = 3.9 \times 10^4$. They observed that optimal actuation frequencies were $F^+ = 0.7$ and 1.3 , and that the highest one was most effective with an optimum for $C_\mu = 0.0123$. Under this forcing conditions, the stall AoA improved from 10° to 18° . Kitsios et al. [24] conducted a LES study using the same airfoil and Reynolds number previously analysed by Tuck and Soria [23]. They realised that the optimal frequencies found in the experiments actually coincided with the baseline shedding frequency (f_{wake}) and its first harmonic ($2f_{wake}$). This was also experimentally confirmed by Buchmann et al. [25]. Kim and Kim [26] numerically investigated flow separation control with SJAs on a NACA23012 at $Re = 2.19 \times 10^6$. They observed maximum lift happened when $F^+ = 1$ and the jet was located in the close vicinity of the separation point. The small rolling vortices generated by the actuator at this low frequency were very unstable and therefore were easily affected by external disturbances, a conclusion previously reported by Amitay and Glezer [20]. Monir et al. [27] used a RANS model to study the effect of SJA parameters on the performance of a NACA23012 wing profile at $Re = 2.19 \times 10^6$. They found that applying SJA tangentially yielded better results than doing it normal to the surface. They concluded that momentum injection into the boundary layer was more efficient in this new configuration. Goodfellow et al. [28] studied experimentally the effects of SJA on separation control and wake topology on a NACA0025 airfoil at $Re = 10^5$ and $AoA = 5^\circ$ and realised that momentum coefficient was the primary control parameter, and that exceeding a given threshold caused a drag decrease of almost 50%. Feero et al. [29] examined the exact same airfoil and Reynolds

number, but at $AoA=10^\circ$. They noticed that the required momentum coefficient to reattach the flow was one order of magnitude lower for excitation frequencies in the range of the vortex shedding frequency than for high frequency. In a later study [30] of the same airfoil and at the same Reynolds number but at $AoA=12^\circ$, they focused on understanding the effect of jet position in controlling the separation. They found that, placing the jet slot close to the separation point, either downstream or upstream, yielded effective results, with a mild advantage for the upstream configuration. Zhang and Samtaney [31] performed a direct numerical simulation (3D-DNS) on a NACA0018 airfoil at $AoA=10^\circ$ and at $Re = 1000$. They studied the effect of three different non-dimensional frequencies ($F^+ = 0.5, 1$ and 4) on airfoil performance. Performances improved in all three cases, the optimum corresponding to $F^+ = 1$. Perhaps one of the latest simulations of SJA applied to airfoils is the one done by Rodriguez et al. [32]. They studied the SD7003 airfoil at $Re = 6 \times 10^4$ at three $AoA=4^\circ, 11^\circ$ and 14° . They observed an aerodynamic efficiency (lift-to-drag ratio) increase of 124% at the highest $AoA=14^\circ$.

In all the studies just cited, the effects of synthetic jets were assessed via parametric analysis, which is a very limited and time consuming approach, particularly so when optimum values of the parameters are sought. In what follows, some of the latest research involving optimisation methods are briefly presented.

Duvigneau and Visonneau [33] coupled the flow solver with an automatic optimisation, which relies on the derivative-free multi-directional search algorithm introduced by Torczon [34], to optimise three parameters of SJA; namely, non-dimensional frequency, velocity amplitude and jet angle. The study was performed on a NACA0015 airfoil at $Re = 8.96 \times 10^5$ and for a range of $AoA \in [12^\circ, 24^\circ]$. By setting the control parameters to their optimal values, the maximum lift was increased by 34%, and the stall angle delayed from 19° to 22° . In a further study [35], they used a derivative-free algorithm to find the optimal SJA location on a NACA0012 airfoil at $Re = 2 \times 10^6$. They considered two $AoA=18^\circ, 20^\circ$ across stall. The results showed that, at an $AoA=20^\circ$ the influence of jet location on lift increase (by 57%) was more noticeable than at $AoA=18^\circ$. Kamari et al. [36] studied the optimisation of four AFC parameters when using constant blowing and sucking on the SD7003 airfoil at $Re = 6 \times 10^4$, they coupled Genetic Algorithms (GA) with Artificial Neural Networks (ANN). They concluded that constant sucking was more effective than using constant blowing. In a further study, using the same methodology, airfoil and Reynolds number, Tadjfar and Kamari [37] optimised five SJA parameters. Two injection configurations, tangent and normal to the boundary layer as well as two $AoA=13^\circ$ and 16° were considered, aerodynamic efficiency was the only objective function. A maximum aerodynamic efficiency of 591% was obtained at $AoA=13^\circ$ using the tangent injection configuration.

The airfoil and Reynolds number chosen for the present study are respectively the Selig-Donovan 7003 (SD7003) and $Re = 6 \times 10^4$. This is due to the fact that for this airfoil and Reynolds number many numerical and experimental data are available in the literature (see for example, [38–44]). SD7003 is a thin airfoil with a thickness-to-chord ratio of 8.5% ($t/C=0.085$) which is often employed in micro air vehicles (MAV). One of the particularities of this airfoil at such a low Reynolds number is the formation of a laminar separation bubble (LSB) on its suction side. LSB is formed when, due to the strong adverse pressure gradient, the laminar boundary layer initially separates from the upper surface and after a laminar-to-turbulent transition, reattaches further downstream. As the angle of attack increases, LSB moves towards the leading edge and reduces its length. Ultimately, at a critical angle, stall AoA , downstream reattachment is not occurring and causes a large recirculation zone which is accompanied by a sudden drop in the lift and a sharp increase in the drag. In the present study, via using a Genetic Algorithm optimisation method, the focus has been placed on demonstrating how different AoA , from pre-stall ($4^\circ, 6^\circ, 8^\circ$) to post-stall (14°), can affect the optimum set of parameters associated with the synthetic jet actuator. For the present airfoil and Reynolds number, it is the first time five SJA parameters are being optimised at these four AoA . The optimisation methodology presented in this paper is completely novel and consists of linking, via using an in-house program developed in Python, a mesh generator (GMSH), a CFD package (OpenFOAM) and a Genetic Algorithm optimiser developed by the authors. After obtaining the two objective functions (maximum lift and maximum efficiency) determined by the CFD simulations, and once transferred to the GA optimiser, the optimiser generates a new set of five Active Flow Control (AFC) parameters, which are being used to automatically create a new mesh and to reset the boundary conditions in the CFD package. Due to the new methodology employed to optimise the AFC parameters, which involved performing over 2200 2D-CFD simulations, it was not possible to perform the simulations in 3D. Nevertheless, as the main aim of the paper was to optimise five AFC parameters for each AoA , the resulting optimised AFC parameters presented in this manuscript are having the maximum possible degree of accuracy.

The remainder of the paper is structured as follows. The problem formulation and numerical methods are presented in section §2, followed by an overview of the optimisation methods in section §3. Results are presented in section §4 and discussed in section §5. Section §6 summarises the main conclusions of the study.

2. Numerical method

2.1. Equations and flow solver

The present study is based on a large number of simulations aiming to optimise the flow around an airfoil at different AoA in order to minimise or maximise the forces acting over it. Although some authors have applied Direct Numerical Simulation (DNS) or Large Eddy Simulation (LES) for the simulation of AFC applications [45]. The use of 3D models for the optimisation study presented in this paper is not feasible due to the extreme demand in computational power. To overcome this drawback, a 2D unsteady Reynolds Averaged Navier-Stokes model (URANS) has been used. To perform all the

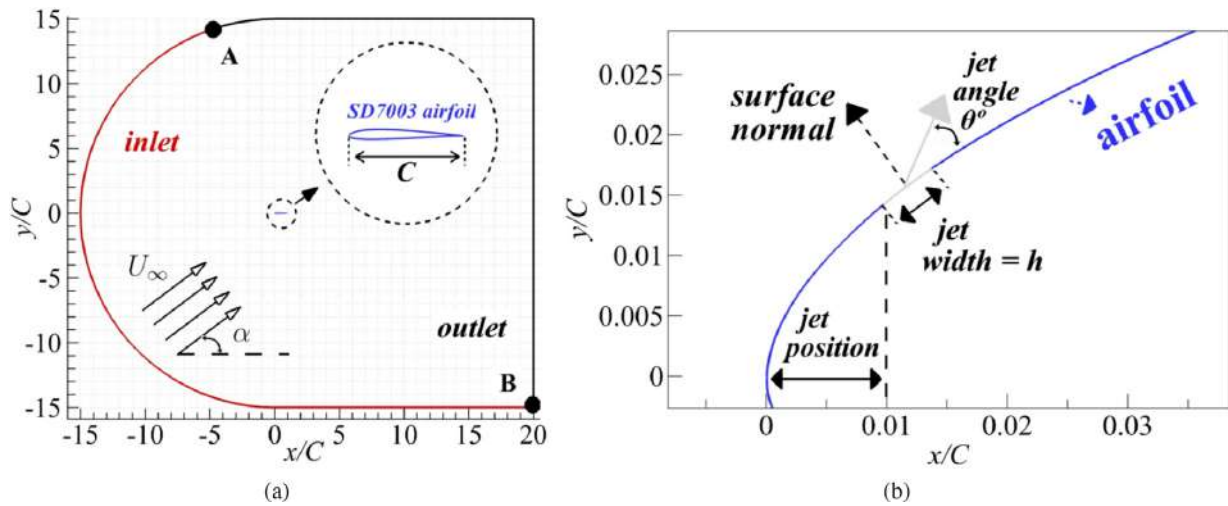


Fig. 1. (a) 2D Computational domain and (b) synthetic jet geometrical design parameters.

simulations a finite volume CFD solver (OpenFOAM) was employed. Also a second order discretization method was used for all parameters. For pressure–velocity coupling the Pressure-Implicit with Splitting of Operators (PISO) scheme [46] was chosen due to its capability in handling unsteady flow. When considering the Navier-Stokes equations under incompressible flow conditions, after substituting each variable by its average and fluctuating values, the resulting averaged continuity and momentum equations are expressed as:

$$\nabla \cdot \bar{\mathbf{u}} = 0 \tag{1}$$

$$\rho \frac{\partial \bar{\mathbf{u}}}{\partial t} + \rho \bar{\mathbf{u}} \cdot \nabla \bar{\mathbf{u}} = -\nabla \bar{p} + (\mu + \mu_t) \nabla^2 \bar{\mathbf{u}} \tag{2}$$

where $\bar{\mathbf{u}}$ and \bar{p} respectively represent the ensemble-averaged velocity and pressure, and μ_t is the turbulence viscosity, which expresses the effects of the fluctuating component of velocity on the averaged field. The Spalart-Allmaras (S-A) one-equation turbulent model [47] has been employed for all the simulations performed.

2.2. Domain and boundary conditions

A sketch of the computational domain containing the SD7003 airfoil with a chord length C is shown in Fig. 1a. The leading edge was placed at the origin of the coordinate system, and the horizontal distance between this point and the inlet was set to $15C$. The outlet domain was located $19C$ downstream of the airfoil trailing edge. The wing profile was fixed at zero degree and the different angles of attack were achieved by tilting the free-stream velocity. For the cases where the active flow control technology is implemented, a groove across which a synthetic jet flows is needed. A generic synthetic jet implementation is sketched in Fig. 1b where a section of the airfoil upper surface, nearby the leading edge, along with the synthetic jet and its geometrical design parameters, jet angle (θ), position (x) and width (h), is presented.

The boundary conditions employed were defined as follows. At the inlet, which was located along the curve connecting the points A and B in anticlockwise direction, see Fig. 1a, a constant velocity profile was imposed and its components were set to $(u, v) \equiv (U_\infty \cos \alpha, U_\infty \sin \alpha)$. Neumann boundary conditions for pressure were employed. Non-slip boundary conditions for velocity and Neumann for pressure were applied on the airfoil surface. At the outlet, which comprises the upper curve between points A and B in Fig. 1a, wound in clockwise direction, Dirichlet boundary conditions for pressure and Neumann boundary conditions for velocity were chosen. Whenever the SJA was implemented, Neumann boundary condition for pressure and Dirichlet boundary condition for velocity were considered. The time dependent velocity profile of the synthetic jet actuator has been defined according to

$$u_j = U_j \sin(2\pi ft) \tag{3}$$

where U_j is the maximum jet velocity, f is the dimensional jet frequency and t is the dimensional time. Notice that the top-hat velocity profile chosen for the SJA is widely used in the literature, see for example [16,18,37]. The evaluation of how different SJ spatial velocity profiles affect the AFC parameters optimisation was left as future work. In order to properly capture the laminar separation bubble (LSB), the free stream turbulence was set as proposed by Catalano and Tognaccini [43].

2.3. Non-dimensional parameters

The non-dimensional groups employed in the present manuscript are introduced in this section.

Table 1
Time-averaged LSB characteristics and airfoil aerodynamic coefficients for different meshes at $\alpha = 8^\circ$.

Mesh	N_{cell}	y^+	x_s/C	x_t/C	x_r/C	C_l	C_d	η
A	26256	4.0	0.033	0.154	0.228	0.941	0.0332	28.30
B	34448	1.0	0.040	0.165	0.246	0.938	0.0329	28.49
C	45466	0.3	0.041	0.170	0.250	0.934	0.0327	28.56
D	92504	0.1	0.041	0.170	0.250	0.934	0.0327	28.56

The definition of the Reynolds number is:

$$Re = \frac{U_\infty C}{\nu} \tag{4}$$

where C is the chord length, U_∞ characterises the free-stream velocity and ν is the kinematic viscosity. The non-dimensional wall coordinate (y^+) is defined as:

$$y^+ = \frac{yu_\tau}{\nu}, \quad u_\tau = \sqrt{\frac{\tau_w}{\rho}} \tag{5}$$

where y is the distance to the wall, u_τ is the friction velocity, ρ stands for the free-stream fluid density and the term τ_w characterises the wall shear stresses. Drag and lift coefficients respectively, are defined as:

$$C_d = \frac{2D}{\rho C U_\infty^2} \tag{6}$$

$$C_l = \frac{2L}{\rho C U_\infty^2} \tag{7}$$

In these equations, D and L are the dimensional drag and lift forces per unit span, respectively. The aerodynamic efficiency is as follows:

$$\eta = L/D = C_l/C_d \tag{8}$$

The definition of the pressure coefficient is given by:

$$C_p = \frac{p - p_\infty}{\frac{1}{2} \rho U_\infty^2} \tag{9}$$

where p is the pressure at any given point and p_∞ is the free-stream pressure. The skin friction coefficient is obtained using the following expression:

$$C_f = \frac{\tau_w}{\frac{1}{2} \rho U_\infty^2} \tag{10}$$

The momentum coefficient associated with the pulsating jet is given by:

$$C_\mu = \frac{h \rho_j U_j^2 \sin \theta}{C \rho U_\infty^2} \tag{11}$$

where h and ρ_j respectively represent the jet width and the pulsating flow fluid density, θ characterises the jet inclination angle with respect to the airfoil surface. The non-dimensional frequency is defined as:

$$F^+ = fC/U_\infty \tag{12}$$

being f the dimensional frequency. The equation characterising the advective time is expressed as:

$$T = tU_\infty/C \tag{13}$$

For the present study, the chord length is taken as one ($C = 1$), the free-stream velocity is equal to one ($U_\infty = 1$), the densities of the synthetic jet and the incoming flow are the same ($\rho_j = \rho = 1$) and the Reynolds number remains constant and equal to $Re = 6 \times 10^4$.

2.4. Mesh sensitivity study

In order to make sure the final CFD results were independent of the employed grid, a mesh sensitivity study was performed for an AoA of 8° . Four different meshes having different resolutions, A, B, C and D (see Table 1), were considered. To properly solve the boundary layer around the airfoil, a hybrid mesh was used to be able to generate a highly refined mesh near the airfoil without drastically increasing the total number of cells. Fig. 2a, shows the full computational domain, Figs. 2b and 2c represent zoom views of the mesh refinement nearby the airfoil surface leading and trailing edges, respectively.

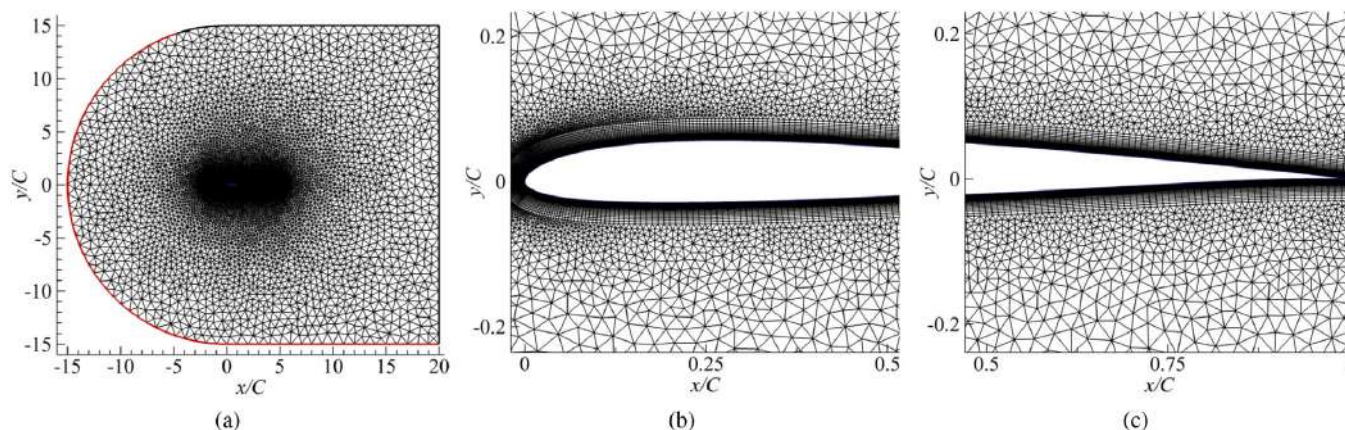


Fig. 2. (a) Overall mesh view, (b) leading edge's and (c) trailing edge's zoomed views of the mesh.

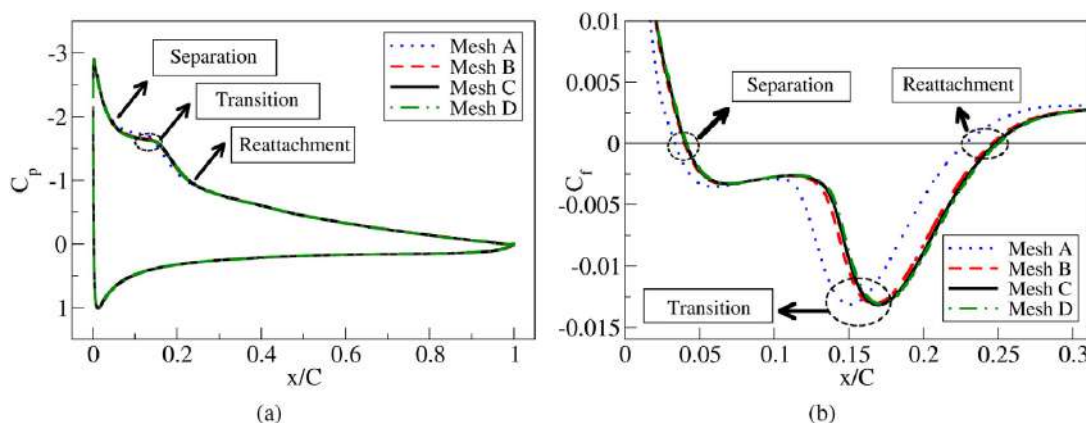


Fig. 3. Distributions of (a) pressure coefficient and (b) skin friction coefficient, for four meshes at $\alpha = 8^\circ$.

In Table 1, the main characteristics of the four different considered meshes (A, B, C and D) are introduced. The coarsest mesh consisted of 26,256 cells, while the finest one was made of 92,504 cells. The third column of Table 1 presents the maximum y^+ value of the first cell layer away from the airfoil surface, as computed after the simulations. The next three columns present the location along the chord where separation, transition to turbulence and reattachment occur, respectively. The separation point is gauged by cancellation of the friction coefficient. This is a particularly important point, as AFC effectively critically depends on its location relative to separation. The separated boundary layer undergoes a turbulent transition, gets re-energised, and reattaches further downstream. The reattachment point can be identified by a second change of sign of the wall shear stress. All these locations can be identified from the skin friction and pressure coefficients distribution presented in Fig. 3, where they are initially introduced. The airfoil lift and drag are reported, alongside the aerodynamic efficiency, in columns 7 through 9 of Table 1. All four meshes, exception made of mesh A, produce very similar results in terms of aerodynamic performances and LSB characteristic properties. Furthermore, C_p and C_f distributions are indistinguishable from one another among meshes B, C and D, as shown in Fig. 3. Quantitatively, mesh C yielded three significant digits accuracy of all parameters considered with about half the resolution of mesh D, rendering it a particularly good choice in terms of compromise between accuracy and computational requirements. This mesh consists of 16,800 quadrilateral cell, distributed in 40 layers of 420 cells around the airfoil surface. The first layer thickness has a maximum y^+ below 0.3, which is well within the viscous sublayer as required by the wall treatment of the Spalart-Allmaras turbulence model.

Three time steps of 7×10^{-5} , 5×10^{-5} and 2×10^{-5} were tested with identical results for the converged solutions. In order to accurately resolve AFC cases, the lowest time step has been chosen and the convergence criterion set to 10^{-6} , such that all residuals are required to fall below this value. Convergence was always achieved before 30 time units, so that the maximum time horizon was set to $T = 30$ for all simulations.

2.5. Baseline computations and numerical validation

Once the mesh has been chosen, it is essential to validate the baseline performances at all AoA. To do so, initially the temporal averaged lift and drag coefficients as a function of AoA are presented in Fig. 4. These graphs compare two sets of experimental results, Exp 89 [38], Exp 95 [39], and four CFD ones, ILES [40], LES [32], the standard $k-\omega$ SST and the $k-\omega$ SST LR, both from Catalano and Tognaccini [43], [44]. The comparison with the results from the present work shows very good agreement. Ranges of pre and post-tall AoA are depicted in Fig. 4a. The lift is properly captured at pre-stall AoA, at

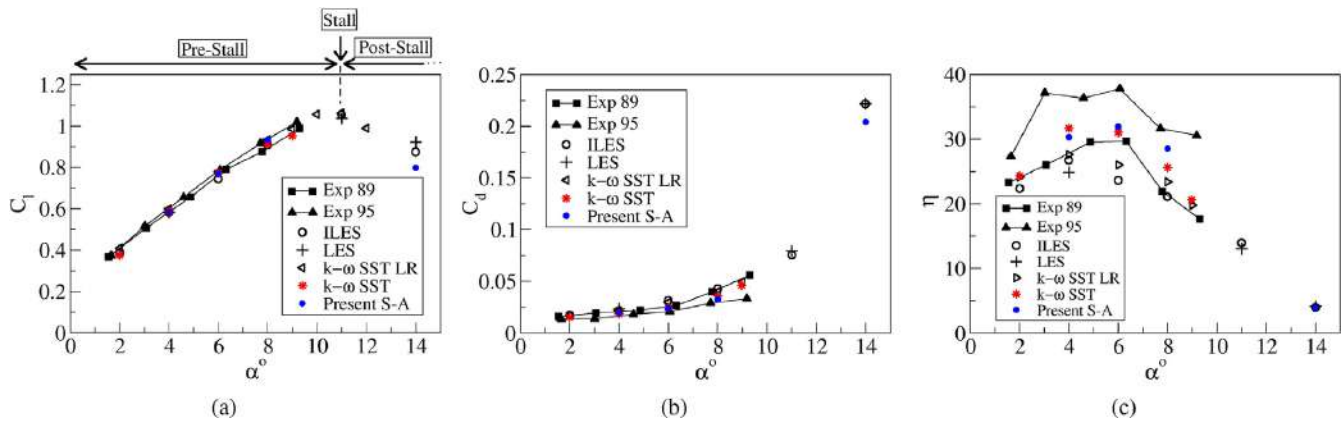


Fig. 4. (a) Lift and (b) drag coefficients as well as (c) aerodynamic efficiency versus the angle of attack and their comparison with some of the numerical and experimental results. Exp 89 [38], Exp 95 [39], ILES [40], LES [32], the standard $k-\omega$ SST and the $k-\omega$ SST LR, [43,44].

Table 2

Aerodynamic coefficients of actuated cases using present S-A model and their comparison with other turbulent models employed by other researchers. The Reynolds number is $Re=6 \times 10^4$.

α°	Cases	F^+	C_μ	θ°	x/C	h/C	C_l	$\epsilon_{C_l}(\%)$	C_d	$\epsilon_{C_d}(\%)$	η	$\epsilon_\eta(\%)$
14	LES [32]	1.0	0.0030	90.00	0.007	0.0070	1.078	—	0.129	—	08.35	—
	Present S-A						1.116	03.52	0.130	00.77	08.58	02.70
13	$k-\omega$ SST $\gamma - Re_\theta$ [37]	3.8	0.0424	23.57	0.040	0.0029	1.432	—	0.057	—	25.12	—
	Present S-A						1.432	00.00	0.065	14.03	22.03	12.30

post-stall, nevertheless, it generates a lower value than the ILES and LES ones. When comparing the drag coefficient (see Fig. 4b), we realised that the S-A model under-estimates the values versus the ones obtained using LES and ILES. In fact, the present drag coefficient values are especially similar to the ones gathered using the $k-\omega$ SST model. As a result, the aerodynamic efficiency (see Fig. 4c), at pre-stall AoA, presents the same differences as observed in the drag coefficient but at post-stall AoA, it has a good agreement with the previous introduced studies.

Fig. 5 shows the comparison of the pressure and skin friction coefficients from the present study, for the baseline cases at AoA 4° , 6° , 8° and 14° , with the numerical ones available in the literature. At pre-stall AoA of 4° , 6° and 8° , it is observed that as the AoA increases, the separation and reattachment points keep moving upstream and the laminar bubble reduces its length. Notice that the friction coefficient maximum and minimum values increase with the AoA increase. It is observed that the results of the current S-A model have a very good agreement with the ones presented by Catalano and Tognaccini [43] when using the $k-\omega$ SST turbulent model. Larger differences are observed in the transition-to-turbulent region and the location of the reattachment point between these two RANS models and the 3D ones [32,40]. These differences were expected, then as stated by Catalano and Tognaccini [43], [44], in order to properly capture the reattachment point, pre-definition of the transition location needs to be implemented. For the present study, it is particularly relevant to determine the location of the separation point, which is very well captured at all AoA (see the right column of Fig. 5). For an AoA of 14° , the present 2D simulation results were compared with the only available results [32,40], see the two bottom graphs in Fig. 5. Despite the fact that at this AoA the flow is fully separated and 3D, the present results agree very well with the ILES ones performed by Galbraith and Visbal [40]. Small differences are observed when comparing with the LES one [32]. It can be seen that when the flow is fully separated, the present RANS model is capable of quite precisely determining the airfoil pressure and skin friction coefficients. The separation point is properly predicted, fully matching the previous researchers work.

In order to further assess the results under actuation condition, the different SJA parameters along with the boundary conditions used by Rodriguez et al. [32] and Tadjfar and Kamari [37] were implemented and studied using our S-A model. The resulting lift and drag coefficients as well as the aerodynamic efficiency were compared in Table 2. ϵ represents the relative error which is defined as $\epsilon_x = (x_{presentS-A} - x_{literature})/x_{literature}$, where x characterises any of the aerodynamic coefficients presented. The comparisons at post-stall AoA of 14° with Rodriguez et al. [32] gave differences of less than 3.6% in all these three parameters. When comparing our results with the ones from Tadjfar and Kamari [37] at AoA 13° , the lift was exactly the same, while the maximum error regarding the drag coefficient was around 14%. The drag coefficient difference is likely due to the different turbulent models used in these two studies and the differences in the mesh density employed to perform this particular simulation.

Based on all the comparisons presented in this section, it can be concluded that the 2D simulations performed generate results fully reliable at these four studied angles of attack, therefore allowing to the present researchers to proceed with the optimisation implementation of the active flow control jets (synthetic jets) on the baseline cases, and study the effects of the five different AFC parameters on the airfoil lift and efficiency.

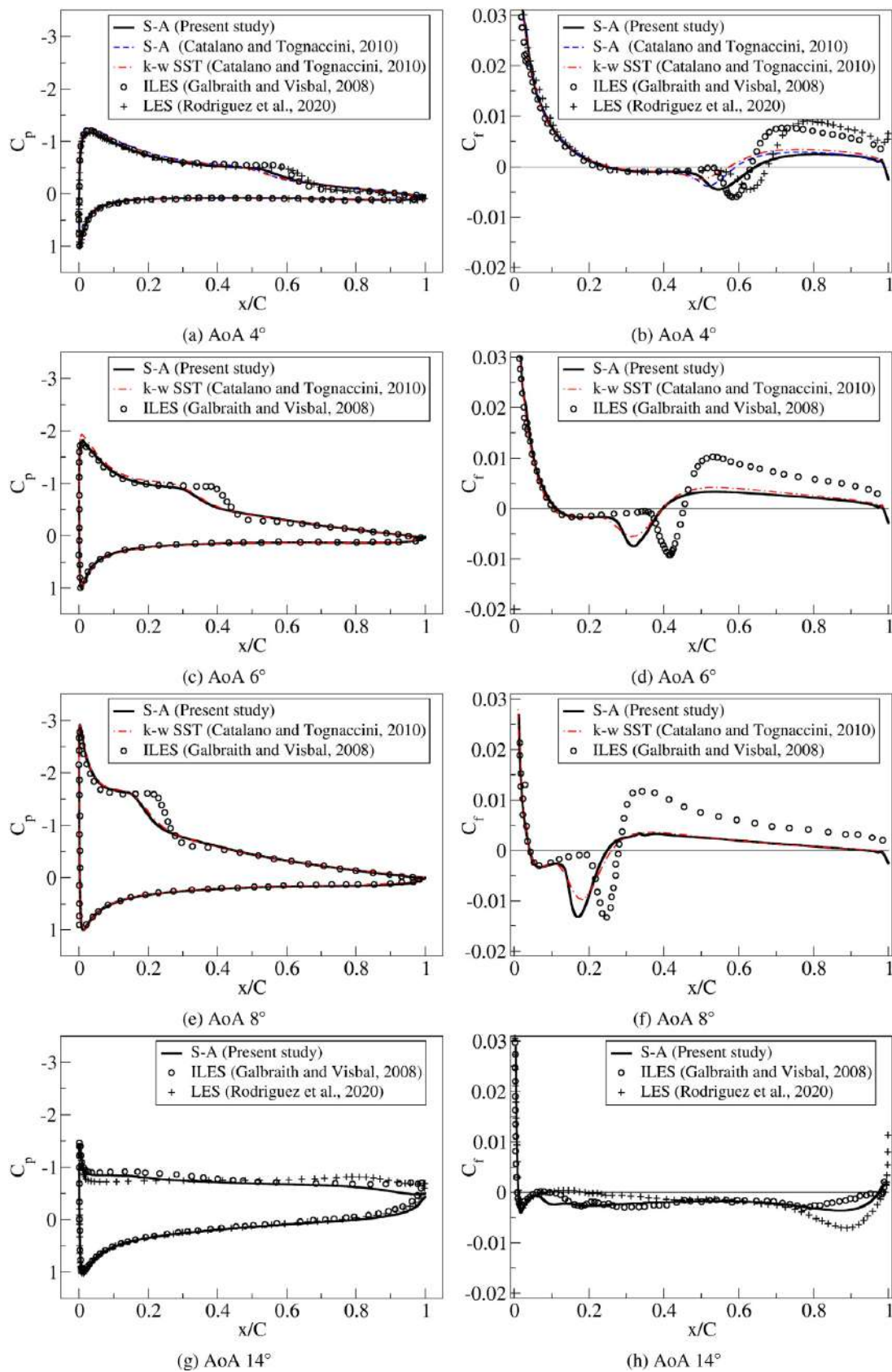


Fig. 5. Distributions of pressure (left column) and skin friction coefficients on the upper surface (right column) for the baseline cases at all angles of attack and their comparison with previous available results. Figures (a) and (b), corresponds to AoA of 4°, figures (c) and (d) characterises the results at 6°, figures (e) and (f) are defining the information at 8° and the information for AoA of 14° is found in figure (g) and (h).

3. Optimisation of AFC parameters

The selection of the values corresponding to the different AFC parameters can be performed through the use of an optimisation method. Optimisation problems are addressed from many different approaches. The classical optimisation techniques are useful in finding the optimum solutions of functions that are continuous and differentiable. These methods use differential calculus techniques, are fast and accurate, but lack the capacity to deal with non-differentiable functions, either objective or restriction functions, which limits their application [48]. Other methods include linear programming (LP) [49], which are a set of techniques to find the best solution of a problem with a linear objective function (single objective problems), and linear equalities and inequalities as restrictions. Their application is limited by the linearity of the functions they require to use. For problems involving AFC applications, it is not possible to use (LP) for this same reason. Nonlinear optimisation methods appear to be more appropriate [50–52].

Among the methods capable of handling non-linearities are the gradient-based methods [53], they use information of the function gradient to select the search direction and, iteratively converge to the optimum solution. These methods can get stuck on local optima and are highly dependent on the starting solution of the iterative method. They are usually efficient, fast and accurate. Their efficiency increases with the accuracy associated with the gradient information computed. Different methods have been proposed to estimate the gradient whenever it can not be directly computed.

Stochastic strategies are those which use random or pseudo-random methods to define the variables along the iterations. They are capable of performing multi-objective optimisation and do not impose restrictions on the objective functions or restrictions behaviour. Their robustness is probably one of the most interesting aspects of these methods and do not usually require gradient information, although some methods can be improved using such information. In comparison with other methods, their main drawback is that they usually need a larger amount of iterations to converge [54–58]

Usually, optimisation methods when coupled with CFD packages are computationally very expensive. When considering the optimisation methods and in order to save computational time, the use of surrogate models is often a typical solution [59]. Artificial Neural Networks or Kriging models are, among many others, two of these surrogate models [60,61]. The results obtained from a surrogate model are often based on a set of previously CFD computed samples and require a training process to ensure an accurate outcome. The accuracy of the results obtained when using a surrogate model is usually lower than the one gathered when performing a CFD simulation. A recent application of a surrogate model in AFC can be found in [37]. In the present paper and in order to guarantee the maximum accuracy of the results the authors decided not to use any surrogate model. All results are gathered from CFD simulations, this could be done thanks to the large computational power available. The computational time required to complete all simulations needed for a given AoA (considering 400 2D-CFD cases) was about 18 days, using a single node of 48 cores in a supercomputer based on two 24 cores Intel Xeon Platinum processor.

A general description of the optimisation method and the configuration chosen is presented in the following sub-section.

3.1. Optimisation method

The problem under study requires the definition of a multi-objective optimisation. Two different strategies can be used to solve such a problem. On one hand, a temporary objective function can be calculated as the weighted sum of the real objective functions. In this way, the multi-objective problem is expressed as a single objective one. The weight values multiplying each original function require a decision, which can greatly affect the final result of the analysis. One should also consider the fact that to obtain the Pareto Front [62], several runs of the optimiser with different weight values will be required. On the other hand, the authors are proposing to use a pure multi-objective approach, which will enable to identify the whole Pareto Front at once, and therefore the best solutions regarding the combination of the whole set of objective functions. A multi-objective optimisation problem can be defined in its minimisation form as Eq. 14.

$$\left\{ \begin{array}{l} \min \quad (f_1(\vec{x}), f_2(\vec{x}), \dots, f_k(\vec{x})), \quad k = 1, \dots, K \\ \text{Subject to:} \\ \quad g_l \quad (\vec{x}) \geq 0, \quad l = 1, \dots, L \\ \quad h_m \quad (\vec{x}) = 0, \quad m = 1, \dots, M \\ \text{Where:} \\ \quad \vec{x} \in X, \quad X \text{ feasible set of decision variables.} \end{array} \right. \quad (14)$$

In order to clarify the nomenclature, the following definitions are stated:

Design Variables (DVs) are the set of decision variables, the independent variables of the optimisation problem: $\vec{x} \in X$.

Objective Functions (FOs) are the set of fitness functions. The functions that express the aptitude of a set of DVs: $f_1(\vec{x}), f_2(\vec{x}), \dots, f_K(\vec{x})$. Being K the number of objectives functions.

Constraints (Ctrts) are the set of expressions that need to be satisfied in order to consider the DVs as feasible. It includes both types, inequality g_l and equality h_m expressions. Being L and M the numbers of inequality and equality constraints, respectively.

In this study a Genetic Algorithm (GA) is used. The reason to use a GA is to capture the Pareto Front in a single optimisation. It is also a very robust method that usually works well regardless of the objective space shape which is unknown for

this case. Furthermore, it is also robust enough to treat configurations that fail and can not be computed due to problems in the automatic mesh generation or any of the automation process involved in the numerical evaluation of each case. Genetic Algorithms were initially proposed by Holland [63] and further developed by Goldberg and Holland [64]. Their methodology is inspired by the natural evolution process, which selects the best fitted individuals to generate new offspring. The GA, including the steps performed to modify the geometry, boundary conditions and mesh for the design variables, is presented in Algorithm 1.

Algorithm 1: Genetic algorithm.

```

InitialisePopulation();
while Stopping criteria is not met do
    ObjectiveFunctionsCalculation();
    BoundaryConditionsDefinition();
    GeometryCreation();
    MeshGeneration();
    CFD-Calculations();
    PostProcess();
    Selection();
    Crossover();
    Mutation();

```

Initially, in the *InitialisePopulation()* function, a random population is generated. The size of all populations is 20 individuals, which has been considered a good trade-off between performance of the method and computational cost. Then the population is prepared and computed in the *ObjectiveFunctionsCalculation()* function, which obtains the objective functions for each individual in the population, as it will be explained later in §3.2. Each individual is prepared using an in-house Python script that links the mesh generator (GMSH), the CFD package (OpenFoam) and the GA. This script automates the process of translating the format of the different packages, modify the mesh and apply the boundary conditions. After the population is computed, the optimisation operators are applied, these are *Selection()*, *Crossover()* and *Mutation()*. In the implementation used in this study the *Selection()* operator employs a $\mu + \lambda$ strategy with a Crowded-Comparison Operator [62]. For the *Crossover()* operator, a Simulated Binary Crossover (SBX) [65] is used and the *Mutation()* operator is performed with Polynomial Mutation [66]. It is important to notice that the optimiser tracks the individuals that survive to the next generation without altering their design variables and does not compute again its objective functions, which is not uncommon when using genetic algorithms. Those individuals beat the odds and pass the crossover and mutation operators without suffering any modifications. In applications that are highly demanding in computational resources and time consuming, it is very important to take this behaviour into account to avoid repeating the CFD analysis. The values of the parameters of the GA used are presented in Table 3.

In the next section the detail of the objective functions and the design variables definition as well as the range employed for each design variable are presented.

3.2. Objective functions and design variables definitions

The aim of this study is to maximise the lift coefficient and the aerodynamic efficiency of an airfoil at different angles of attack. The GA used solves the optimisation problem as a minimisation problem, which means it will minimise the objective functions. Taking this into account, two objective functions f_1 and f_2 were defined, which are minimised when the lift coefficient and the efficiency were maximum:

$$f_1 = -C_l \tag{15}$$

$$f_2 = -\eta \tag{16}$$

The optimisation was performed at four angles of attack, 4°, 6°, 8° and 14°, being four independent optimisation analysis defining the design variables as five AFC parameters associated with the synthetic jet. These parameters were the non-dimensional frequency (F^+), momentum coefficient (C_μ), jet angle (θ), jet position (x/C) and jet width (h/C). A scheme

Table 3
Parameters of the Genetic Algorithm.

Parameter	Value
Population size	20
Probability of crossover	0.9
Probability of mutation	0.1

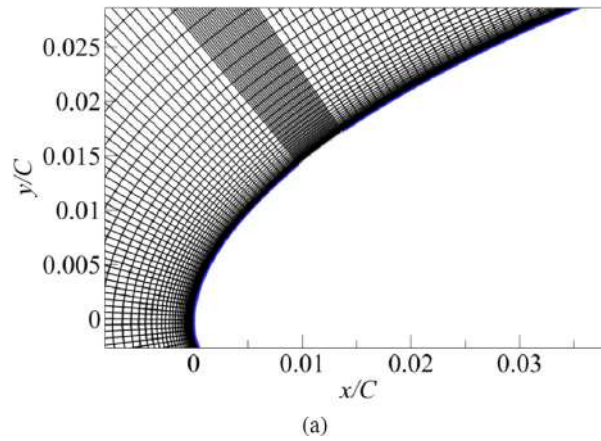


Fig. 6. Mesh view nearby the jet, automatically generated.

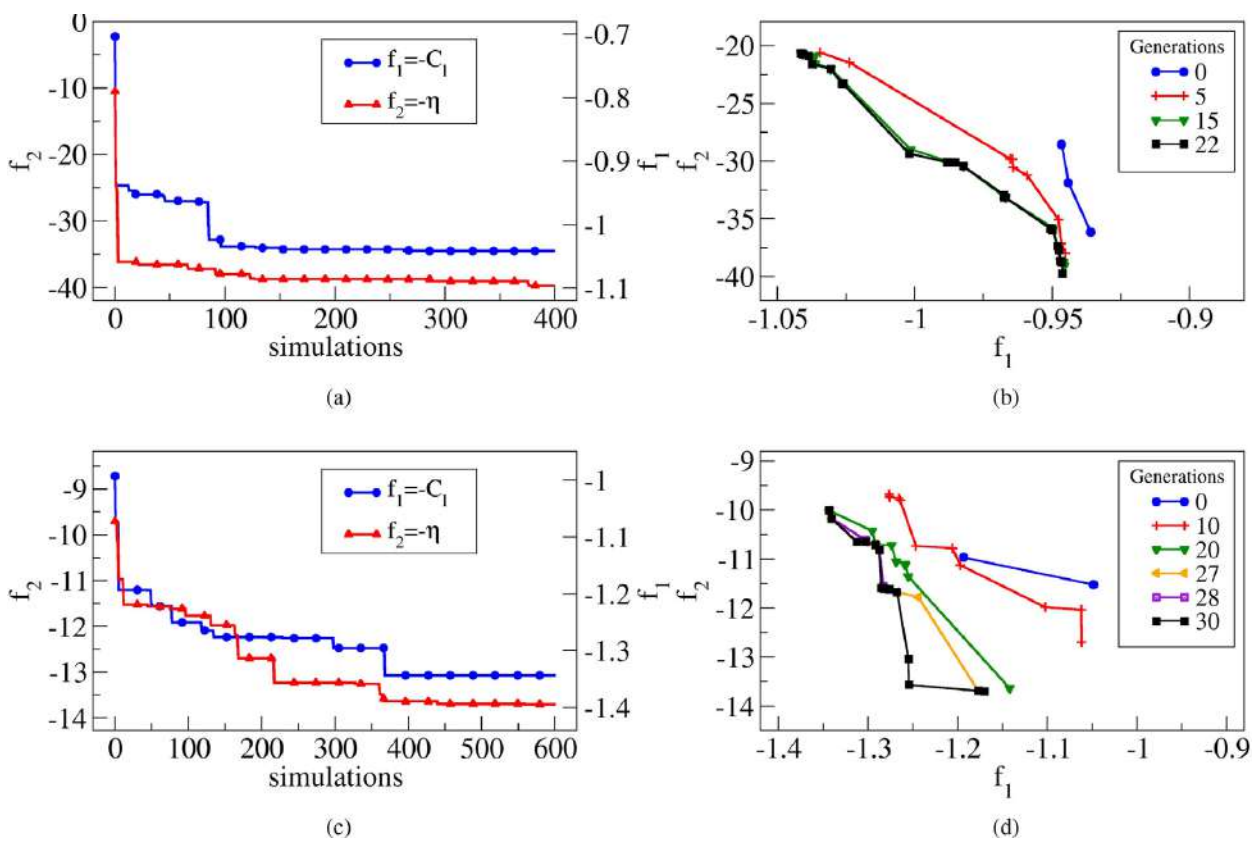


Fig. 7. Evolution of the objective functions as the number of simulated cases increase (a and c). Pareto Front history at several generations (b and d). AoA of 8° is represented in figures (a and b). Figures (c and d) characterise the results at AoA 14°.

representing the geometrical design parameters was introduced in Fig. 1b. Fig. 6 shows a zoomed view around the jet position introduced in Fig. 1b for one of the automatic generated meshes. In the function *BoundaryConditionsDefinition()* from Algorithm 1, the first three design variables (F^+ , C_μ and θ) were selected. In the next step, using the function *GeometryCreation()*, and according to the two last design variables (x/C) and (h/C), a new geometry was created using the GMSH program. Once the new geometrical changes were applied, the function *MeshGeneration()* created a new mesh, deciding as well the number of cells required along the groove width in order to guarantee a good mesh quality. At this point the CFD simulations were ready to start, the function *CFD-Calculations()* was doing so. Finally, the two objective functions were post-processed in *PostProcess()* function and the results were transferred to the three GA operators, already discussed in §3.1.

The process just described was repeated until the stopping criteria was met. In the present study the stopping criteria used consisted in computing a minimum of 400 individuals. The reason why 400 individuals were sufficient is detailed in Fig. 7, which shows the convergence evolution and the Pareto Front history at a pre-stall AoA of 8° and at the post-stall AoA of 14°. At low angles of attack of 4°, 6° and 8°, the number of CFD simulations required to minimise the two objective

Table 4
AFC Design variables and their evaluation ranges for the different angles of attack.

α°	F^+	C_μ	θ°	x/C	h/C
4,6,8	0.1–10	0.0001–0.02	15–165	0.015–0.320	0.005–0.020
14	0.1–10	0.0001–0.02	15–165	0.0001–0.04	0.005–0.015
14	0.1–10	0.0001–0.10	15–165	0.0001–0.04	0.005–0.015

functions (f_1) and (f_2), or in other words, to maximise the lift coefficient (C_l) and the aerodynamic efficiency (η), was around 400. Notice from Fig. 7a that after 300 simulations the two objective functions show a negligible improvement. In order to assure a full convergence of the two objective functions at post-stall AoA, it was initially decided to run 600 simulations (see Fig. 7c), but it was realised that after 400 simulations the objective functions suffered minor modifications. The same conclusion can be reached from the observation of the Pareto Front history's presented in Figs. 7b and 7d for 8° and 14° respectively. Notice that after 15 generations in Fig. 7b and 28 generations in Fig. 7d, the Pareto Front curves suffer minor variations.

The ranges of evaluation for the five AFC design variables and for the four different AoA, are presented in Table 4. At AoA of 4°, 6° and 8°, the ranges of the different variables were $F^+ \in [0.1, 10]$, $C_\mu \in [0.0001, 0.02]$, $\theta^\circ \in [15, 165]$, $x/C \in [0.015, 0.32]$ and $h/C \in [0.005, 0.02]$. The reason for selecting these particular ranges is upon several previous studies. For example, in the literature, frequencies around $F^+ = 1$ are commonly used for the pulsating flows (see for example, [32]). In the present study and considering that the pulsating frequency is an important parameter to activate the boundary layer, we decided to set the limits, ten times smaller and bigger than the baseline one. Regarding the range of momentum coefficients, the upper limit was set based on the maximum momentum coefficient used in the experimental work done by Gilarranz et al. [21] and Goodfellow et al. [28]. In the case of jet width (h/C), we decided to use a larger upper limit in comparison to the one used by Kamari et al. [36] ($h/C = 0.003$). This is due to the fact that after checking their results, we noticed that the optimum solution for this parameter was located around 0.003. The range chosen for the jet position (x/C) was such that the separation point, at each AoA, was always located inside the chosen margins. For the pulsating jet inclination angle (θ°), Kamari et al. [36] set a range varying from 1 to 180 degrees. Since their optimum solutions were located in a region between 65 and 94.6 degrees, we decided to limit the upper and lower bounds of the jet angle to 15 and 165 degrees, respectively. This decision was also taken to reduce the computational cost.

At 14°, initially the same ranges for F^+ , C_μ and θ were employed, but smaller modifications were allowed on the ranges of position (x/C) and width (h/C) of the jet, see the second line of Table 4. The reason for this is that, at an angle of attack of 14°, separation occurs very close to the airfoil leading edge, and as the position of the groove as well as its width have to be placed around the separation point, the ranges of the groove location and width need to be accordingly restricted. Consequently, at 14°, only the initial 4% of the chord length was evaluated by the optimiser. Due to the physical restrictions just explained and to the high curvature of the airfoil near the leading edge, the maximum non-dimensional jet width at 14° was set to a size of $h/C = 0.015$, which is 25% smaller than the maximum jet width employed at pre-stall AoA. As it will be explained in the next sections, the present authors observed that, the maximum efficiency obtained when employing the AFC parameters just defined for AoA 14°, was lower than what other researchers obtained in similar investigations. In order to increase the maximum aerodynamic efficiency, a second set of optimisation tests at 14° was carried out (see the third line of Table 4). All AFC parameters remained unchanged except the momentum coefficient range, in this second optimisation evaluation C_μ was allowed to change in the range $0.0001 < C_\mu < 0.1$. In other words, the maximum momentum coefficient was allowed to be five times larger than the one employed in the previous optimisation case.

4. Results

In the following sections, the optimum AFC parameters to maximise the airfoil lift and efficiency, at three pre-stall angles of attack (4°, 6° and 8°) and also at one post-stall angle of attack (14°), are presented. The main idea of studying the optimum AFC parameters at all these angles of attack is to be able to evaluate how each AFC parameter is changing as the AoA increases, with the hope of finding a pattern which could be used in future applications.

4.1. Pre-stall angles of attack of 4°, 6° and 8°

The aerodynamic efficiency for each of the 400 CFD studied cases at all pre-stall AoA and versus each AFC parameter is shown in Fig. 8. Each column represents the aerodynamic efficiency as a function of the different AFC parameter at given AoA. From left to right, AoA=4°, 6° and 8°. The evolution of the aerodynamic efficiency as a function of a given AFC parameter, for several different AoA, can be observed at each row of Fig. 8. The first row characterises the efficiency versus the non-dimensional frequency for the three studied AoA. Maximum efficiencies are obtained at pulsating frequencies F^+ around 9. Lower frequencies appear of minor interest in terms of having high efficiency. For comparison, the horizontal line introduced in all graphs shows the baseline case efficiency at each AoA. The efficiency values for each particular baseline case is found in Table 5. The second row of graphs presents the efficiency as a function of the momentum coefficient C_μ . For AoA of 4° and 6°, the optimum C_μ is around 0.019 and the momentum coefficient is reduced to about 0.015 as the AoA

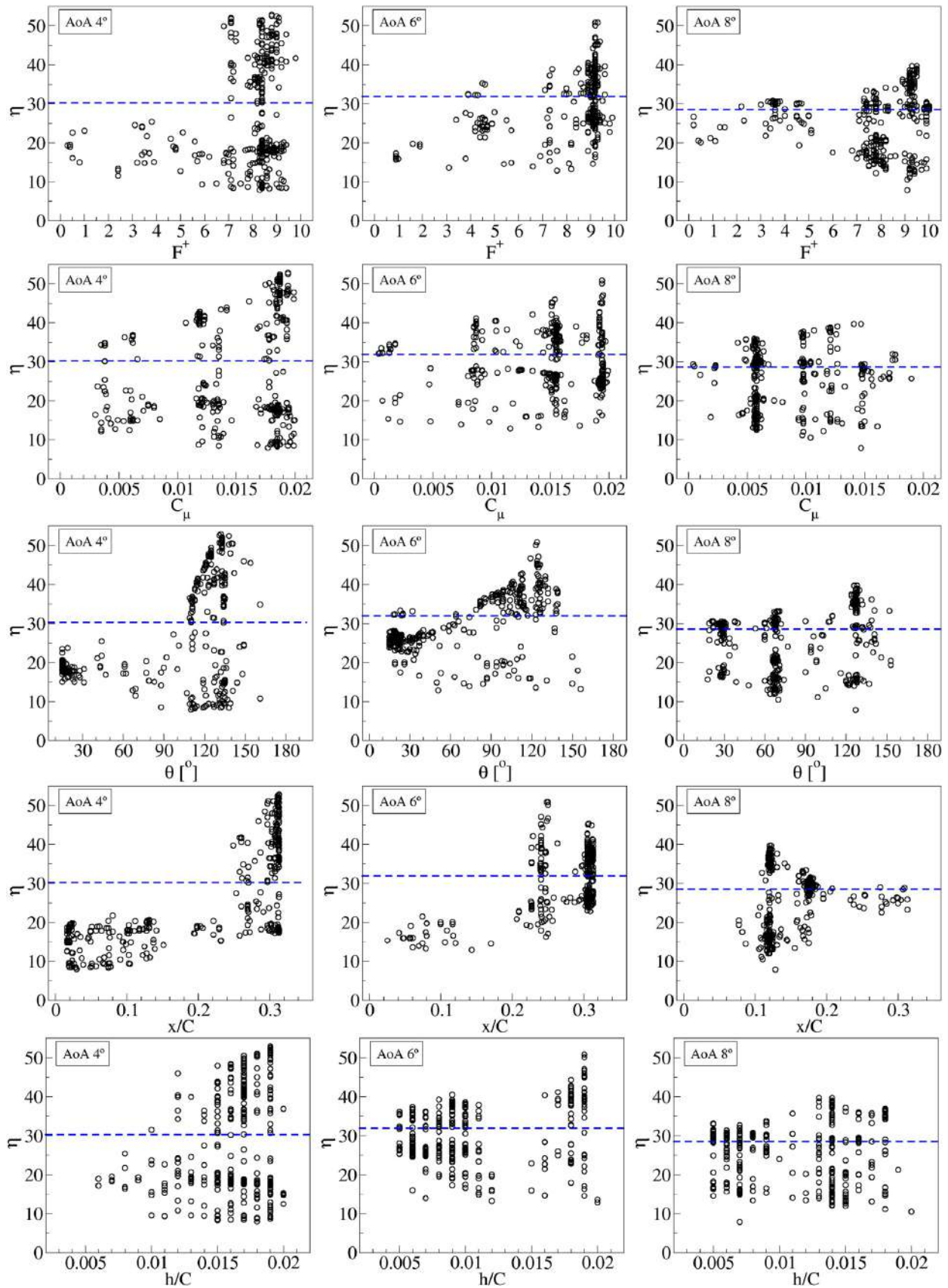


Fig. 8. Aerodynamic efficiency η versus non-dimensional frequency F^+ , momentum coefficient C_μ , jet angle θ° , jet position x/C and jet width h/C for all the CFD cases at AoA of 4° , 6° and 8° are presented in left to right columns respectively. The horizontal dashed line represents the baseline case efficiency for each AoA.

Table 5

Optimum five synthetic jet parameters associated with the maximum lift and maximum efficiency cases at pre-stall angles of attack of 4°, 6° and 8°.

α°	cases	F^+	C_μ	θ°	x/C	h/C	C_l	$C_l\%$	C_d	η	$\eta\%$
4	max lift	9.4	0.0193	015	0.021	0.013	0.6185	+5.76	0.0317	19.51	-35.61
	max efficiency	8.8	0.0194	132	0.313	0.019	0.5740	-1.84	0.0108	52.86	+74.45
	baseline	—	—	—	—	—	0.5848	—	0.0193	30.30	—
6	max lift	9.1	0.0195	015	0.308	0.006	0.8371	+9.14	0.0338	24.76	-22.50
	max efficiency	9.2	0.0194	124	0.250	0.019	0.7802	+1.72	0.0153	50.85	+59.15
	baseline	—	—	—	—	—	0.7670	—	0.0240	31.95	—
8	max lift	8.0	0.0058	067	0.116	0.015	1.0413	+11.45	0.0504	20.66	-27.66
	max efficiency	9.3	0.0147	126	0.122	0.013	0.9460	+1.28	0.0238	39.71	+39.00
	baseline	—	—	—	—	—	0.9340	—	0.0327	28.56	—

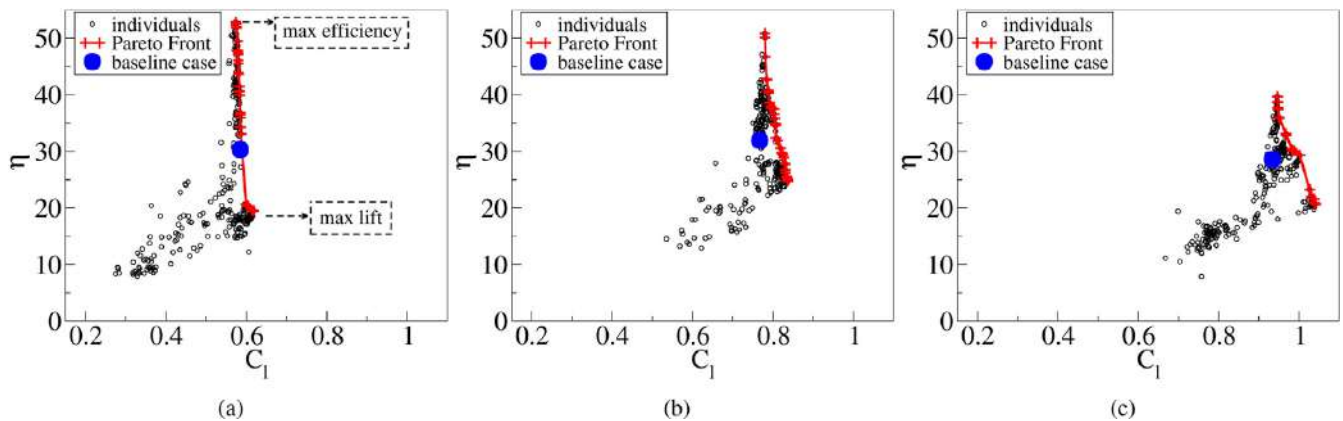


Fig. 9. Pareto Front at angles of attack of (a) 4°, (b) 6° and (c) 8°. The blue dots represent the efficiency versus lift coefficient for the baseline cases at different AoA. (For interpretation of the references to colour in this figure legend, the reader is referred to the web version of this article.)

increases to 8°. This small reduction of the momentum coefficient at 8° is likely to be due to the particularly successful groove location. The next row in Fig. 8 introduces the aerodynamic efficiency as a function of the jet inclination angle θ . The origin of the angular position was presented in Fig. 1b. The optimum jet injection angle is about 130° at AoA 4° and decreases to about 125° as the AoA increases to 8°. What it is particularly interesting to observe is that regardless of the pre-stall AoA chosen, the flow is injected facing upstream. This fact needs to be understood in combination of the groove location, which is presented in the next row of Fig. 8. Groove location clearly moves upstream as the AoA increases, the optimum groove location at 4°, 6° and 8° is respectively $x/C = 0.313$, $x/C = 0.250$ and $x/C = 0.122$. In fact, this evolution was expected. Then, as explained in §2.5, the separation point moves upstream with the increase of AoA. The respective separation and reattachment points for the different studied AoA were, $x/C = 0.2436$ and $x/C = 0.66$ for and AoA of 4°, $x/C = 0.1125$ and $x/C = 0.3958$ at 6°, and $x/C = 0.04$ and $x/C = 0.248$ for an AoA of 8°. As it will be clarified in Fig. 10, the optimum groove location (maximum efficiency) falls inside the laminar bubble for all pre-stall studied AoA. What appears to be more interesting is to observe that the groove location versus the location of the separation point for each AoA, further moves downstream as the AoA increases. The location of the groove is displaced about 29% downstream versus the separation point at AoA 4°, this displacement increases to 122% when the AoA is of 6° and reaches a 205% for an AoA of 8°. The authors observed that when the groove is located just before the transition to turbulence point, for the present study this is particularly happening at 8 degrees AoA, the momentum needed to trigger the flow reattachment can be lower. The final row of Fig. 8 shows the aerodynamic efficiency as a function of the groove width h/C . Optimum groove widths at 4° and 6° are around $h/C = 0.19$ and decrease to $h/C = 0.13$ at 8° AoA. For an AoA of 8°, this reduction appears to be triggered by the advantageous location of the groove inside the laminar bubble, where the transition occurs. In this region, the boundary layer becomes turbulent and it requires a smaller amount of energy to be activated.

Fig. 9, for the three pre-stall AoA, characterises the two objective functions considered in this study, the aerodynamic efficiency and the lift coefficient. In each figure, over 400 points defining each of the CFD simulations are presented. The red broken line represented on the right hand side of each figure is the so called Pareto Front, which indicates the optimum values of the AFC parameters to obtain maximum efficiency, maximum lift and the optimum combination of both. The blue dot shown in each figure represents the airfoil baseline case characteristics associated with each studied AoA. For an AoA of 4° the Pareto Front is almost vertical, the efficiency increase is mostly due to a decrease of the average drag. As the AoA raises, aerodynamic efficiency improvement is due to the lift increase and drag decrease.

The first three tables presented in Appendix A summarise the values of each of the five AFC parameters corresponding to each point of the Pareto Front for AoA 4°, 6° and 8°, respectively introduced in Fig. 9. Descending in the tables, lift and drag coefficients decrease and efficiency increases. The first and the last rows of each table are underlined and correspond to the maximum lift and maximum efficiency, respectively. For an AoA of 8°, the highest obtained efficiency was

Table 6

Optimum five synthetic jet parameters associated with the maximum lift and maximum efficiency cases at a post-stall angle of attack of 14° (small momentum coefficient range). 600 CFD cases.

α°	cases	F^+	C_μ	θ°	x/C	h/C	C_l	$C_l\%$	C_d	η	$\eta\%$
14	max lift	1.5	0.0051	44	0.0082	0.005	1.3435	+68.36	0.1343	10.00	+156.41
	max efficiency	2.4	0.0055	18	0.0097	0.005	1.1702	+46.64	0.0854	13.70	+251.28
	baseline	—	—	—	—	—	0.7980	—	0.2040	03.90	—

39.71, see Table A.3 in Appendix A. Notice that the point of maximum efficiency corresponds to the point of minimum drag. When comparing with the baseline case efficiency, an increase of almost 39% is observed. The values related to the five AFC parameters which generate the maximum aerodynamic efficiency are; non-dimensional frequency $F^+ = 9.3$, momentum coefficient $C_\mu = 0.0147$, jet angle 126° , jet position $12\%C$, $x/C = 0.12$ and jet width $1.3\%C$, $h/C = 0.013$. The values characterising AFC parameters capable of generating the maximum lift are; $F^+ = 8$, $C_\mu = 0.0058$, $\theta = 67^\circ$, $x/C = 0.116$ and $h/C = 0.015$. A maximum lift increase versus the baseline case of around 11% could be obtained. Comparing the lift coefficients of all points defined in the Pareto Front with the baseline case one $C_l = 0.934$ at AoA 8° , see Table A.3 in Appendix A, it is seen an improvement in all optimum cases, whereas when considering the drag coefficient, an improvement (reduction of drag force), only happens when the lift coefficients are below $C_l = 0.985$. In other words, increasing the lift coefficient a value of higher than 0.985 introduces a drag penalty higher than in the non-actuated case. A similar effect is observed at the other two pre-stall studied AoA, see Tables A.1 and A.2 in Appendix A.

Table 5 presents the aerodynamic coefficients (C_l , C_d and η) as well as five SJA parameters (F^+ , C_μ , θ , x/C and h/C) associated with the maximum lift and maximum efficiency cases. These cases represent two points of the Pareto front at each AoA (4° , 6° and 8°). When comparing these optimum cases with the baseline ones, the first thing to realise is that aerodynamic efficiencies can be increased by over 39% for all pre-stall AoA. The maximum efficiency was found to decrease with the AoA increase. During the simulations it was observed that the efficiency increase was linked to the low average value of the drag coefficient. Regardless of AoA, the lift coefficient associated with the highest efficiency cases suffered a variation smaller than $\pm 2\%$ versus the baseline case. The maximum lift coefficient, in percentage versus the baseline case, raised with the AoA increase. For an AoA of 4° the maximum lift coefficient increase was of around 5.7%, reaching a value of about 11.5% when the AoA was 8° . When comparing the jet inclination angles θ required to obtain maximum lift and maximum efficiency, it is observed that the maximum lift is associated with small jet inclination angles, maximum efficiencies are linked with high θ . To understand why it is so, it is needed to study the interaction between the incoming flow and the pulsating jet. This study is presented in §5.4. Regarding the AFC parameters and based on the results presented, maximum aerodynamic efficiencies are linked with high injection angles, high momentum coefficients and high pulsating frequencies. At AoA 8° , the differences in the AFC parameters characterising the maximum lift and the maximum efficiency cases are mostly coming from the angle of the jet and the momentum coefficient. The rest of the parameters are almost in the same range. For the AoA of 4° and 6° the differences in AFC parameters to obtain maximum lift and maximum efficiency reside in the jet inclination angle, the groove width and the groove position.

In reality the effects of the groove location x/C are better observed in Fig. 10. For each pre-stall AoA studied, it is presented the pressure and friction coefficients as a function of the chord length. The comparison between the baseline, maximum efficiency and maximum lift cases is also introduced. From the friction coefficient curves and regardless of the AoA, it is observed that the optimum groove location to obtain the maximum efficiency as well as the maximum lift falls inside the laminar bubble. The only exception is observed at 4° , where the maximum lift is reached when locating the groove almost at the airfoil leading edge. For AoA 6° , the location of the groove to obtain the highest efficiency is slightly upstream than the one needed to obtain maximum lift. At AoA 8° the groove location remains approximately unchanged, for both the maximum efficiency and lift cases. From the friction coefficient curves and considering the highest efficiency cases (red lines), regardless of the AoA, it is observed that the length of the bubble appearing on the airfoil upper surface reduces whenever AFC is applied.

The effect of the AFC parameters on the pressure coefficient can clearly be seen in Figs. 10a, 10c and 10e. Notice that regardless of the AoA, the application of AFC tends to maintain the flow pretty much attached downstream of the AFC jet groove location and therefore, slightly decreasing the pressure at the airfoil upper surface. Such decrease is particularly relevant between the leading edge and synthetic jet location. The pressure is especially low at the groove location, generating as well a decrease on the friction coefficient. In some cases, the use of AFC generates small alternative vortices emanating from the interaction of the main stream with the synthetic jet, and they roll downstream on the airfoil upper surface. Under these conditions, the pressure on the upper airfoil surface decreases, increasing the lift as well as the drag. Evolution of vortical structures on the airfoil surface will be further discussed in §5.

To further understand the effect of actuation on the airfoil upper surface for the three pre-stall AoA of 4° , 6° and 8° , the streamlines along with the turbulence viscosity contours for the baseline and actuated cases are presented in Fig. 11. Regardless of the AoA, all baseline cases show a laminar bubble appearing just after the separation point. Notice that as previously explained in Fig. 10, the laminar bubble length decreases with the AoA increase. For an AoA 8° the bubble appears almost near the leading edge. For all cases, the flow remains reattached downstream of the separation bubble. When observing the highest lift cases (central panel in each sub-figure), a bubble is seen on the airfoil upper surface. This bubble

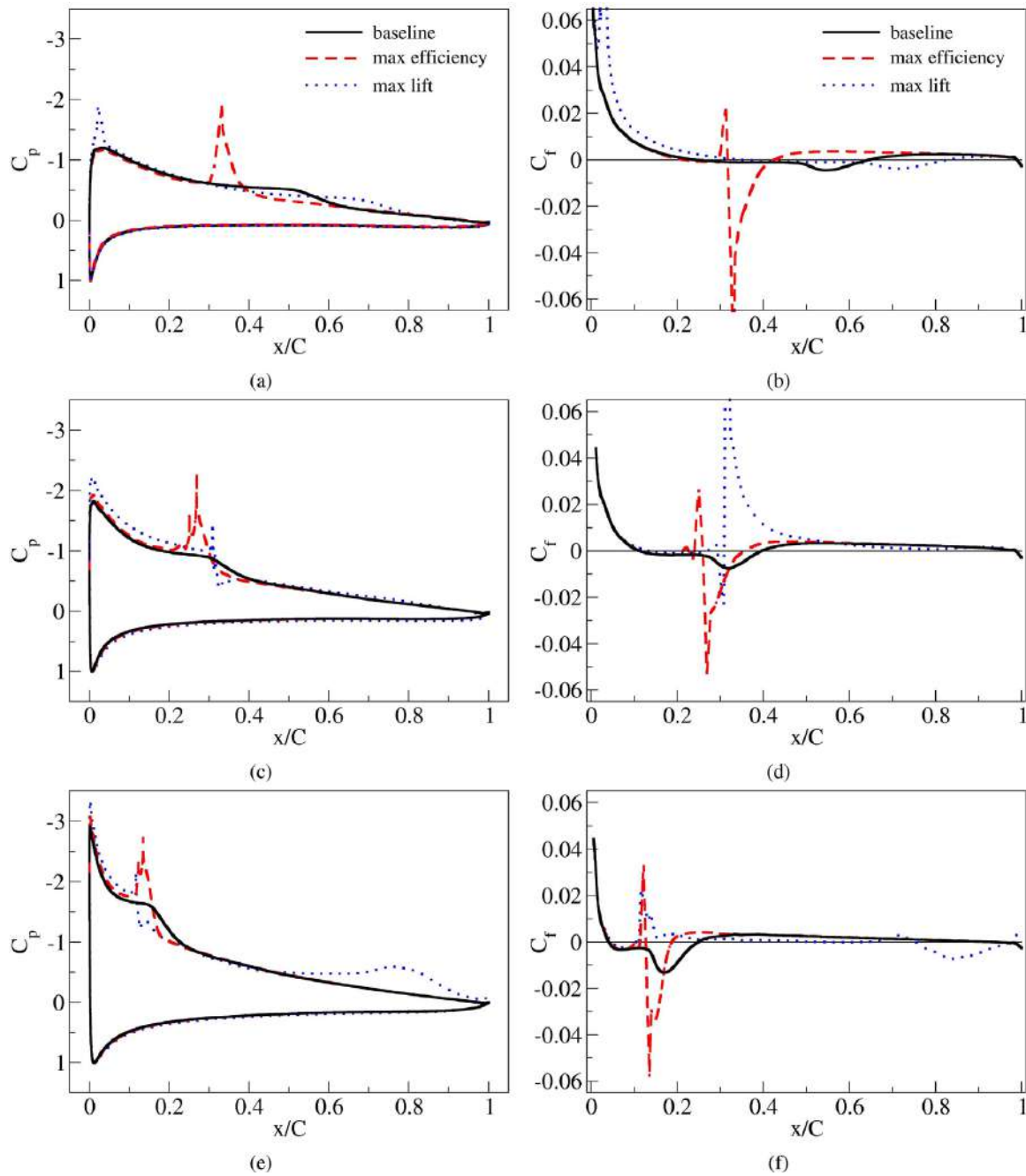


Fig. 10. Distributions of pressure coefficient (C_p) and skin friction coefficient (C_f) for the baseline (black solid lines), maximum efficiency (red dashed lines) and maximum lift (blue dotted lines) cases at three pre-stall AoA. (a), (b) AoA 4° ; (c), (d) AoA 6° ; (e), (f) AoA 8° . (For interpretation of the references to colour in this figure legend, the reader is referred to the web version of this article.)

is related to the pressure distribution introduced in Fig. 10, from where it can be concluded that the highest lift is achieved due to the low pressure distribution along the airfoil upper surface. This pressure is lower than the one for the rest of the cases studied and it is particularly observed upstream of the groove location and also downstream of this point, where the bubble is generated. For an AoA of 4° , this is being accomplished via displacing the laminar bubble further downstream. At 6° , the laminar bubble is drastically reduced relative to the baseline case. At 8° , the lowest upper surface pressure is obtained when removing the laminar separation bubble at the leading edge and generating a large separation bubble around the airfoil position $x/C = 0.8$, the bubble origin and end are respectively located at $x/C = 0.6$ and $x/C = 1$. This large bubble explains the drag increase and the decrease of efficiency in this particular case. It must be kept in mind that, having low pressures at the airfoil upper surface, always tends to increase the drag. The length of the arrows observed in the central and bottom panels characterises the Synthetic Jet momentum coefficient, while their width is proportional to the groove width and their inclination represents the injection angle. The three bottom panels in each sub-figure show the streamlines configuration when the maximum aerodynamic efficiency is obtained. At all AoA, the maximum efficiency is reached when

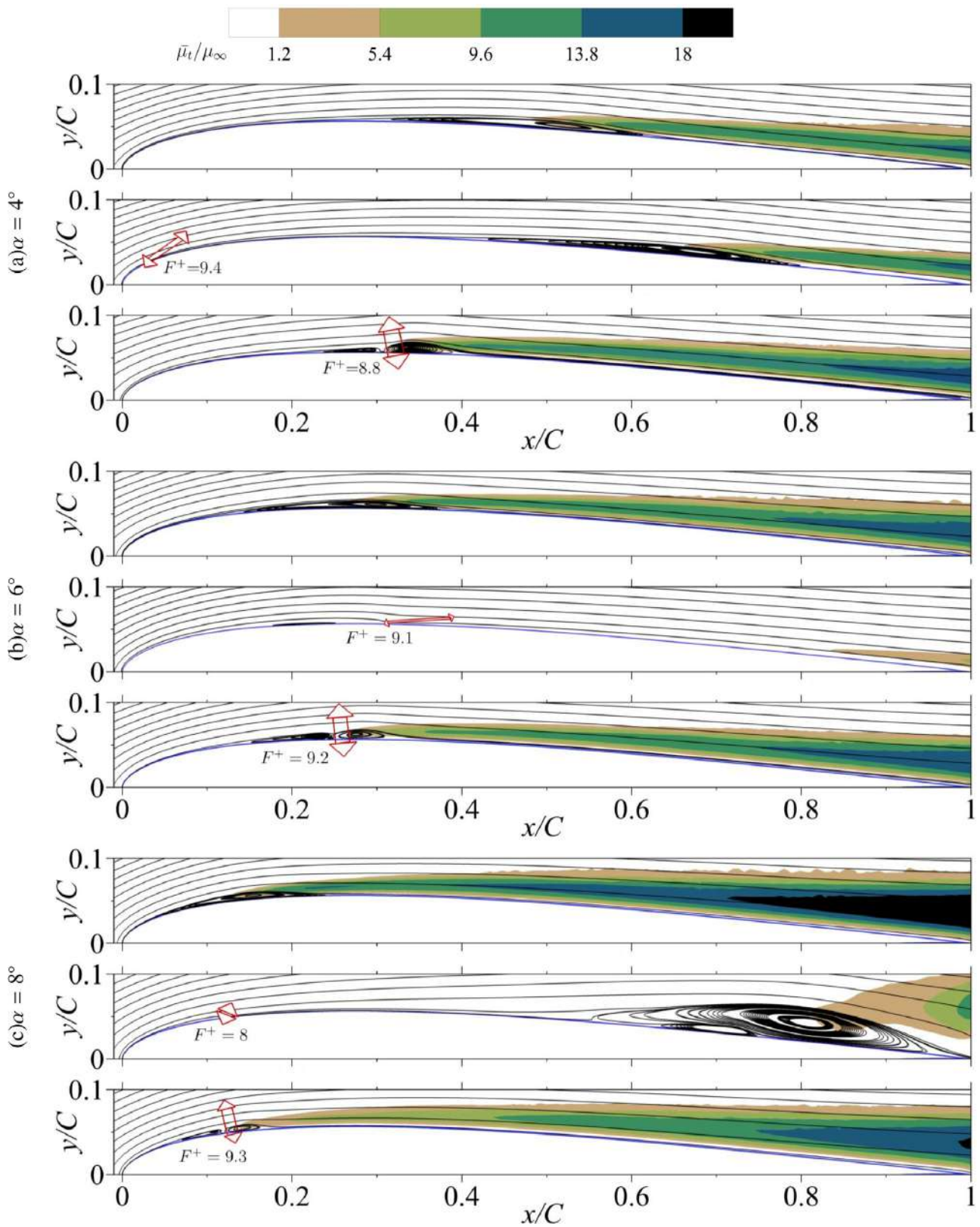


Fig. 11. Streamlines of the temporal average velocity field and contours of turbulence viscosity at the three pre-stall AoA. (a) 4°, (b) 6° and (c) 8°. The baseline, maximum lift and maximum efficiency cases are introduced as the top, central and bottom panel in each sub-figure, respectively. (For interpretation of the references to colour in this figure legend, the reader is referred to the web version of this article.)

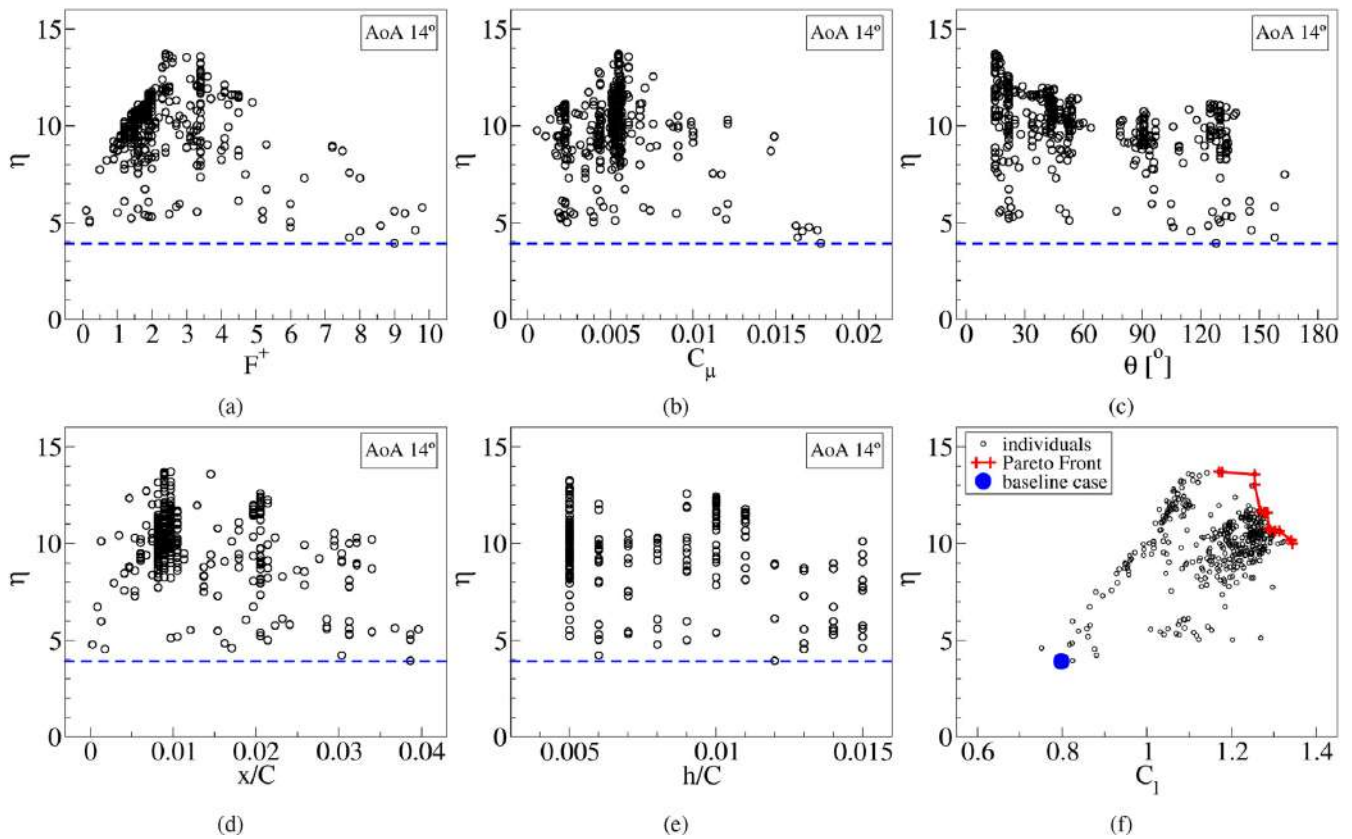


Fig. 12. aerodynamic efficiency versus (a) non-dimensional frequency, (b) momentum coefficient, (c) jet angle, (d) jet position, (e) jet width and (f) lift coefficient at $\alpha = 14^\circ$. The horizontal dashed line and the blue dot represent the baseline case efficiency. (For interpretation of the references to colour in this figure legend, the reader is referred to the web version of this article.)

the flow is attached along the entire airfoil chord and just a small bubble appears downstream of the synthetic jet location. This vortical structure is larger at small AoA. Therefore it seems that at all pre-stall AoA the same physical phenomenon is controlling the flow reattachment. One of the details which is important to highlight is the relationship between the vortical structures observed in Fig. 11 and the evolution of the pressure and friction coefficients presented in Fig. 10. This relation can be clearly seen when observing that the position of the vortical structures presented in the maximum efficiency cases of Fig. 11. Such a position coincides with the sudden drop of the friction coefficient and the sharp increase of the pressure coefficient observed in Fig. 10. From the contours of turbulence viscosity presented in Fig. 11, it is observed that under all conditions studied, the turbulence begins to grow inside the laminar separation bubble and then develops along the upper surface of the airfoil. As soon as transition to turbulence occurs, a turbulent boundary layer is developed and extends until the end of the chord. Flow reattachment occurs after the laminar separation bubble as a consequence of the transition to turbulence.

4.2. Post-stall angle of attack of 14°

In this subsection, the results obtained from the optimisation at the post-stall AoA 14° are presented. Fig. 12, from (a) to (e), introduces the aerodynamic efficiency as a function of each five AFC parameters evaluated in the present manuscript, the AoA was kept constant at 14° . When comparing the aerodynamic efficiency versus the non-dimensional frequency F^+ , Fig. 12a, the maximum efficiency appears at frequencies around $2.5 < F^+ < 3.5$. Notice that at pre-stall conditions, the optimum frequencies were around $F^+ \approx 9$. The aerodynamic efficiency as a function of the momentum coefficient C_μ is presented in Fig. 12b. Maximum efficiency is obtained for momentum coefficients around 0.005, when comparing this C_μ with the optimum ones at pre-stall AoA, it can be concluded the C_μ needed for the present case is over three times lower than the ones previously required. The explanation of why it is so needs to be found when analyzing the injection angle, which is introduced in Fig. 12c, along with the groove location. At post-stall AoA the optimum injection angle is around 18° , indicating the fluid is injected almost tangentially. This is completely different than the optimum jet angles at pre-stall AoA, which were around 120° . This injection angle as well as the momentum coefficient differences, along with the fact that at post-stall AoA there is no laminar bubble, direct the attention to different flow phenomenon to achieve flow attachment. Due to the fact that at post-stall AoA the AFC jet is injected almost tangentially, to further understand the coupling between the main flow and the injected pulsating one, the relation of the main flow reattachment with the Coanda effect should be further studied. At pre-stall AoA the interaction between the AFC jet and the boundary layer flow generates small vortical structures

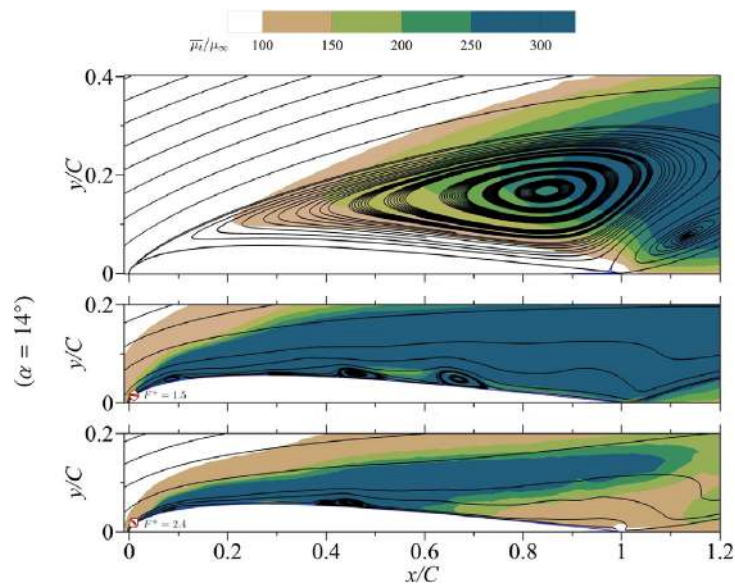


Fig. 13. Streamlines of the temporal average velocity field and contours of turbulence viscosity at the post-stall AoA. of 14° . The baseline, maximum lift and maximum efficiency cases are introduced as the top, central and bottom panel, respectively. (For interpretation of the references to colour in this figure legend, the reader is referred to the web version of this article.)

which are alternatively shed downstream, lowering the local pressure and promoting fluid reattachment. The position of the groove, which is introduced in Fig. 12d, appears to be optimum at around 1% of the chord, which is just the location of the flow separation point. It seems at high AoA, the jet injection needs to be implemented where the separation point is, while at low AoA the optimum position is located further downstream, inside the laminar bubble. From Fig. 12e, it is observed that groove widths around $h/C = 0.005$ seem to be the optimum ones at 14° . These widths are three to four times smaller than the ones needed at pre-stall AoA. Finally the Pareto Front curve characterising the maximum efficiency and maximum lift coefficient points, as well as the optimum combination of them, is presented in Fig. 12f. In order to understand which is the effect of the different AFC parameters on the main flow, the relation between the instantaneous streamlines at different jet pulsating instants and the boundary layer evolution will be further discussed, in §5.4.

The optimum AFC parameters to obtain the maximum efficiency and maximum lift for an AoA of 14° , obtained from the optimisation process and after performing 600 CFD simulations, is presented in Table 6. All optimum points characterising the full Pareto Front curve are introduced in Table A.4, Appendix A. From Tables 6 and A.4 it is observed that the AFC parameters required for maximum lift and maximum efficiency are very similar. The highest variation appears at the jet inclination angle θ , which is of 44° for the maximum lift and reduces to 18° for the maximum efficiency. The second AFC parameter suffering high variations is the F^+ , which for the maximum lift condition decreases by 37% versus the F^+ required for the maximum efficiency. Regarding the groove position, for maximum lift it is displaced upstream about 15% when compared with the groove position required for maximum efficiency. Table 6 shows that a maximum aerodynamic efficiency increase of about 251% can be obtained. When comparing Tables 5 and 6 it becomes clear that efficiency at the pre-stall AoA slightly decreases with the AoA increase, but at post-stall conditions it sharply increases. At post-stall AoA and considering the baseline case, due to the large vortical structure generated above the airfoil, see Fig. 13 top panel, considerable efficiency improvements can be obtained when implementing the AFC technology. In fact, from Table 6 it is observed a lift increase of 46% and a drag decrease of 58%, therefore explaining the large efficiency increase at AoA 14° . From the comparison of Tables 5 and 6 it is seen, for the pre-stall AoA the optimum jet inclination angles to obtain the maximum aerodynamic efficiency are around 120° , while at post-stall the jet inclination angles are of around 18° . But at pre-stall AoA the jet injection angles to obtain maximum lift are similar to the ones to obtain maximum lift and or efficiency at post-stall AoA. When analysing the momentum coefficient, jet injection angle and groove location required at pre and post-stall AoA, clear differences are observed between them, suggesting that the interaction between the incoming flow and the synthetic jet one may be characterised by a different physical phenomenon, further research is required in this regard.

The time averaged streamlines and contours of turbulence viscosity on the airfoil top surface for the baseline, maximum lift and maximum efficiency cases at AoA 14° is presented in Fig. 13. The baseline case (top panel) is characterised by a large separation bubble, which is drastically reduced for the maximum lift and efficiency cases (middle and bottom panels respectively). For the highest lift condition, a small vortex is alternatively generated at a position around $x/C = 0.1$, which keeps rolling downstream onto the airfoil surface, creating a particularly low pressure on the airfoil upper surface and therefore producing the maximum lift. For the maximum efficiency case, a very small vortical structure alternatively appears at the groove location. It seems the boundary layer is slightly separating and reattaching again, maintaining the vortical structure locked in the same position. The same performance was previously observed at 13° AoA by Tadjfar and Kamari [37]. Airfoil profile and Reynolds number were the same in both cases. When comparing the contours of turbulence viscosity

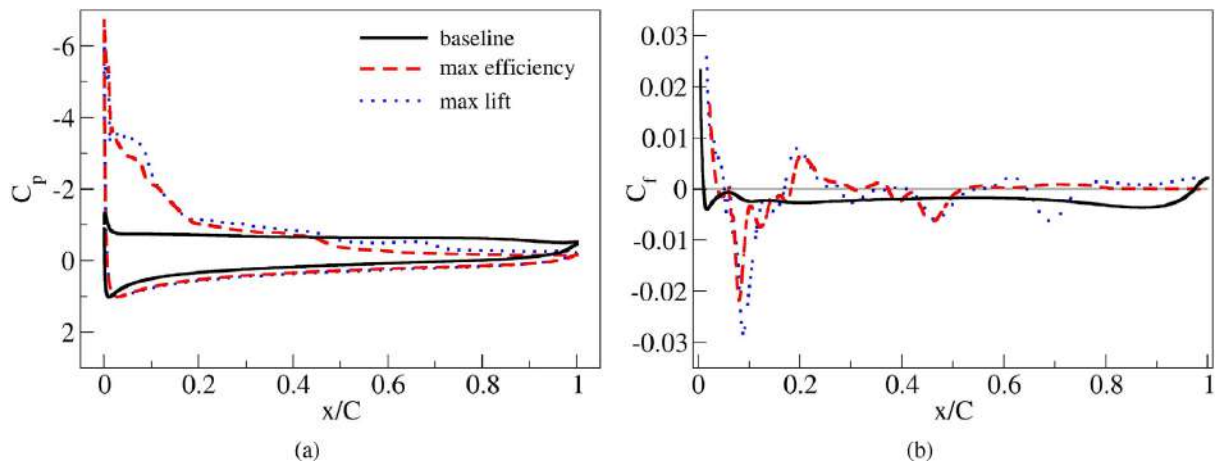


Fig. 14. Distributions of (a) pressure coefficient and (b) skin friction coefficient for the baseline (black solid lines), maximum efficiency (red dashed lines) and maximum lift (blue dotted lines) cases at 14°. (For interpretation of the references to colour in this figure legend, the reader is referred to the web version of this article.)

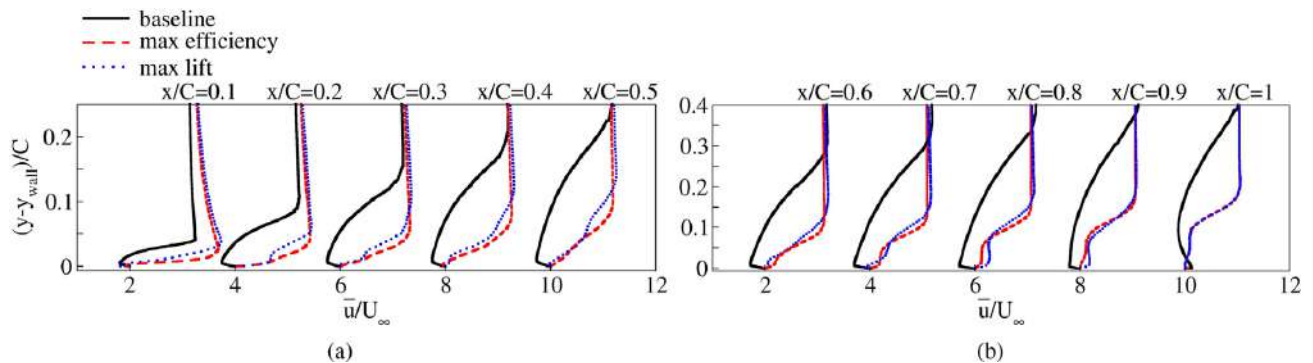


Fig. 15. Mean streamwise velocity profiles at several streamwise locations, (a) from $x/C=0.1$ to $x/C=0.5$ and (b) from $x/C=0.6$ to $x/C=1$, as a function of the normalised wall normal distance. Individual profiles are separated by horizontal offset of 2 with the corresponding zero lines located at 2, 4, 6, 8, 10. The black solid, red dashed and blue dotted lines represent the baseline, maximum efficiency and maximum lift cases, respectively. (For interpretation of the references to colour in this figure legend, the reader is referred to the web version of this article.)

at this post-stall AoA with the ones presented at pre-stall AoA, (see Figs. 13 and 11) it is realised that at post-stall AoA the maximum turbulence viscosity is about an order of magnitude higher. This is due to the fact that at 14° AoA (baseline case) the flow is fully separated. At this post-stall AoA and for the actuated cases, the boundary layer becomes turbulent just after the Synthetic Jet location, the high level of turbulence viscosity associated with the fluid inside the turbulent boundary layer maintains the flow attached along the entire chord length.

The effects on the pressure and friction coefficients when using the optimum AFC parameters at 14° are introduced in Fig. 14. The comparison with the baseline case is also presented. For both optimum AFC cases, on the initial 50% of the chord, the pressure on the upper airfoil surface is drastically reduced, and then increases to a higher value than the one associated with the baseline case. The friction coefficient shows that, for both optimum actuated cases, at around 50% of the chord, a small vortical structure appears. Such structure is already seen in Fig. 13, highlighting the point where the pressure coefficient is beginning to have a value higher than the baseline case one. For both actuated cases, friction coefficient suffers a particular decrease at a position $x/C = 0.1$, which is the point where the small laminar bubble is generated just after the jet, see Figs. 13b and 13 c. When comparing Fig. 14 with Fig. 10, it can be concluded that at post-stall AoA, the pressure and friction coefficients suffer large variations versus the baseline case ones. These changes are minor at pre-stall AoA, therefore explaining the relatively small efficiency variations.

The evolution of the mean streamwise velocity profiles at several streamwise locations, from $x/C=0.1$ to $x/C=1$, as a function of the normalised wall normal distance and for an AoA 14°, is introduced in Fig. 15. The comparison between the baseline, maximum lift and maximum efficiency cases is presented in the same figure. A drastic reduction of the boundary layer thickness is observed when the AFC cases are considered. For the baseline case and when moving downstream, the flow is separated, the vertical position at which negative velocity distribution exists keeps growing therefore indicating the existence of a large vortical structure located onto the airfoil surface, as observed in Fig. 13. For any of the optimum AFC cases presented in Fig. 15 and regardless of the streamwise location chosen, fluid velocity remains always positive, indicating there is no boundary layer separation. Small differences are observed between maximum lift and maximum efficiency cases. At the airfoil trailing edge ($x/C=1$) and for the baseline case, the velocity profile nearby the surface shows a positive velocity

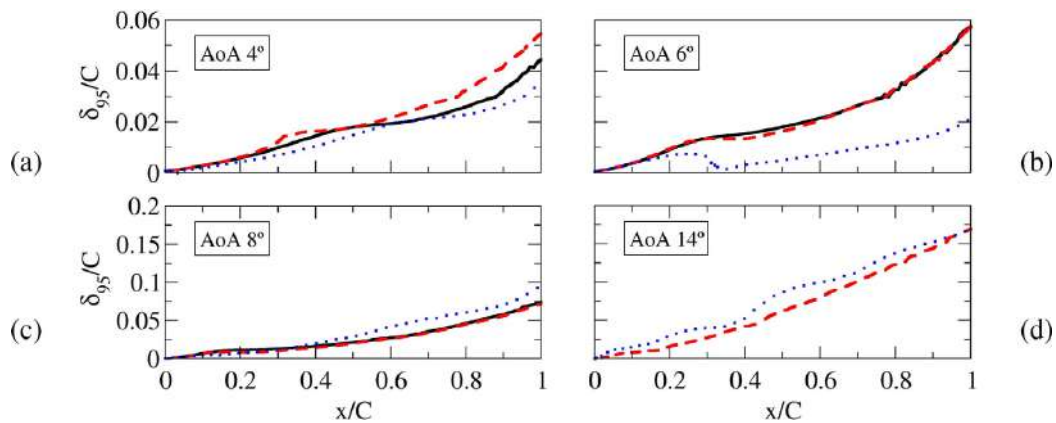


Fig. 16. Boundary layer thickness as a function of the chord length and for the four AoA studied cases; (a) 4°, (b) 6°, (c) 8° and (d) 14°. The black solid, red dashed and blue dotted lines represent the baseline, maximum efficiency and maximum lift cases, respectively. (For interpretation of the references to colour in this figure legend, the reader is referred to the web version of this article.)

sign (see Fig. 15b). This behaviour is linked to the existence of a relatively small vortical structure, turning anticlockwise, and located at the airfoil trailing edge, such structure can be seen in Fig. 13.

5. Discussion

In this section, some physical characteristics of the flow which helps in understanding the implementation effects of the AFC technology are introduced.

5.1. Boundary layer thickness for different AoA and actuation cases

The non-dimensional boundary layer thicknesses as a function of the non-dimensional abscissa axis for AoA of 4°, 6°, 8° and 14° are represented in Fig. 16. The thicknesses for the maximum lift, maximum efficiency and baseline cases are introduced in each figure, except at AoA 14°, where the curve representing the boundary layer thickness for the baseline case is not presented, as the flow is fully separated. The first thing to realise is that for the pre-stall AoA, the boundary layer thickness decreases with the AoA increase. Under these conditions, the AFC technology slightly modifies the boundary layer thicknesses versus the respective baseline cases ones, yet a clear reduction of the BL thickness is observed at AoA 6° under the maximum lift conditions. For AoA of 14° and 8°, the highest efficiency case is characterised by a boundary layer thickness thinner than the one observed for the maximum lift case. At AoA of 4° and 6° the opposite happens, high lift conditions have associated thinner boundary layers than the ones observed at high efficiency conditions. In fact, the streamlines presented in Figs. 11 and 13 help in clarifying the evolution of the boundary layer thicknesses. The location of the groove along with the different jet injection angles could further explain the different trend in boundary layer thicknesses. Further research to understand the mixing phenomenon is needed.

5.2. Further investigation on AoA of 14°

Recalling now the work done by Tadjfar and Kamari [37], where they studied the same airfoil profile at the same Reynolds number and for post-stall AoA of 13° and 16°, they obtained efficiencies much higher than what it is obtained in the present paper at 14° (see Tables 6 and A.4). These differences seem to be mostly due to the 4 times higher momentum coefficient they employed in their study. In the present work the maximum momentum coefficient was limited to avoid using large amounts of energy to drive the synthetic jet. Yet, in order to check if the use of a higher momentum coefficient could further increase the aerodynamic efficiency, a second set of 400 CFD optimisation cases was run. The ranges of the different AFC parameters used for this second set of tests were already presented in the last line of Table 4. Notice that the only difference in the range of the different AFC parameters defined for the new case at 14° introduced in Table 4, resides in the larger momentum coefficient range allowed for this second optimisation process. From now on, this second case will be called the unrestricted momentum coefficient case.

Table 7 introduces the optimised AFC parameters to obtain the new maximum lift and efficiency. When comparing the results presented in Table 7 with the ones previously presented in Table 6, it is observed the efficiency has increased from the previous 251% to the actual 460%. The groove width h/C remains unchanged, the jet injection angle θ has reduced to 15° clearly indicating that tangential injections lead to higher efficiencies, the position of the groove has moved around 180% further downstream, the injection frequency has doubled and the momentum coefficient has increased by over 600%. Based on this information it can be concluded that, for post-stall AoA the momentum coefficient as well as the groove location are essential to obtain high aerodynamic efficiencies. The flow needs to be injected almost tangentially. Under these

Table 7

Optimum five synthetic jet parameters associated with the maximum lift and maximum efficiency cases at a post-stall angle of attack of 14° (large momentum coefficient range). 400 CFD cases.

α°	cases	F^+	C_μ	θ°	x/C	h/C	C_l	$C_l\%$	C_d	η	$\eta\%$
14	max lift	6.7	0.0985	15	0.02854	0.005	1.7635	+121.00	0.0966	18.24	+367.69
	max efficiency	5.2	0.0390	15	0.02764	0.005	1.5690	+096.61	0.0717	21.86	+460.50
	baseline	—	—	—	—	—	0.7980	—	0.2040	03.90	—

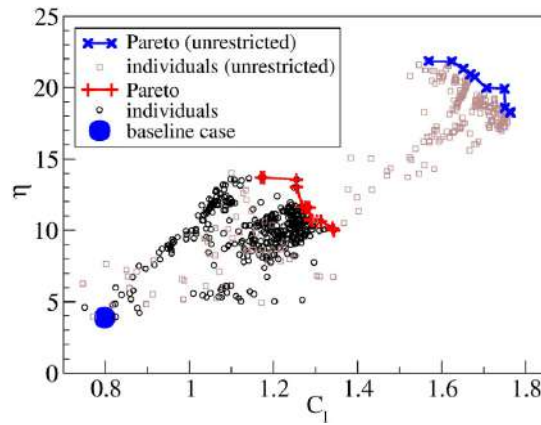


Fig. 17. Comparison of the two Pareto Fronts obtained at AoA 14° with the restricted and unrestricted momentum coefficient.

Table 8

Power ratio obtained for the maximum efficiency case and at pre and post stall AoA.

cases	α°	U_j [m/s]	A_j [m ²]	θ°	W_j [W]	W_G [W]	W_G/W_j
max efficiency	4	1.17	0.019	132	0.00479	0.00425	0.885
	6	1.11	0.019	124	0.00457	0.00435	0.951
	8	1.18	0.013	126	0.00366	0.00445	1.213
	14	1.89	0.005	018	0.00221	0.05930	26.789
	14 (u)	5.49	0.005	015	0.04544	0.06615	1.455

conditions the aerodynamic efficiency is perfectly comparable with the one obtained by Tadjfar and Kamari [37], being the AFC parameters of a similar order of magnitude.

To further visualise the advantages obtained when using an unrestricted momentum coefficient, Fig. 17 is introduced. It compares the former Pareto Front obtained with the restricted momentum coefficient and initially presented in Fig. 12f, with the new Pareto Front obtained with the unrestricted momentum coefficient. The advantages of employing quite unrestricted momentum coefficients are clearly stated. The full values of the new Pareto Front are presented in Table A.5 in Appendix A. In the next subsection the comparison between the different flow structures obtained over the airfoil and generated due to the interaction of the main flow stream and the synthetic jet, are presented and discussed.

5.3. Energy assessment

In the present section in order to determine the effectiveness of the AFC technology, the power per unit length used by the SJA (W_j) and the one gained after the actuation (W_G), at each AoA and for the optimum case of maximum efficiency, is calculated and presented in Table 8. The power required by the synthetic jet is defined in Eq. 17.

$$W_j = \frac{1}{2} \rho_j A_j \sin(\theta) \overline{u_j^3} \tag{17}$$

where $A_j = hl$ is the cross-sectional flow area of the synthetic jets, in the present study as the spanwise length of the airfoil is equal to unity $l = 1$, the area is equivalent to the jet width h . As previously introduced in §2.3, θ is the jet inclination angle with respect to airfoil surface.

The time dependent velocity profile of the synthetic jet actuator to the power three, $\overline{u_j^3}$, has been defined according to [15,17].

$$\overline{u_j^3} = \frac{1}{T/2} \int_0^{T/2} U_j^3 \sin^3(2\pi ft) dt = \frac{4}{3\pi} U_j^3 \tag{18}$$

where U_j represents the maximum jet velocity. The power saved due to the reduction of the drag force when AFC is applied can be given as:

$$W_G = U_\infty (D_{\text{baseline}} - D_{\text{actuated}}) = \frac{\rho U_\infty^3 C}{2} (C_{d_{\text{baseline}}} - C_{d_{\text{actuated}}}) \quad (19)$$

where D and C_d represent the drag force and drag coefficient respectively. The parameter representing the power ratio when AFC is applied reads:

$$W_G/W_j \quad (20)$$

Whenever this parameter becomes negative, it indicates the drag coefficient after the actuation is bigger than the one generated at the baseline case. When this value is positive but smaller than one, it means that despite a drag reduction being observed when AFC is implemented, the energy saved is lower than the one needed to actuate the synthetic jet. Also when the power ratio has values higher than the unity, there is energy saving. All related information is summarised in Table 8 from where it can be stated that under the maximum efficiency conditions at nearly all AoA the power ratio is higher than one. At AoA 14° the power ratio is particularly high. This is perfectly understandable when considering that at this AoA the flow is fully separated under baseline conditions, the application of AFC reattaches the flow drastically reducing the drag forces acting over the airfoil. Nevertheless, if the unrestricted momentum coefficient is employed, (see the row of $14^\circ(u)$ from Table 8) the power ratio drops, although the airfoil is still energetically efficient.

In conclusion, it is interesting to notice that although the AFC technology is effective in modifying lift and drag forces, under some conditions it is energetically efficient. In fact, at the three pre-stall AoA, under baseline conditions, the flow is attached to the airfoil and the application of AFC slightly improves the flow conditions. The drag is slightly increased but the energy used to do so is almost the same as the amount saved (considering the maximum efficiency conditions). At post-stall AoA, the situation is completely different as the flow is fully separated (before actuation). Whenever AFC is applied the flow attaches to the airfoil, causing a large drag reduction. As a result, the energy used is much smaller than the amount saved. From the energy point of view, the conclusion of this sub-section is that Synthetic Jet Actuators are efficient at high AoA and specially at post-stall AoA.

5.4. Flow structures

In the present subsection it will be explained for AoA 6° and 14° , how the vortical structures created by the interaction of the AFC synthetic jet and the main flow, generate, collapse and are being shed downstream. Two injection angles θ of 124° and 15° , which respectively correspond to the cases of maximum efficiency and maximum lift for an AoA of 6° are initially analyzed, see Figs. 18 and 19. For an AoA of 14° , the two maximum efficiency cases corresponding to the restricted and unrestricted momentum coefficient ones are respectively presented in Figs. 20 and 21. In all these figures, a full jet oscillation period is divided in eighth equally spaced time periods. The initial four time periods correspond to the blowing phase, and the remaining four time periods obey to the suction phase. At phase $1/8T$ the synthetic jet has just started to blow fluid and therefore has associated a low injection velocity, the maximum blowing velocity will be reached in the next time period $2/8T$. The time periods $5/8T$ and $6/8T$ characterise the initial and maximum sucking velocities respectively, which are equivalent to the $1/8T$ and $2/8T$ blowing periods. The time periods $4/8T$ and $8/8T$ define the final blowing and sucking periods respectively. At these two time periods the synthetic jet velocity is zero.

Fig. 18, represents the case characterised by an AoA of 6° and an injection angle of $\theta = 124^\circ$. During the blowing phase, at the initial time period $1/8T$, the interaction between the external flow and the low synthetic jet velocity facing upstream generates a small laminar bubble just before the groove location. An even thinner bubble is created just upstream of this one. Downstream of the groove location, at a distance about $x/C = 0.05$ versus the groove position, a third laminar bubble of a size slightly larger than the previous two ones is observed. When the time period is $2/8T$ the blowing velocity is maximum, the two upstream attached vortical structures have decrease in length while slightly increasing in thickness. This is due to the slightly increase of the boundary layer thickness at the groove location. Downstream of the groove location, the former third laminar separation bubble still remains in the same position and directly after the groove, a fourth vortical structure is generated. At the next time period $3/8T$, the synthetic jet blowing velocity is the same as at $1/8T$. This decrease of velocity versus the previous time period enhances the growth of the four vortical structures. A particular large growth is observed on the eddy located just downstream of the jet. The maximum dimension of the vortical structures is observed at $4/8T$, the two upstream structures, which were connected in the previous time periods are now quite independent. The two downstream structures are rather joined and the eddy located just downstream of the jet has now moved upstream into the jet area while considerably increasing its dimension. The external flow simply passes over the four eddy structures drastically reducing the downstream perturbed zone. As soon as the suction phase starts, at time $5/8T$, the former four vortical structures drastically reduce in size while maintaining their central core position. In the next time period $6/8T$, the sucking velocity is maximum, the two upstream structures have almost completely disappeared and the structure just downstream of the jet still remains, although it is largely being dragged into the groove. Finally, the further downstream structure is being pushed slightly downstream. As the time period increases to $7/8T$, and due to the low sucking velocity, the almost dragged downstream structure is regaining intensity and places again just downstream of the groove. The further downstream structure completely collapses while the remaining of one of the upstream structures can still be seen. The

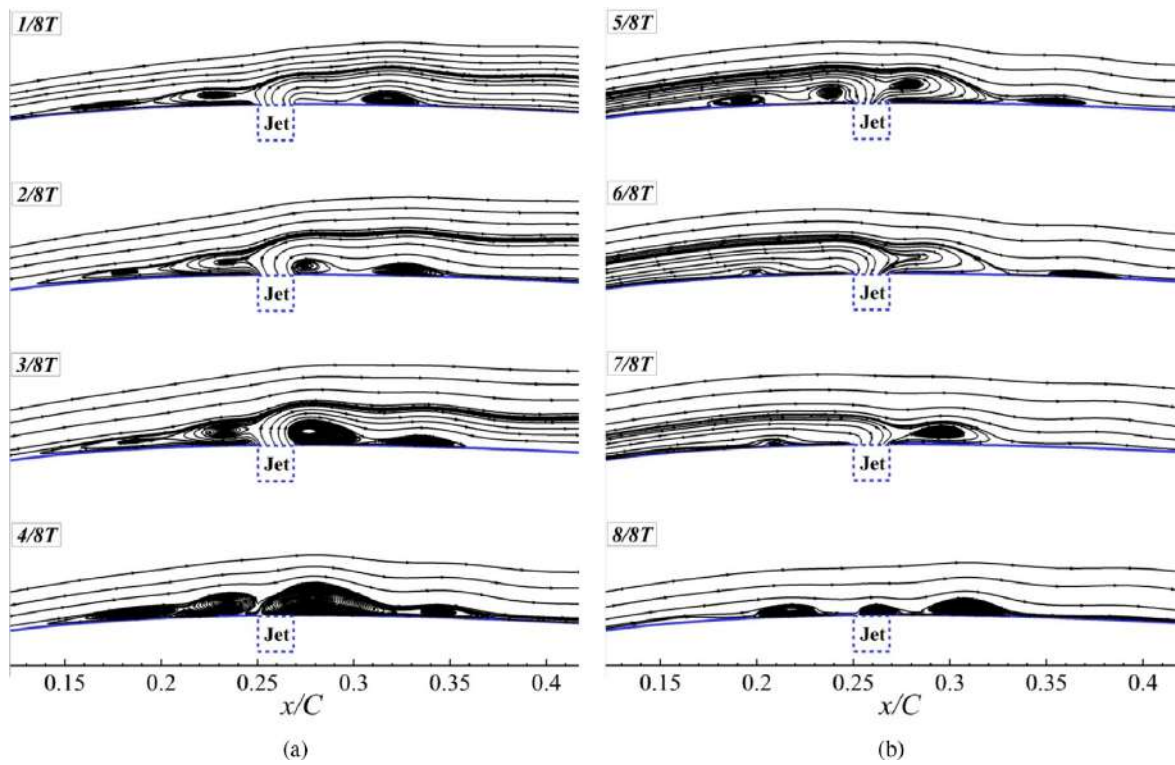


Fig. 18. Instantaneous velocity streamlines at different phases of synthetic jet for the maximum efficiency case at AoA 6° with $F^+ = 9.2$, $C_\mu = 0.0194$, $\theta = 124^\circ$, $x/C = 0.25$ and $h/C = 0.019$.

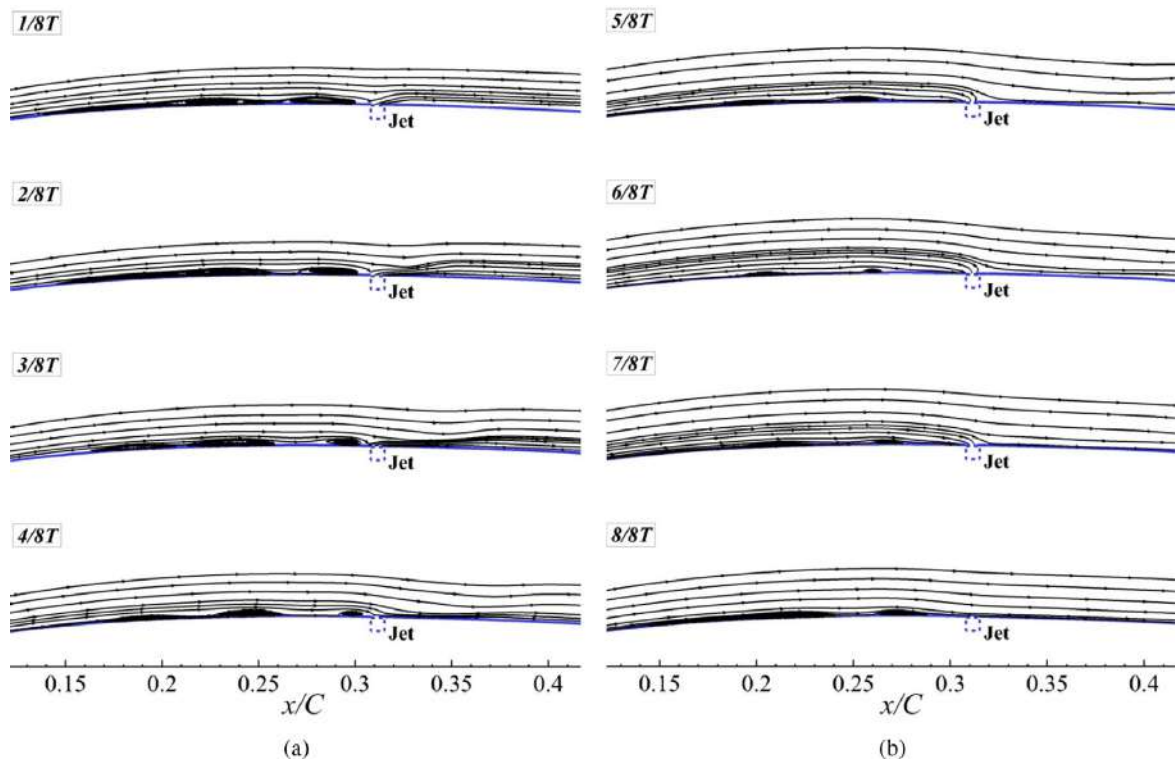


Fig. 19. Instantaneous velocity streamlines at different phases of synthetic jet for the maximum lift case at AoA 6° with $F^+ = 9.1$, $C_\mu = 0.0195$, $\theta = 15^\circ$, $x/C = 0.308$ and $h/C = 0.006$.

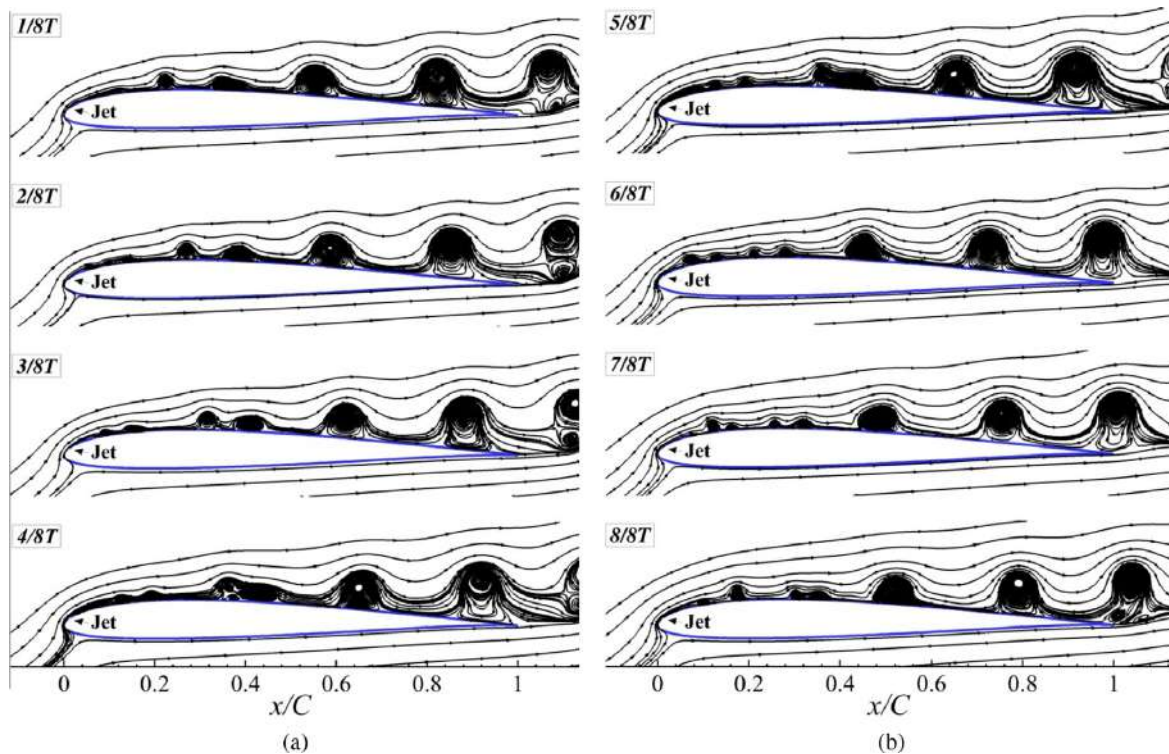


Fig. 20. Instantaneous velocity streamlines at different phases of synthetic jet for the maximum efficiency case at AoA 14° with $F^+ = 2.4$, $C_\mu = 0.0055$, $\theta = 18^\circ$, $x/C = 0.0097$ and $h/C = 0.005$. Restricted momentum coefficient.

last time period characterises the end of the sucking phase, where the sucking velocity is zero, the former upstream and downstream structures have grown in size and a third smaller structure has been created just on the groove zone. This smaller structure will be blown away in the next time period, blowing phase.

Taking the blowing and suction phases globally and when the jet injection angle is of 124° , it can be said that the synthetic jet is creating around the jet zone several small laminar bubbles which keep appearing and disappearing while maintaining the flow outside this area rather attached to the airfoil. All information presented here is based on the 2D CFD RANS simulations. In fact, a further 3D-DNS set of simulations are needed to carefully evaluate the flow interaction just outlined in the present manuscript.

When maintaining the AoA at 6° but changing the jet injection angle to $\theta = 15^\circ$, which characterises the maximum lift case, the evolution of the flow around the jet area is presented in Fig. 19. From the comparison of Figs. 18 and 19 three main details are initially observed. When injecting at small angles, the groove position needs to be moved downstream, the groove width is reduced by over 66% and the eddies previously observed in Fig. 18, are now largely reduced. In fact, the vortical structures previously seen downstream of the groove are now completely gone. Regarding the upstream structures, two to three rather elongated eddies having a very small thickness are observed during the blowing phase, such structures almost disappear during the suction phase. Fig. 19 indicates the boundary layer thickness has to be thinner for the maximum lift case than for the maximum efficiency case, which was analysed in Fig. 18, and this is exactly what Fig. 16 shows for this AoA.

The analysis of the vortex shedding phenomenon for the maximum efficiency case at AoA 14° and when the momentum coefficient was restricted to a maximum value of $C_\mu = 0.02$ is presented in Fig. 20. Blowing and suction phases are characterised by a set of vortical structures generated just downstream of the synthetic jet and rolling onto the airfoil surface. Their dimension grows as they move downstream and once the vortices reach the trailing edge they separate from the airfoil and are being shed downstream. From the observation of time periods between $1/8T$ and $4/8T$, it is seen that during the blowing phase the vortical structures simply move downstream. Very small vortical structures seem to be appearing at the end of the blowing phase. Seen from the airfoil leading edge, the first, rather circular, and the second, much elongated, vortical structures observed at $1/8T$, are approaching each other as they roll downstream, finally joining at time period $5/8T$, which is the beginning of The suction phase. At this particular time period, an elongated laminar bubble is observed just downstream of the jet. In fact, this laminar bubble was initially observed as $3/8T$ and kept growing until reaching the actual time period. On the next time period, $6/8T$, where the suction velocity is maximum, the elongated laminar bubble previously seen wraps up generating a high intensity rounded vortex, which rolls downstream faster than the three smaller vortical structures initially generated at time period $2/8T$ and clearly seen downstream of the laminar bubble at $5/8T$. At time period $8/8T$ the high intensity vortical structure generated at $6/8T$, has already caught one of the three smaller vortical structures initially generated at $2/8T$, and it will take a full synthetic jet oscillation period until it will catch the remaining

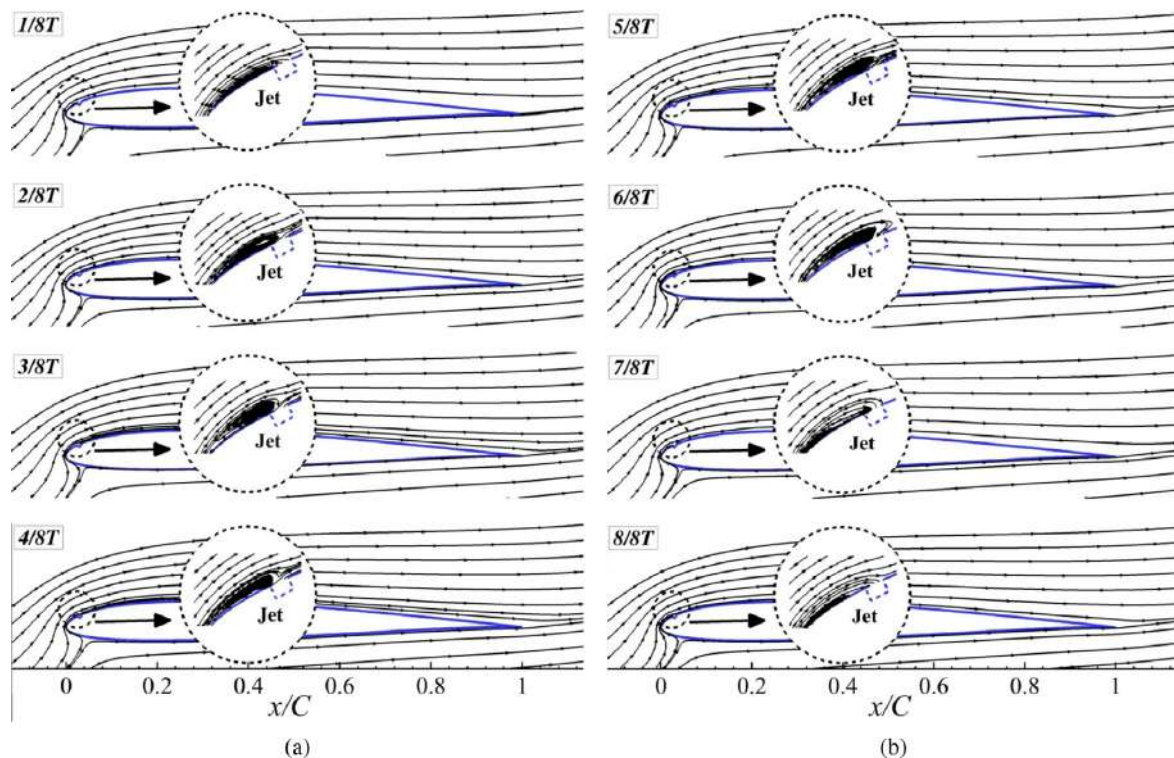


Fig. 21. Instantaneous velocity streamlines at different phases of synthetic jet for the maximum efficiency case at AoA 14° with $F^+ = 5.2$, $C_\mu = 0.039$, $\theta = 15^\circ$, $x/C = 0.02764$ and $h/C = 0.005$. Unrestricted momentum coefficient.

two small vortical structures, until reaching the time period $5/8T$. It can be concluded that the formation of the main vortical structures which will be shed downstream is due to the merging process of several small eddies initially generated at time period $2/8T$, with a higher intensity one generated at time period $6/8T$. This merging process takes a full synthetic jet oscillation cycle, counted from the moment the higher intensity vortex is created.

The final results presented in this paper, Fig. 21, characterise the maximum efficiency case at AoA 14° but with the unrestricted momentum coefficient. In Table 7 it was already stated that for this particular case, the efficiency increase versus the baseline one was of 460%, notice that the efficiency increase associated with Fig. 20 was of 251%. Fig. 21 shows that regardless of the blowing or suction phase chosen, the streamlines are completely attached to the airfoil, just a small elongated laminar bubble slightly changing in size appears upstream of the jet groove. The dimension of the laminar bubble is minimum at the end of the suction phase. One of conclusions from this figure which is one of the conclusions of the present study is that if large momentum coefficients can be employed, the flow can be completely reattached to the airfoil surface. Nevertheless, we observed that the amount of energy required by this AFC actuation was not compensated by the energy saving due to the improved profile performance.

6. Conclusions

The paper evaluates five AFC parameters and optimises their combination to obtain the maximum lift and efficiency for the SD7003 airfoil at three pre-stall and one post-stall AoA. The Reynolds number is kept constant at 6×10^4 .

The paper presents the results of over 2200 2D RANS simulations. 400 CFD cases were run for each of pre-stall AoA, 4° , 6° and 8° . 600 CFD cases were run at 14° with a restricted momentum coefficient and another 400 CFD cases were run at AoA 14° with an unrestricted momentum coefficient. A Genetic algorithm optimiser was linked with a mesh generator and a CFD solver in order to automatically perform the simulations for each new Genetic algorithm generation.

The use of an optimisation tool considering two objective functions, lift coefficient and efficiency, has allowed to obtain for each of the four studied AoA, a Pareto Front which contains all the optimum set of AFC parameters characterising the maximum efficiency, the maximum lift and their optimum combinations.

The use of AFC has improved the efficiency and lift coefficient under all studied angles of attack. The percentage of improvement of both parameters versus the baseline case values is particularly relevant at post-stall AoA.

An aerodynamic efficiency increase of almost 39% was obtained for an AoA of 8° . This efficiency was related to the following values for the different AFC parameters, non-dimensional frequency $F^+ = 9.3$, momentum coefficient $C_\mu = 0.0147$, jet angle 126° , jet position $12\%C$, $x/C = 0.12$ and jet width $1.3\%C$, $h/C = 0.013$. The efficiency increased to 251% when the AoA was 14° and using a restricted momentum coefficient, the AFC parameters associated were, $F^+ = 2.4$; $C_\mu = 0.0055$; $\theta = 18^\circ$,

$x/C = 0.0097$ and $h/C = 0.005$. When using an unrestricted momentum coefficient at AoA of 14° , the efficiency increased to 460%, being the AFC parameters $F^+ = 5.2$; $C_\mu = 0.039$; $\theta = 15^\circ$, $x/C = 0.02764$ and $h/C = 0.005$.

To obtain a maximum aerodynamic efficiency, the synthetic jet optimum inclination angles at pre-stall AoA are about 125° . The jet inclination angles to obtain the maximum lift are around 15° . At post-stall AoA maximum lift and maximum efficiency are obtained when employing jet inclination angles around 18°

At pre-stall AoA the optimum position of the synthetic jet, to obtain the maximum efficiency, is inside the laminar separation bubble corresponding to each angle of attack. For the momentum coefficient restricted case at post-stall AoA, the groove needs to be located just where the separation point is. The momentum coefficient required is several times lower than the one needed at pre-stall AoA, yet the efficiency increase is much higher. For the unrestricted case at 14° , the jet location has moved further downstream, the required momentum coefficient is about seven times larger the one needed for the restricted case at the same AoA and the efficiency has now increased to 460% versus the base case one.

Large momentum coefficients are associated with high frequencies and vice-versa. The required jet width at post-stall AoA is about one third of the one required at pre-stall AoA.

The physics phenomenon characterising the interaction between the boundary layer and the pulsating jet flow is highly dependent on the jet inclination angle and the airfoil angle of attack. Despite the fact the simulations are two dimensional, a further inside into the interaction between the synthetic jet and the external flow is obtained. At pre-stall AoA and when using large injection angles, injecting upstream, a set of small vortical structures are observed. But when the injection angle is facing downstream, downstream vortical structures completely disappear. At post-stall AoA it has been demonstrated that injecting almost tangentially and employing large momentum coefficients completely reattaches the flow to the airfoil, hugely increasing its efficiency.

Acknowledgment

This work was supported by the Spanish and Catalan Governments under grants FIS2016-77849-R and 2017-SGR-00785, respectively. Part of the computations were done in the Red Española de Supercomputación (RES), Spanish supercomputer network, under the grants IM-2019-3-0002 and IM-2020-1-0001. Dr. Jordi Pons-Prats acknowledges the support of the Serra Hunter programme by the Catalan Government.

Appendix A. Full Pareto Front results, at all AoA

Table A.1

All the Optimum cases of Pareto Front at 4° .

F^+	C_μ	θ°	x/C	h/C	C_l	$C_l\%$	C_d	η	$\eta\%$
9.4	0.0193	15	0.021	0.013	0.6185	5.76	0.0317	19.51	-35.61
8.4	0.0183	15	0.020	0.013	0.6141	5.01	0.0314	19.56	-35.44
8.4	0.0134	16	0.111	0.012	0.6047	3.40	0.0297	20.34	-32.84
8.4	0.0134	15	0.131	0.012	0.6019	2.92	0.0295	20.37	-32.75
8.7	0.0121	15	0.131	0.013	0.5987	2.39	0.0289	20.70	-31.70
8.4	0.0135	111	0.307	0.015	0.5867	0.32	0.0177	33.09	9.20
8.4	0.0121	111	0.307	0.012	0.5854	0.10	0.0170	34.26	13.07
8.3	0.0178	110	0.313	0.018	0.5846	-0.03	0.0162	35.94	18.62
8.8	0.0193	109	0.313	0.018	0.5845	-0.04	0.016	36.54	20.59
8.2	0.0177	111	0.313	0.017	0.5843	-0.07	0.0158	36.77	21.35
8.2	0.0178	111	0.313	0.017	0.5843	-0.07	0.0158	36.81	21.51
7.2	0.0193	115	0.313	0.013	0.5826	-0.36	0.0145	39.92	31.76
8.7	0.019	114	0.313	0.018	0.5821	-0.44	0.0143	40.58	33.93
8.5	0.0193	114	0.313	0.017	0.5821	-0.44	0.0143	40.64	34.14
8.8	0.019	115	0.313	0.017	0.5820	-0.46	0.0140	41.46	36.85
8.8	0.0185	119	0.313	0.015	0.5809	-0.65	0.0133	43.64	44.02
8.8	0.0185	119	0.309	0.016	0.5803	-0.75	0.0132	43.66	44.12
8.8	0.0185	120	0.308	0.015	0.5802	-0.77	0.0132	43.92	44.97
9.2	0.0184	121	0.313	0.019	0.5800	-0.80	0.0127	45.53	50.29
7.3	0.0199	123	0.313	0.017	0.5799	-0.83	0.0125	46.07	52.05
8.7	0.0185	123	0.313	0.019	0.5795	-0.89	0.0122	47.15	55.61
8.8	0.0194	123	0.313	0.017	0.5795	-0.90	0.0122	47.43	56.53
9.4	0.0199	123	0.313	0.017	0.5790	-0.99	0.0121	47.78	57.69
8.8	0.0194	125	0.313	0.019	0.5787	-1.04	0.0117	49.45	63.21
7.1	0.0187	133	0.313	0.019	0.5754	-1.60	0.0111	51.78	70.91
7.1	0.0187	133	0.312	0.019	0.5752	-1.63	0.0110	51.95	71.48
7.1	0.0187	133	0.311	0.019	0.5748	-1.70	0.0110	52.02	71.68
8.8	0.0194	131	0.313	0.019	0.5747	-1.71	0.0109	52.54	73.41
8.8	0.0194	132	0.313	0.019	0.5740	-1.84	0.0108	52.86	74.45
		baseline			0.5848		0.0193	30.30	

Table A.2
All the Optimum cases of Pareto Front at 6°.

F^+	C_μ	θ°	x/C	h/C	C_l	$C_l\%$	C_d	η	$\eta\%$
9.1	0.0195	15	0.308	0.006	0.8371	9.14	0.0338	24.76	-22.50
9.1	0.0195	15	0.308	0.007	0.8370	9.13	0.0337	24.79	-22.41
9.1	0.0192	15	0.308	0.006	0.8363	9.03	0.0336	24.88	-22.13
9.1	0.0195	19	0.308	0.006	0.8360	9	0.0332	25.17	-21.22
9.1	0.0195	23	0.307	0.006	0.8345	8.80	0.0327	25.46	-20.31
9.1	0.0195	24	0.313	0.007	0.8344	8.79	0.0327	25.48	-20.25
9.1	0.0192	23	0.307	0.006	0.8337	8.70	0.0326	25.58	-19.93
9.1	0.0195	34	0.307	0.006	0.8311	8.36	0.0317	26.21	-17.96
9.1	0.0198	40	0.307	0.006	0.8310	8.34	0.0310	26.73	-16.33
9	0.0199	47	0.308	0.006	0.8307	8.31	0.0300	27.68	-13.36
9.1	0.0195	47	0.308	0.006	0.8297	8.17	0.0297	27.87	-12.77
9.1	0.0195	55	0.308	0.006	0.8263	7.73	0.0286	28.90	-9.55
9.1	0.0195	59	0.308	0.006	0.8241	7.44	0.0280	29.43	-7.88
9.1	0.0194	59	0.308	0.006	0.8238	7.40	0.0279	29.46	-7.79
9.1	0.0195	62	0.308	0.006	0.8220	7.17	0.0276	29.78	-6.79
9.2	0.0194	66	0.311	0.006	0.8183	6.68	0.0267	30.56	-4.35
9.1	0.0158	64	0.308	0.005	0.8121	5.88	0.0254	31.88	-0.22
9.1	0.0144	64	0.308	0.005	0.8076	5.29	0.0249	32.39	1.38
9.3	0.0194	82	0.311	0.007	0.8071	5.22	0.0233	34.54	8.10
9.3	0.0194	83	0.311	0.007	0.8066	5.16	0.0231	34.84	9.05
9.3	0.0177	82	0.311	0.007	0.8050	4.95	0.0230	34.92	9.29
9.2	0.0158	82	0.308	0.008	0.8046	4.90	0.0225	35.76	11.92
9.2	0.0158	85	0.305	0.009	0.8031	4.70	0.0219	36.58	14.49
9.2	0.0194	91	0.309	0.008	0.8027	4.65	0.0214	37.47	17.27
9.2	0.0194	94	0.311	0.009	0.7989	4.16	0.0212	37.63	17.78
9.2	0.0155	94	0.311	0.009	0.7952	3.68	0.0211	37.67	17.90
9.2	0.0154	95	0.306	0.009	0.7948	3.62	0.0209	37.95	18.78
9.2	0.0155	99	0.309	0.010	0.7918	3.23	0.0205	38.55	20.66
9.2	0.0192	105	0.305	0.018	0.7895	2.93	0.0195	40.34	26.26
9.2	0.0192	106	0.305	0.018	0.7890	2.87	0.0193	40.73	27.48
9.2	0.0192	112	0.305	0.018	0.7849	2.33	0.0184	42.59	33.30
9.2	0.0192	113	0.305	0.018	0.7840	2.21	0.0183	42.77	33.86
9.2	0.0194	119	0.250	0.019	0.7810	1.82	0.0167	46.69	46.13
9.2	0.0194	123	0.250	0.019	0.7805	1.76	0.0155	50.07	56.71
9.2	0.0194	124	0.250	0.019	0.7802	1.72	0.0153	50.85	59.15
		baseline			0.767		0.0240	31.95	

Table A.3
All the Optimum cases of Pareto Front at 8°.

F^+	C_μ	θ°	x/C	h/C	C_l	$C_l\%$	C_d	η	$\eta\%$
8	0.0058	67	0.116	0.015	1.043	11.45	0.0504	20.66	-27.66
8	0.0058	68	0.114	0.015	1.040	11.42	0.0502	20.72	-27.47
7.8	0.0056	68	0.120	0.014	1.039	11.20	0.0498	20.85	-27.02
8.1	0.0058	69	0.120	0.014	1.037	11.02	0.0480	21.57	-24.50
7.8	0.0057	68	0.120	0.007	1.030	10.27	0.0468	22.01	-22.96
7.4	0.0057	68	0.120	0.007	1.026	9.89	0.0440	23.27	-18.55
7.4	0.0056	68	0.120	0.007	1.026	9.85	0.0440	23.30	-18.44
9.9	0.0147	31	0.173	0.007	1.002	7.28	0.0341	29.33	2.66
9.9	0.011	30	0.169	0.013	0.988	5.78	0.0328	30.08	5.28
7.4	0.0104	26	0.173	0.006	0.985	5.46	0.0327	30.08	5.28
7.4	0.0098	30	0.173	0.006	0.982	5.14	0.0323	30.41	6.44
7.7	0.0059	67	0.167	0.005	0.967	3.53	0.0293	32.92	15.22
7.7	0.0058	69	0.166	0.005	0.967	3.53	0.0291	33.14	15.99
7.7	0.0059	71	0.166	0.005	0.967	3.53	0.0291	33.15	16.03
9.3	0.0049	128	0.122	0.014	0.950	1.71	0.0265	35.82	25.37
9.1	0.0056	128	0.122	0.016	0.950	1.71	0.0264	35.97	25.90
9.3	0.0096	126	0.122	0.014	0.948	1.50	0.0253	37.37	30.80
9.4	0.0098	128	0.120	0.014	0.947	1.40	0.0251	37.71	31.99
9.2	0.0121	127	0.123	0.014	0.947	1.40	0.0245	38.65	35.28
9.4	0.0121	128	0.121	0.013	0.946	1.28	0.0244	38.74	35.59
9.3	0.0147	126	0.122	0.013	0.946	1.28	0.0238	39.71	39
		baseline			0.934		0.0327	28.57	

Table A.4
All the Optimum cases of Pareto Front at 14° (restricted momentum coefficient).

F^+	C_μ	θ°	x/C	h/C	C_l	$C_l\%$	C_d	η	$\eta\%$
1.5	0.0051	44	0.0082	0.005	1.3435	68.36	0.1343	10	156.41
1.5	0.0052	44	0.0082	0.005	1.3433	68.33	0.1343	10	156.41
1.5	0.0061	43	0.0082	0.005	1.3403	67.96	0.1318	10.17	60.77
1.5	0.0054	43	0.0082	0.005	1.3123	64.45	0.1232	10.65	173.07
1.5	0.0052	43	0.0082	0.005	1.3025	63.22	0.1223	10.65	173.07
1.6	0.0052	54	0.0089	0.005	1.2914	61.83	0.1207	10.70	174.35
1.6	0.0068	54	0.0089	0.005	1.2873	61.32	0.1190	10.81	177.18
2	0.0056	29	0.0097	0.005	1.2850	61.03	0.1108	11.59	197.18
2	0.0056	34	0.0097	0.005	1.2815	60.59	0.1104	11.60	197.43
2	0.0056	33	0.0097	0.005	1.2761	59.91	0.1099	11.61	197.69
2	0.0056	38	0.0097	0.005	1.2678	58.87	0.1086	11.67	199.23
2.3	0.0061	15	0.0089	0.005	1.2547	57.23	0.0962	13.04	234.36
2.4	0.0061	15	0.0089	0.005	1.2544	57.19	0.0925	13.56	247.69
2.4	0.0055	15	0.0089	0.005	1.1769	47.48	0.0859	13.69	251.02
2.4	0.0055	18	0.0097	0.005	1.1702	46.64	0.0854	13.70	251.28
		baseline			0.798		0.204	3.90	

Table A.5
All the Optimum cases of Pareto Front at 14° (unrestricted momentum coefficient).

F^+	C_μ	θ°	x/C	h/C	C_l	$C_l\%$	C_d	η	$\eta\%$
6.7	0.0985	15	0.0285	0.005	1.764	121	0.0966	18.24	367.69
6.8	0.098	15	0.0285	0.005	1.763	120.86	0.09625	18.31	369.48
4.7	0.0965	25	0.0285	0.005	1.750	119.32	0.09419	18.58	376.41
4.9	0.0965	25	0.0223	0.005	1.749	119.22	0.08777	19.93	411.02
6.7	0.0740	15	0.0276	0.005	1.706	113.79	0.08530	20.00	412.82
6.8	0.0645	15	0.0276	0.005	1.678	110.30	0.08091	20.74	431.79
6.7	0.0615	15	0.0276	0.005	1.668	109.06	0.07967	20.94	436.92
6.7	0.0565	15	0.0276	0.005	1.651	106.90	0.07748	21.31	446.41
7.4	0.0490	15	0.0285	0.005	1.624	103.48	0.07434	21.84	460
5.2	0.0390	15	0.0276	0.005	1.569	96.61	0.0717	21.86	460.5
		baseline			0.798		0.204	3.90	

References

[1] L.N. Cattafesta, M. Sheplak, Actuators for active flow control, *Annu Rev Fluid Mech* 43 (1) (2011) 247–272, doi:10.1146/annurev-fluid-122109-160634.

[2] L. Wang, F.-b. Tian, Numerical simulation of flow over a parallel cantilevered flag in the vicinity of a rigid wall, *Physical Review E* 99 (5) (2019), doi:10.1103/physreve.99.053111.

[3] Y.-C. Cho, W. Shyy, Adaptive flow control of low-reynolds number aerodynamics using dielectric barrier discharge actuator, *Prog. Aerosp. Sci.* 47 (7) (2011) 495–521, doi:10.1016/j.paerosci.2011.06.005.

[4] S. Foshat, Numerical investigation of the effects of plasma actuator on separated laminar flows past an incident plate under ground effect, *Aerosp. Sci. Technol.* 98 (2020) 105646, doi:10.1016/j.ast.2019.105646.

[5] N. Benard, E. Moreau, Electrical and mechanical characteristics of surface AC dielectric barrier discharge plasma actuators applied to airflow control, *Exp Fluids* 55 (11) (2014), doi:10.1007/s00348-014-1846-x.

[6] N. Benard, J. Pons-Prats, J. Periaux, G. Bugeada, P. Braud, J.P. Bonnet, E. Moreau, Turbulent separated shear flow control by surface plasma actuator: experimental optimization by genetic algorithm approach, *Exp Fluids* 57 (2) (2016), doi:10.1007/s00348-015-2107-3.

[7] M. Baghaei, J.M. Bergada, Analysis of the forces driving the oscillations in 3d fluidic oscillators, *Energies* 12 (24) (2019) 4720, doi:10.3390/en12244720.

[8] M. Baghaei, J.M. Bergada, Fluidic oscillators, the effect of some design modifications, *Applied Sciences* 10 (6) (2020) 2105, doi:10.3390/app10062105.

[9] Advances in effective flow separation control for aircraft drag reduction, N. Qin, J. Periaux, G. Bugeada (Eds.), Springer International Publishing, 2020, doi:10.1007/978-3-030-29688-9.

[10] A. Abbas, G. Bugeada, E. Ferrer, S. Fu, J. Periaux, J. Pons-Prats, E. Valero, Y. Zheng, Drag reduction via turbulent boundary layer flow control, *Science China Technological Sciences* 60 (9) (2017) 1281–1290.

[11] A. Glezer, M. Amitay, Synthetic jets, *Annu Rev Fluid Mech* 34 (1) (2002) 503–529.

[12] C. Rumsey, T. Gatski, W. Sellers, V. Vatsa, S. Viken, Summary of the 2004 CFD validation workshop on synthetic jets and turbulent separation control, in: 2nd AIAA Flow Control Conference, 2004, p. 2217.

[13] I. Wygnanski, The variables affecting the control of separation by periodic excitation, in: 2nd AIAA Flow Control Conference, 2004, p. 2505.

[14] N. Findanis, N.A. Ahmed, The interaction of an asymmetrical localised synthetic jet on a side-supported sphere, *J Fluids Struct* 24 (7) (2008) 1006–1020, doi:10.1016/j.jfluidstructs.2008.02.002.

[15] M.G. De Giorgi, C.G. De Luca, A. Ficarella, F. Marra, Comparison between synthetic jets and continuous jets for active flow control: application on a NACA 0015 and a compressor stator cascade, *Aerosp. Sci. Technol.* 43 (2015) 256–280, doi:10.1016/j.ast.2015.03.004.

[16] S. Traficante, M.G. De Giorgi, A. Ficarella, Flow separation control on a compressor-stator cascade using plasma actuators and synthetic and continuous jets, *J Aerosp Eng* 29 (3) (2016) 04015056.

[17] M.G. De Giorgi, S. Traficante, C. De Luca, D. Bello, A. Ficarella, Active flow control techniques on a stator compressor cascade: a comparison between synthetic jet and plasma actuators, in: *Turbo Expo: Power for Land, Sea, and Air*, volume 44748, American Society of Mechanical Engineers, 2012, pp. 439–450.

[18] H. Zhang, S. Chen, Y. Gong, S. Wang, A comparison of different unsteady flow control techniques in a highly loaded compressor cascade, *Proceedings of the Institution of Mechanical Engineers, Part G: Journal of Aerospace Engineering* 233 (6) (2019) 2051–2065.

[19] M. Amitay, D.R. Smith, V. Kibens, D.E. Parekh, A. Glezer, Aerodynamic flow control over an unconventional airfoil using synthetic jet actuators, *AIAA Journal* 39 (2001) 361–370, doi:10.2514/3.14740.

- [20] M. Amitay, A. Glezer, Role of actuation frequency in controlled flow reattachment over a stalled airfoil, *AIAA Journal* 40 (2002) 209–216, doi:[10.2514/3.15052](https://doi.org/10.2514/3.15052).
- [21] J.L. Gilarranz, L.W. Traub, O.K. Rediniotis, A new class of synthetic jet actuators—part i: design, fabrication and bench top characterization, *J Fluids Eng* 127 (2) (2005) 367–376, doi:[10.1115/1.1839931](https://doi.org/10.1115/1.1839931).
- [22] D. You, P. Moin, Active control of flow separation over an airfoil using synthetic jets, *J Fluids Struct* 24 (8) (2008) 1349–1357, doi:[10.1016/j.jfluidstructs.2008.06.017](https://doi.org/10.1016/j.jfluidstructs.2008.06.017).
- [23] A. Tuck, J. Soria, Separation control on a NACA 0015 airfoil using a 2d micro ZNMF jet, *Aircraft Engineering and Aerospace Technology* 80 (2) (2008) 175–180, doi:[10.1108/00022660810859391](https://doi.org/10.1108/00022660810859391).
- [24] V. Kitsios, L. Cordier, J.-P. Bonnet, A. Ooi, J. Soria, On the coherent structures and stability properties of a leading-edge separated aerofoil with turbulent recirculation, *J Fluid Mech* 683 (2011) 395–416, doi:[10.1017/jfm.2011.285](https://doi.org/10.1017/jfm.2011.285).
- [25] N.A. Buchmann, C. Atkinson, J. Soria, Influence of ZNMF jet flow control on the spatio-temporal flow structure over a NACA-0015 airfoil, *Exp Fluids* 54 (3) (2013), doi:[10.1007/s00348-013-1485-7](https://doi.org/10.1007/s00348-013-1485-7).
- [26] S.H. Kim, C. Kim, Separation control on NACA23012 using synthetic jet, *Aerosp. Sci. Technol.* 13 (4–5) (2009) 172–182, doi:[10.1016/j.ast.2008.11.001](https://doi.org/10.1016/j.ast.2008.11.001).
- [27] H.E. Monir, M. Tadjfar, A. Bakhtian, Tangential synthetic jets for separation control, *J Fluids Struct* 45 (2014) 50–65, doi:[10.1016/j.jfluidstructs.2013.11.011](https://doi.org/10.1016/j.jfluidstructs.2013.11.011).
- [28] S.D. Goodfellow, S. Yarusevych, P.E. Sullivan, Momentum coefficient as a parameter for aerodynamic flow control with synthetic jets, *AIAA Journal* 51 (3) (2013) 623–631, doi:[10.2514/1.j051935](https://doi.org/10.2514/1.j051935).
- [29] M.A. Feero, S.D. Goodfellow, P. Lavoie, P.E. Sullivan, Flow reattachment using synthetic jet actuation on a low-reynolds-number airfoil, *AIAA Journal* 53 (7) (2015) 2005–2014, doi:[10.2514/1.j053605](https://doi.org/10.2514/1.j053605).
- [30] M.A. Feero, P. Lavoie, P.E. Sullivan, Influence of synthetic jet location on active control of an airfoil at low reynolds number, *Exp Fluids* 58 (8) (2017), doi:[10.1007/s00348-017-2387-x](https://doi.org/10.1007/s00348-017-2387-x).
- [31] W. Zhang, R. Samtaney, A direct numerical simulation investigation of the synthetic jet frequency effects on separation control of low-re flow past an airfoil, *Physics of Fluids* 27 (5) (2015) 055101, doi:[10.1063/1.4919599](https://doi.org/10.1063/1.4919599).
- [32] I. Rodriguez, O. Lehmkuhl, R. Borrell, Effects of the actuation on the boundary layer of an airfoil at reynolds number $re = 60000$, *Flow, Turbulence and Combustion* 105 (2) (2020) 607–626, doi:[10.1007/s10494-020-00160-y](https://doi.org/10.1007/s10494-020-00160-y).
- [33] R. Duvigneau, M. Visonneau, Simulation and optimization of stall control for an airfoil with a synthetic jet, *Aerosp. Sci. Technol.* 10 (4) (2006) 279–287, doi:[10.1016/j.ast.2006.01.002](https://doi.org/10.1016/j.ast.2006.01.002).
- [34] V.J. Torczon, Multidirectional search: a direct search algorithm for parallel machines, Rice University, 1989 Ph.D. thesis. URL <https://hdl.handle.net/1911/16304>
- [35] R. Duvigneau, A. Hay, M. Visonneau, Optimal location of a synthetic jet on an airfoil for stall control, *J Fluids Eng* 129 (7) (2007) 825–833, doi:[10.1115/1.2742729](https://doi.org/10.1115/1.2742729).
- [36] D. Kamari, M. Tadjfar, A. Madadi, Optimization of SD7003 airfoil performance using TBL and CBL at low reynolds numbers, *Aerosp. Sci. Technol.* 79 (2018) 199–211.
- [37] M. Tadjfar, D. Kamari, Optimization of flow control parameters over SD7003 airfoil with synthetic jet actuator, *J Fluids Eng* 142 (2) (2020), doi:[10.1115/1.4044985](https://doi.org/10.1115/1.4044985).
- [38] M.S. Selig, J.F. Donovan, D.B. Fraser, *Airfoils at low speeds*, HA Stokely, 1989.
- [39] M. Selig, J.J. Guglielmo, A.P. Broeren, P. Giguere, Summary of low-speed airfoil data summary of low-speed airfoil data, Tech. rep., University of Illinois, 1995.
- [40] M. Galbraith, M. Visbal, Implicit large eddy simulation of low Reynolds number flow past the SD7003 airfoil, in: 46th AIAA Aerospace Sciences Meeting and Exhibit, American Institute of Aeronautics and Astronautics, 2008, p. 225, doi:[10.2514/6.2008-225](https://doi.org/10.2514/6.2008-225).
- [41] S. Burgmann, W. Schröder, Investigation of the vortex induced unsteadiness of a separation bubble via time-resolved and scanning PIV measurements, *Exp Fluids* 45 (4) (2008) 675.
- [42] W. Zhang, R. Hain, C.J. Kähler, Scanning PIV investigation of the laminar separation bubble on a SD7003 airfoil, *Exp Fluids* 45 (4) (2008) 725–743.
- [43] P. Catalano, R. Tognaccini, Turbulence modeling for low-reynolds-number flows, *AIAA Journal* 48 (8) (2010) 1673–1685, doi:[10.2514/1.j050067](https://doi.org/10.2514/1.j050067).
- [44] P. Catalano, R. Tognaccini, Rans analysis of the low-reynolds number flow around the sd7003 airfoil, *Aerosp. Sci. Technol.* 15 (8) (2011) 615–626.
- [45] W. Wang, S. Siouris, N. Qin, Hybrid RANS/LES for active flow control, *Aircraft Engineering and Aerospace Technology* 86 (3) (2014) 179–187, doi:[10.1108/aeat-01-2013-0012](https://doi.org/10.1108/aeat-01-2013-0012).
- [46] J.H. Ferziger, M. Perić, R.L. Street, *Computational methods for fluid dynamics, volume 3*, Springer, 2002.
- [47] P. Spalart, S. Allmaras, A one-equation turbulence model for aerodynamic flows, in: 30th aerospace sciences meeting and exhibit, 1992, p. 439, doi:[10.2514/6.1992-439](https://doi.org/10.2514/6.1992-439).
- [48] H.-P. Schwefel, *Numerical optimization of computer models*, John Wiley & Sons, Inc., USA, 1981.
- [49] D.G. Luenberger, Y. Ye, et al., *Linear and nonlinear programming, volume 2*, Springer, 1984, doi:[10.1007/978-3-319-18842-3](https://doi.org/10.1007/978-3-319-18842-3).
- [50] D.-S. Lee, J. Periaux, J. Pons-Prats, G. Bugeđa, E. Oñate, Double shock control bump design optimization using hybridised evolutionary algorithms, in: *Evolutionary Computation (CEC), 2010 IEEE Congress on*, IEEE, 2010, pp. 1–8, doi:[10.1109/cec.2010.5586379](https://doi.org/10.1109/cec.2010.5586379).
- [51] D.-S. Lee, J. Periaux, E. Onate, L.F. Gonzalez, N. Qin, Active transonic aerofoil design optimization using robust multiobjective evolutionary algorithms, *J Aircr* 48 (3) (2011) 1084–1094, doi:[10.2514/1.c031237](https://doi.org/10.2514/1.c031237).
- [52] D.S. Lee, L.F. Gonzalez, J. Periaux, G. Bugeđa, Double-shock control bump design optimization using hybridized evolutionary algorithms, *Proceedings of the Institution of Mechanical Engineers, Part G: Journal of Aerospace Engineering* 225 (10) (2011) 1175–1192, doi:[10.1177/0954410011406210](https://doi.org/10.1177/0954410011406210).
- [53] A. Kendall Atkinson, *An introduction to numerical analysis*, 1988.
- [54] D.E. Goldberg, *Genetic algorithms in search, optimization and machine learning*, Addison-Wesley, Reading, Massachusetts, 1989.
- [55] K. Deb, A. Pratap, T. Meyarivan, Constrained test problems for multi-objective evolutionary optimization, in: *Lecture Notes in Computer Science*, Springer Berlin Heidelberg, 2001, pp. 284–298.
- [56] D. Lee, L.F. Gonzalez, J. Periaux, K. Srinivas, E. Onate, Hybrid-game strategies for multi-objective design optimization in engineering, *Computers and Fluids* 47 (1) (2011) 189–204, doi:[10.1016/j.compfluid.2011.03.007](https://doi.org/10.1016/j.compfluid.2011.03.007).
- [57] D.-S. Lee, L.F. Gonzalez, J. Periaux, K. Srinivas, *Evolutionary Optimisation Methods with Uncertainty for Modern Multidisciplinary Design in Aeronautical Engineering*, in: *Notes on Numerical Fluid Mechanics and Multidisciplinary Design*, Springer Berlin Heidelberg, 2009, pp. 271–284.
- [58] D. Lee, L.F. Gonzalez, J. Periaux, K. Srinivas, Efficient hybrid-game strategies coupled to evolutionary algorithms for robust multidisciplinary design optimization in aerospace engineering, *IEEE Trans. Evol. Comput.* 15 (2) (2011) 133–150, doi:[10.1109/tevc.2010.2043364](https://doi.org/10.1109/tevc.2010.2043364).
- [59] R. Lopez, E. Oñate, A variational formulation for the multilayer perceptron, in: *Artificial Neural Networks – ICANN 2006*, Springer Berlin Heidelberg, 2006, pp. 159–168.
- [60] D.J.J. Toal, N.W. Bressloff, A.J. Keane, Kriging hyperparameter tuning strategies, *AIAA Journal* 46 (5) (2008) 1240–1252, doi:[10.2514/1.34822](https://doi.org/10.2514/1.34822).
- [61] D.J.J. Toal, A.J. Keane, Efficient multipoint aerodynamic design optimization via cokriging, *J Aircr* 48 (5) (2011) 1685–1695, doi:[10.2514/1.c031342](https://doi.org/10.2514/1.c031342).
- [62] K. Deb, A. Pratap, S. Agarwal, T. Meyarivan, A fast and elitist multiobjective genetic algorithm: NSGA-II, *IEEE Trans. Evol. Comput.* 6 (2) (2002) 182–197, doi:[10.1109/4235.996017](https://doi.org/10.1109/4235.996017).
- [63] J.H. Holland, *Adaptation in natural and artificial systems: An introductory analysis with applications to biology, control, and artificial intelligence*, MIT Press, Cambridge, Massachusetts, 1992.
- [64] D.E. Goldberg, J.H. Holland, Genetic algorithms and machine learning, *Mach Learn* 3 (1988) 95–99, doi:[10.1023/A:1022602019183](https://doi.org/10.1023/A:1022602019183).
- [65] K. Deb, R.B. Agrawal, Simulated binary crossover for continuous search space, *Complex systems* 9 (2) (1995) 115–148.
- [66] K. Deb, *Multi-objective optimization using evolutionary algorithms, volume 16*, John Wiley & Sons, Chichester, UK, 2001.



Large Eddy Simulation of optimal Synthetic Jet Actuation on a SD7003 airfoil in post-stall conditions

N.M. Tousei^a, J.M. Bergadà^a, F. Mellibovsky^{b,*}

^a Department of Fluid Mechanics, Universitat Politècnica de Catalunya, Barcelona, 08034, Spain

^b Department of Physics, Aerospace Engineering Division, Universitat Politècnica de Catalunya, Barcelona, 08034, Spain

ARTICLE INFO

Article history:

Received 1 December 2021
Received in revised form 27 May 2022
Accepted 1 June 2022
Available online 10 June 2022
Communicated by Cummings Russell

Keywords:

Active Flow Control
LES/RANS
Optimisation
Aerodynamic efficiency
Flow structure

ABSTRACT

Aerodynamic performances may be optimised by the appropriate tuning of Active Flow Control (AFC) parameters. For the first time, we couple Genetic Algorithms (GA) with an unsteady Reynolds-Averaged Navier-Stokes (RANS) solver using the Spalart-Allmaras (SA) turbulence model to maximise lift and aerodynamic efficiency of an airfoil in stall conditions [1], and then validate the resulting set of optimal Synthetic Jet Actuator (SJA) parameters against well-resolved three-dimensional Large Eddy Simulation (LES). The airfoil considered is the SD7003, at the Reynolds number $Re = 6 \times 10^4$ and the post-stall angle of attack $\alpha = 14^\circ$. We find that, although SA-RANS is not quite as accurate as LES, it can still predict macroscopic aggregates such as lift and drag coefficients, provided the free-stream turbulence is prescribed to reasonable values. The sensitivity to free-stream turbulence is found to be particularly critical for SJA cases. Baseline LES simulation agrees well with literature results, while RANS-SA would seem to remain a valid model to a certain degree. For optimally actuated cases, our LES simulation predicts far better performances than obtained by suboptimal SJA LES computations as reported by other authors [2] for the same airfoil, Re and α , which illustrates the applicability and effectiveness of the SJA optimisation technique applied, despite using the less accurate yet computationally faster SA-RANS. The flow topology and wake dynamics of baseline and SJA cases are thoroughly compared to elucidate the mechanism whereby aerodynamic performances are enhanced.

© 2022 The Author(s). Published by Elsevier Masson SAS. This is an open access article under the CC BY-NC-ND license (<http://creativecommons.org/licenses/by-nc-nd/4.0/>).

1. Introduction

Active Flow Control (AFC) may be applied to airfoils and wings to suppress or postpone flow separation thereby improving aerodynamic performance. One of the main advantages of AFC as compared to passive flow control is that no drag penalty is incurred in off-design conditions. AFC techniques usually fall in one of three different categories [3], namely moving body, plasma and fluidic actuation. Moving body actuators act on the geometry of the body to inject momentum into the flow [4]. Plasma actuators generate fast temporal response jets of ionised fluid by applying large electric potential differences [5–9]. Fluidic actuators (FA), which are by far the most common, inject/suck fluid to/from the boundary layer.

Among fluidic actuators, Synthetic Jet Actuators (SJA, sometimes also called Zero Net Mass Flow Actuators ZNMFA) are of particular interest because of their simplicity and demonstrated capability of suppressing flow separation [10–14]. For instance, SJAs have been shown more effective than Continuous Jet Actuators (CJA) at

comparable power input levels in improving the performances of a stator compressor cascade [15–19]. SJAs do not require an external fluid supply, since their zero net mass flux can be simply obtained with an oscillating membrane (or reciprocating piston) housed inside a tiny cavity just beneath the surface. The back and forth displacement of the membrane alternatively sucks low momentum fluid from the near-wall and injects the fluid back with increased momentum.

A large number of numerical and experimental studies involving SJA implementation on airfoils has been published over the last couple of decades. Most of the research focuses on assessing the combined effect of two SJA parameters, namely the actuation frequency f_j and the jet momentum coefficient C_{μ} . The former is nondimensionalised with the airfoil chord C and the free-stream velocity U_∞ following $f_j/(U_\infty/C)$, while the momentum coefficient is defined as $C_{\mu} = (\rho_j U_j^2 h_j \sin \theta_j)/(\rho_\infty U_\infty^2 C)$, with h_j the jet width, ρ_j and ρ_∞ the jet and far field fluid densities, respectively, U_j the maximum jet velocity and θ_j the jet inclination angle with respect to the surface.

One of the first experimental studies looking into the effect on flow separation over an unconventional symmetric airfoil of the momentum coefficient, frequency and position of a synthetic

* Corresponding author.

E-mail address: fernando.mellibovsky@upc.edu (F. Mellibovsky).

jet actuator was undertaken by Amitay et al. [19], Amitay and Glezer [20]. They found that placing the actuator close to the boundary layer separation point minimised the momentum coefficient required for flow reattachment. Actuating with frequencies of the same order of magnitude as the natural von Kármán vortex-shedding frequency ($f_j \sim f_{VK} \simeq 0.7U_\infty/C$) produced unsteady reattachment, while full flow reattachment could be obtained by actuating at about ten times the vortex-shedding frequency ($f_j/f_{VK} \sim \mathcal{O}(10)$).

The effect of SJA on a NACA0015 airfoil at $Re = 8.96 \times 10^5$ was studied experimentally by Gilarranz et al. [21] and numerically (using LES) by You and Moin [22]. In the experiments, while actuation was rather ineffective below $\alpha \leq 10^\circ$, its effectiveness was seen to largely improve at higher values of α , managing to push the stall angle of attack from $\alpha_s = 12^\circ$ to 18° . At $\alpha > 25^\circ$ the required actuation frequencies needed to obtain high lift coefficients were particularly large. Numerical simulations produced a 70% lift increase for SJA AFC parameters $C_\mu = 0.0123$, $f_j = 1.284U_\infty/C$ and $\theta_j = 30.2^\circ$ with respect to baseline. The same airfoil was experimentally analysed by Tuck and Soria [23] at the lower $Re = 3.9 \times 10^4$, and then simulated numerically via LES [24]. Maximum efficiency was obtained for SJA frequencies $f_j = 0.65U_\infty/C$ and 1.3 in the experiments, intermediate values being not quite so effective. The combination of $C_\mu = 0.0123$ momentum coefficient with the highest frequency delayed stall from $\alpha_s = 10^\circ$ for baseline to 18° . The numerical simulations revealed that the optimal frequencies coincided with the baseline shedding frequency (f_{VK}) and its first harmonic ($2f_{VK}$). The same particulars were observed again by Buchmann et al. [25] in their high-repetition-rate PIV experiments. Itsariyapinyo and Sharma [26] revisited the same airfoil at $Re = 1.1 \times 10^5$ with LES simulations of SJA acting tangentially to the surface precisely at the trailing edge. The lift coefficient was seen to increase linearly when raising the momentum coefficient up to a certain threshold, beyond which point further improvement slowed down and saturated.

Kim and Kim [27] applied flow separation control to a NACA23012 airfoil at $Re = 2.19 \times 10^6$ and $\alpha \in [6^\circ, 22^\circ]$ in 5 different slat/flap/jet configurations using the Reynolds-averaged Navier-Stokes (RANS) equations and the $k-\omega$ SST turbulence model. Low actuation frequencies were found the most adequate to the reduction of the large separated regions, while the jet momentum coefficients required were large. They proposed the implementation of multi-array/multi-location SJA to reduce the required jet velocity, a solution that was successful. The same airfoil and Reynolds number were addressed by Monir et al. [28] in two different configurations using RANS and the Spalart-Allmaras turbulence model. They found that while SJA actuation at $\theta_j = 43^\circ$ could improve aerodynamic efficiency substantially, tangential actuation was by far the optimum.

Experimental studies to evaluate the effects of SJA on separation control and wake topology on a NACA0025 airfoil at $Re = 10^5$ and $\alpha = 5^\circ$ were undertaken by Goodfellow et al. [29]. They noticed that momentum coefficient was the primary control parameter, and obtained up to 50% drag decrease with C_μ above a certain threshold. The same airfoil at the same Reynolds number was analysed by Feero et al. [30], but at the higher $\alpha = 10^\circ$. They reported that momentum coefficients required for flow reattachment were one order of magnitude lower for excitation frequencies about the vortex shedding frequency than for high frequencies. In a later study they considered the effects of jet location at the still larger $\alpha = 12^\circ$ [31]. Flow control was all the more effective by locating the jet slot in the vicinity of the natural separation point. Zhang and Samtaney [32] investigated the dependence of SJA efficacy on excitation frequency for a NACA0018 airfoil at $\alpha = 10^\circ$ and ultralow $Re = 1000$ using three-dimensional Direct Numerical Simulation (DNS). Three different frequencies were assessed

($f_j = 0.5U_\infty/C$, 1 and 4) and, although aerodynamic performances improved in all cases, $f_j = 1U_\infty/C$ was found the optimal.

As an airfoil specifically designed for low Reynolds number applications, the Selig-Donovan 7003 (SD7003) [33,34] has been recently investigated at $Re = 6 \times 10^4$ employing LES [35,36,2]. Breuer [35] tested several inlet turbulence intensities, ranging from nil to $Tu = 11\%$, at $\alpha = 4^\circ$ with the object of understanding its impact on the Laminar Separation Bubble (LSB). He concluded that high Tu values managed to reduce and even suppress the LSB, thereby enhancing aerodynamic performance. Freestream unsteadiness effects were also assessed by Qin et al. [36], this time by exploring different inlet velocity oscillation amplitudes and frequencies, at the same $\alpha = 4^\circ$. Flow separation was delayed and even suppressed during the acceleration phase, while the separation point progressed upstream towards the leading edge in the deceleration phase. Rodriguez et al. [2] applied SJA AFC to the SD7003 in their LES simulations at $\alpha = \{4^\circ, 11^\circ, 14^\circ\}$ and obtained an aerodynamic efficiency increase of up to $\Delta\eta/\eta = 124\%$ at the highest α , actuation being less effective at pre-stall angles of attack.

All research on SJA AFC application to airfoils discussed so far was limited to straightforward parametric explorations merely intended to elucidate the separate effects of the various actuation parameters on aerodynamic performance. There exist, however, a number of studies aiming at systematic optimisation. Duvingneau and Visonneau [37] optimised SJA non-dimensional frequency, velocity amplitude and injection angle on a NACA0015 airfoil at $Re = 8.96 \times 10^5$ and for a range of $\alpha \in [12^\circ, 24^\circ]$. To do so, they coupled their flow solver with an optimisation algorithm first developed by Torczon [38]. An optimum choice of the three SJA parameters produced a lift increase of 34% and a stall angle delay from $\alpha_s = 19^\circ$ to 22° . A study of SJA on a NACA0012 airfoil at $Re = 2 \times 10^6$ and $\alpha = \{18^\circ, 20^\circ\}$ followed shortly after that employed a derivative-free algorithm to find the optimal location for actuation [39]. The influence of jet location on lift was remarkable at $\alpha = 20^\circ$, with up to 57% increase, but not so noticeable at 18° .

Kamari et al. [40] optimised constant blowing and constant suction on the SD7003 airfoil at $Re = 6 \times 10^4$ by coupling Genetic Algorithms (GA) with Artificial Neural Networks (ANN) previously trained with a set of almost 45 CFD runs. Optimal constant suction was shown more effective. The same numerical methods were applied to the same airfoil, at the same Reynolds number and SJA parameters by Tadjfar and Kamari [41], but at $\alpha = 13^\circ$ and 16° and with two alternative injection configurations, namely tangent and normal to the airfoil surface. Aerodynamic efficiency was the objective/target function. Optimal tangent injection at $\alpha = 13^\circ$, produced an astonishing maximum aerodynamic efficiency increase of 591%.

Perhaps the latest, and possibly the most extensive, research in the field of AFC application to airfoils is the one undertaken by Tousi et al. [1]. Five SJA parameters were optimised in a coupled fashion for a SD7003 airfoil at $Re = 6 \times 10^4$ and several pre- and post-stall $\alpha = \{4^\circ, 6^\circ, 8^\circ, 14^\circ\}$ using GA and RANS. The key difference between Tadjfar and Kamari [41] and Tousi et al. [1] resides in the methodology employed. While the former used ANN to estimate most of the SJA AFC parameters, the latter based the entire optimisation process on precise RANS-CFD simulations with the Spalart-Allmaras (SA) turbulence model, which enhances the accuracy of the results at the cost of incurring a high computational burden. This is the first time, to the best of our knowledge, that genetic algorithms have been coupled with an unsteady RANS CFD solver with the aim of optimally tuning a set of SJA AFC parameters to maximise aerodynamic performances of an airfoil in stall conditions. The resulting optimals could not at the time undergo validation against experiments or well-resolved simulations,

nor were the flow mechanisms responsible for optimally enhancing aerodynamic performances examined in any detail.

The study presented here builds up on the optimal SJA AFC configurations found by Tousei et al. [1]. Their analysis implicitly relied on the dubious accuracy of RANS-SA simulations of massively detached wake flows and/or deploying SJA AFC. Literature recommendations as to the setup of computations in regards to the tuning of turbulence model parameters and the prescription of free-stream turbulent viscosity boundary conditions were blindly followed. Here we undertake the ensuing natural step and put the optimisation results thus obtained to the test. We analyse optimal SJA on the SD7003 at $Re = 6 \times 10^4$, at a single post-stall $\alpha = 14^\circ$, with accurate, well-resolved, 3D-LES computations. The object is two-fold. On one side, we evaluate the reliability of RANS-SA simulation in assessing SJA application to airfoils in post-stall conditions at moderate Reynolds numbers. On the other hand, we exploit the higher accuracy of LES simulation to better understand the physics behind SJA AFC application to the SD7003 airfoil.

A wealth of numerical and experimental data is available on the literature for the SD7003 airfoil (see, for example, [33,34,42–46]), which makes it a particularly convenient choice for the study of AFC. The SD7003 is a thin airfoil with a thickness-to-chord ratio $t/C = 8.5\%$ that is often employed in micro air vehicles (MAV) intended to fly at moderate Reynolds numbers. A LSB forms on the suction side at low Reynolds number, even for low to moderate values of α . The strong adverse pressure gradient existing beyond the suction peak on the upper surface causes the laminar boundary layer to detach, but separation is shortly followed by turbulent transition and this induces reattachment. The LSB drifts towards the leading edge and shrinks as α increases. Above a critical value of α , however, the reattachment ceases to occur and the recirculation region bursts and extends into the wake, which results in a sharp drop of lift and a dramatic surge of aerodynamic drag.

The remainder of the paper is structured as follows. The governing equations for LES and RANS-SA turbulence models are presented in §2. Section §3 is devoted to the computational domain, boundary conditions and grid assessment. The results and conclusions are presented in §4 and §5, respectively.

2. Governing equations and numerical modelling

The Navier-Stokes equations for an incompressible Newtonian fluid of density ρ and dynamic viscosity μ ($\nu \equiv \mu/\rho$ is the kinematic viscosity) read

$$\nabla \cdot \mathbf{u} = 0, \quad (1)$$

$$\rho \frac{\partial \mathbf{u}}{\partial t} + \rho(\mathbf{u} \cdot \nabla)\mathbf{u} = -\nabla p + \nabla \cdot (\mu \nabla \mathbf{u}). \quad (2)$$

The advection term can be expressed in conservation form by applying the vector calculus identity $(\mathbf{u} \cdot \nabla)\mathbf{u} = \nabla \cdot (\mathbf{u} \otimes \mathbf{u}) - (\nabla \cdot \mathbf{u})\mathbf{u}$, where \otimes denotes the outer product and the divergence term cancels out due to incompressibility. Taking the ensemble average of the Navier-Stokes equation or applying spatial filtering, yields

$$\nabla \cdot \bar{\mathbf{u}} = 0, \quad (3)$$

$$\rho \frac{\partial \bar{\mathbf{u}}}{\partial t} + \rho \nabla \cdot (\bar{\mathbf{u}} \otimes \bar{\mathbf{u}} + \overline{\mathbf{u}' \otimes \mathbf{u}'}) = -\nabla \bar{p} + \nabla \cdot (\mu \nabla \bar{\mathbf{u}}), \quad (4)$$

where the linear averaging/filtering operator commutes with all operators but the nonlinear term. Switching back to the non-conservation form of the ensemble averaged/filtered advective term following $\nabla \cdot (\bar{\mathbf{u}} \otimes \bar{\mathbf{u}}) = (\bar{\mathbf{u}} \cdot \nabla)\bar{\mathbf{u}} + (\nabla \cdot \bar{\mathbf{u}})\bar{\mathbf{u}}$ and rearranging terms, results in

$$\nabla \cdot \bar{\mathbf{u}} = 0, \quad (5)$$

$$\rho \frac{\partial \bar{\mathbf{u}}}{\partial t} + \rho(\bar{\mathbf{u}} \cdot \nabla)\bar{\mathbf{u}} = -\nabla \bar{p} + \nabla \cdot (\mu \nabla \bar{\mathbf{u}} - \rho \overline{\mathbf{u}' \otimes \mathbf{u}'}). \quad (6)$$

Here, $-\rho \overline{\mathbf{u}' \otimes \mathbf{u}'}$ is the Reynolds stress tensor, which must be modelled using a turbulence model for RANS or a subgrid scale (SGS) model in the case of LES. The turbulence models used in the present RANS and LES are the Spalart-Allmaras (SA) [47] and the Wall-Adapting Local Eddy-Viscosity (WALE) [48], respectively. The accuracy of the former was assessed as acceptable in an earlier study [1], but the choice of LES in the present study is based on its demonstrated capabilities in dealing with turbulent transition as well as unstructured grids [48]. The WALE model is based on a tensor invariant that reproduces correctly wall asymptotic behaviour.

Both turbulence models used by either of the CFD methods employed here approximate the Reynolds stress tensor using the Boussinesq hypothesis, which states that the deviatoric part of the tensor can be written as

$$-\overline{\mathbf{u}' \otimes \mathbf{u}'} - \frac{1}{3}(\nabla \cdot \mathbf{u})\mathbf{I} = -2\nu_t \mathbf{S}. \quad (7)$$

\mathbf{I} denotes the identity matrix, $\mathbf{S} = 1/2(\nabla \bar{\mathbf{u}} + \nabla(\bar{\mathbf{u}})^T)$ is the rate-of-strain tensor, and ν_t is the turbulent kinematic viscosity scalar field, which is the target of the so-called turbulent viscosity models.

The RANS SA model solves a single transport equation for a modified form of the turbulent kinetic viscosity $\tilde{\nu}$ that is the same with ν_t everywhere but in the near-wall region where viscosity effects dominate. Both turbulent viscosities are related by $\nu_t = \tilde{\nu} f_{\nu 1}$, where $f_{\nu 1} = \chi^3 / (\chi^3 + C_{\nu 1}^3)$, $\chi = \tilde{\nu} / \nu$ and $C_{\nu 1} = 7.1$. On the other hand, the LES WALE model, instead of solving a transport equation for ν_t , it models it via SGS, based on the following expression

$$\nu_t = \nu_{sgs} = (C_w \Delta)^2 \frac{(S^d : S^d)^{3/2}}{(\mathbf{S} : \mathbf{S})^{5/2} + (S^d : S^d)^{5/4}} \quad (8)$$

where $S^d = \frac{1}{2}[(\nabla \bar{\mathbf{u}})^2 + (\nabla(\bar{\mathbf{u}})^T)^2] - \frac{1}{3}(\nabla \cdot \bar{\mathbf{u}})^2 \mathbf{I}$ is the traceless symmetric part of the square of the velocity gradient tensor, $\Delta = \sqrt{\Delta x \Delta y \Delta z}$ is the cut-off width used for filtering the flow field, and Δx , Δy and Δz denote grid sizing along the three orthonormal coordinates. The sole parameter of the model has been set to $C_w = 0.325$, which is a standard choice [49,50]. For the RANS-SA optimisation simulations we initially set the free-stream turbulent viscosity to a very low value $\tilde{\nu} / \nu = 10^{-20}$ following Catalano and Tognaccini [51], who claimed that this was required to properly capture the LSB at low pre-stall α , only to find out at the end that the choice was not the most appropriate for post-stall actuated cases.

Numerical computations have been carried out using the OpenFOAM [52] computational fluid dynamics (CFD) solver, which is based on the finite volume method (FVM). LES has been implemented on an unstructured grid using the Linear-Upwind Stabilised Transport (LUST) [52] scheme in discretising the non-linear advective term. This scheme stabilises the solutions while retaining second-order accuracy. Second-order central-differences has been employed for the diffusive term, and an implicit second-order Backward Euler method has been chosen for evolving the equations in time. The pressure-velocity coupling problem has been tackled by the Pressure-Implicit algorithm with Splitting of Operators (PISO) [53]. The stopping criteria for both the pressure and velocity residuals was 10^{-6} .

For the RANS SA simulations, the same discretisation methods were used as for the preliminar optimisation study by Tousei et al. [1]. These were second order discretisation schemes for

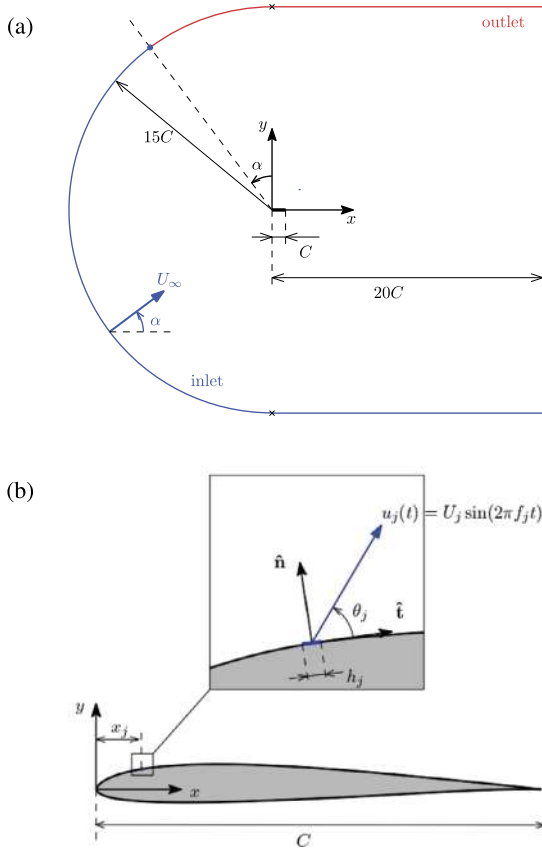


Fig. 1. (a) Computational domain. (b) Synthetic jet parameters. (For interpretation of the colours in the figure(s), the reader is referred to the web version of this article.)

all parameters, and the pressure-velocity coupling PISO scheme, which can cope with transient simulations as required. The averaged solutions presented in the results section, obtained from either LES or SA simulations, are all considered after all initial transients have been overcome.

Each one of the 360 RANS computations required about 84CPUh of supercomputing time at Marenostrum IV – Barcelona Supercomputing Centre, while LES cases consumed 660kCPUh apiece.

3. Domain, boundary conditions and mesh validation

For simplicity, the SD7003 chord length has been taken as $C = 1$ and the free-stream velocity as $U_\infty = 1$ so that the Reynolds number is simply set as $Re = U_\infty C / \nu = 1 / \nu = 6 \times 10^4$ and all simulation parameters (including time and space coordinates) and results are already non-dimensional with length and time-scales C and C / U_∞ , respectively. The computational domain used for both LES and RANS simulations is depicted in Fig. 1. The airfoil (thick black line) is placed with its chord line horizontal and its leading edge at the coordinate origin $(x, y, z) \equiv (0, 0, 0)$. The two-dimensional spanwise projection of the domain is delimited upstream by a half circle of radius $R = 15$ and centred at the origin, two horizontal lines above and below at $y = \pm 15$ and a vertical line downstream at $x = 20$. The angle of attack is prescribed by tilting the inlet velocity, so that the inlet (blue line) and outlet (red) boundaries are not coincident with the geometrical elements just described (Fig. 1a). For the 3D LES computations, a periodic span of 0.2 has been considered, as this size was shown sufficient for capturing the largest spanwise length scales of the flow at $\alpha = 14^\circ$ and $Re = 6 \times 10^4$ [42,2].

The usual boundary conditions have been applied. At inlet (blue line), a uniform velocity profile of free-stream velocity $U_\infty = 1$ and

tilt $\alpha = 14^\circ$ has been prescribed, along with zero normal pressure gradient ($\nabla p \cdot \hat{n} = 0$). At outlet, the roles of pressure and velocity are reversed, so that homogeneous Dirichlet boundary condition is used for pressure ($p = 0$) and homogeneous Neumann ($\nabla \mathbf{u} \cdot \hat{n} = \mathbf{0}$) for velocity. The airfoil surface is treated as an impermeable no-slip wall by setting both velocity ($\mathbf{u} = \mathbf{0}$) and the normal gradient of pressure to zero. On the upper surface of the airfoil, a short portion of length the jet slot width h is cut straight and switched to inlet-type boundary conditions at the jet location for the actuated cases. Here, the time-dependent jet velocity $u_j = U_j \sin(2\pi f_j t)$ is prescribed, with $2U_j$ the jet velocity amplitude and f_j the actuation frequency. The jet velocity is tilted at an angle θ_j with respect to the airfoil surface and the velocity profile simply taken as a top-hat function in the streamwise direction and uniform along the wing span. Homogeneous Neumann boundary conditions are used for pressure at the jet boundary. Finally, periodic boundary conditions are enforced to the lateral boundaries of the domain for three-dimensional simulations.

A sketch representing the synthetic jet design parameters is presented in Fig. 1b. These parameters are the jet location along the chord x_j , the jet width h_j , and the jet angle θ_j (with respect to the airfoil surface), frequency f_j , and momentum coefficient $C_\mu = (h_j \rho_j U_j^2 \sin \theta_j) / (C \rho U_\infty^2)$, with the jet fluid density $\rho_j = \rho = 1$ the same as free-stream density on account of incompressibility.

An unstructured computational grid, consisting of about 28.7 million control volumes has been employed for the LES unactuated baseline case. The mesh was highly refined around the airfoil and along the wake, but left to coarsen in the far-field, as shown in Fig. 2. For the actuated cases, cell count has been increased to nearly 30 million due to the higher grid resolution required to resolve the jet. The spanwise length has been discretised into 48 layers, as shown adequate by previous simulations for this same airfoil at the same Reynolds number and angle of attack [42].

According to Piomelli and Chasnov [54], the near-wall mesh resolution required for wall-resolved LES simulations involving mainly attached boundary layers is $\Delta x^+ = \mathcal{O}(50 - 150)$, $\Delta y^+ < 2$, and $\Delta z^+ = \mathcal{O}(15 - 40)$, where the $+$ superscript denotes wall units. The first cell layer thickness in wall units is $\Delta y^+ = y u_\tau / \nu$, where y is the dimensional normal distance to the wall, $u_\tau = \sqrt{\tau_w / \rho}$ is the friction velocity and τ_w the wall shear stress. Δx^+ and Δz^+ characterise the wall-grid spacing in the streamwise and spanwise directions, respectively, and are obtained from dimensional grid spacing in the same way as Δy^+ . The maximum Δx^+ , Δy^+ and Δz^+ on the upper surface of the airfoil are about 0.2, 0.5 and 18, respectively. The excess resolution in the streamwise wall-parallel direction could have been avoided by resolving the near-wall region with a structured mesh of prisms, which would have resulted in a lower cell count, but due to the massively separated nature of the baseline flow we deemed it prudent to keep cells short.

The resolved-to-total turbulent kinetic energy (TKE) ratio (k_{res} / k_{tot} where $k_{tot} = k_{res} + k_{sgs}$, the total kinetic energy, is the sum of the resolved and modelled parts) provides yet another means of assessing LES mesh quality. The resolved component of TKE is obtained from the velocity field fluctuations of the resolved scales as $k_{res} = (\langle u'u' \rangle + \langle v'v' \rangle + \langle w'w' \rangle) / 2$, whereas the modelled component is $k_{sgs} = \nu_{sgs} / C_k \Delta$. The model parameter was set to a standard $C_k = 0.094$, which combined with the also standard value for $C_\epsilon = 1.048$ results in the classic value for the Smagorinsky constant $C_s = C_k^3 / C_\epsilon = 0.1677$. Sound LES simulations should resolve at least 80% of TKE [55], and this is the case of our baseline simulation, as clearly shown in Fig. 3. The mesh was sufficiently fine to resolve above 95% of TKE in all cases, leaving less than 5% to the sub-grid scale model in the most critical regions, namely the proximal part of the shear layer after boundary layer separation.

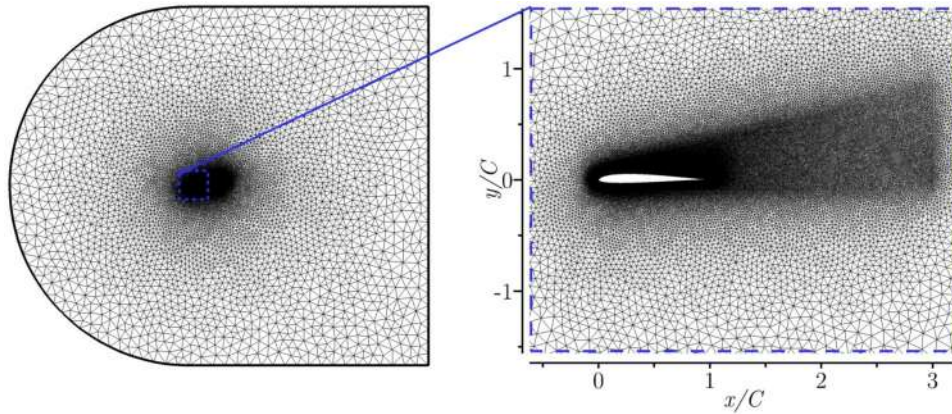


Fig. 2. An overview of LES baseline mesh along with a zoomed view of its near-wall and wake regions.

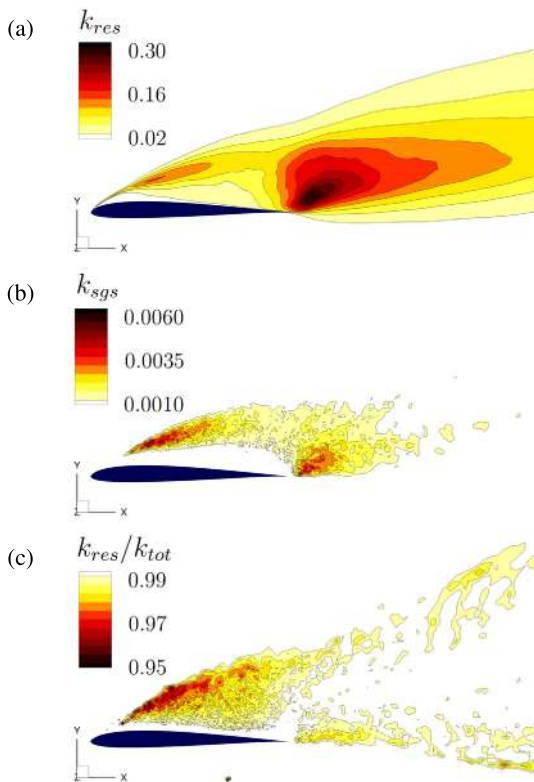


Fig. 3. Resolved k_{res} and b) modelled k_{sgs} parts of the turbulent kinetic energy (TKE). c) Resolved-to-total TKE ratio k_{sgs}/k_{tot} .

The Courant-Friedrichs-Levy number was limited to $CFL < 0.8$ by means of an adaptive time-stepper.

The mesh-independence and time-resolution analyses for the 2D RANS-SA simulations were performed and reported in an earlier study [1], concluding that a hybrid mesh of 45,466 cells and a time step $\Delta t = 2 \times 10^{-5}$ was sufficient to properly capture the flow dynamics and to resolve boundary layers down to the viscous sublayer. The mesh truncation error was estimated at about 0.01% (see table 1 of that paper).

The baseline LES case has been validated against the simulations by Rodriguez et al. [2] and Galbraith and Visbal [42], both corresponding to the same airfoil at the same Reynolds number and angle of attack. The former study employed LES on a grid of nearly 30 million nodes, while the latter used Implicit LES (ILES) on a more modest mesh of about 5.7 million grid points. The values of time-averaged lift (C_l) and drag (C_d) coefficients, along with aerodynamic efficiency ($\eta = C_l/C_d$) and the Strouhal number or

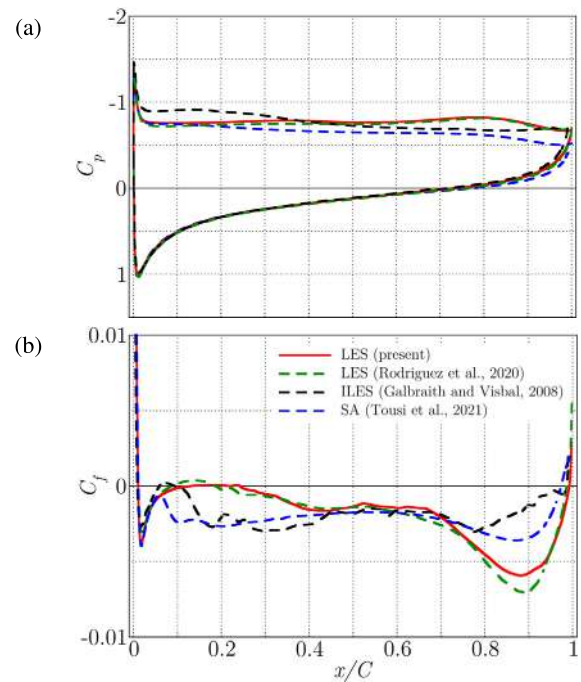


Fig. 4. Spanwise- and time-averaged chord distributions of (a) pressure C_p and (b) skin friction C_f coefficients along the SD7003 surface(s) at $Re = 6 \times 10^4$ and $\alpha = 14^\circ$. Shown are the present LES (solid red), the LES case by Rodriguez et al. [2] (dashed green), ILES by Galbraith and Visbal [42] (dashed black) and SA RANS by Tousi et al. [1] (dashed blue).

von Kármán frequency of vortex shedding (f_{vK}), are presented in Table 1. Current baseline simulation shows very good agreement with Rodriguez et al. [2] (within 1%) and a fairly good match with ILES simulations by Galbraith and Visbal [42]. The mesh and numerical approaches undertaken are sufficiently different that the mesh truncation error can be trusted to be contained within reported discrepancies for average aerodynamic performance parameters and, therefore, amount to less than 1%. RANS-SA results, however, tend to underestimate both aerodynamic force coefficients, particularly so C_d .

Aggregate quantities such as forces are always prone to misleading conclusions due to unnoticed compensation. Local quantities convey a better degree of appreciation as to whether the flow dynamics are being adequately captured. Fig. 4a depicts the chord distribution of the spanwise averaged pressure coefficient $C_p = (p - p_\infty)/(0.5\rho U_\infty^2)$ along both upper and lower surfaces. No apparent differences exist among the various simulations considered for the C_p distribution on the lower surface, except perhaps

Table 1

Literature review of the aerodynamic performances of the SD7003 airfoil at $Re = 6 \times 10^4$ and $\alpha = 14^\circ$. L_x , L_y and L_z are the domain size in the streamwise, cross-stream and spanwise directions, respectively, in units of C . N_{xy} and N_z are the in-plane and spanwise resolutions, and T the time-span of the simulations in C/U_∞ units.

	Domain	$L_x \times L_y$	L_z	N_{xy}	N_z	T	C_l	C_d	f_{vK}	η
LES FVM (Present)	C-grid	35×30	0.2	597,916	48	35	0.895	0.239	0.69	3.744
LES FEM [2]	H-grid	15×16	0.2	467,812	64	65	0.886	0.238	-	3.726
ILES FDM [42]	O-grid	30×30	0.2	47,565	101	15	0.875	0.221	-	3.960
2D-RANS-SA [1]	C-grid	35×30	-	45,466	-	60	0.798	0.204	-	3.911

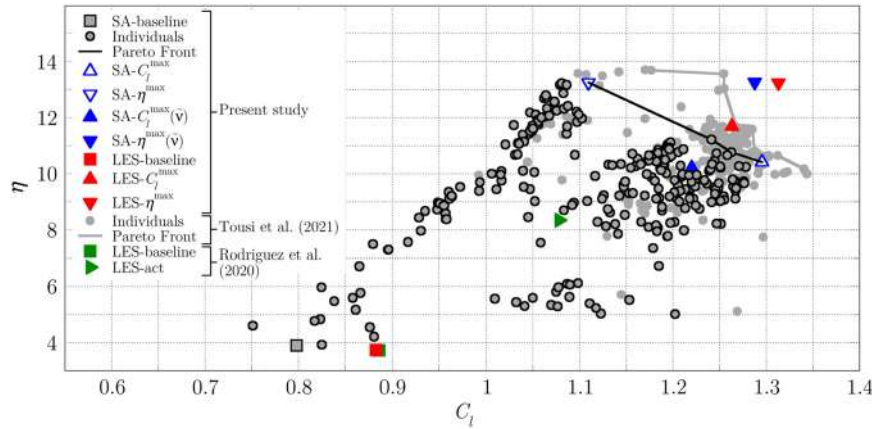


Fig. 5. Optimisation procedure and optimal cases in objective function space (C_l , η).

very slightly in the vicinity of the trailing edge. On the upper surface, the match between present results and Rodriguez et al. [2] is remarkably accomplished, while the ILES of Galbraith and Visbal [42] and the 2D RANS-SA by Tousei et al. [1] are fair but not excellent due to the less precise computational methods employed and the coarser grids. The aforementioned compensation effect is clear for the simulation by Galbraith and Visbal [42], which clearly transfers some lift from the back of the airfoil to the front. The resulting C_l is about the same obtained in the LES simulations, but at the cost of a nose-up shift of the pitching moment coefficient C_m . The skin friction coefficient $C_f = \tau_w/0.5\rho U_\infty^2$ again shows a fair agreement with Rodriguez et al. [2]. The boundary layer separation on the upper surface is, on average, located at $x_{sep} \approx 0.011$, and is also fairly well predicted by ILES and RANS-SA simulations, although downstream from the separation point these present noticeable discrepancies with respect to the two LES simulations. This may challenge the alleged capabilities of RANS-SA to properly reproduce highly separated flows, at least from a quantitative point of view, but since actuation is intended to reduce or even suppress separation, the method might still work acceptably for actuated cases.

4. Results

An optimisation procedure was employed by Tousei et al. [1] to determine optimal SJA parameters in terms of maximising both C_l and η . The set of five SJA parameters, the design variables of the optimisation problem, comprises the actuation frequency f_j , the jet inclination angle with respect to the airfoil surface θ_j , the slot streamwise location measured from the airfoil leading edge x_j , the jet slot width h_j and the jet momentum coefficient $C_\mu \equiv (\rho_j U_j^2 h_j \sin \theta_j)/(\rho_\infty U_\infty^2 C)$. The method coupled a scripted mesh generator (GMSH [56]), a CFD package (OpenFOAM) and a Genetic Algorithm (GA). The GA population size was set to 20 individuals (each one consisting in a CFD case with a different set of prescribed SJA parameters) per generation/iteration, which was considered a reasonable trade-off between method performance and computational cost. The first generation was initialised with a

random set of individuals, and all CFD cases run. The two objective functions, C_l and η , were obtained for each of the simulations and passed onto the GA optimiser, where the *Selection*, *Crossover* and *Mutation* operators were applied to produce a new set of values for the five SJA parameters defining the individuals for the next generation. The Selection phase employed a $\mu + \lambda$ strategy with a *Crowded-Comparison Operator* [57]. Simulated Binary Crossover (SBX) [58] (with a probability of 0.9) and Polynomial Mutation [59] (with a probability of 0.1) were adopted for the Crossover and Mutation phases, respectively. This process was repeated until having completed 18 generations (360 CFD simulations), the overall improvement being found marginal after the sixteenth generation. For a detailed account of the optimisation method used, we refer the reader to Tousei et al. [1]. Each additional individual requires a full CFD simulation, such that aspiring to be overly accurate results in unfeasible optimisation time spans. For this reason, a compromise was done by using two-dimensional RANS simulations with the Spalart-Allmaras model.

Fig. 5 presents a summary of the results obtained along the optimisation process, as seen in objective function space. The 2D RANS-SA baseline case (grey-filled black square) starts at low values of both C_l and η . Actuated cases (grey-filled black circles corresponding to the 360 cases run) progressively move to higher lift coefficient and aerodynamic efficiency values to finally delineate a multi-objective Pareto front (black line) with optimum C_l (up-pointing empty blue triangle) and maximum η (down-pointing empty blue triangle). The optimisation was run further by Tousei et al. [1] by increasing the initial set of 360 cases with an additional 240 runs thus reaching a final population of up to 600 individuals (grey circles and grey line for the second Pareto front), but the final results were still not available by the time the present study began, and the further refinement obtained was anyway expected to be within the accuracy limits of RANS-SA. The LES baseline case (red square), as for Rodriguez et al. [2] (green square), has a larger C_l than the 2D RANS-SA case, as already pointed out, so that it is to be expected that some discrepancies might be encountered when switching from RANS-SA to LES for the optimally actuated cases. In any case, the LES non-optimised actuated case

Table 2

Baseline case, and optimal SJA actuation cases corresponding to maximum lift C_l^{\max} and maximum aerodynamic efficiency η^{\max} . The values of the five actuation parameters (jet frequency f_j , jet momentum coefficient C_μ , jet inclination angle with respect to the airfoil surface θ_j , jet streamwise location from leading edge x_j and jet slot width h_j) are listed alongside the resulting aerodynamic performances.

	SJA parameters					Aerodynamic performance parameters				
	f_j	C_μ	θ_j (°)	x_j	h_j	C_l	C_d	η	$\Delta C_l/C_l$	$\Delta \eta/\eta$
Baseline										
SA [1]						0.798	0.204	3.91		
LES (present)						0.895	0.239	3.74		
LES [2]						0.886	0.238	3.72		
Actuated										
SA- C_l^{\max}	1.6	0.0053	53	0.0097	0.005	1.295	0.129	10.42	+62.3%	+157.4%
SA- $C_l^{\max}(\tilde{\nu})$						1.220	0.1194	10.21	+52.9%	+161.1%
LES- C_l^{\max}						1.263	0.108	11.69	+41.1%	+212.5%
SA- η^{\max}	2.6	0.0055	18	0.0089	0.005	1.109	0.083	13.25	+31.1%	+239.7%
SA- $\eta^{\max}(\tilde{\nu})$						1.288	0.097	13.27	+61.4%	+239.4%
LES- η^{\max}						1.313	0.094	13.96	+46.7%	+273.2%
LES-[2]	1.0	0.0030	90	0.0070	0.007	1.078	0.129	08.35	+21.6%	+124.4%

run by Rodriguez et al. [2] (green triangle) falls largely short of the results expected from the optimisation.

The optimum SJA parameters at either end of the Pareto Front, corresponding to cases SA- C_l^{\max} and SA- η^{\max} , and the resulting aerodynamic performances are presented in Table 2. The case featuring maximum lift achieved a considerable improvement $\Delta C_l/C_l = 62.3\%$ with respect to baseline. Beside improving lift, this actuation setup also enhances aerodynamic efficiency by $\Delta \eta/\eta = 157.4\%$. Meanwhile, the maximum aerodynamic efficiency case boosted it by an impressive $\Delta \eta/\eta = 239.7\%$, retaining still an appreciable $\Delta C_l/C_l = 31.1\%$ increase in lift. Three of the SJA parameters, namely $C_\mu \simeq 0.005$, $x_j \simeq 0.009$ (just upstream of the separation point) and $h_j \simeq 0.005$, take essentially the same value for the two optimal cases considered. The main differences concern the actuation frequency f_j and injection angle θ_j . Maximum efficiency is obtained by actuating almost tangentially with $\theta_j = 18^\circ$ at frequency $f_j = 2.6$, while maximum lift requires larger actuation angle $\theta_j = 53^\circ$ and lower frequency $f_j = 1.6$.

Since the optimally actuated RANS-SA cases might be afflicted by the same shortcomings that plague the baseline run, two LES simulations at the same optimal set of actuation parameters were also undertaken. The results are indicated in Fig. 5 (up-pointing and down-pointing red triangles for the C_l^{\max} and η^{\max} cases, respectively) and accordingly listed in Table 2. While both LES simulations outperformed amply the unoptimised actuated case by Rodriguez et al. [2], the results notably differ from the 2D RANS-SA estimation. While the maximum lift case produced slightly lower C_l and somewhat higher η , the maximum aerodynamic efficiency case yielded remarkably higher C_l without notably modifying η . As a result, the latter case became at once optimal in terms of both C_l and η .

It must be born in mind that optimisation techniques for non-linear problems, GA being no exception, provide no guarantee that the best SJA configuration found is indeed optimal, let alone the absolute optimum. The configurations selected here as *optimal* are thus tagged in the weaker sense that nearly doubling the GA population of RANS-SA individuals did not produce better aerodynamic performances [1] than those obtained here for the two LES cases tested and, more importantly, that the well-resolved simulations widely outperformed available sub-optimal results for the same airfoil and flight conditions.

The discrepancies between 2D RANS-SA and LES simulations, also for the actuated cases, dispute the applicability of the former to low Reynolds number aerodynamics past airfoils at post-stall conditions, even in situations for which boundary layers remain attached through the action of SJA. RANS is specifically designed for

turbulent flow conditions, and performs reasonably provided the model parameters are appropriately tuned. Some models can deal with laminar-turbulent transition, but their reliability is largely dependent on parameter tuning. In the case of the SA turbulence model, this sensitivity extends crucially to the free-stream boundary conditions for the unique turbulent field $\tilde{\nu}$. Following Catalano and Tognaccini [45,51], which states that free-stream turbulent viscosity must be sufficiently low so as to properly capture the LSB at pre-stall α , we set $\tilde{\nu}/\nu = 10^{-20}$ for the SJA optimisation RANS simulations. As it happens, the optimisation process was run in post-stall conditions and with a time-dependent fluidic actuation that crucially acts on the LSB. Such a low turbulent viscosity might be artificially stabilising the laminar flow region and thus inducing wrong results. To check sensitivity to free-stream preturbulence levels, the baseline, maximum lift and maximum aerodynamic efficiency cases were run for a wide range $\tilde{\nu}/\nu \in [10^{-20}, 10^2]$. The results are presented in Fig. 6. Unrealistically high free-stream turbulent viscosity of the order of the fluid viscosity and above ($\tilde{\nu}/\nu \geq 1$) produces unphysical results and must be discarded. At the low-values end of the range, RANS-SA results (blue lines) are fairly stable but diverge considerably from LES (red horizontal lines). Not much is gained at intermediate levels of $\tilde{\nu}/\nu$ for the baseline case, which produces pretty stable but wrong C_l and C_d values all along. The actuated cases, however, traverse a regime $\tilde{\nu}/\nu \in [10^{-6}, 10^{-3}]$ with RANS-SA C_l and C_d values decently close to LES results. The aerodynamic performance of the maximum lift and maximum aerodynamic efficiency cases for $\tilde{\nu}/\nu = 10^{-5}$ are shown in Fig. 5 (filled blue symbols) and listed in Table 2 as SA- $C_l^{\max}(\tilde{\nu})$ and SA- $\eta^{\max}(\tilde{\nu})$, respectively. If not quite on top of the LES results, they at least are much closer and clearly align with the trend. The deviation from the original RANS-SA optimals as obtained from a reduced population of 360 individuals serves as an *a-posteriori* justification for not having waited for the completion of the 600 runs before starting the two *optimal* LES cases. It is clear enough that the error incurred by using RANS-SA in the optimisation process is sufficiently large and unsystematic to consider both Pareto fronts, the preliminar and the refined, as not significantly distinct. The reason for this better agreement between RANS-SA and LES at intermediate values of the free-stream turbulent viscosity, only for actuated cases, remains a mystery. Unfortunately, the apparent improvement of the RANS-SA model with a more appropriate choice for $\tilde{\nu}$ was not known at the time the optimisation process was run and it was later thought inexpedient, on cost-benefit grounds, to re-run it anew. Besides, there is no guarantee that this same value of $\tilde{\nu}/\nu$ will produce accurate results at other post-stall flight regimes or under different SJA operat-

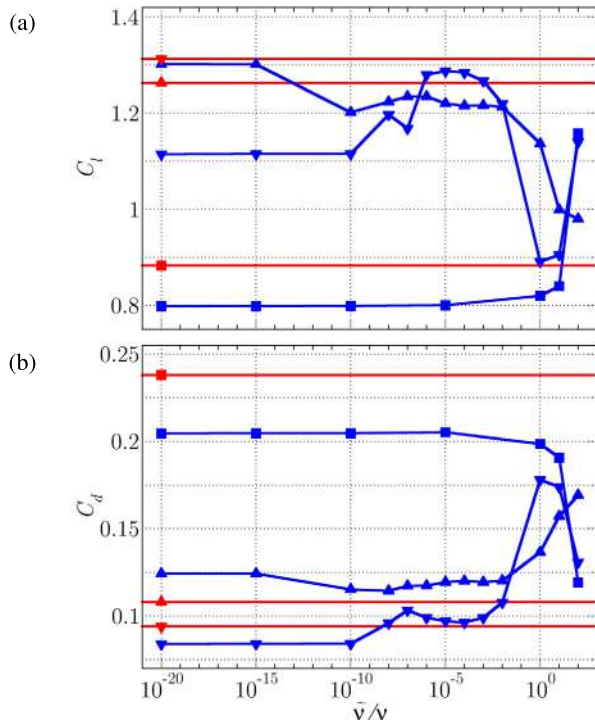


Fig. 6. Results sensitivity to free-stream preturbulence levels as prescribed by \tilde{v}/ν . (a) Average lift coefficient C_l . (b) Average drag coefficient C_d . Baseline (squares), maximum lift (up-pointing triangles) and maximum aerodynamic efficiency (down-pointing triangles) SJA setups are shown for both RANS-SA (blue) and LES (red) computations.

ing conditions. A thorough parametric exploration, far beyond the scope of this study, will be required to cast light on the issue. Breuer [35] observed that high inlet turbulent intensities tend to reduce and even suppress the LSB on the upper surface of the unactuated airfoil. This would explain the sharp drop of C_d and the surge of C_l we observe for the baseline case when high values of \tilde{v} are prescribed at inlet. The LSB shrinks and vanishes and the airfoil performs as in pre-stall conditions on account of the turbulent boundary layer and the delay in its separation. For actuated cases, too high free-stream \tilde{v} over-rides the SJA capabilities and the airfoil behaves much as in the baseline case, all the more so for maximum efficiency SJA.

In the remaining of the manuscript, RANS-SA optimal cases have been considered for $\tilde{v}/\nu = 10^{-5}$ instead of the original runs used for optimisation. Furthermore, since the maximum aerodynamic efficiency case outperforms the maximum lift case in all respects when assessed with these new RANS-SA or LES simulations, only the corresponding set of SJA parameter values will be considered further, as an absolute optimum.

4.1. RANS-SA vs LES comparison of optimally actuated cases

The pressure and skin friction coefficient distributions along the upper and lower surfaces corresponding to the maximum efficiency SJA set of parameters are plotted in Fig. 7 alongside baseline LES results (dashed red line). As expected, SJA manages to reattach the flow over a large portion of the upper surface. The separation point, identified by $C_f = 0$, is retarded for all three actuated simulations, LES- η^{\max} (solid red), SA- $\eta^{\max}(\tilde{v})$ (solid blue) and the sub-optimal LES-act case by Rodriguez et al. [2] (dash-dotted green), with respect to baseline (dashed red line). The separation bubble, though, is short and reattachment is effected shortly behind the jet location. The reattachment contributes to slightly increasing the pressure on the lower surface and, more notably, to enhancing the

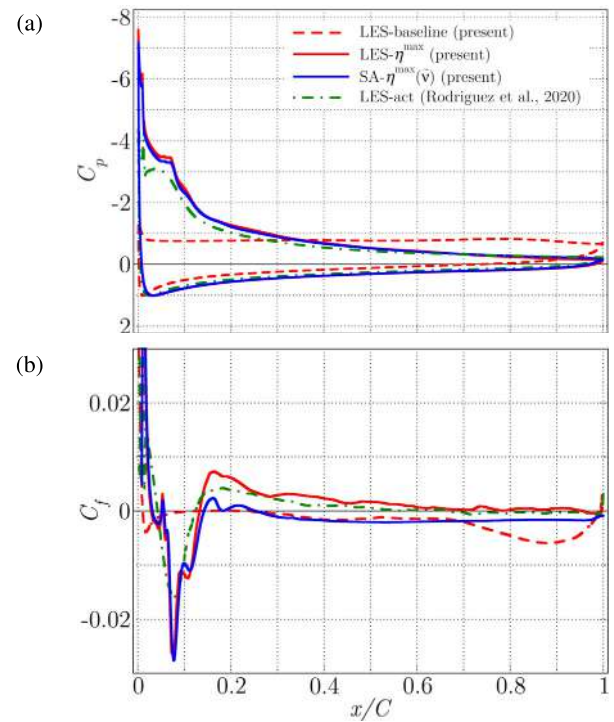


Fig. 7. Optimal SJA vs baseline (a) Pressure C_p and (b) skin friction C_f coefficient distributions. Shown are the LES-baseline (dashed red), the LES- η^{\max} (solid red), RANS SA- $\eta^{\max}(\tilde{v})$ (solid blue) and sub-optimal actuated LES-act case by Rodriguez et al. [2] (dash-dotted green).

suction effect on the upper surface, particularly so along the front half of the airfoil. Suction on the back half is reduced but the net effect is that of a lift increase and a sharp pressure drag reduction. All three SJA cases show similar features. In particular, the SA- $\eta^{\max}(\tilde{v})$ and LES- η^{\max} computations, run with the same SJA parameter values, present very similar pressure distributions, which indicates that the main flow features are being appropriately dealt with also by the less accurate RANS-SA model when free-stream turbulent viscosity is appropriately prescribed to a moderate realistic value. The sub-optimal LES-act produces less suction in the front part of the upper surface and therefore lower lift, as a result of its being suboptimal. Friction distributions are very similar for the LES- η^{\max} and LES-act cases except around the actuation location, where the different actuation parameters produce very different local outcomes. The SA- $\eta^{\max}(\tilde{v})$ reproduces quite accurately the behaviour of C_f in the front part of the airfoil, as comparison with the LES- η^{\max} simulation avows, but the reattachment is not properly fulfilled and the friction remains negative over most of the upper surface when it should in reality be small but positive and decisively contribute to friction drag. The effect on total net drag is however not noticeable, as form drag largely dominates. All in all, 2D RANS-SA simulation seems an appropriate cost-effective tool for extensive optimisation of SJA parameters provided an adequate amount of turbulent viscosity is allowed at the inlet of the domain, and final optimal results are further refined with LES (or DNS if feasible).

Fig. 8 shows colourmaps of the $\langle u'v' \rangle$ component of the Reynolds stress tensor along with a collection of time- and spanwise-averaged streamlines for the baseline and maximum aerodynamic efficiency actuated cases. The baseline separation bubble exhibits similar topologies for the LES-baseline and RANS-SA-baseline simulations. The dynamical behaviour, as represented by $\langle u'v' \rangle$, is however quite different. Streamwise-cross-stream cross-correlation is evenly distributed along the shear layer bounding the separation bubble at the top for RANS-SA-baseline, while

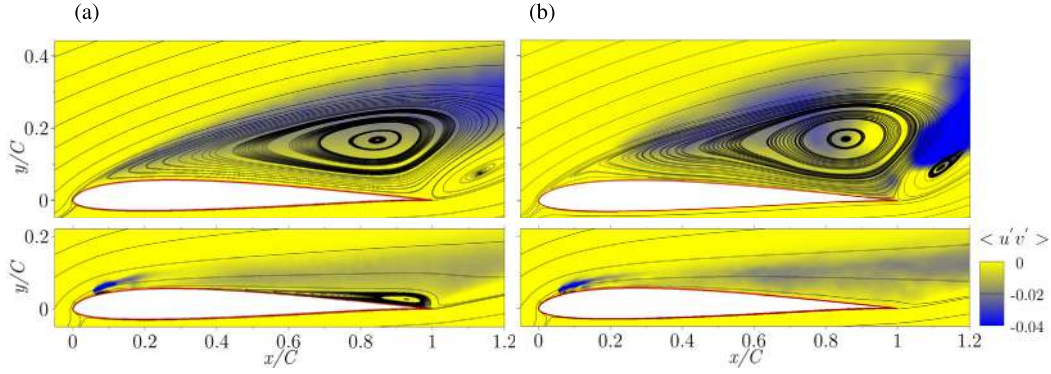


Fig. 8. Spanwise-averaged $\langle u'v' \rangle$ component of the Reynolds stress tensor and time- and spanwise-averaged streamlines. (a) RANS-SA-baseline (top) and RANS-SA- $\eta^{\max}(\bar{v})$ (bottom). (b) LES-baseline (top) and LES- η^{\max} (bottom).

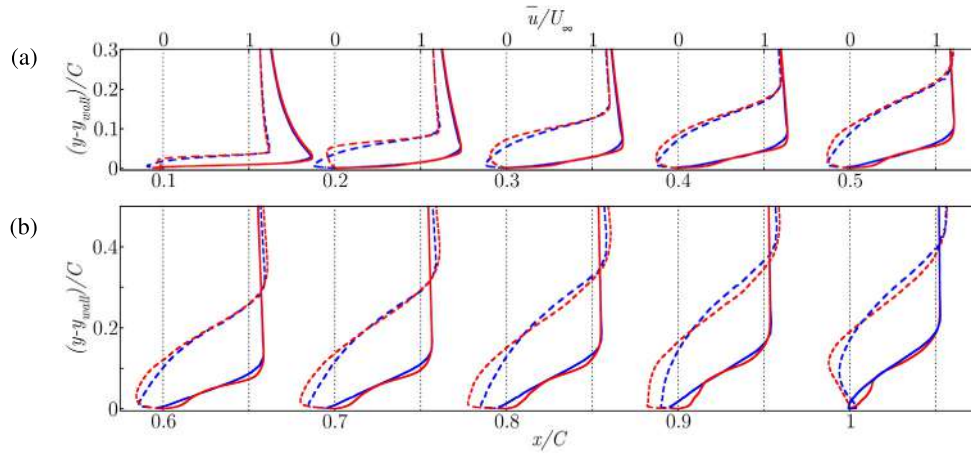


Fig. 9. Evolution of the upper-surface boundary layer along the airfoil. Time- and spanwise-averaged streamwise velocity profiles $\langle u(x, y, z; t) \rangle_{t,z}$ at streamwise coordinates (a) $x/C = 0.1$ through $x/C = 0.5$ and (b) $x/C = 0.6$ through $x/C = 1$, as a function of wall-normal distance. Shown are the baseline (dashed) and actuated (solid) cases, for both LES (red) and RANS-SA (blue) simulations. The actuated cases are LES- η^{\max} and SA- $\eta^{\max}(\bar{v})$.

it is much more concentrated in the vortex formation region at the back of the airfoil for LES-baseline. The RANS-SA model is not expected to behave particularly well in post-stall conditions. Once actuation is switched on, the quality of RANS-SA results improves remarkably. The RANS-SA- $\eta^{\max}(\bar{v})$ and LES- η^{\max} cases display a very similar distribution of $\langle u'v' \rangle$. These are particularly high in the region of the jet as it bends downstream, blown by the incoming flow. Also streamlines reveal a fairly comparable pattern, except that RANS-SA does not manage to completely suppress the separation bubble and a narrow but relatively long recirculation region extends on the upper surface from the trailing edge upstream. The boundary layer is therefore attached for LES but not for RANS-SA. However, the effects on the pressure distribution are not large, and although the friction on the aft portion of the upper surface differs notably, the net lift and drag, which are pressure dominated, do not suffer exceedingly from the inaccuracies incurred by the RANS-SA model.

To clarify the evolution of the boundary layer along the upper surface of the airfoil, the time- and span-averaged velocity profiles are presented in Fig. 9 at several streamwise locations. The baseline case (dashed lines) has the boundary layer already separated at $x = 0.1$, as clear from the reverse flow in the close proximity of the wall. The LES simulation (red), however, features lower recirculation velocity than the RANS-SA computation (blue), but spread over a wider cross-section. The peak of reverse flow is indeed located further from the wall for LES. These differences between the two methods region remain as the separated cross-section widens downstream all the way down to $x = 0.5$, beyond which point RANS-SA starts underpredicting negative streamwise velocity with

respect to LES. Maximum aerodynamic efficiency actuation (solid lines) suppresses separation, notably at $x = 0.2$ and beyond. The reattached boundary layer is very similar for LES and RANS-SA, an indication that the latter method is properly capturing the effects of SJA. The match is very good for $x \leq 0.2$ and gradually deteriorates downstream. Nonetheless, agreement remains acceptable in all respects except for the slight flow reversal RANS-SA predicts in the immediate proximity of the wall over most of the upper surface.

To better characterise the boundary layer in terms of the viscous blockage, the displacement (δ_1) and momentum (δ_2) thicknesses help quantify the near-wall mass-flow and momentum deficits resulting from the effects of viscosity. These are computed following

$$\delta_1 = \int_0^\delta \left(1 - \frac{\hat{u}}{\hat{u}_e}\right) d\hat{y}, \quad (9)$$

$$\delta_2 = \int_0^\delta \frac{\hat{u}}{\hat{u}_e} \left(1 - \frac{\hat{u}}{\hat{u}_e}\right) d\hat{y}, \quad (10)$$

where \hat{y} is the local wall-normal coordinate, \hat{u} the streamwise (wall-parallel) velocity component, \hat{u}_e its value at the boundary layer edge, and δ the boundary layer thickness, formally infinite but in practice the wall-normal distance required to reach the virtually inviscid flow region. As boundary layer thickness we have used $\delta = \delta_\tau$, defined as the wall-normal distance where the shear

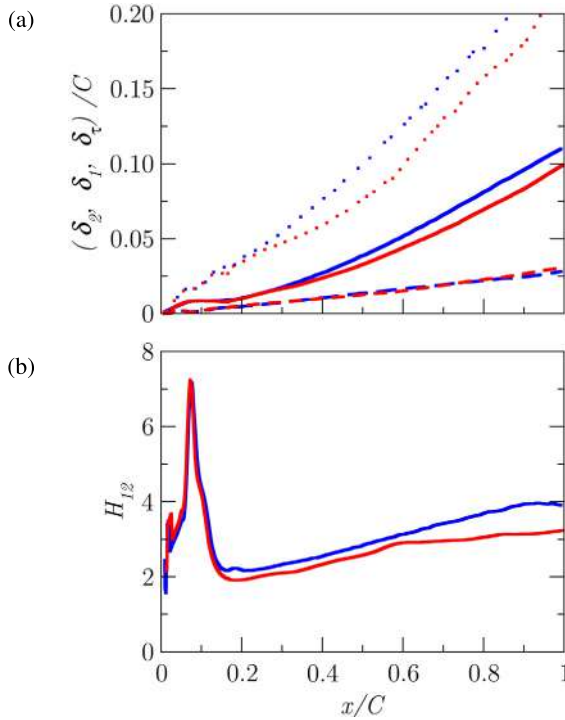


Fig. 10. Evolution of boundary layer characteristic properties along the upper surface of the airfoil for actuated cases LES- η^{\max} (red lines) and RANS-SA- η^{\max} (\bar{v}) (blue). (a) Boundary layer (δ_τ , dotted), displacement (δ_1 , solid), and momentum (δ_2 dashed) thicknesses. (b) Shape factor H .

$\|\tau\|$ is seen to decay a 95% with respect to the maximum value recorded on the airfoil surface τ_w^{\max} ($\|\tau\| < 0.05\tau_w^{\max}$). The evolution of δ_τ , δ_1 , δ_2 and the shape factor $H \equiv \delta_1/\delta_2$ along the upper surface is shown in Fig. 10 for both the LES- η^{\max} and RANS-SA- η^{\max} (\bar{v}) cases. All three thicknesses grow steadily along the chord but are much reduced in relation to baseline (not shown in the figure) following the suppression of boundary layer separation. RANS-SA slightly overestimates δ_1 over the aft half of the airfoil and underestimates δ_2 on the last third. As a result, shape factor is larger in this region for the RANS-SA simulation than for LES. The separation bubble visible in Fig. 8 must be held responsible for the discrepancies. It is also interesting to observe that both actuated cases show particularly large Reynolds stresses values at the injection/suction zone, Reynolds stresses are also observed along the airfoil upper surface especially in the LES- $\max\eta$ case. This fact explains why the boundary layer remains reattached under these conditions.

4.2. Baseline vs optimally actuated case comparison

The three LES simulations for baseline, (allegedly) maximum lift and maximum aerodynamic efficiency cases have been minutely analysed to elucidate the flow mechanism whereby SJA attains enhanced aerodynamic performances at post-stall angles of attack. In order to characterise the time dependence of the flow, five probe arrays were deployed in the flow field as indicated in Fig. 11a. All five probe lines are located in regions where high fluctuation levels are expected, as indicated by the high values of $\langle u'v' \rangle$. Three are distributed along the shear layer resulting from the early separation of the boundary layer, and the remaining two in the very near wake region. The streamwise ($u_{(x,y)}(z, t)$) velocity signal along spanwise probe arrays P_2 (within the shear layer at $(x,y)=(0.098,0.08)$, grey lines) and P_5 (in the near wake at $(x,y)=(1.1,0.08)$, black) have been Fourier-transformed to obtain the Power Spectral Density (PSD) $|\hat{u}_{(x,y)}(z, f)|$ and then spanwise

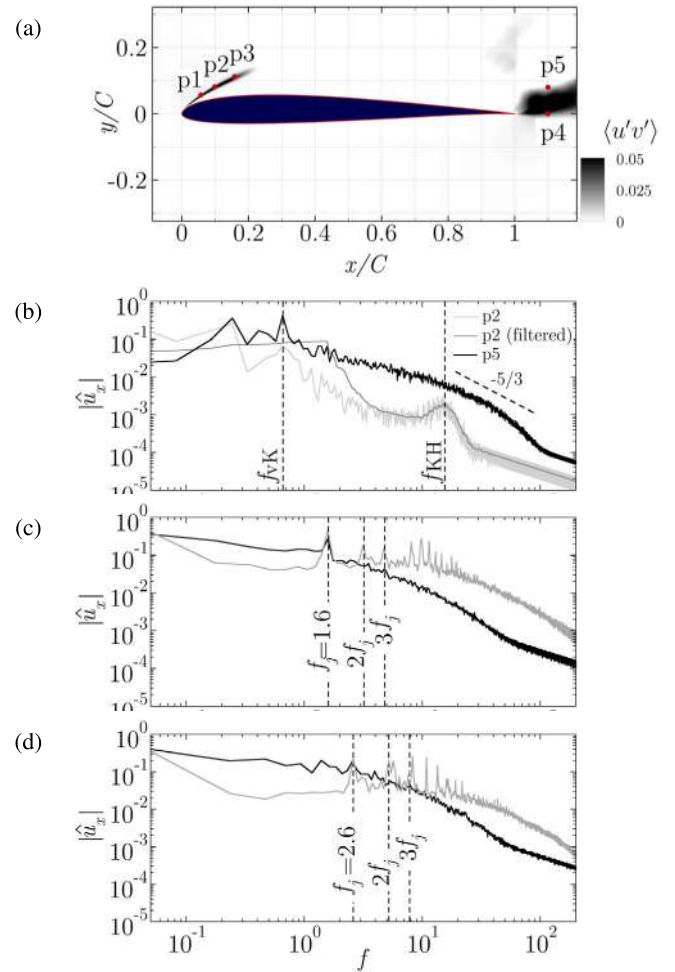


Fig. 11. Power Spectral Density (PSD) of the streamwise velocity signal as recorded from spanwise probe arrays P_2 and P_5 . (a) LES-baseline spanwise-averaged $\langle u'v' \rangle$ colourmap showing the location of the five probe-arrays. Three probes are placed along the shear layer, while the other two are in the very near wake. The PSD of the signals from probes P_2 ($x, y) = (0.098, 0.08)$ and P_5 ($x, y) = (1.1, 0.08)$ are represented for the (b) LES-baseline, (c) LES- C_l^{\max} and (d) LES- η^{\max} cases. Shown are the spectra for the signal read from P_5 (black) and P_2 (light grey), which has been further filtered (dark grey).

averaged into panels Fig. 11b-d for the LES-baseline, LES- C_l^{\max} and LES- η^{\max} cases, respectively. Quadratic interpolation pinpoints the main frequency peaks in the spectrum. For the baseline case, the Strouhal frequency associated with the vortex-shedding of Kármán vortices is identifiable at $f_{vK} = 0.69$, both at locations P_2 and P_5 . The $-5/3$ energy slope that is typical of the inertial range of developed turbulence is also noticeable despite the transitional nature of the flow considered here. Probe P_2 also detects a broadband peak at about $f_{KH} = 15.5$ that may be associated with the passage of Kelvin-Helmholtz vortices. In order to precisely detect the f_{KH} , the filtered signal from probe P_2 is represented as a dark-grey line in Fig. 11b. Probes P_1 and P_3 also record the same phenomenon, albeit with decreasing intensity, while P_4 and P_5 do not in the least reflect it. This is clearly suggestive of a local instability that develops precisely along the shear layer, i.e. a Kelvin-Helmholtz instability.

Actuating with $f_j = 2.6$, as corresponds to the LES- η^{\max} case, the jet frequency is imprinted on the flow and recorded at all probes. The vortex-shedding frequency is superseded by actuation, and no wake vortices are discernible. Several harmonics of the jet actuation frequency are also visible in the spectrum of signals recorded close to the actuation location. The same happens for the

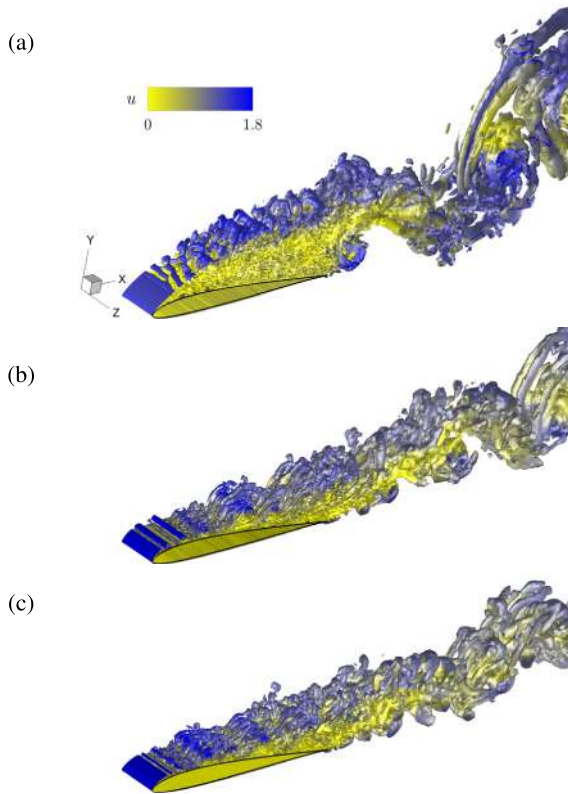


Fig. 12. Instantaneous vortical structures visualised through iso-surfaces of the Q-criterion $Q = 30U_\infty^2/C^2$, coloured by streamwise velocity u . (a) LES-baseline. (b) LES- C_l^{\max} . (c) LES- η^{\max} . (See online movies.)

LES- C_l^{\max} , albeit with the reduced frequency $f_j = 1.6$. Again, the main peak is detected at all probes, while harmonics - a large number of them- are only detected by probes that are sufficiently close to the jet location. The actuation frequency for maximum aerodynamic efficiency (and incidentally also lift) is about 4 times larger than the natural vortex-shedding frequency.

Fig. 12 displays instantaneous vortical structures through Q-criterion iso-surfaces coloured by streamwise velocity. The LES-baseline case (panel a) is characterised by the early separation of the boundary layer and the clear development of Kelvin-Helmholtz vortices along the detached shear layer. These vortices remain predominantly two-dimensional as do all large-scale structures in the vicinity of the airfoil, and are subsumed downstream within the Kármán vortices forming at the top of the wake. The separated region is massive and determines the size of the Kármán vortices that are shed into the wake. The sinuous arrangement of vortices, connected by braids is clearly recognisable and streamwise-cross-stream vortices populate the braid region already one chord distance downstream from the trailing edge.

Actuation drastically reduces the low-speed region above the airfoil and, with it, the width of the wake. Accordingly, lift is enhanced and pressure drag, and along with it total drag, greatly reduced. The SJA-generated spanwise vortices are clearly visible downstream from the jet location as fairly two-dimensional spanwise structures and govern the flow dynamics. They are somewhat more spaced for the LES- C_l^{\max} (panel b) than for the LES- η^{\max} case (panel c), on account of the lower actuation frequency of the latter as compared with the former. Kármán vortex-shedding is completely suppressed for LES- η^{\max} , and highly attenuated for LES- C_l^{\max} , for which case smaller-scale spanwise vortices are visible in the wake that become synchronised with the high-frequency vortices induced by the actuator. Two videos showing the vortical

structures for the LES-baseline and LES- η^{\max} are provided as supplementary data.

5. Conclusions

Following the Synthetic jet Actuation parameters optimisation undertaken by Tousi et al. [1] on the SD7003 airfoil at moderate $Re = 6 \times 10^4$ and post-stall $\alpha = 14^\circ$, we have analysed, using Large Eddy Simulation, the aerodynamic performances and flow properties of optimally actuated scenarios. The original optimisation study, coupled a RANS solver that used the Spalart-Allmaras turbulence model with a Genetic Algorithm specifically devised for maximising either lift or aerodynamic efficiency.

Our Large Eddy Simulation of the baseline case reasonably validated the baseline RANS-SA computation, not without conspicuous discrepancies attributable to the inadequacy of the latter model for the simulation of massively separated flow configurations. However, the two optimal Active Flow Control LES cases, while still producing impressive enhancement of aerodynamic performances, did not align with RANS-SA results as expected. In point of fact, the maximum aerodynamic efficiency case outdoes the other alleged optimum both in terms of aerodynamic efficiency and lift, in this sense constituting an absolute optimum. And not only this, but it also further improves on RANS-SA estimations, with increases from baseline of $\Delta C_l/C_l = 46.7\%$ and $\Delta \eta/\eta = 273.2\%$.

The problem being highly nonlinear, there is no guarantee that the SJA configurations reported here as optimal are indeed absolute optima. They do, however, amply outperform the one SJA study available on the SD7003 airfoil at the same Re and α [2] and produce aerodynamic performances improvements with respect to baseline broadly comparable to those reported in the literature for other airfoils and post-stall flight regimes using alternative optimisation techniques.

A parametric study varying the free-stream turbulent viscosity prescribed at the inlet boundary for actuated simulations with the RANS-SA model reveals that flow topology and aerodynamic performance parameters are highly sensitive, unlike what happens for the baseline case. Turbulent-to-fluid viscosity ratios of around $\tilde{\nu}/\nu \sim 10^{-5}$ enable RANS-SA simulations to better reproduce the actual flow past the actuated airfoil. For these levels of free-stream turbulence, RANS-SA simulation of actuated cases aligned comfortably with LES results, thus proving the convenience of the former for AFC optimisation given their sufficient accuracy and cost-effectiveness. Setting the right amount of free-stream turbulence is however essential, as too low or too large values result in unrealistic flows, possibly due to the poor capabilities of the SA turbulence model for predicting turbulent transition.

The application of optimal (or quasi-optimal) SJA suppresses the boundary layer separation from the upper surface and the shedding of von Kármán vortices in the wake. Actuation-jet-induced spanwise vortices pervade the flow and help maintain quasi-two-dimensionality over a long distance. They also replace the Kelvin-Helmholtz vortices that naturally arise with $f_{KH} \simeq 15.5$ from a shear layer instability of the separated boundary layer for the baseline case. The jet actuation frequency dominates the spectrum of velocity signals far downstream from the jet location, which indicates that actuation is governing the time- and length-scales of the vortical structures in the flow. Kármán vortices, originally shed with a frequency $f_{VK} = 0.69$ for the baseline case are no longer present in the wake nor imprint their periodicity on the spectrum of any of the probe signals.

The dependence of the optimum set of SJA parameters on the angle of attack is a matter worth considering, as also is the sensitivity of aerodynamic performances to suboptimal configurations. Some of the parameters, such as actuation frequency, amplitude and, possibly, injection angle, can be adjusted dynamically, while

others must be necessarily fixed (slot location and width). For these latter, the sensitivity analysis is particularly relevant, as the one-size-fits-all solution is a must. Also, actuation cannot in practice be continuously distributed along the span, as we have considered here. A discrete number of actuators must instead be distributed along the span with a prescribed spacing, and each could potentially be endowed with a different amplitude, phase or even frequency, such that the set of optimisation parameters can be enlarged unboundedly. These detailed analyses will require extremely costly parametric explorations that are beyond the scope of the present study.

Declaration of competing interest

The authors declare that they have no known competing financial interests or personal relationships that could have appeared to influence the work reported in this paper.

Acknowledgements

This work was supported by the Spanish Government under grants FIS2016-77849-R and PID2020-114043GB-I00 and by the Catalan Government under grant 2017-SGR-00785. Computations were performed in the Red Española de Supercomputación (RES), Spanish supercomputer network, under the grants IM-2019-3-0002 and IM-2020-1-0001. F. M. is a Serra-Hünter fellow.

Appendix A. Supplementary material

Supplementary material related to this article can be found online at <https://doi.org/10.1016/j.ast.2022.107679>.






References

- [1] N.M. Tousi, M. Coma, J.M. Bergada, J. Pons-Prats, F. Mellibovsky, G. Bugada, Active flow control optimisation on sd7003 airfoil at pre and post-stall angles of attack using synthetic jets, *Appl. Math. Model.* (2021), <https://doi.org/10.1016/j.apm.2021.05.016>.
- [2] I. Rodriguez, O. Lehmkühl, R. Borrell, Effects of the actuation on the boundary layer of an airfoil at Reynolds number $Re = 60000$, *Flow Turbul. Combust.* 105 (2020) 607–626, <https://doi.org/10.1007/s10494-020-00160-y>.
- [3] L.N. Cattafesta, M. Sheplak, Actuators for active flow control, *Annu. Rev. Fluid Mech.* 43 (2011) 247–272, <https://doi.org/10.1146/annurev-fluid-122109-160634>.
- [4] L. Wang, F. bao Tian, Numerical simulation of flow over a parallel cantilevered flag in the vicinity of a rigid wall, *Phys. Rev. E* 99 (2019), <https://doi.org/10.1103/physreve.99.053111>.
- [5] Y.-C. Cho, W. Shyy, Adaptive flow control of low-Reynolds number aerodynamics using dielectric barrier discharge actuator, *Prog. Aerosp. Sci.* 47 (2011) 495–521, <https://doi.org/10.1016/j.paerosci.2011.06.005>.
- [6] S. Foshat, Numerical investigation of the effects of plasma actuator on separated laminar flows past an incident plate under ground effect, *Aerosp. Sci. Technol.* 98 (2020) 105646, <https://doi.org/10.1016/j.ast.2019.105646>.
- [7] N. Benard, E. Moreau, Electrical and mechanical characteristics of surface AC dielectric barrier discharge plasma actuators applied to airflow control, *Exp. Fluids* 55 (2014), <https://doi.org/10.1007/s00348-014-1846-x>.
- [8] N. Benard, J. Pons-Prats, J. Periaux, G. Bugada, P. Braud, J. Bonnet, E. Moreau, Turbulent separated shear flow control by surface plasma actuator: experimental optimization by genetic algorithm approach, *Exp. Fluids* 57 (2016), <https://doi.org/10.1007/s00348-015-2107-3>.
- [9] M.G. De Giorgi, V. Motta, A. Suma, Influence of actuation parameters of multi-dbd plasma actuators on the static and dynamic behaviour of an airfoil in unsteady flow, *Aerosp. Sci. Technol.* 96 (2020) 105587.
- [10] A. Glezer, M. Amitay, Synthetic jets, *Annu. Rev. Fluid Mech.* 34 (2002) 503–529.
- [11] C. Rumsey, T. Gatski, W. Sellers, V. Vatsa, S. Viken, Summary of the 2004 cfd validation workshop on synthetic jets and turbulent separation control, in: 2nd AIAA Flow Control Conference, 2004, p. 2217.
- [12] I. Wygnanski, The variables affecting the control of separation by periodic excitation, in: 2nd AIAA Flow Control Conference, 2004, p. 2505.
- [13] N. Findanis, N. Ahmed, The interaction of an asymmetrical localised synthetic jet on a side-supported sphere, *J. Fluids Struct.* 24 (2008) 1006–1020, <https://doi.org/10.1016/j.jfluidstructs.2008.02.002>.
- [14] L. Zhiyong, L. Zhenbing, L. Qiang, Z. Yan, Modulation of driving signals in flow control over an airfoil with synthetic jet, *Chin. J. Aeronaut.* 33 (2020) 3138–3148.
- [15] M. De Giorgi, C. De Luca, A. Ficarella, F. Marra, Comparison between synthetic jets and continuous jets for active flow control: application on a NACA 0015 and a compressor stator cascade, *Aerosp. Sci. Technol.* 43 (2015) 256–280, <https://doi.org/10.1016/j.ast.2015.03.004>.
- [16] S. Traficante, M. De Giorgi, A. Ficarella, Flow separation control on a compressor-stator cascade using plasma actuators and synthetic and continuous jets, *J. Aerosp. Eng.* 29 (2016) 04015056.
- [17] M.G. De Giorgi, S. Traficante, C. De Luca, D. Bello, A. Ficarella, Active flow control techniques on a stator compressor cascade: a comparison between synthetic jet and plasma actuators, in: *Turbo Expo: Power for Land, Sea, and Air*, vol. 44748, American Society of Mechanical Engineers, 2012, pp. 439–450.
- [18] H. Zhang, S. Chen, Y. Gong, S. Wang, A comparison of different unsteady flow control techniques in a highly loaded compressor cascade, *Proc. Inst. Mech. Eng., G J. Aerosp. Eng.* 233 (2019) 2051–2065.
- [19] M. Amitay, D.R. Smith, V. Kibens, D.E. Parekh, A. Glezer, Aerodynamic flow control over an unconventional airfoil using synthetic jet actuators, *AIAA J.* 39 (2001) 361–370, <https://doi.org/10.2514/3.14740>.
- [20] M. Amitay, A. Glezer, Role of actuation frequency in controlled flow reattachment over a stalled airfoil, *AIAA J.* 40 (2002) 209–216, <https://doi.org/10.2514/3.15052>.
- [21] J. Gilarranz, L. Traub, O. Rediniotis, A new class of synthetic jet actuators—part I: design, fabrication and bench top characterization, *J. Fluids Eng.* 127 (2005) 367–376, <https://doi.org/10.1115/1.1839931>.
- [22] D. You, P. Moin, Active control of flow separation over an airfoil using synthetic jets, *J. Fluids Struct.* 24 (2008) 1349–1357, <https://doi.org/10.1016/j.jfluidstructs.2008.06.017>.
- [23] A. Tuck, J. Soria, Separation control on a NACA 0015 airfoil using a 2d micro ZNMF jet, *Aircr. Eng. Aerosp. Technol.* 80 (2008) 175–180, <https://doi.org/10.1108/00022660810859391>.
- [24] V. Kitsios, L. Cordier, J.-P. Bonnet, A. Ooi, J. Soria, On the coherent structures and stability properties of a leading-edge separated aerofoil with turbulent recirculation, *J. Fluid Mech.* 683 (2011) 395–416, <https://doi.org/10.1017/jfm.2011.285>.
- [25] N. Buchmann, C. Atkinson, J. Soria, Influence of ZNMF jet flow control on the spatio-temporal flow structure over a NACA-0015 airfoil, *Exp. Fluids* 54 (2013), <https://doi.org/10.1007/s00348-013-1485-7>.
- [26] P. Itsariyapinyo, R.N. Sharma, Large Eddy simulation of a naca0015 circulation control airfoil using synthetic jets, *Aerosp. Sci. Technol.* 82 (2018) 545–556.
- [27] S.H. Kim, C. Kim, Separation control on NACA23012 using synthetic jet, *Aerosp. Sci. Technol.* 13 (2009) 172–182, <https://doi.org/10.1016/j.ast.2008.11.001>.
- [28] H.E. Monir, M. Tadjfar, A. Bakhtian, Tangential synthetic jets for separation control, *J. Fluids Struct.* 45 (2014) 50–65, <https://doi.org/10.1016/j.jfluidstructs.2013.11.011>.
- [29] S.D. Goodfellow, S. Yarusevych, P.E. Sullivan, Momentum coefficient as a parameter for aerodynamic flow control with synthetic jets, *AIAA J.* 51 (2013) 623–631, <https://doi.org/10.2514/1.j051935>.
- [30] M.A. Feero, S.D. Goodfellow, P. Lavoie, P.E. Sullivan, Flow reattachment using synthetic jet actuation on a low-Reynolds-number airfoil, *AIAA J.* 53 (2015) 2005–2014, <https://doi.org/10.2514/1.j053605>.
- [31] M.A. Feero, P. Lavoie, P.E. Sullivan, Influence of synthetic jet location on active control of an airfoil at low Reynolds number, *Exp. Fluids* 58 (2017), <https://doi.org/10.1007/s00348-017-2387-x>.
- [32] W. Zhang, R. Samtaney, A direct numerical simulation investigation of the synthetic jet frequency effects on separation control of low-Re flow past an airfoil, *Phys. Fluids* 27 (2015) 055101, <https://doi.org/10.1063/1.4919599>.
- [33] M.S. Selig, J.F. Donovan, D.B. Fraser, *Airfoils at low speeds*, HA Stokely, 1989.
- [34] M. Selig, J. Guglielmo, A. Broeren, P. Giguere, Summary of low-speed airfoil data summary of low-speed airfoil data, Tech. Rep., University of Illinois, 1995.
- [35] M. Breuer, Effect of inflow turbulence on an airfoil flow with laminar separation bubble: an les study, *Flow Turbul. Combust.* 101 (2018) 433–456.
- [36] S. Qin, M. Koochesfahani, F. Jaber, Large Eddy simulations of unsteady flows over a stationary airfoil, *Comput. Fluids* 161 (2018) 155–170.
- [37] R. Duvigneau, M. Visonneau, Simulation and optimization of stall control for an airfoil with a synthetic jet, *Aerosp. Sci. Technol.* 10 (2006) 279–287, <https://doi.org/10.1016/j.ast.2006.01.002>.
- [38] V.J. Torczon, Multidirectional search: a direct search algorithm for parallel machines, Ph.D. thesis, Rice University, 1989, <https://hdl.handle.net/1911/16304>.
- [39] R. Duvigneau, A. Hay, M. Visonneau, Optimal location of a synthetic jet on an airfoil for stall control, *J. Fluids Eng.* 129 (2007) 825–833, <https://doi.org/10.1115/1.2742729>.
- [40] D. Kamari, M. Tadjfar, A. Madadi, Optimization of SD7003 airfoil performance using TBL and CBL at low Reynolds numbers, *Aerosp. Sci. Technol.* 79 (2018) 199–211.
- [41] M. Tadjfar, D. Kamari, Optimization of flow control parameters over SD7003 airfoil with synthetic jet actuator, *J. Fluids Eng.* 142 (2020), <https://doi.org/10.1115/1.4044985>.

- [42] M. Galbraith, M. Visbal, Implicit large Eddy simulation of low Reynolds number flow past the SD7003 airfoil, in: 46th AIAA Aerospace Sciences Meeting and Exhibit, American Institute of Aeronautics and Astronautics, 2008, p. 225.
- [43] S. Burgmann, W. Schröder, Investigation of the vortex induced unsteadiness of a separation bubble via time-resolved and scanning piv measurements, *Exp. Fluids* 45 (2008) 675.
- [44] W. Zhang, R. Hain, C.J. Kähler, Scanning piv investigation of the laminar separation bubble on a sd7003 airfoil, *Exp. Fluids* 45 (2008) 725–743.
- [45] P. Catalano, R. Tognaccini, Turbulence modeling for low-Reynolds-number flows, *AIAA J.* 48 (2010) 1673–1685, <https://doi.org/10.2514/1.j050067>.
- [46] P. Catalano, R. Tognaccini, Rans analysis of the low-Reynolds number flow around the sd7003 airfoil, *Aerosp. Sci. Technol.* 15 (2011) 615–626.
- [47] P. Spalart, S. Allmaras, A one-equation turbulence model for aerodynamic flows, in: 30th Aerospace Sciences Meeting and Exhibit, 1992, p. 439.
- [48] F. Nicoud, F. Ducros, Subgrid-scale stress modelling based on the square of the velocity gradient tensor, *Flow Turbul. Combust.* 62 (1999) 183–200.
- [49] O. Lehmkuhl, I. Rodriguez, A. Baez, A. Oliva, C. Pérez-Segarra, On the large-Eddy simulations for the flow around aerodynamic profiles using unstructured grids, *Comput. Fluids* 84 (2013) 176–189.
- [50] A.K. Shukla, A. Dewan, Flow and thermal characteristics of jet impingement on a flat plate for small nozzle to plate spacing using les, *Int. J. Therm. Sci.* 145 (2019) 106005.
- [51] P. Catalano, R. Tognaccini, Influence of free-stream turbulence on simulations of laminar separation bubbles, in: 47th AIAA Aerospace Sciences Meeting Including the New Horizons Forum and Aerospace Exposition, 2009, p. 1471.
- [52] C.J. Greenshields, Openfoam user guide version 6, The OpenFOAM Foundation, 2018, p. 237.
- [53] R.I. Issa, Solution of the implicitly discretised fluid flow equations by operator-splitting, *J. Comput. Phys.* 62 (1986) 40–65.
- [54] U. Piomelli, J.R. Chasnov, Large-Eddy simulations: theory and applications, in: *Turbulence and Transition Modelling*, Springer, 1996, pp. 269–336.
- [55] S.B. Pope, Ten questions concerning the large-Eddy simulation of turbulent flows, *New J. Phys.* 6 (2004) 35.
- [56] C. Geuzaine, J.-F. Remacle Gmsh, A 3-d finite element mesh generator with built-in pre-and post-processing facilities, *Int. J. Numer. Methods Eng.* 79 (2009) 1309–1331.
- [57] K. Deb, A. Pratap, S. Agarwal, T. Meyarivan, A fast and elitist multiobjective genetic algorithm: NSGA-II, *IEEE Trans. Evol. Comput.* 6 (2002) 182–197, <https://doi.org/10.1109/4235.996017>.
- [58] K. Deb, R.B. Agrawal, Simulated binary crossover for continuous search space, *Complex Syst.* 9 (1995) 115–148.
- [59] K. Deb, *Multi-Objective Optimization Using Evolutionary Algorithms*, vol. 16, John Wiley & Sons, Chichester, UK, 2001.

Article

A New Hybrid Optimization Method, Application to a Single Objective Active Flow Control Test Case

Martí Coma^{1,2,*}, Navid Monshi Tousi³, Jordi Pons-Prats^{1,4}, Gabriel Bugeada^{1,5} and Josep M. Bergada³

- ¹ Centre Internacional de Mètodes Numèrics a l'Enginyeria (CIMNE), Edifici C1, Gran Capitan, 08034 Barcelona, Spain; jordi.pons-prats@upc.edu (J.P.-P.); bugeda@cimne.upc.edu (G.B.)
- ² Department of Physics, Aeronautics Division, Universitat Politècnica de Catalunya, Barcelona Tech (UPC), Edifici GAIA, Rambla de Sant Nebridi, 22, 08222 Terrassa, Spain
- ³ Department of Fluids Mechanics, Universitat Politècnica de Catalunya, Barcelona Tech (UPC), Edifici TR4, C/Colom, 9, 08222 Terrassa, Spain; navid.monshi.tousi@upc.edu (N.M.T.); josep.m.bergada@upc.edu (J.M.B.)
- ⁴ Department of Physics, Aeronautics Division, Universitat Politècnica de Catalunya, Barcelona Tech (UPC), Edifici C3, Esteve Terrades, 5, 08860 Castelldefels, Spain
- ⁵ Department of Civil and Environmental Engineering, Universitat Politècnica de Catalunya, Barcelona Tech (UPC), Edifici C1, Gran Capitan, 08034 Barcelona, Spain
- * Correspondence: mcoma@cimne.upc.edu; Tel.: +34-932057016; Fax: +34-934016517

Abstract: Genetic Algorithms (GA) are useful optimization methods for exploration of the search space, but they usually have slowness problems to exploit and converge to the minimum. On the other hand, gradient based methods converge faster to local minimums, although are not so robust (e.g., flat areas and discontinuities can cause problems) and they lack exploration capabilities. This article presents a hybrid optimization method trying to combine the virtues of genetic and gradient based algorithms, and to overcome their corresponding drawbacks. The performance of the Hybrid Method is compared against a gradient based method and a Genetic Algorithm, both used alone. The rate of convergence of the methods is used to compare their performance. To take into account the robustness of the methods, each one has been executed more than once, with different starting points for the gradient based method and different random seeds for the Genetic Algorithm and the Hybrid Method. The performance of the different methods is tested against an optimization Active Flow Control (AFC) problem over a 2D Selig–Donovan 7003 (SD7003) airfoil at Reynolds number 6×10^4 and a 14 degree angle of attack. Five design variables are considered: jet position, jet width, momentum coefficient, forcing frequency and jet inclination angle. The objective function is defined as minus the lift coefficient ($-C_l$), so it is defined as a minimization problem. The proposed Hybrid Method enables working with N optimization algorithms, multiple objective functions and design variables per optimization algorithm.

Keywords: Hybrid Methods; Genetic Algorithms; gradient-based methods; optimization; Active Flow Control; Synthetic Jets



Citation: Coma, M.; Tousi, N.M.; Pons-Prats, J.; Bugeada, G.; Bergada J.M. A New Hybrid Optimization Method, Application to a Single Objective Active Flow Control Test Case. *Appl. Sci.* **2022**, *12*, 3894. <https://doi.org/10.3390/app12083894>

Academic Editor: Vincent A. Ciciello

Received: 15 March 2022

Accepted: 9 April 2022

Published: 12 April 2022

Publisher's Note: MDPI stays neutral with regard to jurisdictional claims in published maps and institutional affiliations.



Copyright: © 2022 by the authors. Licensee MDPI, Basel, Switzerland. This article is an open access article distributed under the terms and conditions of the Creative Commons Attribution (CC BY) license (<https://creativecommons.org/licenses/by/4.0/>).

1. Introduction

Optimization methods usually excel in exploration or exploitation, they have to make a trade-off between those characteristics. The balance between exploration and exploitation capabilities will affect the usability of the optimization method. A method that excels in exploitation may lack the capacity to find the candidate regions and get stuck in local minima. On the other hand, a method that excels in exploration may lack the capacity to quickly converge to a refined solution, but it can find the candidate regions efficiently. Evolutionary bio-inspired methods usually excel in exploration capabilities and gradient based methods usually excel in exploitation capabilities.

Traditionally, bio-inspired optimization methods provide good exploration capabilities with robustness in providing global minimum. Nevertheless, this requires a large number

of evaluations of the objective functions, this being its main drawback, especially when dealing with applications to industry and engineering. We can see examples of this type of solution using particle swarm optimization algorithms in microwave engineering at A. Lalbakhsh and Smith [1], or resonator antennas at A. Lalbakhsh and Esselle [2]. Genetic Algorithms have also been used on environmental sensing problems at Lalbakhsh et al. [3], or improving satellite darkness at Lalbakhsh et al. [4]. Gray Wolf Optimization has been used for the solution of flow measurement and instrumentation problems at [5].

In practice, one could think in a sequential combination of different optimization methods in order to combine their main advantages and to overcome the different limitations of each one. For instance, first use an evolutionary algorithm (e.g., a Genetic Algorithm) to perform an exploration and, next, use its results to start a gradient based method (e.g., a conjugate gradient) to exploit the interesting regions found by the evolutionary algorithm. If we do that with all the individuals provided by the evolutionary method, the total computational cost would be even more prohibitive. However, one could also think of applying a deterministic improvement with only a reduced set of promising individuals. This is considered a form of hybridization. An example of this kind of hybridization can be found at Kelly Jr and Davis [6], which proposes a combination of a Genetic Algorithm and a k-nearest neighbors classification algorithm. Another example of hybridization with multiple algorithms is proposed at Jih and Hsu [7]. In this case, a Genetic Algorithm and dynamic programming is used to address vehicle routing optimization problems. Other examples can be found at El-Mihoub et al. [8], Kulcke and Lorenz [9].

Other forms of hybridization are the definition of new operators, including multi-population methods. A multi-population Hybrid Method was proposed in Lee et al. [10] where games strategies were combined with bio-inspired optimization methods. In this approach there are different players, all of them using Genetic Algorithms applied to the solution of different complementary optimization problems.

This approach was used for the optimization of aeronautic shape configurations in Lee et al. [10], Lee et al. [11] and D. S. Lee and Srinivas [12]. This was applied in the optimization of composite structure design at Lee et al. [13].

In this paper, an extended implementation of this approach combining a player using a Genetic Algorithm with another player using a conjugate gradient is presented and tested against a single objective problem on an Active Flow Control device optimization. The performance of this approach is compared with the use of the Genetic Algorithm and the conjugate gradient methods used alone.

There are two players:

- One population-based for exploration, which could be an evolutionary algorithm or swarm intelligence.
- One which tries to improve a selection of the most promising individuals coming from the population of the bio-inspired algorithm which uses a deterministic gradient based method.

2. Hybrid Method Description

In this section, the proposed Hybrid Method is described. Hybrid Methods have been researched by Lee et al. [10] among others. In the work of Lee et al. [10], there are different optimization algorithms inside the Hybrid Method that are also called *players*, as it uses the Nash games concepts and hybridizes a Nash game with a global Pareto player. In Lee et al. [10], the authors use Genetic Algorithms for all optimization algorithms (i.e., players) which compound the Hybrid Method. When working with two objective functions, it uses three players. The first one is the Pareto player or global player and it deals with the whole problem, two objective functions and all design variables. The other two players are the Nash players, and each one only deals with one objective function. The design variables are also split between the two Nash players, resulting in each Nash player working with a subset of the search space.

The proposed Hybrid Method, which has been derived from the one proposed by Lee et al. [10], enables working with N players, multiple objective functions and design variables per player, and a different optimization algorithm for each player. The structure of the method is divided into three main components:

- **General Algorithm:** It contains the initialization of the player, the main optimization loop and the post-process of the optimization. It is not intended to be changed for different variants of the Hybrid Method.
- **Migration epoch algorithm:** It is the function that defines the exchange of information between the different players. It defines which individuals are migrated between players, under which circumstances, etc.
- **Immigrate methods:** The immigrate method is a function that has to be defined for each type of player. The way each optimization algorithm used as a player can incorporate and use an individual highly depends on the internal algorithm of each type of player. This function defines how each type of player incorporates the individuals that emigrate into them.

The Hybrid Method interlaces the execution of its internal optimization algorithms. Each player runs one iteration of its optimization algorithm, then a migration epoch occurs before the other method runs one iteration of its own algorithm. The migration epoch is the mechanism that allows the exchange of information between players. The information exchanged by the players are the design variables of a selection of individuals. The migration epoch implementation is what defines the main functionality of the Hybrid Method. The general algorithm of the Hybrid Method is described in Algorithm 1.

Algorithm 1: General algorithm of the Hybrid Method

```

foreach player do
  | player-Initialize;
while not stop criteria is met do
  | foreach player do
  | | player-Generate;
  | | player-Compute;
  | | MigrationEpoch(players[i]);
foreach player do
  | player-PostProcess;
PostProcess;

```

In this article, the optimization method selected to perform the exploration is a Genetic Algorithm based on the NSGAI [14]. Other population based optimization algorithms, such as differential evolution, particle swarm optimization, etc., could also be used here. The Genetic Algorithm is known for its robustness and exploration capabilities and it is one of the most widely used optimization algorithms for complex problems. It should perform the task well in exploring the full search space. On the other hand, the method selected for the exploitation is a conjugate gradient [15]. As shown in Algorithm 1, first of all, the *Initialize* process for each player is called. These methods are called once and are used to initialize each optimization algorithm. After the initialization of each optimization algorithm, the optimization loop is started. Inside the loop, as mentioned above, each optimization player runs one iteration before the migration epoch. One iteration consists of generating a set of new individuals (i.e., a set of design variables) and computing them. For the Genetic Algorithm player, the genetic operators of selection, crossover and mutation are performed inside the *Generate* process, which yields a new population, known as the offspring. After the population is computed, the *MigrationEpoch* process is called, and after

that the conjugate gradient runs an iteration of its algorithm starting with the migrated individual, and the process repeats until the stop criteria is met.

The *MigrationEpoch* process is responsible for managing the exchange of information between the different players. The definition of this process is what defines most of the hybrid algorithm. For example, it defines the criteria of which individuals migrate between players, how often they migrate, etc. The internal algorithm of the *MigrationEpoch* process that describes the Hybrid Method presented and tested in this article is detailed in Algorithm 2.

Algorithm 2: Hybrid Method With Gradient Game

After computing a full iteration of a player the *MigrationEpoch(this-player)* function does:

```

if iter = 0 then
  foreach player do
    | player-Immigrate(this-player-Bestfits);
  else
    if this-player-Bestfits < players[0]-Bestfits then
      foreach player do
        | player-Immigrate(this-player-Bestfits);
    else
      | GetMinBestfits;
      | this-player-Immigrate(Bestfit);

```

The tested Hybrid Method combines two players (i.e., optimization algorithms). One player is intended to perform the exploration of the full search space. The second player is responsible for the exploitation of the promising regions found by the first one. The Hybrid Method shares information between the two players, in a bidirectional way, to overcome the main drawbacks of the optimization algorithms that is formed of. It tries to achieve a fast rate of convergence and to avoid getting stuck at local minimums.

The Hybrid Method initially runs the Genetic Algorithm player. After the first iteration, the best individual found by the Genetic Algorithm is transferred to the conjugate gradient player (first *if* of the Algorithm 2). The *player-Bestfits* is the individual with the best objective function found so far, and it is stored for each player. It is updated every time a better individual is found. The conjugate gradient player will use this individual as the starting point of its internal algorithm for its own iteration. The iteration of the conjugate gradient consists of computing the gradient at the location of the starting point and performing a line search in the direction of the gradient. After the iteration of the conjugate gradient, another migration epoch occurs. If the best individual found by the conjugate gradient outperforms the best individual found by the Genetic Algorithm, then the best individual of the conjugate gradient is sent to the Genetic Algorithm.

If the first conditional is not met, a second *if* condition is evaluated, taking into account the values of the objectives functions achieved so far. The inner *if* condition compares the objective function of the last evaluated player (*this-player*) against the objective function of the first player, which in this case is a Genetic Algorithm. The condition *this-player-Bestfits < players[0]-Bestfits* is clear in a single-objective optimization case, as it is a direct comparison between values of the objective function. If the objective function of *this-player* is better (lower) than the first player, this individual is migrated to the other player.

If the objective function of *this-individual* is not better, the inner *else* part of the algorithm is conducted. In the function *GetMinBestfits*, a search for the best individual (*Bestfit*) among all players is performed, and the individual is migrated to *this-player*, the last player that was executed.

For the full comprehension of the hybrid algorithm, it is important to specify the *Immigrate* process. This process is defined for each player, and its implementation depends on the type of optimization algorithm, and it affects the general hybrid algorithm. It has one input parameter, the individual that has been selected to migrate into this player. The *Immigrate* process is responsible for incorporating the individual into the player. The *Immigrate* process of the Genetic Algorithm substitutes the design variables of the last individual of its internal population with the one that comes from the conjugate gradient. This introduces the genetic information of this individual into the population. In the next iteration, the design variables of this individual will be used in the genetic operators.

In order not to repeat computations, the conjugate gradient player only performs a new iteration when the Genetic Algorithm one provides a best individual different than in the previous global iteration.

On the other hand, the Genetic Algorithm player always incorporates to the population the best individual coming from the conjugate gradient, even if it is the same as in any previous global iteration. The stochastic nature of the Genetic Algorithm can benefit from maintaining the best individual in the population at each iteration. There is a probability that the best individual is not selected in the genetic operators, and to keep the best individual in the population, keeping its genetic information can help to converge in that region. One could think about problems with elitism, but the method only forces one individual to remain in the population, the absolute best so far. If this happens for too long, most probably the optimization has converged, and in case it is not converged, the algorithm should still be capable to explore other regions with the mutation operator and the stochastic nature of the Genetic Algorithm.

For more clarity, the general algorithm with two players, the Genetic Algorithm as the first player and the conjugate gradient as the second one, is schematized at Figure 1. As mentioned previously, a migration epoch occurs after each iteration of each player. This executes the process detailed in the Algorithm 2, enabling the possibility of exchanging information between the two players.

The configuration of the Genetic Algorithm is specified in Table 1 and the configuration of the conjugate gradient is specified in Table 2. The configuration of both optimization algorithms is the same when running alone and when running as a player of the Hybrid Method.

Table 1. Parameters of the Genetic Algorithm.

Parameter	Value
Crossover operator	Simulated Binary Crossover [16]
Mutation operator	Polynomial Mutation [17]
Selection operator	$\mu + \lambda$ & Crowded-Comparison Operator [14]
Probability of crossover	0.9
Probability of mutation	0.1
Population size	20

Table 2. Parameters of the conjugate gradient algorithm.

Parameter	Value
Search Direction Method	Fletcher-Reeves [18]
Optimal Step Size Method	Golden Section [19]
Epsilon for numerical differentiation	1.0×10^{-6}
First step size	1.0×10^{-3}
Optimal step size tolerance	1.0×10^{-3}

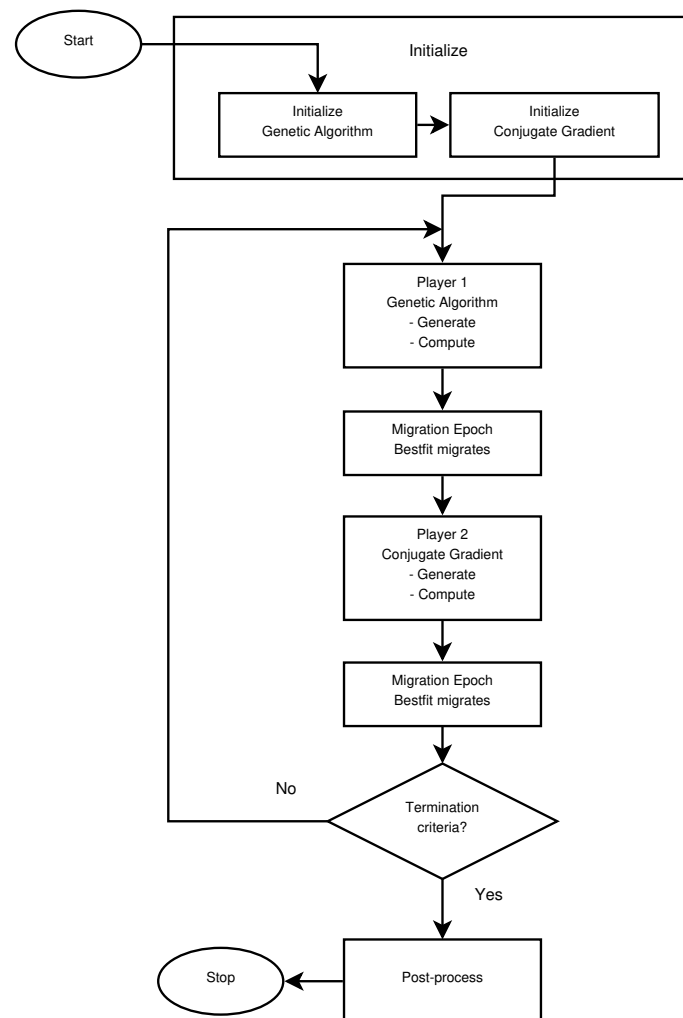


Figure 1. General algorithm of the tested Hybrid Method.

One of the main drawbacks of the proposed Hybrid Method, using both population and gradient-based optimization methods, is that it requires the independent configuration of each optimization method for each player. In this case, the configuration of the Hybrid Method requires the configuration of the Genetic Algorithm and the conjugate gradient players. On the other hand, it also enables the possibility to fine tune the players to perform better, but in cases with high computational costs, it is difficult to perform tests with different configuration values. Another drawback of the Hybrid Method is that the parallelization of the evaluations of the individuals can become more ineffective because each method may have its optimum number of CPUs which may be different for each method. For example, in this case, the evaluation of the Genetic Algorithm population can benefit from using 20 CPUs, one for each individual of the population because they can be computed at the same time. On the other hand, to evaluate the individuals of the conjugate gradient, the parallelization is not that clear. The individuals to compute the gradient can be evaluated at the same time, in this case there are eleven individuals, the central point plus two for each design variable. The line search could also be parallelized, but it is not in the implementation used in this study. The difference in the parallelization capabilities between players could result in an under utilization of the computational resources at some stages of the process.

3. Numerical Results

In order to evaluate the performance of the proposed Hybrid Method, it has been compared against two classical optimization methods, a plain conjugate gradient and a

plain Genetic Algorithm. The conjugate gradient method is the same as that which forms part of the Hybrid Method, but running on its own. The Genetic Algorithm used to compare the hybrid algorithm is also the same that forms part of the Hybrid Method, but also running alone. To take into account the random component of the Genetic Algorithm and the strong dependence on the starting point of the conjugate gradient, multiple optimizations with each algorithm have been conducted.

Two optimizations have been conducted with the Genetic Algorithm, starting with different random populations. The Hybrid Method was also run twice, starting with the same random populations as the Genetic Algorithm, so both methods started with the same populations. Finally, the conjugate gradient was run six times, starting with six individuals of the first random population generated by one of the Genetic Algorithms.

All the optimization methods have been tested against the same test case. The test case consists of a single objective optimization of an Active Flow Control optimization problem based on the work of Tousi et al. [20]. The objective of that work is to determine the optimum parameters of the Synthetic Jet actuator design at different angles of attack in a multiple objective optimization problem. The test case details for the comparison of optimization algorithms are presented in Section 3.1.

3.1. Test Case Description

The test case focuses on the optimization of an Active Flow Control device, more precisely, a Synthetic Jet actuator. The device is tested on a SD7003 airfoil at an angle of attack of 14 degrees. For the comparison between the optimization algorithms, which is the main objective of this work, a single optimization problem with five design variables has been used. The objective function is to maximize the lift coefficient, and to do so the objective function is set to:

$$f = -C_l$$

At high angles of attack, the Synthetic Jet can greatly affect the flow structure, improving the lift coefficient. The Synthetic Jet actuator, if set properly, can help to reattach the flow to the airfoil or to almost avoid the detachment of the flow.

The design variables are the same as the previous work by Tousi et al. [20]. For a full explanation and detail of the Synthetic Jet actuator design variables meaning refer to [20]. The five design variables are:

- F^+ Non-dimensional frequency.
- C_μ Momentum coefficient.
- θ Jet inclination angle.
- x/C Non-dimensional jet position.
- h/C Non-dimensional jet width.

The evaluation range of each design variable is shown in Table 3. The same ranges are used with all optimization algorithms.

Table 3. Active Flow Control design variables and their evaluation ranges.

Design Variable	Minimum Value	Maximum Value
F^+	0.1	10
C_μ	0.0001	0.02
θ°	5	175
x/C	0.001	0.3
h/C	0.005	0.015

The flow has been solved with an unsteady Reynolds averaged Navier–Stokes model (URANS), using the OpenFOAM software. Other models, like direct numerical simulation (DNS) or large eddy simulation (LES) could be used to solve the Synthetic Jet simulation, but their computational cost is too high to perform so many optimizations with the avail-

able resources. In addition, there is no need to use such precise solvers to evaluate the performance of the Hybrid Method. More details on the solver used can be consulted at [20], as this study uses the same model.

The mesh used, see Figure 2a, is one of the meshes previously evaluated in [20], although having a smaller number of cells (34,448) than the final one employed in that paper, the maximum y^+ after the simulation was $y^+ = 1$. The mesh nearby the Synthetic Jet actuator is presented in Figure 2b. The run time of the simulation has been adjusted to 30 time units, which as shown in [20] is sufficient to reach convergence. It is important to note that this study is not about the Synthetic Jet actuator optimization, but to compare the optimization algorithms in a real world application with a significant computational cost and complexity. The study of the physical problem is not the main purpose of this study, which justifies reducing the precision of each CFD simulation in order to reduce the overall computational cost.

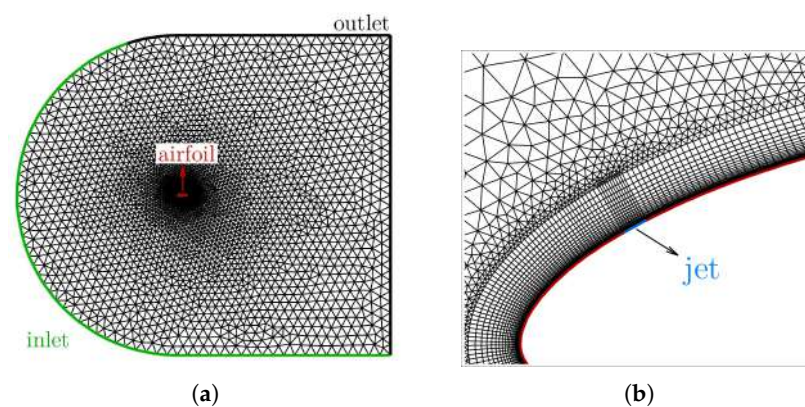


Figure 2. Full mesh of the domain (a) and Mesh nearby the Synthetic Jet actuator (b).

In Figure 3, the temporal averaged streamlines and pressure field for the non-actuated case is presented. This configuration is called the baseline. From the streamlines, it can be seen that the flow is fully separated and the airfoil is under stall conditions.

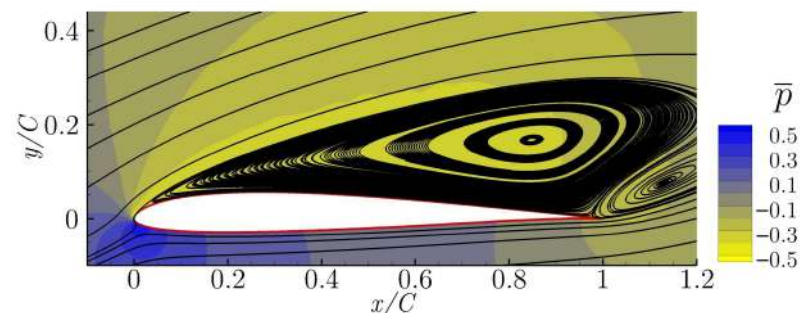


Figure 3. Averaged streamlines and pressure field of baseline case ($C_l = 0.80$).

3.2. Results from the Optimizations Methods

This section introduces the results obtained for the proposed comparison. The convergence of the different optimization algorithms are shown in Figure 4. The results shown in the graph of Figure 4 reflect the problems encountered by the gradient based method. Most runs of the conjugate gradient initially improve faster than the Genetic Algorithm but then get stuck between $C_l \approx 1.35$ and $C_l \approx 1.45$ (except for two runs that get stuck at $C_l \approx 0.8$ and $C_l \approx 1.25$, respectively). Those lift coefficient values are achieved with almost 100 evaluations of the objective function for each optimization of the conjugate gradient. The strong dependence of the conjugate gradient on the starting point is also reflected on these results, as it presents very different solutions between runs than the other methods.

In all cases, the conjugate gradient method was stopped because the algorithm found a local minimum and could not compute the gradient to further improve the results.

On the other hand, the Genetic Algorithm provides optimal solutions similar to the conjugate gradient, but with a higher computational cost, approximately four times higher. Both runs of the Genetic Algorithm achieve values of the objective function in the range of the conjugate gradient results. One of the runs achieves a better objective function than all of the conjugate gradient runs, with a value of $C_l = 1.49$. It is important to note that the Genetic Algorithm optimizations could run additional iterations and achieve better results, but with a high computational cost.

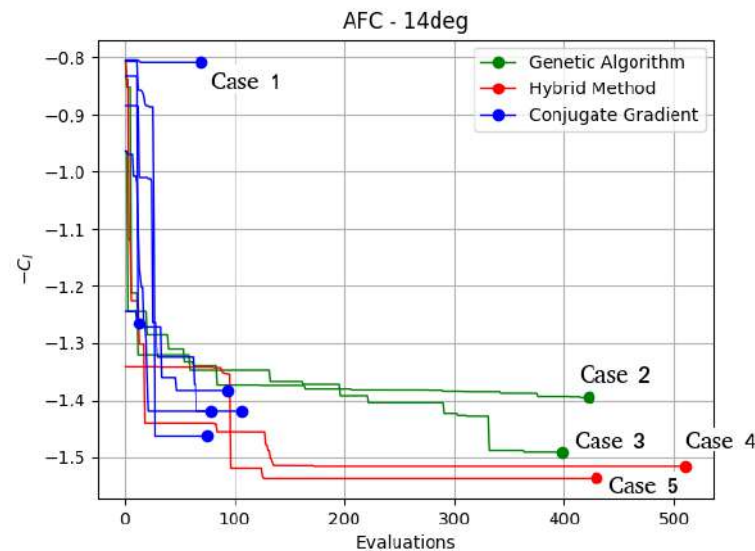


Figure 4. Comparative of the convergence of the different optimization methods.

The Hybrid Method is the method that achieved better results, outperforming all runs of the other algorithms in both of its runs. During the first iterations, it achieved a convergence rate similar to the conjugate gradient. However, the improvement of the solution has continued, avoiding being trapped in any local minimum. It is also the most robust, as both runs are very similar in their performance. Both Hybrid Method runs outperformed all the other optimization methods with a $C_l = 1.52$ and $C_l = 1.54$. One run of the Genetic Algorithm achieved a comparable solution ($C_l = 1.49$), but it took more than twice the computational cost of the Hybrid Method. Case 3, with a lift coefficient of $C_l = 1.49$, obtained by the Genetic Algorithm with around 375 objective function evaluations, improves the baseline lift coefficient by 86%. Cases 4 and 5, obtained by the Hybrid Method runs, achieved a lift coefficient of $C_l = 1.52$ and $C_l = 1.54$, respectively. Both runs needed around 125 objective function evaluations, which is 67% the number of evaluations of case 3, with an increase in the lift coefficient of 90% and 93%, respectively, from the baseline. The best lift coefficient achieved by each optimization is presented in Table 4. The mean (\bar{C}_l) and standard deviation (σ) of the lift coefficient achieved by each optimization method is also presented. The Hybrid Method presents the best lift coefficient mean ($C_l = 1.53$) followed by the Genetic Algorithm ($C_l = 1.44$) and the conjugate gradient ($C_l = 1.29$). The conjugate gradient is the least robust, with a standard deviation of $\sigma = 0.2458$, but four of the six optimizations achieved similar results than the Genetic Algorithm with less computational effort.

Looking at these results, one can conclude that the proposed Hybrid Method performs much more robustly than the conjugate gradient method and much faster than the Genetic Algorithm.

Table 4. Best lift coefficient of each optimization case, means and standard deviation.

	Genetic Algorithm	Hybrid Method	Conjugate Gradient
C_l	1.39	1.52	0.81
			1.26
	1.49	1.54	1.38
			1.42
			1.42
			1.46
$\overline{C_l}$	1.44	1.53	1.29
σ	0.07071	0.01414	0.2458

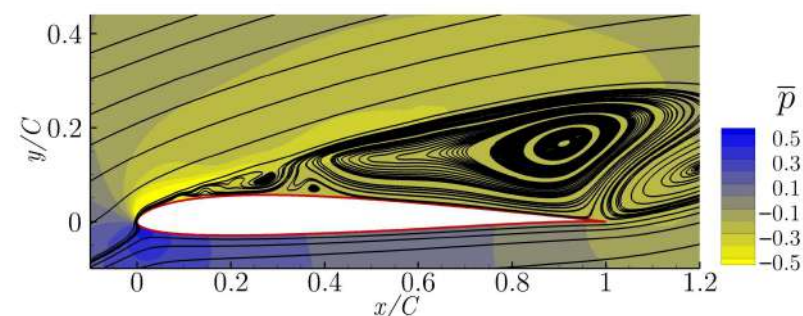
3.3. Results Based on the Fluid Flow Performance

This subsection provides a comparison between the characteristics of the flow field corresponding to each of the optimal solutions labeled in Figure 4. The lift coefficient and design variables of each of the optimal solutions are presented in Table 5. For a full explanation of the flow structure and details on the Synthetic Jet actuator performance, the reader is directed to [20].

Table 5. Values of the lift coefficient and design variables of the five labeled cases.

Case	C_l	F^+	C_μ	θ°	x/C	h/C
1	0.81	8.6	1×10^{-4}	136	3×10^{-1}	5×10^{-3}
2	1.39	0.3	1.47×10^{-2}	24	1×10^{-3}	1.4×10^{-2}
3	1.49	3.2	1.92×10^{-2}	8	2×10^{-2}	5×10^{-3}
4	1.52	6.7	2×10^{-2}	7	2.6×10^{-2}	5×10^{-3}
5	1.54	9.9	2×10^{-2}	5	1.97×10^{-2}	5×10^{-3}

As explained in the Section 3.1, the flow without the Synthetic Jet actuator is fully detached, see Figure 3. The objective of the Synthetic Jet actuator is to prevent or minimize flow separation. The averaged streamlines and pressure field of the optimized cases are presented and discussed in this section. The flow field corresponding to Case 1 is presented in Figure 5. Despite the fact that the flow separation is slightly delayed versus the baseline case, a large vortical structure is still observed over the airfoil.

**Figure 5.** Averaged streamlines and pressure field of the Case 1 ($C_l = 0.81$).

In Figure 6, the averaged streamlines and pressure field obtained from case 2 is presented. It shows a late reattachment of the flow, which improves the lift coefficient of the baseline by 74%. This solution has been obtained by one of the Genetic Algorithm's runs, with around 400 evaluations of the objective function. The resulting lift coefficient is $C_l = 1.39$.

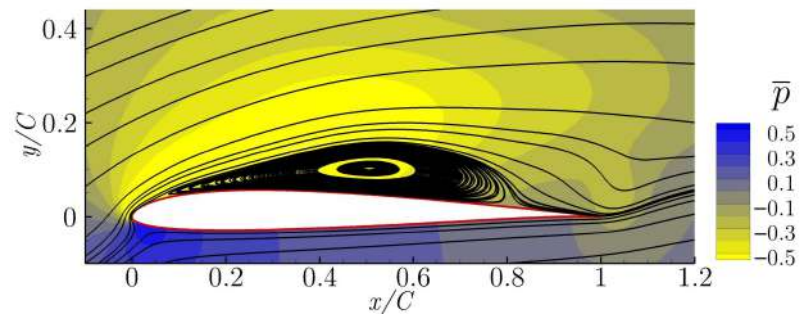


Figure 6. Averaged streamlines and pressure field of case 2 ($C_l = 1.39$).

The averaged streamlines and pressure fields of cases 3, 4 and 5 are presented in Figures 7–9, respectively. All of them show a complete flow reattachment, with very minor differences in the size of the laminar bubble appearing close to the airfoil leading edge. The bubbles are in fact located near the Synthetic Jet position, just downstream of it, as can be seen in the above mentioned figures. The optimization of the flow control actuation parameters has managed to successfully reattached the flow along the entire airfoil chord.

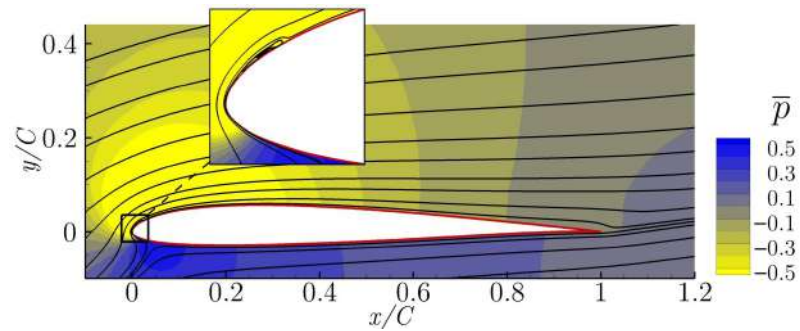


Figure 7. Averaged streamlines and pressure field of case 3 ($C_l = 1.49$).

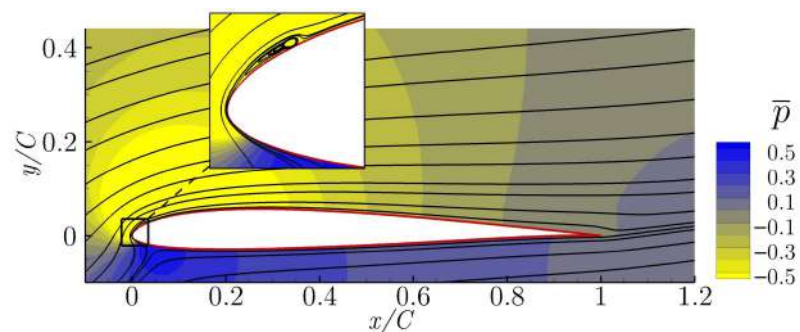


Figure 8. Averaged streamlines and pressure field of case 4 ($C_l = 1.52$).

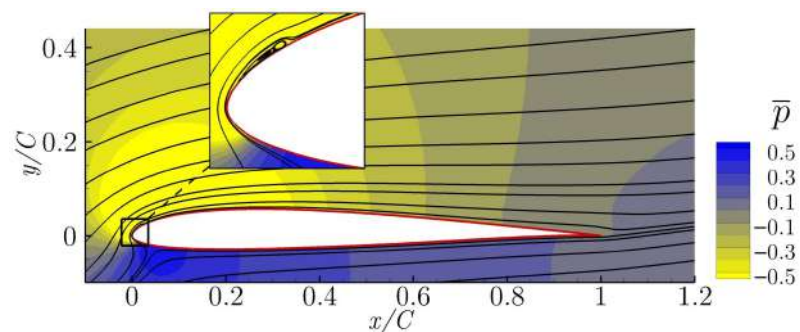


Figure 9. Averaged streamlines and pressure field of case 5 ($C_l = 1.54$).

4. Discussion

This article presents a new Hybrid Method which combines two optimization methods (a Genetic Algorithm and a conjugate gradient) of a very different nature. The test case used to evaluate the performance of the new Hybrid Method is a single objective optimization with five design variables associated with a Synthetic Jet actuator. The CFD simulations are solved using a URANS model, which has proven precise enough to capture the active flow actuator effect and to compare between different designs. For the test case of the Synthetic Jet actuator, the Hybrid Method has outperformed both of the traditional optimization algorithms. The new Hybrid Method successfully combines the best characteristics of both optimization algorithms. It shows a great convergence rate, like a gradient based method, but without the lack of robustness that usually comes with gradient based methods and complex applications. The increase in robustness is provided by the Genetic Algorithm player which avoids local minimums. The strategy to exchange information between the two optimization algorithms proposed in this Hybrid Method has proven efficient to overcome the main drawbacks of both classical optimization methods, and the result is an optimization method capable of exploring and exploiting the full search space.

The future work aims to further test the new Hybrid Method in a multi-objective optimization problem such as the one introduced in Tousi et al. [20]. In high CPU demanding applications, such a Synthetic Jet actuator optimization is important when working with optimization algorithms that require a low number of evaluations of the physical model, and the new Hybrid Method has proven a good option.

Author Contributions: Conceptualization, M.C., N.M.T., J.P.-P., G.B. and J.M.B.; methodology, M.C. and N.M.T.; software, M.C. and N.M.T.; validation, M.C., N.M.T., J.P.-P., G.B. and J.M.B.; formal analysis, M.C., N.M.T., J.P.-P., G.B. and J.M.B.; investigation, M.C., N.M.T., J.P.-P., G.B. and J.M.B.; resources, N.M.T. and J.M.B.; data curation, M.C. and N.M.T.; writing—original draft preparation, M.C.; writing—review and editing, M.C., N.M.T., J.P.-P., G.B. and J.M.B.; visualization, M.C. and N.M.T.; supervision, J.P.-P., G.B. and J.M.B. All authors have read and agreed to the published version of the manuscript.

Funding: This research has been partially supported through the Severo Ochoa Centre of Excellence (2019-2023) under the grant CEX2018-000797-S funded by MCIN/AEI/10.13039/501100011033.

Acknowledgments: The third author, Jordi Pons-Prats, is a Serra Hunter Fellow.

Conflicts of Interest: The authors declare no conflict of interest.

References

1. Lalbakhsh, A.; Afzal, M.U.; Esselle, K.P.; Smith, S. Design of an artificial magnetic conductor surface using an evolutionary algorithm. In Proceedings of the 2017 International Conference on Electromagnetics in Advanced Applications (ICEAA), Verona, Italy, 11–15 September 2017; Volume 1, pp. 885–887.
2. Lalbakhsh, A.; Afzal, M.U.; Esselle, K.P. Multiobjective Particle Swarm Optimization to Design a Time-Delay Equalizer Metasurface for an Electromagnetic Band-Gap Resonator Antenna. *IEEE Antennas Wirel. Propag. Lett.* **2017**, *16*, 912–915. [[CrossRef](#)]
3. Lalbakhsh, A.; Simorangkir, R.B.; Bayat-Makou, N.; Kishk, A.A.; Esselle, K.P. Chapter 2—Advancements and artificial intelligence approaches in antennas for environmental sensing. In *Artificial Intelligence and Data Science in Environmental Sensing*; Asadnia, M., Razmjou, A., Beheshti, A., Eds.; Cognitive Data Science in Sustainable Computing, Academic Press: Cambridge, MA, USA, 2022; pp. 19–38. [[CrossRef](#)]
4. Lalbakhsh, A.; Pitcairn, A.; Mandal, K.; Alibakhshikenari, M.; Esselle, K.P.; Reisenfeld, S. Darkening Low-Earth Orbit Satellite Constellations: A Review. *IEEE Access* **2022**, *10*, 24383–24394. [[CrossRef](#)]
5. Karami, A.; Roshani, G.H.; Nazemi, E.; Roshani, S. Enhancing the performance of a dual-energy gamma ray based three-phase flow meter with the help of grey wolf optimization algorithm. *Flow Meas. Instrum.* **2018**, *64*, 164–172. [[CrossRef](#)]
6. Kelly, J.D., Jr.; Davis, L. A Hybrid Genetic Algorithm for Classification. *IJCAI* **1991**, *91*, 645–650.
7. Jih, W.R.; Hsu, J.Y.J. Dynamic vehicle routing using hybrid Genetic Algorithms. In Proceedings of the 1999 IEEE International Conference on Robotics and Automation (Cat. No. 99CH36288C), Detroit, MI, USA, 10–15 May 1999; Volume 1, pp. 453–458.
8. El-Mihoub, T.A.; Hopgood, A.A.; Nolle, L.; Battersby, A. Hybrid Genetic Algorithms: A Review. *Eng. Lett.* **2006**, *13*, 124–137.
9. Kulcke, M.; Lorenz, W.E. Utilizing Gradient Analysis within Interactive Genetic Algorithms. *eCAAD* **2016**, *2*, 359–364.

10. Lee, D.; Gonzalez, L.F.; Periaux, J.; Srinivas, K.; Onate, E. Hybrid-Game Strategies for multi-objective design optimization in engineering. *Comput. Fluids* **2011**, *47*, 189–204. [[CrossRef](#)]
11. Lee, D.; Periaux, J.; Pons-Prats, J.; Bugada, G.; Oñate, E. Double Shock Control Bump design optimization using hybridised evolutionary algorithms. In Proceedings of the IEEE Congress on Evolutionary Computation, Barcelona, Spain, 18–23 July 2010; Volume 1, pp. 1–8.
12. Lee, D.S.; Gonzalez, L.F.; Périaux, J.; Srinivas, K. Efficient Hybrid-Game Strategies Coupled to Evolutionary Algorithms for Robust Multidisciplinary Design Optimization in Aerospace Engineering. *IEEE Trans. Evol. Comput.* **2011**, *15*, 133–150. [[CrossRef](#)]
13. Lee, D.; Morillo, C.; Bugada, G.; Oller, S.; Onate, E. Multilayered composite structure design optimisation using distributed/parallel multi-objective evolutionary algorithms. *Compos. Struct.* **2012**, *94*, 1087–1096. [[CrossRef](#)]
14. Deb, K.; Pratap, A.; Agarwal, S.; Meyarivan, T. A fast and elitist multiobjective genetic algorithm: NSGA-II. *IEEE Trans. Evol. Comput.* **2002**, *6*, 182–197. [[CrossRef](#)]
15. Shewchuk, J.R. *An Introduction to the Conjugate Gradient Method without the Agonizing Pain*; Technical Report; Carnegie Mellon University, Pittsburgh, PA, USA, 1994.
16. Deb, K.; Agrawal, R.B. Simulated binary crossover for continuous search space. *Complex Syst.* **1995**, *9*, 115–148.
17. Deb, K. *Multi-Objective Optimization Using Evolutionary Algorithms*; John Wiley & Sons: Chichester, UK, 2001; Volume 16.
18. Fletcher, R. *Practical Methods of Optimization*; John Wiley & Sons: Hoboken, NJ, USA, 2013.
19. Brent, R.P. *Algorithms for Minimization without Derivatives*; Prentice-Hall: Englewood Cliffs, NJ, USA, 1973.
20. Tousi, N.; Coma, M.; Bergadà, J.; Pons-Prats, J.; Mellibovsky, F.; Bugada, G. Active Flow Control optimisation on SD7003 airfoil at pre and post-stall angles of attack using Synthetic Jets. *Appl. Math. Model.* **2021**, *98*, 435–464. [[CrossRef](#)]

Article

Discharge Coefficients of a Heavy Suspension Nozzle

Carlos Rio-Cano ¹, Navid M. Tousi ², Josep M. Bergada ^{2,*} and Angel Comas ³

¹ Mechanical Engineering Department, Universitat Politècnica de Catalunya, 08034 Barcelona, Spain; carlos.rio-cano@upc.edu

² Fluid Mechanics Department, Universitat Politècnica de Catalunya, 08034 Barcelona, Spain; navid.monshi.tousi@upc.edu

³ Heat Engines Department, Universitat Politècnica de Catalunya, 08034 Barcelona, Spain; angel.comas@upc.edu

* Correspondence: josep.m.bergada@upc.edu; Tel.: +34-937398771

Abstract: The suspensions used in heavy vehicles often consist of several oil and two gas chambers. In order to perform an analytical study of the mass flow transferred between two gas chambers separated by a nozzle, and when considering the gas as compressible and real, it is usually needed to determine the discharge coefficient of the nozzle. The nozzle configuration analyzed in the present study consists of a T shape, and it is used to separate two nitrogen chambers employed in heavy vehicle suspensions. In the present study, under compressible dynamic real flow conditions and at operating pressures, discharge coefficients were determined based on experimental data. A test rig was constructed for this purpose, and air was used as working fluid. The study clarifies that discharge coefficients for the T shape nozzle studied not only depend on the pressure gradient between chambers but also on the flow direction. Computational Fluid Dynamic (CFD) simulations, using air as working fluid and when flowing in both nozzle directions, were undertaken, as well, and the fluid was considered as compressible and ideal. The CFD results deeply helped in understanding why the dynamic discharge coefficients were dependent on both the pressure ratio and flow direction, clarifying at which nozzle location, and for how long, choked flow was to be expected. Experimentally-based results were compared with the CFD ones, validating both the experimental procedure and numerical methodologies presented. The information gathered in the present study is aimed to be used to mathematically characterize the dynamic performance of a real suspension.

Keywords: discharge coefficients; real compressible flow; Computational Fluid Dynamics (CFD); choked flow; analytical solutions based on experimental data



Citation: Rio-Cano, C.; Tousi, N.M.; Bergada, J.M.; Comas, A. Discharge Coefficients of a Heavy Suspension Nozzle. *Appl. Sci.* **2021**, *11*, 2619. <https://doi.org/10.3390/app11062619>

Academic Editor: Maria Grazia De Giorgi

Received: 8 February 2021

Accepted: 11 March 2021

Published: 15 March 2021

Publisher's Note: MDPI stays neutral with regard to jurisdictional claims in published maps and institutional affiliations.



Copyright: © 2021 by the authors. Licensee MDPI, Basel, Switzerland. This article is an open access article distributed under the terms and conditions of the Creative Commons Attribution (CC BY) license (<https://creativecommons.org/licenses/by/4.0/>).

1. Introduction

Hydro-pneumatic suspensions consist on two or more oil chambers and a couple of gas ones. During the alternative displacement of the suspension, oil and gas flows back and forth between two consecutive chambers often separated by one or several nozzles or valves, therefore generating the smooth suspension displacement characteristic of such devices. Figure 1 introduces a typical heavy vehicle suspension, where several oil and gas chambers can be observed. To mathematically evaluate the dynamic fluid variations associated with the compression and extension of a given suspension, it is required to obtain the dynamic discharge coefficient of the different nozzle shapes separating the gas chambers. The discharge coefficient is defined as $c_d = \frac{\dot{m}}{\dot{m}_t}$, where \dot{m} characterizes the real mass flow flowing through the nozzle, while \dot{m}_t is the mass flow obtained using a theoretical equation. For the suspension configuration presented in Figure 1, the gas chambers consist of a constant volume chamber and a variable volume one. Compressible gas, generally nitrogen, flows between two chambers through a narrow passage of constant cross-section, a nozzle. In the suspension of the present study, the pressure in both nitrogen chambers is time-dependent, which is the reason why it is important to determine the discharge coefficient variation for a real compressible flow under transient conditions.

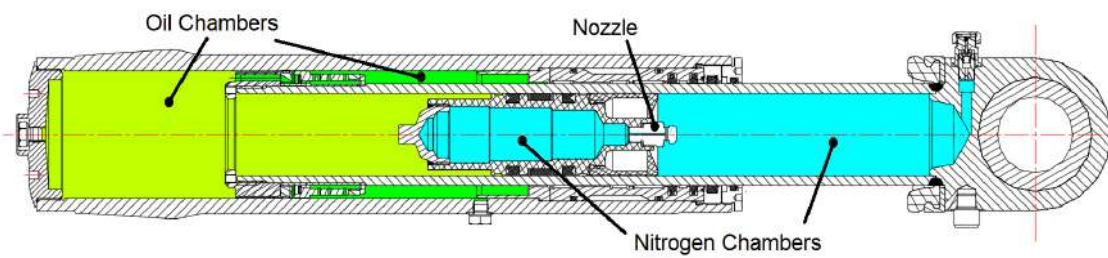


Figure 1. Scheme of a typical heavy vehicle suspension.

The main advantage of knowing the discharge coefficient of a given nozzle is that it allows to determine the real mass flow through the nozzle via employing theoretical equations. From the existing literature, several traditional experimental procedures [1,2] are described to experimentally determine the discharge coefficients on nozzles under real flow compressible conditions. The accuracy of these methods is good for a limited range of pressures, but it is jeopardized in applications involving high pressure metering. One of the most relevant early papers on non-ideal gas flow through orifices is the work undertaken by Johnson [3], where an expression for one-dimensional real flow through nozzles and based on the Beattie-Bridgeman equation was developed. The specific heat ratio was considered to be constant. Air at room temperature and for 10 MPa pressure differential was used as working fluid, and he observed a deviation of 3.5 percent for critical flow in nozzles when employing real versus ideal gas equations. Bober and Chow [4], using Methane as working fluid and for a pressure differential of 23 MPa between chambers, compared the ideal and real gas flow performance through a venturi-shaped nozzle using the Redlich-Kwong equation. Under choked flow conditions, the difference between ideal and real gas models was about 20%. Based on these early papers, it became clear that real gas effects had to be considered if precision metering was required.

Kouremenos et al. [5] and Kouremenos and Antonopoulos [6], based on the Lee-Kesler and Redlich-Kwong equations of state, described a constant entropy process via using three isentropic exponents. A set of simulations and experimental measurements of real compressible flow through convergent divergent nozzles, at very high pressure differentials, were recently undertaken by Kim et al. [7,8] and Nagao et al. [9,10]. They observed that, for a given range of Reynolds numbers, the discharge coefficient exceeded unity. This fact was previously reported by Nakao [11] experimentally. They realized that the molecules' vibrational energy had to be considered in the non-equilibrium thermodynamic process. Working with hydrogen, Ding et al. [12] observed the discharge coefficient was not just dependent on the Reynolds number but also on the throat diameter, stagnation pressure and stagnation temperature. They realized that the compressibility factor (Z) was changing in opposite direction than the discharge coefficient and concluded that the compressibility factor was likely the most important parameter when studying the discharge coefficient. They also noticed that, due to real gas effects, the fluid density at the nozzle throat became smaller than the theoretical one. In most of the research undertaken previously, the theoretical work was not supported by an experimental method, which could allow working directly with the experimental data. These aspects were covered in Reference [13], where, for constant section short nozzles, an expression defining the discharge coefficient was developed using an experimental method and a gas flow model based on the Lee-Kesler equation of state [14]. Experimental results were compared with the ones obtained from the new developed equation, observing that, for tests performed using nitrogen up to 7.6 MPa pressure differential, a good correlation was obtained.

Computational Fluid Dynamic (CFD) applications are gaining reliability every day. The consideration of the gas as real and compressible, under sonic or supersonic flow conditions, is still not fully extended. In reality, turbulent models quite often have some difficulties in dealing with such kind of flows. Nevertheless, there are many industrial applications where sonic, and even supersonic, flow is used. CFD simulations on compressible flow through valves, whether purging or relief ones, have recently been performed

in Reference [15,16]. The modeling of flow ejectors under sonic flow conditions was considered in Reference [17–21]. Some of the recent papers simulating compressible flow conditions at high Mach numbers inside nozzles are Reference [22–25].

From all these studies, it is particularly relevant to highlight the work done by Farzaneh-Gord et al. [15], where they numerically evaluated the exit flow of natural gas through a purging valve, during its opening time. They considered the gas as real and compressible, being the maximum pressure differential of 3.5 MPa. As a turbulent model, the standard $k - \epsilon$ was selected. They concluded supersonic flow was to be expected at the pipe outlet. García-Todolí et al. [16] performed CFD simulations on air valves under compressible flow condition. They showed how CFD models are efficient to represent the behavior of air entering and leaving the valve. The maximum pressure differential studied was 0.1 MPa. In their analysis, they used the realizable $k - \epsilon$ turbulent model and their results matched very well with the experimental data. Mazzelli et al. [17] performed numerical and experimental analyses in order to check the effectiveness of the commonly-used computational techniques when predicting ejector flow characteristics at supersonic flow conditions. For the numerical part, they considered the working fluid as an ideal gas. They tested different Reynolds-averaged Navier–Stokes (RANS) turbulent models, among them, the $k - \omega$ SST and $k - \epsilon$ realizable ones, and observed that, in general, all turbulent models generated very similar results, although epsilon-based models were more accurate at low pressure differentials (around 0.2 MPa). The different pressure differentials they evaluated were of 0.2, 0.35, and 0.5 MPa. On the other hand, they stated that the main differences between the numerical and experimental results appeared when comparing 2D and 3D models. Lakzian et al. [18] performed a compressible 2D RANS simulation on an air ejector pump. In their analysis, they assumed the working fluid as ideal gas and the walls were treated as adiabatic. Pressure differentials of 0.5, 0.6, 0.7, and 0.8 MPa were considered. They used a $k - \epsilon$ realizable turbulent model along with a wall function and a very good agreement with experimental data was obtained. They concluded that the main sources of entropy are the mixing and normal shock occurred in the mixing chamber and diffuser, respectively. Arias and Shedd [21] used CFD to develop a 3D model of compressible flow across a venturi in which obstacles were located inside. Air was considered as compressible and was treated as ideal gas. The turbulent model they used was RNG $k - \epsilon$ and the maximum pressure differential was about 0.1 MPa. The results showed that the obstacles located at the converging nozzle of the venturi causes negligible pressure losses, while other obstacles that generate wakes in the flow are responsible for the largest pressure drop. Discharge coefficients of critical nozzles used for flow measurement under compressible flow conditions were evaluated by Ding et al. [22]. Fluid was considered as real, the standard $k - \epsilon$ turbulent model with a wall function was employed in all simulations. Nozzle roughness was considered, being the maximum pressure differential between nozzle inlet-outlet of 120 MPa. They observed that, when the nozzle roughness was very small, and for pressure differentials until 1 MPa, the effect on the discharge coefficient was negligible. Sonic and supersonic flow inside micro/nanoscale nozzles was studied by Darbandi and Roohi [23]. They used a density-based solver (rhoCentralFoam) employed in OpenFOAM. Second order spatial discretization scheme along with a first order Euler-scheme for time integration were implemented. They observed supersonic flow was impossible to set in nanoscales once Knudsen number exceeded a given value. Zhao et al. [24] numerically studied the fuel flow in a nozzle considering the fuel compressibility. They used the RANS method with a Realizable $k - \epsilon$ turbulent model and they investigated the effect of injection pressure on the fuel flow under fuel compressibility conditions. They concluded that the nozzle discharge coefficient for compressible flow was larger than when fluid was considered as incompressible.

According to the authors knowledge, the nozzle configuration studied in the present paper, which has a T shape, has not been previously studied under real gas compressible flow conditions, and just the work done by Farzaneh-Gord et al. [15] presents some similarities. In fact, under incompressible flow conditions, a similar shape was studied by

Reference [26,27], where it was stated the discharge coefficient was highly dependent on the flow direction. The present study consists of the following parts: initially, the test rig employed to do all experimental tests is introduced, and then the mathematical equations used to analytically determine the flow parameters are presented. In a third stage, the Computational Fluid Dynamics (CFD) methodology employed to numerically evaluate the compressible flow between the two tanks is introduced. Next, the experimentally-based and numerical results are presented and compared. Finally, the discharge coefficients as a function of the Reynolds number, and for both flow directions, are presented and discussed, and the paper ends with the conclusions.

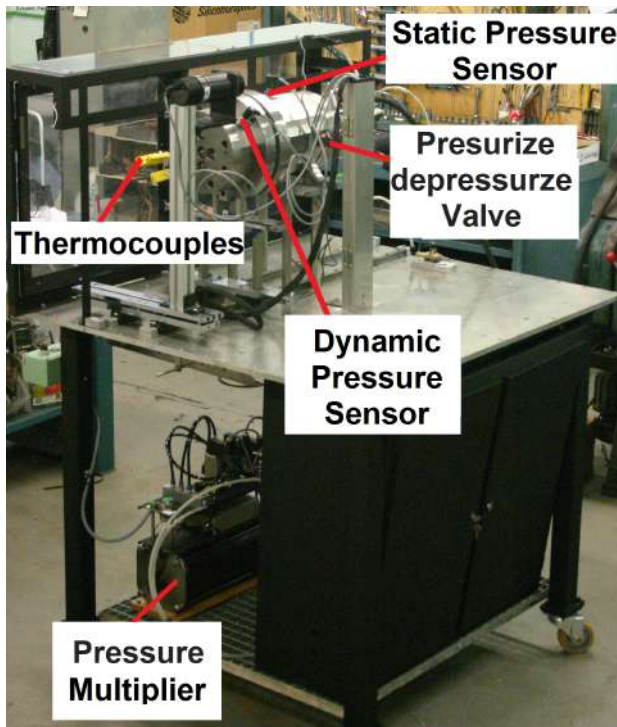
2. Experimental Test Rig

Since the primary idea in the present paper was to experimentally determine the directional dynamic discharge coefficients for a real gas, air, the test rig introduced in Figure 2 was created. Figure 2a,b, respectively, show a general view of the test rig and the two reservoirs. Figure 2c presents a schematic view of the two reservoirs central section with the different transducers employed. Apart of the two reservoirs, the test rig consisted of a stopper cylinder, which was employed to displace the shutter valve located inside the large reservoir; see Figure 2c. When this valve was closed, it prevented the fluid from flowing between the two reservoirs, allowing to pressurize each of them independently. The volume of each reservoir was of 2288.48 and 700.18 cm³. Notice that the volume of the large reservoir was slightly increasing as the shutter valve was opening. Therefore, in order to know at each instant which was the real volume, a position transducer was attached to the stopper cylinder. The pressure multiplier in conjunction with the pressurize-depressurize valve were connected to the large reservoir and allowed to set the required pressure in the reservoir chambers. A static and a dynamic pressure transducer were connected to each reservoir; this was done due to the uncertainty of the static transducer in properly measuring the dynamic pressure variations. The fluid temperature was aimed to be measured by several dynamic thermocouples placed on the internal reservoirs walls; one of them was located in the large reservoir, and three were placed on the smaller one, and then larger temperature variations were expected in there.

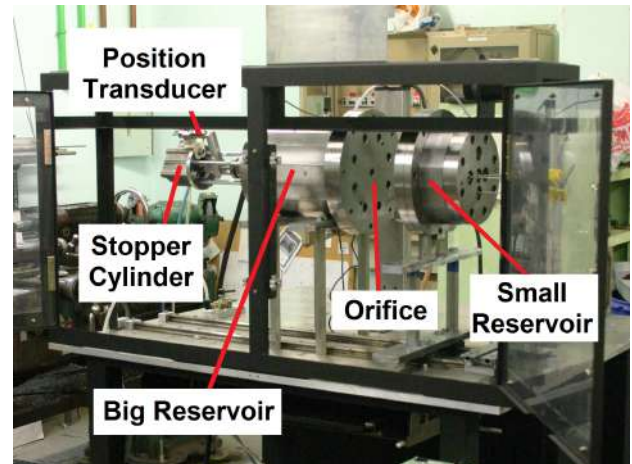
It is important to notice that the dynamic thermocouples were welded to the internal walls of the reservoirs; therefore, the measured temperature was, in reality, the internal wall temperature, which may not be exactly the same as the fluid temperature, specially under dynamic conditions. Considering known the dynamic temperature at the upstream reservoir, Kagawa et al. [2] identified the susceptibility of the pressure response to temperature changes in a reservoir at natural conditions, and suggested the use of an upstream isothermal chamber to guarantee no temperature variation. This idea appears to be a good solution since it reduces the number of variables, and assuming pressure is a known variable, it would be possible to mathematically determine the temperature, heat transfer, and the mass flow downstream by means of integration. The main difficulty lies in achieving no upstream temperature variation during the discharge, Kagawa et al. [2] suggested stuffing extremely thin steel wool or copper wire in the upstream reservoir to obtain isothermal conditions. For the present experimental test rig, and in order to tend to achieve isothermal conditions during experimentation, both reservoirs walls were constructed with a thickness of 35 mm.

The main characteristics of the different transducers were: the static pressure sensors were from Keller series model 21/21PRO, capable of measuring pressures of 10 MPa and having a resolution of 100 Pa. To properly evaluate the dynamic pressure, Kistler transducers model 601A were used; their resolution was of 100 Pa, and the time response was of 1 μs. Dynamic temperature was measured using low inertia Nammac thermocouples model E6-20, and their resolution was of 0.01 °C. The transducer used to measure the position of the shutter valve was a LVDT type, model CGA-2000 from TE connectivity, and its resolution was of 0.001 mm. The dynamic variables were recorded, thanks to an in-house LabVIEW program specifically developed for this application. Table 1 introduces

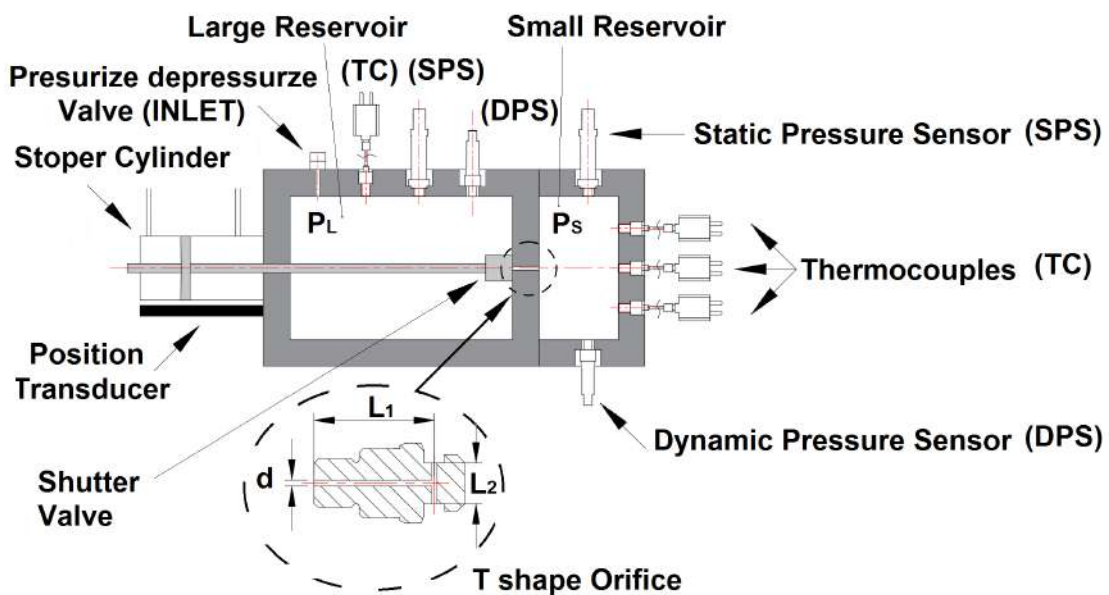
the initial absolute pressure on both reservoirs employed in each experimental test, as well as in each CFD case. The main dimensions of the T shape nozzle are defined in Figure 2c. The constant section nozzle diameter of both the horizontal and vertical nozzle branches was $d = 1.5 \text{ mm}$, the horizontal branch length (L_1) was $L_1 = 29.5 \text{ mm}$, and the length of the vertical branch (L_2) was $L_2 = 10 \text{ mm}$.



(a)



(b)



(c)

Figure 2. (a) Test rig main view. (b) The two reservoirs with their pressure and temperature transducers; (c) schematic view of the reservoirs and the transducers localization.

The process followed to perform the simulations was a function of the flow direction, and it was depending on which of the two reservoirs was initially pressurized. In other words, it depends on if the discharge was from the large to the small reservoir (L-to-S) or from the small to the large (S-to-L) one. It is important to notice that the T shape nozzle was always kept in the same position, regardless of the flow direction.

Table 1. Initial absolute pressure at both reservoirs for all different experimental tests performed and for all Computational Fluid Dynamic (CFD) simulations undertaken.

Pressure large reservoir (MPa)	0.4	0.6	0.9	1.1	1.2	0.1	0.1	0.1	0.1	0.4	0.4	1.1	0.1	0.4
											CFD	CFD	CFD	CFD
Pressure small reservoir (MPa)	0.1	0.1	0.1	0.1	0.4	0.4	0.6	0.9	1.1	1.2	0.1	0.1	0.6	1.2
											CFD	CFD	CFD	CFD

The measurements done when the large reservoir was pressurized started with the shutter valve open and both reservoirs at the atmospheric pressure, 0.1 MPa absolute pressure. Under these conditions, the shutter valve was closed, and the large reservoir was filled with air, passing through the pressurize-depressurize valve, until reaching the required pressure. Then, the pressurize-depressurize valve was closed. The last step consisted of opening the shutter valve, which was accomplished by pressurizing the stopper cylinder, and the flow was allowed to go from the large to the small reservoir. The stopper cylinder position, the static, and dynamic pressure, as well as the internal walls temperature, on both reservoirs, were recorded using an external computer, and thanks to a labVIEW program. For tests at which the fluid was going from the small reservoir to the large one, the same procedure was used but initially both reservoirs were pressurized at the pressure required for the small reservoir. After closing the shutter valve and using the pressurize-depressurize valve, the pressure at the large reservoir was decreased until obtaining the one needed. It is important to highlight at this point that each test was done ten times, and the resulting curves presented in the results section are the average value of the ten measurements done for each variable.

3. Mathematical Equations and Analytical Process Followed to Determine the Physical Variables

From the experimental tests, it was soon realized that, as the temperature transducers were welded to the reservoirs internal walls, in reality, they were measuring the temperature of the wall and not the fluid temperature at each reservoir. The measured temperature was almost constant in both reservoirs, and it was used to instantaneously estimate the heat transferred through the walls. Therefore, providing that the only trustworthy dynamic information in both reservoirs was the temporal pressure evolution, the methodology employed to determine the mass flow between reservoirs was based on the following equations, developed by the authors in a former paper [13]. Equation (1) was obtained from the application of the energy equation in the upstream reservoir, it characterizes the temporal mass variation in the upstream reservoir, $\frac{dm_u}{dt}$, as a function of the tank's temperature T_u , the heat transferred to the fluid $\frac{dQ_u}{dt}$, the upstream pressure temporal variation $\frac{dp_u}{dt}$, the variation of the compressibility factor versus the temperature and specific volume $\frac{\partial Z_u}{\partial T}$, $\frac{\partial Z_u}{\partial v}$, the mass of the fluid in the upstream reservoir m_u , the enthalpy h_u , and the internal energy u_u associated with the upstream fluid. The heat transferred across the walls of the reservoir was estimated based on the Fourier equation $Q = -\lambda \frac{dT}{dx} |_{x=0'}$ being the value of the thermal conductivity $\lambda = 54 \left(\frac{W}{mK}\right)$. Equations (2) and (3) arise from the differentiation of the real gas equations applied to the upstream and downstream reservoirs, $p_u \nabla_u = Z_u m_u R_u T_u$; $p_d \nabla_d = Z_d m_d R_d T_d$, and they link the pressure, volume,

temperature, mass flow, and compressibility factor temporal variations existing in the respective upstream and downstream reservoirs. Equation (4) simply characterizes the mass transfer balance. In all these equations, sub-indices *u* and *d* stand for upstream and downstream, respectively.

$$\frac{dm_u}{dt} = \frac{\frac{1}{p_u} \frac{dp_u}{dt} - \frac{1}{m_u c_v} \left[\frac{1}{T_u} + \frac{1}{Z_u} \left(\frac{\partial Z_u}{\partial T} \right)_v \right] \frac{dQ_u}{dt}}{\frac{1}{m_u} - \frac{1}{Z_u} \left(\frac{\partial Z_u}{\partial v} \right)_T \frac{v_u}{(m_u)^2} + \frac{1}{m_u c_v} \left[\frac{1}{T_u} + \frac{1}{Z_u} \left(\frac{\partial Z_u}{\partial T} \right)_v \right] \left[RT_u^2 \left(\frac{\partial Z_u}{\partial T} \right)_v - (h_u + u_u) \right]}, \quad (1)$$

$$\frac{dT_u}{dt} = \frac{T_u}{p_u} \frac{dp_u}{dt} + \frac{T_u}{v_u} \frac{dv_u}{dt} - \frac{T_u}{m_u} \frac{dm_u}{dt} - \frac{T_u}{Z_u} \frac{dZ_u}{dt}, \quad (2)$$

$$\frac{dT_d}{dt} = \frac{T_d}{p_d} \frac{dp_d}{dt} + \frac{T_d}{v_d} \frac{dv_d}{dt} - \frac{T_d}{m_d} \frac{dm_d}{dt} - \frac{T_d}{Z_d} \frac{dZ_d}{dt}, \quad (3)$$

$$\frac{dm}{dt} = \frac{dm_d}{dt} = -\frac{dm_u}{dt}. \quad (4)$$

An in-house computer program was created to solve the preceding Equations (1)–(4) with a Runge-Kutta method based on DVERK from the International Mathematics and statistics library, (IMSL). The air density was determined every time step using the Lee-Kesler equation iteratively as performed by Plocker and Knapp [28]. According to this equation, the compressibility factor as a function of the reduced parameters, can be expressed as:

$$Z^{(r)} = \left(\frac{P_r v_r}{T_r} \right) = 1 + \frac{B}{v_r} + \frac{C}{v_r^2} + \frac{D}{v_r^5} + \frac{c_4}{T_r^3 v_r^2} \left(\beta + \frac{\gamma_1}{v_r^2} \right) e^{-\frac{\gamma_1}{v_r^2}}. \quad (5)$$

The parameters *B*, *C*, *D*, *c*₄, *β*, and *γ*₁, for various gases, can be determined from Reference [5]. *P_r*, *T_r*, and *v_r* stand for reduced pressure, reduced temperature, and reduced specific volume, respectively.

According to Lee and Kesler [14], the compressibility factor can be defined as:

$$Z = Z^{(0)} + \frac{\omega}{\omega^{(R)}} \left(Z^{(R)} - Z^{(0)} \right), \quad (6)$$

where *Z^(R)* and *Z⁽⁰⁾* are the compressibility factors for a reference fluid and simple fluid, respectively, while *ω^(R)* and *ω* stand for the acentric factors of the reference and working fluids.

Considering known the pressure and temperature in a given location and time, the following steps were used to calculate the fluid compressibility factor. Initially, the reduced upstream pressure and temperature (*P_r* and *T_r*) were obtained based on the working fluid critical properties (*P_c*; *T_c*) and the values of the pressure and temperature. When introducing the values of *P_r* and *T_r* in Equation (5), introducing, as well, the values of the parameters given for a simple fluid and obtained from reference [5], the value of *v_r* could be determined. Substituting the value of *v_r* in the same Equation (5), the corresponding compressibility factor for a simple fluid *Z⁽⁰⁾* was obtained. Following the same procedure just described, but using the values of the parameters characterizing the reference fluid, which, for the present study, was n-octane, and values obtained from Reference [5], the value of *Z^(R)* was determined. Substituting the compressibility factors *Z⁽⁰⁾* and *Z^(R)* in Equation (6) and considering the acentric factor values *ω^(R)* = 0.3978 and *ω* = 0.039, the compressibility factor for the working fluid could finally be obtained. This procedure allows to determine the compressibility factor and the fluid density at any position and time, and just the values of the pressure and temperature are required at the generic location where the information is needed.

To be able to determine the instantaneous mass at each reservoir, the pressure evolution was measured in both reservoirs at any time; the volume of both reservoirs was also

known, and the fluid temperature, as well as the compressibility factor, were estimated based on the previous equations. The variation of the fluid mass between two consecutive time steps allowed to calculate the instantaneous mass flow leaving one reservoir and entering the other one. The only problem associated with this methodology was that the fluid temperature had to be estimated. As previously defined by Kagawa et al. [2] and Comas et al. [13], if the reservoirs were large enough, the fluid temperature was likely to remain constant. Yet, which were the required dimensions to fulfill this condition, for each particular case, was not clearly stated.

Based on the previous information, the instantaneous space averaged fluid velocity at the nozzle minimum section $S = \frac{\pi d^2}{4}$ was determined as presented in Equation (7). The fluid velocity at the critical section was determined based on the experimentally-based mass flow \dot{m} , the nozzle section S , and the fluid downstream density ρ_d .

$$\vartheta = \frac{\dot{m}}{S\rho_d}. \quad (7)$$

To determine the Mach number, the sound speed was initially obtained from Equation (8), when substituting Equations (7) and (8) in Equation (9), the Mach number at the nozzle critical section was obtained.

$$c^2 = \left(\frac{\partial p}{\partial \rho}\right)_s = -v^2 \left(\frac{\partial p}{\partial v}\right)_s, \quad (8)$$

$$M = \frac{\vartheta}{c}. \quad (9)$$

On the other hand, and due to the fact that the pressure differential between both reservoirs was relatively small, as in Table 1, the following equation was employed to calculate the theoretical mass flow.

$$\dot{m}_t = \frac{\pi D^2}{4} \sqrt{\frac{2\gamma}{\gamma-1} p_u \rho_u \left(\left(\frac{p_d}{p_u}\right)^{\frac{2}{\gamma}} - \left(\frac{p_d}{p_u}\right)^{\frac{\gamma+1}{\gamma}} \right)}. \quad (10)$$

The instantaneous discharge coefficient was determined at each time step by comparing the real and theoretical mass flows. Actually, the discharge coefficient at each time step was obtained according to Equation (11).

$$c_d = \frac{\dot{m}}{\dot{m}_t}, \quad (11)$$

where \dot{m} is the real mass flow obtained based on the temporal variation of the mass in the upstream reservoir, which was determined from the experimental upstream and downstream pressure evolution, the initial fluid temperature, and after calculating the compressibility factor, as well as the fluid temperature evolution, at each time step. \dot{m}_t is the mass flow obtained via using Equation (10).

At each instant, the Reynolds number was determined using the following equation.

$$Re = \frac{4\dot{m}}{\pi D \mu}, \quad (12)$$

where μ is the fluid dynamic viscosity.

4. Dynamic Computational Fluid Dynamic Simulations

In order to be able to analyze the dynamic flow evolution between the two reservoirs, several 3D Computational Fluid Dynamic (CFD) simulations were undertaken. The working fluid was air, and it was considered as ideal and compressible. Some recent papers in which the fluid was considered as ideal and compressible and working under similar

pressure differentials are Reference [17,18]. In the present paper, the simulations were performed under dynamic conditions, therefore matching the experimental test conditions.

Figure 3 shows the two reservoirs separated by the T shape nozzle, and the dimensions of both reservoirs and the T shape nozzle were the same as the ones used in the experimental tests. The only difference was the shutter valve needed in the experimental test rig, as in Figure 2c, which was not required in the CFD simulations. The mesh employed was generated using GMSH, and it was unstructured and consisted of 126,633 cells. The OpenFOAM software was used for all 3D simulations, and finite volumes is the approach OpenFOAM uses to discretize Navier–Stokes equations. The solver rhoCentralFoam was used for all tests, and the spatial discretization was set to second order being the first order Euler scheme the one used for time discretization. The maximum Courant number was kept below 0.8, being the time step around 5×10^{-8} s. Turbulence intensity was set to 0.05% in all cases. The realizable $k - \epsilon$ turbulent model, along with a wall function, as previously used by Lakzian et al. [18], were employed in all the simulations. The maximum y^+ on the wall of the nozzle was about 90. Volumetric Dirichlet pressure and temperature boundary conditions were initially set in both reservoirs, Newman boundary conditions for pressure and temperature were set in all walls, and Dirichlet boundary conditions for velocity were established in all walls. Regarding the heat transfer, all walls were set as adiabatic. To compare with the experimental results, four simulations were performed; in two of them, the flow was going from the large to the small reservoir, and the respective L-to-S reservoirs pressures were 0.4–0.1 MPa and 1.1–0.1 MPa. In the other two simulations, the fluid was flowing from the small to the large reservoir, being the S-to-L reservoirs pressures, respectively, of 0.6–0.1 MPa and 1.2–0.4 MPa; see Table 1.

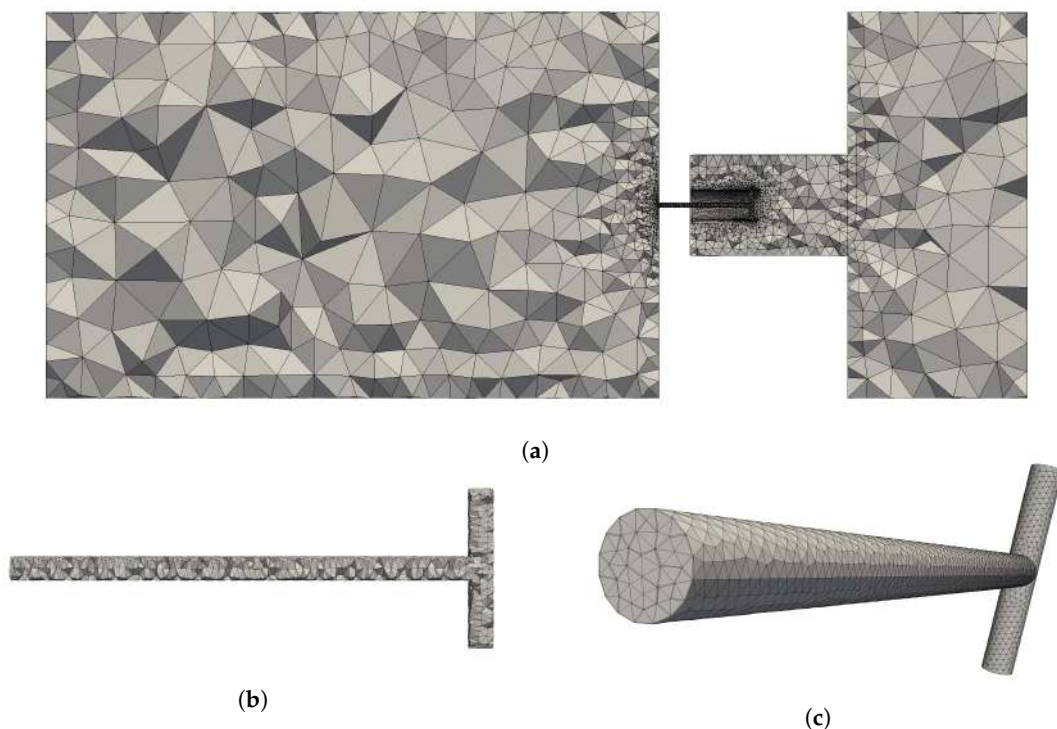


Figure 3. (a) Reservoirs main mesh; (b) T shape nozzle section mesh; (c) T shape nozzle mesh general view.

5. Results and Discussion

In the present section, initially the measured temporal pressure evolution inside the reservoirs is compared with the ones obtained from the CFD simulations. The same is later being done with the temporal temperature at the upstream reservoirs. Next, the time-dependent mass at each reservoir is also compared between CFD and experimentally-based results, which is followed by the temporal mass flow comparison. The time-dependent

Mach numbers at the respective critical sections and the discharge coefficients versus the Reynolds number are presented next. At the end of this section, a figure showing the flow inside the nozzle and for both flow directions is introduced. In this figure, the critical sections where the flow becomes sonic and the locations where supersonic flow is to be expected are clearly stated.

Figure 4 presents the temporal pressure variation measured in both reservoirs for the different initial pressure differentials introduced in Table 1. Each curve is, in reality, the average one obtained after performing each test ten times. Although not presented in Figure 4, the standard deviation of each point was smaller than 1% for all tests performed. From Figure 4a, it is observed the discharge lasts about two seconds, regardless of the initial pressure differential existing between the two reservoirs. In fact, the time needed to complete the discharge suffers an increase of about 22.5% when comparing the discharge from 0.4 to 0.1 MPa with the 1.1 to 0.1 MPa one. This phenomenon is clearly understandable then the higher the upstream pressure the higher is the mass to be transferred from one reservoir to the other. Notice that the initial mass of fluid in the downstream reservoir is the same for all cases presented in Figure 4a, except the case at which the initial downstream pressure is of 0.4 MPa, being the upstream pressure of 1.2 MPa. This case shows clear differences versus the rest of the discharges; then, the time required to complete the discharge is about 10% shorter than the one needed to complete the discharge when the upstream/downstream reservoir pressures were 0.4 and 0.1 MPa, respectively. In fact, the discharge time is directly related to the initial fluid density ratio $\rho_{upstream} / \rho_{downstream}$ between reservoirs, given the rest of the parameters, reservoirs volumes, and initial fluid temperature as constant, the smaller the initial upstream/downstream density ratio $\rho_{upstream} / \rho_{downstream}$, and the shorter the discharge time.

From the observation of the temporal pressure decay when the flow goes from the small reservoir to the large one, as in Figure 4b, it is realized that the discharge time obeys to the same upstream/downstream density rule just presented. It is interesting, as well, to observe that, when comparing discharge times for the same pressure differential and opposite flow directions, the discharge time is larger when the fluid goes from the small to the large reservoir. This is likely linked to the resistance the T shape nozzle is presenting when the fluid flows in such direction. The time the flow remains under choked conditions it is expected to depend on such resistance. This point is to be clarified in the remaining part of the paper. Figure 4 also compares the pressure decay and increase measured experimentally with the ones obtained from the CFD simulations, two cases are compared for each flow direction. The comparison shows a very good agreement, generating the same discharge times and final pressures as the ones measured experimentally. Small discrepancies are observed in the final pressure values when the flow goes from the small to the large reservoir, a discrepancy of 4.4% is observed for a discharge from 1.2 to 0.4 MPa, and the variation reaches 11.3% for a discharge from 0.6 to 0.1 MPa. Such relatively small discrepancies are understandable when considering that, in the CFD simulations, the process is considered as adiabatic, the fluid is considered as ideal, and the large volume remains constant.

Figure 5 presents the fluid temperature evolution in both reservoirs and for the four cases numerically evaluated. When the discharge is from the large to the small reservoir, as in Figure 5a, the fluid temperature on the large reservoir suffers a decrease of less than 20°, and the increase of the fluid temperature in the small reservoir lies between 55° and 85°; such a large increase is perfectly understandable when considering the reduced volume of this particular reservoir and that the walls are considered adiabatic. Notice, as well, that the temperature decrease and increase are directly dependent on the pressure ratio between reservoirs. When the flow goes from the small to the large reservoir, as in Figure 5b, the temperature decrease in the small tank oscillates between 50° and 70°, and a maximum temperature rise of around 30° is observed in the large reservoir.

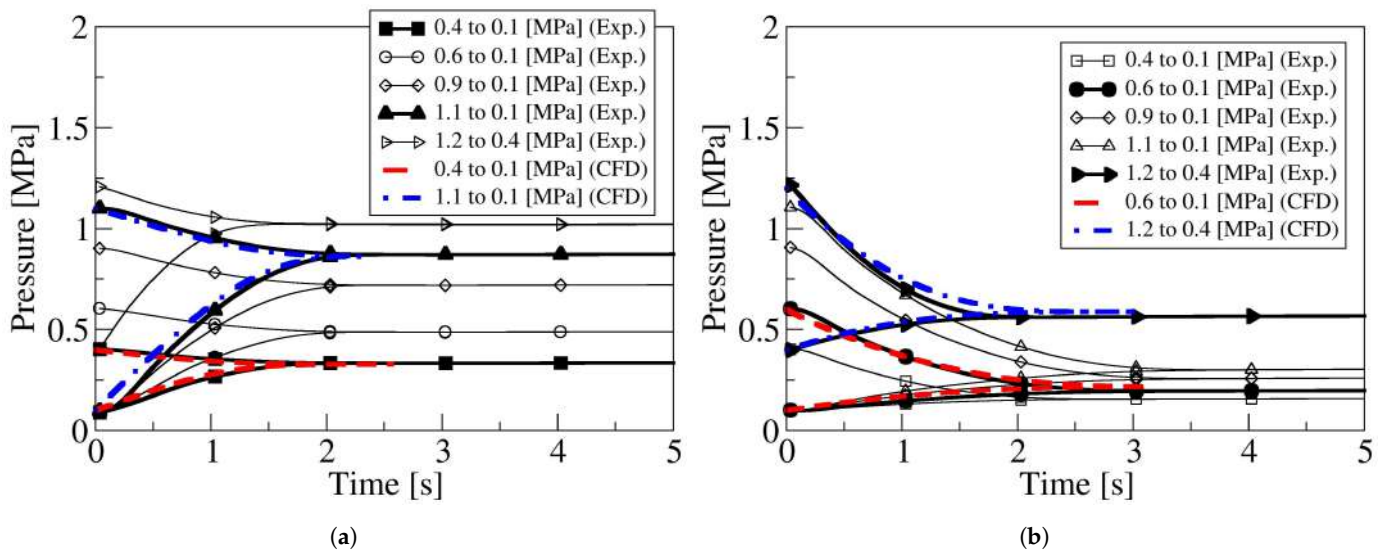


Figure 4. Measured temporal pressure variation in both reservoirs, comparison between experimental and CFD results. (a) Flow from large to small reservoir. (b) Flow from small to large reservoir. Five different pressure decays are considered for each flow direction; see Table 1.

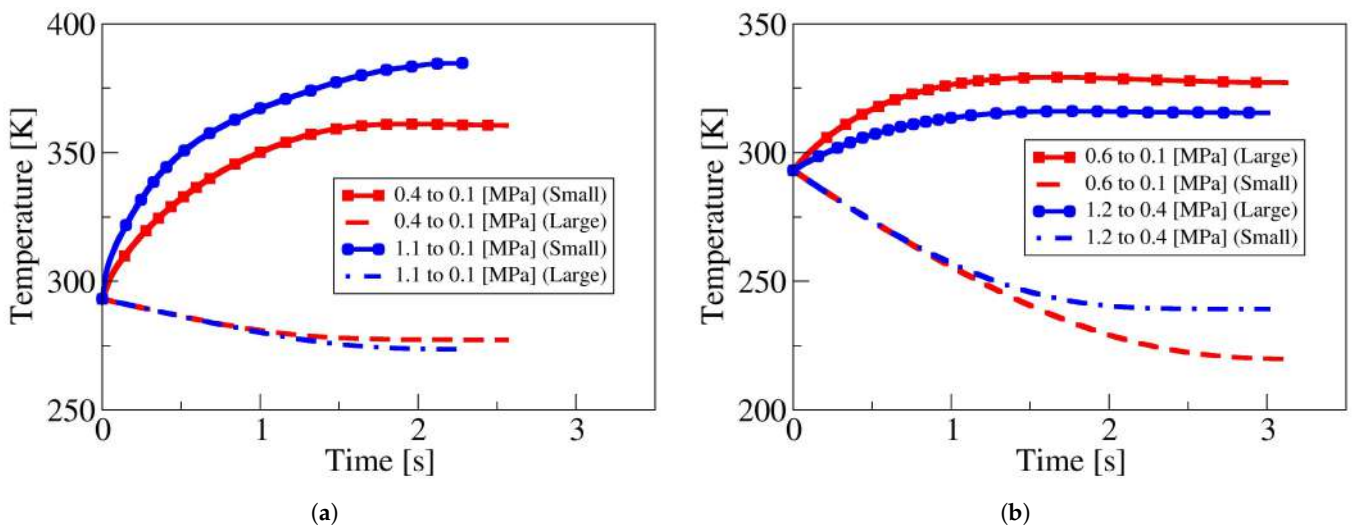


Figure 5. Numerical temperature evolution in the upstream and downstream reservoirs. (a) The flow goes from the large to the small reservoir. (b) The flow goes from the small to the large reservoir.

A point which needs to be considered, and which could help to explain why the discharge from the small to the large reservoir takes longer than the one in the opposite direction, is that, regardless of the flow direction, the temperature variation at the small reservoir is several times larger than the one observed at the large one. Another possible explanation needs to be found in the possible existence of a flow restriction under these conditions, therefore reducing the effective flow section. In fact, the most plausible explanation is likely to be the different nozzle resistance the fluid is facing when flowing in opposite directions. These hypotheses will be analyzed in the remaining part of the paper.

Figure 6 introduces the experimentally-based fluid temperature temporal variation on both reservoirs for the two flow directions and for all pressure differentials evaluated; see Table 1. Figure 6a,b characterize the temperature decrease in the large and small reservoirs when the flow goes from the large to the small and from the small to the large reservoirs, respectively. The fluid temperature evolution in both reservoirs obtained from the CFD simulations is also presented for comparison.

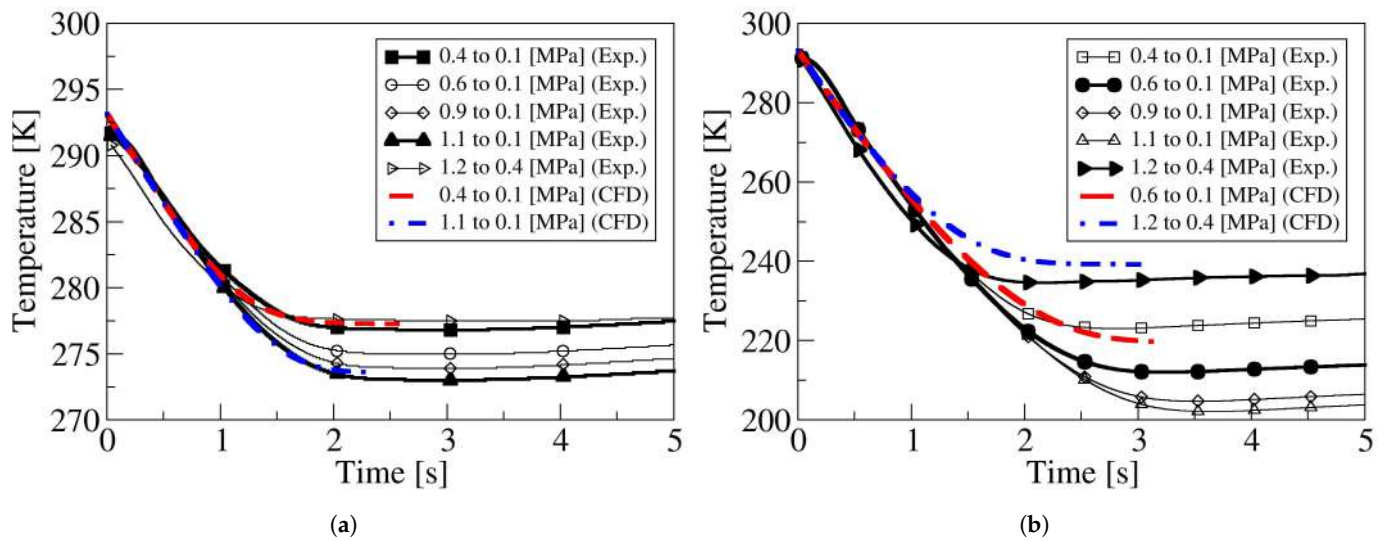


Figure 6. Experimentally-based and numerical temperature decay in the upstream reservoir. (a) The flow goes from the large to the small reservoir. (b) The flow goes from the small to the large reservoir.

The first thing to be observed is that the fluid temperature decay is proportional to the initial pressure ratio between reservoirs, and the higher the pressure ratio, the higher the fluid temperature decay in the upstream reservoir. As previously observed, the temperature drop is particularly high in the small reservoir. Temperature decreases of over 50° are observed in the small reservoir, and such decrease is of less than 20° in the large one. When comparing the temperature evolution experimentally-based with the CFD one, a particularly good agreement is observed in the large reservoir, and a maximum difference between experimental and numerical results of about 3.3% is observed in the small reservoir when the discharge is from 0.6 to 0.1 MPa. The experimentally-based results generate final temperatures slightly lower than the ones obtained via CFD simulations. As the walls were assumed adiabatic in the CFD simulations, Figure 6 confirms this assumption; then, the heat transferred through the walls appears to be negligible.

Based on the experimental pressure temporal evolution and the calculated temperature, the temporal mass variation at each reservoir for both flow directions and for all different pressures studied is presented in Figure 7. The same figure presents, as well, the mass decay/increase obtained via CFD. Figure 7a,b introduce the reservoirs temporal mass variation when the air flows from the L-to-S and S-to-L reservoirs, respectively. As previously observed, when the discharge is from 1.2 to 0.4 MPa, the discharge time is minimum, and this is due to the small density ratio associated to the fluid. Regardless of the flow direction, the curves representing the temporal mass variation on both reservoirs are, for the discharge initial first second, having a constant pendent, but, during the next 1.5 discharge seconds, the curves are rounded. The constant pendent is likely to indicate choked flow conditions. The curves of the Mach number versus time should clarify this hypothesis.

The instantaneous mass flow flowing between the two reservoirs for all pressures studied and for both flow directions, is presented in Figure 8. Notice that the information presented in this figure was directly extracted from Figure 7. For each pressure ratio, Figure 7 presents two curves, representing the mass decrease in one reservoir and the mass increase in the other; therefore, each of the mass flow curves could be obtained twice, considering the mass decrease and increase in the respective reservoirs. Since both mass flow curves were almost identical, in Figure 8, just the curves representing the mass flow decrease in the upstream reservoir are presented. Figure 8a characterizes the mass flow between reservoirs when the fluid is going from the large to the small reservoir. Notice that, as the pressure ratio increases, the mass flow also increases. In reality, this mass flow increase associated with the pressure ratio increase is due to the upstream

fluid density increase. It is as interesting to see that, as the pressure ratio increases, the overall discharge time, and the time at which the flow remains under sonic conditions, also increases; Figure 9 shall further clarify this point. Figure 8b presents the mass flow for the fluid going from the small to the large reservoir. It is interesting to realize that, regardless of the pressure ratio evaluated, the discharge time lasts almost a second longer than when the flow goes in the opposite direction. As already observed in Figure 8a, for a discharge from 1.2 to 0.4 MPa, the pendent of the mass flow curve is much higher than for the rest of the cases evaluated, clearly showing that the initial downstream density plays an important role when considering the discharge temporal evolution and final time, and such time decreases with the density ratio decrease.

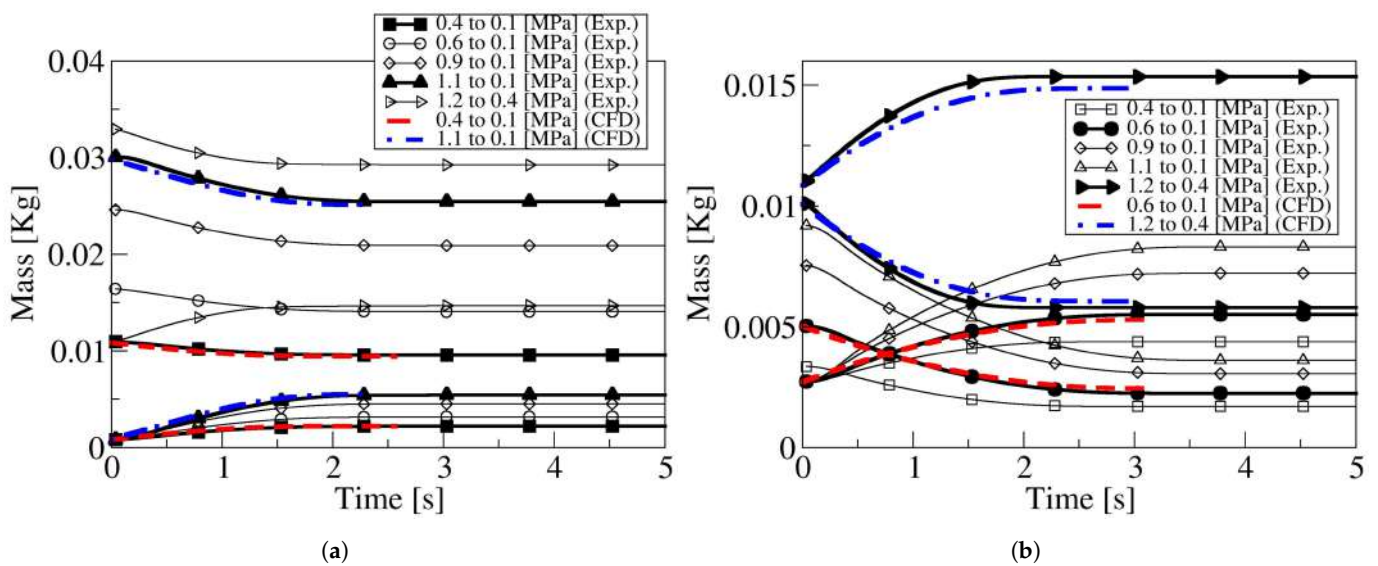


Figure 7. Temporal mass variation in each reservoir based on experimental data and for all pressures studied. (a) Flow from large to small reservoir. (b) Flow from small to large reservoir.

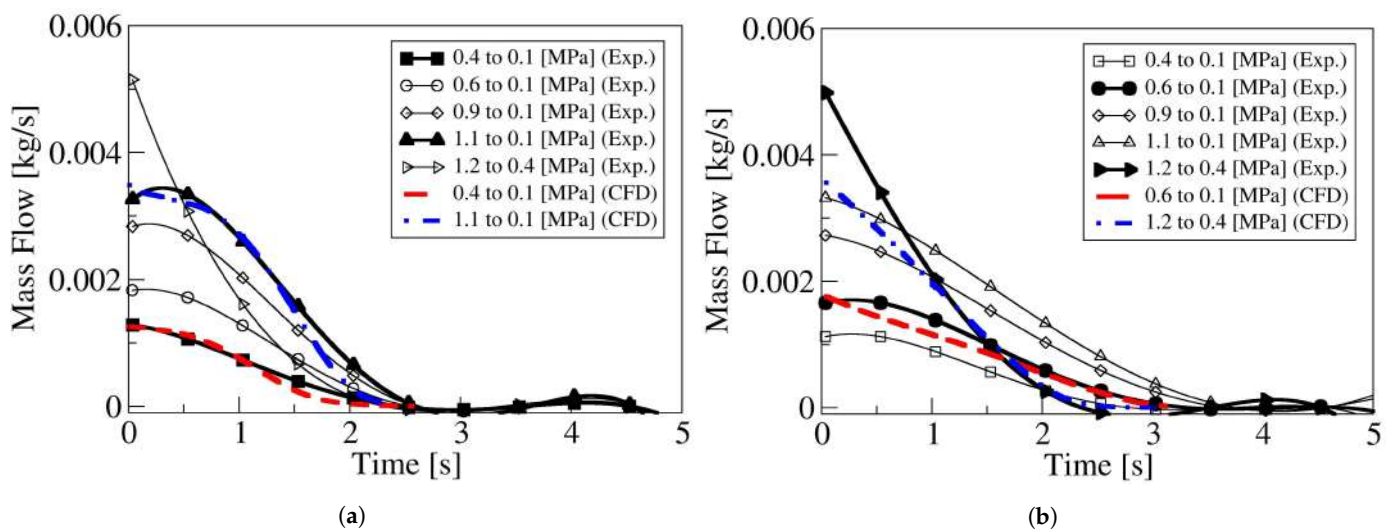


Figure 8. Mass flow between reservoirs, based on experimental data and for all pressures studied. (a) Flow from large to small reservoir. (b) Flow from small to large reservoir.

Figure 8 also compares the mass flow obtained experimentally with the numerical one, and the agreement appears to be very good for all cases studied; just when the discharge is from 1.2 to 0.4 MPa, and the flow goes from the small to the large reservoir, the pendent of the mass flow during the initial 0.5 s shows some discrepancy. In fact, already, in Figure 7b, clear differences in the temporal mass evolution are observed for this particular discharge.

When comparing Figure 8a,b, for any given pressure differential, it is observed that, at time zero, the mass flow, when the fluid goes from L-to-S, is slightly larger than when the fluid goes from the S-to-L, indicating the flow is seeing a higher restriction when the fluid is going from S-to-L reservoir.

Figure 9a,b introduce the Mach number temporal evolution at the nozzle minimum section as a function of the pressure differential and for the two flow directions, L-to-S and S-to-L reservoirs, respectively. The information presented obeys the cases where numerical and experimentally-based results can be compared. When the fluid goes from the large to the small reservoir, the flow is initially sonic, and the time during which the flow remains under sonic conditions increases with the pressure ratio increase, as in Figure 9a. When the fluid is flowing from the small to the large reservoir, and for initial respective pressures of 1.2 MPa and 0.4 MPa, the discharge is sonic during a very small time. But, when the initial reservoirs pressure is of 0.6 MPa and 0.1 MPa, respectively, the time at which the flow remains sonic is of nearly 1 s, which is almost the same time observed when the fluid goes from the large to the small reservoir, and, for a respective pressure of 1.1 MPa and 0.1 MPa, compare figures Figure 9a,b.

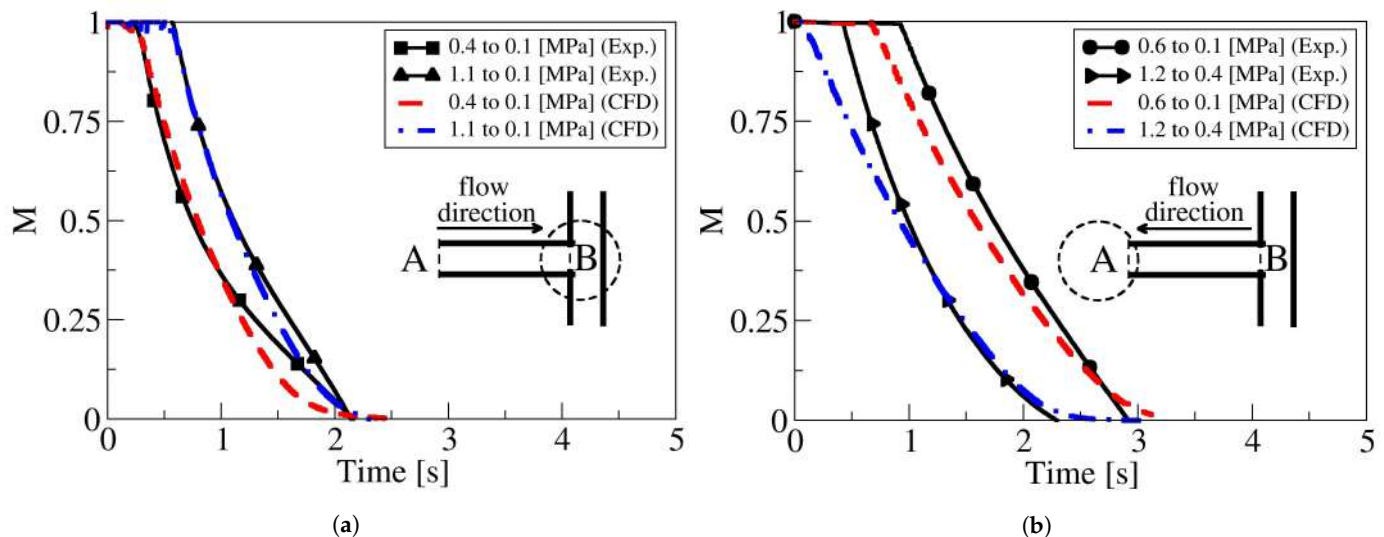


Figure 9. Temporal evolution of the maximum Mach number obtained at the nozzle separating the two reservoirs. Comparison between the numerical results and the experimentally-based ones. (a) Flow from large to small reservoir. (b) Flow from small to large reservoir.

The reason why the fluid remains sonic during a longer time, when the flow goes from S-to-L reservoirs, is likely to be caused by the sudden flow restriction the fluid is suffering when the flow enters the horizontal section of the nozzle and coming from the two T shape branches. The two T shape branches promote the existence of a flow restricted section at the horizontal nozzle inlet, restricting, as well, the entrance of the fluid from a vertical plane, the fluid can only move vertically in the two vertical branches of the T nozzle. In reality, this effect is creating a smaller effective section of the flow in this case than when flow goes from large to small reservoir. In other words, the nozzle resistance to the fluid is larger when the flow goes from the small to the large reservoir; therefore, the mass flow is also smaller. In fact, when comparing the mass flow curves for the same pressure drop presented in Figure 8a,b, it can be clearly seen that the mass flow is higher during the initial times when the fluid goes from the L-to-S reservoir. At this point, it must be highlighted that the location where the Mach number values are computed is always where the spatially averaged Mach number is maximum. Such location is at the end of the horizontal nozzle, beginning of the T junction, when the flow goes from L-to-S reservoir, and at the end of the horizontal nozzle and beginning of the large tank, when the flow goes from the S-to-L reservoir. Such different locations were expected; then, regardless of the

flow direction, the fluid at the entrance of the horizontal nozzle has to be subsonic and accelerates along it.

The temporal discharge coefficients as a function of the Reynolds number, and for the four cases at which CFD and experimentally-based results are generated, is presented in Figure 10. The variations of the discharge coefficient when the flow goes from the large to the small tank, and vice versa, is given in Figure 10a,b, respectively. For both flow directions, the numerical and experimentally-based results are presented for the pressure differentials studied using both methodologies.

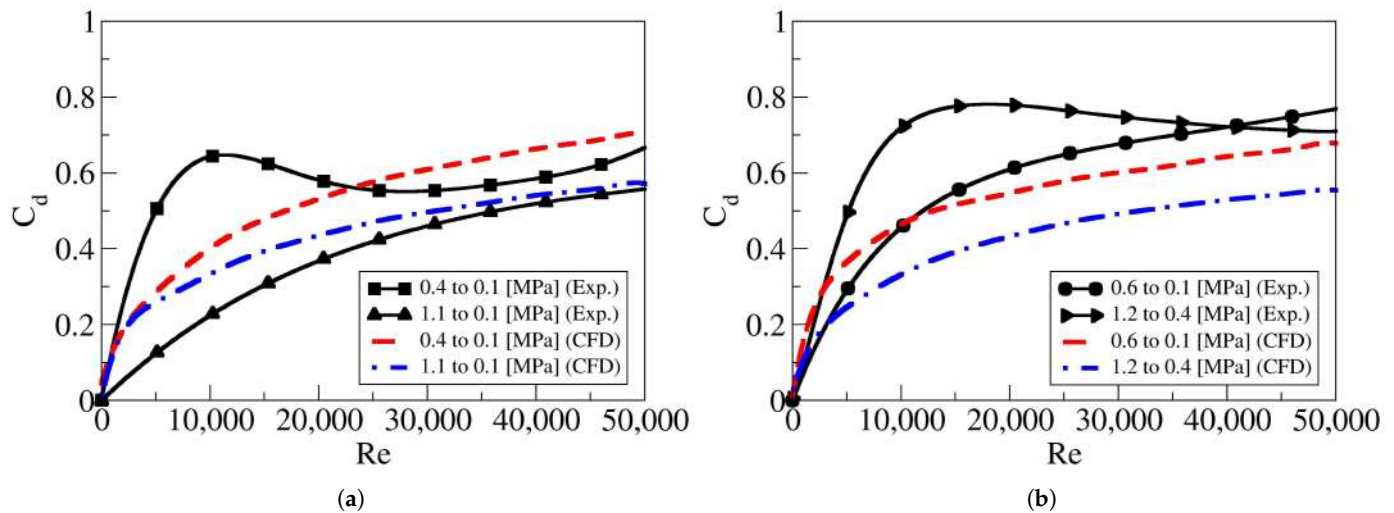


Figure 10. Nozzle discharge coefficient based on experimental data and for all pressures studied. (a) Flow from large to small reservoir. (b) Flow from small to large reservoir.

The first thing to notice is that, for a given flow direction, the discharge coefficient shows a very similar temporal trend, regardless of the pressure ratio evaluated. In fact, it is to be expected that the discharge coefficient depends on the Reynolds number but not on the pressure ratio between reservoirs. Some differences are observed between the discharge coefficients obtained numerically and the ones obtained based on experimental data, particularly at low Reynolds numbers. Authors believe such differences are due to the differences in fluid temperature between experimental and CFD results appearing at the end of the discharge. However, for a given flow direction, the asymptotic values of the discharge coefficients are almost the same regardless of the methodology employed to calculate them. The discharge coefficients obtained when the flow is going from the large to the small reservoir are slightly higher than the ones obtained when the flow is going in the opposite direction. This supports what has been presented until the moment, which is the time required to discharge from the small to the large reservoir is larger than the one needed when the discharge is from the large to the small tank. In other words, the fluid is finding more resistance to flow from the small to the large reservoir than in opposite direction. As explained before, this must be due to the restriction the fluid is observing when flowing from the two T branches and entering the horizontal one.

In order to obtain a single curve representing the evolution of the discharge coefficient as a function of the Reynolds number, and for each flow direction, at each Reynolds number, the average discharge coefficient was determined. The mathematical equation of the resulting curves is presented in Equation (13), which represents the generic equation for the discharge coefficient as a function of the Reynolds number and for both flow directions. The parameters $a_0 \dots a_{10}$ characterizing the discharge coefficient curve for each flow direction are defined in Table 2. Notice that, as in Figure 10b, the maximum Reynolds number is 50,000, and the parameters given in the first two rows of Table 2 are valid for this Reynolds number range. Nevertheless, based on the results from the CFD simulations,

a second set of parameters valid for a Reynolds number range $1000 \leq Re \leq 130,000$ are also presented in the last two rows of Table 2.

$$C_d = a_0 + a_1 Re + a_2 Re^2 + \dots + a_{10} Re^{10}. \quad (13)$$

Table 2. Constant values of the discharge coefficient equation for two different range of Reynolds number and different flow directions, large to small reservoirs, and vice versa.

Reynolds Range	Flow Direction	a_0	a_1	a_2	a_3	a_4	a_5	a_6	a_7	a_8	a_9	a_{10}
1 to 50,000	L to S	1.470×10^{-1}	2.625×10^{-5}	-9.852×10^{-10}	3.077×10^{-14}	-8.131×10^{-19}	1.774×10^{-23}	-2.904×10^{-28}	3.252×10^{-33}	-2.300×10^{-38}	9.184×10^{-44}	-1.572×10^{-49}
	S to L	3.608×10^{-2}	1.053×10^{-4}	-5.156×10^{-9}	-1.795×10^{-13}	3.144×10^{-17}	-1.407×10^{-21}	2.351×10^{-26}	1.988×10^{-31}	-1.406×10^{-35}	2.063×10^{-40}	-1.047×10^{-45}
1000 to 130,000	L to S	1.480×10^{-1}	2.566×10^{-5}	-8.676×10^{-10}	1.981×10^{-14}	-2.541×10^{-19}	7.886×10^{-25}	2.838×10^{-29}	-4.980×10^{-34}	3.824×10^{-39}	-1.481×10^{-44}	2.350×10^{-50}
	S to L	6.400×10^{-2}	5.258×10^{-5}	-4.250×10^{-9}	2.382×10^{-13}	-8.453×10^{-18}	1.909×10^{-22}	-2.779×10^{-27}	2.594×10^{-32}	-1.499×10^{-37}	4.884×10^{-43}	-6.857×10^{-49}

One of the advantages of performing 3D-CFD simulations is that it allows to carefully analyze the flow evolution inside the nozzle. The flow field dynamics given as instantaneous velocity contours at both ends of the horizontal pipe, for both flow directions, reservoir pressures and at three different time instants, 0.02 s, 0.5 s, and 1 s, is introduced in Figure 11. Each column characterizes the time at which the velocity field is presented. The initial two rows of Figure 11 show the flow field at both horizontal nozzle ends when the fluid goes from the L-to-S reservoir, and the initial upstream-downstream pressure on each tank is 0.4 MPa–0.1 MPa and 1.1 MPa–0.1 MPa, respectively. The final two rows show the velocity field that, when the flow goes from the S-to-L reservoir, the upstream-downstream initial pressures are 0.6 MPa–0.1 MPa and 1.2 MPa–0.4 MPa, respectively.

When the fluid goes from the large to the small reservoirs, and for the two pressure ratios studied, during the initial milliseconds, $t = 0.02$ s, the fluid reaches sonic conditions at the horizontal nozzle outlet just before the T junction, and supersonic flow conditions are observed as the fluid expands to the two lateral vertical branches; see the first and second rows of Figure 11. At $t = 0.5$ s, and for upstream-downstream initial pressures of 0.4 MPa–0.1 MPa, the fluid has become subsonic at all points, the maximum spatial averaged velocity is 239 m/s, which corresponds to $M = 0.74$, and the fluid still remains detached when entering the T junction. After 1 s of the origin of the discharge, the maximum fluid velocity has decreased to 120 m/s, but the flow keeps being detached at the T junction entrance. But, when the L-to-S reservoirs initial pressure is of 1.1 MPa and 0.1 MPa, respectively, after 0.5 s, the flow is still under sonic conditions, and the Mach number and the associated spatial averaged velocities at the inlet and outlet of the horizontal pipe are of $M = 0.53$ (176 m/s) and $M = 0.99$ (310 m/s), respectively. The respective values of the Mach number in these two pipe locations are of 0.45 and 0.56, after the initial second of the discharge.

The discharge when the fluid flows from the small to the large reservoir at initial pressures of 0.6 MPa and 0.1 MPa, respectively, is presented in the third row of Figure 11. Now, the maximum Mach number appears at the entrance of the large reservoir, and horizontal pipe outlet, as expected according to the theory [29,30]. At time $t = 0.02$ s, the respective Mach numbers and spatial averaged fluid velocities at the horizontal pipe inlet and outlet are $M = 0.6$ (198 m/s) and $M = 1$ (353 m/s). For these particular initial pressures, and after 0.5 s, the flow still remains under sonic conditions, and the inlet and outlet Mach numbers and fluid velocities are $M = 0.59$ (190 m/s) and $M = 1$ (317 m/s), respectively. At this point, it is important to realize that under sonic conditions, the spatial averaged fluid velocity depends on the instantaneous fluid temperature. When comparing these figures with the ones characterizing the initial pressure drop of 1.2 MPa to 0.4 MPa, presented as the bottom row of Figure 11, it is realized that now just at the initial instants, $t = 0.02$ s, the flow is sonic, but the pressure drop is not large enough to generate a supersonic expansion as the fluid enters the large reservoir. After 0.5 s, the discharge is completely subsonic, being the horizontal pipe inlet and outlet Mach numbers and

associated spatial averaged fluid velocities of $M = 0.57$ (182 m/s) and $M = 0.73$ (230 m/s), respectively. At this point, it is interesting to observe the agreement between the CFD results presented in Figures 9 and 11, noticing that the time during which flow is sonic has a perfect match for all pressures studied.

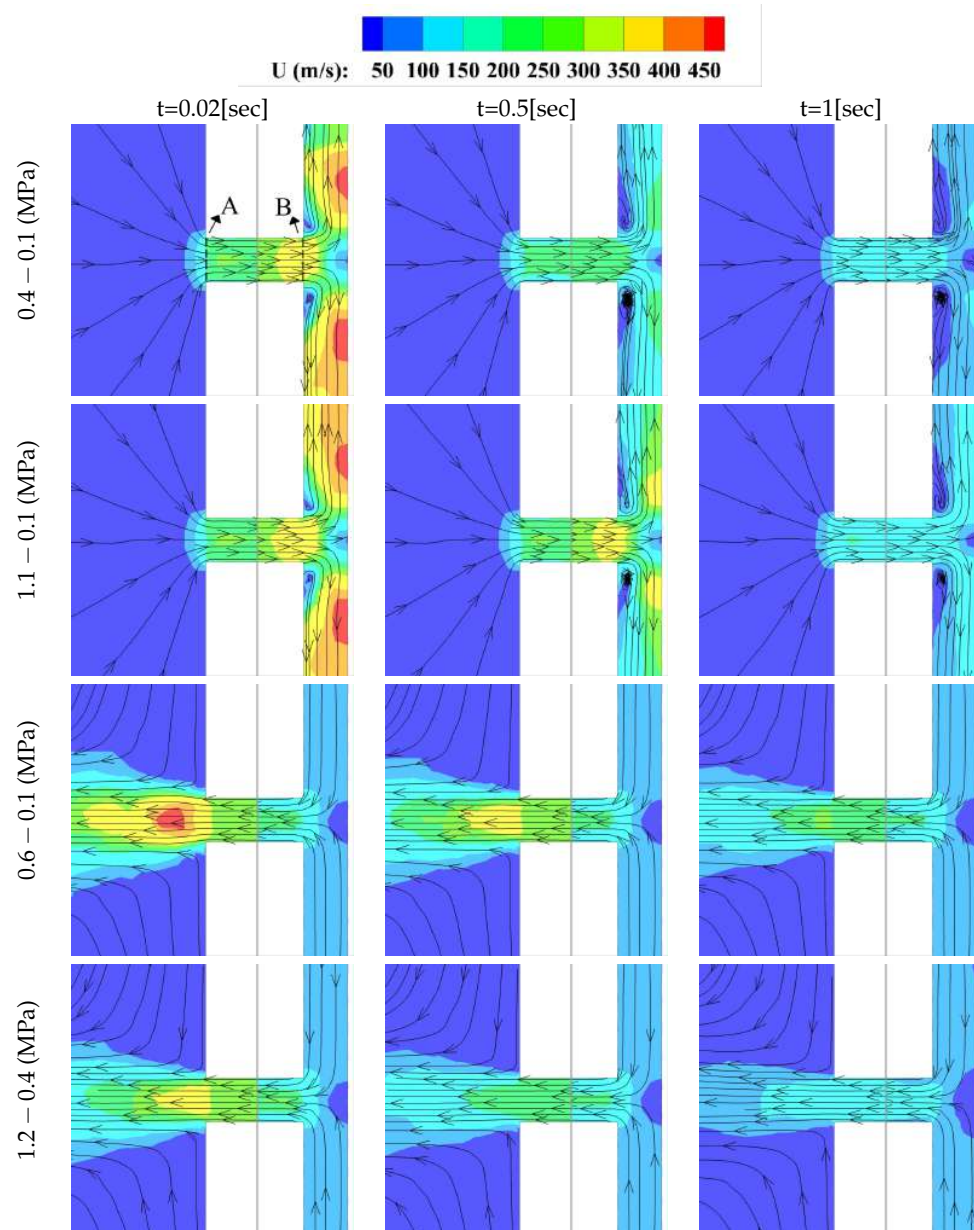


Figure 11. Velocity contours of all CFD cases studied and at three instants, 0.02, 0.5, and 1 s. The first and second rows represent the fluid evolution when the fluid goes from the L-to-S reservoir, and the respective upstream/downstream initial pressures are 0.4 MPa–0.1 MPa and 1.1 MPa–0.1 MPa. The third and fourth rows characterize the two cases when the flow goes from S-to-L reservoir, being the upstream/downstream initial pressures of 0.6 MPa–0.1 MPa and 1.2 MPa–0.4 MPa, respectively.

The observations made in Figure 11 are clarifying why, during the experimental tests and CFD simulations, the discharge time was larger when the flow was flowing from the S-to-L reservoir than when flowing in the opposite direction; see all figures between Figures 4 and 8. Notice, as well, from Figure 8, that the maximum mass flow at time zero is always larger when the flow is going from the L-to-S reservoir than when going from the S-to-L one, clearly indicating the added difficulty for the fluid to flow from the small

to the large reservoir. This difficulty can be understood when analyzing the inlet section under both flow conditions. When the flow goes from the large to small reservoir, the flow enters the horizontal nozzle from any direction, 360 degrees, but, when the flow goes from the small to the large reservoir, initially, the fluid needs to enter from the two ends of a T branch and then the fluid needs to enter the horizontal nozzle from the two sides of the T branch, therefore facing a particularly narrow inlet when compared to the opposite fluid direction. The effects of this higher flow restriction, when the fluid is going from the small to the large reservoir, can also be observed when analyzing the discharge coefficients in both flow directions. Notice that the discharge coefficient, when the fluid is going from the S-to-L reservoir, is asymptotically smaller than when the fluid flows from the L-to-S reservoir; see Equation (13) and Table 2.

The work presented in the present manuscript consisted of evaluating the discharge coefficient of a T shape nozzle under compressible flow conditions. Experimental and numerical analyses were performed. Numerical simulations clarified where the sonic conditions are to be expected. Discharge coefficients were dependent on the flow direction and the Reynolds number, and they agree well with the ones obtained by Comas et al. [13] and Nagao et al. [9], specially when considering the different nozzle length to diameter ratio. In the CFD simulations, the fluid was considered as ideal, and similar CFD simulations were performed by Lakzian et al. [18] and Mazzelli et al. [17], where the fluid was considered as ideal, as well, and studied under similar pressure differentials and the same turbulence model. From the comparison of the present study with Reference [9,13,17,18], it can be concluded that the error generated by the CFD simulations is small and acceptable under the engineering applications point of view.

6. Conclusions

The discharge time is proved to be directly related to the upstream/downstream density ratio. The discharge coefficients on both flow directions of a T shape nozzle, and considering the fluid as compressible and real, were obtained in the present manuscript based on experimental data. The same information was obtained from CFD simulations. The CFD simulations performed showed a good match with the experimental results and allowed understanding of the differences of the temporal flow evolution inside the nozzle at different flow directions. The exact locations where the flow was sonic, and even supersonic, were detected, allowing further modification of the T shape nozzle design in future applications. The theoretical methodology presented was based on the experimental data and proved to be very accurate and reliable, particularly when temporal pressure and temperature were known. The final equations characterizing the discharge coefficient as a function of the Reynolds number and for both flow directions are provided.

Author Contributions: Conceptualization, A.C. and J.M.B.; methodology, C.R.-C., N.M.T., and J.M.B.; experimentation, C.R.-C.; software, A.C. and N.M.T.; validation, N.M.T. and J.M.B.; formal analysis, A.C. and J.M.B.; investigation, C.R.-C., N.M.T., A.C., and J.M.B.; data curation, C.R.-C. and N.M.T.; writing—original draft preparation, N.M.T. and J.M.B.; writing—review and editing, J.M.B.; visualization, N.M.T. and J.M.B.; supervision, J.M.B.; project administration, A.C. and J.M.B.; funding acquisition, C.R.-C., J.M.B., and A.C. All authors have read and agreed to the published version of the manuscript.

Funding: Part of the computations were done in the Red Española de Supercomputación (RES), Spanish supercomputer network, under the grant IM-2020-1-0001.

Institutional Review Board Statement: Not applicable.

Informed Consent Statement: Not applicable.

Data Availability Statement: Not applicable.

Conflicts of Interest: The authors declare no conflict of interest.

References

1. ISO6358. Pneumatic fluid power-components using compressible fluids. In *Determination of Low-Rate Characteristics*; Technical Report; ISO Standards Org: Geneva, Switzerland, 1989.
2. Kagawa, T.; Wang, T.; Ishii, Y.; Terashima, Y.; Morozumi, T.; Mogami, T.; Oneyama, N. Determination of flow rate characteristics of small pneumatic valves using isothermal chamber by pressure response. In *Proceedings of the 7th Symposium on Fluid Control Measurement and Visualization*, Sorrento, Italy, 25–28 August 2003.
3. Johnson, R.C. Calculations of real-gas effects in flow through critical-flow nozzles. *J. Basic Eng. Trans. ASME Ser. D* **1964**, *86*, 519–526. [[CrossRef](#)]
4. Bober, W.; Chow, W. Nonideal gas effects for the venturi meter. *ASME J. Fluid. Eng.* **1991**, *113*, 301–304. [[CrossRef](#)]
5. Kouremenos, D.; Antonopoulos, K.; Kakatsios, X. A correlation of the isentropic exponents of real gases. *Int. J. Heat Fluid Flow* **1988**, *9*, 410–414. [[CrossRef](#)]
6. Kouremenos, D.; Antonopoulos, K. Sound velocity and isentropic exponents of real air on its compressibility chart. *Int. J. Heat Fluid Flow* **1991**, *12*, 137–141. [[CrossRef](#)]
7. Kim, H.; Lee, J.; Park, K.; Setoguchi, T.; Matsuo, S. A study of the critical nozzle for flow rate measurement of high-pressure hydrogen gas. *J. Therm. Sci.* **2007**, *16*, 28–32. [[CrossRef](#)]
8. Kim, J.H.; Kim, H.D.; Setoguchi, T.; Matsuo, S. Computational study on the critical nozzle flow of high-pressure hydrogen gas. *J. Propuls. Power* **2008**, *24*, 715–721. [[CrossRef](#)]
9. Nagao, J.; Matsuo, S.; Mohammad, M.; Setoguchi, T.; Kim, H.D. Numerical study on characteristics of real gas flow through a critical nozzle. *Int. J. Turbo Jet-Engines* **2012**, *29*, 21–27. [[CrossRef](#)]
10. Nagao, J.; Matsuo, S.; Suetsugu, S.; Setoguchi, T.; Kim, H.D. Characteristics of high Reynolds number flow in a critical nozzle. *Int. J. Hydrog. Energy* **2013**, *38*, 9043–9051. [[CrossRef](#)]
11. Nakao, S. Development of critical nozzle flow meter for high pressure hydrogen gas flow measurements. *Proc. JSME Fluid Dyn. Sect. Kanazawa Jpn. G* **2005**, *201*, 2005.
12. Ding, H.; Wang, C.; Zhao, Y. Flow characteristics of hydrogen gas through a critical nozzle. *Int. J. Hydrog. Energy* **2014**, *39*, 3947–3955. [[CrossRef](#)]
13. Comas, A.; Rio-Cano, C.; Bergada, J. A novel method to determine the discharge coefficient of constant section nozzles under compressible dynamic flow conditions. *J. Fluids Eng.* **2019**, *141*, 071108. [[CrossRef](#)]
14. Lee, B.I.; Kesler, M.G. A generalized thermodynamic correlation based on three-parameter corresponding states. *AIChE J.* **1975**, *21*, 510–527. [[CrossRef](#)]
15. Farzaneh-Gord, M.; Pahlevan-Zadeh, M.S.; Ebrahimi-Moghadam, A.; Rastgar, S. Measurement of methane emission into environment during natural gas purging process. *Environ. Pollut.* **2018**, *242*, 2014–2026. [[CrossRef](#)] [[PubMed](#)]
16. García-Todolí, S.; Iglesias-Rey, P.L.; Mora-Meliá, D.; Martínez-Solano, F.J.; Fuertes-Miquel, V.S. Computational determination of air valves capacity using cfd techniques. *Water* **2018**, *10*, 1433. [[CrossRef](#)]
17. Mazzelli, F.; Little, A.B.; Garimella, S.; Bartosiewicz, Y. Computational and experimental analysis of supersonic air ejector: Turbulence modeling and assessment of 3D effects. *Int. J. Heat Fluid Flow* **2015**, *56*, 305–316. [[CrossRef](#)]
18. Lakzian, E.; Hajian, M.; Farahmand, A. The entropy generation rate minimization for a proposed air ejector for the carpet industry. *Meccanica* **2018**, *53*, 145–159. [[CrossRef](#)]
19. Smolka, J.; Bulinski, Z.; Fic, A.; Nowak, A.J.; Banasiak, K.; Hafner, A. A computational model of a transcritical R744 ejector based on a homogeneous real fluid approach. *Appl. Math. Model.* **2013**, *37*, 1208–1224. [[CrossRef](#)]
20. Macia, L.; Castilla, R.; Gamez-Montero, P.J.; Camacho, S.; Codina, E. Numerical simulation of a supersonic ejector for vacuum generation with explicit and implicit solver in openfoam. *Energies* **2019**, *12*, 3553. [[CrossRef](#)]
21. Arias, D.A.; Shedd, T.A. CFD Analysis of Compressible Flow Across a Complex Geometry Venturi. *J. Fluids Eng.* **2007**, *129*, 1193–1202. [[CrossRef](#)]
22. Ding, H.; Wang, C.; Zhao, Y. Surface roughness effect on flow measurement of real gas in a critical nozzle. *Measurement* **2015**, *68*, 82–91. [[CrossRef](#)]
23. Darbandi, M.; Roohi, E. Study of subsonic–supersonic gas flow through micro/nanoscale nozzles using unstructured DSMC solver. *Microfluid. Nanofluidics* **2011**, *10*, 321–335. [[CrossRef](#)]
24. Zhao, J.; Liu, W.; Zhao, J.; Grekhov, L. Numerical investigation of gas/liquid two-phase flow in nozzle holes considering the fuel compressibility. *Int. J. Heat Mass Transf.* **2020**, *147*, 118991. [[CrossRef](#)]
25. Kumar, A.; Ghobadian, A.; Nouri, J.M. Assessment of cavitation models for compressible flows inside a nozzle. *Fluids* **2020**, *5*, 134. [[CrossRef](#)]
26. Lichtarowicz, A.; Duggins, R.; Markland, E. Discharge coefficients for incompressible non-cavitating flow through long orifices. *J. Mech. Eng. Sci.* **1965**, *7*, 210–219. [[CrossRef](#)]
27. Bergada, J.; Codina, E. Discharge coefficients for a four nozzle two flapper servovalve. In *Proceedings of the 46th National Conference on Fluid Power*, Chicago, IL, USA, 23–24 March 1994; Volume 1, pp. 213–218.
28. Plocker, U.; Knapp, H. Save time in computing density. *Hydrocarb. Process.* **1976**, *55*, 199–201.
29. Zucrow, M.; Hoffman, J. *Gas Dynamics*; John Wiley & Sons: Hoboken, NJ, USA, 1976; Volume 1.
30. Bergada Grañó, J.M. *Mecánica de Fluidos: Breve Introducción Teórica con Problemas Resueltos*, 3rd ed.; Universitat Politècnica de Catalunya; Iniciativa Digital Politècnica, Barcelona, Spain: 2017.

6.2 Conference Papers

5TH INTERNATIONAL CONFERENCE ON ADVANCES IN MECHANICAL ENGINEERING ISTANBUL 2019, 17-19 DECEMBER 2019

ACTIVE FLOW CONTROL ON SD7003 AIRFOIL USING SYNTHETIC JETS

Navid M Tousi^{1*}, Josep M Bergada¹, Ivette Rodriguez²

ABSTRACT

The present paper focuses on applying the Active Flow Control (AFC) technology on the Selig-Donovan 7003 (SD7003) airfoil at Reynolds number 60,000, the idea is to employ synthetic jets in order to modify the lift and drag forces acting on the airfoil. In this study two angles of attack (AoA) are considered, two (AFC) parameters the jet momentum coefficient and forcing frequency are studied. All the CFD simulations are performed in two dimensions and using the Spalart-Allmaras turbulent model. The primary motivation behind the current examination is to find out the optimum frequency and momentum coefficient of the pulsating jets to minimize the drag and maximize the lift coefficients. Results are showing that, as the angle of attack increases, the application of the (AFC) technology becomes more effective, allowing to considerably increase the airfoil efficiency. For example, for (AoA) of 14 degrees the airfoil efficiency was increased by 98% versus the non-actuated case.

Keywords: Active Flow Control, synthetic jets, CFD RANS simulation, SD7003 airfoil

1. INTRODUCTION

The reduction of drag and increasing of lift have a considerable influence in fuel consumption and improvement of stability, endurance, and maneuverability of airplanes. Active Flow Control (AFC), based on addition of momentum at precise locations of the boundary layer, is one of the methods with good potential to do so. Cattafesta and Sheplak [1] classified the active flow control techniques into the following solutions: 1-moving body actuators that have the purpose of inducing local fluid motion without the need of adding mass. 2-plasma actuators that have been studied recently due to their fast time response and finally 3-fluidic actuators, which are the most common type of actuators, and their primary function is to inject/suck fluid to/from the boundary layer. Among the different fluidic actuators, the devices involving zero-net-mass-flux oscillatory jets or synthetic jets have shown good feasibility for industrial applications and effectiveness in controlling flow separation (e.g., Glezer and Amitay [2], Rumsey et al. [3], Wygnanski [4], Findanis and Ahmed [5]). The application of synthetic jets to control flow separation is based on their ability to stabilize the boundary layer by adding/removing momentum to/from the boundary layer with the formation of vortical structures. The vortical structures in turn promote boundary layer mixing and hence momentum exchange between the outer and inner parts of the boundary layer. In the recent decades, these jets have been implemented on different airfoils and have been studied by many researchers using various numerical models. Donovan et al. [6] used the Reynolds-averaged Navier Stokes (RANS) equations approach to compute the flow around a NACA0012 airfoil using a synthetic jet. A significant increase in lift (29%) was observed in the post-stall regime. They observed, an important actuation parameter was the amplitude of the jet velocity, which is an essential term to define the momentum coefficient. In his experiments, McCormick [7] observed that, to have a positive effect on the lift coefficient, the momentum coefficient must be at least 0.002 for $Re = 500000$. Gillaranz et al. [8] experimentally observed a weak dependency on frequency for angles of attack smaller than 10 degrees and when using a NACA0015 profile. Following Gillaranz et al. [8] experiments, You and Moin [9] performed a CFD model using Large Eddy Simulation (LES) on the same airfoil to investigate the mechanism for separation control, they observed that the synthetic-jet actuation not only stabilizes the boundary layer, but also enhances mixing between inner and outer parts of the boundary layer. Kim and Kim [10] studied the effects of synthetic jets on separation flow control on NACA23012 airfoil at Reynolds number 1,200,000. They solved unsteady Reynolds-averaged Navier–Stokes (URANS) equations with $k-w$ SST turbulent model. To control the separation on the airfoil NACA23012, Monir et al. [11] applied synthetic jets, he also used

¹ Department of Fluid Mechanics, Universitat Politècnica de Catalunya, BarcelonaTECH, 08034, Barcelona, Spain

² Department of Heat Engines, Universitat Politècnica de Catalunya, BarcelonaTECH, 08034, Barcelona, Spain

*E-mail address: navid.monshi.tousi@upc.edu, josep.m.bergada@upc.edu, ivette.rodriguez@upc.edu

URANS with k- ω SST turbulent model. In their study it was demonstrated that tangential (AFC) jets were more effective than jets blowing at an angle.

In the present study, the Selig-Donovan 7003 (SD7003) airfoil at Reynolds number 60,000 is numerically studied, the main reason why this particular profile was chosen is that, there is considerable numerical and experimental data available in the literature on this airfoil and for the same Reynolds number. The main aim of the work is to increase the airfoil efficiency, at different angles of attack. Notice that from the different (AFC) technologies, periodic forcing is going to be employed, then based on several previous investigations [12-14], periodic forcing is the most effective way to activate the boundary layer and therefore requires the minimum amount of energy to obtain the maximum airfoil efficiency.

2. NUMERICAL METHOD

2.1. FLOW SOLVER

A second order two-dimensional finite volume CFD solver (OpenFOAM) for unsteady Reynolds averaged Navier-Stokes equations (URANS) have been used with an implicit scheme. The Spalart-Allmaras (S-A) model was implemented as the turbulence model. The equation for the pressure has been solved using the Geometric Algebraic Multigrid (GAMG) solver, available in OpenFOAM. This particular solver has been shown to be highly scalable for the number of coarse-level grid cells that are likely to appear in the mesh generated. A standard smoother has also been employed for the velocity solver. The pressure-coupling algorithm (Pressure Implicit with Splitting of Operators) (PISO) was used.

2.2. DOMAIN AND BOUNDARY CONDITIONS

The SD7003 airfoil with a chord length C was placed in the computational domain introduced in Figure 1. The leading edge was located in the center of coordinate system, and the horizontal distance between this point and the inlet was set to $15C$, while the outlet was situated $19C$ downstream of the airfoil trailing edge. Instead of considering different domains at different angles of attack, the wing profile was fixed at zero degree and the different angles of attack were achieved by decomposing the free-stream velocity into the x and y components.

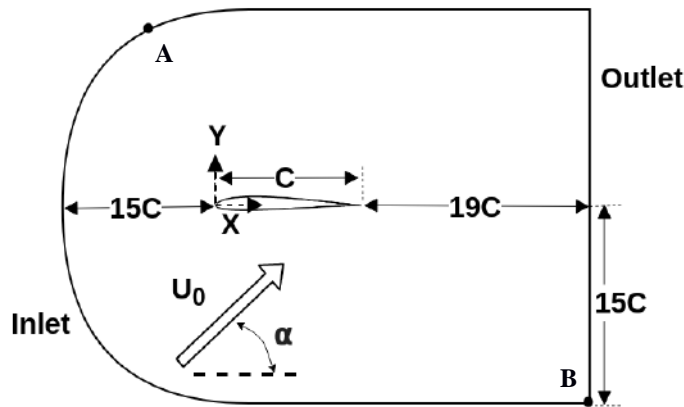


Figure 1. Computational domain

To solve the problem, the following boundary conditions were used. At the inlet, which is located along the curve connecting points A and B in figure 1, a constant velocity profile was imposed and its components were set to $(u, v, w) \equiv (U_0 \cos \alpha, U_0 \sin \alpha, 0)$, Newman boundary conditions for pressure were employed. The no-slip boundary condition was applied at the airfoil. At the outlet, which again is located between points A and B in figure 1, but now turning clockwise, Dirichlet boundary conditions for pressure and Newman boundary conditions for velocity were selected. In order to properly capture the laminar separation bubble (LSB), the turbulent viscosity was set to the 10^{-20} in the free-stream flow, as proposed by [15].

2.3. NON-DIMENSIONAL PARAMETERS

The different non dimensional parameters used in the present paper are defined blow.

Lift and drag coefficients are defined as:

$$C_d = \frac{2F_d}{\rho C U_0^2}$$

$$C_l = \frac{2F_l}{\rho C U_0^2}$$

Where C = chord length, U_0 = free-stream velocity and ρ = free-stream fluid density, F_d and F_l are the dimensional drag and lift forces, respectively.

The airfoil efficiency is defined as:

$$\text{airfoil efficiency} = \frac{C_l}{C_d}$$

The pressure coefficient is defined as following:

$$C_p = \frac{P - P_0}{\frac{1}{2} \rho U_0^2}$$

where P_0 is the free-stream pressure.

The skin friction coefficient is obtained using:

$$C_f = \frac{\tau_w}{\frac{1}{2} \rho U_0^2}$$

where τ_w represents the wall shear stresses.

The momentum coefficient is given as:

$$C_\mu = \frac{h(\rho U_{\max}^2) \sin \theta_j}{C(\rho U_0^2)}$$

where h = jet width, U_{\max} = maximum jet velocity, θ_j = jet inclination angle with respect to the airfoil surface.

The non-dimensional frequency is:

$$F^+ = f \frac{C}{U_0}$$

where f is dimensional frequency.

2.4. MESH SENSITIVITY STUDY

To make sure that the final results are independent of the grid chosen, a grid sensitivity study was performed for an (AoA) of 8 degrees. Four different meshes having different resolutions, A, B, C and D, see table 1, were studied. In order to properly solve the boundary layer around the airfoil, a hybrid mesh was used to be able to generate a highly refined mesh near the airfoil without drastically increasing the total number of cells. In Figure 2, a detail of the mesh refinement used is depicted.

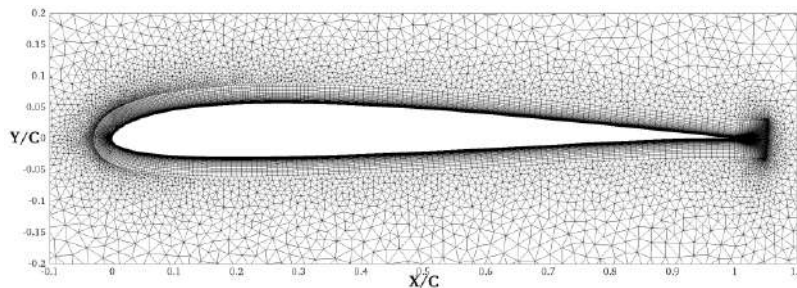


Figure 2. Computational mesh

In Table 1, the characteristics of the four different meshes evaluated are introduced. The coarsest mesh consisted of 26,256 cells, while the finest one had 92,504 cells. The second column of table 1 defines the maximum values of y^+ obtained after the simulations, the three final columns respectively represent the points of flow separation, transition to turbulent and reattachment as a function of the chord length. It is important to realize that in order to efficiently employ the (AFC) technology, the location of the synthetic jet is a particularly relevant parameter, this is why the flow separation point is needed. From the pressure coefficient (C_p) and skin friction coefficient (C_f) distributions, presented in Figure 3, it can be seen that meshes B, C, and D, gave very similar results in terms of separation, transition and reattachment locations. Mesh A resulted in larger discrepancies in these regions, especially in the separation point which is of particular importance in this study. Due to the similarities in the results, obtained from meshes C and D, and also considering the smaller computational power required for mesh C than for mesh D, it was decided to choose mesh C as the one to be used for the rest of the simulations.

Table 1. LSB characteristics at $\alpha = 8^\circ$ for four different meshes

<i>Mesh</i>	N_{cell}	y^+	X_s/C	X_t/C	X_{reat}/C
A	26,256	4	0.033	0.154	0.228
B	34,448	1	0.040	0.165	0.246
C	45,466	0.3	0.041	0.17	0.25
D	92,504	0.1	0.041	0.17	0.25

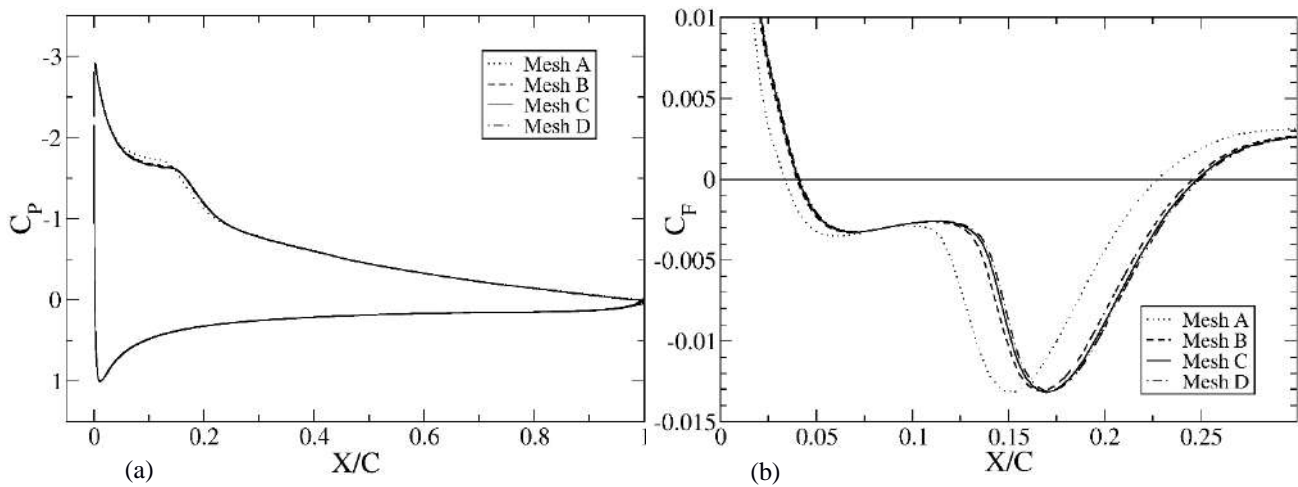


Figure 3. Distributions of (a) pressure coefficient and (b) skin friction coefficient, for four meshes at $\alpha = 8^\circ$

2.5. SOLVER VALIDATION

In order to validate the initial computational results at angles of attack 8 and 14 degrees, the pressure C_p and skin friction C_f coefficients obtained from the respective non actuated baseline cases, were compared with the numerical data available in the literature. For an angle of attack of 8 degrees, numerical results from ILES [16], LES [17] and k-w SST [18] turbulent models, are available, while at 14 degrees, results were only compared with the only available ILES [16] result. In Figures 4 and 5, the C_p and C_f coefficients at 8 and 14 degrees obtained from the present simulations, are compared with those obtained from previous scholars.

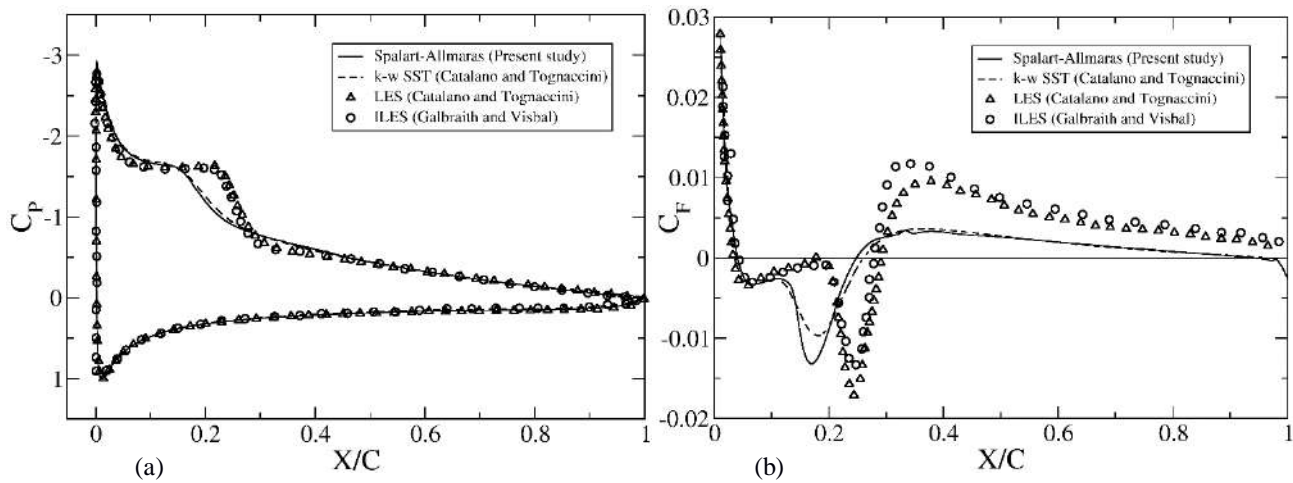


Figure 4. Distributions of (a) pressure coefficient and (b) skin friction coefficient, at $\alpha = 8^\circ$

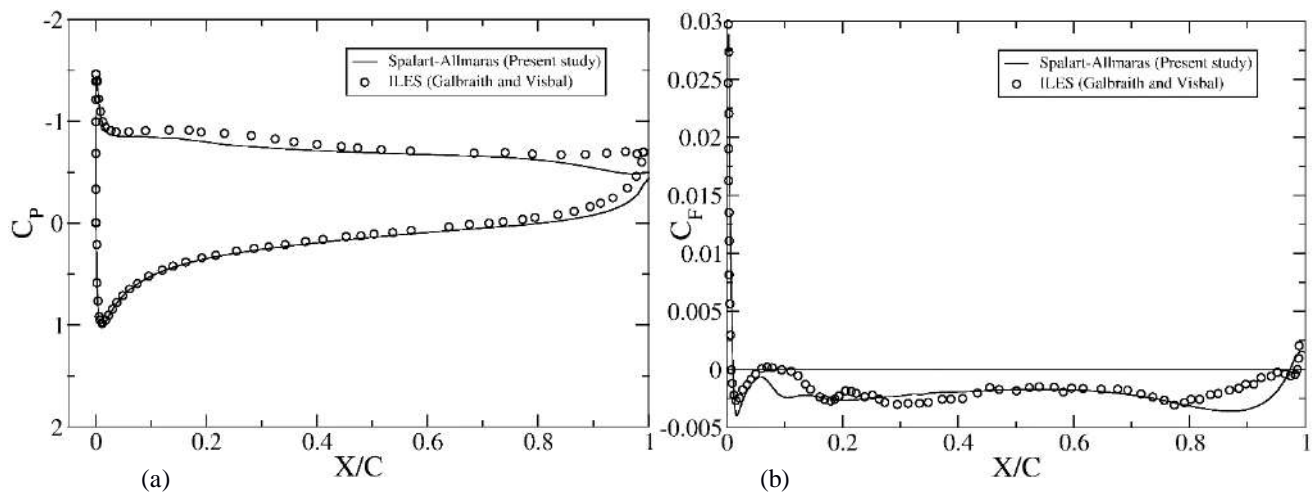


Figure 5. Distributions of (a) pressure coefficient and (b) skin friction coefficient at $\alpha = 14^\circ$

At an angle of attack of 8 degrees, as it is observed from Figure 4, the results of the current S-A model have a very good agreement with the ones presented by [n] and when using the kw-SST turbulent model. Larger differences between these two RANS models and the ILES [16] and LES [17] ones are observed, yet all curves show a similar trend regardless of the model employed, and what it is more important for the present study, the flow separation point is exactly at the same location in all these cases. Figure 5, shows that at the post-stall region, $\alpha = 14$ degrees, the present results agree very well with the ILES ones performed by Galbraith and Visbal [16]. It appears that when the flow is fully separated, the present RANS model is capable of more precisely determine the airfoil pressure and skin friction coefficients. Based on these comparisons, it can be concluded that the 2D simulations performed generate results fully trustable at these two angles of attack studied, therefore allowing to the present researchers to proceed with the implementation of the active flow control jets (synthetic jets) on the baseline cases, and study the effects of the different (AFC) parameters on the airfoil efficiency (C_l/C_d).

3. ACTIVE FLOW CONTROL

After performing the baseline case validations, and for an angle of attack of 8 degrees, synthetic jets were applied at a location of 0.01C upstream of the flow separation point obtained for this particular angle of attack. In addition, the groove width and (AFC) jet inclination angle were set to 0.005C and 90 degrees respectively. In this study, only two (AFC) parameters, forcing frequency and momentum coefficient, were studied and their effects on the airfoil efficiency were compared with the respective baseline case. Table 2, introduces the results obtained for an angle of attack 8 degrees, notice that three momentum coefficients of 0.001, 0.002, 0.005, were considered, for each of them five non-dimensional frequencies of 1, 2, 3, 5, 10 were studied. The respective columns of table 2 represent the angle of attack, the momentum coefficient, the non-dimensional frequency, the drag and lift coefficients and the airfoil efficiency.

Table 2. Active flow control cases $\alpha = 8^\circ$

α	C_μ	F^+	C_d	C_l	C_l/C_d
8°	0.001	1	0.0429	0.912	21.25
		2	0.0398	0.936	23.5
		3	0.0378	0.87	23.01
		5	0.0384	0.72	18.80
		10	0.0851	0.701	8.24
	0.002	1	0.043	0.9	20.84
		2	0.04	0.93	23.2
		3	0.039	0.873	22.15
		5	0.04	0.697	17.42
		10	0.074	0.71	9.5
	0.005	1	0.0473	0.901	19.05
		2	0.0433	0.919	21.21
		3	0.0422	0.868	20.56
		5	0.044	0.67	15.21
		10	0.069	0.68	9.86
Baseline case			0.0327	0.934	28.57

The first thing to realize from Table 2, is that for all momentum coefficients studied, the cases with $F^+=2$ gave the best airfoil efficiency, while those with non-dimensional frequencies of 5 and 10 resulted in the lowest airfoil efficiency. Moreover, the lowest drag coefficients achieved, belongs to the cases with $F^+=3$, whereas the highest lift coefficient correspond to the cases with the non-dimensional frequency of 2. In general, by fixing the frequency and increasing the momentum coefficients the efficiency of the airfoil was decreasing, except for the frequency of $F^+=10$, this is likely be due to the fact that at this particular angle of attack the boundary layer is not strong enough to receive very large momentum jets and boundary layer tripping appears. The maximum efficiency was obtained for a momentum coefficient of 0.001 and a non-dimensional frequency of $F^+=2$.

From the baseline simulation at an angle of attack of 14 degrees, it was obtained that the flow separation point was appearing at $X_s/C = 0.01$, the (AFC) groove was located at a non-dimensional distance versus the airfoil leading edge of 0.0017 and the groove non dimensional width employed was of 0.005.

At an angle of attack of 14 degrees, see table 3 the benefits of using (AFC) were more evident, since the efficiency of the airfoil in all of the studied cases raised between a minimum of 43% and a maximum of 98%. The case with $C_\mu = 0.005$ and $F^+ = 2$ had the lowest drag coefficient, while the highest lift belongs to the case with $C_\mu = 0.005$ and $F^+ = 1$. Nevertheless, the highest airfoil efficiency was obtained for $C_\mu = 0.002$ and $F^+ = 2$, its value was of 7.76. It should be noted that the uncontrolled case at $\alpha = 14$ degrees had an efficiency of 3.90. Additionally, another trend observed from Table 3 is that, regardless of the momentum coefficient, when increasing the forcing frequency, the lift coefficient tends to decrease, although at $F^+ = 5$ a small increase is observed. In other words, regardless of the momentum coefficient used, when the non-dimensional pulsating frequency was $F^+ = 1$, the highest lift coefficient was obtained.

Table 3. Active flow control cases at $\alpha = 14^\circ$

α	C_μ	F^+	C_d	C_l	C_l/C_d	
14°	0.002	1	0.182	1.055	5.79	
		2	0.121	0.941	7.76	
		3	0.125	0.880	7	
		5	0.119	0.894	7.51	
		10	0.143	0.838	5.85	
	0.005	1	0.148	1.123	7.58	
		2	0.119	0.911	7.64	
		3	0.127	0.867	6.81	
		5	0.119	0.885	7.41	
		10	0.149	0.833	5.59	
	Baseline case			0.204	0.798	3.90

In order to visualize the flow field around the airfoil for the optimum (AFC) conditions, Figures 6 and 7 were generated. Figure 6a characterizes the streamlines for the baseline case and Figure 6b is showing the flow field around the airfoil for the optimum conditions previously established, the angle of attack is 8 degrees. Notice that both figures show almost the same flow field, just in figure 6a a small laminar bubble can be observed. The streamlines for the baseline case and for the optimum actuated case when the angle of attack is of $\alpha = 14$ degrees are presented in Figures 7a and 7b respectively. When comparing Figures 7a and 7b it is clear that the size of LSB is drastically reduced when (AFC) is applied, explaining why a considerable lift enhancement along with a rise in airfoil efficiency were obtained.

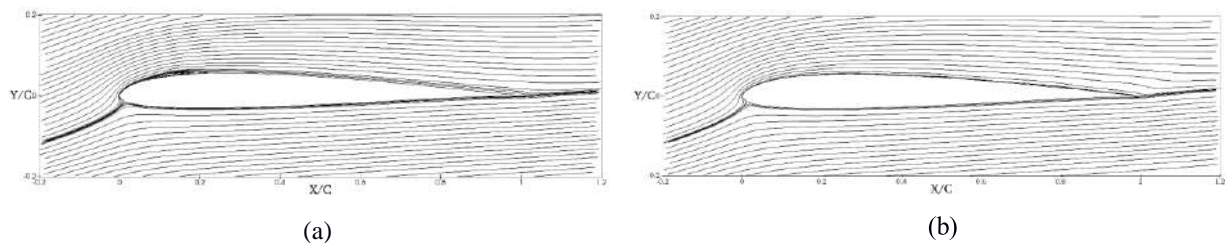


Figure 6. Streamlines at $\alpha = 8^\circ$, for the (a) baseline case and the (b) actuated case of ($C_\mu = 0.001$ and $F^+ = 2$)

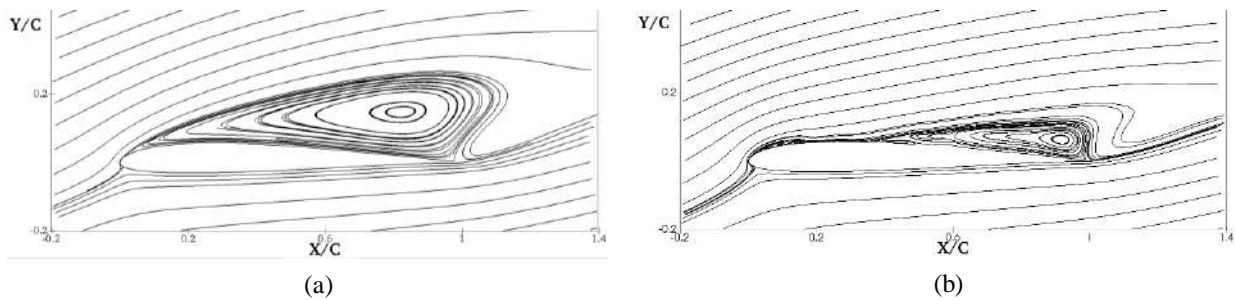


Figure 7. Streamlines at $\alpha = 14^\circ$, for the (a) baseline case and the (b) actuated case of ($C_\mu = 0.002$ and $F^+ = 2$)

4. CONCLUSION

The Active Flow Control (AFC) technology on the Selig-Donovan 7003 (SD7003) airfoil at Reynolds number 60,000 and for two angles of attack, 8 and 14 degrees has been numerically applied.

For both angles of attack, initially the baseline case solutions were compared with the results obtained by previous scholars, therefore validating the 2D simulations without (AFC).

From the baseline case solutions and for each angle of attack, the flow separation point was obtained. In the present paper and for an angle of attack of 8 degrees, the (AFC) groove was placed 1% upstream of the separation point. For an angle of attack of 14 degrees, the (AFC) groove was located from the airfoil leading edge, at a non-dimensional distance of 0.0017.

A set of momentum coefficients and non-dimensional frequencies were studied. For an angle of attack of 8 degrees and regardless of the momentum coefficient employed, the maximum efficiency was obtained for non-dimensional frequencies of $F^+ = 2$, yet no efficiency improvement was obtained versus the baseline case one.

For an angle of attack of 14 degrees, the maximum airfoil efficiency was obtained when using a momentum coefficient of 0.002 and a non-dimensional frequency of $F^+ = 2$. The maximum efficiency obtained was almost twice the one obtained without (AFC).

REFERENCES

- [1] Cattafesta III, L. N., & Sheplak, M. (2011). Actuators for active flow control. *Annual Review of Fluid Mechanics*, 43, 247-272.
- [2] Glezer, A., & Amitay, M. (2002). Synthetic jets. *Annual review of fluid mechanics*, 34(1), 503-529.
- [3] Rumsey, C., Gatski, T., Sellers, W., Vatsa, V., & Viken, S. (2004, January). Summary of the 2004 CFD validation workshop on synthetic jets and turbulent separation control. In *2nd AIAA Flow Control Conference* (p. 2217).
- [4] Wygnanski, I. (2004). The variables affecting the control of separation by periodic excitation. In *2nd AIAA Flow Control Conference* (p. 2505).
- [5] Findanis, N., & Ahmed, N. A. (2008). The interaction of an asymmetrical localised synthetic jet on a side-supported sphere. *Journal of Fluids and Structures*, 24(7), 1006-1020.
- [6] Donovan, J., Kral, L., & Cary, A. (1998, January). Active flow control applied to an airfoil. In *36th AIAA Aerospace Sciences Meeting and Exhibit* (p. 210).
- [7] McCormick, D. (2000, January). Boundary layer separation control with directed synthetic jets. In *38th Aerospace Sciences Meeting and Exhibit* (p. 519).
- [8] Gilarranz, J. L., Traub, L. W., & Rediniotis, O. K. (2005). A new class of synthetic jet actuators—Part I: Design, fabrication and bench top characterization. *Journal of fluids engineering*, 127(2), 367-376.
- [9] You, D., & Moin, P. (2008). Active control of flow separation over an airfoil using synthetic jets. *Journal of Fluids and Structures*, 24(8), 1349-1357.
- [10] Kim, S. H., & Kim, C. (2009). Separation control on NACA23012 using synthetic jet. *Aerospace Science and Technology*, 13(4-5), 172-182.
- [11] Monir, H.E; Tadjfar, M; & Bakhtian, A. (2014). Tangential synthetic jets for separation control. *Journal of fluid and Structures*, 45, 50-65.
- [12] Daham Jeremy A., Morgans A.S., Lardeau S. (2012). Feedback control for form-drag reduction on a bluff body with a blunt trailing edge. *J. Fluid Mech.* 704; 360-387.

- [13] Joseph P., Amadolèse X., Aider JL. (2012). Drag reduction on the 25o slant angle Ahmed reference body using pulsed jets. *Exp. Fluids* 52: 1169-1185.
- [14] Vukasinovic B., Rusak Z., Glezer A. (2010). Dissipative small-scale actuation of turbulent shear layer. *J Fluid Mech.* 656; 51-81.
- [15] Catalano, P., & Tognaccini, R. (2010). Turbulence modeling for low-reynolds-number flows. *AIAA journal*, 48(8), 1673-1685.
- [16] Galbraith, M., & Visbal, M. (2008, January). Implicit large eddy simulation of low Reynolds number flow past the SD7003 airfoil. In *46th AIAA Aerospace Sciences Meeting and Exhibit* (p. 225).
- [17] Catalano, P., & Tognaccini, R. (2009). Influence of free-stream turbulence on simulations of laminar separation bubbles. In *47th AIAA Aerospace Sciences Meeting including The New Horizons Forum and Aerospace Exposition* (p. 1471).
- [18] Catalano, P., & Tognaccini, R. (2011). RANS analysis of the low-Reynolds number flow around the SD7003 airfoil. *Aerospace Science and Technology*, 15(8), 615-626.

Optimization of synthetic jet actuation on a SD7003 airfoil in stall conditions

Navid M Tousi,^{1,*} Reda El Mansy,¹ Fernando Mellibovsky,² and Josep M Bergada¹

¹Department of Fluids Mechanics, Universitat Politècnica de Catalunya, Barcelona, 08034, Spain

²Department of Physics, Aeronautics Division, Universitat Politècnica de Catalunya, Barcelona, 08034, Spain

We optimise a set of Synthetic Jet (SJ) Active Flow Control (AFC) parameters on a SD7003 airfoil in order to maximise lift and aerodynamic efficiency. 2D-RANS with the Spallart Almaras (SA) turbulence model is employed in the optimisation process. The optimal set of SJ parameters is then tested using LES. Comparison between 2D RANS-SA and 3D LES results shows the necessity of tuning the SA model parameters to further improve the reliability of a 2D-simulation-based optimisation. Notwithstanding this, both RANS-SA and LES results show that airfoil efficiency can be drastically improved with SJ AFC.

INTRODUCTION

Increasing lift and reducing drag have major effects on fuel usage, stability, durability and maneuverability of aircraft. Active Flow Control (AFC) technologies consist of adding/subtracting momentum to/from the main flow in convenient locations in order to interact with the boundary layer, and delay or promote its separation. Moreover, it has the advantage over passive flow control techniques of not introducing drag penalty in off-design conditions. Among different AFC methods, Synthetic Jet Actuators (SJA) have gained particular attention because of their simplicity and high capability in controlling flow separation. The number of adjustable parameters is large, and finding the optimum is extremely resource-intensive at best, if not altogether unfeasible. In the present study we search for optimal SJA design parameters at a post stall Angle of Attack (14°) for SD7003 airfoil and $Re=60,000$ by coupling a Genetic Algorithm (GA) optimizer, a mesh generator (GMSH) and a CFD package (OpenFOAM). The optimisation relies on 2D RANS simulations [1, 2], so that Large Eddy Simulation (LES) computation of both the baseline and optimally actuated cases has been undertaken to assess the accuracy. The optimum found largely outperforms previously assessed suboptimal SJA AFC [3].

RESULTS

All CFD simulations in the optimization process were run using 2D RANS with the Spalart Allmaras (SA) turbulence model. The SA-baseline case was run on a grid of 45,466 cells and with a time step of 2×10^{-5} , which were shown adequate [1]. For the 3D runs, an unstructured mesh consisting of almost 30 million cells was deployed with sufficient density for a wall-resolved LES simulation, and WALE was chosen as the Sub-grid Scale model.

In the optimisation process, two independent objective functions, the lift coefficient C_l and the aerodynamic efficiency $\eta = L/D$ (lift-to-drag ratio), were considered along with five design variables, namely jet position x , width h , injection angle θ , actuation frequency f and the momentum coefficient C_μ .

Fig 1 shows all simulations in objective-function space (C_l - η). Almost all actuated cases (gray circles) were

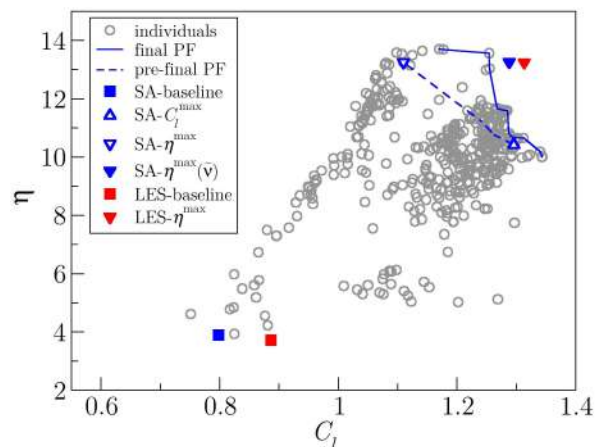


FIG. 1. Pareto Front (η vs C_L) for the SD7003 airfoil at $Re = 60000$ and 14° .

successful in improving aerodynamic performances as compared to the SA-baseline case (blue square). The optimum cases for maximum lift $SA-C_l^{\max}$ (empty up-pointing triangle) and maximum efficiency ($SA-\eta^{\max}$) (empty down-pointing triangle) are located at the ends of the segment representing the so-called Pareto Front (PF) line. The Pareto Front considered here (PF, dashed line) corresponds to results obtained halfway through the optimisation process, after close to 400 CFD runs. Further optimisation yields the final Pareto front (solid blue lines) [1] after 600 CFD runs, but it was not available at the time LES simulations were performed. The LES-

TABLE I. Baseline case, and optimal SJA actuation cases corresponding to maximum lift C_l^{\max} and maximum aerodynamic efficiency η^{\max} , as obtained halfway through the optimisation process, after 400 CFD runs. The values of the five actuation parameters are listed alongside corresponding aerodynamic performances.

cases	F^+	C_μ	θ°	x/C	h/C	C_l	C_d	η	$\Delta\bar{C}_l/\bar{C}_l$	$\Delta\eta/\eta$
SA-baseline						0.798	0.2040	03.90		
LES-baseline						0.895	0.239	03.74		
$SA-C_l^{\max}$	1.6	0.0053	53	0.0097	0.005	1.295	0.129	10.42	+62.3%	+157.4%
$SA-\eta^{\max}$						1.109	0.083	13.25	+31.1%	+239.7%
$SA-\eta^{\max}(\bar{v})$	2.6	0.0055	18	0.0089	0.005	1.288	0.097	13.27	+61.4%	+239.4%
$LES-\eta^{\max}$						1.313	0.094	13.96	+46.7%	+273.2%

baseline (red square) is in a good agreement with literature results [1]. The close-to-optimal $\text{LES-}\eta^{\max}$ (filled red down-pointing triangle) was run with the same SJA design parameters as the $\text{SA-}\eta^{\max}$.

The optimum SJA design parameters associated with the maximum lift (C_l^{\max}) and maximum efficiency (η^{\max}) are gathered in Table I. When comparing these two sets of parameters small differences are observed in almost all parameters with exception of the jet inclination angle θ and the actuation frequency. Highest efficiency is obtained by injecting almost tangentially to the wall ($\theta = 18^\circ$) at frequency noticeably higher than that of natural vortex-shedding. Close inspection of the results for $\text{SA-}\eta^{\max}$ and $\text{LES-}\eta^{\max}$ reveals clear discrepancies that are attributable to a high sensitivity of RANS-SA simulations to turbulence model parameters, in particular to free-stream turbulent viscosity ($\tilde{\nu}$). Tuning this parameter yields more realistic results, as clear from the $\text{SA-}\eta^{\max}(\tilde{\nu})$ (blue down-pointing triangle), which corresponds to the same AFC case but with duly adjusted $\tilde{\nu}$.

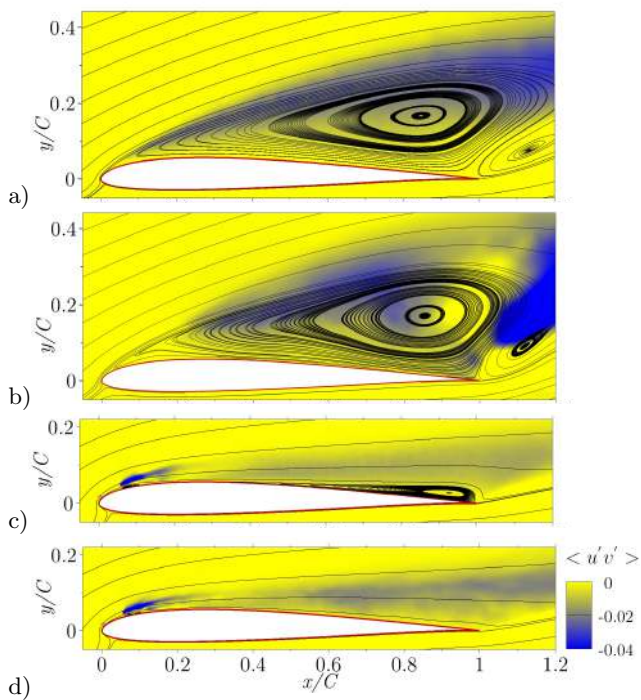


FIG. 2. Spanwise-averaged $\langle u'v' \rangle$ component of the Reynolds stress tensor and time- and spanwise-averaged streamlines. (a) SA-baseline (b) LES-baseline (c) $\text{SA-}\eta^{\max}(\tilde{\nu})$ and (d) $\text{LES-}\eta^{\max}$.

Fig 2 shows colourmaps of the $\langle u'v' \rangle$ component of the Reynolds stress tensor along with a collection of time- and spanwise-averaged streamlines for the SA and LES baselines (a and b) and maximum aerodynamic efficiency AFC cases (c and d). The baseline separation bubble exhibits similar features for the LES-baseline and RANS-SA-baseline simulations. However, the dynamic

behaviour as shown by $\langle u'v' \rangle$ is quite different. The RANS-SA model is not expected to behave particularly well in post-stall conditions. Once actuation is switched on, the quality of RANS-SA results improves significantly. The distribution of $\langle u'v' \rangle$ become very similar, especially in the jet region. Also streamlines of actuated cases are matching in almost every location except that RANS-SA does not manage to completely suppress the separation bubble at the trailing edge. The instantaneous vortical structures, represented through Q-criterion iso-surfaces and coloured by streamwise velocity, are shown in Fig. 3 for the both the baseline and optimum AFC LES runs.

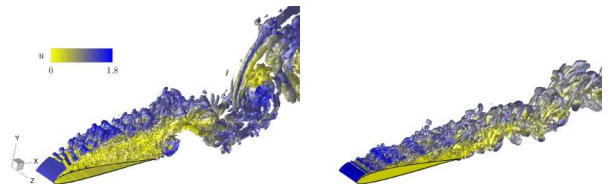


FIG. 3. Instantaneous vortical structures visualised through iso-surfaces of the Q-criterion $Q = 30U_\infty^2/C^2$, coloured by streamwise velocity u . LES-baseline (left). $\text{LES-}\eta^{\max}$ (right).

CONCLUSIONS

We illustrate the capabilities of coupling 2D RANS computations and genetic algorithms to optimise active flow control on airfoils in stall conditions. Adequately tuning the turbulent model parameters is key to obtaining sufficiently accurate RANS simulations and, therefore, to rendering the optimisation process reliable. In the case of the Spallart Almaras model, adjusting free-stream turbulent viscosity $\tilde{\nu}$ is paramount when dealing with AFC applications. LES simulations confirm the applicability of the optimisation process in finding optimum AFC configurations. Aerodynamic efficiency may be increased by about 270% with respect to baseline, according to LES runs, even beyond the 240% increase promised by RANS-SA during the optimisation procedure.

* navid.monshi.tousi@upc.edu

- [1] N. Tousi, M. Coma, J. Bergadà, J. Pons-Prats, F. Mellibovsky, and G. Bugeada, Active flow control optimisation on sd7003 airfoil at pre and post-stall angles of attack using synthetic jets, *Applied Mathematical Modelling* **98**, 435 (2021).
- [2] M. Tadjfar and D. Kamari, Optimization of flow control parameters over SD7003 airfoil with synthetic jet actuator, *Journal of Fluids Engineering* **142**, 10.1115/1.4044985 (2020).
- [3] I. Rodriguez, O. Lehmkuhl, and R. Borrell, Effects of the actuation on the boundary layer of an airfoil at Reynolds number $\text{Re} = 60000$, *Flow, Turbulence and Combustion* **105**, 607 (2020).



PERFORMANCE OF HYBRID OPTIMIZATION METHODS APPLIED TO ACTIVE FLOW CONTROL DEVICES

Martí Coma^{1,2*}, Navid M. Tousi¹, Jordi Pons-Prats^{1,2}, Josep M. Bergadà¹
and Gabriel Bugada^{1,2}

1: Universitat Politècnica de Catalunya. Barcelona Tech (UPC)
Edificio C1, Gran Capitan, 08034
Gran Capitan, 08034, Barcelona, Spain
Tel. (+34) 934016494 / Fax. (+34) 934016894
e-mail:

marti.coma,navid.monshi.tousi,jordi.pons-prats,josep.m.bergada,gabriel.bugada@upc.edu,
<http://www.upc.edu>

2: Centre Internacional de Mètodes Numèrics a l'Enginyeria (CIMNE)
Edificio C1, Gran Capitan, 08034
Barcelona, Spain. Tel. (+34) 932057016 / Fax. (+34) 934016517
e-mail: mcoma, jpons, bugeda@cimne.upc.edu, <http://www.cimne.com>

Abstract. *Genetic Algorithms (GA) are optimization methods that are usually very robust but have a slow convergence to the exact minimum. On the other hand, Gradient Based methods which converge better, are not so robust, and can get stuck in local minimums or flat areas. In this article a Hybrid optimization method is presented and its performance is compared against a Gradient Based method and a Genetic Algorithm. The comparison is established with a Gradient Based method, which is a Conjugate Gradient, and a Genetic Algorithm, based on a $\mu + \lambda$ strategy. The Hybrid methods combine the two above-mentioned methods. Each Hybrid implementation is composed of a GA and a Conjugate Gradient which share information at each iteration, to try overcome individual-method limitations and achieve a better performance. The strategy used for sharing information among each method is based on games theory, more specifically Nash Games. The use of a coupling based on competitive players enhances the overall performance of the method pushing each one with the improvements of the other one. This enables an efficient management of the individuals, and the optimum ones, ensuring a good balance when dealing with elite individuals. A performance comparison is done with the optimization of an Active Flow Control (AFC) over a 2D Selig-Donovan 7003 (SD7003) airfoil at Reynolds number 6×10^4 and 14 degrees of attack. Five design variables are considered: jet position, jet width, momentum coefficient, forcing frequency and jet inclination angle. The fluid flow problem is solved using Computational Fluid Dynamics (CFD) with the Spalart-Allmaras turbulent model. The motivation behind the current study is to evaluate the performance of the Hybrid methods in a physical problem with a computationally expensive objective function.*

Keywords: Hybrid Optimization Methods, Optimization, Population-based Methods, Gradient-based Methods, Evolutionary Techniques, Active Flow Control, Synthetic Jet

1 INTRODUCTION

Optimization methods search for a good trade-off between exploration and exploitation. These two aspects are usually associated with different optimization techniques and approaches. For example, Evolutionary Algorithms are usually very robust and have great exploration capabilities, but they lack precision to find the exact minimum efficiently. On the other hand, Gradient Based methods are very efficient exploiting minimums, assuming function continuity, differentiability and convexity.

In order to mitigate the drawbacks of each method, different hybridizations have been proposed. At least three main strategies can be found in the literature. The first strategy is the definition of new operators, similar to the traditional genetic operators (namely selection, crossover and mutation), but with improved local search capabilities. The second group combines two optimization methods, ideally one with great exploration capabilities and the other focused on exploitation. Both methods share information to increase the performance. The last group is composed by multi-population strategies.

An example of hybridization on Genetic Algorithms can be found at Cheng et al. [1]. The article describes the hybridization of genetic operators (crossover and mutation) combining global and local methods. Another example is Wang et al. [2], which defines a new selection operator, a new mutation operator and local search operators. Other examples of operator hybridization can be found in Weare et al. [3], Valls et al. [4] and Ho et al. [5].

Regarding the combination of two methods, Kelly Jr and Davis [6] combines a Genetic Algorithm with k-nearest neighbors classification algorithm, as hybridization and Genetic Algorithms are not only used in optimization. In the vehicle routing field, Jih and Hsu [7] uses Genetic Algorithms hybridized with Dynamic Programming. The Dynamic Programming algorithm produces a first approach to the solution, and the Genetic Algorithm starts from those results. Another example of hybridization combining different methods is the work of El-Mihoub et al. [8], which presents an hybridization of a Genetic Algorithm with other local search algorithms. The assessed ones are Lamarckian learning, Baldwinian Learning, and an hybrid Lamarckian-Baldwinian model. The work treats the balancing and communication between the different methods.

Regarding the strategy, which defines multiple populations working in parallel and sharing genetic information, there are different approaches. For example, Ho et al. [5] defines an hybrid Genetic Algorithm with multiple population, applied to Vehicle routing problem, with each population using different operators. Another approach is presented by Berger and Barkaoui [9] who splits the objective functions in one population and the restrictions in another, and shares the information between them. The work of Lee et al. [10] propose an hybrid Genetic Algorithms based on the Nash Games, splits the problem (objective functions and design variables) into two different populations, and a third one which deals with the overall problem, receiving information back and forth with the two others.

2 PROPOSED HYBRID METHOD AND REFERENCE OPTIMIZATION METHODS

In this section the proposed Hybrid Method is presented, as well as the used Genetic Algorithm and the Gradient Method. The performance comparison has been done with the two methods that the hybrid method combines, but running separately.

2.1 Proposed hybrid method description

The proposed Hybrid Method consists of a combination of two optimization algorithms, called players. According to the classification of hybridization types presented in the *Sec. 1 Introduction*, this falls into the second type. The first player, mainly, dedicated to exploration is a Genetic Algorithm, explained in detail in *Sec. 2.2 Genetic Algorithm*. The second player, dedicated to exploitation is a Conjugate Gradient, explained in detail in *Sec. 2.3 Conjugate Gradient*. Both players run sequentially, one after the other. The players pause its progression after each iteration. At this moment a *Migration Epoch* occurs, and both algorithms share information. This is inspired in the evolution of the species, where different populations exchange individuals at some point, and then continue its own evolution on its own after another migration occurs.

The fittest individual found by the Genetic Algorithm player migrates to the Conjugate Gradient one. On the other side, the best individual from the Genetic Algorithm player migrates to the Conjugate Gradient one.

The Genetic Algorithm player receives the individual substituting the less fitted individual in its current population with the one that comes from the Conjugate Gradient one. On the other hand, the Conjugate Gradient player treats the individual from the Genetic Algorithm one as a new seed and starts to optimize from there.

After some testing on the Hybrid Method, the Conjugate Gradient was modified to overcome some instabilities when running inside the Hybrid Method as a player. The step size is the distance increased during the line search in the design variables space. During the line search process the step size is recomputed using the Brent Method [11]. In case of the step size becomes zero, the iteration is considered finished and the default step size value is set. Then, the player is ready for the next seed, that will arrive from the Genetic Algorithm.

2.2 Genetic Algorithm

Genetic Algorithms were initially proposed by Holland [12], further developed by Goldberg and Holland [13] and more recently evolved by Deb et al. [14] which proposes different new operators. The methodology of Genetic Algorithm mimics the natural evolution process, which selects the best fitted individuals to generate new offspring, which tend to be better fitted than its predecessors.

The Genetic Algorithm used as a reference in this study is based on the NSGAI implementation developed by Deb et al. [14]. The main algorithm and operators are the same as the original published by the authors, but some modifications have been included, mainly to parallelize the evaluation of the objective functions. The *Selection()* operator employs a $\mu + \lambda$ strategy with a Crowded-Comparison Operator, proposed by Deb et al. [14]. For the *Crossover()* operator, a Simulated Binary Crossover (SBX) operator, also proposed by Deb and Agrawal [15] is used and the *Mutation()* operator is performed with Polynomial Mutation proposed by Deb [16]. The values of the configuration of the different operators are presented in the Tab.1.

2.3 Conjugate Gradient

A Conjugate Gradient, which is explained in detail by Shewchuk et al. [17], has been used. The Conjugate Gradient has been coded with the capability to compute the nec-

Table 1: Parameters of the Genetic Algorithm.

Parameter	Value
Population size	20
Probability of crossover	0.9
Probability of mutation	0.1

essary individuals to obtain the gradient approximation in parallel. It needs the values of the design variables corresponding to the current individual, and a $\pm\epsilon$ for each one in order to approximate the value of the gradient using a finite differences scheme. This defines different sets of design variables corresponding to different designs whose objective functions can be computed in parallel, as they are independent between them. After the gradient is computed, the minimum in this direction is found using a line search method. This method needs information about the objective function at certain points, but it generates the points one by one, after the evaluation of the objective function of the previous point is computed. Because of that, the evaluations of the individuals can not be run in parallel. Tab.2 presents the configuration for the Conjugate Gradient.

Table 2: Parameters of the Conjugate Gradient.

Parameter	Value
Search Direction Method	Fletcher Reeves [18]
Optimal Step Size Method	Brent Method [11]
Epsilon for numerical differentiation	10^{-6}
Optimal step size tolerance	10^{-3}

3 CASE OF STUDY

We have proceed to make a comparison between the different algorithms by solving the optimization of the parameters of an Active Flow Control (AFC) device over a 2D Selig-Donovan 7003 (SD7003). The Reynolds number of the free stream is set to 6×10^{-4} and the angle of attack is 14 degrees.

Five design variables are taken into account for the optimization of the AFC. These are, the jet position x/C , jet width h/C , momentum coefficient C_μ , forcing frequency F^+ and jet inclination angle θ° . The fluid is solved using Computational Fluid Dynamics (CFD) with the Spalart-Allmaras turbulent model. A complete explanation of the AFC case used in this study can be found at Tousi et al. [19]. The case computed in the paper differs from the original one in the mesh size and the number of objective functions which is now set to 1. As the goal of this study is to compare the performance of different optimization methods, and not the flow structure of the AFC, the mesh size has been enlarged to reduce the computational time at each iteration. The mesh size is about 36000 cells. A new mesh is generated for each individual as some of the design variables affect the geometry of the AFC device location.

The boundaries for the design variables are presented at Tab.3.

The objective of the optimization problem is to maximize the lift coefficient C_l . The implementation of the optimizer always treats the optimization as a minimization problem,

Table 3: AFC Design variables and their evaluation ranges.

F^+	C_μ	θ°	x/C	h/C
[0.1, 10]	[0.0001, 0.02]	[5, 175]	[0.001, 0.3]	[0.005, 0.015]

the objective function f is set to $-C_l$.

$$f = -C_l \quad (1)$$

4 RESULTS

In this section, the results obtained for the three different optimization methods are presented. The Genetic Algorithm and the Hybrid Method have been run twice with different random seeds, in order to evaluate the robustness of the methods, as both methods have a stochastic component due to the Genetic Algorithm operators (Mutation and Crossover). The Conjugate Gradient has been run 6 times with different initial individuals (the first 6 individuals from the first generation of one of the Genetic Algorithms have been used). The Conjugate Gradient does not have a random behavior, but is highly dependent on the initial seed if the objective space has local minimums. To extract relevant statistical data, more runs with different seeds are needed, but as the study case is computationally very expensive, the results are evaluated looking at the tendency of the convergence graphs.

The convergence as a function of the number of evaluations of the CFD problem is presented in Fig.1. In this case, the performance of the convergence of the Hybrid Method is better than the Genetic Algorithm, and in addition it is more robust. The results of both runs of the Hybrid Method are better and more consistent than the Genetic Algorithm ones. The Hybrid Method took advantage of the internal Conjugate Gradient player to converge much faster to better results. On the other hand, analyzing the results of the Conjugate Gradient alone, one of the runs got stuck at a local minimum at the beginning of the analysis. Another one spent about 80 evaluation without improving the initial seed. And four of them were able to improve the initial seeds, but after around 100 iterations got stuck achieving better results than the Genetic Algorithm (at the same number of evaluations). Finally, comparing the Hybrid method against the Conjugate Gradient, the Hybrid Method has a convergence speed similar to the Conjugate Gradient, but does not get stuck and at around 150 evaluations reaches its best results.

As explained in *Sec. 2.1 Proposed hybrid method description*, the three methods are capable of parallelizing the evaluations of the individuals in some parts of the algorithm. The level of parallelization that can be achieved is not the same for each algorithm. The evaluation of all the individuals belonging to the same population can be performed in parallel whereas the line search method is not parallelized because each design is obtained sequentially after the evaluation of the previous one. This makes that the improvement on the performance of the different algorithms when using parallel capabilities is not the same. In order to take into account this phenomena two additional graphics are presented. These graphics shows the convergence with a different x axis, which takes into account the speedup of each algorithm due to the parallelization capabilities. The graphics consider that all evaluations of the objective functions takes the same amount of time, which is not always true. It depends on the solver used to evaluate the objective function (for

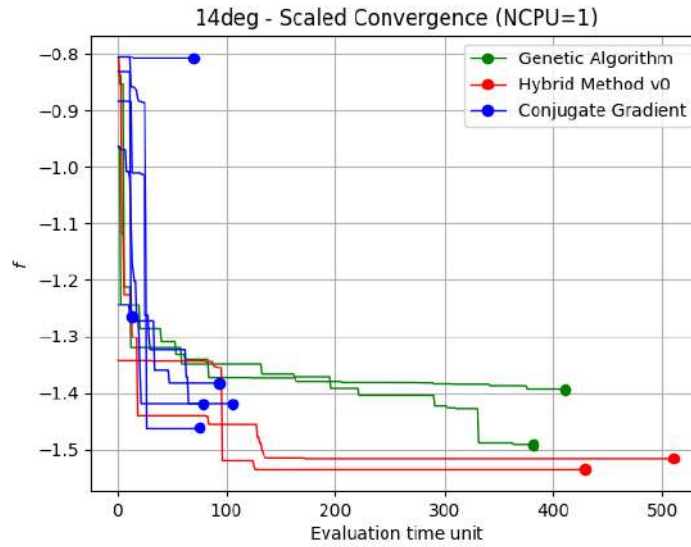


Figure 1: Convergence with 1 CPU.

example, an iterative process inside the objective function evaluation may take more or less iterations, and thus time, depending on the exact condition, i. e. design variables), but it gives a clear idea of the parallelization capabilities of each optimization algorithm. 11 CPU is the maximum number of CPU that the Conjugate Gradient can take advantage for five design variables, as it can only compute in parallel the objective functions needed to calculate the gradient, twice the number of design variables plus the current point. And 20 CPU is the maximum number of CPU that the Genetic Algorithm can use with a population of 20 individuals, as no assynchronization strategy is implemented and it needs the whole population computed before generating a new offspring.

The graphics in Fig.2 and Fig.3 shows the scaled convergence for 11 and 20 CPU, respectively. The algorithm that most benefits from the availability of CPU is the Genetic Algorithm, as it can parallelize all evaluations in chunks of the population size. The Conjugate Gradient is the algorithm that benefits less of the availability of the results, as the line search is not parallelized. The Hybrid Method also takes advantage of the parallelization, but the improvement is mainly noticed up to 11 CPU, as the Conjugate Gradient player can not benefit from more CPU, defines the bottleneck.

The Genetic Algorithm should run additional iterations in order to clearly identify the converged solution when using 11 and 20 CPU. It is currently still running, but the problem is computationally high demanding and this are the results so far.

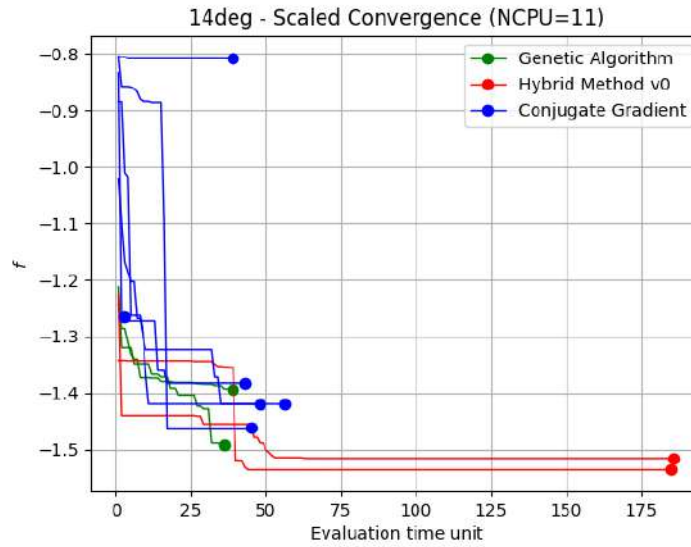


Figure 2: Convergence with 11 CPU.

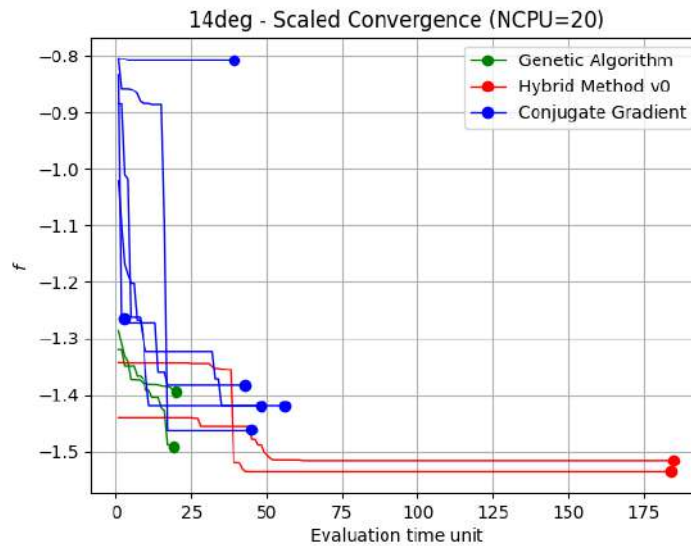


Figure 3: Convergence with 20 CPU.

5 CONCLUSIONS

The present article describes the application of three different optimization strategies to a complex and high-demanding problem. Although the problem definition has been simplified, as described in the 1, each individual evaluation of the objective function is taking around 12 hours, making the whole optimization analysis a costly process. Due to the computational cost, the aim of the proposed methods is to speed up the analysis while keeping the robustness on the solution, as well as its convergence to the accurate optimum.

The proposed Hybrid Algorithm has demonstrated a general better performance than the traditional Genetic Algorithm and Conjugate Gradient methods. The algorithm suc-

cessfully takes advantage of the strengths of each player. Each of them contributes to analyze the search space from the global and local search point of view, and the shared information along the process facilitates the speed up of each individual player. The result of this cooperation is reflected on the general behavior of the method. The Conjugate Gradient needs a good seed, close to the minimum which requires previous knowledge in the problem, which is not always available. This seed-dependence could greatly affect the final performance of the method.

When considering the availability of a large number of computational resources, the Genetic Algorithm has an advantage, and could outperform the Hybrid Method. What could determine if the Genetic Algorithm outperforms the Hybrid Method is the fact that the multiple CPU graphs are showing the ideal case that all evaluations of the objective functions takes the same amount of time. If that is not the case, the benefits of increasing the number of CPU are less than the shown by the presented results.

The planned future work is to evaluate better the performance of the algorithms with regards to the number of CPU. The optimizations should be run with different number of CPU in order to compare the real time, and not only applying a scale factor considering that all individuals take the same amount of time to evaluate. The main issue with this tests is to obtain enough computational resources.

Another future work is to evaluate the performance of the Hybrid Method when dealing with multi objective functions. It has not been stated before but the Hybrid Method is extended to multi objective problems, and will be tested using the same problem described by Tousi et al. [19].

ACKNOWLEDGEMENTS

This work was supported by the Spanish and Catalan Governments under grants FIS2016-77849-R and 2017-SGR-00785, respectively. Part of the computations were done in the Red Española de Supercomputación (RES), Spanish supercomputer network, under the grants IM-2019-3-0002 and IM-2020-1-0001.

Third author, Jordi Pons-Prats, acknowledges the support of Serra Hunter programme from Generalitat de Catalunya.

REFERENCES

- [1] R. Cheng, M. Gen, and Y. Tsujimura. A tutorial survey of job-shop scheduling problems using genetic algorithms, part ii: hybrid genetic search strategies. *Computers & Industrial Engineering*, 36(2):343–364, 1999.
- [2] Y. Wang et al. A new hybrid genetic algorithm for job shop scheduling problem. *Computers & Operations Research*, 39(10):2291–2299, 2012.
- [3] R. Weare, E. Burke, and D. Elliman. A hybrid genetic algorithm for highly constrained timetabling problems. *Department of Computer Science*, 1995.
- [4] V. Valls, F. Ballestin, and S. Quintanilla. A hybrid genetic algorithm for the resource-constrained project scheduling problem. *European Journal of Operational Research*, 185(2):495–508, 2008.

- [5] W. Ho, G. T. Ho, P. Ji, and H. C. Lau. A hybrid genetic algorithm for the multi-depot vehicle routing problem. *Engineering Applications of Artificial Intelligence*, 21(4):548–557, 2008.
- [6] J. D. Kelly Jr and L. Davis. A hybrid genetic algorithm for classification. In *IJCAI*, volume 91, pages 645–650, 1991.
- [7] W.-R. Jih and J. Y.-J. Hsu. Dynamic vehicle routing using hybrid genetic algorithms. In *Proceedings 1999 IEEE International Conference on Robotics and Automation (Cat. No. 99CH36288C)*, volume 1, pages 453–458. IEEE, 1999.
- [8] T. A. El-Mihoub, A. A. Hopgood, L. Nolle, and A. Battersby. Hybrid genetic algorithms: A review. *Engineering Letters*, 13(2):124–137, 2006.
- [9] J. Berger and M. Barkaoui. A parallel hybrid genetic algorithm for the vehicle routing problem with time windows. *Computers & Operations Research*, 31(10):2037–2053, 2004.
- [10] D. Lee, J. Periaux, J. Pons-Prats, G. Bugada, and E. Oñate. Double shock control bump design optimization using hybridised evolutionary algorithms. In *Evolutionary Computation (CEC), 2010 IEEE Congress on*, pages 1–8. IEEE, 2010.
- [11] R. P. Brent. *Algorithms for minimization without derivatives*. Courier Corporation, 2013.
- [12] J. H. Holland. *Adaptation in natural and artificial systems: an introductory analysis with applications to biology, control, and artificial intelligence*. MIT Press, Cambridge, Massachusetts, Jan. 1992.
- [13] D. E. Goldberg and J. H. Holland. Genetic algorithms and machine learning. *Machine Learning*, 3:95–99, 1988. doi:10.1023/A:1022602019183.
- [14] K. Deb, A. Pratap, S. Agarwal, and T. Meyarivan. A fast and elitist multiobjective genetic algorithm: NSGA-II. *Evolutionary Computation, IEEE Transactions on*, 6(2):182–197, Apr 2002. ISSN 1089-778X. doi:10.1109/4235.996017.
- [15] K. Deb and R. B. Agrawal. Simulated binary crossover for continuous search space. *Complex systems*, 9(2):115–148, 1995.
- [16] K. Deb. *Multi-objective optimization using evolutionary algorithms*, volume 16. John Wiley & Sons, Chichester, UK, 2001.
- [17] J. R. Shewchuk et al. An introduction to the conjugate gradient method without the agonizing pain, 1994.
- [18] R. Fletcher. *Practical methods of optimization*. John Wiley & Sons, 2013.
- [19] N. Tousi, M. Coma, J. Bergadà, J. Pons-Prats, F. Mellibovsky, and G. Bugada. Active flow control optimisation on sd7003 airfoil at pre and post-stall angles of attack using synthetic jets. *Applied Mathematical Modelling*, 2021.

Square cylinder downstream of two different-velocity streams

Reda El Mansy,^{1,*} Navid M Tousi,¹ Josep M Bergada,¹ and Fernando Mellibovsky²

¹*Department of Fluids Mechanics, Universitat Politècnica de Catalunya, Barcelona, 08034, Spain*

²*Department of Physics, Aeronautics Division, Universitat Politècnica de Catalunya, Barcelona, 08034, Spain*

We study the flow past a square cylinder immersed in the wake of an upstream splitter plate separating two different-velocity streams. The bottom stream Reynolds number, $Re_B = 56$ is kept constant for all cases, while the top-to-bottom Reynolds numbers ratio $R \equiv Re_T/Re_B$ is in the range $R \in [1, 6.5]$, corresponding to a variation of the bulk Reynolds number $Re \equiv (Re_T + Re_B)/2 \in [56, 210]$. The onset of vortex-shedding, at $R = 2.1 \pm 0.1$ (corresponding to $Re = 86.8 \pm 2.8$), is pushed to higher Re as compared to the square cylinder in the classic configuration. The three-dimensionality is triggered by a mode-C-type instability at $R \simeq 3.1$ ($Re \simeq 115$) with wavelength $\lambda_z \simeq 2.5 \pm 0.1$, similar to the mode reported for square cylinders placed at an incidence. For a velocity ratio $R = 3.4$ the flow is period-doubled and exhibits three spanwise symmetries: a mirror reflection and two spatiotemporal symmetries. The road to spatio-temporal chaos is initiated thereafter with a modulational period-doubling tertiary bifurcation at $R \in (3.4, 3.8)$ that also doubles the spanwise periodicity. The resulting nonlinear solution repeats after four vortex shedding cycles and retains only a spatiotemporal invariance consisting in the evolution by half a period followed by mirror reflection about a streamwise-cross-stream plane. At slightly higher values $R \geq 4$, the flow becomes spatio-temporally chaotic, but the main features of mode C are still observable.

INTRODUCTION

The uniform flow past square cylinders has long served as a canonical problem for the study of bluff body aerodynamics. Two main flow structures, modes A- and B-type, are reported in the wake transition regime [1–4], their respective occurrence starting at Reynolds number values $Re^A \simeq 160 \pm 2$ and $Re^B \simeq 204 \pm 5$, with wavelengths $\lambda_z^A/D \simeq 5.1 \pm 0.1$ and $\lambda_z^B/D \simeq 1.3 \pm 0.1$ at onset [5]. These two modes were confirmed via linear stability analysis by [6], who also found a third quasi-periodic mode QP called mode S. Sheard et al. [7] observed that the QP mode evolves into a period-doubling mode C and becomes dominant when the square cylinder is placed at an incidence.

The present study exploits a large number of both 2D and 3D DNS runs to try and understand the effects on the flow of immersing the cylinder in the interface of two-different velocity streams at varying velocity ratio $R \equiv Re_T/Re_B$. Nektar++, an open source code based on the spectral/hp element method has been employed throughout. A 2D in-plane mesh consisting of $N_{xy} = 95294$ 6th-order quadrilateral elements has been used for all simulations with time step $\Delta t = 0.0012$. The computational domain is shown in figure 1. The splitter plate of length $6.5D$ is placed upstream from the square cylinder of side D , leaving a $2.5D$ gap. The upstream and downstream domain dimensions are $L_x^u = 9.5D$ and $L_x^d = 25.5D$, respectively, and the cross-stream height is $L_y = 16D$. According to Floquet stability analysis, periodic spanwise lengths from $5D$ to $10D$, discretised with 28 to 80 Fourier modes, have been deployed.

RESULTS

The linear stability analysis presented in figure 2 shows that the flow remains two-dimensional for velocity ratios $R \leq 3.1$. The spanwise wavelength associated to the on-

set of three dimensionality and characterizing the dominant unstable mode is $\lambda_z = 2.5 \pm 0.1$, and remains fairly unaltered up to $R = 4$. A second unstable mode arises at $R = 6.5$, with much shorter associated spanwise wavelength of $\lambda_z = 1.5$.

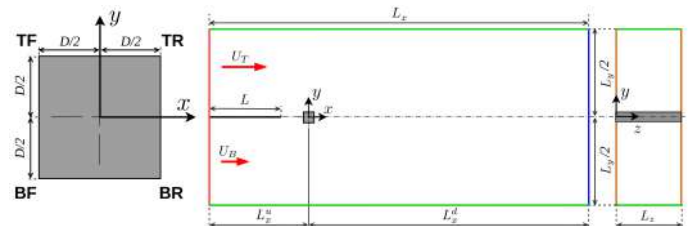


FIG. 1. Computational domain.

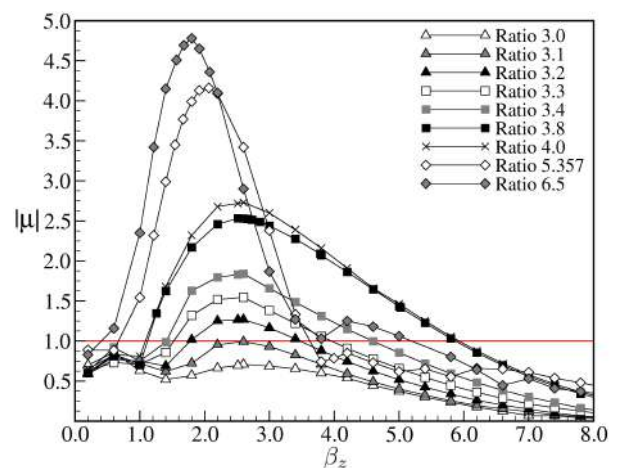


FIG. 2. Stability analysis of the two-stream flow past the square cylinder for $Re_B = 56$. Least stable Floquet multipliers (μ) as a function of wavenumber (β) for velocity ratios in the range $R \in [3, 6.5]$.

DNS reveals that the actual period of the solution doubles upon three-dimensionalisation, the flow repeating it-

self every two complete vortex-shedding cycles. The period doubling is however dynamically trivial, as it merely translates the preservation of a spatio-temporal symmetry consisting of the evolution over one vortex-shedding cycle followed by reflection about appropriately chosen streamwise-cross-stream planes that, together with spanwise reflection about another set of planes, replace the former spanwise invariance of two-dimensional vortex shedding. At slightly large values of R , however, a second period-doubling occurs, this time dynamically relevant that finally breaks these two remaining spanwise symmetries and leaves the flow invariant after four complete vortex-shedding cycles.

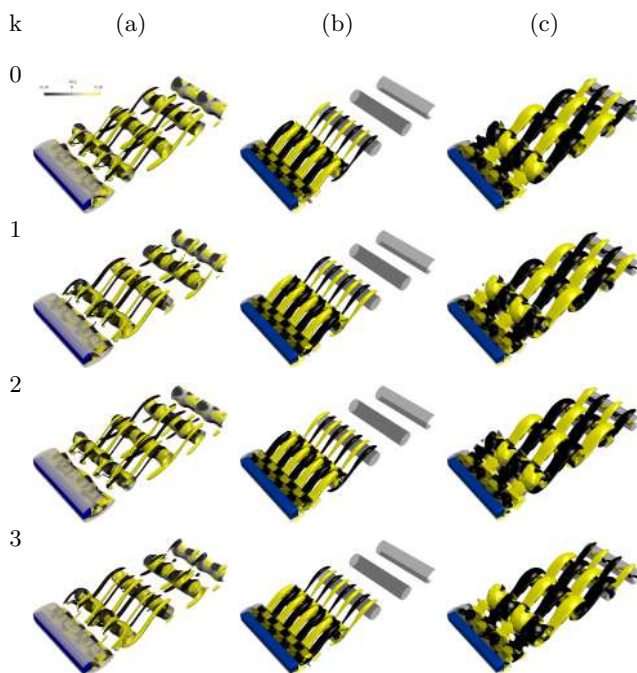


FIG. 3. Instantaneous snapshots of (a) the three-dimensional solution at $R = 3.8$, (b) dominant eigenmode for $(R, \lambda_z) = (3.8, 2.5)$ and (c) dominant eigenmode for $(R, \lambda_z) = (3.8, 5)$, at four consecutive crossings of the Poincaré section. $Q = 0.0001$ is used to display nonlinear three-dimensional vortical structures.

The period-four solution is illustrated in figure 3a for $R = 3.8$. The previous spanwise wavelength $\lambda_z = 2.5$ is preserved to a large extent, but the actual periodicity is now the full $\lambda_z = L_z = 5$. Hard to notice, but nevertheless present, is the symmetry that leaves the solution invariant after evolution over two consecutive vortex-shedding cycles followed by reflection about appropriately chosen streamwise-cross-stream planes. The spanwise periodicity $\lambda_z = 5$ is doubtless unrelated to a mode A instability despite the compatible wavelength. The typical features of mode A are absent from the wake, while mode C vortical structures clearly prevail, albeit with a two-fold subharmonic spanwise modulation. In order to discard any involvement of mode A in the solu-

tion observed at $R = 3.8$, 4 consecutive normalised snapshots of the dominant mode for wavelengths $\lambda_z = 2.5$ and 5, both unstable according to figure 2, are shown in figures 3b and c, respectively. The spatial structure of the dominant eigenmode is clearly the same for both wavelengths, with minor differences that are perfectly imputable to a continuous transformation from one to the other. Moreover, the two modes are definitely of the C type, that is subharmonic, as normalised snapshots of the eigenmode taken exactly two vortex-shedding cycles apart are identical in all respects, and those taken only one vortex-shedding cycle apart are related by the existing space-time symmetry. Therefore, the actual frequency and symmetry-breaking of the nonlinear solution at $R = 3.8$ is not explained by a period-doubling bifurcation that affects also the already unstable two-dimensional vortex-shedding solution.

CONCLUSIONS

We present 2D and 3D simulations to unveil the flow over a square cylinder subject to streams of different velocities separated by an upstream splitter plate. Three-dimensionalisation of the flow occurs at a velocity ratio $R = 3.1$, according to linear stability analysis. A unique dominant unstable mode (a type-C mode characterized by a period-doubling and a spatio-temporal symmetry involving the spanwise direction) of characteristic wavelength $\lambda_z \simeq 2.5D$, is observed for velocity ratios between $3.1 \leq R \leq 4$, although the nonlinear branch of solutions undergoes a tertiary period-doubling instability that starts the route towards chaotic dynamics.

* Reda.mohamed.yousif@upc.edu

- [1] A. Sohankar, C. Norberg, and L. Davidson, Simulation of three-dimensional flow around a square cylinder at moderate Reynolds numbers, *Phys. Fluids* **11**, 288 (1999).
- [2] A. Saha, G. Biswas, and K. Muralidhar, Three-dimensional study of flow past a square cylinder at low Reynolds numbers, *Int. J. Heat Fluid Fl.* **24**, 54 (2003).
- [3] S. Luo, Y. Chew, and Y. Ng, Characteristics of square cylinder wake transition flows, *Phys. Fluids* **15**, 2549 (2003).
- [4] H. Bai and M. Alam, Dependence of square cylinder wake on Reynolds number, *Phys. Fluids* **30**, 015102 (2018).
- [5] S. Luo, X. Tong, and B. Khoo, Transition phenomena in the wake of a square cylinder, *J. Fluid. Struct.* **23**, 227 (2007).
- [6] J. Robichaux, S. Balachandar, and S. Vanka, Three-dimensional Floquet instability of the wake of square cylinder, *Phys. Fluids* **11**, 560 (1999).
- [7] G. Sheard, M. Fitzgerald, and K. Ryan, Cylinders with square cross-section: wake instabilities with incidence angle variation, *J. Fluid Mech.* **630**, 43 (2009).